Научном већу Института за физику Београд

Београд 16.oктобар 2018.

Предмет:
Молба за покретање поступка за избор у звање научни сарадник

С обзиром да испуњавам критеријуме прописане од стране Министарства просвете, науке и технолошког развоја за стицање звања научни сарадник, молим Научно веће Института за физику Београд да покрене поступак за мој избор у наведено звање.

У прилогу достављам:

1. Мишљење руководиоца пројекта са предлогом чланова комисије за избор у звање
2. Стручну биографију
3. Преглед научне активности
4. Елементе за квалитативну и квантитативну оцену научног доприноса са доказима
5. Списак објављених научних радова и њихове копије
6. Податке о цитираности
7. Уверење о одбрањеној докторској дисертацији

С поштовањем,
др Бојан Стојадиновић

Научном већу Института за физику Београд

Београд 16.oktobar 2018.

Предмет:
Мишљење руководиоца пројекта о избору др Бојана Стојадиновића у звање научни сарадник

Бојан Стојадиновић је од 01.04.2013. године запослен у Центру за физику чврстог стања и нове материјале, а од 2016. године је ангажован у оквиру лабораторије за физику нано-композитних структура и биовибрационy спектроскопију Института за физику у Београду, где ради на пројекту ОИ171032 који финансира Министарство за просвету и науку Републике Србије и чији је руководилац др Зорана Дохчевић-Митровић.
У звање истраживач сарадник изабран је децембра 2014. године, а реизабран у исто звање децембра 2017. године. Кандидат се на Институту за физику бави проблемима везаним за карактеризацију и синтезу чистих и допираних нанопрахова и танких филмова бизмут ферита ($BiFeO_3$), као коаутор је објавио 14 радова у међународним часописима (од којих су 5 из категорије M21a). Из свих наведених разлога, сагласна сам са покретањем поступка за избор др Бојана Стојадиновића у звање научни сарадник.

За састав комисије за избор Бојана Стојадиновића у звање научни сарадник предлажем:

1. др Зорану Дохчевић-Митровић, научног саветника Института за физику Београд
2. др Новицу Пауновића, научног сарадника Института за физику Београд
3. др Димитрија Степаненка, вишег научног сарадника Института за физику Београд
4. др Растка Василића, ванредног професора Физичког факултета

др Зорана Дохчевић-Митровић
Руководилац пројекта ОИ171032

У Београду,
16.10.2018.

1. Биографски подаци о кандидату

Др Бојан Стојадиновић је рођен у Пожаревцу, Република Србија, 23. маја 1988. године. Завршио је Пожаревачку гимназију, са одличним успехом. Основне студије је уписао 2007. године на Физичком факултету, Универзитета у Београду, на смеру Примењена физика и информатика. Основне студије је дипломирао јуна 2011. године. Мастер студије је уписао на Физичком факултету, Универзитета у Београду, смер Теоријска и експериментална физика и завршио јуна 2012. године са просеком 10.00, где је мастер рад са темом „*Испитивање електронске структуре нанокристала церијум диоксида скенирајућом тунелском микроскопијом*“ урадио у Центру за физику чврстог стања и нове материјале Института за физику. Исте године уписује докторске студије, ужа научна област: Физика кондензоване материје и статистичка физика.

Кандидат је започео истраживачки рад на Институту за физику Београд септембра 2011. године, а запослен је од 01.04.2013. године у Центру за физику чврстог стања и нове материјале. Од 2016. године је ангажован у оквиру лабораторије за физику нано-композитних структура и биовибрациону спектроскопију Института за физику у Београду на пројекту ОИ171032 чији је руководилац др Зорана Дохчевић-Митровић. У звање истраживач сарадник изабран је децембра 2014. године, а реизабран у исто звање децембра 2017. године.

Кандидат је током 2016. године био учесник школе у Бечу под називом *„Training School and 6th Workshop on FEBIP (Focused Electron Beam Induced Processing) 2016“* у оквиру *COST* акције *CELINA (Chemistry for Electron-Induced Nanofabrication)*, а имао је и једну посету Универзитету Гете у Франкфурту у оквиру билатералне сарадње са Немачка којом је руководио др Братислав Маринковић. Почетком 2017. године је био на краћем боравку на *STSM (Short-term scientific missions)* пројекту, у оквиру *COST* акције *CELINA,* под називом *„Ferroelectric properties of* $BiFeO_3$ *thin films as monitored by nano-granular sensor structures prepared by focused electron beam induced deposition“,* у истој групи на Гете Универзитету у Франкфурту. Др Бојан Стојадиновић до сада има 14 објављених научних радова, 12 радова из категорије М21 (од чега су 5 из категорије М21а) и 2 рада из категорије М22.

Докторску дисертацију под називом „*Утицај 4f допаната на мултифероичне особине* $BiFeO_3$ *наноматеријала*“, урађену под руководством др Зоране Дохчавић-Митровић, одбранио је 28.09.2018. на Физичком факултету у Београду.

2. Преглед научне активности др Бојана Стојадиновића

Др Бојан Стојадиновић се бави истраживањима која спадају у област физике кондензоване материје и заснивају се на испитивању утицаја различитих 4f допаната (Ce, Pr и Ho) на структурне, вибрационе, диелектричне, фероелектричне и магнетне особине $BiFeO_3$ керамика и нанопрахова са циљем проналажења оптималног допанта и концентрације допаната који доводе до повећања електричне отпорности $BiFeO_3$, а самим тим и до побољшања фероелектричних, диелектричних и мултифероичних особина. Испитиване су и локалне електричне особине зрнастог танког $BiFeO_3$ филма у циљу бољег разумевања разлика у електричним особинама између унутрашњости зрна и границе зрна у овим наноструктурама, што може бити од значаја за примену $BiFeO_3$ танких филмова у сензорима и меморијама рачунара.

Кандидат је за синтезу нанопрахова и керамика користио хидротермалну, сол-гел методу и методу самосагоревања, а танки филмови су направљени методом танких превлака (*spin-coating* техника). Кандидат је коришћењем карактеризационих техника скенирајуће тунелске микроскопије и спектроскопије (*STM/STS*), микроскопије на бази атомских сила (*AFM*) и микроскопије на бази пиезоелектричног ефекта (*PFM*) испитивао локалне електричне и фероелектричне особине зрнастих наноструктурних филмова са циљем да се детаљније проуче механизми проводности унутар зрна и на граници зрна који у великој мери одређују фероелектричне особине танких филмова. Од оптичких карактеризационих метода кандидат је радио на уређајима за спектроскопску елипсометрију и раманску спектроскопију. Током досадашњег рада кандидат је овладао коришћењем теоријских модела (*Cole-Cole* и *UDR* моделе) којима се описују процеси диполне релаксације и доприноси који потичу од струје цурења на граници зрна и поларизације просторног наелектрисања.

Истраживачки рад и научни резултати које је до сада остварио др Бојан Стојадиновић могу се груписати у пет тема:

- Испитивање структурних, вибрационих и електричних особина $BiFeO_3$ поликристалних керамика и нанопрахова допираних празеодимијумом, церијумом и холмијумом,
- Испитивање локалних електричних особина на зрнима и границама зрна $BiFeO_3$ танког филма,
- Испитивање вибрационих и оптичких особина недопираних и итријум допираних $BiFeO_3$ поликристалних керамика и нанопрахова,
- Испитивање вибрационих и оптичких особина нанопрахова никл-цинк ферита, композита никл-цинк ферита и баријум титаната, Al_2O_3/ZnO слојева, TiO_2 танких филмова и Mg допираних CeO_2 нанопрахова,
- Мапирање топографије и испитивање електронске структуре CeO_2 и La допираних TiO_2 нанопрахова AFM и STM/STS техникама.

2.1. Испитивање структурних, вибрационих и електричних особина $BiFeO_3$ поликристалних керамика и нанопрахова допираних празеодимијумом, церијумом и холмијумом

Први део истраживања је био посвећен испитивању диелектричних и фероелектричних особина (на собној температури) $BiFeO_3$ керамика допираних Pr и Ce јонима ($Bi_{1-x}Pr(Ce)_xFeO_3$, $0\leq x\leq 0.1$) које су синтетисане методом самосагоревања. Утврђено је да је, у случају највеће концентрације допаната (у $Bi_{0.90}Pr_{0.10}FeO_3$ и $Bi_{0.90}Ce_{0.10}FeO_3$ узорцима), дошло до делимичне структурне фазне трансформације из ромбоедарске у орторомбичну ($Bi_{0.90}Pr_{0.10}FeO_3$ узорак) и псеудотетрагоналну ($Bi_{0.90}Ce_{0.10}FeO_3$ узорак) фазу, што је довело до промена у фероелектричним и диелектричним својствима ових материјала. Диелектрична и фероелектрична својства $BiFeO_3$ керамике су побољшана Pr допирањем због смањења концентрације кисеоничних ваканција и утицаја поларизације просторног наелектрисања. Што се тиче Ce допираних керамика, показано је да 3 mol% допирања церијумом доводи до побољшања диелектричних и фероелектричних особина, док повећана концентрација Ce јона доводи до деградације диелектричних и фероелектричних особина услед појаве параелектричне псеудотетрагоналне фазе и присуства проводне секундарне $Bi_2Fe_4O_9$ фазе. Описани резултати објављени су у једном раду у врхунском међународном часопису:

- **B. Stojadinović**, Z. Dohčević-Mitrović, N. Paunović, N. Ilić, N. Tasić, I. Petronijević, D. Popović, B. Stojanović, "Comparative study of structural and electrical properties of Pr and Ce doped $BiFeO_3$ ceramics synthesized by auto-combustion method", J. Alloy. Compd. 657 (2016) 866-872 (M21a).

Кандидат се бавио и испитивањем утицаја холмијума као допанта на структурне, диелектричне, фероелектричне и магненте особине $BiFeO_3$ нанопрахова ($Bi_{1-x}Ho_xFeO_3$, $0\leq x\leq 0.15$) синтетисаних сол-гел методом. Установљено је да при већим концентрацијама допирања ($x\geq 0.1$) узорци постају двофазни, тј. долази до делимичног структурног фазног прелаза из ромбоедарске у орторомбичну *Pnma* фазу, која постаје доминантна у 15 mol% Ho допираном узорку. Фреквентно зависна комплексна диелектрична пропустљивост $Bi_{1-x}Ho_xFeO_3$ нанопрахова на собној температури је анализирана помоћу комбинованог модела који укључује Кол-Кол (*Cole-Cole*) релаксациони модел и UDR (*Universal dielectric response*) модел да би се проценили ефекти струје цурења и поларизације просторног наелектрисања на укупну диелектричну пропустљивост. Утврђено је да је доминантно присуство орторомбичне *Pnma* фазе у $Bi_{0.85}Ho_{0.15}FeO_3$ узорку утицало на смањење струје цурења и довело до значајног повећања поља пробоја у односу на остале $Bi_{1-x}Ho_xFeO_3$ нанопрахове. Испитивањем фероелектричних особина $Bi_{1-x}Ho_xFeO_3$ нанопрахова, показано је да су фероелектричне особине $Bi_{0.85}Ho_{0.15}FeO_3$ узорка значајно побољшане у јаким пољима (50 kV/cm и 100 kV/cm) на ниским фреквенцијама. Уочена је изразита фреквенцијска зависност реманентне поларизација као и нагли пораст њене вредности са опадањем фреквенције. Закључено је да се у јаким пољима на ниским фреквенцијама дефектни комплекси, настали током процеса синтезе $Bi_{1-x}Ho_xFeO_3$ узорака, лакше оријентишу дуж правца спонтане поларизације, прате процес преокретања поларизације домена и на тај начин доприносе побољшању својствене поларизације $Bi_{0.85}Ho_{0.15}FeO_3$ узорка. $Bi_{0.85}Ho_{0.15}FeO_3$ узорак испољава феромагнетно (ФМ) уређење на собној температури као и недопиран узорак. Присуство ФМ је последица нарушења антиферомагнетног уређења (које је карактеристично за недопиран $BiFeO_3$ материјал у ромбоедарској $R3c$ фази) услед смањења димензије честица (кристалита) које постају мање од периода спинске циклоиде. Побољшање феромагнетних особина у односу на недопиран $BiFeO_3$ је последица додатног смањења димензије честица (кристалита) и присуства доминантне орторомбичне $Pnma$ фазе. У орторомбичној фази долази до нагињања FeO_6 октаедара и до значајније промене Fe–O веза и Fe–O–Fe углова између антиферомагнетно спрегнутих Fe јона, што проузрокује слабљење суперизменске интеракције, нарушење спинске циклоиде и доводи до побољшања феромагнетних особина. Описани резултати објављени су у једном раду у врхунском међународном часопису:

- **Bojan Stojadinović**, Zorana Dohčević-Mitrović, Dimitrije Stepanenko, Milena Rosić, Ivan Petronijević, Nikola Tasić, Nikola Ilić, Branko Matović, Biljana Stojanović, “Dielectric and ferroelectric properties of Ho-doped $BiFeO_3$ nanopowders across the structural phase transition”, Ceram. Int. 43 (2017) 16531-16538 (M21a).

2.2. Испитивање електричних особина на зрнима и границама зрна $BiFeO_3$ танког филма

Кандидат је испитивао зрнасте танке $BiFeO_3$ филмове синтетисане методом танких превлака са циљем да се детаљније проуче механизми проводности унутар зрна и на граници зрна који у великој мери одређују фероелектричне особине танких филмова. Скенирајућим техникама (AFM, PFM) показано је да димензија фероелектричних домена одговара димензији појединачних зрна. Струја цурења је израженија на границама зрна, а по први пут је уочена и појава хистерезиса у електричним особинама унутар зрна. Кандидат је коришћењем модела за описивање транспорта наелектрисања у полупроводницима се испитивала природа механизама струје цурења унутар зрна и на граници зрна. Показано је да унутар зрна на нижим напонима доминира Омска проводност, на средњим Шоткијев механизам, а на вишим Фаулер-Нортхаимов механизам провођења. Такође је показао да је струја цурења најизраженија на граници зрна, а за опис механизма провођења на граници зрна се није могао применити ни један познат модел транспорта наелектрисања. Локална електрична мерења на унутрашњости зрна су показала хистерезисно понашање при спорим променама напона, како у локалној густини стања, тако и у положају средине енергијског процепа, док на границама зрна није уочено хистерезисно понашање. Описани резултати објављени су у једном раду у врхунском међународном часопису:

- **B. Stojadinović**, B. Vasić, D. Stepanenko, N. Tadić, R. Gajić, Z. Dohčević-Mitrović, "Variation of electric properties across the grain boundaries in $BiFeO_3$ film", J. Phys. D: Appl. Phys. 49 (2016) 045309 (M21).

2.3. Испитивање вибрационих и оптичких особина недопираних и итријум допираних $BiFeO_3$ поликристалних керамика и нанопрахова

Кандидат је раманском спектроскопијом пратио утицај одређеног горива и температуре на чистоћу $BiFeO_3$ керамика. Мерењем раманских спектара детектовао је присуство/одсуство секундарних фаза ($Bi_2Fe_4O_9$ и $Bi_{25}FeO_{40}$) у зависности од коришћеног горива и од примењене температуре. Узорци добијени коришћењем уреe као горива у самосагоревајућој методи и винске киселине као горива у сол-гел методи су показали најчистије ромбоедарске R3c фазе. Иако се поменутим методама добијају чисти $BiFeO_3$ материјали, неопходно их је синтеровати ради добијања већих густина керамика због даље примене. Описани резултати објављени су у једном раду у врхунском међународном часопису:

- N. Ilić, J Bobić, **B. Stojadinović**, A. Džunuzović, M Vijatović Petrović, Z. Dohčević-Mitrović, B. Stojanović, “Improving of the electrical and magnetic properties of $BiFeO_3$ by doping with yttrium”, Mater. Res. Bull. 77 (2016) 60-69 (M21).

Кандидат је раманском спектроскопијом утврдио да код допираних узорака $BiFeO_3$ са итријумом (Y) долази до ширења и померања модова ка вишим енергијама, што потврђује субституционалну уградњу лакшег Y јона на место Bi, и изазива велике структурне промене ромбоедарске фазе, чиме је потврђен резултат из XRD мерења. Кандидат је коришћењем метода спектроскопске елипсометрије одредио вредности енергијских процепа применом Тауцовог модела. Закључено је да са повећањем садржаја Y долази до повећања енергијском процепа у $Bi_{1-x}Y_xFeO_3$ узорцима. Овакво понашање је објашњено ефектом фононског ограничења, који описује повећање енергијског процепа са смањењем димензија наночестица (уочено у SEM мерењима). Описани резултати објављени су у једном раду у врхунском међународном часопису:

- N. Ilić, A. Džunuzović, J. Bobić, **B. Stojadinović**, P. Hammer, M. Vijatović Petrović, Z. Dohčević-Mitrović, B. Stojanović, “Structure and properties of chemically synthesized $BiFeO_3$. Influence of fuel and complexing agent”, Ceram. Int. 41 (2015) 69-77 (M21).

Кандидат је коришћењем метода спектроскопске елипсометрије испитивао оптичке особине $BiFeO_3$ нанопраха синтетисаног хидротермалном методом. Применом Тауцовог модела на мерења псеудодиелектричне функције је утврдио да нанопрах $BiFeO_3$ поседује вредност енергијског процепа од око 2.71 eV, што је у сагласности са литературом. Описан резултат објављен је у једном раду у врхунском међународном часопису:

- M. Čebela, D. Zagorac, K. Balatović, J. Radaković, **B. Stojadinović**, V. Spasojević, R. Hercigonja, “$BiFeO_3$ perovskites: A multidisciplinary approach to multiferroics”, Ceram. Int. 43 (2017) 1256-1264 (M21a).

2.4. Испитивање вибрационих и оптичких особина нанопрахова никл-цинк ферита, композита никл-цинк ферита и баријум титаната, Al_2O_3/ZnO слојева, TiO_2 танких филмова и Mg допираних CeO_2 нанопрахова

Кандидат је раманском спектроскопијом испитивао вибрационе особине никл-цинк ферита и мултифероичног композита никл-цинк ферита и баријум титаната са варирањем односа никла и цинка. Код узорака никл-цинк ферита ($Ni_{1-x}Zn_xFe_2O_4$, x=0.0, 0.3, 0.5, 0.7, 1.0) синтетисаних самосагоревајућом методом раманском спектроскопијом је потврђено доминантно присуство кубичне структуре и јасно је уочена трансформација из никл ферита у цинк ферит са променом односа никла и цинка у нанопраховима. Код мултифероичних композита никл-цинк ферита (y $Ni_{1-x}Zn_xFe_2O_4$-(1-y)BT, x=0.3, 0.5, 0.7, y=0.5) синтетисаних самосагоревајућом методом такође је вариран однос никла и цинка у једињењу никл-цинк ферита, док је однос никл-цинк ферита и баријум титаната био једнак. Кандидат је раманском спектроскопијом утврдио да је у поменутим узорцима присутан мали садржај секундарних фаза и јасно уочљива трансформација из никл ферита у цинк ферит са варирањем садржаја никла и цинка у никл-цинк фериту. Описани резултати објављени су у једном раду у врхунском међународном часопису и једном раду у међународном часопису:

- A. Džunuzović, M. Vijatović Petrović, **B. Stojadinović**, N. Ilić, J. Bobić, C. Foschini, M. Zaghete, B. Stojanović, “Multiferroic (NiZn)Fe_2O_4–$BaTiO_3$ composites prepared from nanopowders by auto-combustion method”, Ceram. Int. 41 (2015) 13189-13200 (M21).
- A. S. Džunuzović, N. I. Ilić, M. M. Vijatović Petrović, J. D. Bobić, **B. Stojadinović**, Z. Dohčević-Mitrović, B. D. Stojanović, “Structure and properties of Ni-Zn ferrite obtained by auto-combustion method”, J. Magn. Magn. Mater. 374 (2015) 245-251 (M22).

Раманском спектроскопијом су праћене промене у структурним-вибрационим особинама Al_2O_3/ZnO слојева у зависности од времена деловања ПЕО процеса. Описани резултати објављени су у једном раду у врхунском међународном часопису:

- S. Stojadinović, N. Tadić, N. Radić, **B. Stojadinović**, B. Grbić, R. Vasilić, “Synthesis and characterization of Al_2O_3/ZnO coatings formed by plasma electrolytic oxidation”, Surf. Coat. Tech. 276 (2015) 573-579 (M21).

Кандидат је испитивао вибрационе особине ласерски синтерованих TiO_2 танких филмова и утврдио доминантно присуство анатас фазе у овим једињењима. Денковолуцијом раманских модова Лоренцијанским профилима утврђен је померај ка вишим енергијама и смањење интензитета, тј. повећање ширине TiO_2 раманских модова. У литаратури је познато да се смањење интензитета, тј. повећање ширине раманских модова може приписати појави кисеоничних ваканција, које се могу квантитативно детектовати недеструктивном раманском спектроскопијом. Појава кисеоничних ваканција као дефеката, директно утиче на локалну кристалну симетрију, што доводи до помераја раманских модова ка вишим енергијама и смањења интензитета, тј. повећања ширине фонона. Добијене информације откривају да ласерски третман чува кристалну структуру наночестица TiO_2 и индукује настанак структурних дефеката у облику кисеоничних ваканција, чија концентрација се повећава у узорцима третираним са већом ласерском флуктуацијом. Описани резултати објављени су у једном раду у врхунском међународном часопису:

- M. Radović, G. Dubourg, S. Kojić, Z. Dohčević-Mitrović, **B. Stojadinović**, M. Bokorov, V. Crnojević-Begnin, „Laser sintering of screen-printed TiO_2 nanoparticles for improvement of mechanical and electrical properties“, Ceram. Int. 44 (2018) 10975-10983 (M21a).

Кандидат је испитивао вибрационе и оптичке особине Mg допираних CeO_2 нанопрахова синтетисаних SPRT методом, коришћењем метода раманске спектроскопије и спектроскопске елипсометрије. Раманском спектроскопијом је поред карактеристичног CeO_2 мода флуоритне кубичне структуре на око 455 cm^{-1} уочен мод на око 600 cm^{-1} који се јавља услед појаве кисеоничних ваканција у Mg допираним CeO_2 нанопраховима. Интензитет овога мода, који је пропоционалан концентрацији ваканција, расте са допирањем, што се одражава на енергетски процеп ових материјала и њихова фотокаталитичка својства. Применом Тауцовог модела на мерења спектроскопске елипсометрије утврђено је да са повећањем садржаја Mg енергијски процеп опада због формирања локализованих стања унутар енергијског процепа CeO_2 нанопрахова, која потичу од Mg^{2+} јона и кисеоничних ваканција. Описани резултати објављени су у једном раду у међународном часопису:

- B. Matović, J. Luković, **B. Stojadinović**, S. Aškrabić, A. Zarubica, B. Babić, Z. Dohčević-Mitrović, “Influence of Mg doping on structural, optical and photocatalytic performances of ceria nanopowders”, Process. Appl. Ceram. 11 (2017) 304-310 (M22).

2.5. Мапирање топографије и испитивање електронске структуре CeO_2 и La допираних TiO_2 нанопрахова AFM и STM/STS техникама

Кандидат је скенирајућим микроскопским техникама мапирао морфологије зрна у нанопраховима CeO_2 и La допираних TiO_2 узорака и из I-V мерења на зрнима одредио вредности енергијских процепа коришћењем модела диференцијалне проводности. Описани резултати објављени су у три рада у врхунским међународним часописима:

- M. Radović, **B. Stojadinović**, N. Tomić, A. Golubović, B. Matović, I. Veljković, Z. Dohčević-Mitrović, “Investigation of surface defect states in CeO_{2-y} nanocrystals by Scanning–tunneling microscopy/spectroscopy and ellipsometry”, J. Appl. Phys. 116 (2014) 234305 (M21).
- M. Grujić-Brojčin, S. Armaković, N. Tomić, B. Abramović, A. Golubović, **B. Stojadinović**, A. Kremenović, B. Babić, Z. Dohčević-Mitrović, M. Šćepanović, “Surface modification of sol-gel synthesized TiO_2 nanoparticles induced by La-doping”, Mater. Charact. 88 (2014) 30-41 (M21a).
- A. Golubović, N. Tomić, N. Finčur, B. Abramović, I. Veljković, J. Zdravković, M. Grujić-Brojčin, B. Babić, **B. Stojadinović**, M. Šćepanović, “Synthesis of pure and La-doped anatasenanopowders by sol-gel and hydrothermal methods and their efficiency in photocatalytic degradation of alprazolam”, Ceram. Int. 40 (2014) 13409-13418 (M21).

3. Елементи за квалитативну оцену научног доприноса

3.1. Квалитет научних резултата

3.1.1. Значај научних резултата

Кандидат се у току досадашњег рада бавио испитивањем утицаја 4*f* допаната на мултифероичне особине $BiFeO_3$ наноматеријала. Проблеми везани за примену $BiFeO_3$ се односе на постојање струје цурења, која се јавља услед појаве бизмутових и кисеоничних ваканција у материјалу. Струја цурења је одговорна за нарушење фероелектричних особина, доводи до смањења реманентне поларизације и повећања диелектричних губитака код $BiFeO_3$ материјала. Такође, додатни проблем приликом синтезе $BiFeO_3$ материјала је појава секундарних фаза ($Bi_2Fe_4O_9$ и $Bi_{25}FeO_{40}$) које су проводне. Кандидат је дао значајан допринос разумевању утицаја одређених 4f допаната (Ce, Pr и Ho) и показао да диелектричне и мултифероичне особине $BiFeO_3$ наноматеријала веома зависе од врсте синтезе, као и од врсте структурног фазног прелаза условљеног типом и концентрацијом допанта. Такође, кандидат је утврдио разлику у локалним електричним особинама $BiFeO_3$ танког филма између унутрашњости и границе зрна и уочио појаву хистерезиса у електричним особинама унутрашњости зрна, што може бити од значаја за потенцијалну примену ових структура у сензорима и меморијама рачунара.

3.1.2. Параметри квалитета часописа

Кандидат др Бојан Стојадиновић је објавио укупно 14 радова у међународним часописима и то:

- 1 рад у врхунском међународном часопису *Journal of Alloys and Compounds* (IF = 3.133, SNIP = 1.321),
- 3 рада у врхунском међународном часопису *Ceramics International* (IF = 3.057, SNIP = 1.167),
- 1 рад у врхунском међународном часопису *Journal of Physics D: Applied Physics* (IF = 2.772, SNIP = 0.920),
- 2 рада у врхунском међународном часопису *Ceramics International* (IF = 2.758, SNIP = 1.253),
- 1 рад у врхунском међународном часопису *Ceramics International* (IF = 2.605, SNIP = 1.662),
- 1 рад у врхунском међународном часопису *Materials Research Bulletin* (IF = 2.435, SNIP = 0.855),
- 1 рад у врхунском међународном часопису *Journal of Applied Physics* (IF = 2.210, SNIP = 1.130),
- 1 рад у врхунском међународном часопису *Surface and Coatings Technology* (IF = 2.199, SNIP = 1.347),
- 1 рад у врхунском међународном часопису *Materials Characterization* (IF = 1.925, SNIP = 2.034),
- 1 рад у међународном часопису *Journal of Magnetism and Magnetic Materials* (IF = 2.357, SNIP = 1.341),
- 1 рад у међународном часопису *Processing and Application of Ceramics* (IF = 1.152, SNIP = 0.792).

Укупан импакт фактор објављених радова др Бојана Стојадиновића износи 35.475.

3.1.3. Позитивна цитираност научних радова кандидата

Према бази *Scopus*, радови др Бојана Стојадиновића су цитирани 121 пут, од чега 116 пута изузимајући аутоцитате. Према овој бази Хиршов индекс кандидата је 7.

3.1.4. Додатни библиометријски показатељи

Додатни библиометријски показатељи су приказани у следећој табели:

	ИФ	М	СНИП
Укупно	35.475	116	17.409
Усредњено по чланку	2.534	8.286	1.2435
Усредњено по аутору	4.740	15.542	2.277

3.1.5. Међународна сарадња

Међународне активности др Бојана Стојадиновића обухватају:

- Учешће у школи одржаној у Бечу (Аустрија) под називом *„Training School and 6th Workshop on FEBIP (Focused Electron Beam Induced Processing) 2016“* у оквиру *COST* акције *CELINA (Chemistry for Electron-Induced Nanofabrication),*
- Посету Универзитету Гете у Франкфурту у оквиру билатералне сарадње са Немачка којом је руководио др Братислав Маринковић,
- Учешће на STSM *(Short-term scientific missions)* пројекту, у оквиру *COST* акције *CELINA,* под називом *„Ferroelectric properties of* $BiFeO_3$ *thin films as monitored by nano-granular sensor structures prepared by focused electron beam induced deposition“,* на Гете Универзитету у Франкфурту.

3.2. Нормирање броја коауторских радова, патената и техничких решења

Свих 14 радова др Бојана Стојадиновића су експерименталне природе, што подразумева сарадњу више институција. Имајући то у виду, број коаутора на појединим радовима је већи од 7 и нормирањем бодова тих радова у складу са Правилником Министарства о поступку, начину вредновања и квантитативном исказивању научноистраживачких резултата, укупан нормирани број М бодова кандидата је 107, што је и даље знатно више од захтеваног минимума од 16 М бодова за избор у звање научни сарадник.

3.3. Учешће у пројектима, потпројектима и пројектним задацима

Кандидат је од 01.04.2013. на пројекту *Физика наноструктурних оксидних материјала и јако корелисаних система*, ОИ171032 чији је руководилац др Зорана Дохчевић-Митровић.

3.4. Утицај научних резултата

Утицај научних резултата кандидата је наведен у одељку 3.1 овог извештаја. Пун списак радова и подаци о цитираности из *Scopus* базе су дати у прилогу.

3.5. Конкретан допринос кандидата у реализацији радова у научним центрима у земљи и иностранству

Кандидат је своје истраживачке активности реализовао у Инстититу за физику Београд. Кандидат је дао допринос објављеним радовима и кључни допринос у свим радовима где је први аутор. Његов допринос се огледа у синтези, карактеризацији, примени модела, интерпретацији и презентацији нумеричких резултата, као и писању научних чланака.

4. Елементи за квантитативну оцену научног доприноса

Остварени М-бодови по категоријама публикација

Категорија	М-бодова по публикацији	Број публикација	Укупно М бодова	Нормирани број М бодова
M21a	10	5	**50**	**43.39**
M21	8	7	**56**	**42.99**
M22	5	2	**10**	**10**
M34	0.5	10	**5**	**4.611**
M70	6	1	**6**	**6**

Поређење оствареног броја М-бодова са минималним условима потребним за избор у звање научног сарадника

	Потребно	Остварено	Остварено (нормирано*)
Укупно	16	**127**	**106.991**
M10+M20+M31+M32+M33+M41+M42	10	**127**	**106.991**
M11+M12+M21+M22+M23	6	**127**	**106.991**

* Нормирање бодова је извршено у складу са Прилогом 1 Правилника.

5. Списак радова др Бојана Стојадиновића

5.1. Радови у врхунским међународним часописима (M21 и M21a):

1. M. Radović, B. Stojadinović, N. Tomić, A. Golubović, B. Matović, I. Veljković, Z. Dohčević-Mitrović, "Investigation of surface defect states in CeO_{2-y} nanocrystals by Scanning−tunneling microscopy/spectroscopy and ellipsometry", J. Appl. Phys. 116 (2014) 234305. M21, IF 2.210, SNIP 1.130
2. N. Ilić, A. Džunuzović, J. Bobić, B. Stojadinović, P. Hammer, M. Vijatović Petrović, Z. Dohčević-Mitrović, B. Stojanović, "Structure and properties of chemically synthesized $BiFeO_3$. Influence of fuel and complexing agent", Ceram. Int. 41 (2015) 69–77. M21, IF 2.758, SNIP 1.253
3. M. Grujić-Brojčin, S. Armaković, N. Tomić, B. Abramović, A. Golubović, B. Stojadinović, A. Kremenović, B. Babić, Z. Dohčević-Mitrović, M. Šćepanović, "Surface modification of sol-gel synthesized TiO_2 nanoparticles induced by La-doping", Mater. Charact. 88 (2014) 30–41. M21a, IF 1.925, SNIP 2.034
4. A. Golubović, N. Tomić, N. Finčur, B. Abramović, I. Veljković, J. Zdravković, M. Grujić-Brojčin, B. Babić, B. Stojadinović, M. Šćepanović, "Synthesis of pure and La-doped anatasenanopowders by sol–gel and hydrothermal methods and their efficiency in photocatalytic degradation of alprazolam", Ceram. Int. 40 (2014) 13409-13418. M21, IF 2.605, SNIP 1.662
5. A. Džunuzović, M. Vijatović Petrović, B. Stojadinović, N. Ilić, J. Bobić, C. Foschini, M. Zaghete, B. Stojanović, "Multiferroic $(NiZn)Fe_2O_4$–$BaTiO_3$ composites prepared from nanopowders by auto-combustion method", Ceram. Int. 41 (2015) 13189–13200. M21, IF 2.758, SNIP 1.253
6. S. Stojadinović, N. Tadić, N. Radić, B. Stojadinović, B. Grbić, R. Vasilić, "Synthesis and characterization of Al_2O_3/ZnO coatings formed by plasma electrolytic oxidation", Surf. Coat. Tech. 276 (2015) 573–579. M21, IF 2.199, SNIP 1.347
7. B. Stojadinović, Z. Dohčević-Mitrović, N. Paunović, N. Ilić, N. Tasić, I. Petronijević, D. Popović, B. Stojanović, "Comparative study of structural and electrical properties of Pr and Ce doped $BiFeO_3$ ceramics synthesized by auto-combustion method", J. Alloy. Compd. 657 (2016) 866–872. M21a, IF 3.133, SNIP 1.321
8. B. Stojadinović, B. Vasić, D. Stepanenko, N. Tadić, R. Gajić, Z. Dohčević-Mitrović, "Variation of electric properties across the grain boundaries in $BiFeO_3$ film", J. Phys. D: Appl. Phys. 49 (2016) 045309. M21, IF 2.772, SNIP 0.920
9. N. Ilić, J Bobić, B. Stojadinović, A. Džunuzović, M Vijatović Petrović, Z. Dohčević-Mitrović, B. Stojanović, "Improving of the electrical and magnetic properties of $BiFeO_3$ by doping with yttrium", Mater. Res. Bull. 77 (2016) 60–69. M21, IF 2.435, SNIP 0.855
10. Maria Čebela, Dejan Zagorac, Katarina Balatović, Jana Radaković, Bojan Stojadinović, Vojislav Spasojević, Radmila Hercigonja, "$BiFeO_3$ perovskites: A multidisciplinary approach to multiferroics", Ceram. Int. 43 (2017) 1256-1264. M21a, IF 3.057, SNIP 1.167

11. Bojan Stojadinović, Zorana Dohčević-Mitrović, Dimitrije Stepanenko, Milena Rosić, Ivan Petronijević, Nikola Tasić, Nikola Ilić, Branko Matović, Biljana Stojanović, “Dielectric and ferroelectric properties of Ho-doped $BiFeO_3$ nanopowders across the structural phase transition”, Ceram. Int. 43 (2017) 16531-16538. M21a, IF 3.057, SNIP 1.167
12. M. Radović, G. Dubourg, S. Kojić, Z. Dohčević-Mitrović, B. Stojadinović, M. Bokorov, V. Crnojević-Begnin, „Laser sintering of screen-printed TiO_2 nanoparticles for improvement of mechanical and electrical properties“, Ceram. Int. 44 (2018) 10975-10983. M21a, IF 3.057, SNIP 1.167

5.2. Радови у међународним часописима (M22):

1. A. S. Džunuzović, N. I. Ilić, M. M. Vijatović Petrović, J. D. Bobić, B. Stojadinović, Z. Dohčević-Mitrović, B. D. Stojanović, “Structure and properties of Ni-Zn ferrite obtained by auto-combustion method”, J. Magn. Magn. Mater. 374 (2015) 245-251. M22, IF 2,357, SNIP 1.341
2. Branko Matović, Jelena Luković, Bojan Stojadinović, Sonja Aškrabić, Aleksandra Zarubica, Biljana Babić, Zorana Dohčević-Mitrović, “Influence of Mg doping on structural, optical and photocatalytic performances of ceria nanopowders”, Process. Appl. Ceram. 11 (2017) 304-310. M22, IF 1,152, SNIP 0.792

5.3. Саопштења на међународним конференцијама (M34):

1. M. Radović, B. Stojadinović, N. Tomić, I. Veljković, S. Aškrabić, A. Golubović, B. Matović, Z. Dohčević-Mitrović, 2nd Conference of The Serbian Ceramic Society, Belgrade, Serbia, O-3, page 42, June 2013.
2. N. I. Ilić, A. S. Džunuzović, J. D. Bobić, M. M. Vijatović-Petrović, B. S. Stojadinović, Z. D. Dohčević-Mitrović, B. D. Stojanović, COST MP0904 Action, Krakow, Poland, 2-3rd September 2013.
3. N. I. Ilić, B. S. Stojadinović, A. S. Džunuzović, J. D. Bobić, Z. D. Dohčević-Mitrović, B. D. Stojanović, 13th Young Researchers Conference – Materials Science and Engineering, 10-12 december, 2014.
4. Bojan Stojadinović, Zorana Dohčević-Mitrović, Nikola Ilić, Nikola Tasić, Biljana Stojanović, Ivan Petronijević, Dušan Popović, 3rd Conference of The Serbian Society for Ceramic Materials, P-34, page 104, June 2015.
5. Nikola Ilić, Bojan Stojadinović, Adis Džunuzović, Jelena Bobić, Nikola Tasić, Lavinia Curecheriu, Zorana Dohčević-Mitrović, Biljana Stojanović, 3rd Conference of The Serbian Ceramic Society, Belgrade, Serbia, O-6, page 58, June 2015.

6. Adis Džunuzović, Nikola Ilić, Mirjana Vijatović Petrović, Jelana Bobić, Bojan Stojadinović, Zorana Dohčević-Mitrović, Biljana Stojanović, 3rd Conference of The Serbian Ceramic Society, Belgrade, Serbia, P-47, page 117, June 2015.
7. Nenad Tadić, Andriana Peleš, Rastko Vasilić, Nenad Radić, Bojan Stojadinović, Boško Grbić, Stevan Stojadinović, Advanced Ceramics and Applications IV, Belgrade, Serbia, September 2015.
8. Bojan Stojadinović, Zorana Dohčević-Mitrović, Dimitrije Stepanenko, Milena Rosić, Ivan Petronijević, Nikola Tasić, Nikola Ilić, Branko Matović, Biljana Stojanović, 4th Conference of the Serbian Society for Ceramic Materials, Belgrade, Serbia, P-22, page 86, June 2017.
9. M. Rosić, D. Zagorac, J. Zagorac, Z. Dohčević-Mitrović, B. Stojadinović, K. Đuriš, B. Matović, 4th Conference of the Serbian Society for Ceramic Materials, Belgrade, Serbia, P-11, page 76, June 2017.
10. B. Stojadinović, M. Radović, N. Tadić, S. Stojadinović, I. Belča, Z. Dohčević-Mitrović, 3rd International Meeting on Materials Science for Energy Related Applications, Belgrade, Serbia, Solid Electrolytes and oxide materials, page 13, september 2018.

5.4. Одбрањена докторска дисертација (М70):

1. Б. Стојадиновић, „Утицај 4*f* допаната на мултифероичне особине $BiFeO_3$ наноструктура“, Универзитет у Београду, Физички факултет (2018).

Scopus

Author details

About Scopus Author Identifier

i The Scopus Author Identifier assigns a unique number to groups of documents written by the same author via an algorithm that matches authorship based on a certain criteria. If a document cannot be confidently matched with an author identifier, it is grouped separately. In this case, you may see more than one entry for the same author.

×

< Return to search results 1 of 1

Print Email

Stojadinović, Bojan S.

Follow this Author

View potential author matches

University of Belgrade, Laboratory for Nanocomposite Structures and Biovibrational Spectroscopy, Belgrade, Serbia
Author ID: 56346684200
Other name formats: Stojadinović, Bojan | Stojadinović, B. | Stojadinović, Bojan S. | Stojadinović, B. | Stojadinovic, B. S.

Subject area: Materials Science | Physics and Astronomy | Engineering | Chemical Engineering | Chemistry

Document and citation trends:

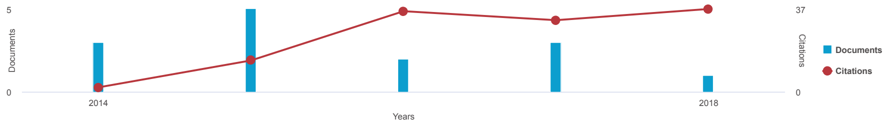

h-index: ⓘ
7

View *h*-graph

Documents by author
14

Analyze author output

Total citations
121 by 115 documents

View citation overview

Get citation alerts + Add to ORCID ⓘ Request author detail corrections

14 Documents | Cited by 115 documents | 49 co-authors | Author history

View in search results format >

Sort on: Date (newest)

Export all Add all to list Set document alert Set document feed

Document title	Authors	Year	Source	Cited by
Laser sintering of screen-printed TiO_2 nanoparticles for improvement of mechanical and electrical properties View abstract ⌄ KOBSON View at Publisher Related documents	Radović, M., Dubourg, G., Kojić, S., (...), Bokorov, M., Crnojević-Bengin, V.	2018	Ceramics International 44(9), pp. 10975-10983	0
Dielectric and ferroelectric properties of Ho-doped $BiFeO_3$ nanopowders across the structural phase transition View abstract ⌄ KOBSON View at Publisher Related documents	Stojadinović, B., Dohčević-Mitrović, Z., Stepanenko, D., (...), Matović, B., Stojanović, B.	2017	Ceramics International 43(18), pp. 16531-16538	1
Influence of Mg doping on structural, optical and photocatalytic performances of ceria nanopowders View abstract ⌄ KOBSON View at Publisher Related documents	Matović, B., Luković, J., Stojadinović, B., (...), Babić, B., Dohčević-Mitrović, Z.	2017	Processing and Application of Ceramics 11(4), pp. 304-310	0
$BiFeO_3$ perovskites: A multidisciplinary approach to multiferroics View abstract ⌄ KOBSON View at Publisher Related documents	Čebela, M., Zagorac, D., Batalović, K., (...), Spasojević, V., Hercigonja, R.	2017	Ceramics International 43(1), pp. 1256-1264	9
Improving of the electrical and magnetic properties of $BiFeO_3$ by doping with yttrium View abstract ⌄ KOBSON View at Publisher Related documents	Ilić, N.I., Bobić, J.D., Stojadinović, B.S., (...), Dohčević-Mitrović, Z.D., Stojanović, B.D.	2016	Materials Research Bulletin 77, pp. 60-69	9

Document title	Authors	Year	Source	Cited by
Comparative study of structural and electrical properties of Pr and Ce doped BiFeO$_3$ ceramics synthesized by auto-combustion method	Stojadinović, B., Dohčević-Mitrović, Z., Paunović, N., (...), Popović, D., Stojanović, B.	2016	Journal of Alloys and Compounds 657, pp. 866-872	9
View abstract ⌄ KOBSON View at Publisher Related documents				
Variation of electric properties across the grain boundaries in BiFeO$_3$ film	Stojadinović, B., Vasić, B., Stepanenko, D., (...), Gajić, R., Dohčević-Mitrović, Z.	2015	Journal of Physics D: Applied Physics 49(4),045309	2
View abstract ⌄ KOBSON View at Publisher Related documents				
Multiferroic (NiZn) Fe$_2$ O$_4$ –BaTiO$_3$ composites prepared from nanopowders by auto-combustion method	Dzunuzovic, A.S., Petrovic, M.M.V., Stojadinovic, B.S., (...), Zaghete, M.A., Stojanovic, B.D.	2015	Ceramics International 41(10PartA), pp. 13189-13200	9
View abstract ⌄ KOBSON View at Publisher Related documents				
Structure and properties of Ni-Zn ferrite obtained by auto-combustion method	Džunuzović, A.S., Ilić, N.I., Vijatović Petrović, M.M., (...), Dohčević-Mitrović, Z., Stojanović, B.D.	2015	Journal of Magnetism and Magnetic Materials 374, pp. 245-251	30
View abstract ⌄ KOBSON View at Publisher Related documents				
Synthesis and characterization of Al$_2$ O$_3$ /ZnO coatings formed by plasma electrolytic oxidation	Stojadinović, S., Tadić, N., Radić, N., (...), Grbić, B., Vasilić, R.	2015	Surface and Coatings Technology 276, pp. 573-579	16
View abstract ⌄ KOBSON View at Publisher Related documents				
Structure and properties of chemically synthesized BiFeO$_3$. Influence of fuel and complexing agent	Ilić, N.I., Džunuzović, A.S., Bobić, J.D., (...), Dohčević-Mitrović, Z.D., Stojanović, B.D.	2015	Ceramics International 41(1), pp. 69-77	7
View abstract ⌄ KOBSON View at Publisher Related documents				
Investigation of surface defect states in CeO$_{2-y}$ nanocrystals by Scanning-tunneling microscopy/spectroscopy and ellipsometry	Radović, M., Stojadinović, B., Tomić, N., (...), Veljković, I., Dohcević-Mitrović, Z.	2014	Journal of Applied Physics 116(23),234305	4
View abstract ⌄ KOBSON View at Publisher Related documents				
Surface modification of sol-gel synthesized TiO$_2$ nanoparticles induced by La-doping	Grujić-Brojčin, M., Armaković, S., Tomić, N., (...), Dohčević-Mitrović, Z., Šćepanović, M.	2014	Materials Characterization 88, pp. 30-41	21
View abstract ⌄ KOBSON View at Publisher Related documents				
Synthesis of pure and La-doped anatase nanopowders by sol-gel and hydrothermal methods and their efficiency in photocatalytic degradation of alprazolam	Golubović, A., Tomić, N., Finčur, N., (...), Stojadinović, B., Šćepanović, M.	2014	Ceramics International 40(8 PART B), pp. 13409-13418	4
View abstract ⌄ KOBSON View at Publisher Related documents				

Display: 20 ⌄ results per page

1

^ Top of page

Scopus

Citation overview

< Back to author details

Export Print

This is an overview of citations for this author.

Author *h*-index : 7 View *h*-graph ?

14 Cited Documents from"Stojadinović, Bojan S."

+ Add to list

Author ID:56346684200

Date range: 2014 to 2018

☐ Exclude self citations of selected author

☐ Exclude self citations of all authors

☐ Exclude citations from books

Update

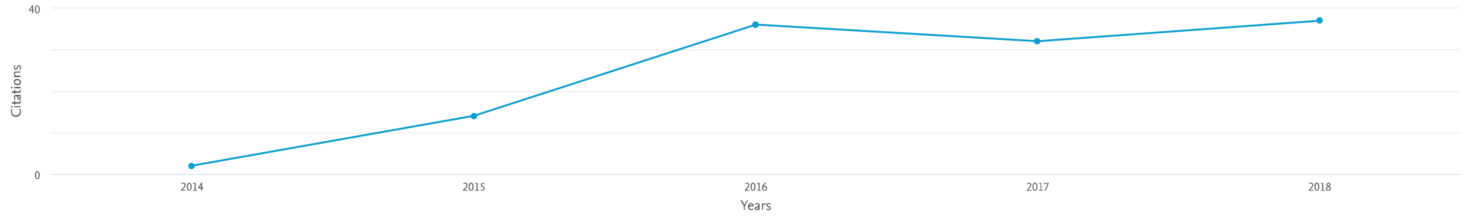

Sort on: Date (newest)

☐ Page Remove

	Documents	Citations	<2014	2014	2015	2016	2017	2018	Subtotal	>2018	Total
		Total	0	2	14	36	32	37	121	0	121
☐ 1	Laser sintering of screen-printed TiO<inf>2</inf>nanoparticl...	2018							0		0
☐ 2	Dielectric and ferroelectric properties of Ho-doped BiFeO<in...	2017						1	1		1
☐ 3	Influence of Mg doping on structural, optical and photocatal...	2017							0		0
☐ 4	BiFeO<inf>3</inf>perovskites: A multidisciplinary approach t...	2017					1	8	9		9
☐ 5	Improving of the electrical and magnetic properties of BiFeO...	2016				1	3	5	9		9
☐ 6	Comparative study of structural and electrical properties of...	2016				3	4	2	9		9
☐ 7	Variation of electric properties across the grain boundaries...	2015				1		1	2		2
☐ 8	Multiferroic (NiZn) Fe<inf>2</inf>O<inf>4</inf>–BaTiO<inf>3<...	2015				2	2	5	9		9
☐ 9	Structure and properties of Ni-Zn ferrite obtained by auto-c...	2015		1	6	4	11	8	30		30
☐ 10	Structure and properties of chemically synthesized BiFeO<inf...	2015			1	4		2	7		7
☐ 11	Synthesis and characterization of Al<inf>2</inf>...	2015				10	4	2	16		16
☐ 12	Investigation of surface defect states in CeO<inf>2-y</inf>n...	2014				1	2	1	4		4
☐ 13	Surface modification of sol-gel synthesized TiO<inf>2</inf>n...	2014		1	6	8	4	2	21		21
☐ 14	Synthesis of pure and La-doped anatase nanopowders by sol-ge...	2014			1	2	1		4		4

Display: 20 results per page

1

^ Top of page

About Scopus

What is Scopus
Content coverage
Scopus blog
Scopus API
Privacy matters

Language

日本語に切り替える
切换到简体中文
切換到繁體中文
Русский язык

Customer Service

Help
Contact us

Универзитет у Београду ФИЗИЧКИ ФАКУЛТЕТ
Студентски трг 12, 11000 Београд
Поштански фах 44
Тел. 011 7158 151, 3281 375
ПИБ 100039173, Мат. бр. 07048190

University of Belgrade FACULTY OF PHYSICS
Studentski trg 12, 11000 Belgrade
Postal Box 44
Phone +381 11 7158 151, Fax +381 11 3282 619
www.ff.bg.ac.rs, dekanat@ff.bg.ac.rs

УНИВЕРЗИТЕТ У БЕОГРАДУ
ФИЗИЧКИ ФАКУЛТЕТ
Бр. 418/8
28.9. 2018 год.
БЕОГРАД СТУДЕНТСКИ ТРГ 12
П. ФАХ 44

На основу члана 161 Закона о општем управном поступку («Службени Лист СРЈ» број 33/97 и 31/01), и члана 120 Статута Универзитета у Београду - Физичког факултета, по захтеву БОЈАНА СТОЈАДИНОВИЋ, дипломираног физичара, издаје се следеће

УВЕРЕЊЕ

БОЈАН СТОЈАДИНОВИЋ, дипломирани физичар, дана 28. септембра 2018. године, одбранио је докторску дисертацију под називом

"УТИЦАЈ 4f ДОПАНАТА НА МУЛТИФЕРОИЧНЕ ОСОБИНЕ BiFeO3 НАНОСТРУКТУРА"

пред Комисијом Универзитета у Београду - Физичког факултета, и тиме испунио све услове за промоцију у ДОКТОРА НАУКА – ФИЗИЧКЕ НАУКЕ.

Уверење се издаје на лични захтев, а служи ради регулисања права из радног односа и важи до промоције, односно добијања докторске дипломе.

Уверење је ослобођено плаћања таксе.

ДЕКАН ФИЗИЧКОГ ФАКУЛТЕТА

Проф. др Јаблан Дојчиловић

БИОГРАФИЈА

БОЈАНА СТОЈАДИНОВИЋ

Дисертација под називом **"УТИЦАЈ 4f ДОПАНАТА НА МУЛТИФЕРОИЧНЕ ОСОБИНЕ BiFeO3 НАНОСТРУКТУРА"** пријављена дана **29. септембра 2016. године.** На седници Наставно-научног већа Факултета одржаној дана **26. октобра 2016. године** одређена је Комисија за оцену испуњености услова и оправданост предложене теме за израду докторске дисертације у саставу:

др Зорана Дохчевић-Митровић
проф. др Стеван Стојадиновић
проф. др Растко Василић.

На седници Наставно-научног већа Факултета одржаној дана **23. новембра 2016. године** усвојен је извештај комисије за тему и одређен ментор: **др Зорану Дохчевић-Митровић, научног саветника Института за физику.** На седница Већа научних области природно-математичких наука Универзитета у Београду одржаној дана **26. децембра 2016. године** одобрен је рад на дисертацији. Урађена дисертација предата дана **22. јуна 2018. године.**

На седници Наставно-научног већа Факултета одржаној дана **28. јуна 2018. године** одређена је Комисија за преглед и оцену докторске дисертације у саставу:

др Зорана Дохчевић-Митровић
проф. др Растко Василић
доц. др Божидар Николић
др Борислав Васић

На седници Наставно-научног већа Факултета одржаној дана **12. септембра 2018. године** усвојен је извештај комисије за преглед и оцену и одређена Комисија за одбрану докторске дисертације у саставу:

др Зорана Дохчевић-Митровић
проф. др Растко Василић
доц. др Божидар Николић
др Борислав Васић

На седници Већа научних области природно-математичких наука Универзитета у Београду одржаној дана **24. септембра 2018. године** одобрена је одбрана дисертације. Дисертација одбрањена дана **28. септембра 2018. године.**

3rd International Meeting on Materials Science
for Energy Related Applications

CERTIFICATE OF PARTICIPATION

Herewith it is certified that

BOJAN STOJADINOVIĆ

participated in
3rd International Meeting on Materials Science
for Energy Related Applications,
held in Belgrade, Serbia,
on September 25th - 26th, 2018.

Belgrade, Serbia
September 26th, 2018.

Dr. Igor Pašti
University of Belgrade
Organizing Committee
of 3IMMSERA

PHYSICAL CHEMISTRY 2018

3rd International Meeting
on

Materials Science for Energy Related Applications

BOOK OF ABSTRACTS

September 25-26, 2018
University of Belgrade - Faculty of Physical Chemistry, Belgrade

KTH
ROYAL INSTITUTE OF TECHNOLOGY
Stockholm, Sweden

UNIVERSITY OF BELGRADE
FACULTY OF PHYSICAL CHEMISTRY
Belgrade, Serbia

THE SOCIETY OF
PHYSICAL CHEMISTS OF SERBIA
Belgrade, Serbia

STABILITY OF F-CENTER DEFECTS DURING THE THERMAL TREATMENT OF NANOCRYSTALLINE CeO_{2-y}

B. Stojadinović[1], M. Radović[2], N. Tadić[3], S. Stojadinović[3], I. Belča[3], Z. Dohčević-Mitrović[1]*

[1]*Laboratory for nanocomposite structures and biovibrational spectroscopy, Institute of Physics, University of Belgrade, Belgrade, Serbia*
[2]*Nano and Microelectronics Group, BioSense Institute, Novi Sad, Serbia*
[3]*Faculty of Physics, University of Belgrade, 11000 Belgrade, Serbia*

The formation of different F center defect states inside the ceria gap have a strong impact on the optical, catalytic, and magnetic properties of ceria nanocrystals [1-4]. These types of defects are registered in various oxide nanomaterials, such as MgO [5] HfO_2 [6] and TiO_2 [7] and are usually formed at the nanoparticle surface during the process of synthesis. Non-stoichiometry at normal atmospheric conditions is more pronounced in nanocrystalline CeO_{2-y} composed of very small crystallites [8], due to the increase of surface-to-volume ratio of the nanocrystals, which reduces the formation energy of oxygen vacancies positioned close to a crystallite surface. Therefore, particle size has important influence on the formation of oxygen vacancy defects. The presence of oxygen nonstoichiometry in nanocrystalline CeO_{2-y} yields mix valence state of Ce ions. Namely, excess electrons that are left behind an oxygen release can be localized on 4f states of Ce ions changing the valence state of Ce^{4+} ions to Ce^{3+}, or can be localized on the oxygen vacancies forming F centers [9]. In this paper we focused our attention to the influence of annealing process on the microstructural changes of nanocrystalline CeO_{2-y} and stability of oxygen vacancy defects *i.e.* F center defects. Nanocrystalline CeO_{2-y} powders were synthesized by the self-propagating room temperature method (SPRT) and were annealed in air at different temperatures in the range 200 – 800 °C. Structural and vibrational properties were investigated by X-ray diffraction and Raman spectroscopy methods. Scanning tunneling microscopy/spectroscopy (STM/STS) have been employed to probe the electronic properties of as-prepared and annealed CeO_{2-y} samples, because STM/STS can get more accurate relation between particle size and electronic properties compared with optical spectroscopy. X-ray diffraction analysis demonstrated that all

samples crystallized into fluorite type structure of CeO_2 and no amorphous or any other phase was detected. As-prepared CeO_{2-y} was composed of very small crystallites with the highest strain value due to the increased oxygen vacancy concentration and presence of Ce^{3+} ions. In annealed samples, crystallite size and microstrain significantly changed above 400 °C. The crystallite size was increased from 2.2 (as –prepared sample) to 44 nm (sample annealed at 800 °C). Microstrain values in the CeO_{2-y} samples annealed at higher temperatures decreased with increasing temperature of annealing, pointing at improved stoichiometry of these samples. Analysis of the Raman spectra has shown that the concentration of oxygen vacancies was the largest in as –prepared CeO_{2-y} sample and drastically decreased in samples annealed at 600 °C and 800 °C. STS spectra revealed that besides the filled and empty *4f* states ($4f^1$and $4f^0$states), different types of F center defects states were formed inside the band gap of as-prepared CeO_{2-y}. These additional states were ascribed to occupied and empty F^+ and F^0 center defect states [10]. With increasing of the annealing temperature up to 400 °C only the F^0 center defect states subsisted, whereas the localized F^+ states disappeared. In the sample annealed at 600 °C, F^0 states were barely visible whereas $4f^1$ and $4f^0$ states were shifted towards the valence and conduction band leading to the increase of the band gap. In the CeO_{2-y} sample annealed at 800 °C no evidence of 4 *f* or defect states was present and the band gap approached the value of 4.3 eV. It can be concluded that readsorption of oxygen on the F^0 defects is much slower than that on the F^+ defects. At temperatures above 600 °C, the CeO_{2-y} oxygen vacancies were healed by oxygen intake, resulting in the improved stoichiometry of the temperature treated samples. These observations gave a new insight for understanding the reconstruction of defect sites at CeO_{2-y} surface at higher temperatures.

References

[1] L. Truffault *et al.*, J. Nanosci. Nanotechnol. 2011, 11, 4019.
[2] A. Corma *et al.*, Nature Mater. 2004, 3, 394.
[3] A. Trovarelli, Catalysis by Ceria and Related Materials, Imperial College Press, London, 2002.
[4] N. Paunović *et al.*, Nanoscale 2012, 4, 5469.
[5] T. König *et al.*, J. Am. Chem. Soc. 2009, 131, 17544.
[6] D. Muñoz Ramo *et al.*, Phys. Rev. B 2007, 75, 205336.
[7] N. Serpone, J. Phys. Chem. B 2006, 110, 24287.
[8] S Aškrabić *et al.*, J. Raman Spectrosc. 2012, 43 (1), 76.
[9] Xiaoping Han *et al.*, Phys. Rev. B 2009, 79, 100403(R).
[10] M. Radović *et al.*, J. Appl. Phys. 2014, 116, 234305.

The Serbian Society for Ceramic Materials
The Academy of Engineering Sciences of Serbia
Institute for Multidisciplinary Research - University of Belgrade
Institute of Physics - University of Belgrade
Vinča Institute of Nuclear Sciences - University of Belgrade

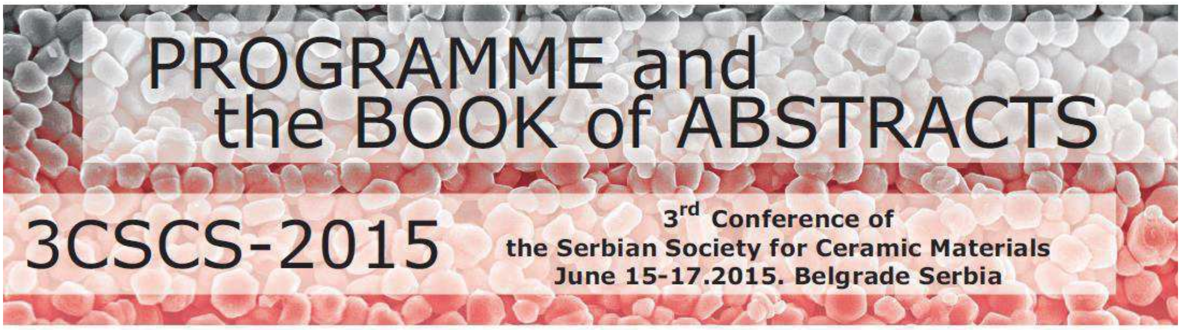

PROGRAMME and the BOOK of ABSTRACTS

3CSCS-2015

3rd Conference of
the Serbian Society for Ceramic Materials
June 15-17.2015. Belgrade Serbia

Edited by:
Branko Matović
Zorica Branković
Dušan Bućevac
Vladimir V. Srdić

O-6

IMPROVED ELECTRICAL AND MAGNETIC PROPERTIES IN Y DOPED $BiFeO_3$ CERAMICS

Nikola Ilić[1], Bojan Stojadinović[2], Adis Džunuzović[1], Jelena Bobić[1], Nikola Tasić[1], Lavinia Curecheriu[3], Zorana Dohčević-Mitrović[2], Biljana Stojanović[1]

[1]Institute for Multidisciplinary Research, University of Belgrade, Belgrade, Serbia
[2]Institute of Physics, University of Belgrade, Belgrade, Serbia
[3]Faculty of Physics, "Alexandru Ioan Cuza" University, Iasi, Romania

Bismuth ferrite ($BiFeO_3$) is considered one of the most promising single phase multiferroic materials thanks to the fact it exhibits ferroelectric and antiferromagnetic properties in the same time in very wide range of temperatures (up to 370 °C). Difficulties in obtaining pure $BiFeO_3$ phase and dense ceramics, together with occurrence of leakage currents have prevented application of $BiFeO_3$. Substitution of Bi^{3+} or Fe^{3+} ions with some transition metal or rare earth ions can improve both electrical and magnetic properties by reducing leakage currents and introducing weak ferromagnetism through structural changes.

Y doped bismuth ferrite, $Bi_{1-x}Y_xFeO_3$, was synthesized by auto-combustion method using urea as a fuel. Precursor powders were annealed, pressed and sintered. Powders and ceramic samples were characterized by XRD, SEM, Raman, impedance spectroscopy, ferroelectric and magnetic measurements.

X-ray diffractograms and Raman spectra showed no presence of secondary phases. SEM images indicated lowering of grain size with higher concentration of Y^{3+}. Electrical resistance is highly improved even at 1 % of Y, while 10 % of Y was necessary to break spiral spin structure, leading to weak ferromagnetism.

The Serbian Society for Ceramic Materials
The Academy of Engineering Sciences of Serbia
Institute for Multidisciplinary Research - University of Belgrade
Institute of Physics - University of Belgrade
Vinča Institute of Nuclear Sciences - University of Belgrade

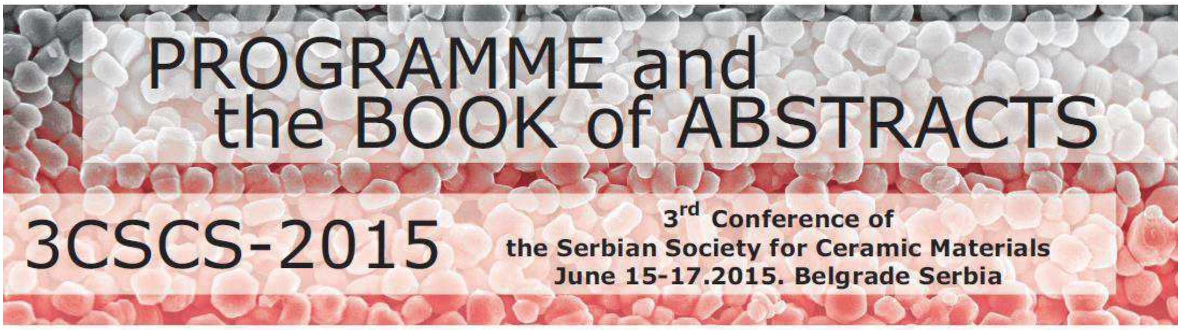

PROGRAMME and the BOOK of ABSTRACTS

3CSCS-2015

3rd Conference of
the Serbian Society for Ceramic Materials
June 15-17.2015. Belgrade Serbia

Edited by:
Branko Matović
Zorica Branković
Dušan Bućevac
Vladimir V. Srdić

mullite powder was compacted at 4.0 GPa in the temperature range 1100-1500 °C with step of 100 °C for 60 s. The measured densities of sintered samples rise with increasing the sintering temperature due to recrystallization of mullite particles. The particles of the starting powder are agglomerated while the microstructure of sintered samples reveals needle-like grains. The needles become elongated with increasing the temperature of sintering process and reach the grain length about 5 μm at 1400 and 1500 °C whereas the grains at 1500 °C are wider.

P-34

COMPARATIVE STUDY OF STRUCTURAL AND ELECTRICAL PROPERTIES OF Pr(Ce)-DOPED $BiFeO_3$ CERAMICS BY AUTO-COMBUSTION METHOD

Bojan Stojadinović[1], Zorana Dohčević–Mitrović[1], Nikola Ilić[2], Nikola Tasić[2], Biljana Stojanović[2], Ivan Petronijević[3], Dušan Popović[3]

Center for Solid State Physics and New Materials, Institute of Physics,
University of Belgrade, Serbia
Institute for Multidisciplinary Research, University of Belgrade, Serbia
[3]*Faculty of Physics, University of Belgrade, Serbia*

Polycrystalline ceramics of pure and Pr(Ce) doped $BiFeO_3$ ($Bi_{1-x}Pr(Ce)_xFeO_3$, x=0.03, 0.05 and 0.1) were synthesized by auto–combustion method using urea as fuel. The structural, vibrational, morphological, dielectric and ferroelectric properties of $Bi_{1-x}Pr(Ce)_xFeO_3$ polycrystalline ceramics at room temperature were examined by X–ray diffraction (XRD), Raman spectroscopy, Scanning electron microscopy and dielectric and ferroelectric measurements. The XRD and SEM measurements showed that the crystallite (particle) size of doped samples decreased. XRD and Raman measurements revealed the structural phase transition from rhombohedral to orthorhombic (pseudotetragonal) phase in the samples doped with 10% of Pr(Ce).

The pristine $BiFeO_3$ exhibited non-saturated P-E loop, typical for conductive $BiFeO_3$. The room-temperature P-E loop study of doped samples showed that partial substitution of Bi^{3+} ions with $Pr^{3+(4+)}$ and $Ce^{3+(4+)}$ ions reduced the concentration of oxygen vacancies and leakage current of $BiFeO_3$, although the saturation and remnant polarization in doped samples were lower than in pristine $BiFeO_3$. The saturation polarization increased (decreased) with Pr(Ce) doping. Up to 10% of Pr(Ce) substitution, significant reduction of dielectric loss and low-frequency dielectric constant dispersion was noticed. The structural transition influenced the ferroelectric and dielectric properties of Pr(Ce) doped $BiFeO_3$.

The Serbian Society for Ceramic Materials
The Academy of Engineering Sciences of Serbia
Institute for Multidisciplinary Research - University of Belgrade
Institute of Physics - University of Belgrade
Vinča Institute of Nuclear Sciences - University of Belgrade

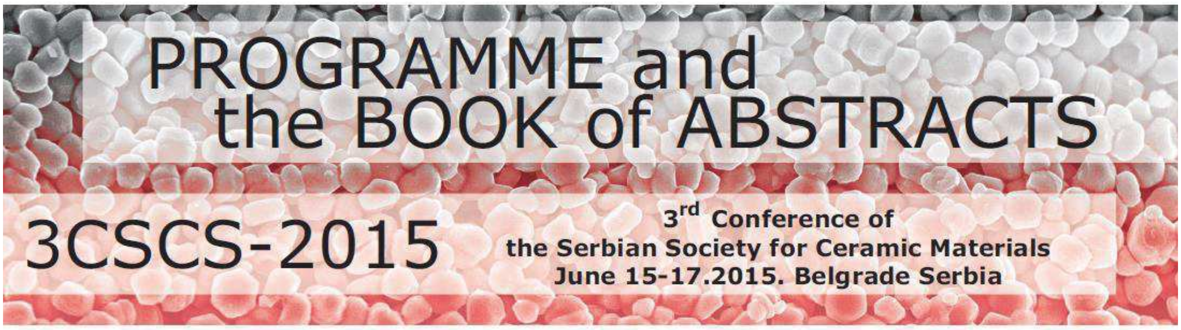

PROGRAMME and the BOOK of ABSTRACTS

3CSCS-2015

3rd Conference of
the Serbian Society for Ceramic Materials
June 15-17.2015. Belgrade Serbia

Edited by:
Branko Matović
Zorica Branković
Dušan Bućevac
Vladimir V. Srdić

P-47

STRUCTURE AND CHARACTERIZATION OF $BaTiO_3$-$Ni_{(1-x)}Zn_{(x)}Fe_2O_4$ COMPOSITES

Adis Džunuzović[1], Nikola Ilić[1], Mirjana Vijatović Petrović[1],
Jelena Bobić[1], Bojan Stojadinović[2], Zorana Dohčević-Mitrović[2],
Biljana Stojanović[1]

[1]*Institute for Multidisciplinary Research, Belgrade University, Serbia*
[2]*Institute of Physics, Belgrade, Serbia*

$NiZnFe_2O_4$ (NZF) powder was prepared by auto-combustion method starting from nickel, zinc and iron nitrates. Thermal treatment was performed at 1000 °C for 1 h after which the nickel ferrite powder was formed. Barium titanate (BT) powder was prepared with same method using titanyl nitrate and barium nitrate as a starting reagents. Multiferroic composites with formula $BaTiO_3$– $Ni_{(1-x)}Zn_xFe_2O_4$ ($x = 0.3$, 0.5, 0.7) were prepared by mixing chemically obtained NZF and BT powders in the planetary mill for 24 h. Powders were pressed and sintered at 1170 °C for 4 h. Samples were characterized by XRD, Raman, SEM, IR. Magnetic and electrical measurements were also carried out. X-ray and Raman measurements confirmed the presence of NZF, BT phases and the traces of barium ferrite phase. The microstructure of the ceramics shows (Fig. 1.) the formation of polygonal (NZF grains), rounded (BT grains) and plate like grains (barium ferrite phase). The impedance analyses of multifferoic composites at 200 ºC have shown the contribution of both, grain and grain boundary resistivity.

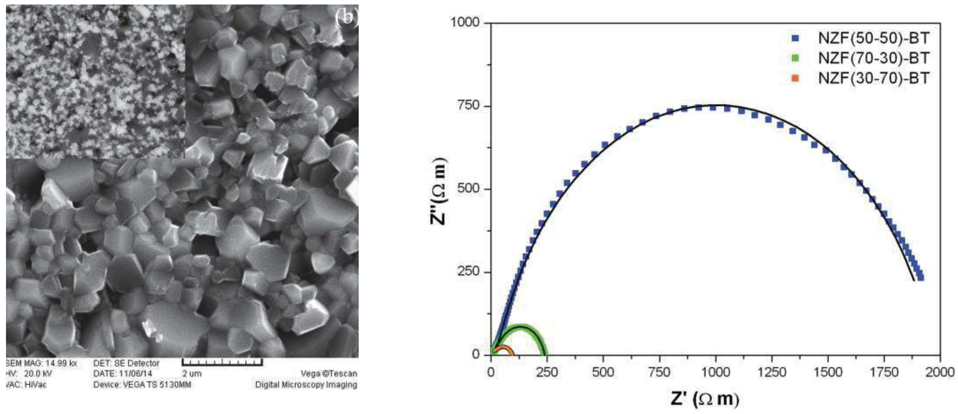

Figure 1. SEM images of NZF(50-50)-BT and impedance measurements

The Serbian Society for Ceramic Materials
Institute for Multidisciplinary Research, University of Belgrade
Institute of Physics-University of Belgrade
Center of Excellence for the Synthesis, Processing and Characterization of Materials for use in Extreme Conditions "CEXTREME LAB" - Institute of Nuclear Sciences "Vinča", University of Belgrade
Faculty of Mechanical Engineering, University of Belgrade

PROGRAMME AND THE BOOK OF ABSTRACTS

4th Conference of The Serbian Society for Ceramic Materials

June 14-16, 2017
Belgrade, Serbia
4CSCS-2017

Edited by:
Branko Matović
Zorica Branković
Dušan Bučevac
Vladimir V. Srdić

P-22

INCREASE OF THE BREAKDOWN FIELD IN $BiFeO_3$ NANOPOWDERS WITH Ho DOPING

Bojan Stojadinović[1], Zorana Dohčević-Mitrović[1], Dimitrije Stepanenko[1],
Milena Rosić[4], Ivan Petronijević[2], Nikola Tasić[3], Nikola Ilić[3],
Branko Matović[4] , Biljana Stojanović[3]

[1]Center for Solid State Physics and New Materials, Institute of Physics Belgrade, University of Belgrade, Pregrevica 118, 11080 Belgrade, Serbia
[2]Faculty of Physics, University of Belgrade, Studentski trg 12-16, 11000 Belgrade, Serbia
[3]Institute for Multidisciplinary Research, University of Belgrade, Kneza Višeslava 1, 11000 Belgrade, Serbia
[4]Institute for Nuclear sciences "Vinča", Materials Science Laboratory, University of Belgrade, 11000 Belgrade, Serbia

$Bi_{1-x}Ho_xFeO_3$ (x = 0, 0.05, 0.07, 0.10, 0.12, and 0.15) nanopowders were synthesized by sol-gel method. The structural, vibrational, ferroelectric and dielectric properties of $Bi_{1-x}Ho_xFeO_3$ samples at room temperature were examined by X–ray diffraction (XRD), Raman spectroscopy, ferroelectric and dielectric measurements. Higher content of Ho dopant (x = 0.10, 0.12, and 0.15) induced partial phase transformation from rhombohedral to orthorhombic phase, confirmed from XRD and Raman spectroscopy, where the content of orthorhombic phase is about 69% in 15% Ho-doped sample.

The appearance of orthorhombic phase substantially influences the electrical properties of $Bi_{1-x}Ho_xFeO_3$ nanopowders. We have found that only 15% Ho-doped sample withstands strong applied fields (up to 100 kV/cm) at lower frequencies without breakdown. Analyzing the frequency dependence of permittivity, applying UDR and Cole-Cole models, we obtained that dc conductivity significantly decreases with higher Ho content, reaching the lowest value for 15% Ho doped sample. The dielectric loss values were reduced and low for 12% and 15 % doped samples. These results imply that the appearance of orthorhombic structure suppresses the conductive properties of $BiFeO_3$ nanopowders.

The Serbian Society for Ceramic Materials
Institute for Multidisciplinary Research, University of Belgrade
Institute of Physics-University of Belgrade
Center of Excellence for the Synthesis, Processing and Characterization of Materials for use in Extreme Conditions "CEXTREME LAB" - Institute of Nuclear Sciences "Vinča", University of Belgrade
Faculty of Mechanical Engineering, University of Belgrade

PROGRAMME AND THE BOOK OF ABSTRACTS

4th Conference of The Serbian Society for Ceramic Materials

June 14-16, 2017
Belgrade, Serbia
4CSCS-2017

Edited by:
Branko Matović
Zorica Branković
Dušan Bučevac
Vladimir V. Srdić

P-11

ELECTRONIC PROPERTIES INVESTIGATION OF $CaMnO_3$ DOPED WITH Gd USING THEORETICAL AND EXPERIMENTAL METHODS

Milena Rosić[1,2], Dejan Zagorac[1,2], Jelena Zagorac[1,2], Zorana Dohčević-Mitrović[3], Bojan Stojadinović[3], Katarina Đuriš[4], Branko Matović[1,2]

[1]Laboratory for Material Science, Institute of Nuclear Sciences „Vinča“, University of Belgrade, Belgrade, Serbia
[2]Center for the Synthesis, Processing and Characterization of Materials for use in Extreme Conditions, Belgrade, Serbia
[3]Center for Solid State Physics and New Materials, Institute of Physics Belgrade, University of Belgrade, Belgrade, Serbia
[4]Max Planck Institute for Solid State Research, Stuttgart, Germany

$CaMnO_3$-based ceramics doped with gadolinium has become a matter of great scientific interest, because of their physical, electronic and magnetic properties, and many intriguing phenomena, such as colossal magnetoresistance (CMR) involving potential applications in magnetic memory devices and sensors. Electronic properties of $CaMnO_3$ doped with different amount of gadolinium were investigated using combination of experimental and theoretical methods. Spectroscopic Ellipsometry has been used to study electronic properties and band gap variation as function of Gd doping (up to 20% Gd). Furthermore, for each of the structure candidates, a local optimization on the *ab initio* level using density-functional theory (DFT), hybrid (B3LYP) and the Hartree–Fock (HF) method was performed.

P-12

CHARACTERIZATION OF IRON IN THE HYDROTHERMAL DICKITE FROM JEDLINA ZDROJ (NOWA RUDA, LOWER SILESIA, POLAND)

Bratislav Ž. Todorović[1], Pavle I. Premović[2]

[1]Faculty of Technology, University of Niš, Leskovac, Serbia
[2]Laboratory for Geochemistry, Cosmochemistry and Astrochemistry, University of Niš, Serbia

In recent years, considerable attention has been given to the genesis of dickite in sedimentary conditions. One way to obtain an objective evaluation of the nature of a

The Serbian Ceramic Society
The Academy of Engineering Sciences of Serbia
Institute for Multidisciplinary Research - University of Belgrade
Institute of Physics - University of Belgrade
Vinča Institute of Nuclear Sciences - University of Belgrade

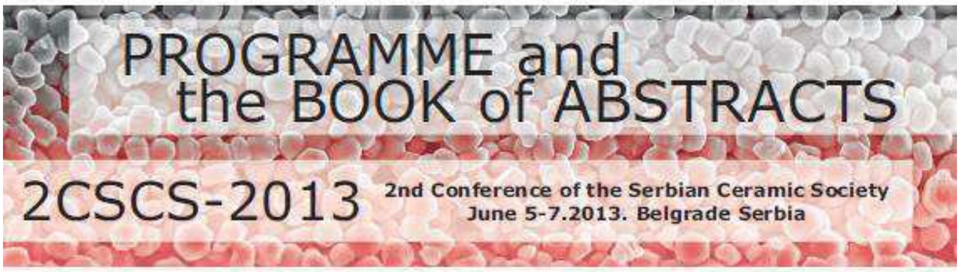

PROGRAMME and the BOOK of ABSTRACTS

2CSCS-2013

2nd Conference of the Serbian Ceramic Society
June 5-7.2013. Belgrade Serbia

Edited by:
Snežana Bošković
Vladimir V. Srdić
Zorica Branković

O-3

INVESTIGATION OF DEFECT ELECTRONIC STATES IN CeO_2 NANOCRYSTALS SYNTHESIZED BY SPRT, HYDROTHERMAL AND PRECIPITATION METHOD

Marko Radović [1], Bojan Stojadinović[1], Nataša Tomić[1], Ivana Veljković[2], Sonja Aškrabić[1], Aleksandar Golubović[1], Branko Matović[3], Zorana Dohčević-Mitrović[1]

[1]*Institute of Physics, University of Belgrade, Belgrade, Serbia*
[2]*Institute for Multidisciplinary Research, University of Belgrade, Serbia*
[3]*Institute of Nuclear sciences "Vinča", University of Belgrade, Belgrade, Serbia*

The present work examines the influence of various synthesis methods on the formation of defect electronic states in the band structure of CeO_{2-y} nanocrystals. Characterization of structural properties and determination of average crystallite size was performed using X-ray diffraction spectroscopy. Raman spectroscopy technique provides an insight into the concentration of oxygen vacancies and vibrational properties of ceria nanocrystals. Scanning tunneling microscopy and scanning tunneling spectroscopy measurements were performed on the CeO_{2-y} nanocrystals and the measurements were compared with available literature data for the electronic band structure of cerium dioxide. The differences in defect electronic states within the band gap were detected among the differently prepared CeO_{2-y} nanocrystals. Optical properties of CeO_{2-y} nanocrystals were investigated by spectroscopic ellipsometry. Through the critical points analysis of ellipsometric data we were able to establish direct relationship between observed variations in electronic structure and optical transitions. This study revealed that synthesis process strongly influences the formation of different oxygen vacancy complexes which, on the other side, have dominant influence on optical, transport and magnetic properties of ceria based materials. In order to reach full potential of these materials it is of great importance to elucidate which type of synthesis process provides better ceria performances.

Serbian Ceramic Society Conference
ADVANCED CERAMICS AND APPLICATION IV
New Frontiers in Multifunctional Material Science and Processing

Serbian Ceramic Society
Institute for Testing of Materials
Institute of Chemistry Technology and Metallurgy
Institute for Technology of Nuclear and Other Raw Mineral Materials
School of Electrical Engineering and Computer Science of Applied Studies

PROGRAM AND THE BOOK OF ABSTRACTS

Serbian Academy of Sciences and Arts, Knez Mihailova 35
Serbia, Belgrade, 21-23. September 2015.

P14

Photocatalytic properties of Al_2O_3/ZnO coatings formed by plasma electrolytic oxidation on aluminum substrate

N. Tadić[1], A. Peleš[2], N. Radić[3], B. Stojadinović[4], B. Grbić[3], R. Vasilić[1], S. Stojadinović[1]
[1] University of Belgrade, Faculty of Physics, Studentski trg 12-16, 11000 Belgrade, Serbia
[2] Institute of Technical Sciences SASA, Knez Mihailova 35/4, 11000 Belgrade, Serbia
[3] University of Belgrade, Institute of Chemistry, Technology and Metallurgy, Department of Catalysis and Chemical Engineering, Njegoševa 12, 11000 Belgrade, Serbia
[4] University of Belgrade, Institute of Physics, Pregrevica 118, 11080 Belgrade, Serbia

Mixed Al_2O_3/ZnO coatings obtained by plasma electrolytic oxidation process (PEO) of aluminum in water solution boric acid and borax with addition ZnO nanoparticles. The oxide coatings were characterized by Scanning electron microscopy equipped with energy dispersive x-ray spectroscopy, x-ray diffraction, and Raman spectroscopy. It was found that chemical and phase compositions strongly depend on PEO time. It was shown that photocatalytic activity was improved by longer time of PEO process.

P15

Structural and optical properties of chemically deposited copper selenide thin films

M. Petrovic[1], M. Gilic[1], B. Hadzic[1], M. Romcevic[1], N. Romcevic[1], J. Trajic[1], Z. Lazarevic[1]
[1]Institute of Physics, University of Belgrade, Pregrevica 118, Belgrade, Serbia

Copper selenides are interesting metal chalcogenide semiconductor materials. They exist in many phases and structural forms: different stoichiometries such as CuSe (mineral klockmannite), Cu_2Se, Cu_2Se_x, $CuSe_2$ (mineral marcasite), á - Cu_2Se, Cu_3Se_2 (mineral umagnite), Cu_5Se_4 (mineral athabaskite), Cu_7Se_4 etc. as well with non - stoichiometric form such as $Cu_{2-x}Se$ (mineral berzelianite) and can be constructed into several crystallographic forms (monoclinic, cubic, tetragonal, hexagonal, etc.). Copper selenides in different stoichiometries are semiconductors with p - type conductivity, and have been widely used in optical filters, solar cells, photo detectors, supersonic materials…

The paper describes the structural and optical properties of copper selenide thin films. The films of tree different thicknesses (56.75, 79.74 and 172.70 nm) were grown by thermal evaporation on glass substrate, at room temperature and pressure better than 1 mPa. The surface morphology of thin films was investigated by atomic force microscopy (AFM). Formation of Cu - Se thin films is concluded to proceed unevenly, in the form of islands which later grew into agglomerates. The structural characterization of Cu - Se thin film was investigated using X - ray diffraction pattern. The presence of two - phase - system is observed. The first one is low - pressure modification of $CuSe_2$. The second phase is solid solution of Cu in Se. The Raman spectroscopy was used to identify and quantify the individual phases presented in the Cu - Se films. The results of Raman spectroscopy are in good agreement with XRD results, and the presence of two phases in our system, the trigonal Se and orthorhombic $CuSe_2$, is confirmed once again.

13th INTERNATIONAL MEETING ON FERROELECTRICITY

The 13th International Meeting on Ferroelectricity (IMF-13) - for the first time in the history of these Meetings - welcomes participants to Kraków, in Poland. The IMF-13 is to deal, as it was the case in previous IMF conferences, with ferroelectricity in a broad sense, i.e. with the ferroelectric and ferroelectric-based materials, relaxors, multiferroics, piezoelectrics, ferroelectric polymers, composites and thin films, to mention only a few topics. Hundreds of participants from almost 40 countries of the world meet together for a week to present not only basic research, new discoveries, new ideas, new experimental techniques, but also new applications of ferroelectrics and materials possessing ferroelectric properties. Perhaps I am not alone of the opinion that the importance of ferroelectrics in the science and their wide practical applications are reciprocally proportional to the knowledge about these materials, even among the physicists. That is why such Meetings need be organised, and the 4-year cycle makes them always attractive and gives an opportunity to get to know the score, through intensive scientific programme with lectures and contributions delivered by extraordinary speakers and experienced experimentalists and theorists, gathered in one place and at the same time. Thus, we believe that the IMFs provide an extraordinary opportunity not only to report on or to present what has already been published, but they will also be a platform for heated discussions, in search of new ideas for ferroelectricity in the macro- micro- and nano-scale. Yet, advances in the physics of ferroelectrics, and the presence of ferroelectrics in different branches of science should attract those who look forward to "an event" which might bring about a change in the mainstream of contemporary ferroelectric physics. That is why the IMF-13 should be treated as a Meeting that provokes asking the question: Is there still or is there not anything exciting about the physics of ferroelectrics? The book of abstracts, id est a kind of a state-of-the-art in the ferroelectricity in 2013, seems to answer this question. It proves once again that the current physics of ferroelectricity is an internationally highly-competitive

area. We thus hope that the programme of the IMF-13 presentations and poster sessions will further the understanding that PhD students and young scientists have of the most important trends in ferroelectricity. On the other hand, outstanding speakers and scientists with internationally recognised achievements, who accepted our invitation to deliver plenary lectures, guarantee the extensive knowledge to be served in the best way. Our words of gratitude go to you who have accepted our invitation and you who have come to Kraków, the city of beauty which never passes, and the city which provides favourable atmosphere for scientific adventures. We believe that the time spent on IMF-13 will be unforgettable from the scientific, as well as cultural, point of view.
(A note: it is not necessary to worry that this is the 13th Meeting in the 13th year of this century. The bad, if any, influence of the number thirteen, "on whatever", has not been scientifically proved yet.).

We wish you interesting and fruitful IMF-13!

On behalf of the Organizing Committee

Krystian Roleder
General Chair of the IMF-13

EFFECT OF FUEL ON THE AUTO-COMBUSTION SYNTHESIZED MULTIFERROIC $BiFeO_3$

0412

N. I. Ilić (1), A. S. Džunuzović (1), J. D. Bobić (1), M. M. Vijatović-Petrović (1), B. S. Stojadinović (2), Z. D. Dohčević-Mitrović (2) and B. D. Stojanović (1)
1. Institute for Multidisciplinary Research, University of Belgrade, Belgrade, Serbia;
2. Institute of Physics, University of Belgrade, Belgrade, Serbia

e: niksentije@gmail.com

Bismuth ferrite is one of the most promising single multiferroic materials. It exhibits ferroelectric and antiferromagnetic behavior in wide range of temperatures. Many new applications arise due to possibility of magnetization reorientation by electric field and polarization reorientation by magnetic field [1]. Main problem in usage of $BiFeO_3$ is difficulty of obtaining pure phase ceramic and high conductivity as a result of Fe non-stoichiometry [2].

$BiFeO_3$ powders were prepared by auto-combustion method starting from iron and bismuth nitrates. After the process of self-ignition, fine precursor powders were thermally treated for various periods at different temperatures and heating rates. Several fuel to oxidizer ratios (F/O) were examined, and X-rays diffraction results showed that in case of citric acid as a fuel, the purest $BiFeO_3$ perovskite phase was obtained for F/O = 1/1 and calcination at 600 °C by 4 hours. However, some Bi_2O_3, $Bi_2Fe_4O_9$ and $Bi_{25}FeO_{39}$ secondary phases remains in all powders. Effect of other fuels (sucrose, urea) [2,3] and sintering regimes are still to be investigated. Powders were characterized by SEM/EDS, TG/DTA, Raman scattering, particle size distribution and BET surface area measurements. Impedance measurements of $BiFeO_3$ ceramics are planned.

---

1. Hill N. A.: Why Are There so Few Magnetic Ferroelectrics? Journal of Physical Chemistry B, 2000; 104; 6694 – 6709
2. Carvalho T. T., Tavares P. B.: Synthesis and thermodynamic stability of multiferroic $BiFeO_3$. Materials Letters, 2008; 62; 3984 – 3986
3. Farhadi S., Zaidi M.: Bismuth ferrite ($BiFeO_3$) nanopowder prepared by sucrose-assisted combustion method: A novel and reusable heterogeneous catalyst for acetylation of amines, alcohols and phenols under solvent-free conditions. Journal of Molecular Catalysis A: Chemical, 2009; 299; 18 – 25

THIRTEENTH YOUNG RESEARCHERS' CONFERENCE
MATERIALS SCIENCE AND ENGINEERING

December 10-12, 2014, Belgrade, Serbia
Serbian Academy of Sciences and Arts, Knez Mihailova 36

Program and the Book of Abstracts

Materials Research Society of Serbia
&
Institute of Technical Sciences of SASA

December 2014, Belgrade, Serbia

X/7

Effect of Y-doping on structure and properties of multiferroic $BiFeO_3$ ceramics

Nikola Ilić[1], Bojan Stojadinović[2], Adis Džunuzović[1],
Jelena Bobić[1], Zorana Dohčević-Mitrović[2], Biljana Stojanović[1]
[1]Institute for Multidisciplinary Research, University of Belgrade, Kneza Višeslava 1, 11000 Belgrade, Serbia, [2]Institute of Physics, University of Belgrade, Pregrevica 118, Belgrade, Serbia

Bismuth ferrite ($BiFeO_3$) exhibits ferroelectric and antiferromagnetic properties up to very high temperatures, and is, consequently, considered one of the most promising single phase multiferroic materials. Doping with Y^{3+} was tested in terms of improving electrical and magnetic properties. $Bi_{1-x}Y_xFeO_3$ was synthesized by auto-combustion method using urea as a fuel. Precursor powders were annealed, pressed and sintered. Powders and ceramic samples were characterized by XRD, SEM, Raman, electrical and magnetic measurements. X-ray diffractograms and Raman spectra showed transition from rhombohedral to orthorhombic structure at 10 % Y^{3+} content. SEM images indicated reduction in grain size with higher concentration of Y^{3+}.

X/8

The role of mechanochemistry in preparation of high dielectric constant and low-loss electroceramics

Piotr Dulian [1], W. Bąk [2], Cz. Kajtoch [2], K. Wieczorek-Ciurowa[1]
[1]Faculty of Chemical Engineering and Technology, Cracow University of Technology, 24, Warszawska Str., 31-155 Cracow, Poland, [2]Institute of Physics, Pedagogical University, 2, Podchorążych Str., 30-084 Cracow, Poland,

High-energy ball milling process of solids often offers unique opportunities for the creation of value-added materials especially with perovskite structure. These studies are aimed to explain the advantages of the mechanochemical synthesis of polycrystalline ceramics with ultrahigh dielectric constants and low dielectric losses.

The results of comparison the syntheses' results using mechanochemical and high-temperature treatments are presented. Additionally, the influence of impurities from ball milling processes is considered.

Acknowledgements: The study was supported by the National Science Centre Poland, Project DEC-2012/05/N/ST8/03764, DS/C-1/KWC/2013-14, and by the EU, project POIG UDA-POIG-01.03.02-12-055/12-01.

Available online at www.sciencedirect.com

ScienceDirect

Ceramics International 41 (2015) 69–77

CERAMICS INTERNATIONAL

www.elsevier.com/locate/ceramint

Structure and properties of chemically synthesized $BiFeO_3$. Influence of fuel and complexing agent

Nikola I. Ilić[a], Adis S. Džunuzović[a], Jelena D. Bobić[a], Bojan S. Stojadinović[b], Peter Hammer[c], Mirjana M. Vijatović Petrović[a], Zorana D. Dohčević-Mitrović[b], Biljana D. Stojanović[a,*]

[a]Institute for Multidisciplinary Research, University of Belgrade, Kneza Višeslava 1, Belgrade, Serbia
[b]Institute of Physics, University of Belgrade, Pregrevica 118, Belgrade, Serbia
[c]Chemistry Institute, UNESP-University Estadual Paulista, Professor Francisco Degni s/n, Araraquara, SP, Brazil

Received 16 June 2014; received in revised form 29 July 2014; accepted 6 August 2014
Available online 15 August 2014

Abstract

Perovskite, single multiferroic bismuth ferrite was prepared by two chemical methods: auto-combustion and soft chemical route. Influence of different fuels and complexing agents and thermal treatment on purity of bismuth ferrite powders and density of bismuth ferrite ceramics were investigated. X-ray diffraction technique (XRD) indicated that optimal temperatures and times for calcination and sintering are 600 °C for 2 h and 800 °C for 1 h with quenching, respectively. Scanning electron microscopy (SEM) analysis showed that soft route synthesized samples formed softer agglomerates and smaller grains with less secondary phases. Powders and pellets were characterized by Brunauer–Emmett–Teller (BET) specific surface area analysis, particle size distribution, Fourier transform infrared spectroscopy (FT-IR), dilatometry, Raman spectroscopy, X-ray photoelectron spectroscopy (XPS), dielectric and magnetic measurements. Resistivity and origin of electrical resistance were studied by means of impedance measurements.

Keywords: A. Powders: chemical preparation; B. Electron microscopy; B. X-ray methods; D. Bismuth ferrite

1. Introduction

Bismuth ferrite (BF) is lately attracting great attention being one of a very few single multiferroic materials at room temperature. BF is ferroelectric up to 830 °C and antiferromagnetic below 370 °C [1], but nanoparticles can also manifest weak ferromagnetic behavior. Unlike other ferroelectric materials with asymmetric unit cells, BF has symmetric rhombohedral perovskite structure, but possesses spontaneous polarization due to lone electron pairs on Bi^{3+} ions [2]. This kind of ferroelectricity allows BF to has magnetic properties in the same time, considering that magnetic materials have partially filled d or f-orbitals with strong repulsive Culon interactions and symmetric unit cells [3,4].

Multiferroic materials have great potential for different applications, primarily for information storage devices [5], but also in sensors, additives, spintronic devices [6], actuators [7], transducers [8], filters, attenuators [9], satellite communication, bubble devices, permanent magnets [10]. BF also has some uses unrelated to its multiferroic properties. It has been examined as a catalyst [11], photocatalyst [12], pigment, material for infrared detectors, optoelectronics and solar cells [13]. Aside from many potential applications, materials such as bismuth ferrite are very interesting from theoretical point of view, for better understanding of multiferroic behavior origin and nature.

BF was intensively studied from the 1960 [2], but difficulties in obtaining single phased material and achieving stable electrical properties have prevented wider application. Although phase diagrams of Bi_2O_3–Fe_2O_3 system show presence of perovskite bismuth ferrite phase up to 830 °C, it is assumed that this phase is metastable, and decomposes eventually to mullite type phase

---

*Corresponding author. Tel.: +381 11 2085057; fax: +381 11 2085062.
E-mail addresses: niksentije@gmail.com (N.I. Ilić), bstojanovic80@yahoo.com (B.D. Stojanović).

http://dx.doi.org/10.1016/j.ceramint.2014.08.020
0272-8842/

($BiFe_2O_4$) and sillenite ($Bi_{25}FeO_{39}$) phases even at significantly lower temperatures [14]. Volatility of bismuth can also disturb the system's stoichiometry.

The main problem with electrical properties is low resistance originating from secondary phases and divalent iron ions, which are inevitably present in some degree [15]. For this reason, it is very hard to obtain saturated polarization loops [16]. Attempts to overcome this problem by controlling sintering atmosphere, doping with other elements or making solid solutions were made [7,15,17].

All this repressed exploration of BF, but the discovery of large remnant polarization in BF thin films in the 2000s have returned interest in this material [2]. It was presumed that this is a consequence of strain present in thin films, but recently has been shown that even bulk BF single crystals have this large polarization [18].

Many routes were reported for synthesis of BF in an effort to obtain pure phased material: solid state [9,16], mechanochemical [19], synthesis from the melt of alkaline salts [20], hydrothermal [21,22], different methods from solutions (auto-combustion [11,14,23], sol–gel [6,24], Pechini [25], co-precipitation [9,26], soft chemical route [10,27], sonochemical and microemulsion techniques [28]). None of them was completely successful, so removal of secondary phases was tried to be done by leaching in diluted mineral acids [24,28] or with different thermal treatments including quenching [9,29], spark plasma sintering [26], rapid liquid phase sintering [15,30], microwave sintering [31], sintering in different atmospheres [15], etc.

Auto-combustion synthesis is based on redox reaction between nitrate ions and organic fuels. Large amount of energy and gasses releases during this process, forming crystalline compounds in form of fluffy ash. In reality, the product is just partly crystallized, and some organic compounds remains in it, so further thermal treatment is necessary [32]. Heat of combustion and gas evolution are dependent on nature of the fuel and fuel to oxidant ratio (*F*/*O*), and they have crucial impact on powder characteristics.

Many advanced materials were successfully synthesized by this method. Its main advantages are simplicity of the process and completion of the reaction so fast (it lasts only few seconds) that many defects are introduced into structure during it, which lowers required sintering temperatures and, hence, helps in obtaining nanomaterial [33]. Soft chemical route is similar to auto-combustion synthesis, but in it solutions are just dried without any combustion. Complexing agents prevent precipitation, so the product is amorphous resin.

In this paper, BF was synthesized by auto-combustion and soft chemical methods. In case of auto-combustion synthesis, several organic compounds were used as fuels: citric acid, sucrose and urea. In soft chemical route two complexing agents (citric and tartaric acids) were compared with reaction without complexing agent. It is known that chemical synthesis routes are mainly referred to powders, and such way obtained materials are very rarely processed to ceramics. In this study, an attempt was made to obtain dense and pure phased ceramic samples of BF with nanosized grains. The influence of fuel or complexing agent on phase composition of powders and ceramics was investigated. The purest materials were chosen for further characterization and study of electric and magnetic properties. As the smallest amount of secondary phases was obtained for urea synthesized BF, some of the results will be presented only for it.

2. Experimental procedure

BF precursor powders were prepared by two methods: auto-combustion and soft chemical route. Both techniques are very simple, fast and of low-cost. Chemicals used for synthesis are $Bi(NO_3)_3 \cdot 6H_2O$ (Alfa Aesar, 98.0%), $Fe(NO_3)_3 \cdot 9H_2O$ (Alfa Aesar, 98.0–101.0%), NH_4OH (Lach Ner, 25%), HNO_3 (65%), citric acid (Carlo Erba, 99.5–100.5%), sucrose (Alfa Aesar, 99%), urea (Riedel-de Haen, 99.0–100.5%) and tartaric acid (Saphoma, 99.9%).

Syntheses are schematically presented in Fig. 1. In auto-combustion synthesis, nitrates of iron and bismuth were dissolved in minimal amounts of distilled water and 3 M nitric acid, respectively. Solutions were mixed together for a while, and saturated solution of fuel was added. Molar ratios of metal nitrate oxidants (*O*) to fuels (*F*) were calculated using summary valences of reactants according to approach suggested by Jain et al. [34], which is very useful to estimate required quantity of fuel for conducting reaction to its end. In case of citric acid and sucrose fuels, pH value was raised with ammonia solution in order to promote complexing ability of fuels and introduce amino ions required for combustion initiation. In case of urea as a fuel this is not necessary because the fuel itself contains amino groups. Solutions were heated at 80–90 °C under continuous stirring until they turn into a sticky mass. Temperature was then raised to about 150 °C and resins were dried after which self ignition occurs. Reaction is very exothermic, and open flame may appear. Voluminous ash which retains into dish is precursor powder.

In soft chemical route, metal nitrates were dissolved in minimal amounts of distilled water and diluted nitric acid, and solution of complexing agent was added to them. Solutions were heated and stirred at 90–100 °C until completely dried.

All precursor powders were ground in a mortar and calcined at 600 °C for 2 h at the heating rate of 10 °C/min. Ceramic samples were prepared by pressing the calcined powders under

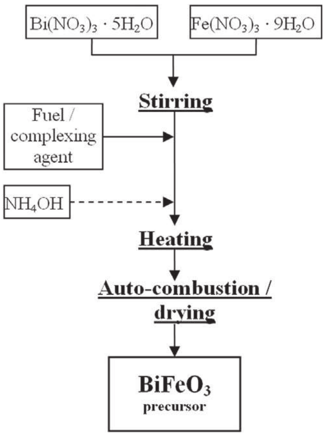

Fig. 1. Scheme of auto-combustion and soft route syntheses of bismuth ferrite.

pressure of 294 MPa (auto-combustion obtained powders) or 196 MPa (soft route obtained powders) and sintering at 800 °C. Samples were placed into preheated oven and quenched after 1 h. In preliminary experiments, other temperatures and times for calcination and sintering were also carried out, but did not show just as good results. Similar optimal thermal treatments were revealed by other authors [9,14,19].

Powders and ceramics were characterized by DTA/TG (SETARAM Labsys TG-DTA/DSC system), XRD (Model Phillips PW1710, Cu Kα radiation, 1°/min), BET (Micrometrics Gemini 2360), particle size distribution (Coulter LS Particle Size Analyzer 230), SEM (Model TESCAN SM-300) equipped with back-scattered electron detector (BSE) and energy-dispersive X-ray spectroscopy (EDS), dilatometer (Linseis, model 4L70-2000), Raman (TriVista 557 Raman system with the mixed Ar/Kr laser line (λ=514.5 nm) as an excitation source with an incident laser power less than 60 mW in order to minimize heating effect), and an FT-IR (Bruker Equinox-55). XPS (UNI-SPECS UHV System, Berlin, Germany) was carried out at a pressure of less than 10^{-7} Pa. The Mg Kα line was used, and the analyzer pass energy was set to 10 eV. The inelastic background of the Fe 3p electron core-level spectra was subtracted using Shirley's method. Ceramic pellets were also characterized by dielectric (HP 4284A, frequencies from 20 Hz to 1 MHz), impedance (HIOKI 3532-50 LCR HiTESTER, frequencies from 42 Hz to 1 MHz) and magnetic measurements (SQUID, Quantum Design).

3. Results and discussion

TG curve for BF tartaric precursor powder (Fig. 2) showed significant loss of mass of about 43%. Loss below 150 °C accompanied with an endothermic peak on the DTA curve corresponds to evaporation of water. Several exothermic peaks in interval from 150 to 280 °C, correspond to combustion of residual organics, and it is followed with mass loss of around 30%. Constant mass confirms that organics were completely gone up to 510 °C, and above this temperature only crystallization of amorphous bismuth ferrite takes place. However, expressed peaks of new phase formation were not observed.

Powders obtained by auto-combustion method contain much less water and organics with less than 1% mass loss, since they were synthesized at higher temperature.

The energy released in auto-combustion reaction is maximal for $F/O=1$, but maximal energy release may not always be desirable. As desired products are often metastabile, it may be necessary to lower the temperature of synthesis, so fuels are used in excess or deficit. Also, with excess fuel, oxygen from air is partly used for reaction, and those additional released gasses make product particles smaller. In our study, different fuel to oxidizer ratios were tried in the auto-combustion synthesis route and the best one was chosen based on the powders' XRD result. The purest BF phase was formed with F/O ratio 1 for citric acid, 3 for sucrose and 1–1.5 for urea. Optimal pH values were between 6 and 7 for citric acid and sucrose, and around 1 for urea.

X-ray diffraction patterns for calcined powders presented in Fig. 3 showed good matching with the data of JCPDC card 74-2016 only in case of urea fuel in auto-combustion method (BF urea) and tartaric acid in soft method (BF tartaric). Small peaks belonging to sillenite ($Bi_{25}FeO_{39}$) and mullite type ($Bi_2Fe_4O_9$) phases are present as well. For similar synthesis routes, other authors have obtained optimal calcinations temperatures of 500–650 °C with small amounts of sillenite

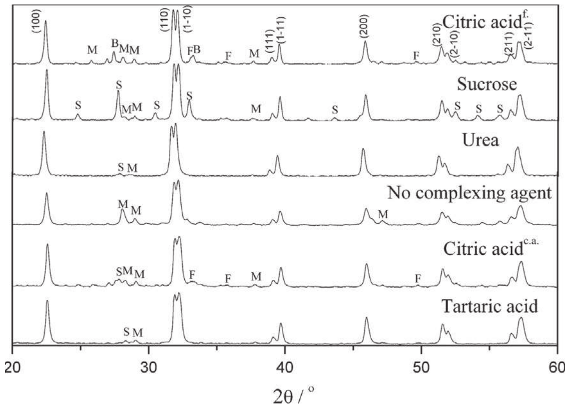

Fig. 3. XRD patterns of differently obtained BF powders calcined at 600 °C for 2 h. Secondary phases are marked: S – sillenite ($Bi_{25}FeO_{39}$), M – mullite type phase ($Bi_2Fe_4O_9$), F – α-Fe_2O_3 and B – Bi_2O_3. Superscripts f. and c.a. denote the citric acid used as a fuel and complexing agent, respectively.

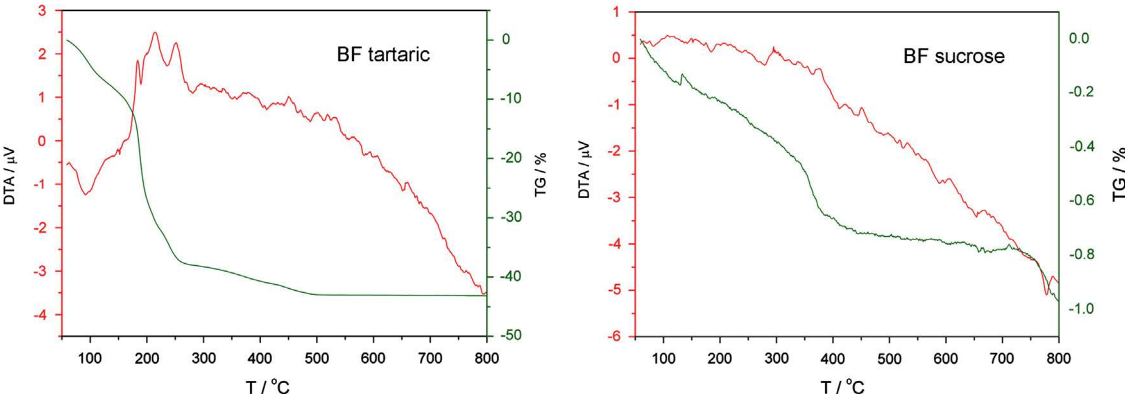

Fig. 2. DTA/TG curves for BF tartaric and BF sucrose precursor powders.

phase [14], sillenite and mullite type phases [27] or with no secondary phases [10].

FT-IR spectra of calcined BF powders are presented in Fig. 4. Strong peak at 550 and smaller one at 450 cm^{-1} correspond to stretching and bending vibrations of Fe–O bonds. Some residual nitro groups are detected by the small peaks at 815 and 1385 cm^{-1}. Band at 1630 cm^{-1} fits to H_2O bending vibrations, while the broad band at 3300–3600 cm^{-1} corresponds to stretching of bonds in H_2O and –OH groups, originating from adsorbed water from air.

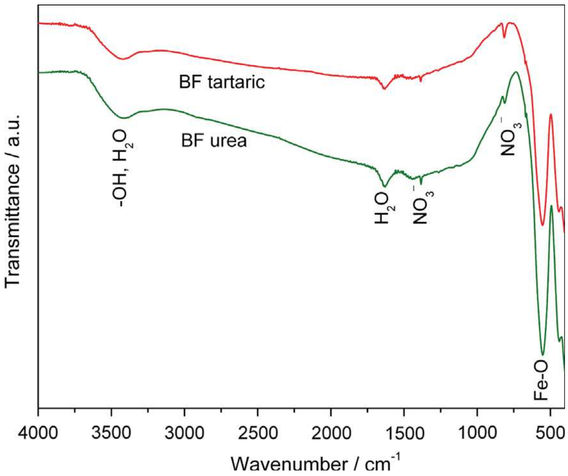

Fig. 4. FT-IR spectra of calcined BF urea and BF tartaric powders.

SEM micrographs of calcined powders (Fig. 5) showed large degree of agglomeration. Sizes of primary particles of all BF powders are between 200 nm and 600 nm, but agglomerates are 2–10 μm large. Agglomerates seem to be hard, especially in case of citric acid as a fuel and soft route synthesis without complexing agent. They were not broken even after dispersing in ethanol with ultrasonic probe. Such hard agglomerates will not be completely broken even after pressing, and they are big problem for achieving high density of ceramics. Beside small pores between particles, there are much larger pores between agglomerates, which do not strive to disappear during sintering process. Other authors obtained particles of similar size for chemically synthesized BF powders calcined at 550 °C for 3 h [27] and 400 °C for 2 h [10] (with smaller agglomeration in this case). At 450 °C and 650 °C for 3 h, Sakar et al. have recorded flower like and granular particles [27].

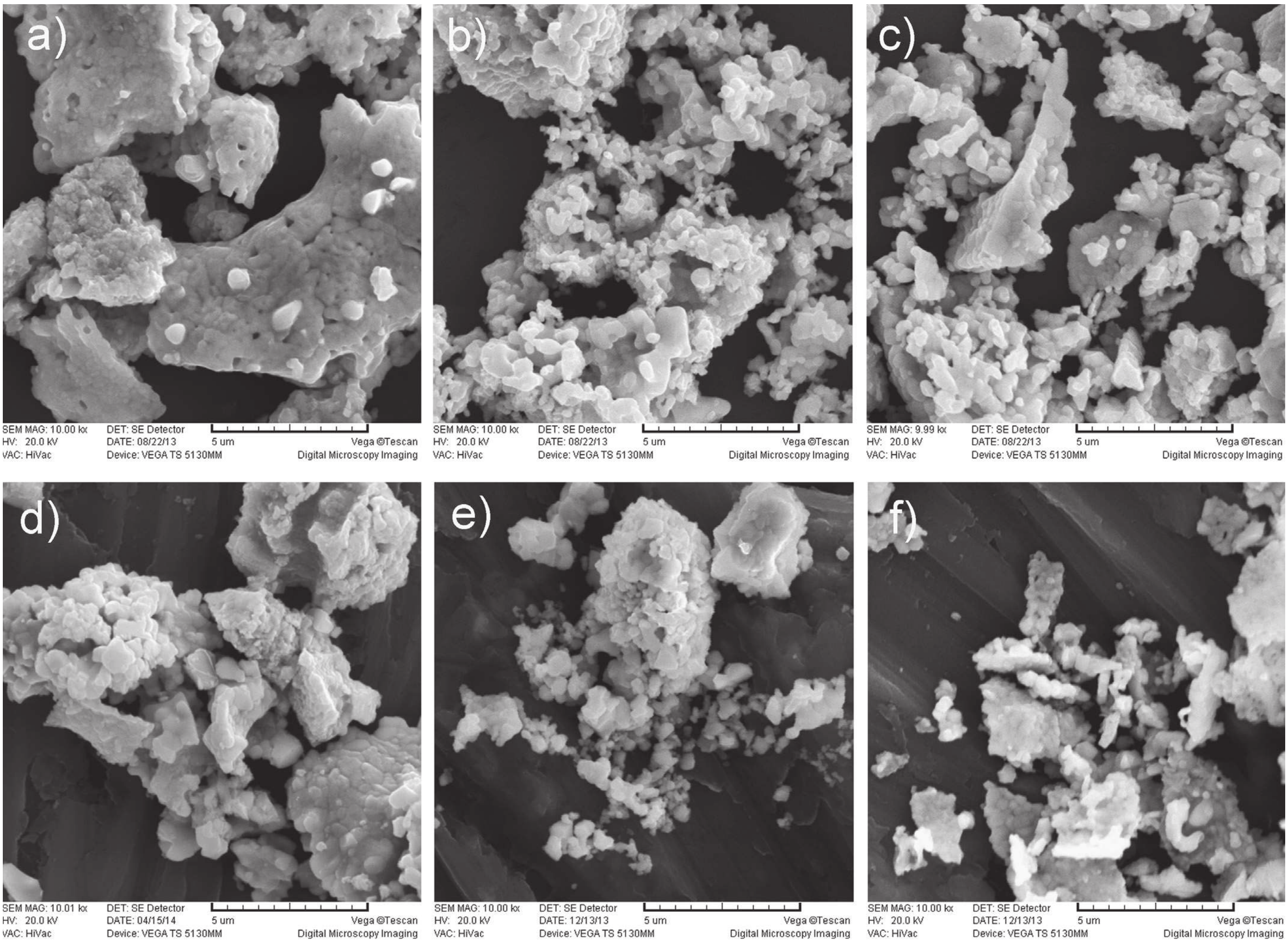

Fig. 5. SEM images of BF powders calcined at 600 °C for 2 h, prepared with (a) citric acid (fuel), (b) sucrose, (c) urea, (d) no complexing agent, (e) tartaric acid and (f) citric acid (complexing agent).

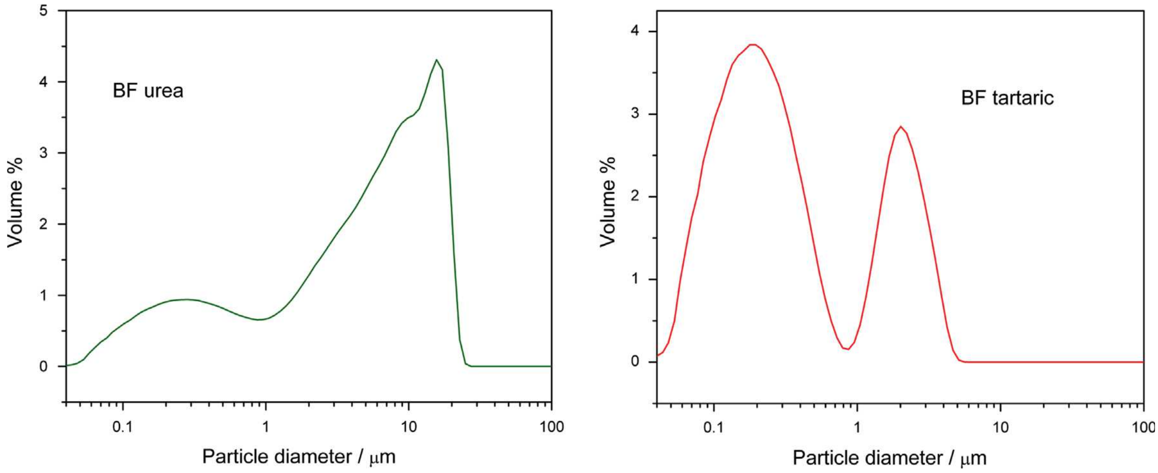

Fig. 6. Particle size distribution of BF urea and BF tartaric powders.

BET isotherm data point out small specific surface area of calcined powders, with 0.33 m^2/g for BF urea and 2.92 m^2/g for BF tartaric. The possible explanation is formation of hard agglomerates, with particles so close to each other that adsorbing gas cannot penetrate within. Particle size analysis (Fig. 6) pointed out bimodal particle size distribution, confirming presence of agglomerates. BF urea powder consists of primary particles ~0.3 μm large and agglomerates of around 15 μm, while these sizes for BF tartaric powder are ~0.2 μm and 2 μm. Calculated mean particle sizes are 7.2 μm for urea and 0.8 μm for tartaric acid synthesized BF.

Dilatometry measurements for calcined and pressed BF urea powder presented in Fig. 7 showed start of shrinkage at 630 °C. At higher temperatures, shrinkage is very fast, and it reaches 7.5% up to 830 °C. It is not possible to heat sample above this temperature because of melting. Based on these results, and considering problem with decomposition of perovskite phase at high temperatures, three different thermal treatments were tried: sintering at 750 °C for 4 h and sintering at 800 and 820 °C for 1 h with quenching. The purest and most dense ceramics was obtained at 800 °C, and all presented results are for these samples.

Densities of green and sintered samples were determined by geometrical measurements and Archimedes method, respectively. As listed in the table in Fig. 7, green densities are between 50 and 60%, and sintered ones between 68 and 90% of theoretical. Larger green density generally means larger density after sintering, but soft route synthesized materials showed different behavior. SEM images of powders in Fig. 5 could explain this. Tartaric acid synthesized powder has smaller agglomerates than powders obtained with citric acid and without complexing agent. Larger agglomerates are easier to be pressed, because of smaller number of contacts between them, requiring smaller compacting energy. That means that total green porosity is smaller, but pores are larger. Pellets with smaller pores densify more effectively, and sintered density is higher although it was lower before sintering. Best densities were achieved with urea in auto-combustion and tartaric acid in soft synthesis, which was confirmed with SEM analysis in Fig. 11 as well.

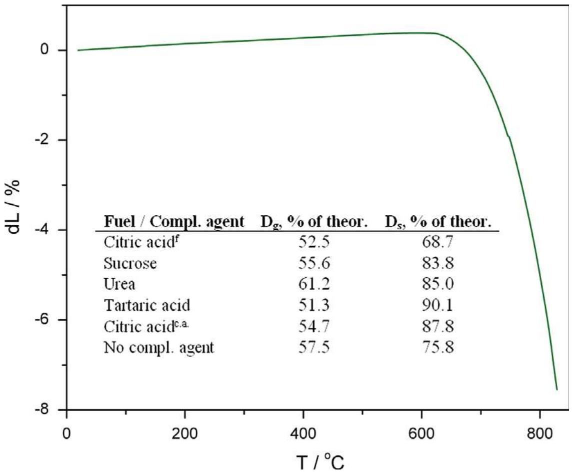

Fuel / Compl. agent	D_g, % of theor.	D_s, % of theor.
Citric acid^f	52.5	68.7
Sucrose	55.6	83.8
Urea	61.2	85.0
Tartaric acid	51.3	90.1
Citric acid$^{c.a.}$	54.7	87.8
No compl. agent	57.5	75.8

Fig. 7. Dilatometry curve for BF urea with inserted data for green (D_g) and sintered (D_s) densities of differently prepared BF pellets.

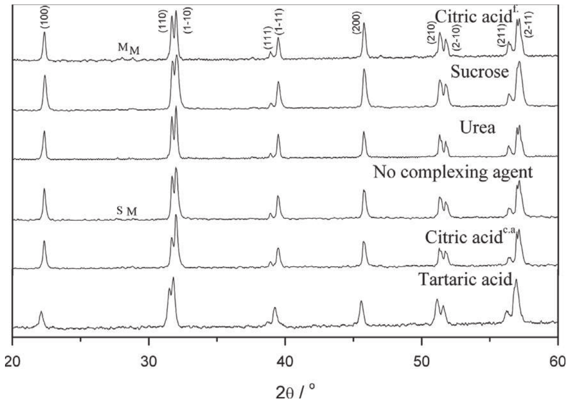

Fig. 8. XRD patterns of differently obtained BF samples sintered at 800 °C for 1 h. Secondary phases are marked: S – sillenite ($Bi_{25}FeO_{39}$) and M – mullite type phase ($Bi_2Fe_4O_9$). Superscripts f. and c.a. denote the citric acid used as a fuel and complexing agent, respectively.

XRDs of the sintered samples (Fig. 8) all indicate quite low content of secondary phases according to small intensity of peaks at $2\theta = 27°–28°$, but exact conclusion cannot be claimed having in mind that sillenite phase is often present in amorphous form. Besides, peaks of mullite type phase could be partially hidden by perovskite and sillenite phases which scatter X-rays more intensively [35].

The Raman spectra of BF urea are presented in Fig. 9. The sample exhibits rhombohedral structure. It is well known that rhombohedral BF with R3c symmetry has 4 A_1 and 9 E modes. The Raman spectra were fitted using the Lorentzian-type profile and the position of each Raman mode is written on the image. The Raman mode positions are in good agreement with literature data [36,37].

Fe $2p_{3/2}$ XPS spectra of BF pellets are presented in Fig. 10. The spectra were deconvoluted into four components. The small sub-peak at binding energy of 708 eV was attributed to a substoichiometric FeO_x phase $(0.5 < x < 1)$, consisting of Fe sites containing oxygen vacancies. The component at 709.6 eV was assigned to the divalent iron ions, while peaks at 710.9 and 712.5 eV were attributed to trivalent iron ions surrounded with O^{2-} and OH^- ions. Content of Fe^{2+} ions is possible to be calculated using ratio of these peaks. Around 51% of iron ions in BF urea and 43% in BF tartaric were in Fe(II) oxidation state. This can also indicate presence of oxygen vacancies and possible low resistivity of BF ceramics.

Large pores could be seen in BSE SEM images of all sintered samples (Fig. 11). Different phases are visible in different shades in these shots. The most abundant phase is BF phase. EDS results showed that darker grains correspond to the mullite type phase, and brighter grains to the heavier, sillenite phase. Except difference in color, difference in size and shape of grains is obvious. Mullite type phase grains are smaller and rectangular, inserted into perovskite grains, while sillenite occurs in large irregular grains.

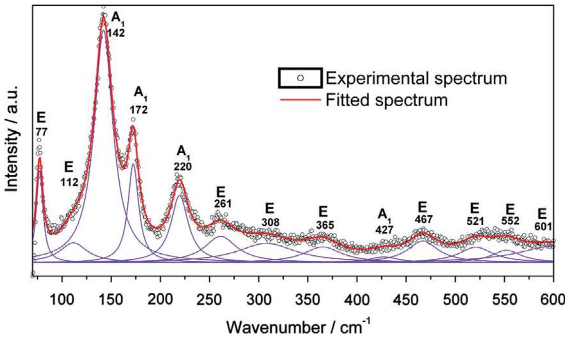

Fig. 9. Room-temperature Raman spectra of BF urea sample (circles) together with calculated spectra (full lines).

Diffusion of Bi^{3+} ions was reported to control the formation of BF during solid state reaction [9]. Beside perovskite phase, it can be assumed that large irregular grains of Bi rich, sillenite phase could be formed on the grains surface, and iron rich, mullite type phase in inner parts in the form of small rectangular grains. Additionally, metastabile BF phase may be decomposed as mentioned in Section 1, so forming of certain amounts of sillenite and mullite type phases is difficult to be avoided. Furthermore, impurities in the starting material disturb the equilibrium between oxides of iron(III) and bismuth.

Insets in Fig. 11 represent fracture surfaces of samples. The surface is representative for auto-combustion synthesized samples, while for samples obtained by soft route grains are much larger inside the sample than at the surface. Therefore, looking at the free surface, there is a significant difference between auto-combustion and soft route synthesized samples. Ceramics obtained by soft method have much smaller grains (500 nm–5 μm, compared to 2–20 μm size of auto-combustion synthesis), and smaller amount of secondary phases, especially in the case of tartaric acid as a complexing agent. Inside the samples there is no significant difference between synthesis methods, except for sucrose prepared material, which has remarkably larger grains than others. BF tartaric material has slightly smaller pores than others, indicating that agglomerates in BF tartaric powder were softer and their breaking more successful than for the other powders.

Dependencies of the dielectric constant (ε′) and dielectric losses (tan δ) on temperature at different frequencies for BF urea ceramics are presented in Fig. 12. Dielectric constant is quite large above 300 °C, with a major peak at 470 °C. Dielectric losses are less than 1 below 250 °C, and they rise at higher temperatures exhibiting two peaks at 370 and 440 °C. This kind of behavior is related to Maxwell–Wagner phenomena, caused by

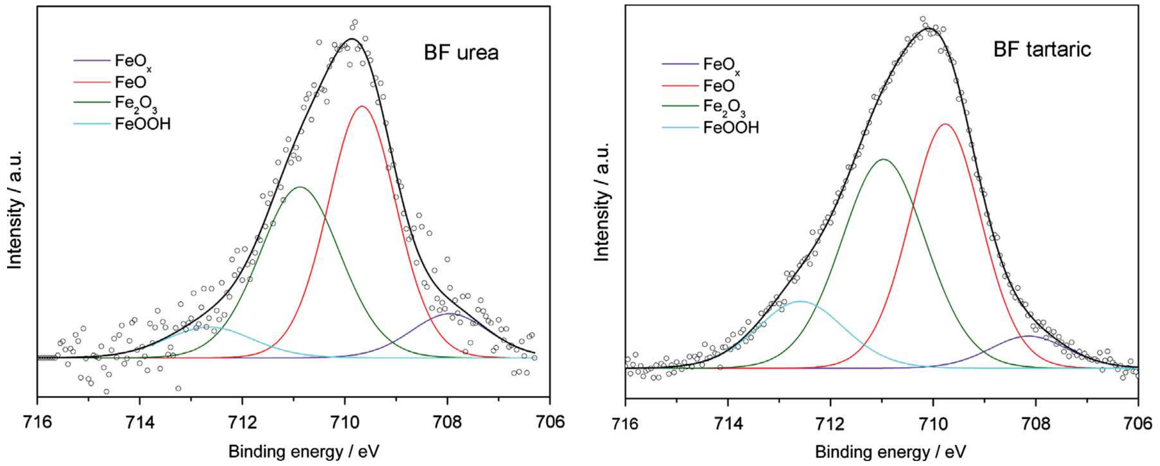

Fig. 10. Fe $2p_{2/3}$ XPS spectrum of BF urea and BF tartaric ceramic samples.

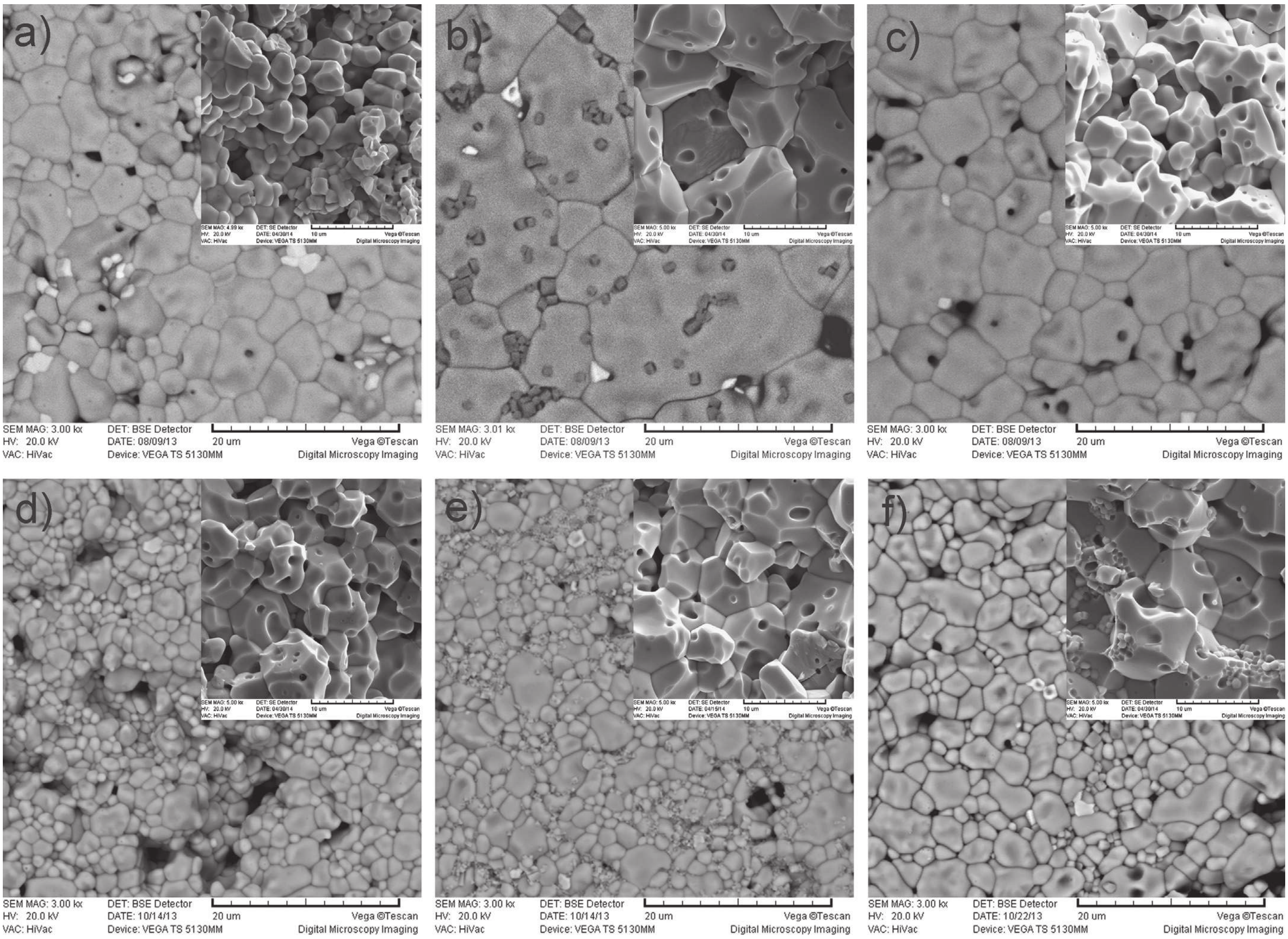

Fig. 11. SEM BSE images of BF pellets sintered at 800 °C for 1 h, prepared with (a) citric acid (fuel), (b) sucrose, (c) urea, (d) no complexing agent, (e) tartaric acid and (f) citric acid (complexing agent).

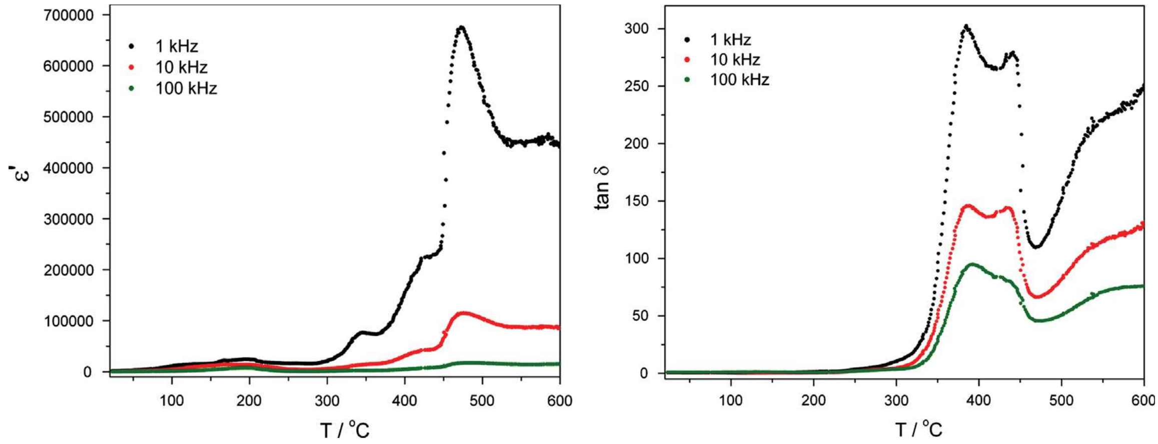

Fig. 12. Dielectric constant and dielectric loss vs. temperature for BF urea ceramic sample at different frequencies.

inhomogeneity in conductivity, which can lead to accumulation of surface charge at the interfaces [38]. The inhomogeneity in conductivity could exist between grains and grain boundaries of the perovskite phase, but also between it and secondary phases.

Fig. 13 represents the dependence of the imaginary part of the complex impedance, Z'', on real part of the complex impedance, Z', for BF urea and BF tartaric samples at room temperature. Results were fitted using ZView2 software,

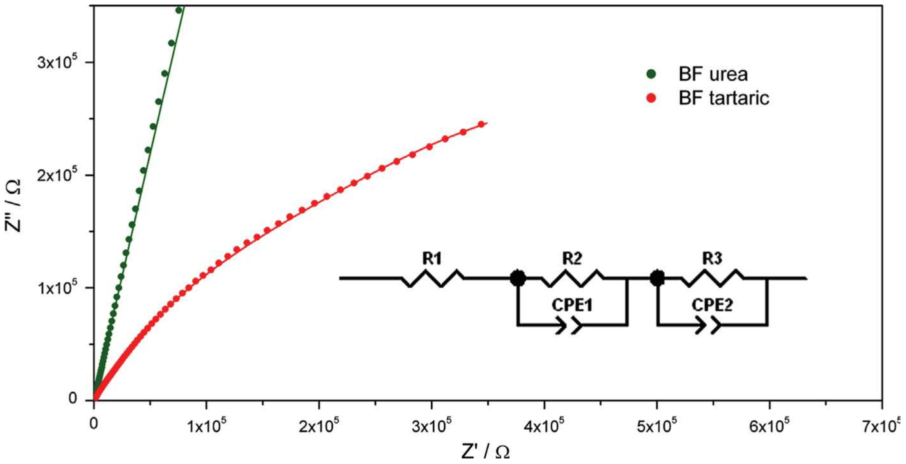

Fig. 13. Impedance plots for BF urea and BF tartaric samples at room temperature.

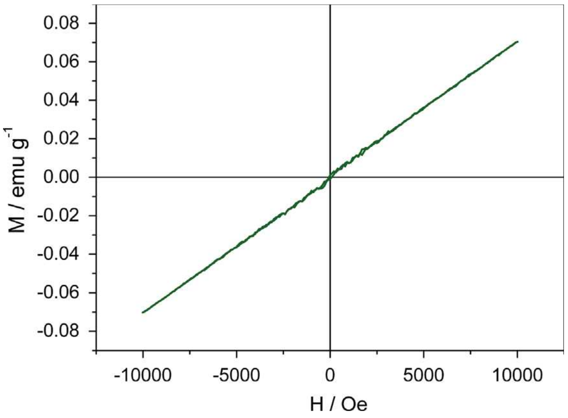

Fig. 14. Magnetization vs. magnetic field plot for sintered BF urea sample.

showing good agreement with the electric circuit presented with inset in Fig. 13. For BF urea, resistivity originates mostly from grain boundaries, while grains contribute with less than 10% of total resistance. Calculated resistivity has an order of magnitude of 10^8 Ω (10^7 Ω cm) at room temperature, which is quite low compared to 10^{10} Ω cm resistance of monocrystalline BF, reported by Palai et al. [39], suggesting the existence of Fe^{2+} ions and secondary phases as the main charge carriers. Although XPS analysis showed less Fe^{2+} ions in BF tartaric than in BF urea, resistivity of BF tartaric sample determined by impedance measurements is one order of magnitude smaller, and contribution of grains in total resistance was significantly higher (around 50%). BF tartaric sample have smaller porosity and, therefore, better contact between grains, which could explain smaller resistance and, in particular, smaller grain boundary resistance.

As mentioned in Section 1, bismuth ferrite is antiferromagnetic, but although each Fe^{3+} ion is surrounded by six other Fe^{3+} ions with opposite angular magnetic spin directions, their spins do not annul completely, so there are some resulting magnetic moments. These moments have cycloidal ordering with period of around 64 nm, which means that particles smaller than 64 nm are weekly ferromagnetic [2,18].

In our study, magnetic measurements showed typical antiferromagnetic behavior with no hysteresis loop up to 10 kOe fields, as depicted in Fig. 14. This kind of response was expected because grains are much larger than 64 nm, so cycloidal magnetic ordering is complete and resulting moment is zero. Sakar et al. [27] have recorded weakly ferromagnetic BF nanopowder, explaining this behavior by coupling between antiferromagnetic core and ferromagnetic surface of particles.

4. Conclusion

Two chemical methods from solution (auto-combustion and soft route) using several organic fuels and complexing agents were investigated in order to obtain rhombohedral perovskite bismuth ferrite phase. Samples obtained using urea in case of auto-combustion and tartaric acid in case of soft route showed the best outcome. XRD, Raman and EDS analyses resulted in very low amount of secondary phases in these two materials. SEM analysis showed that soft route synthesized ceramics possess smaller grains than auto-combustion synthesized ceramics. The densities achieved by soft route are larger. The Fe^{2+} percentage, determined by XPS has the lowest value of about 43% of total Fe ions for samples obtained using tartaric acid. Resistivity determined by impedance spectroscopy is rather low. BF ceramics showed antiferromagnetic properties.

Although auto-combustion and soft chemical methods have good potential in obtaining bismuth ferrite, for achieving better properties for multiferroic application, BF should be doped and/or synthesis and processing modified in order to produce higher densities and smaller grains, which will be the subject of our future work.

Acknowledgments

The authors would like to acknowledge the financial support of the Ministry of Education, Science and Technological Development of the Republic of Serbia (which also provides scholarship for the author Nikola Ilić), Project no. III 45021 and EU Project COST IC 1208 action. Special thanks for the useful discussion and characterization of samples to Prof. Paula Vilarinho and her group from Aveiro University, Portugal, Prof. M.A. Zaghete, from UNESP-IQ, Araraquara, Brasil and Dr. Lavinia Curecheriu from the Faculty of Physics, Alexandru Ioan Cuza University, Iasi, Romania.

References

[1] G.A. Smolenskii, I.E. Chupis, Ferroelectromagnets, Sov. Phys. Uspekhi 25 (1982) 475–493.

[2] R. Safi, H. Shokrollahi, Physics, chemistry and synthesis methods of nanostructured bismuth ferrite ($BiFeO_3$) as a ferroelectro-magnetic material, Prog. Solid State Chem. 40 (2012) 6–15.

[3] Nicola A. Spaldin, Magnetic Materials, Fundamentals and Applications, second edition, Cambridge University Press, Cambridge, 2011.

[4] N.A. Hill, Why are there so few magnetic ferroelectrics?, J Phys. Chem. B 104 (2000) 6694–6709.

[5] W. Eerenstein, N.D. Mathur, J.F. Scott, Multiferroic and magnetoelectric materials, Nature 442 (2006) 759–765.

[6] T.-J. Park, G.C. Papaefthymiou, A.J. Viescas, A.R. Moodenbaugh, S.S. Wong, Size-dependent magnetic properties of single-crystalline multiferroic $BiFeO_3$ nanoparticles, Nano Lett. 7 (2007) 766–772.

[7] A. Chaudhuri, K. Mandal, Study of structural, ferromagnetic and ferroelectric properties of nanostructured barium doped bismuth ferrite, J. Magn. Magn. Mater. 353 (2014) 57–64.

[8] R. Grigalaitis, M.M. Vijatović Petrović, J.D. Bobić, A. Dzunuzovic, R. Sobiestianskas, A. Brilingas, B.D. Stojanović, J. Banys, Dielectric and magnetic properties of $BaTiO_3$–$NiFe_2O_4$ multiferroic composites, Ceram. Int. 40 (2014) 6165–6170.

[9] M.S. Bernardo, T. Jardiel, M. Peiteado, A.C. Caballero, M. Villegas, Reaction pathways in the solid state synthesis of multiferroic $BiFeO_3$, J. Eur. Ceram. Soc. 31 (2011) 3047–3053.

[10] S. Ghosh, S. Dasgupta, A. Sen, H.S. Maiti, Low-temperature synthesis of nanosized bismuth ferrite by soft chemical route, J. Am. Ceram. Soc. 88 (2005) 1349–1352.

[11] S. Farhadi, M. Zaidi, Bismuth ferrite ($BiFeO_3$) nanopowder prepared by sucrose-assisted combustion method: a novel and reusable heterogeneous catalyst for acetylation of amines, alcohols and phenols under solvent-free conditions, J. Mol. Catal. A: Chem. 299 (2009) 18–25.

[12] X. Yang, Y. Zhang, G. Xu, X. Wei, Z. Ren, G. Shen, G. Han, Phase and morphology evolution of bismuth ferrites via hydrothermal reaction route, Mater. Res. Bull. 48 (2013) 1694–1699.

[13] V. James, P.P. Rao, S. Sameera, S. Divya, Multiferroic based reddish brown pigments: $Bi_{1-x}M_xFeO_3$ (M = Y and La) for coloring applications, Ceram. Int. 40 (2014) 2229–2235.

[14] T.T. Carvalho, P.B. Tavares, Synthesis and thermodynamic stability of multiferroic $BiFeO_3$, Mater. Lett. 62 (2008) 3984–3986.

[15] H.Y. Dai, Z.P. Chen, T. Li, R.Z. Xue, J. Chen, Structural and electrical properties of bismuth ferrite ceramics sintered in different atmospheres, J. Supercond Nov. Magn. 26 (2013) 3125–3132.

[16] M. Thrall, R. Freer, C. Martin, F. Azough, B. Patterson, R.J. Cernik, An in situ study of the formation of multiferroic bismuth ferrite using high resolution synchrotron X-ray powder diffraction, J. Eur. Ceram. Soc. 28 (2008) 2567–2572.

[17] J. Xie, Y. Liu, C. Feng, X. Pan, Preparation and characterization of Zr^{4+}-doped $BiFeO_3$ ceramics, Mater. Lett. 96 (2013) 143–145.

[18] G. Catalan, J.F. Scott, Physics and applications of bismuth ferrite, Adv. Mater. 21 (2009) 2463–2485.

[19] Z. Marinković-Stanojević, L. Mančić, T. Srećković, B. Stojanović, Mechanochemical synthesis of bismuth ferrite, J. Min. Metall. Sect. B 49 (2013) 27–31.

[20] A. Hernández-Ramírez, A. Martínez-Luévanos, A.F. Fuentes, A.-G. D. Nelson, R.C. Ewing, S.M. Montemayor, Molten salts activated by high-energy milling: a useful, low-temperature route for the synthesis of multiferroic compounds, J. Alloys Compd. 584 (2014) 93–100.

[21] D. Cai, J. Li, T. Tong, D. Jin, S. Yu, J. Cheng, Phase evolution of bismuth ferrites in the process of hydrothermal reaction, Mater. Chem. Phys. 134 (2012) 139–144.

[22] K. Chybczyńska, P. Ławniczak, B. Hilczer, B. Leska, R. Pankiewicz, A. Pietraszko, L. Kepinski, T. Kaluski, P. Cieluch, F. Matelski, B. Andrzejewski, Synthesis and properties of bismuth ferrite multiferroic flowers, J. Mater. Sci. 49 (2013) 2596–2604.

[23] H. Seema, S.K. Durrani, K. Saeed, I. Mohammadzai, N. Hussain, Auto-combustion synthesis and characterization of multiferroic ($BiFeO_3$) materials, in: Proceedings of the JPMS Conference Issue, Materials, 2010.

[24] A. Kumar, K.L. Yadav, Magnetic, magnetocapacitance and dielectric properties of Cr doped bismuth ferrite nanoceramics, Mater. Sci. Eng. B: Adv. 176 (2011) 227–230.

[25] E.C. Aguiar, M.A. Ramirez, F. Moura, J.A. Varela, E. Longo, A. Z. Simoes, Low-temperature synthesis of nanosized bismuth ferrite by the soft chemical method, Ceram. Int. 39 (2013) 13–20.

[26] R. Mazumder, D. Chakravarty, D. Bhattacharya, A. Sen, Spark plasma sintering of $BiFeO_3$, Mater. Res. Bull. 44 (2009) 555–559.

[27] M. Sakar, S. Balakumar, P. Saravanan, S.N. Jaisankar, Annealing temperature mediated physical properties of bismuth ferrite ($BiFeO_3$) nanostructures synthesized by a novel wet chemical method, Mater. Res. Bull. 48 (2013) 2878–2885.

[28] N. Das, R. Majumdar, A. Sen, H.S. Maiti, Nanosized bismuth ferrite powder prepared through sonochemical and microemulsion techniques, Mater. Lett. 61 (2007) 2100–2104.

[29] S.T. Zhang, M.H. Lu, D. Wu, Y.F. Chen, N.B. Ming, Larger polarization and weak ferromagnetism in quenched $BiFeO_3$ ceramics with a distorted rhombohedral crystal structure, Appl. Phys. Lett. 87 (2005) 262907.

[30] A.K. Pradhan, K. Zhang, D. Hunter, J.B. Dadson, G.B. Loutts, P. Bhattacharya, R. Katiyar, J. Zhang, D.J. Sellmyer, U.N. Roy, Y. Cui, A. Burger, Magnetic and electrical properties of single-phase multiferroic $BiFeO_3$, J. Appl. Phys. 97 (2005) 093903.

[31] W. Cai, C. Fu, W. Hu, G. Chen, X. Deng, Effects of microwave sintering power on microstructure, dielectric, ferroelectric and magnetic properties of bismuth ferrite ceramics, J. Alloys Compd. 554 (2013) 64–71.

[32] S.T. Aruna, A.S. Mukasyan, Combustion synthesis and nanomaterials, Curr. Opin. Solid State Mater. 12 (2008) 44–50.

[33] S. Lorentzou, K. Karadimitra, C. Agrafiotis, A.G. Konstandopoulos, New routes for ferrite powders synthesis, Partec (2004).

[34] S.R. Jain, K.C. Adiga, V.R. Pai Verneker, A new approach to thermochemical calculations of condensed fuel-oxidizer mixtures, Combust. Flame 40 (1981) 71–79.

[35] M. Valant, A.-K. Axelsson, N. Alford, Peculiarities of a solid-state synthesis of multiferroic polycrystalline $BiFeO_3$, Chem. Mater. 19 (2007) 5431–5436.

[36] D. Kothari, V.R. Reddy, V.G. Sathe, A. Gupta, A. Banerjee, A. M. Awasthi, Raman scattering study of polycrystalline magnetoelectric $BiFeO_3$, J. Magn. Magn. Mater. 320 (2008) 548–552.

[37] Y. Yang, J.Y. Sun, K. Zhu, Y.L. Liu, J. Chen, X.R. Xing, Raman study of $BiFeO_3$ with different excitation wavelengths, Physica B 404 (2009) 171–174.

[38] V. Kumar, A. Gaur, N. Sharma, J. Shah, R.K. Kotnala, High temperature dielectric and magnetic response of Ti and Pr doped $BiFeO_3$ ceramics, Ceram. Int. 39 (2013) 8113–8121.

[39] R. Palai, R.S. Katiyar, H. Schmid, P. Tissot, S.J. Clark, J. Robertson, S.A. T. Redfern, G. Catalan, J.F. Scott, β Phase and γ-β metal–insulator transition in multiferroic $BiFeO_3$, Phys. Rev. B 77 (2008) 014110.

Materials Research Bulletin 77 (2016) 60–69

Contents lists available at ScienceDirect

Materials Research Bulletin

journal homepage: www.elsevier.com/locate/matresbu

Improving of the electrical and magnetic properties of $BiFeO_3$ by doping with yttrium

Nikola I. Ilić[a,*], Jelena D. Bobić[a], Bojan S. Stojadinović[b], Adis S. Džunuzović[a], Mirjana M. Vijatović Petrović[a], Zorana D. Dohčević-Mitrović[b], Biljana D. Stojanović[a]

[a] Institute for Multidisciplinary Research, University of Belgrade, Kneza Višeslava 1, 11000 Belgrade, Serbia
[b] Center for Solid State Physics and New Materials, Institute of Physics, University of Belgrade, Pregrevica 118, 11000 Belgrade, Serbia

ARTICLE INFO

Article history:
Received 15 July 2015
Received in revised form 30 December 2015
Accepted 9 January 2016
Available online 13 January 2016

Keywords:
Chemical synthesis
Impedance spectroscopy
Electrical properties
Ferroelectricity
Multiferroics

ABSTRACT

Bismuth ferrite is one of the most promising multiferroic materials, and the main barriers for exploiting all of its specific properties are difficulties in obtaining pure, high resistive material with nanosized grains. Doping of $BiFeO_3$ with different transition metals and rare earth elements is often used way for overcoming these obstacles. Yttrium doped bismuth ferrite, $Bi_{1-x}Y_xFeO_3$ ($x=0$; 0.01; 0.03; 0.05; 0.1), was prepared by auto-combustion method. X-ray diffraction patterns and Raman results showed that partial phase transition from rhombohedral to orthorhombic structure took place at around 10 mol% of Y. Effect of Y doping on microstructure was studied from SEM micrographies, showing the reduction of grain size in doped samples. Electrical measurements showed continuous improvement of resistivity with Y doping, whereas the values of saturation and remnant polarizations exhibit maximums at around 5 mol% of Y. Yttrium doping also enhanced magnetic properties, leading to weak ferromagnetism.

1. Introduction

Properties of materials which result in spontaneous polarization, magnetization and deformation which can be controlled by an applied electric field, magnetic field and stress are called ferroelectricity, ferromagnetism and ferroelasticity, respectively [1]. These properties (also called ferroic properties) have been thoroughly studied and used widely for years in various devices and components. But nowadays, very interesting potential applications arises for materials which possess two or three of ferroic properties at the same time. Those materials are usually called multiferroic materials. Some other similar properties (antiferromagnetism, ferrimagnetism, ferrotoroidicity) are often also considered ferroic [2].

There are two main types of multiferroic materials. Composite multiferroics consist of two different phases, each of whom possesses one ferroic property. That means that they could be made from many different materials, so they are very numerous and many new materials have the potential to be investigated. Single multiferroics on the other hand have two or all three ferroic properties in only one phase. They are very rare, because of different origin of ferroic properties, which normally exclude one another [3]. Both types of multiferroics, composite and single ones, have some advantages and disadvantages. Aside from scarcity of single multiferroics, coefficient of correlation between different properties in them is often too small for some multifunctional application. These coefficients are significantly larger in composite multiferroics, but are limited only to boundary between different phases [4].

Bismuth ferrite (BF) has a rhombohedral perovskite structure, with almost cubic unit cell ($a_{rh}=3.965$ Å, $\alpha_{rh}=89.40°$) though it is usually described using hexagonal axes. Hexagonal c-axis is directed along [111] axes of pseudocubic cell and hexagonal cell ($a_{hex}=5.58$ Å, $c_{hex}=13.90$ Å) is consisted of six formula units of $BiFeO_3$ [5]. It is single multiferroic material, exhibiting ferroelectric and antiferromagnetic properties in the same phase. Aside from its multiferroicity, BF exhibit properties which could be interesting to those dealing with pigments, solar cell materials, photocatalysts and optoelectronics thanks to a relatively small band gap of about 1.8–2.8 eV [6–9].

With very wide temperature range of multiferroic behavior ($T_C=830\,°C$, $T_N=370\,°C$) [10], BF belongs to the materials with greatest potential for different kind of application, but still has unsolved problems in bringing out the best from its extraordinary properties. That is the reason for such numerous studies about BF in the last 15 years. Main obstacles which are still to be overcome

---

[*] Corresponding author.
E-mail addresses: niksentije@gmail.com (N.I. Ilić), bstojanovic80@yahoo.com (B.D. Stojanović).

http://dx.doi.org/10.1016/j.materresbull.2016.01.018
0025-5408/

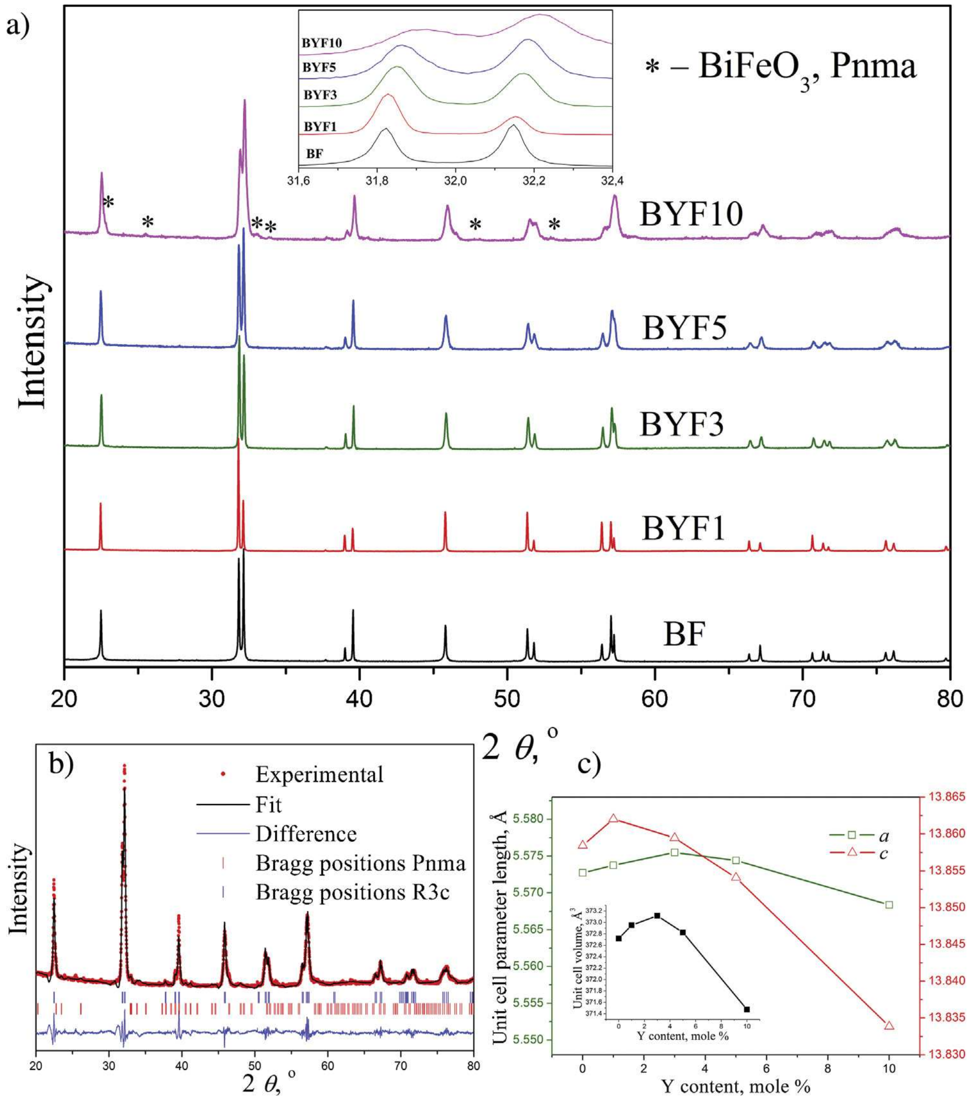

Fig. 1. XRD patterns with enlarged 2θ region between 31.6° and 32.4° in the inset (a), rietveld refinement for the sample BYF10 (b) and characteristic values of unit cell vs. composition (c) for BF and BYF ceramic samples.

are occurrence of leakage currents and insufficiently expressed magnetic properties.

Authors are still arguing about the mechanism of conduction in BF: Qi et al. [11] reported that partially substituting Fe^{3+} in the B site, Ti^{4+} ions increase the dc resistivity by more than three orders of magnitude, while Ni^{2+} ions in the same conditions reduce resistivity, so the main mechanism for conduction in BF ceramics is formation of O^{2-} vacancies and their movement. Dai et al. [12] reported that after sintering in different atmospheres, BF with more oxygen vacancies, but the lowest portion of Fe^{2+} is the most resistive, concluding the main charge carriers are electrons and not O^{2-} vacancies. Most authors highlight one of those two mechanisms [4,13]. Possible Bi^{3+} vacancies and secondary phases are rarely considered [14,15].

Low electrical resistivity of BF disables manifestation of ferroelectric behavior. The resistivity of BF was successfully improved by doping, especially in case of aliovalent ions [11,16–18]. In case of doping with isovalent ions, opinions are divided. Improvement of resistivity by A-site[1] substitution with isovalent ions was explained by smaller content of volatile Bi^{3+} ions and, therefore, less pronounced unstoichiometry [19–23]. For this reason, although slightly decreasing ferroelectric polarization by the elimination of its cause (Bi^{3+} ions with lone $6s^2$ electron pair) [1]. substitution of A-site ion is often used method for synthesis of BF with improved ferroelectric properties. There are also some studies reporting higher current density in isovalently substituted BF [24,25]. Substitution of Bi^{3+} in BF was additionally reported to promote formation of perovskite BF phase, reducing the amount of secondary phases in this way [17,24,26–28]. More success in obtaining highly resistive BF has been achieved in two-dimensional materials — in the form of thin films [29,30].

Antiferromagnetic materials still do not have many applications, but BF is not typical representative. Its antiferromagnetism is originating from Fe^{3+} ions, and is of G-type, meaning all first neighboring Fe^{3+} ions have opposite magnetic spin directions. What is interesting in BF is that these spins are not completely opposite, and there is some small resulting moment. This kind of structure is called canted spin structure, and it usually leads to weak ferromagnetism, but in BF, magnetic spins have another level of organization arranging them in spiral structures with a period of 62 nm, destroying magnetization in bulk material [31]. This means that one way of creating ferromagnetism in BF is by limiting the

---

[1] With regard to ABO_3 perovskite chemical formula.

growth of its particles or grains under 62 nm [32]. The other way could be breaking of spiral spin structure by substitution of Bi^{3+} ions with isovalent ions of different size as it was tried with many rare earth and transition metal ions [19,25,28,33,34].

Another important obstacle in BF application is difficulty in obtaining pure and dense BF ceramics. BF phase exhibits instability area between 447 °C and 767 °C [15] in which it is spontaneously decomposed to secondary phases (mullite type phase, $Bi_2Fe_4O_9$, and sillenite type phase, $Bi_{25}FeO_{39}$). It is hard to conduct sintering of powder and in the same time to completely avoid this temperature interval. Together with the large bismuth loss at high temperatures, this is a huge barrier for densification of BF ceramics. That is the reason why so many studies about BF operate with powders. Magnetic properties are manifested and could be easily measured in powders, but for electrical and multiferroic properties, and also applications based on them, it is usually necessary to make dense ceramics.

Mechanisms of isovalent substitution-driven improvement of resistivity, polarization and magnetization are still not known, but there are implications that it is mainly driven by the average size of the A-site ion, and not by the dopant nature. The most probable reason is change in the Goldschmidt tolerance factor and, therefore, lowering the angle of the Fe—O—Fe bonds, which controls both magnetic and conduction properties leading also to structural transition [35–38].

Y^{3+} effective ionic radius of 1.02 Å for coordination number (CN) 8 is significantly smaller than 1.17 Å for Bi^{3+} in the same coordination [39] (for CN = 12, like it is in BF, Bi^{3+} has effective ionic radius of 1.36 Å [35], but there is no data for Y^{3+} in that coordination), so it is a candidate for the A-ion-size-caused changes. For this reason, an attempt of improving purity, electrical and magnetic properties of BF by doping with yttrium was conducted in this study. BF materials with 1, 3, 5 and 10 mol% of Bi^{3+} ions substituted with Y^{3+} ions were synthesized by the auto-combustion method, and then characterized and their properties compared with those of undoped BF samples. The doped samples were named according to Y content — from BYF1 to BYF10.

2. Experimental

$Bi_{1-x}Y_xFeO_3$ (x = 0, 0.01, 0.03, 0.05 and 0.1) was synthesized by auto-combustion method using $Bi(NO_3)_3 \cdot 6H_2O$ (Alfa Aesar, 98.0%), $Y(NO_3)_3 \cdot 6H_2O$ (Sigma–Aldrich, 99.8%), $Fe(NO_3)_3 \cdot 9H_2O$ (Alfa Aesar, 98.0–101.0%), urea (Riedel-de Haen, 99.0–100.5%), HNO_3 (65%). Auto-combustion synthesis method used here was already described in our previous paper [40]. It starts from the solution, so it is very convenient for homogeneous incorporation of small amount of doping metal cations. Precursor powders obtained after fuming combustion and drying were grinded in agate mortar and calcined at 600 °C for 2 h (heating rate 5 °C/min). Powders were grinded again and then pressed at 294 MPa. Samples were put in an oven preheated to 800 °C and taken out to room temperature after 1 h. Sintering was conducted in a closed dish together with a small amount of Bi_2O_3 powder which has diminished Bi evaporation by producing Bi-rich atmosphere.

Powders and ceramics were characterized by XRD (Brucker AXS D8, Ni-filtered Cu Kα radiation), SEM (Model TESCAN SM-300), Raman (TriVista 557 Raman system with the mixed Ar/Kr laser line (λ = 514.5 nm) as an excitation source with an incident laser power less than 60 mW in order to minimize the heating effect). Ceramic pellets were also characterized by ellipsometry (high resolution variable angle spectroscopic ellipsometer (SOPRA GES5E-IRSE), incidence angle $\theta_i = 65°$, in a wide spectral range 1.5–5.0 eV), ferroelectric (Radiant Precision Multiferroic Analyzer, at frequency of 2 Hz), impedance (HIOKI 3532-50 LCR HiTESTER, frequencies from 42 Hz to 1 MHz, temperatures between 50 and 250 °C) and magnetic measurements (SQUID, Quantum Design). Ceramics pellets were coated with silver electrodes for electrical characterization.

3. Results and discussion

3.1. X-ray diffraction

X-ray diffractograms of sintered BYF pellets are presented in Fig. 1a. Perovskite rhombohedral BF phase with very low presence of secondary mullite type phase ($Bi_2Fe_4O_9$) was formed. Unlike many different dopants (including Y) which have prevented [17,24,26–28] or enhanced [25,41] secondary phases formation, according to the results of this study Y content does not significantly affect product's purity. However, it makes noticeable changes in the structure of the crystal lattice. All diffraction peaks shift to higher 2θ angle with Y doping. At the same time, pairs in double peaks tend to merge into single ones. The gradual change is most obvious in the enlarged (1 1 0) and (1 −1 0) peaks presented in the inset of Fig. 1a. From the structural point of view, this means that the unit cell parameters are changing and strains are emerging, but also that crystallite size is decreasing. In one point, the change in unit cell parameters is enough large to induce gradual transferring of rhombohedral lattice system into orthorhombic one. Performed using FullProf Suite toolbar, the Rietveld refinement (Fig. 1b) of diffraction pattern for BYF10 sample indicates 6.6% of orthorhombic phase. Calculated lattice parameters are plotted in Fig. 1c, implying that unit cell slowly expands with smaller substitution rate, and then shrinks. With Y^{3+} ions smaller than Bi^{3+} this does not make much sense, but the effect of vacancies could explain it. With such small Y^{3+} ions concentration, average A-site ion size has smaller influence on unit cell size than eventual change in vacancies concentration. Less volatile Y^{3+} ions prevent evaporation of Bi^{3+} (explained in more detail in Section 3.3) and, therefore, vacancies formation, so average unit cell is expanding up to 3% of Y. Only at higher content the effect of smaller Y^{3+} ion size prevails and unit cell starts to shrink. The theoretical densities of ceramic samples were calculated using fitted unit cell parameters. Together with relative densities obtained using Archimedes' principle, theoretical densities are presented in Table 1.

The rhombohedral-orthorhombic structural transition for Y concentrations of around 10 mol% was also found in other studies [27,42]. Many other dopants cause this characteristic structural

Table 1
Densities of ceramic samples and fitted values of grain and grain boundary resistivities in BF and BYF ceramic samples at 250 °C.

Sample	Theoretical density (g cm^{-1})	ρ, % of theoretical density	$R_{g.}$ (Ωm)	$R_{g.b.}$ (Ωm)
BF	8.36	82	3.86×10^2	9.34×10^2
BYF1	8.33	75	1.92×10^3	1.06×10^4
BYF3	8.26	78	2.74×10^3	1.64×10^4
BYF5	8.20	80	1.03×10^4	1.94×10^4
BYF10	8.12[a]	72	1.19×10^4	3.84×10^4

[a] 8.07 for R3c phase and 8.90 for Pnma phase.

transition at some substitution degree [14,36,43,44], implying that the size of A-site ion and not some other characteristic is deciding for the structure.

3.2. Raman spectroscopy

Raman spectra of BYF ceramics in the wavenumber range 70–650 cm^{-1} are presented in Fig. 2. BiFeO$_3$ has 13 Raman active modes, which are not well resolved at room temperature [19,45]. In this range, three A$_1$ and five E modes can be clearly seen in BF sample and they are labeled in Fig. 2. The Raman spectra of BYF ceramic samples showed that the A$_1$ and E modes are of lower intensity, broadened and shifted to higher wavenumbers with increasing content of yttrium. This is particularly evident for the A$_1$ modes at 146, 171 and 220 cm^{-1}, which are related to Bi—O covalent bonds [46]. With reduction in average A-site ion mass, it is expected for modes to be shifted to higher wavenumbers. Besides, decreased peak intensities indicate declined stereochemical activity of A-site ion (since Y^{3+} ion does not possess a lone electronic pair) [34]. However, all BF modes are still present, so it is evident that although Bi—O bonds are partially replaced with Y—O bonds and there are significant structural changes, the rhombohedral phase, and not the orthorhombic one, prevails.

3.3. Scanning electron microscopy

Micrographs taken on fracture surfaces of the ceramic samples (Fig. 3) indicate that the grain size is reduced more than twice (from 4–10 μm to 1–3 μm) in Y doped samples. However, Y content of higher than 1 mole% has not further affected the grain size, so grains of doped samples are of similar size and morphology. Intragranular porosity present in undoped BF (probably originated from fast grain boundary movement) is disappearing at doping levels above 1 mol%. Intergranular porosity on the other hand increases, and all doped samples have smaller densities than BF (Table 1), but relative density is increasing with higher Y content up to 5 mol%. Y^{3+} ions are less mobile than Bi^{3+} ions at the sintering temperature (800 °C compared to 1450 °C reported for sintering of YFeO$_3$ [47]), and they slow down the solid state reaction, preventing the grain growth and lagging of pores inside grains, but lowering the final density. As a consequence of smaller mobility, Y would concentrate in the grain boundaries, which can explain a density improvement of doped samples with more Y: smaller coverage of grain boundaries with Bi^{3+} ions prevents its volatilization from the grains as well, decreasing the concentration of Bi^{3+} and O^{2-} vacancies and leading to slightly improved densities.

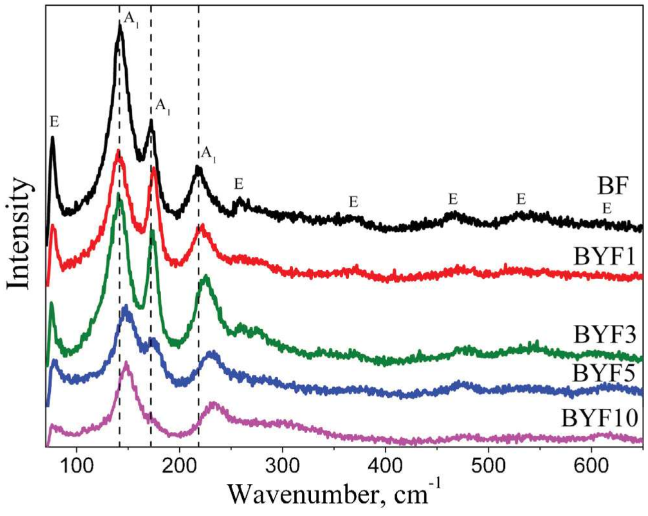

Fig. 2. Room-temperature Raman spectrum of BF and BYF ceramic samples.

If this presumption is correct, conductivities of both grains and grain boundaries would be markedly improved thanks to less mobile Y^{3+} ions at the surface and smaller number of vacant places having a role of charge carriers. Small density of the sample BYF10 could be explained with formation of new orthorhombic phase, which may require different temperature for densification. Many dopants were reported to inhibit the grain growth [24,41], and other authors have also assumed that doped BF may require slightly higher sintering temperatures [44].

3.4. Impedance spectroscopy

Fig. 4 represents characteristic complex impedance plots of Y doped BF ceramics at 250 °C. Data were fitted using ZView2 software, treating the sample as equivalent electrical circuit presented in the inset of Fig. 4. The complex impedance, Z is composed of its real and imaginary parts, Z' and Z'':

$$Z = Z' - jZ'' \tag{1}$$

The best fit was achieved comparing with three parallel resistor-constant phase element pairs lined in a row. Each pair manifests electrical properties (resistivity and capacitance) of some part of the material, and graphically looks like a semicircle. Semicircle at the lowest frequencies exists due to electrode and/or potentially formed conductive phases. It is usually not clearly visible. Middle frequencies semicircle (right in Fig. 4) represents grain boundary contribution to resistivity, while that of grains is at high frequencies (left in Fig. 4). Resistivities of grains and grain boundaries could be estimated from diameters of the corresponding semicircle. The obtained values for all samples at 250 °C are presented in Table 1. It is obvious from both Fig. 4 and Table 1 that resistivity is markedly improving with increasing the doping level. At the same time, grain boundaries have greater contribution to the total resistance than grains. Continuous resistivity rise is not in complete agreement with previous report that there is a decrease in resistivity at the temperature induced rhombohedral to orthorhombic phase transition in BF [5], and this could mean that Y is strongly influencing not only the structure, but also conduction mechanism.

The explanation for increasing electrical resistivity of BF by doping with Y^{3+} (or some other isovalent ion) mainly used by other authors is reduced unstoichiometry because of the lower volatility of dopant comparing to Bi [19–22] which does not sound very probable having in mind such low levels of doping. But if the fitted values of grain and grain boundary resistivity (presented in Table 1) are plotted as their dependence on composition (Fig. 5), similar conclusion can be brought out. Grain resistivity is improving almost linearly with doping level, while grain boundary resistivity show sharp increase with small amount of Y, and then increase linearly with Y content. If the assumption from the Section 3.3, predicting that Y^{3+} ions concentrate in the grain boundaries during the solid state reaction, was made again, the sharp increase could be explained. As grain boundaries contain only few ionic layers, even 1% of non-volatile dopant would make the boundaries significantly more resistive. Fewer vacancies in the grain boundaries mean fewer vacancies inside grains too, but 1% of dopant cannot make so pervasive change in grains containing most of the material, so the grain resistivity is not markedly improved. In higher content, Y occupies almost complete grain boundaries, increasing the grain boundary resistivity and disabling volatilization of Bi$_2$O$_3$, preventing formation of bismuth and oxygen vacancies and raising the grain resistivity as well as the grain

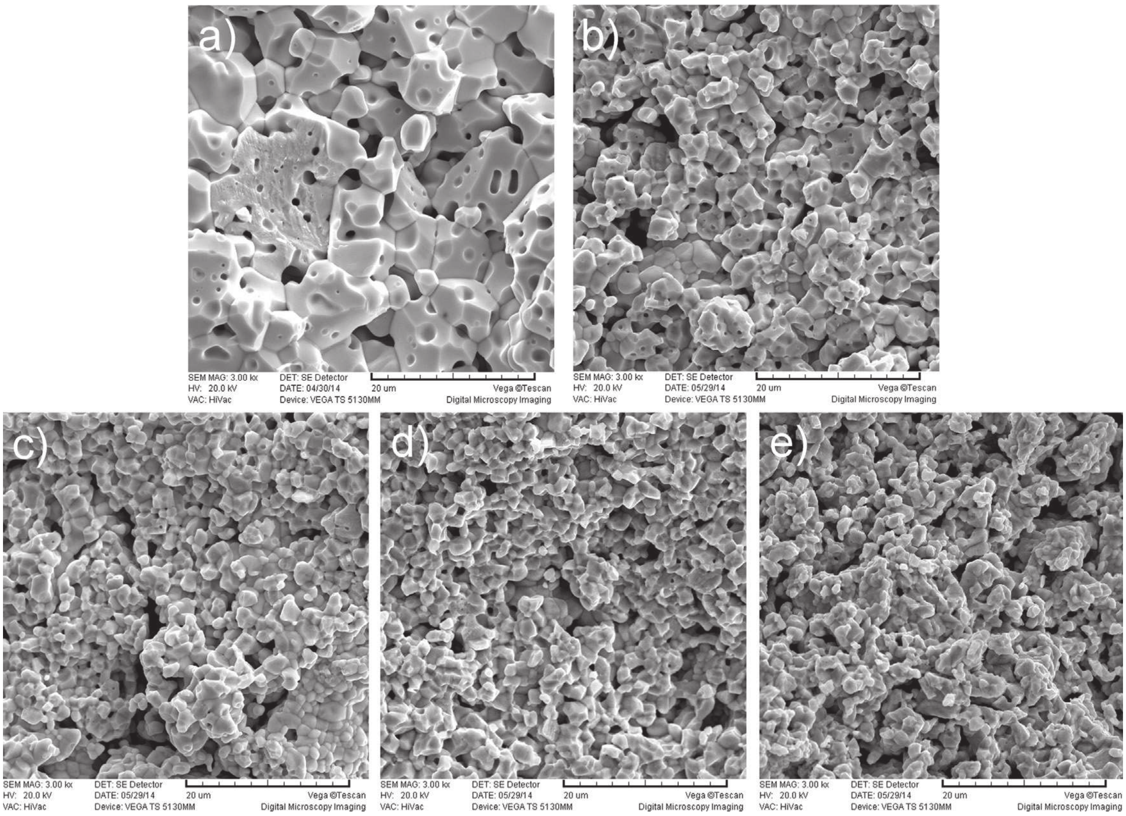

Fig. 3. SEM images of BF and BYF ceramic samples at fracture surfaces: BF (a), BYF1 (b), BYF3 (c), BYF5 (d) and BYF10 (e).

boundary resistivity. However, without precise characterization of grain boundaries, this cannot be firmly claimed.

The porosity of ceramics must also be considered as one of the conduction decisive factors. The air barrier is preventing charge mobility between separate grains, so they must move through the smaller surface. Taking this into account, obtained resistivities should be modified because of decreased area available for the charge transfer and extended effective thickness of the samples. With the assumption that the pores are uniformly distributed through ceramics, it is possible to estimate the change of area, so obtained resistivities should be multiplied with appropriate density factor (from 0.82 to 0.73). All these approximations do not make a significant change in general conducting behavior. Still, they could partly explain the resistivity increase in more porous, Y doped ceramics.

Other effects of dopant on electrical resistivity cannot be excluded. Yang et al. [35] reported that indirect influence of the average size of A-site ion on the band structure by buckling of Fe—O—Fe angle leads to more insulating character.

Another impedance related function useful for defining of electrical properties is the complex modulus. It could be derived from the complex impedance function Z using Eq (2) [48]:

$$M = j\omega C_c Z = j\omega C_c (Z' - jZ'') = \omega C_c Z'' + j\omega C_c Z' = M' + jM'', \qquad (2)$$

where ω is angular frequency ($\omega = 2\pi f$) and C_c is the capacitance of the empty cell dependent of the sample dimensions. $C_c = \varepsilon_0 S/d$,

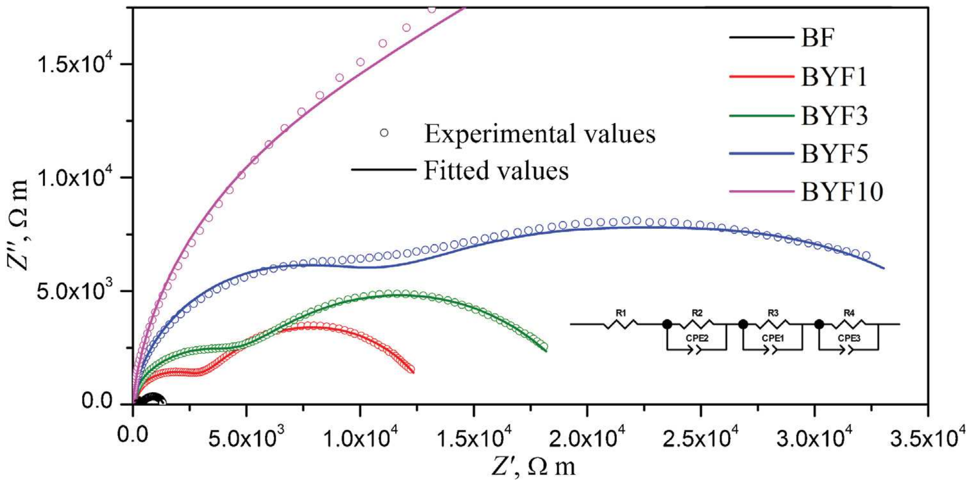

Fig. 4. Impedance plots of BF and BYF ceramic samples at 250 °C.

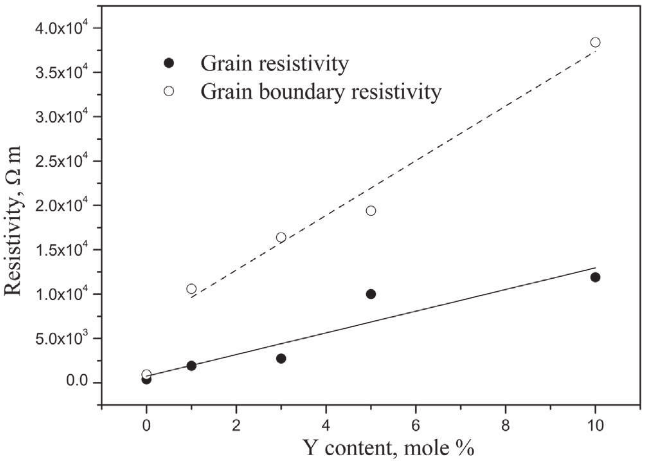

Fig. 5. Dependence of grain and grain boundary resistivity on Y content in BYF ceramics at 250 °C.

where ε_0 is vacuum permittivity ($\varepsilon_0 = 8.854 \times 10^{-12}\,\mathrm{F\,m^{-1}}$), S area of the sample covered with electrode, and d its thickness (separation between electrodes). Dimensionless quantities M' and M'' are the real and imaginary part of complex impedance function M, taking the values of $\omega C_c Z''$ and $\omega C_c Z'$, respectively. It is possible to get more information about conductivity from the plotted M''–f graphs. All samples exhibited strong temperature dependent relaxation, with large shift of the M'' peak to the higher frequency with higher temperature, which is becoming less expressed with doping (Fig. 6(a) and (b)). The shift indicates that the hopping of charge carriers dominates at higher temperatures [49]. The conclusion is that in BF ceramic samples conduction is thermally activated, but that becomes less pronounced with higher content of Y. There is also a shift in the peak position and shape with level of doping (Fig. 6(c) and (d)), again suggesting that charge carriers become less thermally activable.

Activation energies for conduction and relaxation processes could be calculated by applying Arrhenius equation (Eq. (3)) to various measured quantities:

$$x = x_0 e^{-E_a/k_b T}, \tag{3}$$

where x represents certain physical quantity (grain conductivity, grain boundary conductivity, dc conductivity, relaxation time), x_0 is pre-exponential factor, E_a is activation energy, k_b Boltsman constant ($k_b = 1.38 \times 10^{-23}\,\mathrm{J\,K^{-1}}$) and T absolute temperature. Grain and grain boundary conductivities were obtained as reciprocal values of the appropriate resistivities, dc conductivity was estimated from the plateau position in total conductivity dependence on frequency and relaxation times were calculated like reciprocal values of angular frequency at the M''–f peak positions. The Eq. (4), obtained after taking natural logarithm of both sides of the Eq. (3), could be easily fitted linearly confirming Debye like behavior. Needed energies could be calculated from the slopes of the fitted lines.

$$\ln(x) = \ln(x_0) - \frac{E_a}{k_b} \times \frac{1}{T}. \tag{4}$$

Activation energies of grain and grain boundary conductivities are plotted in Fig. 7, and all obtained energy values are presented in Table 2. It is obvious that Y as a dopant is reducing activation energies, making electrical properties less temperature-dependent. Differences in grain and grain boundary activation energies

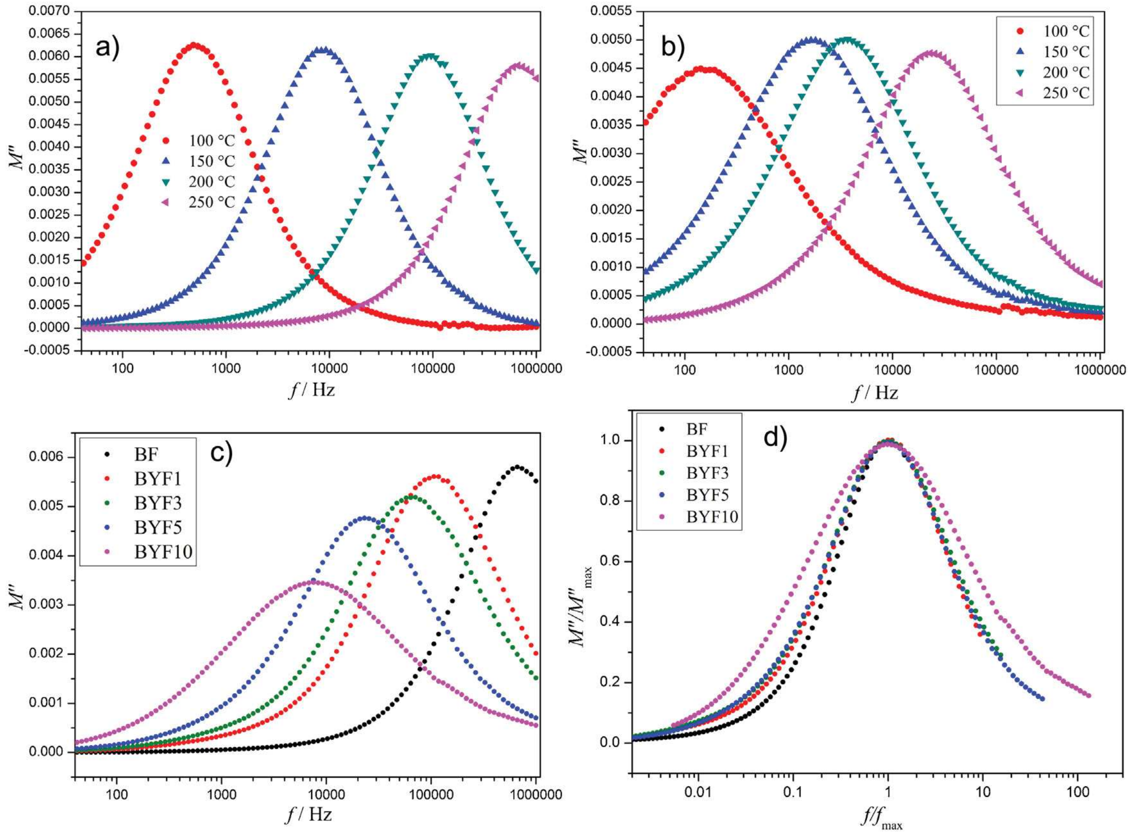

Fig. 6. Modulus curves for BF (a) and BYF5 (b) samples at different temperatures, and modulus curves (c) and normalized modulus curves (d) for BF and BYF ceramic samples at 250 °C.

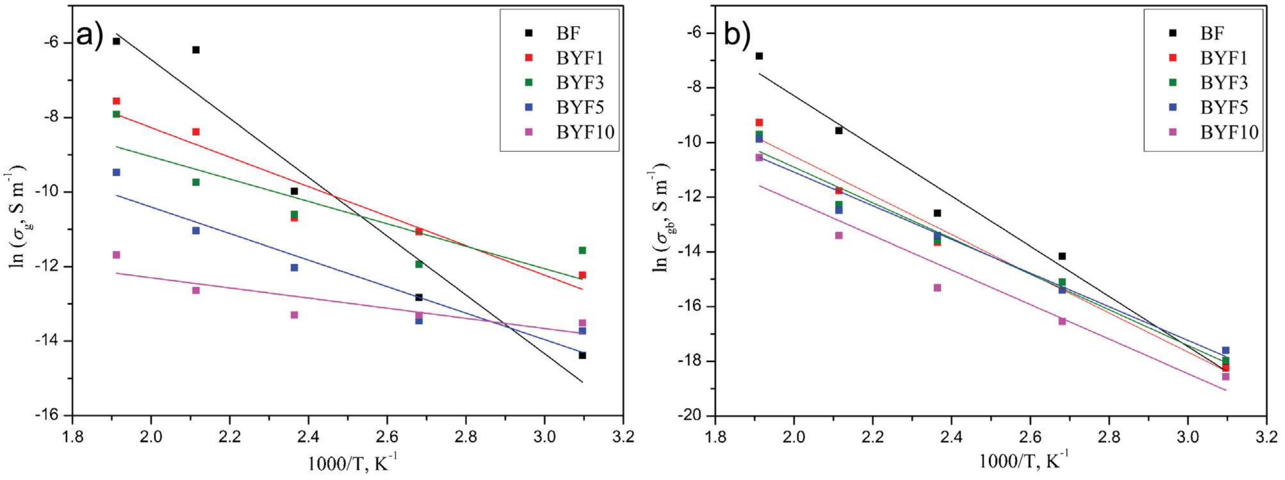

Fig. 7. Activation energies for grain (a) and grain boundary (b) conductivities for BF and BYF ceramic samples.

lead to conclusion that different type of charge carriers is responsible for conduction in them. Several possible charge carriers could cause occurrence of leakage currents in BF. In Kröger–Vink notation system [50] their formation could be presented by the following reactions:

$$O_O^{x} \rightarrow 1/2O_2 + V_O^{\bullet\bullet} + 2e' \quad (5)$$

$$Bi_{Bi}^{x} + 3e' \rightarrow Bi_{(g)} + V_{Bi}''' \quad (6)$$

$$Fe_{Fe}^{x} + e' \rightarrow Fe_{Fe}' \quad (7)$$

Other carriers like interstitial or foreign ions, or those originating from secondary phases could not be excluded, but in simplified system only 3 mentioned charge carrier types are considered: Bi^{3+} and O^{2-} vacancies and electrons. Being involved in all reactions, in certain equilibrium between Fe^{3+} reduction and formation of O^{2-} and Bi^{3+} vacancies, the electrons could be absent even when the O^{2-} vacancies are formed.

Since grain conductivity was shown to be more temperature stabile than grain boundary conductivity, and the same relationship exists between Y doped and undoped BF, the following assumption could be made. The main charge carriers in undoped BF are O^{2-} and Bi^{3+} vacancies, especially in grain boundaries, where they are more prone to be formed. With yttrium doping, the role of electrons, originated from Fe^{3+} to Fe^{2+} reduction (reverse Reaction (7)), is growing. The increase in temperature does not markedly affect electron movement, but vacancies are more mobile at higher temperatures, and that would explain why grain boundary resistivity changes faster with rise in temperature than grain resistivity, which is illustrated in the example of BYF3 ceramic sample in Fig. 8. There is even stabile grain resistivity region up to 100 °C depicting the electron hopping conducting behavior.

With Y addition, number of vacancies is decreasing, so grain boundary resistivity increases fast like it is obvious from Fig. 5. Grain resistivity also increases with Y doping, but only because conduction in grains also partly originates from the vacancies. Electron conductivity could be even improved, since electron-consuming Reaction (6) is prevented, but that is apparently not the case. With smaller number of vacancies, the total resistivity of Y doped BF is significantly less temperature-dependent. It is therefore possible to say that Y is changing the conduction mechanisms in BF ceramics.

Values of activation energies from Table 2 indicate that the same charge carriers (vacancies) are mostly responsible for grain boundary conduction, dc conduction and relaxation, but also grain conduction in undoped BF, while in grains of doped samples the case is different, and electrons are becoming more probable charge carriers.

3.5. Spectroscopic ellipsometry measurements

The band gap energies of BF and Y-doped BF ceramics were estimated using spectroscopic ellipsometry. The pseudo-dielectric function $<\varepsilon>$ was obtained directly from the measurements of the ellipsometric angles Ψ and Δ [51]:

$$<\varepsilon>= \sin^2\theta\left[\frac{1+\tan^2\theta(1-\rho)^2}{(1+\rho)^2}\right], \rho = \tan(\Psi)e^{i\Delta} \quad (8)$$

The imaginary part of the pseudo-dielectric function, $\varepsilon_2(E)$, is deduced from the ellipsometric measurements by applying two-phase model approximation (air/BYF ceramics) [52]. The energy gap (E_g) can be determined from ε_2 applying the Tauc formalism

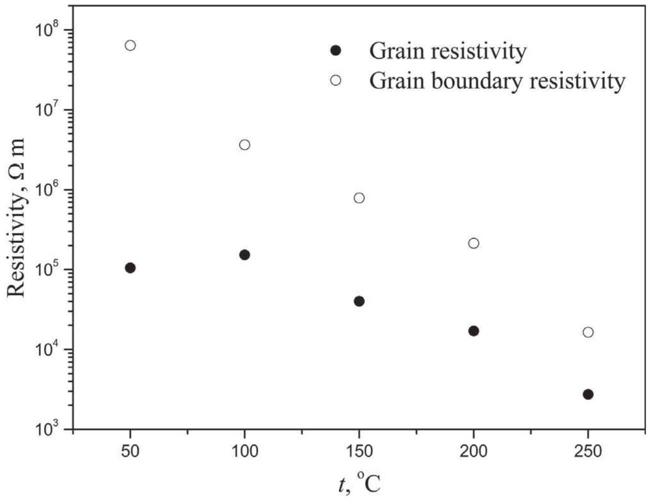

Fig. 8. Dependence of grain and grain boundary resistivities on temperature in the case of BYF3 ceramic sample.

Table 2
Activation energies for grain ($E_{c,g}$), grain boundary ($E_{c,gb}$) and dc ($E_{a,dc}$) conductivities and relaxation (E_r) in BF and BYF ceramic samples.

Sample	$E_{c,g}$ (eV)	$E_{c,gb}$ (eV)	$E_{a,dc}$ (eV)	E_r (eV)
BF	0.68	0.79	0.66	0.81
BYF1	0.34	0.62	0.56	0.77
BYF3	0.26	0.56	0.49	0.63
BYF5	0.29	0.53	0.43	0.54
BYF10	0.12	0.54	0.42	0.61

[53]. For the energies close to the E_g and in a case of direct transition, the following equation can be applied:

$$\varepsilon_2 E^2 \sim (E - E_g)^{1/2} \quad (9)$$

The plots $(<\varepsilon_2>E^2)^2$ vs. E for BYF samples are shown in Fig. 9. The direct band gap values for BYF ceramic samples were determined from extrapolation of the linear part of $(<\varepsilon_2>E^2)^2 - E$ to zero $(<\varepsilon_2>E^2)^2$ value. It was found that the band gap value increased from 2.36 eV for pure BF to 2.48 eV for BYF10. Such blue shift of the band gap with increasing Y content can be explained by the quantum size effect [54], which causes the change in the electronic band structure. This conclusion is in agreement with SEM analysis, which has shown that the grain size had decreased with increasing percent of Y. The change in band gap energy is very interesting for construction of materials with desired semiconducting properties. The change in band gap energy is very interesting for construction of materials with desired semiconducting properties.

3.6. Ferroelectric measurements

Ferroelectric hysteresis loops of ceramic samples presented in Fig. 10 show that the leakage currents are so high in the case of undoped BF (inset in Fig. 10), that it is impossible to induce any polarization without conduction, even with very small fields of 2 kV cm^{-1}. For all doped samples, electrical resistivity was high enough to measure proper ferroelectric loops, but as in many other bulk polycrystalline BF materials saturation was not achieved as it has been done in BF single crystals and thin films [5]. The reason is mostly the conduction, which is, although reduced, still substantial and leads to the electrical break up in higher fields, but partly also impossibility of making pellets thin enough to produce larger fields in them with used device. That is why it is not possible to talk about remnant or saturation polarization and coercive field, but it is possible to compare those values for different samples at certain field strength. At electrical field of 60 kV cm^{-1}, remnant (P_R) and saturation (P_S) polarizations are increasing for increased Y content up to 5 mol%, and reach P_R of 0.32 μC cm^{-2} and P_S of 0.64 μC cm^{-2} in case of BYF5 sample, while coercive field is around 25 kV cm^{-1}. Obtained values for the BYF5 sample are in concurrence to those from literature for similar compositions at similar conditions (Table 3), showing slightly larger polarizations and coercive field. The reduction of polarization values in sample BYF 10 corresponds to the formation of paraelectric orthorhombic phase [42], but could also be a consequence of decreased total number of 6s^2 lone electron pairs, which cause the ferroelectricity in BF. The changes of structure and resistivity have been considered more important than decreased stereochemical activity of the A-site ion [55,56]. Since there is still a significant amount of ferroelectric rhombohedral phase, the ferroelectric hysteresis is present in BYF10.

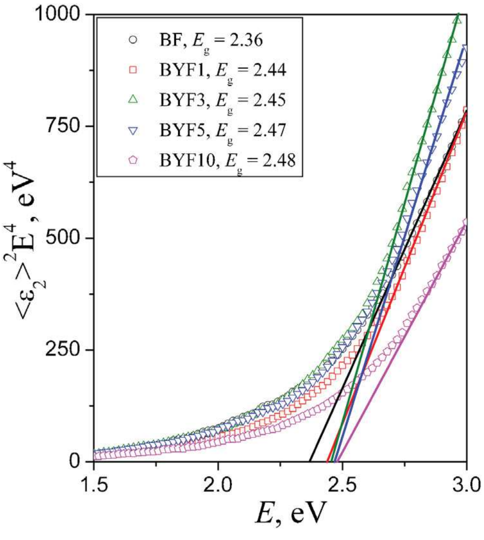

Fig. 9. Tauc plots for direct band gap transition for BF and BYF ceramic samples.

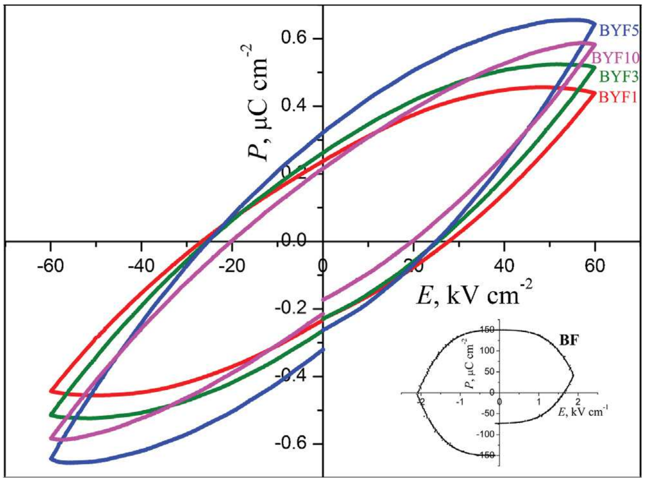

Fig. 10. Ferroelectric hysteresis loops for BF (inset) and BYF ceramic samples.

3.7. Magnetic characterization

Magnetization dependences on magnetic field for BF and BYF ceramics are presented in Fig. 11. Obtained loops are not saturated, so all the results will be assigned to certain field strength, similarly to ferroelectric measurements. Undoped BF showed typical antiferromagnetic behavior due to spiral arrangement of magnetic spins. With Y partially substituting Bi, saturation magnetization is gradually increasing, and at 5 mol% of Y it is possible to notice very weak ferromagnetic loop. The concentration of Y required for breaking spiral spin structure coincides with the phase transition from rhombohedral to orthorhombic, and ferromagnetic hysteresis loop, though still weak, occurs at 10 mol% of Y, with magnetization of ~0.13 emu g^{-1} at 10 kOe field and remnant magnetization just below 0.03 emu/g. The values of remnant magnetization and coercive field for BYF10 are compared with similar materials in Table 3. They are comparable to many Bi substituted BF systems (some of them also Y doped) [19,20,24,26,42], but lower than some others with Y [22,27,28]. Significantly higher magnetic field strengths of the latter comparing to those used in this study can explain this result. The coercive field strength of around 2.5 kOe in the case of the $Bi_{0.9}Y_{0.1}FeO_3$ sample is very large comparing to similar compositions [19,22,28,34], implying that more point defects, which pin domain walls, are formed [57]. That could be expected for the auto-combustion synthesis route [58].

Table 3
Comparison of the ferroelectric and magnetic parameters of BYF5 and BYF10 ceramics with other doped BF ceramics or powders.

Ferroelectric characteristic values					Ferromagnetic characteristic values					Ref.
Dopant	P_R (μC cm^{-2})	P_S (μC cm^{-2})	E_C (kV cm^{-1})	E (kV cm^{-1})	Dopant	M_R (emu g^{-1})	M_S (emu g^{-1})	H_C (kOe)	H (kOe)	
Y 5%	0.32	0.64	25	60	Y 10%	0.03	0.13	2.5	10	This study
Y 5%	0.15	0.30	10	20	Y 20%	0.11	6.27	0.01	20	[28]
Y 10%	0.03	0.16	8	47	Y 15%	–	3	–	60	[22]
Y 30%	2.5	–	15	110	Y 30%	0.09	0.31	0.15	1	[19]
Gd 20%	0.9	1.5	35	75	Gd 20%	–	2	–	30	[36]
Pr 15%	0.10	0.22	7	15	Pr 10%	–	0.003	–	5	[26]
Ba 20%	0.03	0.35	8	27	Ba 20%	5	13	0.9	15	[16]
La 10%	2	6	10	70	La 10%	0.04	0.8	0.25	15	[59]

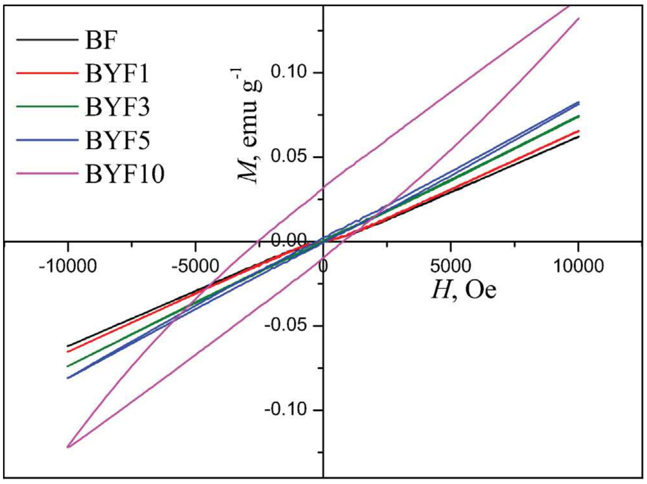

Fig. 11. Magnetic hysteresis loops for BF and BYF ceramic samples.

4. Conclusions

Yttrium doped bismuth ferrite ceramics were prepared by auto-combustion synthesis method. Up to 5 mol%, Y ions are well incorporated into the structure of bismuth ferrite, slightly changing Fe—O—Fe angle and unit cell size, but above this amount, change in the size of the average A-site ion is big enough to start inducing structural transition from rhombohedral to orthorhombic symmetry. Morphology is also changing, with smaller grains and larger porosity in doped ceramics. The resistivity is continuously increasing with Y content. Accumulation of Y^{3+} ions in the grain boundaries, where they replace mobile Bi^{3+} ions, slowing down the solid state reaction and preventing evaporation of Bi_2O_3 and formation of charge carriers, explain the changes in morphology and conduction. It is not only conductivity affected with Y content in BF, but also the mechanism of conduction. Charge carriers are transferring from vacancy prevailing to electron prevailing. Electrical properties are less temperature-dependent in doped BF and that is a good sign for potential application. Both ferroelectric and magnetic properties are affected by the change in composition and structure. Polarization values start to increase with doping, but after the structural transition ferroelectricity is declining. Weak ferromagnetism is arising in the 10 mol% Y doped sample due to the break in the spiral structure of magnetic spins. Large electrical and magnetic coercive fields indicate that a large number of defects, acting like pinning points for domain walls movement, are introduced into the structure with fast auto-combustion synthesis route. The weak rise of band gap with Y substitution was deduced from the spectroscopic ellipsometry. All the results indicate that Y induce improvement in electrical and magnetic properties of BF, and is one of the potential dopants for modeling the material with specific properties.

Acknowledgments

The authors would like to acknowledge the financial support of the Ministry of Education, Science and Technological Development of the Republic of Serbia (which also provides the scholarship for the author Nikola Ilić), project No. III 45021 and EU project COST IC 1208 action. Special thanks to Prof. Adelina Ianculescu from Polytechnics University of Bucharest, Romania for X-ray diffraction measurements, Dr. Lavinia Curecheriu from the Faculty of Physics, Alexandru Ioan Cuza University, Iasi, Romania for help regarding magnetic characterization and to Nikola Tasić from Institute for Multidisciplinary Research, University of Belgrade, Serbia for ferroelectric measurements.

References

[1] N.A. Hill, A. Filippetti, Why are there any magnetic ferroelectrics? J. Magn. Magn. Mater. 242–245 (2002) 976–979.
[2] W. Eerenstein, N.D. Mathur, J.F. Scott, Multiferroic and magnetoelectric materials, Nature 442 (2006) 759–765.
[3] N.A. Hill, Why are there so few magnetic ferroelectrics? J. Phys. Chem. B 104 (2000) 6694–6709.
[4] R. Safi, H. Shokrollahi, Physics chemistry and synthesis methods of nanostructured bismuth ferrite ($BiFeO_3$) as a ferroelectro-magnetic material, Prog. Solid State Chem. 40 (2012) 6–15.
[5] G. Catalan, J.F. Scott, Physics and applications of bismuth ferrite, Adv. Mater. 21 (2009) 2463–2485.
[6] X. Yang, Y. Zhang, G. Xu, X. Wei, Z. Ren, G. Shen, G. Han, Phase and morphology evolution of bismuth ferrites via hydrothermal reaction route, Mater. Res. Bull. 48 (2013) 1694–1699.
[7] V. James, P.P. Rao, S. Sameera, S. Divya, Multiferroic based reddish brown pigments: $Bi_{1-x}M_xFeO_3$ (M = Y and La) for coloring applications, Ceram. Int. 40 (2014) 2229–2235.
[8] B. Ramachandran, A. Dixit, R. Naik, G. Lawes, M.S.R. Rao, Charge transfer and electronic transitions in polycrystalline $BiFeO_3$, Phys. Rev. B 82 (2010) 012102.
[9] R.V. Pisarev, A.S. Moskvin, A.M. Kalashnikova, T. Rasing, Charge transfer transitions in multiferroic $BiFeO_3$ and related ferrite insulators, Phys. Rev. B 79 (2009) 235128.
[10] G.A. Smolenskii, I.E. Chupis, Ferroelectromagnets, Sov. Phys. Uspekhi 25 (1982) 475–493.
[11] X. Qi, J. Dho, R. Tomov, M.G. Blamire, J.L. MacManus-Driscoll, Greatly reduced leakage current and conduction mechanism in aliovalent-ion-doped $BiFeO_3$, Appl. Phys. Lett. 86 (2005) 062903.
[12] H.Y. Dai, Z.P. Chen, T. Li, R.Z. Xue, J. Chen, Structural and electrical properties of bismuth ferrite ceramics sintered in different atmospheres, J. Supercond. Novel Magn. 26 (2013) 3125–3132.
[13] K. Sardar, J. Hong, G. Catalan, P.K. Biswas, M.R. Lees, R.I. Walton, J.F. Scott, S.A.T. Redfern, Structural, spectroscopic, magnetic and electrical characterization of Ca-doped polycrystalline bismuth ferrite, $Bi_{1-x}Ca_xFeO_{3-x}/2$ ($x \leq 0.1$), J. Phys.-Condens. Mat. 24 (2012) 045905.
[14] D.C. Arnold, Composition-driven structural phase transitions in rare-earth-doped $BiFeO_3$ ceramics: a review, IEEE T. Ultrason. Ferr. 62 (2015) 62–82.
[15] T. Rojac, A. Bencan, B. Malic, G. Tutuncu, J.L. Jones, J.E. Daniels, D. Damjanovic, $BiFeO_3$ ceramics: processing electrical and electromechanical properties, J. Am. Ceram. Soc. 97 (2014) 1993–2011.

[16] A. Chaudhuri, K. Mandal, Study of structural ferromagnetic and ferroelectric properties of nanostructured barium doped bismuth ferrite, J. Magn. Magn. Mater. 353 (2014) 57–64.

[17] S.K. Pradhan, B.K. Roul, Electrical behavior of high resistivity Ce-doped $BiFeO_3$ multiferroic, Physica B 407 (2012) 2527–2532.

[18] K. Kalantari, I. Sterianou, S. Karimi, M.C. Ferrarelli, S. Miao, D.C. Sinclair, I.M. Reaney, Ti-doping to reduce conductivity in $Bi_{0.85}Nd_{0.15}FeO_3$ ceramics, Adv. Funct. Mater. 21 (2011) 3737–3743.

[19] L. Luo, W. Wei, X. Yuan, K. Shen, M. Xu, Q. Xu, Multiferroic properties of Y-doped $BiFeO_3$, J. Alloy. Compd. 540 (2012) 36–38.

[20] M. Luo, P.H. Zhou, Y.F. Liu, X. Wang, J.L. Xie, Influence of Y-doping on structure microwave dielectric and magnetic bahaviors in $BiFeO_3$, Physica B 450 (2014) 1–6.

[21] V. Singh, S. Sharma, P.K. Jha, M. Kumar, R.K. Dwivedi, Effect of Y^{3+} substitution on structural electrical and optical properties of $BiFeO_3$ ceramics, Ceram. Int. 40 (2014) 1971–1977.

[22] R.K. Mishra, D.K. Pradhan, R.N.P. Choudhary, A. Banerjee, Effect of yttrium on improvement of dielectric properties and magnetic switching behavior in $BiFeO_3$, J. Phys.-Condens. Matter 20 (2008) 045218.

[23] A.Z. Simoes, F.G. Garcia, C.S. Riccardi, Rietveld analysis and electrical properties of lanthanum doped $BiFeO_3$ ceramics, Mater. Chem. Phys. 116 (2009) 305–309.

[24] K.S. Nalwa, A. Garg, Phase evolution, magnetic and electrical properties in Sm-doped bismuth ferrite, J. Appl. Phys. 103 (2008) 044101.

[25] D. Varshney, P. Sharma, S. Satapathy, P.K. Gupta, Structural magnetic and dielectric properties of Pr-modified $BiFeO_3$ multiferroic, J. Alloy. Compd. 584 (2014) 232–239.

[26] N. Kumar, N. Panwar, B. Gahtori, N. Singh, H. Kishan, V.P.S. Awana, Structural dielectric and magnetic properties of Pr substituted $Bi_{1-x}Pr_xFeO_3$ $(0 \leq x \leq 0.15)$ multiferroic compounds, J. Alloy. Compd. 501 (2010) L29–L32.

[27] N.V. Minh, D.V. Thang, Dopant effects on the structural optical and electromagnetic properties in multiferroic $Bi_{1-x}Y_xFeO_3$ ceramics, J. Alloy. Compd. 505 (2010) 619–622.

[28] F. Bao Lin, X. Hao, X. Zhao Xian, Structure and multiferroic properties of Y-doped $BiFeO_3$ ceramics, Chin. Sci. Bull. 55 (2010) 452–456.

[29] T.P. Gujar, V.R. Shinde, C.D. Lokhande, Nanocrystalline and highly resistive bismuth ferric oxide thin films by a simple chemical method, Mater. Chem. Phys. 103 (2007) 142–146.

[30] V.R. Palkar, R. Pinto, $BiFeO_3$ thin films: novel effects, Pramana-J. Phys. 58 (2002) 1003–1008.

[31] D. Lebeugle, D. Colson, A. Forget, M. Viret, A.M. Bataille, A. Gukasov, Electric-field-induced spin flop in $BiFeO_3$ single crystals at room temperature, Phys. Rev. Lett. 100 (2008) 227602.

[32] T.-J. Park, G.C. Papaefthymiou, A.J. Viescas, A.R. Moodenbaugh, S.S. Wong, Size-dependent magnetic properties of single-crystalline multiferroic $BiFeO_3$ nanoparticles, Nano Lett. 7 (2007) 766–772.

[33] X. Zhang, Y. Sui, X. Wang, Y. Wang, Z. Wang, Effect of Eu substitution on the crystal structure and multiferroic properties of $BiFeO_3$, J. Alloys Compd. 507 (2010) 157–161.

[34] T.D. Rao, T. Karthik, S. Asthana, Investigation of structural magnetic and optical properties of rare earth substituted bismuth ferrite, J. Rare Earth 31 (2013) 370–375.

[35] C.-H. Yang, D. Kan, I. Takeuchi, V. Nagarajan, Jan Seidel, Doping $BiFeO_3$: approaches and enhanced functionality, Phys. Chem. Chem. Phys. 14 (2012) 15953–15962.

[36] W. Hu, Y. Chen, H. Yuan, G. Li, Y. Qiao, Y. Qin, S. Feng, Structure magnetic and ferroelectric properties of $Bi_{1-x}Gd_xFeO_3$ nanoparticles, J. Phys. Chem. C 115 (2011) 8869–8875.

[37] D. Kan, L. Palova, V. Anbusathaiah, C.J. Cheng, S. Fujino, V. Nagarajan, K.M. Rabe, I. Takeuchi, Universal behavior and electric-field-induced structural transition in rare-earth-substituted $BiFeO_3$, Adv. Funct. Mater. 20 (2010) 1108–1115.

[38] D. Kan, V. Anbusathaiah, I. Takeuchi, Chemical substitution-induced ferroelectric polarization rotation in $BiFeO_3$, Adv. Mater. 23 (2011) 1765–1769.

[39] R.D. Shannon, Revised effective ionic radii and systematic studies of interatomic distances in halides and chalogenides, Acta Cryst. A 32 (1976) 751.

[40] N.I. Ilić, A.S. Džunuzović, J.D. Bobić, B.S. Stojadinović, P. Hammer, M.M. Vijatović Petrović, Z.D. Dohčević-Mitrović, B.D. Stojanović, Structure and properties of chemically synthesized $BiFeO_3$. Influence of fuel and complexing agent, Ceram. Int. 41 (2015) 69–77.

[41] M.S. Bernardo, T. Jardiel, M. Peiteado, A.C. Caballero, M. Villegas, Sintering and microstructural characterization of W^{6+} Nb^{5+} and Ti^{4+} iron-substituted $BiFeO_3$, J. Alloy. Compd. 509 (2011) 7290–7296.

[42] Y.-J. Wu, X.-K. Chen, J. Zhang, X.-J. Chen, Structural transition and enhanced magnetization in $Bi_{1-x}Y_xFeO_3$, J. Magn. Magn. Mater. 324 (2012) 1348–1352.

[43] A.I. Iorgu, F. Maxim, C. Matei, L.P. Ferreira, P. Ferreira, M.M. Cruz, D. Berger, Fast synthesis of rare-earth (Pr^{3+}, Sm^{3+} Eu^{3+} and Gd^{3+}) doped bismuth ferrite powders with enhanced magnetic properties, J. Alloy. Compd. 629 (2015) 62–68.

[44] T. Karthik, T.D. Rao, A. Srinivas, S. Asthana, A-Site Cation disorder and Size variance effects on the physical properties of multiferroic $Bi_{0.9}RE_{0.1}FeO_3$ Ceramics ($RE = Gd^{3+}$, Tb^{3+}, Dy^{3+}), arXiv 1206 (2016) 5606.

[45] D. Kothari, V.R. Reddy, V.G. Sathe, A. Gupta, A. Banerjee, A.M. Awasthi, Raman scattering study of polycrystalline magnetoelectric $BiFeO_3$, J. Magn. Magn. Mater. 320 (2008) 548–552.

[46] M.K. Singh, S. Ryu, H.M. Jang, Structure, structural phase transitions, mechanical properties, defects-Polarized Rama n scattering of multiferroic $BiFeO_3$ thin films with pseudo-tetragonal symmetry, Phys. Rev. B 72 (2005) 132101.

[47] X. Yuan, Y. Sun, M. Xu, Effect of Gd substitution on the structure and magnetic properties of $YFeO_3$ ceramics, J. Solid State Chem. 196 (2012) 362–366.

[48] E. Barsoukov, J.R. Macdonald, Impedance Spectroscopy Theory, Experiment, and Applications, second edition, John Wiley & Sons, Inc., Hoboken, New Jersey, 2005.

[49] R.N.P. Choudhary, C. Behera, P.R. Das, R.R. Das, Development of bismuth-based electronic materials from Indian red mud, Ceram. Int. 40 (2014) 12253–12264.

[50] F.A. Kröger, H.J. Vink, Relations between the concentrations of imperfections in crystalline solids, Solid State Phys. 3 (1956) 307–435.

[51] H. Fujiwara, Spectroscopic Ellipsometry Principles and Applications, John Wiley and Sons Ltd., Chichester, England, 2003.

[52] H.G. Tompkins, E.A. Irene, Handbook of Ellipsometry, William Andrew, Norwich, 2005.

[53] J. Tauc, R. Grigorovici, A. Vancu, Optical properties and electronic structure of amorphous germanium, Phys. Stat. Sol. 15 (1966) 627–637.

[54] L. Brus, Electronic wave functions in semiconductor clusters: experiment and theory, J. Phys. Chem. 90 (1986) 2555–2560.

[55] P. Pandit, S. Satapathy, P. Sharma, P.K. Gupta, S.M. Yusuf, V.G. Sathe, Structural dielectric and multiferroic properties of Er and La substituted $BiFeO_3$ ceramics, Bull. Mater. Sci. 34 (2011) 899–905.

[56] H.Y. Dai, T. Li, R.Z. Xue, Z.P. Chen, Y.C. Xu, Effects of europium substitution on the microstructure and electric properties of bismuth ferrite ceramics, J. Supercond. Novel Magn. 25 (2012) 109–115.

[57] Nicola A. Spaldin, Magnetic Materials, Fundamentals and Applications, second edition, Cambridge University Press, Cambridge, 2011.

[58] S. Lorentzou, K. Karadimitra, C. Agrafiotis, A.G. Konstandopoulos, New Routes for Ferrite Powders Synthesis, Partec, 2004.

[59] P. Priyadharsini, A. Pradeep, B. Sathyamoorthy, G. Chandrasekaran, Enhanced multiferroic properties in La and Ce co-doped $BiFeO_3$ nanoparticles, J. Phys. Chem. Solids 75 (2014) 797–802.

AIP Journal of Applied Physics

Investigation of surface defect states in CeO2-y nanocrystals by Scanning−tunneling microscopy/spectroscopy and ellipsometry

Marko Radović, Bojan Stojadinović, Nataša Tomić, Aleksandar Golubović, Branko Matović, Ivana Veljković, and Zorana Dohčević-Mitrović

Citation: Journal of Applied Physics **116**, 234305 (2014); doi: 10.1063/1.4904516
View online: http://dx.doi.org/10.1063/1.4904516
View Table of Contents: http://scitation.aip.org/content/aip/journal/jap/116/23?ver=pdfcov
Published by the AIP Publishing

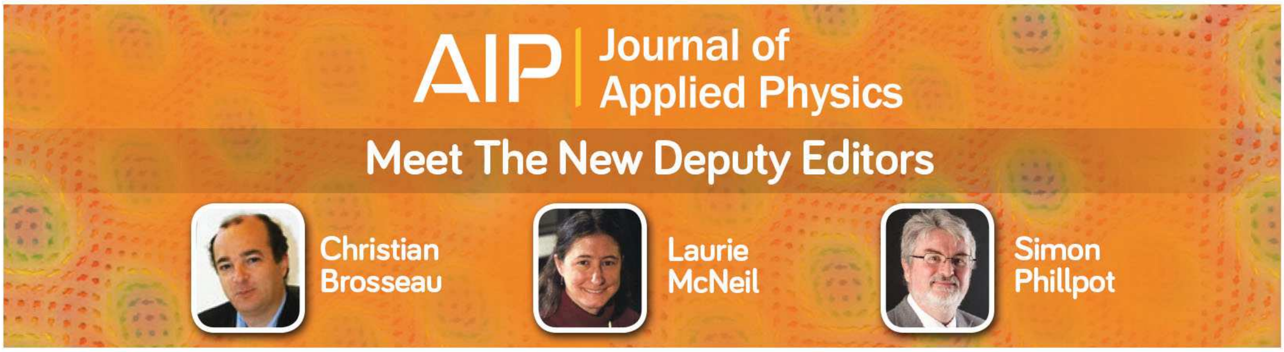

JOURNAL OF APPLIED PHYSICS **116**, 234305 (2014)

Investigation of surface defect states in CeO_{2-y} nanocrystals by Scanning−tunneling microscopy/spectroscopy and ellipsometry

Marko Radović,[1] Bojan Stojadinović,[1] Nataša Tomić,[1] Aleksandar Golubović,[1]
Branko Matović,[2] Ivana Veljković,[3] and Zorana Dohčević-Mitrović[1,a)]
[1]*Institute of Physics, Pregrevica 118, University of Belgrade, 11 000 Belgrade, Serbia*
[2]*Institute for Nuclear sciences “Vinča,” Materials Science Laboratory, University of Belgrade, 11 000 Belgrade, Serbia*
[3]*Institute for Multidisciplinary Research, Kneza Viseslava 1a, University of Belgrade, 11 000 Belgrade, Serbia*

(Received 19 September 2014; accepted 7 December 2014; published online 18 December 2014)

Synthesis process strongly influences the nanocrystalline CeO_{2-y} defective structure. The presence of surface defects, in the form of oxygen vacancies in different charge states (F centers), can change the electronic properties of ceria nanocrystals. Nanocrystalline CeO_{2-y} samples were synthesized using three different methods (precipitation, self-propagating room temperature, and hydrothermal synthesis). Raman spectroscopy was used to identify the presence of oxygen vacancies which presumably were formed at the nanoparticle surface. The defect concentration depended on the crystallite size of differently prepared CeO_{2-y} samples. Scanning tunneling microscopy/spectroscopy and ellipsometry were employed to investigate the electronic band structure of defective CeO_{2-y} nanocrystals. Scanning tunneling spectroscopy measurements demonstrated that inside the band gap of CeO_{2-y} nanocrystals, besides the filled 4 f states, appeared additional states which were related to occupied and empty F center defect states. From the ellipsometric measurements, using the critical points model, the energy positions of different F centers states and the values of the reduced band gap energies were determined. The analysis of obtained data pointed out that depending on the synthesis method, different types of F centers (F^+ and F^0) can be formed in the CeO_{2-y} nanocrystals. The formation of different F center defect states inside the ceria gap have a strong impact on the electrical, optical, and magnetic properties of ceria nanocrystals. © *2014 AIP Publishing LLC*. [http://dx.doi.org/10.1063/1.4904516]

I. INTRODUCTION

During the 20th century, CeO_2 based materials were widely applied in catalysis of automotive exhaust gases,[1,2] glass polishing,[3] high storage capacitors,[4] superconductor structures,[5] and gas sensors.[6] With significant expansion of nanotechnology, from the beginning of the 21st century, new areas of application emerged, such as solid oxide fuel cells[7,8] and spintronics.[9,10] Special interest was devoted to the optical properties of nanocrystalline ceria materials due to the appearance of new effects characteristic for nanosized materials. The application of ceria in the optical technologies, such as inorganic UV filters,[11] solar cells,[12,13] electrochromic smart windows,[14] and photocatalytic systems[15,16] requires precise control of the electronic band gap structure. For the ceria applications in oxide phosphorus materials[17] and optical conversion,[18] it is important to introduce additional electronic states inside the band gap. These electronic states can originate from the oxygen vacancies, whose concentration can be controlled by selecting the synthesis process or by a careful choice of the dopant.

In this paper, CeO_{2-y} nanocrystals were synthesized by three different methods in order to investigate the influence of different synthesis methods on the formation of oxygen vacancies, which can be formed as abundant defects on the surface of ceria nanocrystals. The combined research performed by scanning tunneling microscopy (STM)/scanning tunneling spectroscopy (STS) and spectroscopic ellipsometry enabled to identify the electron trapping sites, i.e., F^0 or F^+ centers, and to obtain better insight into the electronic band gap structure of differently prepared CeO_{2-y} nanopowders. The better knowledge of the electronic band gap structure of nanocrystalline ceria is crucial for the application of this material in the field of catalysis and spintronics.

II. EXPERIMENT

A. Materials synthesis

1. *Hydrothermal method*

Cerium (III) nitrate hexahydrate ($Ce(NO_3)_3 \times 6H_2O$), Acros Organics 99.5%) and Polyvinylpyrrolidone (PVP) (Aldrich) were used as starting materials. During a synthesis procedure, 1 g of PVP was mixed with 40 ml of distilled water under vigorous magnetic stirring at room temperature, until homogeneous solution was obtained. 3 mmol of cerium source was slowly added to the PVP solution (also under vigorous stirring at room temperature) in order to obtain a well-dissolved solution. No pH adjustment was made. Homogeneous solution was transferred into an autoclave and prepared at 200 °C for 6 h ($T = 200\,^\circ C$, $t = 6\,h$). The precipitate was washed with distilled water and dried at 80 °C overnight.

---

[a] Author to whom correspondence should be addressed. Electronic mail: zordoh@ipb.ac.rs

0021-8979/2014/116(23)/234305/8/$30.00

2. Self propagating room temperature synthesis (SPRT)

In this experiment, starting reactants were cerium nitrate hexahydrate ($Ce(NO_3)_3 \times 6H_2O$) (Acros Organics 99.5%) and sodium hydroxide (Carlo Erba). Hand-mixing of nitrates with NaOH was performed in alumina mortar for approximately10 min until mixture got light brown. After being exposed to air for 4 h, the mixture was suspended in water. Rinsing out of $NaNO_3$ (four times with distilled water and twice with ethanol) was performed in centrifuge at 3500 rpm for 10 min. The precipitate was dried at 60 °C overnight. The reaction can be written as follows:

$$2[(Ce(NO_3)_3 \times 6H_2O] + 6NaOH + (1/2 - y)O_2 \rightarrow 2CeO_{2-y} + 6NaNO_3 + 15H_2O. \quad (1)$$

3. Precipitation method

The $Ce(SO_4)_2 \times 4H_2O$(Acros Organics) was dissolved in distilled water and formed a clear solution with a concentration of 0.4 M. The ammonia solution (Carlo Erba, 25%) was added drop-wise to the solution at room temperature (with continuous magnetic stirring) until the desired pH value was achieved (~9). Yellow suspension appeared and gradually became brown in color with continuous addition of the ammonium solution. The resulting room-temperature precipitate was filtered and washed with distilled water for several times, dried at 80 °C in air and calcinated at 200 °C for 4 h. The corresponding chemical reactions are

$$Ce(SO_4)_2 + 4NH_4OH \rightarrow Ce(OH)_4 \downarrow + 2(NH_4)_2SO_4 \quad (2)$$

$$Ce(OH)_4 \rightarrow CeO_2 + 2H_2O. \quad (3)$$

The samples produced by hydrothermal, SPRT, and precipitation methods are labeled as $H{-}CeO_{2\text{-}y}$, $S{-}CeO_{2\text{-}y}$, and $P{-}CeO_{2\text{-}y}$ for brevity.

4. Samples preparation

The X-ray diffraction (XRD) measurements were performed on powder samples. The Raman and ellipsometric measurements were performed on powder samples pressed into the pellets. For the STM/STS measurements, the synthesized ceria nanopowders were dispersed in ethanol and treated in the ultrasonic tub for 20 min in order to minimize the number of agglomerated particles. One drop of obtained suspension was deposited on a freshly cleaved, grounded highly ordered pyrolitic graphite (HOPG) surface, and after drying was loaded in the microscope chamber.

B. Materials characterization

The crystalline phase of cerium dioxide nanocrystals was studied by XRD method on a Siemens D-5000 diffractometer with Cu Kα radiation. The diffraction patterns were recorded over the 2θ range from 20° to 80°. The STM and STS measurements were carried out using Omicron scanning probe microscope (SPM) VT AFM 25. The micro-Raman spectra were collected in the backscattering configuration using a Jobin Yvon T64000 spectrometer equipped with a nitrogen-cooled CCD detector. The argon ion (Ar^+) laser line at $\lambda = 514.5$ nm was used as an excitation source. Ellipsometric measurements were performed at $\theta_i = 70°$ incidence angle in the UV−V is spectral range, using variable angle spectroscopic ellipsometer (SOPRA GES5E–IRSE) of the rotating polarizer type. The high resolution spectra were collected with a step of 0.02 eV and prolonged exposure time.

III. RESULTS AND DISCUSSION

In Fig. 1 are shown the XRD patterns of the investigated samples with the Miller indices which correspond to the XRD peaks of CeO_2. All samples crystallized into fluorite type structure of CeO_2 and no amorphous or any other phase was detected. The average crystallite sizes (L_0) were calculated using Wiliamson-Hall method[19] and obtained values are also presented in Fig. 1. The diffraction peaks of CeO_2 samples, produced by SPRT and precipitation method, are broadened indicating that these samples are composed of very fine, nanometric size particles of lower crystallinity. The hydrothermal method produced significantly larger crystallites in comparison with SPRT and precipitation methods and consequently, the XRD pattern of this sample resembles to the XRD spectrum of well-crystallized sample.

Raman spectroscopy is more sensitive to structural disorder induced by oxygen vacancies than XRD method. In nonstoichiometric oxides like $CeO_{2\text{-}y}$, the oxygen vacancies are usually formed in the surface layer[20] and the presence of defects, as well as, defect concentration distribution can be

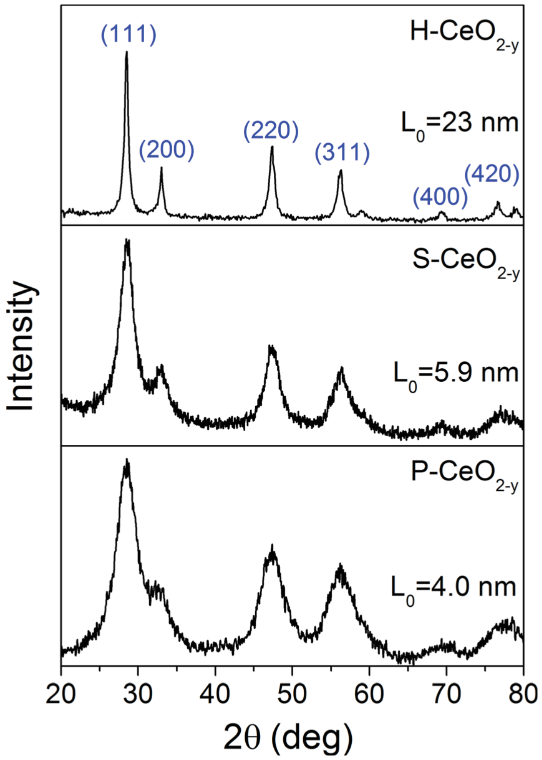

FIG. 1. XRD patterns of $CeO_{2\text{-}y}$ nanopowders synthesized by hydrothermal ($H{-}CeO_{2\text{-}y}$), SPRT ($S{-}CeO_{2\text{-}y}$) and precipitation ($P{-}CeO_{2\text{-}y}$) method, together with a corresponding average crystallite size values.

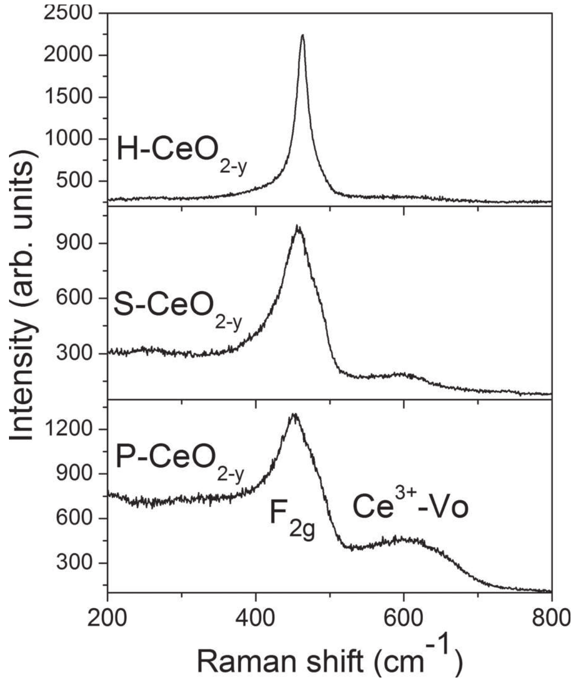

FIG. 2. Room-temperature Raman spectra of differently synthesized CeO_{2-y} nanocrystals.

successfully investigated by Raman spectroscopy.[21] In Fig. 2 are presented the Raman spectra of differently synthesized CeO_{2-y} nanocrystals in the spectral range 350–750 cm^{-1}, where the F_{2g} mode and oxygen-vacancy-related Raman modes are positioned. The F_{2g} mode frequency and linewidth are essentially determined by the particle size, size distribution, and the presence of defects like oxygen vacancies.[22–24] In a case of $H-CeO_{2-y}$ sample, with the largest crystallite size, the F_{2g} mode is narrow and positioned at 463 cm^{-1}, very close to the value for bulk CeO_2 sample (464.4 cm^{-1}).[23] In the case of $S-CeO_{2-y}$ and $P-CeO_{2-y}$ samples, with much smaller crystallite size, the F_{2g} peak is very broad, asymmetric, and shifted to lower frequencies (458 cm^{-1} and 454 cm^{-1}, respectively).

The other mode positioned around 600 cm^{-1} originates from Ce^{3+}–oxygen vacancy (V_O) complexes. The intensity of this mode is proportional to the concentration of oxygen vacancies.[24–26] From Fig. 2, it can be seen that $P-CeO_{2-y}$ sample has the highest intensity of vacancy mode, implying that this sample contains the highest concentration of oxygen vacancies. In the case of $S-CeO_{2-y}$ sample, the concentration of oxygen vacancies is lower, whereas $H-CeO_{2-y}$ sample has the lowest concentration of oxygen vacancies, because the corresponding Raman mode is barely visible. The observed behavior of the oxygen vacancy mode in investigated samples is expected, having in mind that $P-CeO_{2-y}$ sample has the smallest average crystallite size and consequently, the highest concentration of defects is expected to be found in this sample.

The STM/STS measurements present powerful tool for direct investigation of the electronic structure of nanomaterials. Using Raman spectroscopy, we have observed significant variations in the oxygen vacancy concentration in analyzed samples. Having in mind that defect states are abundant on the surface of nanoparticles, we applied STM/STS technique to examine how the presence of defects influences the electronic structure of synthesized ceria samples. Electronic band structure of stoichiometric CeO_2 is composed of O2p valence band states and 5d conduction band (CB) states. Inside the O2p−Ce5d band gap, there is narrow and localized Ce 4*f* band composed of empty $4f^0$ states. By measuring the change in the tunneling current with the bias voltage, between the STM tip and ceria nanocrystals, information about the electronic density of states can be obtained.[27] Current vs. voltage spectra are shown in Fig. 3(a) for the $H-CeO_{2-y}$, $S-CeO_{2-y}$, and $P-CeO_{2-y}$ samples together with the STM images of individual nanocrystals on which the STS measurements were performed. The crystallite size of individual nanocrystals was in good agreement with the average crystallite size obtained from XRD data.

In Fig. 3(b) are shown the differential conductance spectra (dI/dV) of investigated samples.

For the negative bias voltage, the information about the occupied electronic states can be obtained. The most prominent occupied band around −3 V, in all investigated samples from the Fig. 3(b), corresponds to the O2p band.[28,29] When the oxygen vacancies are formed, part of Ce^{4+} atoms is reduced to Ce^{3+} atoms, resulting in a partial filling of the Ce 4*f* states. As a consequence, the Ce 4*f* band splits into occupied $4f^1$ and unoccupied $4f^0$ states. The occupied $4f^1$ states in CeO_2, detected by XPS measurements, were positioned around 1.2–1.5 eV above the top of the valence band.[30] In all investigated samples, $4f^1$ states appear about 0.7–1eV above

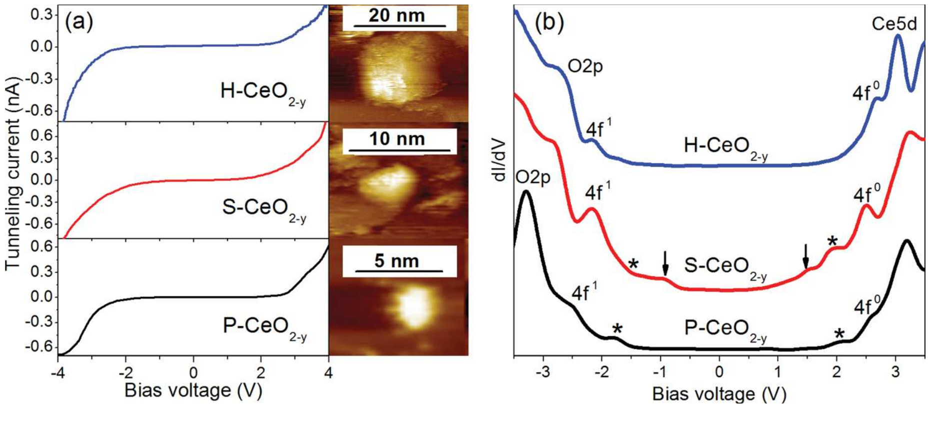

FIG. 3. (a) Current vs. voltage curves together with STM images of single ceria nanocrystals. Images were taken at $V_{bias} = 3$ V and I = 100–300 pA. (b) Differential conductance spectra (dI/dV) for $H-CeO_{2-y}$, $S-CeO_{2-y}$, and $P-CeO_{2-y}$ samples. Arrows and asterisks indicate the position of dI/dV maxima which belong to F^+ and F^0 center defect states.

the valence band. In the case of S–$CeO_{2\text{-y}}$ and P–$CeO_{2\text{-y}}$ samples, besides the $4f^1$ states, we have detected another occupied defect electronic states marked with arrows and asterisks in Fig. 3(b). In the S–$CeO_{2\text{-y}}$ sample, these states appear as dI/dV peaks, approximately at −1 V and −1.5 V. For the P−$CeO_{2\text{-y}}$ sample, occupied states appear at −1.7 V, whereas no similar states are detected for H−$CeO_{2\text{-y}}$ sample. According to the paper of Jerratsch *et al.*,[31] two peaks above the valence band in the differential conductance spectra of defective CeO_2 films were ascribed to the splitting of the occupied $4f^1$ band. On the other side, the DFT calculations performed by Han *et al.*[32] on defective CeO_2 structure revealed that for increasing vacancy concentration, the electrons are localized not only on 4*f* states but also on the vacancy sites. This is manifested as further splitting of the gap states into empty and full states. Therefore, the gap states have substantial contributions from the electrons on the oxygen vacancy site in the case of high oxygen deficiencies.[32]

Surface defects like oxygen vacancies can trap two, one, or none electrons forming F^0, F^+ and F^{++} centers. F^0 and F^+ centers form localized occupied and empty states in the band gap, whereas F^{++} centers form only localized empty states near the conduction band. These types of defects are registered in various oxide nanomaterials, such as MgO,[33] HfO_2,[34] and TiO_2.[35] The STS measurements performed on defect rich surface of MgO[33] showed that the additional states were formed in the band gap of MgO. These states were ascribed to empty and occupied F center defect states. The appearance of these states in MgO supports our findings in ceria samples. In our recently published paper,[36] we have demonstrated that ceria nanocrystals synthetized by SPRT and precipitation methods exhibited different luminescence properties which originated from different F center defect states. PL spectra have shown that F^+ centres were dominant in the CeO_2 sample synthesized by SPRT method, whereas F^0 centres were the major defects in CeO_2 sample synthesized by precipitation method. Furthermore, the EPR analysis of these samples confirmed the existence of paramagnetic F^+ centers only in ceria samples produced by SPRT method.[36]

For positive bias voltage, the information about the empty electronic states can be obtained. The most prominent empty state around 3 V corresponds to the Ce 5d states which presents the upper part of the CB.[29] At approximately 2.5 V, we have $4f^0$ states which form the lower part of CB. Just below the $4f^0$ state, additional defect electronic states emerge in S−$CeO_{2\text{-y}}$ and P−$CeO_{2\text{-y}}$ samples which are marked with arrows and asterisks in Fig. 3(b). These peaks correspond to the empty states of F centers. The appearance of oxygen vacancy related empty electronic state, at similar energy, was detected by STS measurements performed on defect rich surface of ZnO nanorods.[37] Continuous rise of differential conductance spectrum for S−$CeO_{2\text{-y}}$ sample, starting from 1 V, indicates significant presence of unoccupied electronic trap states which can originate from different kinds of F center states, i.e., from F^0, F^+ or F^{++} centers. In the case of P−$CeO_{2\text{-y}}$ sample, there is one visible empty state at 2 V and in a case of H−$CeO_{2\text{-y}}$ sample, there are no visible empty states below the $4f^0$ band.

Another effect which can lead to the appearance of the peaks in the differential conductance spectra of metal and semiconductor nanoparticles is the so called Coulomb charging effect, where electron transport between the STM tip and nanocrystal is governed by electron-electron repulsion inside the spatially confined nanostructures.[38,39] This phenomena manifest as staircase behavior in the I(V) curves. The I/V curves of our investigated samples are flat and the absence of Coulomb staircases is evident.

Spectroscopic ellipsometry is a complementary technique to the STS measurements for the investigation of the electronic band structure and defect electronic states in nanomaterials. Additional motivation for using ellipsometry in this study lies in the fact that it is very sensitive method to the changes in the surface structure of the nanocrystals, where most of the defects are concentrated.

Optical properties of differently synthesized cerium dioxide nanocrystals were investigated using spectroscopic ellipsometry in the 2–5 eVspectral region. From the measurements of ellipsometric angles Ψ and Δ, by using the two-phase model approximation ($CeO_{2\text{-y}}$ nanoparticles/air), we have obtained the pseudo-dielectric function spectra.[40] The measurement of pseudo-dielectric function enables direct determination of real and imaginary parts of the complex dielectric function $\varepsilon(E) = \varepsilon_1(E) + i\varepsilon_2(E)$. The standard critical points (CPs) model for the dielectric function, in the case of 1D and 3D CPs ($m \neq 0$), is given by[41–43]

$$\varepsilon(E) = C - Ae^{i\varphi}(E - E_0 + i\Gamma)^m, \tag{4}$$

and for 2D, CPs ($m = 0$) can be written as

$$\varepsilon(E) = C - Ae^{i\varphi}\ln(E - E_0 + i\Gamma), \tag{5}$$

where A, E_0, Γ, and φ are the amplitude, energy threshold, broadening, and the excitonic phase angle of CP, respectively. The factor m determines the dimensionality of the critical point ($m = -1/2$ for 1D, $m = 0$ for 2D and $m = 1/2$ for 3D CP). To perform a line-shape analysis of the structures in the $\varepsilon(E)$ and to obtain the parameters of the critical points for ceria nanocrystals, we used the expressions from the articles of Albornoz *et al.*[44] and León *et al.*[45] to fit the second derivative spectra of the imaginary part of the dielectric function ($d^2\varepsilon_2/dE^2$).

The second derivative spectra of $\varepsilon_2(E)$ (open symbols) for all investigated samples are shown in Fig. 4(a), together with numerical fits (solid lines) based on CP model. An appropriate level of smoothing was applied in order to suppress the noise in the derivative spectra without distorting the line shape. We have used six critical points to describe the observed features in the spectra and the obtained parameters are presented in Table I.

The value of excitonic phase angle φ, for each CP, was obtained as the best-fit parameter. The obtained φ values were non-integer multiples of $\pi/2$ ($0 \leq \varphi \leq \pi/2$ for 3D and 1D CP and $0 \leq \varphi \leq 3\pi/2$ for 2D CP), due to the excitonic effects[43,44] which are expected to be more pronounced in confined systems like ceria nanocrystals.

Numerical modeling of ellipsometry data was carried out having in mind that defect structure of ceria nanocrystals can be well described by the core-shell model.[20] According

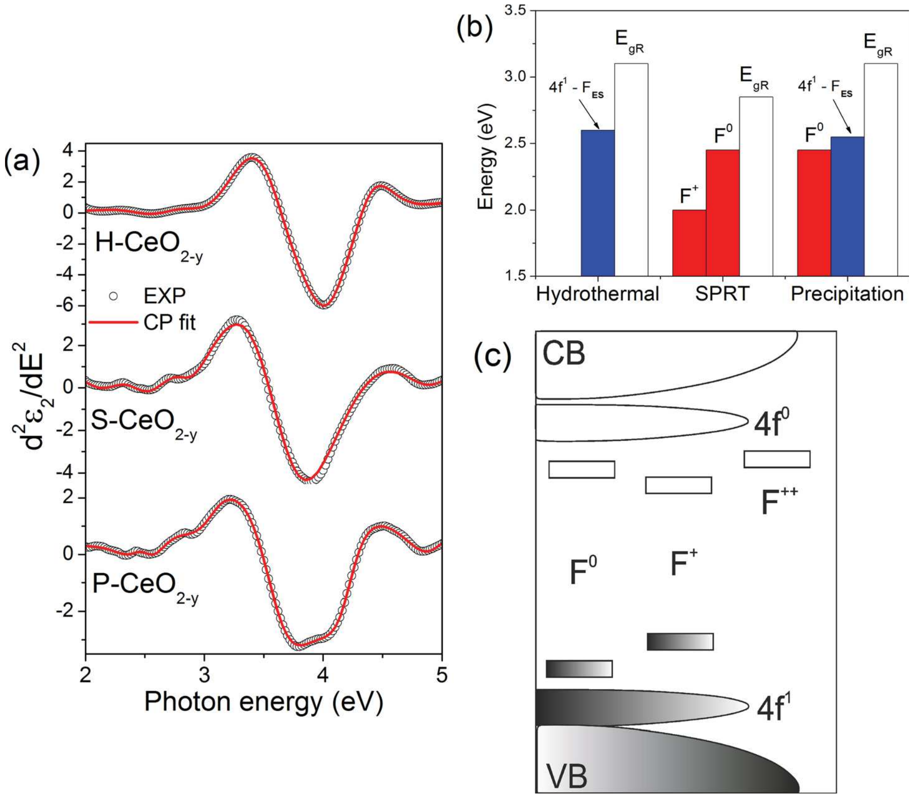

FIG. 4. (a) Numerical fits of the $d^2\varepsilon_2/dE^2$ spectra (open symbols) using the CP lineshape analysis is given by solid (red) lines, (b) energy values of the reduced band gap and defect electronic states transitions obtained from CP model fitting, and (c) schematic representation of the electronic band gap structure of $CeO_{2\text{-}y}$ nanocrystals.

to this model, the surface shell of ceria nanocrystals is defect rich,[20] whereas the core is essentially bulk-like CeO_2. Therefore, the interband transitions related to the fundamental band gap features were well fitted with 3D line shape. The interband transitions which originate from defect shell were best fitted with 2D line shape, whereas for the electronic transition related to the surface oxygen species, 1D line shape yielded slightly better fit than 2D line shape.

The most prominent peak at around 4 eV in the $d^2\varepsilon_2/dE^2$ spectra of the synthesized samples from Fig. 4(a) corresponds to the optical band gap of bulk cerium dioxide, i.e., the transition from O 2p to the Ce $4f^0$ states.[29] This transition is split into two states ($^2F_{5/2}$ and $^2F_{7/2}$), because of the spin−orbit interaction,[46] so we fitted the main peak with two CPs (peaks 4 and 5 in Table I). The first CP is located at 3.6 eV for $S{-}CeO_{2\text{-}y}$ and $P{-}CeO_{2\text{-}y}$ and at 3.73 eV for $H{-}CeO_{2\text{-}y}$ sample. Obtained energy values match the energy of optical band gap transition in CeO_2.[47] Second CP of this transition, at 4.2 eV for $S{-}CeO_{2\text{-}y}$ and $P{-}CeO_{2\text{-}y}$ samples and at 4.27 eV for $H{-}CeO_{2\text{-}y}$ sample, corresponds to the transition from O 2p states into the upper part ($^2F_{7/2}$) of the $4f^0$ states. We can observe from fitting parameters that spin−orbit splitting in the $S{-}CeO_{2\text{-}y}$ and $P{-}CeO_{2\text{-}y}$ samples ($\Delta_{SO} = 0.6$ eV) is higher than for bulk sample ($\Delta_{SO} = 0.25$ eV), probably due to the strong electron confinement in nanocrystals.[48] The O2p→$4f^0$ transition is characteristic transition for bulk CeO_2 so it was treated as 3D CP.

TABLE I. Fit parameters of the CPs.

CP	$H{-}CeO_{2\text{-}y}$	$S{-}CeO_{2\text{-}y}$	$P{-}CeO_{2\text{-}y}$
E_1 (eV)	…	2	2.45
Γ_1 (eV)	…	0.32	0.2
E_2 (eV)	2.6	2.44	2.55
Γ_2 (eV)	0.25	0.3	0.24
E_3 (eV)	3.2	2.86	3.1
Γ_3 (eV)	0.46	0.24	0.28
E_4 (eV)	3.73	3.6	3.59
Γ_4 (eV)	0.36	0.58	0.43
E_5 (eV)	4.27	4.2	4.2
Γ_5 (eV)	0.24	0.67	0.24
E_6 (eV)	4.8	4.95	4.96
Γ_6 (eV)	0.4	0.45	0.36

In the lower energy region from the main peak in Fig. 4(a), additional structures appear in the $d^2\varepsilon_2/dE^2$ spectra which originate from the presence of defect electronic states in the $CeO_{2\text{-}y}$ gap. The assignments of these CPs are given as follows:

- *F center states*
  The CPs at the lowest energies (2–2.45 eV) from Table I were ascribed to different F center types of defects. F centers are characteristic for defect-rich shell of ceria nanocrystals and in a case of interband transitions which correspond to F center states, the best fits were obtained with 2D line shape.

  In a case of $S{-}CeO_{2\text{-}y}$ sample, CP at 2 eV corresponds to the transition marked with arrows in Fig. 3(b). Previous results on HfO_2 (Ref. 34) and TiO_2 (Ref. 35) have pointed out that singly occupied vacancies (F^+ centers) introduce electronic states deeper in the band gap. Therefore, we ascribed CP at 2 eV to the F^+ center type of defect. These deep localized states appear only in $S{-}CeO_{2\text{-}y}$ sample. In a case of P$-$CeO$_{2\text{-y}}$ sample, the CP at 2.45 eV corresponds to the transition marked with asterisk in Fig. 3(b). This interband transition can correspond to F^0 type of defects for which the characteristic is that the occupied/empty electronic states lie closer to the valence/conduction band.[34] For H$-$CeO$_{2\text{-y}}$ sample, there are no pronounced CP peaks which can correspond to F$^+$ or F^0 states and we have not observed any additional states in the differential conductance spectra of this sample too. Therefore, it is reasonable to assume that the concentration of the F centers is very low, which is in accordance with the Raman spectrum of this sample.

- *$4f^1$ – F center empty states ($4f^1$ – Fes)*
  Second CP from Table I at energies 2.55 (2.6) eV for P$-$CeO$_{2\text{-y}}$ (H$-$CeO$_{2\text{-y}}$), can correspond to the transition from $4f^1$ state to the empty states of F centers (Fes). Since this transition involves electronic states characteristic for the defect-rich shell of ceria nanocrystals, the best fit was obtained with 2D line shape.

  In the case of S$-$CeO$_{2\text{-y}}$ sample, the second CP in the d$^2\varepsilon_2$/dE^2 spectra at 2.44 eV (marked with asterisk in Fig. 3(b)) can correspond to the transition between full and empty electronic states of F^0 type of defects. This transition is already seen in the STS spectrum of P$-$CeO$_{2\text{-y}}$ sample.
- *$4f^1 \rightarrow 4f^0$ transition*
  The critical-point energies at 2.85 eV, 3.1 eV, and 3.2 eV for S$-$CeO$_{2\text{-y}}$, P$-$CeO$_{2\text{-y}}$, and H$-$CeO$_{2-y}$ samples can originate from $4f^1 \rightarrow 4f^0$ transition. The 2D line shape yielded the best fit for this transition. The appearance of $4f^1$ and F center defect states reduces the band gap of CeO$_{2\text{-y}}$ samples[49,50] and shifts the absorption edge more towards the visible region. Such behavior is contrary to the quantum confinement model predictions (increase in energy gap (E$_g$) with decreasing particle size). Although the confinement effect is present, particularly for S$-$CeO$_{2\text{-y}}$ and P$-$CeO$_{2\text{-y}}$ nanocrystalline samples, the dominant role in the band gap behavior with decreasing particle size comes from the formation of $4f^1$ and F center defect states in the gap.[50] As $4f^1 \rightarrow 4f^0$ transition reduces the optical band gap of ceria, we named it as reduced band gap (E$_{gR}$). According to the selection rules for dipole transition such a transition would be generally forbidden or would have low oscillator strength. However in nanosystems, this transition can be allowed due to the breaking of the selection rules in confined nanocrystals.

Finally, the critical-point energies at 4.8 eV, 4.95 eV, and 4.96 eV, in the d$^2\varepsilon_2$/dE^2 spectra of H$-$CeO$_{2-y}$, S$-$CeO$_{2\text{-y}}$, and P$-$CeO$_{2\text{-y}}$ samples, may be assigned to the oxygen species adsorbed on the surface of CeO$_{2\text{-y}}$ nanocrystals.[51] The electronic transitions ascribed to adsorbed oxygen were slightly better fitted with1D than 2D lineshape. The adsorbed oxygen probably form linear chains on the ceria surface, similar to the one-dimensional Pt oxide chains formed when the atomic oxygen covered the Pt(111) surface.[52] Critical point analysis of chain-like structures can be well described with 1D CPs.[53]

In Fig. 4(b) presented are the reduced band gap value energies together with the corresponding energies of F center defect electronic states transitions obtained from CP model fitting, whereas in Fig. 4(c), proposed is the schematic representation of the electronic band structure of defective CeO$_{2\text{-y}}$ nanocrystals. It is important to mention here that there is some discrepancy in the critical point energies observed in ellipsometric spectra and energies between the corresponding peaks in the differential conductance spectra. This can be explained by the fact that STS measurements were carried out on a single CeO$_{2\text{-y}}$ nanocrystals, whereas the ellipsometric measurements were performed on the nanocrystalline samples composed of different crystallite sizes which contribute to the final CP energy with different weights.

It is known from the literature that the formation of the F centers in ceria nanostructures is responsible for the appearance of very interesting effect, the ferromagnetism (FM) at room temperature. Extensive studies have been performed on the magnetic properties of ceria nanostructures and the results have demonstrated that charge state of oxygen vacancy is crucial for the establishment of the ferromagnetism in CeO$_2$.[9,54–58] It is already shown[56,57] that F$^+$ center type of defects mediates ferromagnetic ordering in CeO$_{2\text{-y}}$, whereas in a case of F^0 centers, electrons are in a singlet (S = 0) state and can only mediate weak antiferromagnetic interaction. In order to support the obtained results and the arguments on the formation of F centers in our samples, we have measured the magnetization vs. magnetic field for P$-$CeO$_{2\text{-y}}$ and S$-$CeO$_{2\text{-y}}$ samples at room temperature and compared it with bulk CeO$_2$ sample. These spectra are presented in Fig. 5. The bulk sample shows weak diamagnetic response, what is expected for stoichiometric cerium dioxide with Ce^{4+} ions in the $4f^0$ electronic configuration. On the other hand, S$-$CeO$_{2\text{-y}}$ sample exhibits ferromagnetism at room temperature indicating that majority of oxygen vacancies, as the main mediators of FM ordering, is in the F$^+$ charge state. For P$-$CeO$_{2\text{-y}}$ sample, magnetization behavior is very similar to the bulk sample leading us to conclude that majority of oxygen vacancies is in the F^0 charge state. These findings are in complete agreement with conclusions from Ref. 36.

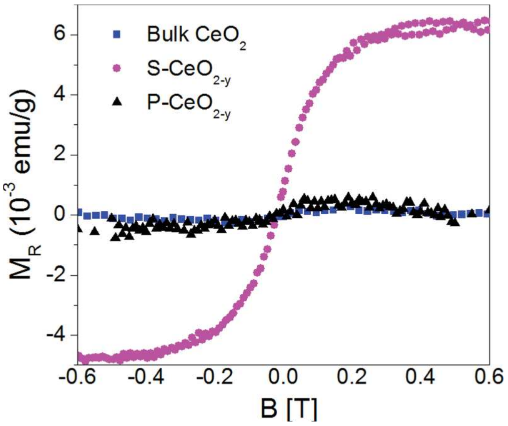

FIG. 5. Room temperature magnetization versus magnetic field for bulk, P$-$CeO$_{2\text{-y}}$, and S$-$CeO$_{2\text{-y}}$ samples.

This study has demonstrated that several types of F centers can be formed in the nanocrystals depending on the synthesis method. Particle size has important influence on the formation of F centers, since we have seen that H$-$CeO$_{2\text{-y}}$ sample with the largest crystallite size has the lowest concentration of F center defects. In a case of samples with much lower crystallite sizes (S$-$CeO$_{2\text{-y}}$ and P$-$CeO$_{2\text{-y}}$), the charge state of oxygen vacancies, i.e., the type of F centers formed, has significant influence on the energy band structure and magnetic properties of defective CeO$_{2\text{-y}}$ nanomaterials.

IV. SUMMARY

The CeO$_{2\text{-y}}$ nanopowders were synthesized by hydrothermal, SPRT, and precipitation methods. XRD and Raman spectroscopy measurements showed that ceria sample produced by hydrothermal method had the largest crystallite size, whereas the CeO$_{2\text{-y}}$ samples produced by SPRT and precipitation methods, had much smaller crystallite size. The highest oxygen vacancy concentration was found in the sample produced by precipitation method. Combined STM/STS and ellipsometry measurements revealed that different types of F center defects were formed in the band gap of CeO$_{2\text{-y}}$ samples. In the case of S$-$CeO$_{2\text{-y}}$ sample, both F^0 and F$^+$ centers were formed inside the gap, whereas for P$-$CeO$_{2\text{-y}}$ sample, only F^0 centers were detected. In the H$-$CeO$_{2\text{-y}}$ sample, no similar defect states were detected. Magnetic measurements confirmed our findings. By summarizing the obtained results, we have concluded that not only the concentration but also the charge state of oxygen vacancies, i.e., the formation of different types of F centers has significant impact on the band structure and optical and magnetic performance of the synthesized ceria nanocrystals.

ACKNOWLEDGMENTS

The authors would like to acknowledge Dr. Novica Paunović for magnetic measurements. This work was financially supported by the Serbian Ministry of Education, Science and Technological development under the Project Nos. ON171032 and III45018.

[1] H. C. Yao and Y. F. Yu Yao, J. Catal. **86**, 254 (1984).

[2] E. C. Su, C. N. Montreuil, and W. G. Rothschild, Appl. Catal. **17**, 75 (1985).

[3] B. E. Gillman and S. D. Jacobs, Appl. Opt. **37**, 3498 (1998).

[4] A. Walkenhorst, M. Schmitt, H. Adrian, and K. Petersen, Appl. Phys. Lett. **64**, 1871 (1994).

[5] S. Kanakaraju, S. Mohan, and A. K. Sood, Thin Solid Films **305**, 191 (1997).

[6] H. J. Beie and A. Gneorich, Sens. Actuators, B **4**, 393 (1991).

[7] B. C. H. Steele, Solid State Ionics **129**, 95 (2000).

[8] B. C. H. Steele and A. Heinzel, Nature (London) **414**, 345 (2001).

[9] X. Chen, G. Li, Y. Su, X. Qui, L. Li, and Z. Zou, Nanotechnology **20**, 115606 (2009).

[10] A. Thurber, K. M. Reddy, V. Shutthanandan, M. H. Engelhard, C. Wang, J. Hays, and A. Punnoose, Phys. Rev. B **76**, 165206 (2007).

[11] L. Truffault, Q. W. Yao, D. Wexler, I. P. Nevirkovets, K. Konstantinov, T. Devers, and S. Nightingale, J. Nanosci. Nanotechnol. **11**, 4019 (2011).

[12] A. Corma, P. Atienzar, H. García, and J.-Y. Chane-Ching, Nature Mater. **3**, 394 (2004).

[13] M. Lira-Cantu and F. C. Krebs, Sol. Energy Mater. Sol. Cells **90**, 2076 (2006).

[14] A. Verma, A. K. Bakhshi, and S. A. Agnihotry, Sol. Energy Mater. Sol. Cells **90**, 1640 (2006).

[15] F. Chen, Y. Cao, and D. Jia, Appl. Surf. Sci. **257**, 9226 (2011).

[16] P. Ji, J. Zhang, F. Chen, and M. Anpo, Appl. Catal., B **85**, 148 (2009).

[17] X. Liu, S. Chen, and X. Wang, J. Lumin. **127**, 650 (2007).

[18] N. Shehata, K. Meehan, I. Hassounah, M. Hudait, N. Jain, M. Clavel, S. Elhelw, and N. Madi, Nanoscale Res. Lett. **9**, 231 (2014).

[19] G. K. Williamson and W. Hall, Acta Metall. **1**, 22 (1953).

[20] L. Wu, H. J. Wiesmann, A. R. Moodenbaugh, R. F. Klie, Y. Zhu, D. O. Welch, and M. Suenaga, Phys. Rev. B **69**, 125415 (2004).

[21] Z. V. Popović, Z. D. Dohčević-Mitrović, N. Paunović, and M. Radović, Phys. Rev. B **85**, 014302 (2012).

[22] W. H. Weber, K. C. Hass, and J. R. McBride, Phys. Rev. B **48**, 178 (1993).

[23] J. E. Spanier, R. D. Robinson, F. Zhang, S. W. Chan, and I. P. Herman, Phys. Rev. B **64**, 245407 (2001).

[24] J. R. McBride, K. C. Hass, B. D. Poindexter, and W. H. Weber, J. Appl. Phys. **76**, 2435 (1994).

[25] M. D. Hernandez-Alonso, A. B. Hugria, A. Martinez-Arias, J. M. Coronado, J. C. Conesa, J. Soria, and M. Fernandez-Garcia, Phys. Chem. Chem. Phys. **6**, 3524 (2004).

[26] Z. D. Dohčević-Mitrović, M. Grujić-Brojčin, M. Šćepanović, Z. V. Popović, S. Bošković, B. Matović, M. Zinkevich, and F. Aldinger, J. Phys.: Condens. Matter **18**, S2061 (2006).

[27] N. Yao and Z. L. Wang, *Handbook of Microscopy for Nanotechnology* (Kluwer Academic Publisher, Boston, 2005).

[28] D. D. Koelling, A. M. Boring, and J. H. Wood, Solid State Commun. **47**, 227 (1983).

[29] N. V. Skorodumova, R. Ahuja, S. I. Simak, I. A. Abrikosov, B. Johansson, and B. I. Lundqvist, Phys. Rev. B **64**, 115108 (2001).

[30] M. A. Henderson, C. L. Perkins, M. H. Engelhard, S. Thevuthasan, and C. H. F. Peden, Surf. Sci. **526**, 1 (2003).

[31] J. F. Jerratsch, X. Shao, N. Nilius, H. J. Freund, C. Popa, M. V. Ganduglia-Pirovano, A. M. Burow, and J. Sauer, Phys. Rev. Lett. **106**, 246801 (2011).

[32] X. Han, J. Lee, and H. I. Yoo, Phys. Rev. B **79**, 100403(R) (2009).

[33] T. König, G. H. Simon, H. P. Rust, G. Pacchioni, M. Heyde, and H. J. Freund, J. Am. Chem. Soc. **131**, 17544 (2009).

[34] D. Muñoz Ramo, J. L. Gavartin, A. L. Shluger, and G. Bersuker, Phys. Rev. B **75**, 205336 (2007).

[35] N. Serpone, J. Phys. Chem. B **110**, 24287 (2006).

[36] S. Aškrabić, Z. D. Dohčević-Mitrović, V. D. Araújo, G. Ionita, M. M. de Lima, Jr., and A. Cantarero, J. Phys. D: Appl. Phys. **46**, 495306 (2013).

[37] M. Herrera-Zaldívar, J. Valenzuela-Benavides, and U. Pal, Opt. Mater. **27**, 1276 (2005).

[38] W. Lu, B. Wang, K. Wang, X. Wang, and J. G. Hou, Langmuir **19**, 5887 (2003).

[39] T. Baron, P. Gentile, N. Magnea, and P. Mur, Appl. Phys. Lett. **79**, 1175 (2001).

[40] H. Fujiwara, *Spectroscopic Ellipsometry Principles and Applications* (John Wiley and Sons Ltd., Chichester, 2003).

[41] P. Lautenschlager, M. Garriga, S. Logothetidis, and M. Cardona, Phys. Rev. B **35**, 9174 (1987).

[42] S. Logothetidis, P. Lautenschlager, and M. Cardona, Phys. Rev. B **33**, 1110 (1986).

[43] L. Viña and M. Cardona, Phys. Rev. B **34**, 2586 (1986).

[44] J. G. Albornoz, R. Serna, and M. León, J. Appl. Phys. **97**, 103515 (2005).

[45] M. León, S. Levcenko, A. Nateprov, A. Nicorici, M. Merino, R. Serna, and E. Arushanov, J. Phys. D: Appl. Phys. **40**, 740 (2007).

[46] M. Marabelli and P. Wachter, Phys. Rev. B **36**, 1238 (1987).

[47] S. Guo, H. Arwin, S. N. Jacobsen, K. Järrendahl, and U. Helmersson, J. Appl. Phys. **77**, 5369 (1995).

[48] O. Voskoboynikov, C. P. Lee, and O. Tretyak, Phys. Rev. B **63**, 165306 (2001).

[49] I. Kosacki and H. U. Anderson, Ionics **6**, 294 (2000).

[50] P. Patsalas, S. Logothetidis, L. Sygellou, and S. Kennou, Phys. Rev. B **68**, 035104 (2003).

[51] A. Bensalem, J. C. Muller, and F. Bozon-Verduraz, J. Chem. Soc. Faraday Trans. **88**, 153 (1992).

[52] S. P. Devarajan, J. A. Hinojosa, Jr., and J. F. Weaver, Surf. Sci. **602**, 3116 (2008).

[53] S. Loughin, R. H. French, L. K. De Noyer, W.-Y. Ching, and Y.-N. Xu, J. Phys. D: Appl. Phys. **29**, 1740 (1996).

[54] A. Sundaresan, R. Bhargavi, N. Rangarajan, U. Siddesh, and C. N. R. Rao, Phys. Rev. B **74**, 161306(R) (2006).

[55] A. Tiwari, V. M. Bhosle, S. Ramachandran, N. Sudhakar, J. Narayan, S. Budak, and A. Gupta, Appl. Phys. Lett. **88**, 142511 (2006).

[56] L. R. Shah, B. Ali, H. Zhu, W. G. Wang, Y. Q. Song, H. W. Zhang, S. I. Shah, and J. Q. Xiao, J. Phys.: Condens. Matter **21**, 486004 (2009).

[57] N. Paunović, Z. Dohčević-Mitrović, R. Scurtu, S. Aškrabić, M. Prekajski, B. Matović, and Z. V. Popović, Nanoscale **4**, 5469 (2012).

[58] V. Fernandes, P. Schio, A. J. A. de Oliveira, W. A. Ortiz, P. Fichtner, L. Amaral, I. L. Graff, J. Varalda, N. Mattoso, W. H. Schreiner, and D. H. Mosca, J. Phys.: Condens. Matter **22**, 216004 (2010).

Ceramics International 44 (2018) 10975–10983

Contents lists available at ScienceDirect

Ceramics International

journal homepage: www.elsevier.com/locate/ceramint

Laser sintering of screen-printed TiO_2 nanoparticles for improvement of mechanical and electrical properties

M. Radović[a,*], G. Dubourg[a], S. Kojić[b], Z. Dohčević-Mitrović[c], B. Stojadinović[c], M. Bokorov[d], V. Crnojević-Bengin[a]

[a] Nano and Microelectronics Group, BioSense Institute, Novi Sad, Serbia
[b] Faculty of Technical Sciences, University of Novi Sad, Serbia
[c] Laboratory for Nanocomposite Structures and Biovibrational Spectroscopy, Institute of Physics Belgrade, University of Belgrade, Serbia
[d] University Laboratory for Electronic Microscopy, University of Novi Sad, Serbia

ARTICLE INFO

Keywords:
A. Sintering
B. Microstructure-final
C. Mechanical properties
D. TiO_2

ABSTRACT

Conducted research presents a rapid and cost-effective approach to technological processing of screen-printed films with anatase TiO_2 nanoparticles, by utilizing the high fluence laser radiation. The influence of laser sintering on the screen-printed films was characterized with optical and scanning electron microscopy, energy-dispersive X-ray (EDX) spectroscopy, Raman spectroscopy, nanoindenter measurements and current vs voltage measurements. Investigation of surface morphology of screen-printed films revealed that higher laser fluences caused significant decrease in film thickness, trough evaporation of organic additives used in the paste matrix. EDX mapping of carbon content in untreated and laser sintered surface confirmed removal of organic additives. Laser sintering stimulated breaking of large agglomerates into much finer nano-sized particles and promoted formation of necking between individual grains. Crystal structure and vibrational properties of anatase TiO_2 nanoparticles was monitored with Raman spectroscopy before and after laser sintering. Obtained results point out that anatase polymorph was preserved during the sintering process, without appearance of other phases. From observation of the behavior of the most intense E_g Raman active mode it was deduced that laser sintering provoked a formation of structural defects i.e. oxygen vacancies in TiO_2 nanoparticles, whose concentration increased in the samples treated with higher laser fluences. Mechanical properties of untreated and laser sintered samples were investigated with nanoindenter measurements using several load forces, in order to carefully probe the Young modulus and mechanical hardness. From the analysis of collected data, we established that overall improvement of the mechanical properties with laser sintering originates from formation of very dense ceramic layer with enhanced interconnectivity between individual TiO_2 nanoparticles. Measurements of current vs voltage characteristics clearly demonstrated that increase in laser fluence leads to drastic increase in current values and improvement of electric conductivity.

1. Introduction

Recent technological and industrial advancements have imposed a staggering need for robust, scalable, cost-effective and innovative solutions for processing of coatings (thick and thin films), foils, bulk surfaces and other types of functional materials. Driven by the needs for cleaner energy, environmental protection and efficient health care, some of the classical energy sources such as UV radiation [1–3], plasma [4–6] and laser radiation [7–9], have found new fields of application in present days. Among these technologies, laser surface texturing has emerged as a versatile tool for improvement of solar cells efficiency [10–12], photocatalytic performance [13], biosensing applications [14,15] and even textile processing [16,17]. Constant development introduced a large variety of laser sources for functionalization of surfaces, ranging from UV region to NIR wavelengths, that can operate in a constant flux or in a pulse mode. Pulsed lasers have recently gained a lot of attention since their pulses can be tuned down to nanosecond [18], picosecond [19] and femtosecond [20,21] intervals. One of the most important advantages of laser processing over the other above mentioned technologies, lies in its spatial resolution. With an appropriate choice of optics or optical fibers, a laser spot can be reduced to micron sizes, enabling very precise localized heating of the target surface without damaging the substrate, which is especially suitable for flexible substrates [22]. Laser processing is also a very effective tool for

---

[*] Correspondence to: Biosense Institute, Dr. Zorana Đinđića 1, 21000 Novi Sad, Serbia.
E-mail address: marrad@bioisense.rs (M. Radović).

https://doi.org/10.1016/j.ceramint.2018.03.181
Received 13 March 2018; Received in revised form 20 March 2018; Accepted 20 March 2018

rapid prototyping (excluding the need for stencils and masks), and can be easily optimized for roll-to-roll and other types of large scale production methods.

Titanium based materials (Ti metal and TiO_2) have been extensively studied for their interaction with laser radiation because of several fascinating effects that were observed. Laser treatment of Ti metal surfaces and TiO_2 films leads to the appearance of laser-induced periodic surface structures (LIPSS) with improved morphological and optical characteristics [23,24]. Another interesting effect was observed during laser treatment of TiO_2 nanoparticles in reducing (Ar) ambient or in colloidal suspension, when the interaction of the laser plume with the target produces the so called "black titania", with a very interesting structural, photovoltaic and photocatalytic properties [25,26]. Most common polymorphs of TiO_2: rutile (tetragonal, *P*42/*mnm*), anatase (tetragonal, *I*41/*amd*), and brookite (orthorombic, *Pbca*/mmm), are particulary suited for laser treatment because all these structural phases exhibit an optical band gap in the visible region. Having established the abovementioned facts, it is clearly understandable why most of the research attention is devoted to enhancement of the dye sensitized solar cells (DSSC) performance trough optimization of basic parameters of the laser treatment method [13,22,27–29].

Available database provides an extensive coverage of literature about the improvement of optical and photovoltaic properties of nanostructured TiO_2 films and coatings with various laser treatment methods. In order to take full advantage of these methods, it is essential to evaluate an effect of laser sintering on the behavior of TiO_2 nanoparticles and to gain better insight into fundamental features of investigated oxide material. The vital importance of this evaluation is based on the fact that mechanical properties, in terms of hardness and elastic modulus, are the key elements that assure both the structural integrity and reliability in various fields of applications.

The aim of this work was to investigate the influence of laser sintering on morphology, structural, mechanical and electrical transport characteristics of the screen-printed films with TiO_2 nanoparticles. One of the first milestones was to achieve controllable technological process for laser sintering of screen-printed nanoparticles, which would induce removal of organic components of the paste (dispersant and binder) and promote sintering of titanium dioxide into dense ceramic material. In the first phase of research we investigated the influence of laser sintering on chemical composition of printed paste matrix and crystallinity of TiO_2 nanoparticles, using EDX and Raman spectroscopy. EDX mapping of untreated and laser sintered surface revealed that laser sintering causes decrease of carbon content and appearance of non-stoichiometry. Raman spectra of treated films showed that anatase crystal structure was preserved, but oxygen deficiency increased in the samples treated with higher laser fluence. From the analysis of SEM images and nanoindenter measurements we established that increase in the laser fluence led to decrease of film thickness and better interconnectivity between TiO_2 nanoparticles, resulting in increase in Young modulus and mechanical hardness. Within such framework, it is possible to offer a cost-effective solution for rapid and large-scale fabrication of ceramic films and coatings on different substrates that could find potential application in electronic devices and advanced technologies.

2. Experimental

One of the main ideas behind the conducted research was to use a simple technology for the functionalization of TiO_2 nanoparticles, such as screen-printing, and to combine it with laser sintering for thermal treatment and improvement of various physical properties of the printed films (Fig. 1). Undertaken multidisciplinary approach can be easily optimized for large scale production of solar cells, sensors and photocatalytic devices [13,22,30]. We deliberately chose a common microscope glass slide as substrate (Fig. 1) and easily accessible commercial TiO_2 nanoparticles, in order to emphasize the low-cost aspect of the utilized technologies and to make it easily applicable to other nanomaterials and substrates.

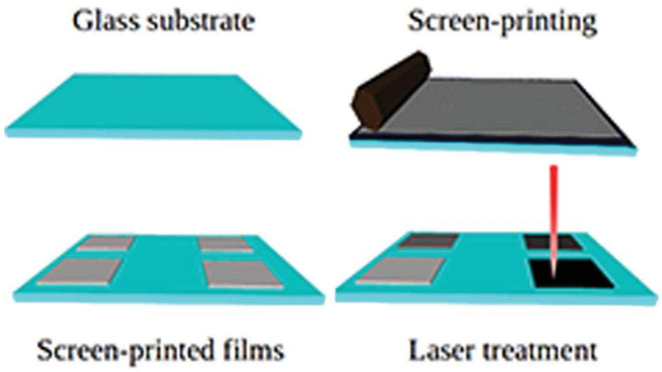

Fig. 1. Schematic representation of multidisciplinary approach undertaken in this research: preparation of microscope glass slide as substrate, screen printing process for the deposition of TiO_2 nanoparticles, and laser sintering of the printed films as a post-processing step.

For the preparation of the functional paste, 2 g of PVP (Sigma-Aldrich) were initially dissolved in 10 ml of ethanol (Sigma-Aldrich). 1 g of anatase TiO_2 nanopowder (Sigma-Aldrich, particle size < 25 nm) was dispersed in 400 μl of terpineol (Sigma-Aldrich), followed by addition of 600 μl of PVP solution. Obtained suspensions were treated with ultrasonic horn for 10 min. Thus prepared paste was deposited on the cleaned microscope-glass substrate using a low-cost screen printing technique (Fig. 1) with EKRA 2H semi-industrial screen printer, in order to obtain a matrix of screen printed films on the glass substrate.

The next step was to apply a very precise and rapid processing technology, such as high-power laser radiation (Fig. 1), and to optimize the parameters of laser treatment of the target surface, with the aim of achieving a controllable sintering of the screen-printed films and improving desired properties of the nanomaterials. The laser treatment of printed films was carried out by using a diode-pumped Nd:YAG laser cutter Rofin-Sinar Power Line D–100, operating in the NIR range at 1064 nm. In order to accomplish a uniform sintering of the surface on the entire sample, the length of the line scanned by the laser was designed to be 5 mm, with line intervals of 20 μm. Frequency of the laser pulse was set at 65 kHz, and, in order to obtain sufficient pulse overlapping, the speed of displacement was adjusted to 1000 mm/s. Afterwards, the laser fluence was varied by adjusting the laser pump current. Several samples were prepared. One sample was kept untreated, in order to serve as a reference, while 4 remaining samples were treated with input current values of 25 A, 26 A, 27 A and 28 A, which correspond to laser fluences of 0.15 J/cm^2, 0.17 J/cm^2, 0.19 J/cm^2 and 0.21 J/cm^2, respectively.

Optical microscopy/profilometry measurements were performed with Huvitz HRM-300 microscope, equipped with Bioimager automatized stage. SEM images were collected on JEOL JSM 6460 LV device in the backscattering geometry. EDX measurements were carried out on Hitachi TM3030 electron microscope, coupled with Bruker Xflash EDX detector. The micro-Raman spectra were collected using Jobin Yvon T64000 spectrometer, equipped with a nitrogen-cooled CCD detector. The $\lambda = 532$ nm line of solid state Nd:YAG laser was used as an excitation source, with an incident laser power less than 40 mW, in order to minimize the heating effects. Investigation of mechanical properties was performed on Agilent G200 nanoindenter. Current vs voltage curves were measured on Yokogawa-Hewlett-Packard 4145A semiconductor probe analyzer.

3. Results and discussion

Fig. 2a), b), c) and d) present the images of untreated and laser sintered samples taken with 500× magnification on optical profilometer. These images show that laser sintering introduces a shift in the

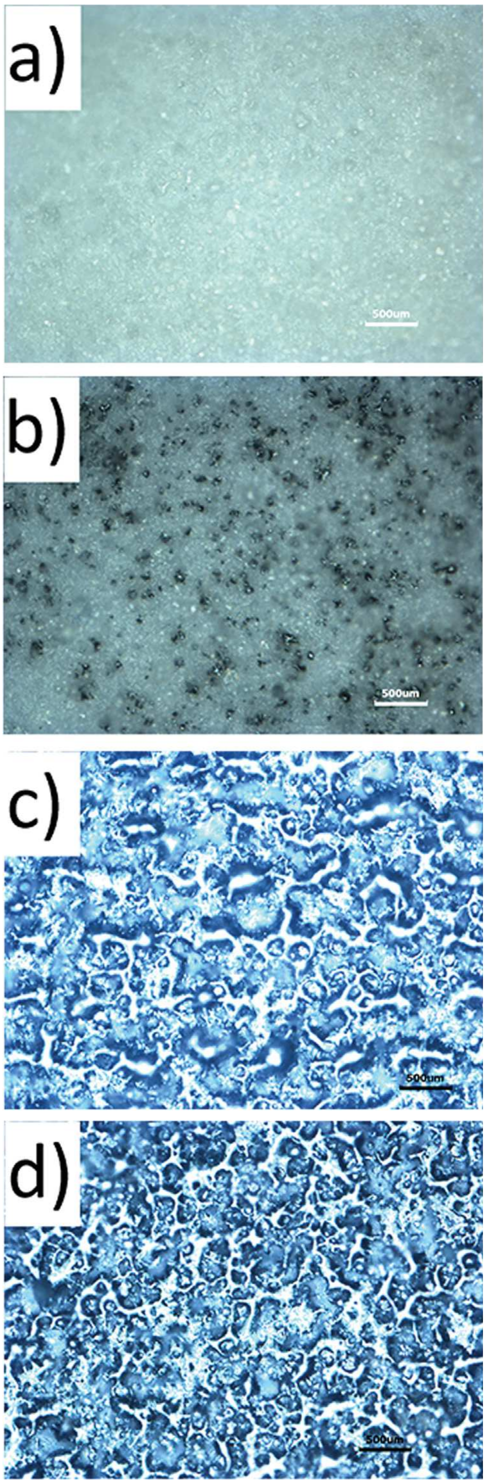

Fig. 2. Comparison of optical microscopy images between a) untreated and samples sintered with b) 0.15 J/cm^2, c) 0.17 J/cm^2 and d) 0.19 J/cm^2 laser fluences, taken with 500 × magnification.

apparent color of printed films, from white for the untreated TiO_2 to black for the sample treated with laser fluence of 0.19 J/cm^2. The sample treated with the highest laser fluence shows significant changes in the topology, manifested as a formation of new, melted structures that exhibit better interconnectivity of the material in the surface layer. The change in contrast in these images reveals that laser sintered surface strongly diffuses the incident light, due to micro-scale reorganization of the surface roughness and porosity. It is important to mention that the laser sintering with fluence higher than 0.19 J/cm^2 results in the ablation of printed films, leading to loss of the nanomaterial and formation of large voids on the film surface. Similar fluence threshold (200 mJ/cm^2) for ablation of the screen printed TiO_2 nanoparticles was reported by Pu et al. [28]. For this reason, the highest laser fluence that was used in this research was set at 0.19 J/cm^2.

SEM measurements were performed in order to gain better insight into the influence of laser sintering on the microstructure of screen printed films. Fig. 3a), b), c) and d) present the captured images of the surface morphologies for the untreated and laser sintered samples. Variation in the film thickness with an increasing laser fluence was determined from the profile images shown in the right part of the Fig. 3a), b), c) and d). The insets in Fig. 3a), b), c) and d) show high magnification SEM images. The SEM image of the untreated screen-printed film reveals a porous surface containing micron sized particles (see the inset of Fig. 3a)) that are much larger than the original anatase nanoparticles (20–30 nm) used for the preparation of the paste. Such clusters are formed by agglomeration of individual TiO_2 nanoparticles, held-together by dried organic binder and dispersant.

In a recent study [22], the same effect was observed for similar paste with ethyl cellulose and terpineol matrix. It is important to mention that in the presented research we used pure anatase TiO_2 nanoparticles, unlike in the majority of previous studies, where P-25 TiO_2 nanoparticles (Evonink Degussa P-25) were used [22,27,31,32]. The P-25 mixture is composed of anatase and rutile phases in the 80%: 20% ratio, for which it is difficult to uncouple the contributions from individual phases to the investigated physical properties. Therefore, pure anatase nanoparticles were chosen in order to easily follow the behavior of a single TiO_2 polymorph during laser treatment. Furthermore, it is interesting to note that for temperatures higher than 500 °C this polymorph starts to transform into rutile phase [33]. Such feature of the material is a good indicator of the local distribution of temperatures in printed films during laser treatment.

Increase in laser fluence induces observable modifications of the surface morphology in the form of melted droplets, as shown in Fig. 3c) and d). The appearance of melted droplets in the printed film is a direct result of breaking of large agglomerates. These agglomerates are reduced into much finer nanoparticles (see inset in Fig. 3d)), whose dimensions are close to the initial size of anatase nanoparticles used in the paste preparation. Breaking of the agglomerates is accomplished by laser thermal evaporation of organic components (PVP and terpineol) whose evaporation temperatures are below 500 °C [22,34]. Additionally, the laser treatment produced sintering of the TiO_2 nanomaterial, which can be observed as formation of necking between individual nanoparticles and better mutual connectivity (inset in Fig. 2d)). In this sintered material, a higher compactness of TiO_2 nanoparticles can be detected, accompanied by dramatic increase in specific surface area. All of the mentioned features reveal great potential for practical applications of the laser sintered films.

The values of film thickness were estimated using the profile SEM images of printed films shown in Fig. 3. The obtained results are shown in Fig. 4 and compared with values obtained from optical profilometry of images shown in Fig. 2a), b), c) and d). Both techniques gave very similar values and the same trend. Film thickness for the untreated sample was around 40 µm, whereas with the laser sintering the film thickness decreased to 10 µm. Decrease in film thickness can be directly correlated to removal of organic binder components with laser radiation, taking into account the fact that oxide material has much higher evaporation temperature. Evaporation of organic additives supports closer packing of the nanoparticles, and formation of dense ceramic material, resulting in the observed film thickness decrease.

Chemical composition and spatial distribution of constitutional elements in laser sintered films was investigated with EDX spectroscopy. Large area EDX maps of the untreated and the laser sintered film were measured using SEM microscope, equipped with EDX detector. SEM image of the investigated area is presented in Fig. 5a), showing

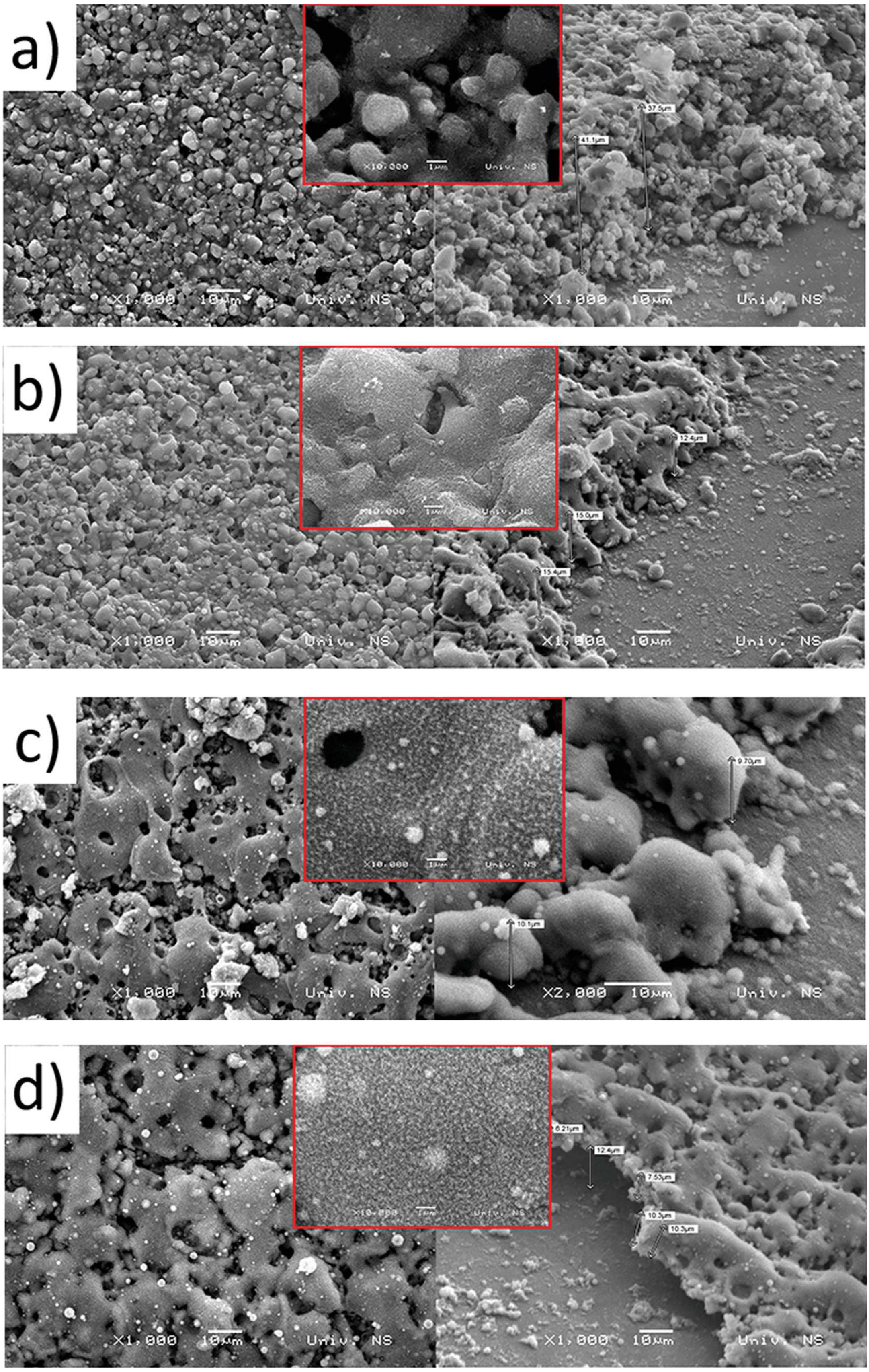

Fig. 3. SEM images of a) untreated and laser sintered screen-printed films with TiO_2 nanoparticles, using b) 0.15 J/cm^2, c) 0.17 J/cm^2 and d) 0.19 J/cm^2 laser fluences.

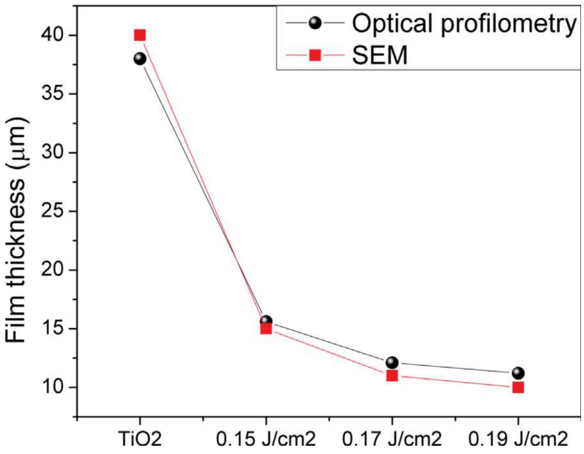

Fig. 4. Variation in film thickness with laser fluence, determined from optical profilometry and SEM images.

laser sintered (0.19 J/cm^2) surface on the left side, and untreated film on the right side. The main features in measured EDX spectra were assigned to titanium (Ti), oxygen (O) and carbon (C) species. Other impurities were not detected. Ti and O signature originates from the oxide nanoparticles, whereas C signature corresponds to the organic additives used for the paste matrix. Fig. 5b), c), d) present the corresponding C, O and Ti EDX maps of the untreated surface and film sintered at 0.19 J/cm^2. When comparing the presented maps with the SEM image, one can clearly see that laser treatment leads to significant changes in the spatial distribution of carbon atoms. Carbon content is lower in the laser sintered surface than in the untreated part. The O map (Fig. 5c) shows a slight decrease in the oxygen content in the sintered surface, whereas Ti map does not show any visible changes in distribution of this element. Lower concentration of O species in treated surface is a signature of non-stoichiometry. Deviation from ideal stoichiometry can originate from a formation of oxygen vacancies in anatase TiO_2 structure, caused by high energy laser radiation. Obtained data lead us to conclusion that the process of laser sintering of screen-printed films induces evaporation of carbon components in the printed film and preserves chemical composition of the oxide nanoparticles. The results also indicate that there is still a certain presence of carbon species in the treated film, and that laser sintering did not entirely remove organic components of the printed paste matrix.

Raman spectroscopy represents a very powerful tool for investigation of nanostructured materials and surfaces. It provides the essential information about crystalline phase and degree of crystallinity of TiO_2 nanoparticles in the printed paste matrix. Moreover, it could be viable tool for assessing the TiO_2 nanocrystals stoichiometry.Fig. 6a) presents Raman spectra of untreated and laser sintered samples, in the spectral region where the first order anatase TiO_2 phonon modes are dominant. Within the spectrum of untreated TiO_2 five distinct modes can be ascribed to phonon modes of anatase TiO_2 crystal structure. Raman modes positioned at 145, 197 and 639 cm^{-1} belong to E_g modes, whereas modes at 398 cm^{-1} and 517 cm^{-1} correspond to the B_g phonon modes [35,36]. Among these modes, E_g mode at around 145 cm^{-1} exhibited noticeable changes. This mode is broader and shifted to higher frequencies with respect to its bulk counterpart. Such behavior can be ascribed to the quantum size effects, strain or non-stoichiometry [37,38]. All Raman modes of anatase crystal structure can be observed in laser treated samples too, providing clear evidence that in these samples, besides the anatase phase, the presence of other phases was not detected. Therefore, it can be concluded that during the laser treatment, local sintering temperature did not exceed 500 °C that instigates transition towards rutile structure [33]. The intensity of this mode, as well as signal-to-noise ratio, decreased in the films treated with higher laser fluence. The SEM analysis of the samples indicated transformation of the surface morphology, i.e an appearance of much finer nanoparticles with higher specific surface area and enhanced porosity. The observed changes in the Raman spectra of films treated with higher laser fluence can be ascribed to increased porosity. However, another reason for the changes can be found in the formation of oxygen vacancies and lack of Ti-O bonds, particularly at the samples` surface. Oxygen vacancies are the most prevalent defects in metal oxides like TiO_2, and their formation is more favorable in anatase than in rutile phase [39]. Furthermore, a novel treatment of hydrogenation of TiO_2 surface, which provoked high disorder in surface layers, led to formation of stable reduced TiO_2, followed by drastic change in color, e.

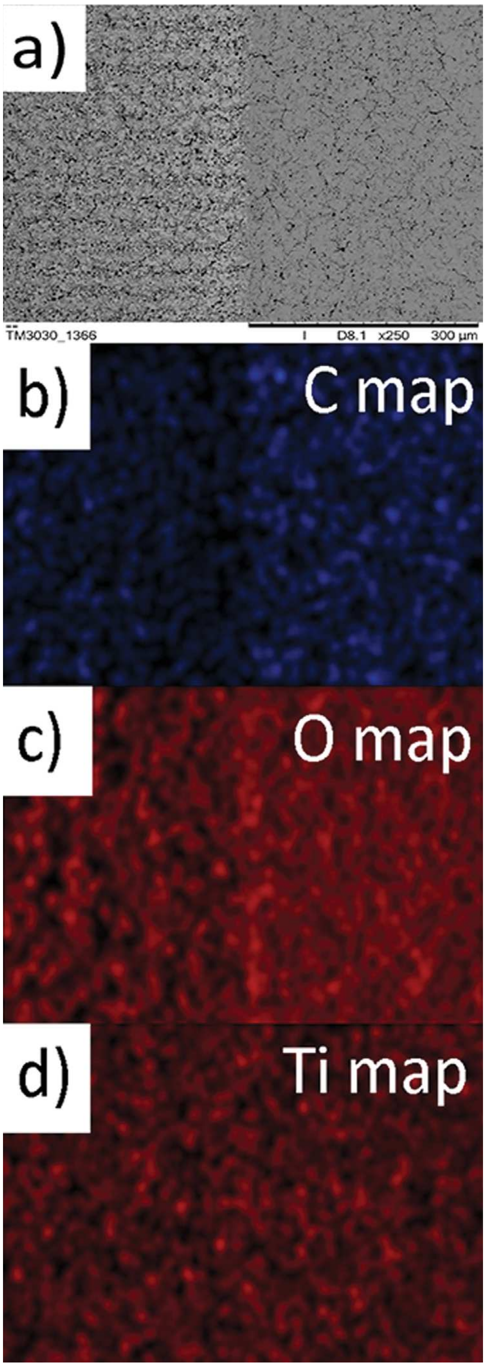

Fig. 5. a) SEM image of the laser sintered (left) and untreated surface (right) of screen-printed film. Laser fluence used for sintering was set at 0.19 J/cm^2. b), c) and d) Corresponding carbon, oxygen and titanium EDX maps of untreated and treated parts. (For interpretation of the references to color in this figure, the reader is referred to the web version of this article.)

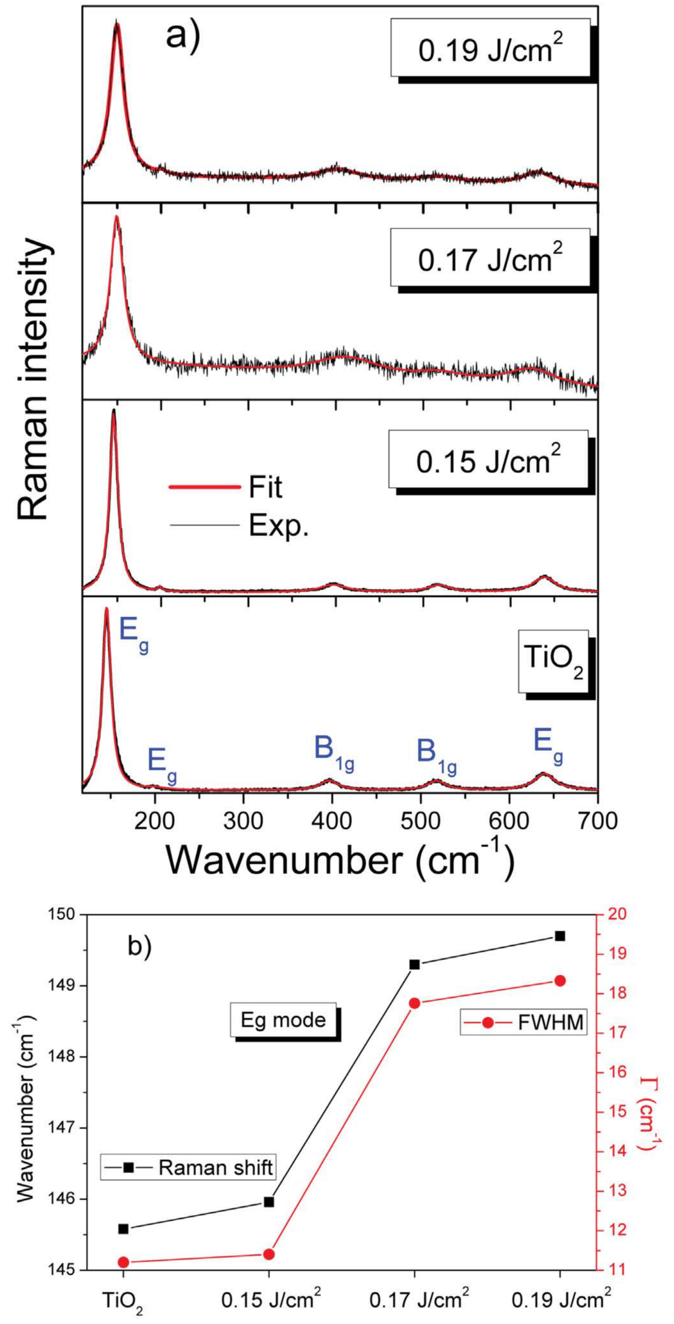

Fig. 6. a) First-order Raman spectra (black curve), together with Lorentzian fits (red curve) for the untreated and laser treated samples. b) Variation in the most-intense Eg mode position and linewidth with the laser fluence. (For interpretation of the references to color in this figure legend, the reader is referred to the web version of this article.)

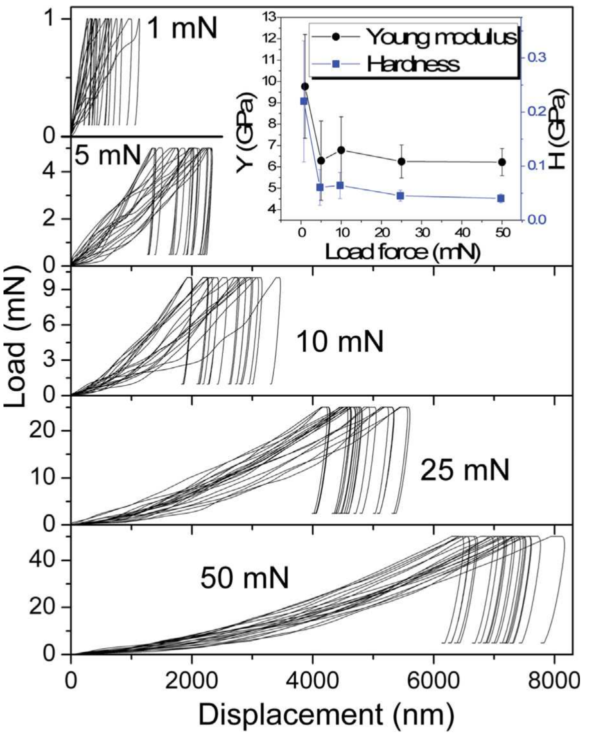

Fig. 7. Load versus displacement curves for untreated sample, measured at 1 mN, 5 mN, 10 mN, 25 mn and 50 mN.

g., darkening of the nanomaterial [40,41]. Based on these findings, it is reasonable to assume that during the laser treatment of TiO_2 films, oxygen vacancy defects are formed in the surface layer, as confirmed by EDX map of O species (Fig. 5c)). Also, formation of oxygen vacancies is accompanied by color change of treated samples from white to black, as observed in the optical microscopy images (see Fig. 2).

Deconvolution of the Raman spectra was performed by Lorentzian profile (red curves in Fig. 6a)). The main effect of the laser sintering manifested as an increase in linewidth and blueshift of the TiO_2 phonon modes. Pronounced blueshift and broadening of E_g mode at 145 cm^{-1} was detected in the films treated with higher laser fluence. In their paper, Parker and Siegel [42] demonstrated that shift and broadening of Raman modes in anatase and rutile polymorphs can be solely ascribed to oxygen stoichiometry, which can be quantitatively assessed by nondestructive Raman spectroscopy. The appearance of oxygen vacancies as defects, directly influences local crystal symmetry and affects the force constants of the E_g mode, leading to a frequency blueshift and increase in phonon damping. The Fig. 6b) presents values of the frequency and linewidth for the most intense E_g mode. Keeping in mind the quantitative estimation of O/Ti ratio from Ref. [42], and knowing the position and bandwidth of E_g mode (Fig. 6b)), we can estimate that the O/Ti ratio is about 1.99 for the sample treated with the lowest laser fluence, whereas for the sample treated with the highest laser fluence this ratio decreased to 1.96. Obtained information reveals that laser treatment preserves crystal structure of TiO_2 nanoparticles and induces formation of structural defects in the form of oxygen vacancies, concentration of which increases in the samples treated with higher laser fluence.

Mechanical properties of untreated and laser sintered screen-printed films with TiO_2 nanoparticles were studied using nano-indentation technique. Aiming to obtain better statistics and more reliable data, Young modulus and hardness were carefully probed using several load-forces, and several measurements points on the surface of samples. The Fig. 7 shows 20 load-displacement curves, measured for each load (1 mN, 5 mN, 10 mN, 25 mN and 50 mN), only for the untreated sample. Values of load-forces are chosen to discriminate the influence of the glass substrate on the resulting characteristics of the investigated samples. For each load-force, 20 measurements were taken in rectangular array on different spots on the surface of investigated sample. The adopted approach offers a proper insight into mechanical properties, because localized defects, impurities and irregularities can very often produce an incorrect conclusion about Young modulus and hardness. Based on the obtained measurements for the untreated sample, one can see that, with an increase in the applied load, the curves shift to higher values of displacements on sample surface (higher penetration depth). This is due to the fact that TiO_2 nanoparticles in as-printed film are loosely bound by the paste matrix.

Values of Young modulus and hardness are calculated from the averaged load-displacement curves, using the Oliver-Pharr method [43]

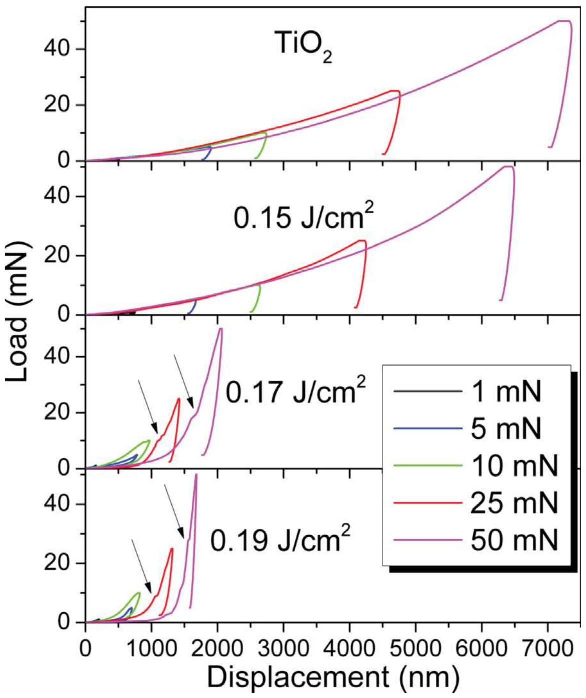

Fig. 8. Averaged load vs displacement curves for the untreated and laser treated samples, measured at 1 mN, 5 mN, 10 mN, 25 mn and 50 mN.

for each load-force and the results are presented in the inset of Fig. 7. With increase in the applied load, the values of Young modulus and hardness decrease. Large standard deviations and very low displacement into sample surface for 1 mN and 5 mN suggest that the measurements performed at these values of load forces are not reliable. This can be expected, since these are the lowest load forces that can be probed with nanoindenter.

Following the investigation of untreated sample, special attention was devoted to the influence of laser sintering on mechanical properties of screen-printed films. For the purpose of quantitative analysis, we averaged 20 measurements obtained for each load-force (like in Fig. 7), and also for each laser fluence that was used for sintering. The Fig. 8 presents comparison of the obtained averaged load displacement curves for untreated and laser sintered samples. From Fig. 8 it can be easily noticed that, with the increasing laser fluence, the curves shift towards lower penetration depth compared to untreated film. For sample treated with the highest laser fluence, the load–displacement curve shows maximum shifting toward lower penetration depth, which directly confirms our assumption that laser treatment process induces localized sintering and hardening of the printed film with TiO_2 nanoparticles. For the samples treated with laser fluences of 0.17 J/cm^2 and 0.19 J/cm^2, and for the highest load-forces (25 mN and 50 mN), we can detect deviation from the expected behavior in load displacement curves as the non-uniform increase in displacement and appearance of critical points (marked with arrows in Fig. 8). Such features can originate from surface roughness, local defects and non-homogeneities in the printed film [44]. Appearance of these defects can produce false values of Young modulus and hardness so it is not advisable to calculate mechanical parameters from the curves possessing such features.

Having in mind that measurements for the lowest applied loads are not reliable and that for the highest applied loads critical points affect the measurements, we chose the curves measured at 10 mN for the calculation and comparison of mechanical parameters for the untreated and laser sintered films. Young modulus and hardness were calculated from the measured load–displacement curves at 10 mN load and their values are presented in the Fig. 9. The obtained values for hardness provide information about the resistance of the screen-printed film to deformation caused by applied load force, whereas the Young modulus can be interpreted as the ability of the printed film to recover in its initial shape and form (stiffness of the material). For the untreated sample we obtained the lowest values of modulus, reflecting the low connectivity between the grains in the screen-printed matrix. For sample treated with highest laser fluence we measured substantial increase in Young modulus and hardness values. Presented results are in good agreement with SEM measurements, since it was established that the first stage of laser sintering process induces formation of necking between nanoparticles, yielding a dense and compact TiO_2 layer. The observed process strongly resembles a transition of micro-porous powdered material towards a solid ceramic one.

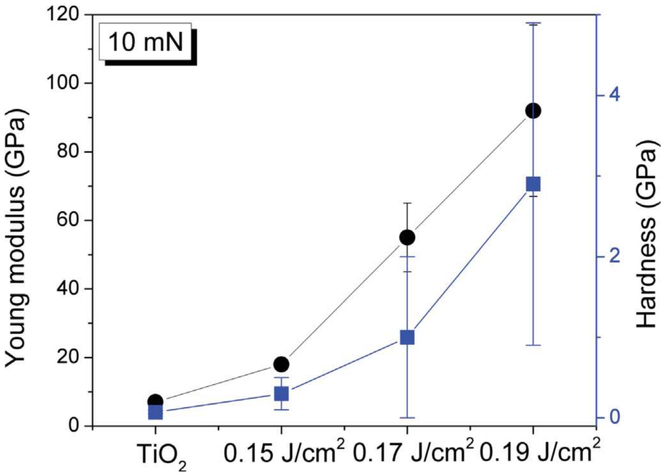

Fig. 9. Comparison of Young modulus and hardness values for untreated and laser treated samples. Presented values were calculated for 10 mN maximum load, from the curves presented in Fig. 7.

The significant increase in modulus and hardness values with laser treatment shows that sintered surfaces exhibit very good recovery characteristics and improved resistance to applied load. Compared to literature data for films prepared with pulsed magnetron sputtering (hardness $H = 8$ GPa, Young modulus $E = 170$ GPa) [45], modified physical vapor deposition technique (H: 0.1–4.4 GPa, E: 20–122 GPa) [46], nanocellulose composites ($H = 3.4$ GPa) [47] and for dip coating ($H = 0.69$ GPa) [48], the values obtained in the presented research reveal that the applied laser treatment produced successful sintering of the oxide nanoparticles into ceramic material. It is important to keep in mind the fact that applied technological processes in this work are by far cost-effective than the ones reported in the literature. Gaillard et al. [46] reported 4.4 GPa value for the hardness of anatase polymorph, but this value was obtained after additional sintering of the laser treated TiO_2 film. Anatase is a very interesting material, because it is stable at lower temperatures (< 500 °C) and ambient pressure, so it mainly occurs in nanocrystalline form. For this reason, it is very important to characterize its fundamental mechanical properties in order to expand the scope of applications of anatase polymorph in advanced technologies. For temperatures higher than 500 °C, anatase starts to transform into rutile polymorph, which naturally possesses much higher hardness and Young modulus [49]. At very high temperatures and pressures, achieved by laser sintering in diamond cell, anatase can transform into cotunnite polymorph, the hardest known oxide [50]. This polymorph exhibits extremely high hardness and Young modulus, comparable even to the artificial diamond. The 2.9 GPa obtained in this research, for the film treated with 0.19 J/cm^2, is lower than the one reported for the films developed with pulsed magnetron sputtering [45] and sintered laser treated film [46]. This is probably due to the fact that not all organic additives were removed during the laser treatment process, as we have seen from the EDX maps. Analysis of the conducted research and comparison with literature database provides substantial room for

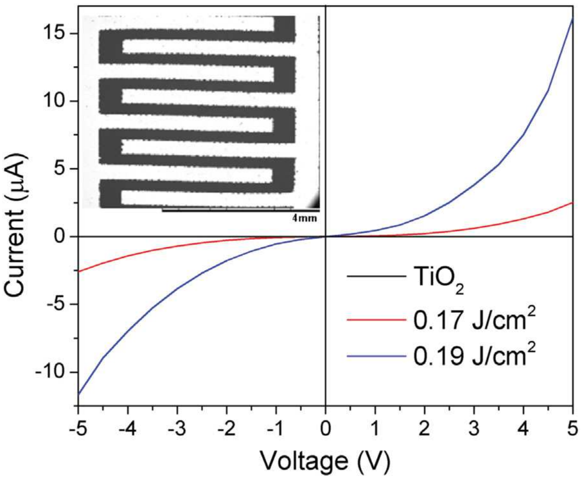

Fig. 10. Current vs voltage curves for untreated and samples sintered at 0.17 J/cm^2 and 0.19 J/cm^2 laser fluences, measured in the − 5 to 5 V range. The inset shows SEM image of the screen-printed interdigitated electrodes.

further improvement.

Formation of necking between individual nanoparticles is one of the most important features of the sintering process, with strong impact on the application of these materials in advanced technologies. Electronic transport in devices based on semiconductor oxide nanomaterials is essentially dependent on the formation of necking and good connectivity among nanoparticles [51]. Aiming to investigate the effect of laser fluence on conductivity of screen-printed films, we measured the current versus voltage characteristics in the DC regime. For successful and reliable measurements, the first step was to prepare the Ag interdigitated electrodes on glass substrate with screen-printing technique. The SEM image of interdigitated electrodes is shown in the inset of Fig. 10. The next step was to print the prepared paste with anatase TiO_2 nanoparticles on top of the electrodes and, finally, printed films were laser sintered using the same parameters in order to obtain identical values of the laser fluence. The Fig. 10 shows I(V) curves for the untreated and samples sintered with 0.17 J/cm^2 and 0.19 J/cm^2 laser fluences, measured in the − 5 to 5 V range. All measured curves exhibit typical semiconductor response, with an evident deviation from linear behavior originating from non-ohmic contacts between printed paste matrix and silver electrodes.

Fig. 10 clearly demonstrates that increase in laser fluence induces significant increase in the current values. For untreated sample, the profile of I(V) curve corresponds to the material with poor conductivity (9 nA at 5 V), whereas for the sample treated with 0.19 J/cm^2 we have order of magnitude higher current (16.6 μA at 5 V). Generally, DC transport properties of the porous nanomaterial, where nanoparticles are packed together, are governed by the grain-boundary resistance, since the resistance at these contacts is much higher than the resistance across single nanoparticle [52]. During sintering process, most of these grain boundaries disappear as the nanoparticles form neck-like structures and the grains connect together. In this case, the grain conductivity becomes dominant, and increase in current values can be detected, as shown in Fig. 10. Improvement of DC conductivity with laser sintering is essential for optimum performance of these materials in gas sensors and photovoltaic devices.

4. Conclusion

Analysis of the obtained results clearly indicates that laser treatment leads to significant improvement of mechanical properties of the screen-printed films. Laser induced evaporation of organic components in the paste matrix enabled total reorganization of the surface morphology, through breaking of the agglomerates into more compact and denser material with nanostructured surface roughness. The investigation of chemical composition in untreated and laser sintered films with EDX spectroscopy, revealed that carbon content is lower in the laser treated film due to evaporation of organic additives. The investigation of crystal structure and vibrational properties, performed with Raman spectroscopy, pointed out that anatase crystal structure is preserved during the laser sintering without presence of other phases, and that implementation of higher laser fluences led to increased non-stoichiometry in the TiO_2 nanoparticles. Nanoindenter measurements were carried out at several applied loads (1 mN, 5 mN, 10 mN, 25 mN and 50 mN), in order to carefully probe the Young modulus and mechanical hardness. Based on refined measurements, it was established that laser treatment induces sintering and hardening of the oxide material into dense ceramic coating with enhanced resistance to mechanical deformation and recovery characteristics. Benefiting from improved mechanical properties and formation of necking between individual nanoparticles during laser sintering process, a dramatic increase in DC conductivity was detected. Combination of the two simple technologies (screen-printing and laser processing) in the presented research offers a cost-effective solution to design and fabrication of semiconductor electrical devices with enhanced mechanical properties.

Acknowledgment

This work is supported by the Serbian Ministry of Education, Science and Technological Development through the projects III44006 and OI171032.

References

[1] J.M. Boyce, Modern technologies for improving cleaning and disinfection of environmental surfaces in hospitals, Antimicrob. Resist. Infect. 5 (2016) 1–10.

[2] W. Ke, G. Fang, J. Wan, H. Tao, Q. Liu, L. Xiong, P. Qin, J. Wang, H. Lei, G. Yang, M. Qin, X. Zhao, Y. Yan, Efficient hole-blocking layer-free planar halide perovskite thin-film solar cells, Nat. Commun. 6 (2015) 6700 (1-7).

[3] S. Zen, Y. Inoue, R. Ono, Low temperature (150 °C) fabrication of high-performance TiO_2 films for dye-sensitized solar cells using ultraviolet light and plasma treatments of TiO_2 paste containing organic binder, J. Appl. Phys. 117 (2015) 103302 (1-5).

[4] V.D. Dao, L.L. Larina, H.S. Choi, Suppression of charge recombination in dye-sensitized solar cells using the plasma treatment of fluorine-doped tin oxide substrates, J. Electrochem. Soc. 162 (2015) H903–H909.

[5] O.V. Penkov, M. Khadem, W.S. Lim, D.E. Kim, A review of recent applications of atmospheric pressure plasma jets for materials processing, J. Coat. Technol. Res. (2015).

[6] L.T. Phan, S.M. Yoon, M.W. Moon, Plasma-based nanostructuring of polymers: a review, Polymers 9 (2017) 417 (1-24).

[7] C.P. Eduardo, A.C.C. Aranha, A. Simões, M.S. Bello-Silva, K.M. Ramalho, M. Esteves-Oliveira, P.M. de Freitas, J. Marotti, J. Tunér, Laser treatment of recurrent herpes labialis: a literature review, Lasers Med. Sci. (2013).

[8] F. Mangano, L. Chambrone, R. van Noort, C. Miller, P. Hatton, C. Mangano, Direct metal laser sintering titanium dental implants: a review of the current literature, Int. J. Biomater. (2014) (Article ID461534).

[9] C. Kerse, H. Kalaycıoğlu, P. Elahi, B. Çetin, D.K. Kesim, Ö. Akçaalan, S. Yavaş, M.D. Aşık, B. Öktem, H. Hoogland, R. Holzwarth, F.O. Ilday, Ablation-cooled material removal with ultrafast bursts of pulses, Nature 537 (2016) 84–88.

[10] G. Mincuzzi, A.L. Palma, A. Di Carlo, T.M. Brown, Laser processing in the manufacture of dye-sensitized and perovskite solar cell technologies, ChemElectroChem 3 (2016) 9–30.

[11] M. Colina, A. Morales-Vilches, C. Voz, I. Martín, P. Ortega, A. Orpella, G. López, R. Alcubilla, Laser induced forward transfer for front contact improvement in silicon heterojunction solar cells, Appl. Surf. Sci. 336 (2015) 89–95.

[12] J.A. Spechler, K.A. Nagamatsu, J.C. Sturm, C.B. Arnold, Improved efficiency of hybrid organic photovoltaics by pulsed laser sintering of silver nanowire network transparent electrode, ACS Appl. Mater. Interfaces 7 (2015) 10556–10562.

[13] T. Huang, J. Lu, R. Xiao, Q. Wu, W. Yang, Enhanced photocatalytic properties of hierarchical three-dimensional TiO_2 grown on femtosecond laser structured titanium substrate, Appl. Surf. Sci. 403 (2017) 584–589.

[14] C. Fenzl, P. Nayak, T. Hirsch, O.S. Wolfbeis, H.N. Alshareef, A.J. Baeumner, Laser-scribed graphene electrodes for aptamer-based biosensing, ACS Sens. 2 (2017) 616–620.

[15] A. Kuchmizhak, E. Pustovalov, S. Syubaev, O. Vitrik, Y. Kulchin, A. Porfirev, S. Khonina, S. Kudryashov, P. Danilov, A. Ionin, On-fly femtosecond-laser fabrication of self-organized plasmonic nanotextures for chemo- and biosensing applications, ACS Appl. Mater. Interfaces 8 (2016) 24946–24955.

[16] O. Hung, C.A. Kan, Study of CO_2 laser treatment on colour properties of cotton-

based fabrics, Coatings 7 (2017) 131 (1-14).

[17] R. Nayak, R. Padhye, The use of laser in garment manufacturing: an overview, Fash. Text. 3 (2016) 5 (1-16).

[18] D.V. Ta, A. Dunn, T.J. Wasley, R.V. Kay, J. Stringer, P.J. Smith, C. Connaughton, J.D. Shephard, Nanosecond laser textured superhydrophobic metallic surfaces and their chemical sensing applications, Appl. Surf. Sci. 357 (2015) 248–254.

[19] H. Zhang, J. Di, M. Zhou, Y. Yan, R. Wang, An investigation on the hole quality during picosecond laser helical drilling of stainless steel 304, Appl. Phys. A 119 (2015) 745–752.

[20] K. Sugioka, J. Xu, D. Wu, Y. Hanada, Z. Wang, Y. Cheng, K. Midorikawa, Femtosecond laser 3D micromachining: a powerful tool for the fabrication of microfluidic, optofluidic, and electrofluidic devices based on glass, Lab Chip 14 (2014) 3447–3458.

[21] G.D. Tsibidis, C. Fotakis, E. Stratakis, From ripples to spikes: a hydrodynamical mechanism to interpret femtosecond laser-induced self-assembled structures, Phys. Rev. B 92 (2015) 041405 (1-6).

[22] A. Hadi, M. Alhabradi, Q. Chen, H. Liu, W. Guo, M. Curioni, R. Cernik, Z. Liu, Rapid fabrication of mesoporous TiO_2 thin films by pulsed fibre laser for dye sensitized solar cells, Appl. Surf. Sci. 428 (2018) 1089–1097.

[23] T.M. Tanvir Ahmmed, C. Grambow, A. Kietzig, Fabrication of micro/nano structures on metals by femtosecond laser micromachining, Micromachines 5 (2014) 1219–1253.

[24] B. Hopp, T. Smausz, M. Lentner, J. Kopniczky, C. Tápai, T. Gera, T. Csizmadia, M. Ehrhardt, P. Lorenz, K. Zimmer, Stability investigation of laser darkened metal surfaces, Appl. Phys. A 123 (2017) 598 (1-8).

[25] M. Tian, M. Mahjouri-Samani, G. Eres, R. Sachan, M. Yoon, M.F. Chisholm, K. Wang, A.A. Puretzky, C.M. Rouleau, D.B. Geohegan, G. Duscher, Structure and formation mechanism of black TiO_2 nanoparticles, ACS Nano 9 (2015) 10482–10488.

[26] X. Chen, L. Liu, F. Huang, Black titanium dioxide (TiO_2) nanomaterials, Chem. Soc. Rev. 44 (2015) 1861–1885.

[27] H. Kim, G.P. Kushto, C.B. Arnold, Z.H. Kafafi, A. Piqué, Laser processing of nanocrystalline TiO_2 films for dye-sensitized solar cells, Appl. Phys. Lett. 85 (2004) 464–466.

[28] M.J. Pu, J.Z. Chen, I.C. Cheng, KrF excimer laser irradiated nanoporous TiO_2 layers for dye-sensitized solar cells: influence of laser power density, Ceram. Int. 39 (2013) 6183–6188.

[29] M.A. Gondal, A.M. Ilyas, U. Baig, Pulsed laser ablation in liquid synthesis of ZnO/TiO_2 nanocomposite catalyst with enhanced photovoltaic and photocatalytic performance, Ceram. Int. 42 (2016) 13151–13160.

[30] G. Dubourg, A. Segkos, J. Katona, M. Radović, S. Savić, G. Niarchos, C. Tsamis, V. Crnojević-Bengin, Fabrication and characterization of flexible and miniaturized humidity sensors using screen-printed TiO_2 nanoparticles as sensitive layer, Sensors 17 (2017) 1854 (1-13).

[31] J. Kim, J. Kim, M. Lee, Laser welding of nanoparticulate TiO_2 and transparent conducting oxide electrodes for highly efficient dye-sensitized solar cell, Nanotechnology 21 (2010) 345203 (6pp).

[32] H. Pan, S. Hwan Ko, N. Misra, C.P. Grigoropoulos, Laser annealed composite titanium dioxide electrodes for dye-sensitized solar cells on glass and plastics, Appl. Phys. Lett. 94 (2009) 071117.

[33] C. Perego, R. Revel, O. Durupthy, S. Cassaignon, J.P. Jolivet, Thermal stability of TiO_2-anatase: impact of nanoparticles morphology on kinetic phase transformation, Solid State Sci. 12 (2010) 989–995.

[34] F. Haaf, A. Sanner, F. Straub, Polymers of *N*-vinylpyrrolidone: synthesis, characterization and uses, Polym. J. 17 (1985) 143–152.

[35] T. Ohsaka, F. Izumi, Y. Fujiki, Raman spectrum of anatase, TiO_2, J. Raman Spec. 7 (1978) 321.

[36] J.-G. Li, T. Ishigaki, X. Sun, Anatase, brookite, and rutile nanocrystals via redox reactions under mild hydrothermal conditions: phase-selective synthesis and physicochemical properties, J. Phys. Chem. C 111 (2007) 4969–4976.

[37] W.F. Zhang, Y.L. He, M.S. Zhang, Z. Yin, Q. Chen, Raman scattering study on anatase TiO_2 nanocrystals, J. Phys. D: Appl. Phys. 33 (2000) 912–916.

[38] A.L. Bassi, D. Cattaneo, V. Russo, C.E. Bottani, E. Barborini, T. Mazza, P. Piseri, P. Milani, F.O. Ernst, K. Wegner, S.E. Pratsinis, Raman spectroscopy characterization of titania nanoparticles produced by flame pyrolysis: the influence of size and stoichiometry, J. Appl. Phys. 98 (2005) 074305.

[39] B.J. Morgan, G.W. Watson, Intrinsic n-type defect formation in TiO_2: a comparison of rutile and anatase from GGA + *U* calculations, J. Phys. Chem. C 114 (2010) 2321–2328.

[40] X. Chen, L. Liu, P.Y. Yu, S.S. Mao, Increasing solar absorption for photocatalysis with black hydrogenated titanium dioxide nanocrystals, Science 331 (2011) 746–750.

[41] X. Pan, M.-Q. Yang, X. Fu, N. Zhang, Y.-J. Xu, Defective TiO2 with oxygen vacancies: synthesis, properties and photocatalytic applications, Nanoscale 5 (2013) 3601–3614.

[42] J.C. Parker, R.W. Siegel, Calibration of the Raman spectrum to the oxygen stoichiometry of nanophase TiO2, Appl. Phys. Lett. 57 (1990) 943–945.

[43] W.C. Oliver, G.M. Pharr, Measurement of hardness and elastic modulus by instrumented indentation: advances in understanding and refinements to methodology, J. Mater. Res. 19 (2011) 3.

[44] L. Qian, M. Li, Z. Zhou, H. Yang, X. Shi, Comparison of nano-indentation hardness to microhardness, Surf. Coat. Technol. 195 (2005) 264–271.

[45] O. Zywitzki, T. Modes, H. Sahm, P. Frach, K. Goedicke, D. Glöß, Structure and properties of crystalline titanium oxide layers deposited by reactive pulse magnetron sputtering, Surf. Coat. Technol. 180–181 (2004) 538–543.

[46] Y. Gaillard, V.J. Rico, E. Jimenez-Pique, A.R. González-Elipe, Nanoindentation of TiO_2 thin films with different microstructures, J. Phys. D: Appl. Phys. 42 (2009) 145305 (9pp).

[47] C. Schütz, J. Sort, Z. Bacsik, V. Oliynyk, E. Pellicer, A. Fall, L. Wågberg, L. Berglund, L. Bergström, G. Salazar-Alvarez, Hard and transparent films formed by nanocellulose-TiO_2 nanoparticle hybrids, PLos One 7 (2012) e45828.

[48] H. Yaghoubi, N. Taghavinia, E.K. Alamdari, A.A. Volinsky, Nanomechanical properties of TiO_2 granular thin films, Appl. Mater. Interface 2 (2010) 2629–2636.

[49] M.J. Mayo, R.W. Siegel, A. Narayanasamy, W.D. Nix, Mechanical properties of nanophase TiO_2 as determined by nanoindentation, J. Mater. Res. 5 (1990) 1073–1082.

[50] R. Ahuja, L.S. Dubrovinsky, High-pressure structural phase transitions in TiO_2 and synthesis of the hardest known oxide, J. Phys.: Condens. Matter 14 (2002) 10995–10999.

[51] N. Barsan, U. Weimar, Conduction model of metal oxide gas sensors, J. Electroceram. 7 (2001) 143.

Surface & Coatings Technology 276 (2015) 573–579

Contents lists available at ScienceDirect

Surface & Coatings Technology

journal homepage: www.elsevier.com/locate/surfcoat

Synthesis and characterization of Al_2O_3/ZnO coatings formed by plasma electrolytic oxidation

S. Stojadinović [a,*], N. Tadić [a], N. Radić [b], B. Stojadinović [c], B. Grbić [b], R. Vasilić [a]

[a] University of Belgrade, Faculty of Physics, Studentski trg 12-16, 11000 Belgrade, Serbia
[b] University of Belgrade, Institute of Chemistry, Technology and Metallurgy, Department of Catalysis and Chemical Engineering, Njegoševa 12, 11000 Belgrade, Serbia
[c] University of Belgrade, Institute of Physics, Pregrevica 118, 11080 Belgrade, Serbia

ARTICLE INFO

Article history:
Received 10 April 2015
Revised 4 June 2015
Accepted in revised form 7 June 2015
Available online 9 June 2015

Keywords:
Plasma electrolytic oxidation
ZnO
Al_2O_3
Photoluminescence
Photocatalytic activity

ABSTRACT

Mixed Al_2O_3/ZnO coatings are prepared by conventional DC plasma electrolytic oxidation (PEO) of aluminum in boric acid and borax solution containing ZnO nanoparticles. Scanning electron microscopy equipped with energy dispersive x-ray spectroscopy, x-ray diffraction, and Raman spectroscopy were employed to monitor morphological, structural, and chemical changes of obtained oxide coatings. It was found that chemical and phase compositions strongly depend on PEO time. Photoluminescence and photodegradation of methyl orange served as a tool to estimate potential application of Al_2O_3/ZnO coatings. Photoluminescence measurements showed that clearly observable bands inherent to Al_2O_3 and ZnO are present in formed coatings, pointing at oxygen vacancies as the main source of photoluminescence. Longer PEO processing times proved beneficial for enhanced photocatalytic activity.

1. Introduction

Zinc oxide (ZnO), a wide band gap semiconductor ($Eg = 3.37$ eV) with large exciton binding energy, is an important material in various fields of application due to its low cost and excellent physical and chemical properties, such as high melting point (1975 °C), high thermal and chemical stability, a large piezoelectric coefficient, high electrochemical coupling coefficient, broad range of radiation absorption and high photostability [1]. For this reason, ZnO is an excellent candidate for solar cell [2], light-emitting diodes in the blue and UV regions [3], ultraviolet photoconductive detectors [4], piezoelectric transducers [5], photocatalyst [6], etc.

The aim of this work was to examine the possibility of formation of ZnO based coatings on aluminum substrate by plasma electrolytic oxidation (PEO) and to probe their photoluminescent (PL) and photocatalytic properties. PEO is an economic, efficient, and environmentally friendly processing technology capable of producing in-situ oxide coatings on some metals (aluminum, magnesium, titanium, zirconium, tantalum, etc.) as well as on their alloys [7]. The PEO process is coupled with the formation of plasma, as indicated by the presence of microdischarges on the metal surface when the supplied voltage is higher than a critical value (known as the breakdown voltage) [8]. The microdischarging results in localized high temperature (10^3 K to 10^4 K) and high pressure (~10^2 MPa), and various processes including plasma-chemical, electrochemical, and thermodynamical reactions occur at the microdischarge sites [9]. These processes allow the formation of oxide coatings that contain crystalline and amorphous phases with constituent species originating both from metal and electrolyte. Having in mind that such severe conditions exist on the surface during the PEO process, we assumed that the deposition of ZnO nanoparticles from electrolyte is possible and that obtained oxide coatings may be interesting for various applications.

2. Experimental details

Rectangular samples cut from the commercially available aluminum (99.9% purity) were used as working electrodes in the experiment. The dimensions of the samples were 25 mm × 10 mm × 0.25 mm. The working electrodes were sealed with insulation resin leaving only active surface with an area of 1.5 cm^2 accessible to the electrolyte. Before the anodization, samples were degreased in acetone, ethanol, and distilled water, using ultrasonic cleaner, and dried in a warm air stream. During the anodization, the electrolyte circulated through the chamber–reservoir system and the temperature of the electrolyte was maintained at (20 ± 0.5) °C. Water solution of 0.1 M boric acid (H_3BO_3) + 0.05 M borax ($Na_2B_4O_7 \cdot 10H_2O$) was used as a supporting electrolyte. Commercially available ZnO powder was used as a source of nanoparticles and added to the supporting electrolyte in the concentration of 2 g/L ZnO. The average size of ZnO nanoparticle was estimated to be around 28 nm (calculated by Williamson–Hall method using obtained XRD patterns). Anodizing was carried out at a current density of 150 mA/cm^2.

---

[*] Corresponding author.
E-mail address: sstevan@ff.bg.ac.rs (S. Stojadinović).

http://dx.doi.org/10.1016/j.surfcoat.2015.06.013
0257-8972/

After the anodization, samples were rinsed in distilled water to prevent additional deposition of electrolyte components during drying.

Scanning electron microscope (SEM) JEOL 840A equipped with energy dispersive x-ray spectroscopy (EDS) was used to characterize morphology and chemical composition of formed oxide coatings. The crystallinity of oxide coatings was analyzed by x-ray diffraction (XRD), using a Rigaku Ultima IV diffractometer in Bragg–Brentano geometry, with Ni-filtered CuKα radiation ($\lambda = 1.54178$ Å). Diffraction data were acquired over the scattering angle 2θ from 20° to 80° with a step of 0.020° and acquisition rate of 2°/min.

Micro-Raman spectra were collected at room temperature using the TriVista 557 Raman system equipped with a nitrogen-cooled CCD detector in the backscattering configuration. The $\lambda = 532$ nm line of solid state laser was used as an excitation source.

PL spectral measurements were taken on a Horiba Jobin Yvon Fluorolog FL3-22 spectrofluorometer at room temperature, with a Xe lamp as the excitation light source. The obtained spectra were corrected for the spectral response of the measuring system and spectral distribution of the Xe lamp.

For photocatalytic activity evaluation, the photodegradation of aqueous methyl orange (MO) solution at room temperature was used as a model reaction. The concentration of MO solution was 8 mg/L. Samples of 15 mm × 10 mm active surface area were immersed into 10 mL of MO solution and placed on the holder, 5 mm above the bottom of the reactor, with magnetic stirrer located under the holder. Prior to illumination, the solution and the catalyst were magnetically stirred in the dark for 30 min to achieve adsorption–desorption equilibrium. The MO solution was then irradiated under lamp that simulates solar radiation (Solimed BH Quarzlampen), with a power consumption of 300 W, housed 25 cm above the top surface of the solution. Illumination intensity on the top of the photocatalytic reactor was 850 lx. A fixed quantity of MO solution was removed every 2 h to measure the absorption and then concentration, using UV–VIS spectrometer (Thermo Electron Nicolet Evolution 500). After each measurement of MO concentration, probe solution was returned back to the photocatalytic reactor. MO has a maximum absorbance at 464 nm, which was used as a wavelength for monitoring MO degradation. The absorbance was converted to MO concentration in accordance with a standard curve showing a linear relationship between the concentration and the absorbance at this wavelength. Prior to the photocatalysis, MO solution was tested for photolysis in the absence of the photocatalyst in order to examine its stability. The lack of change in MO concentration after 12 h of irradiation revealed that degradation was only due to the presence of the photocatalyst. The reproducibility of the results was verified by performing each test several times.

3. Results and discussion

3.1. Morphology, chemical, and phase composition of Al_2O_3/ZnO coatings

Time variation of anodization voltage of aluminum at 150 mA/cm^2 in electrolyte containing 0.1 M H_3BO_3 + 0.05 M $Na_2B_4O_7 \cdot 10H_2O$ + 2 g/L ZnO is shown in Fig. 1. From the beginning of anodization, the voltage increases roughly linearly with time to about 400 V with average slope of 34 V/s (stage I in Fig. 1) resulting in the constant rate of increase of the compact barrier oxide film thickness [10]. During this stage, the main part of the total current passing through the barrier oxide film is ionic current which forms oxide film. Throughout the anodization electrons are injected into the conduction band of the aluminum oxide film and accelerated by the electric field producing avalanches by an impact ionization mechanism [11]. When the avalanche electronic current reaches a certain critical value the breakdown of the barrier oxide films occurs. The point of dielectric breakdown can be identified by an apparent deflection from linearity in the voltage–time curve, starting from so-called breakdown voltage. At this point, a large number of small-sized microdischarges evenly distributed over the whole sample surface appear. After the breakdown, anodization voltage still increases, but the voltage-time slope decreases towards relatively constant value of the anodization voltage (Stage II in Fig. 1).

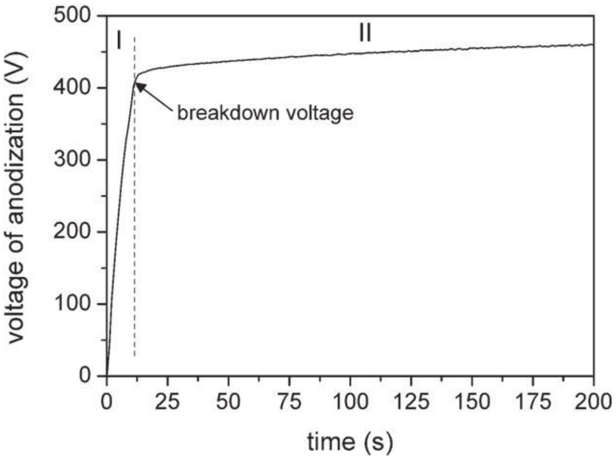

Fig. 1. Time variation of voltage during galvanostatic anodization of aluminum at 150 mA/cm^2 in electrolyte containing 0.1 M H_3BO_3 + 0.05 M $Na_2B_4O_7 \cdot 10H_2O$ + 2 g/L ZnO.

Multiple coexisting processes such as oxide formation, dissolution and dielectric breakdown are typical for PEO [12]. At the beginning of the anodization, oxide layer grows at the aluminum/oxide and oxide/electrolyte interfaces as a result of migration of O^{2-}/OH^- and Al^{3+} ions across the oxide assisted by a strong electric field. The proposed chemical reactions at the aluminum/oxide interface are [13]:

$$2Al + 3O^{2-}_{solid} \rightarrow Al_2O_3 + 6e^-, \quad (1)$$

$$Al \rightarrow Al^{3+}_{solid} + 3e^-. \quad (2)$$

Simultaneously, at the oxide/electrolyte interface the following reaction takes place:

$$2Al^{3+}_{solid} + 9H_2O \rightarrow Al_2O_3 + 6H_3O^+. \quad (3)$$

During the PEO process, components of the electrolyte are drawn into the discharge channels. Alongside, aluminum is melted out of the substrate, enters the discharge channels, and gets oxidized. In the following step, oxidized metal is ejected from the channels into the coating surface in contact with the electrolyte and in that way increases the coating thickness around the channels. At last, discharge channels get cooled and the reaction products are deposited onto its walls. The ZnO nanoparticles take part in this process through the electrophoretic and microdischarging mechanisms. Due to the electrophoretic effect, the ZnO nanoparticles move in the direction of anode and locally high temperature and pressure induced at the microdischarge sites result in deposition of the ZnO nanoparticles on the surface of oxide coatings.

SEM micrographs of the surface coatings obtained at various stages of PEO process are shown in Fig. 2. Numerous microdischarge channels with different diameters and shapes, as well as regions resulting from the rapid cooling of molten material, decorate the surface of the coatings. Results of the EDS analyses of surface coatings in Fig. 2 are shown in Table 1. Main elements of the coatings are Al, O, and Zn. The concentration of Zn increases with PEO time. Although one may expect incorporation of boron from the electrolyte into the surface coatings obtained by PEO [14], we were not able to detect its presence utilizing EDS analysis, possibly because its concentration is below the detection limit of our equipment. Fig. 3 shows SEM micrograph and EDS of two different regions on surface coating processed for 5 min (Table 2). Due to a high sparking strength in microdischarge channel oxide coating in the surrounding area is mainly composed of aluminum and oxygen (spectrum

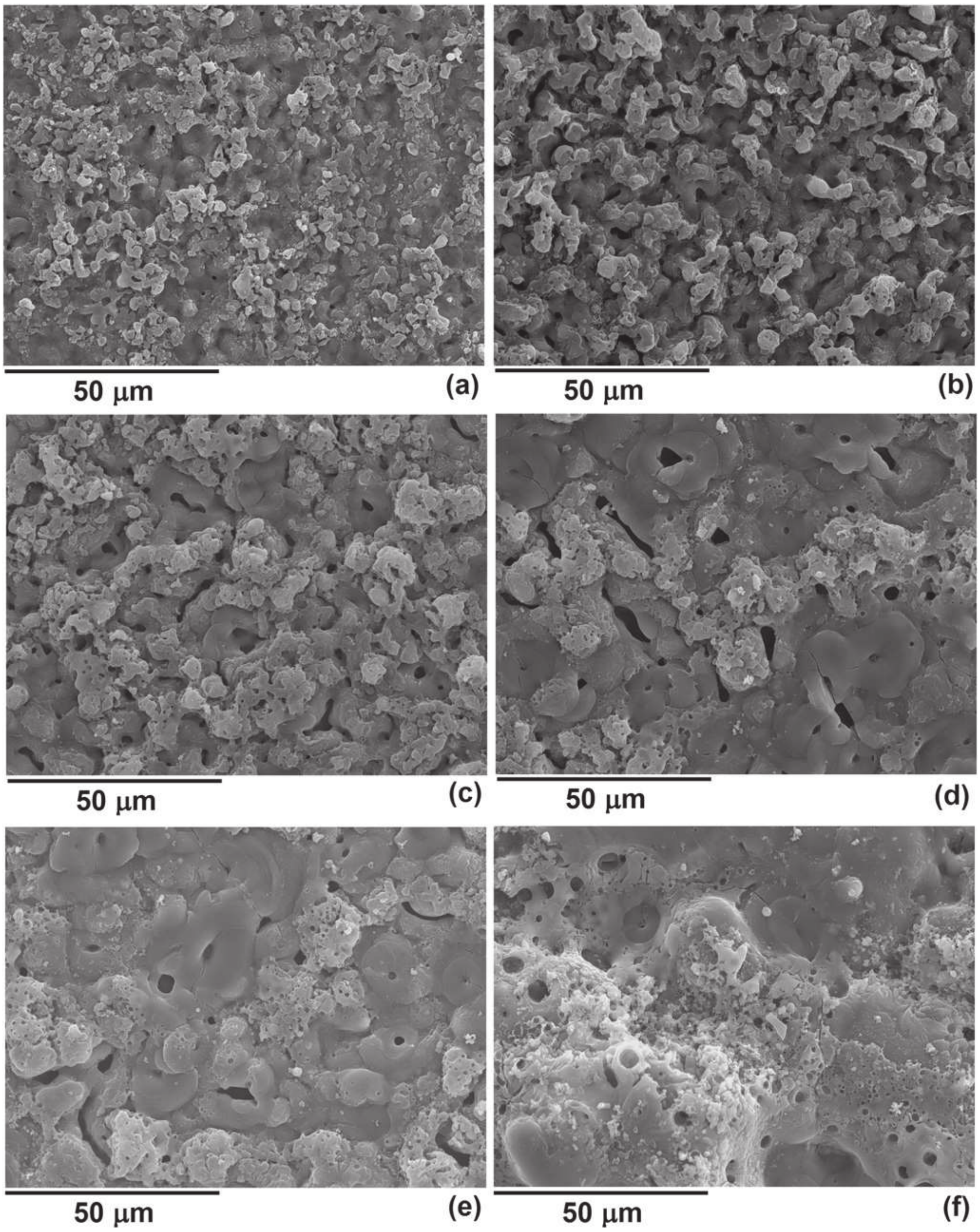

Fig. 2. SEM micrographs of surface coatings formed at various stages of PEO process: (a) 1 min; (b) 3 min; (c) 5 min; (d) 10 min; (e) 15 min; (f) 30 min.

2), while grains observed on the surface contain significant amount of zinc (spectrum 1).

SEM micrographs of polished cross sections of PEO coatings grown on aluminum are presented in Fig. 4. Relatively dense layers, thick about 4.9 µm, 6.6 µm and 8.8 µm are formed after 10 min, 15 min and 30 min of PEO, respectively. The results of line scan EDS analysis in ten points on cross-sectioned surface formed by PEO for 15 min (Fig. 4b) are given in Table 3. Elemental Zn (originating from ZnO nanoparticles) was detected through entire depth of the coating, but its content gradually increases towards outer layer of oxide coating.

Table 1
EDS analyses of oxide coatings in Fig. 2.

Sample	PEO time [s]	Atomic [%]		
		O	Al	Zn
Fig. 2a	1	45.17	54.49	0.34
Fig. 2b	3	53.73	45.75	0.52
Fig. 2c	5	55.12	43.46	1.42
Fig. 2d	10	58.12	40.10	1.78
Fig. 2e	15	59.12	38.85	2.03
Fig. 2f	30	65.66	26.40	7.94

The XRD patterns of surface coatings obtained after various PEO times are shown in Fig. 5. The coatings are partially crystallized and mostly composed of gamma alumina and alpha alumina. Patterns in Fig. 5 suggest that during the first minute of anodization, amorphous alumina is formed, while after 3 min amorphous alumina becomes moderately crystallized. Diffraction peaks attributed to gamma alumina phase indicate crystallization of amorphous alumina. Amorphous alumina transforms into gamma alumina under annealing temperatures ranging from 800 °C to 950 °C [15]. After about 10 min from the onset of PEO, gamma alumina transforms into alpha alumina. Alpha alumina is thermodynamically stable at all temperatures, whereas gamma alumina is metastable and starts to transform into alpha alumina at temperature above 1000 °C. With prolonged PEO times, alpha alumina phase becomes the dominant crystalline form of aluminum oxide.

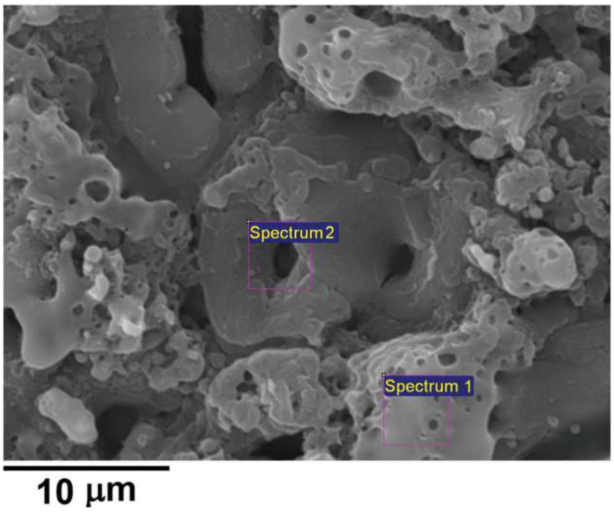

Fig. 3. SEM micrograph with marked positions of EDS spectra in Table 2 of oxide coating formed by PEO for 5 min.

XRD pattern of pure ZnO powder that was used as a source of ZnO nanoparticles is shown in Fig. 6. The peaks corresponding to (1 0 0), (0 0 2), (1 0 1), (1 0 2), (1 1 0), (1 0 3), and (1 1 2) planes are in accord with the typical wurtzite type structure of ZnO crystals. Peaks corresponding to unknown/unidentified phases were not observed in XRD pattern, indicating high purity of ZnO powder. Nevertheless, we were not able to detect any peaks corresponding to ZnO in XRD patterns of surface coatings obtained after different PEO times (Fig. 5). The main reason for this is the low concentration of uniformly dispersed ZnO nanoparticles all over the surface coatings. In order to investigate whether ZnO nanoparticles are present in oxide coatings, we performed Raman measurements (Fig. 7). Raman spectrum of ZnO powder (Fig. 7d) is characterized by a strong band at about 438 cm^{-1} corresponding to the E_2 mode, which is the strongest Raman mode in the wurtzite crystal structure of ZnO [16]. The Raman band at about 329 cm^{-1} is assigned to acoustic mode, while the weak Raman bands at about 381 cm^{-1} and 410 cm^{-1} are assigned to overtone of A_1 and E_1 transverse optical phonons [17]. Strong E_2 mode can be identified on all Raman spectra of the surface coatings formed by PEO. Strong bands at about 418 cm^{-1} and 379 cm^{-1} correspond to A_{1g} and E_g Raman active modes of alpha alumina [18]. These bands can be identified on Raman spectra of Al_2O_3/ZnO coatings formed after ten or more minutes of PEO, which is in agreement with XRD measurements (Fig. 5). The main E_2 mode of ZnO exhibits slight broadening due to interference with active mode E_g at about 431 cm^{-1} of alpha alumina [18].

3.2. Photoluminescent and photocatalytic properties of Al_2O_3/ZnO coatings

Evolution of the PL emission spectra of Al_2O_3/ZnO coatings formed during the PEO process is shown in Fig. 8. PL emission spectra in Fig. 8a feature a very intense and sharp band centered at about 385 nm, one visible broad band centered at about 510 nm, and a weak ultraviolet band centered at about 327 nm. On the PL emission spectra in Fig. 8b in addition to the visible broad band a sharp band at about 693 nm appears. Some of these PL bands are related to the PL of Al_2O_3 and other to the ZnO. In order to explain the spectra we performed PL measurements of surface coating formed in the supporting electrolyte without ZnO powder (0.1 M boric acid + 0.05 M borax), as well as the pure ZnO powder (Fig. 9).

Table 2
EDS analysis of oxide coating in Fig. 3 formed by PEO for 5 min.

	Atomic [%]		
	O	Al	Zn
Spectrum 1	63.96	30.99	5.04
Spectrum 2	49.94	49.42	0.64

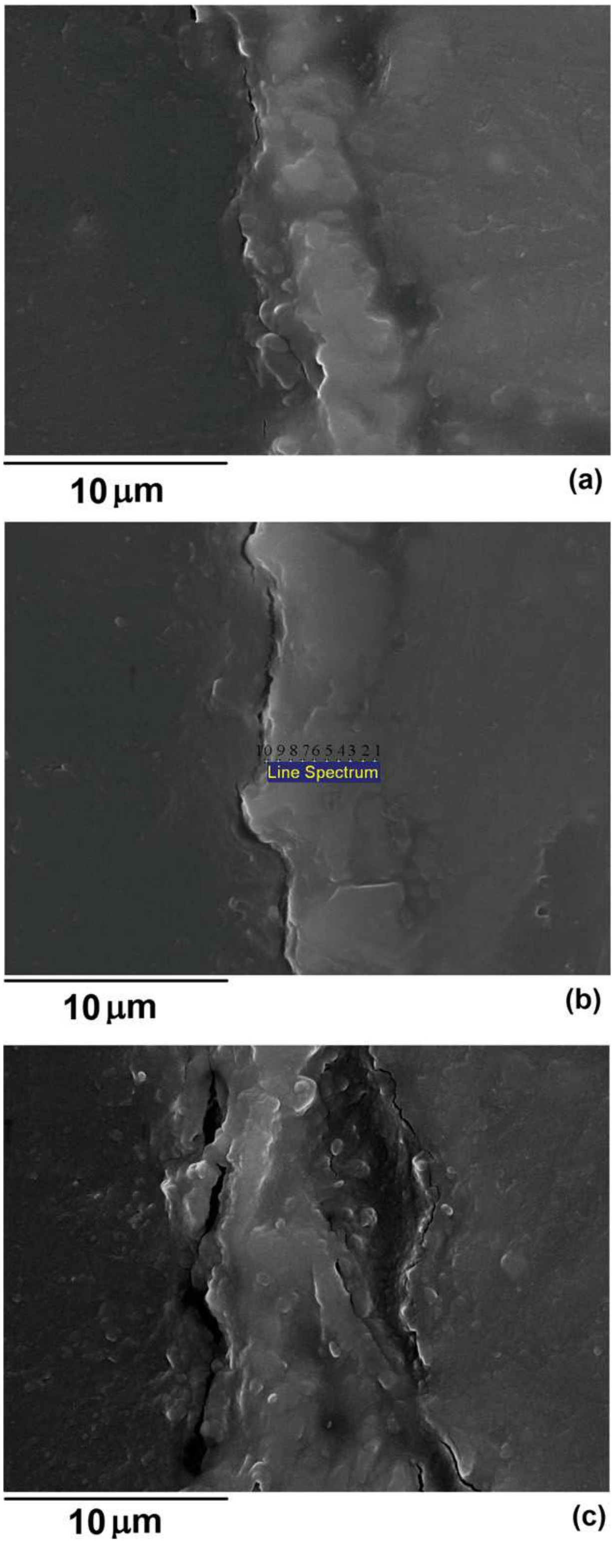

Fig. 4. SEM micrographs of polished cross-section of oxide coatings formed by PEO process for: (a) 10 min; (b) 15 min; (c) 30 min.

PL spectra of ZnO powder consist of a relatively weak near-ultraviolet emission band centered at about 385 nm and one broad green emission band centered at about 510 nm. It is generally acknowledged that the green emission of the ZnO is due to oxygen vacancy and

Table 3
Cross-sectional EDS analysis of oxide coatings in Fig. 4b.

	Atomic [%]		
	O	Al	Zn
Point 1	36.29	63.56	0.15
Point 2	42.08	57.68	0.23
Point 3	41.05	58.69	0.26
Point 4	43.80	55.92	0.28
Point 5	44.61	55.16	0.23
Point 6	48.19	51.53	0.28
Point 7	51.45	48.29	0.26
Point 8	50.36	49.18	0.46
Point 9	50.83	48.43	0.74
Point 10	51.09	47.58	1.28

zinc vacancy related defects [19], while the ultraviolet emission is attributed to the radiative recombination of free excitons [20]. On the other hand, wide PL bands of Al_2O_3 occur in the range from 300 nm to 600 nm and the PL centers are defect centers related to oxygen vacancies in oxide films (F and F^+ centers) [21]. In the PL emission spectra of Al_2O_3 coating formed by PEO, bands at about 327 nm and 693 nm are related to F^+ centers in alpha alumina [21,22]. PL of Al_2O_3 coating is much weaker than the corresponding PL of Al_2O_3/ZnO coating formed under the same anodic conditions (current density and time of anodization). This indicates that the main contribution in PL for Al_2O_3/ZnO coatings comes from ZnO deposited on the surface of such coatings. Band at 693 nm from alpha alumina can be detected in PL emission spectra of Al_2O_3/ZnO coatings formed after 10 min (Fig. 7b), which is also in agreement with XRD and Raman measurements (Fig. 4).

Fig. 8 shows that both near ultraviolet and green bands of Al_2O_3/ZnO coatings increase with time of PEO, but unlike in the case of PL of ZnO powder, ultraviolet PL band is much more intense than the green PL band. Wang et al. showed that Al_2O_3 buffer layer leads to an increase of the ultraviolet and a decrease of green bands of ZnO [23]. They proposed that the green band quenching of the ZnO films growing on Al_2O_3 buffer layer was due to the decrease in the concentration of oxygen vacancies. Namely, the oxygen atoms drift from the Al_2O_3 layer and occupy oxygen vacancies in ZnO film during its growth, thus improving its crystallization. Some authors have reported that the improvement the crystalline quality of ZnO (low structural defects, oxygen vacancies, zinc interstitials, and decrease in the impurities) may cause the appearance of a sharp and strong ultraviolet emission and a suppressed and/or weak green emission [24–26].

The efficiency of MO photodegradation for Al_2O_3/ZnO coatings formed after various PEO times is shown in Fig. 10. C_0 is the initial concentration of MO and C is the concentration after time t. Fig. 10 clearly implies that photoactivity of Al_2O_3/ZnO coatings increases with PEO time. Since it is well known that alumina is not photocatalytically active, it can be proposed that the increase in activity with PEO time is a consequence of the oxide layer thickening, resulting in an increase of highly dispersed ZnO phase content. This statement is supported by previously discussed EDS, XRD, and Raman spectra. Also, improved activity of ZnO/Al_2O_3 photocatalyst coincides with increase of PL intensity (Fig. 8). It is widely accepted that PL intensity reflects the rate of electron/hole recombination; in other words, materials with low PL intensity have high PA and vice versa. Following this reasoning, one can conclude that the nature of photoactive centers in ZnO/Al_2O_3 oxide coatings remains unchanged with prolonged PEO time, i.e., there is only an increase of their number within the oxide layer.

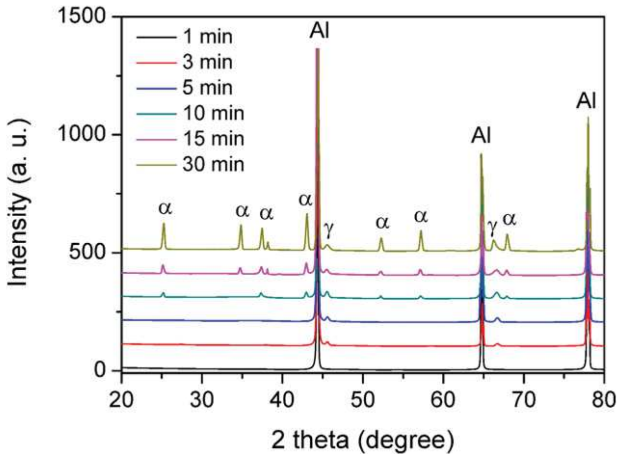

Fig. 5. XRD patterns of oxide coatings formed at various stages of PEO process.

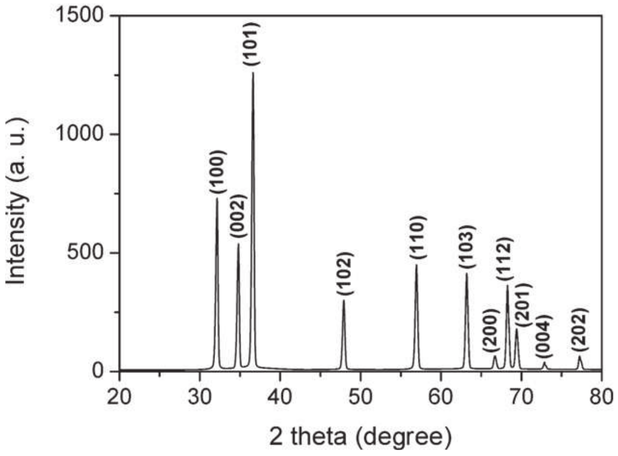

Fig. 6. XRD pattern of used ZnO powder.

It should be stressed that there is inhomogeneity in ZnO distribution within the oxide layer and ZnO is predominantly deposited in the outer layer of oxide coating. This observation imposes a question about more detailed consideration of nonuniform distribution of ZnO within the oxide coating. It seems that surface charge of ZnO plays an important role in the course of coating preparation. The pH value around 8 of the electrolytic solution we used in this experiment is beneath the isoelectric point that corresponds to the value of pH from around 10 indicating that surface of ZnO particles is positively charged [27]. Therefore, there are repulsive forces between the anode and positively charged ZnO particles, allowing only a small quantity of ZnO to be incorporated into oxide coatings in the early stages of PEO process. The incorporation of ZnO into oxide coating at this stage is related to its trapping by the outer layer due to locally high temperatures and significant turbulence

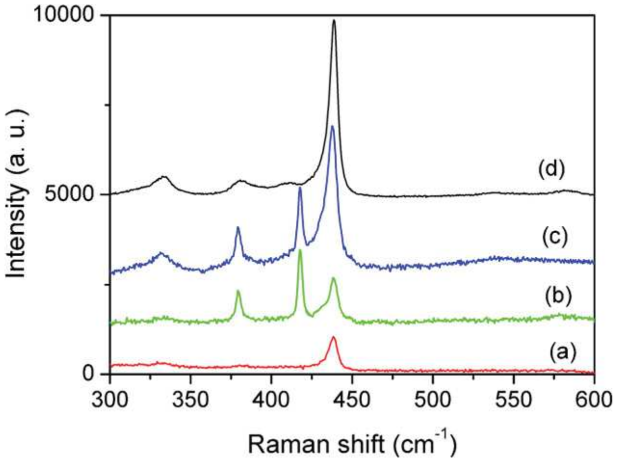

Fig. 7. (a) Raman spectrum of oxide coating formed after 3 min of PEO; (b) Raman spectrum of oxide coating formed after 10 min of PEO; (c) Raman spectrum of oxide coating formed after 15 min of PEO; (d) Raman spectrum of ZnO powder.

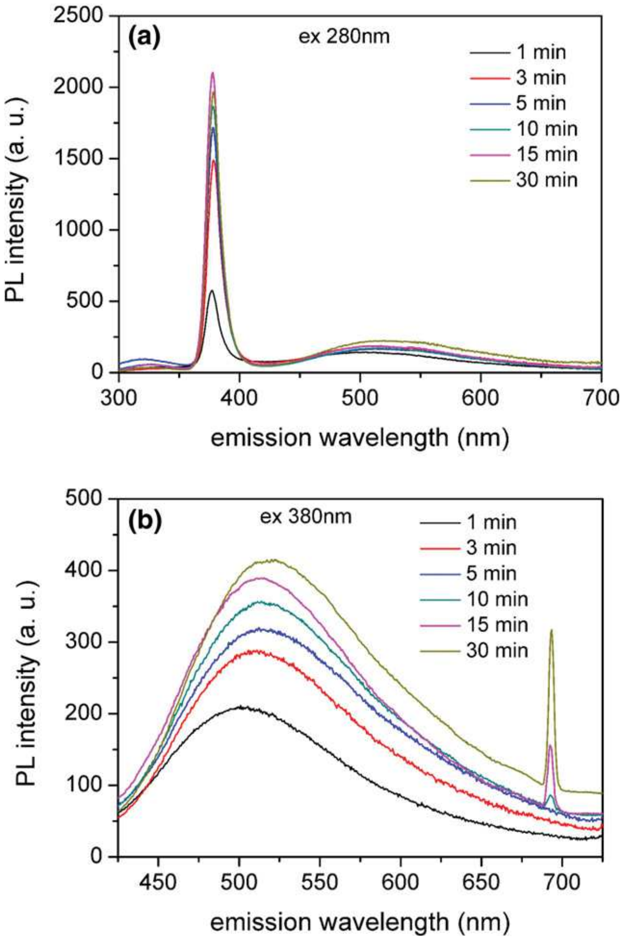

Fig. 8. Evolution of PL emission spectra of Al_2O_3/ZnO coatings formed during the PEO process: (a) emission PL spectra excited at 280 nm; (b) emission PL spectra excited at 380 nm.

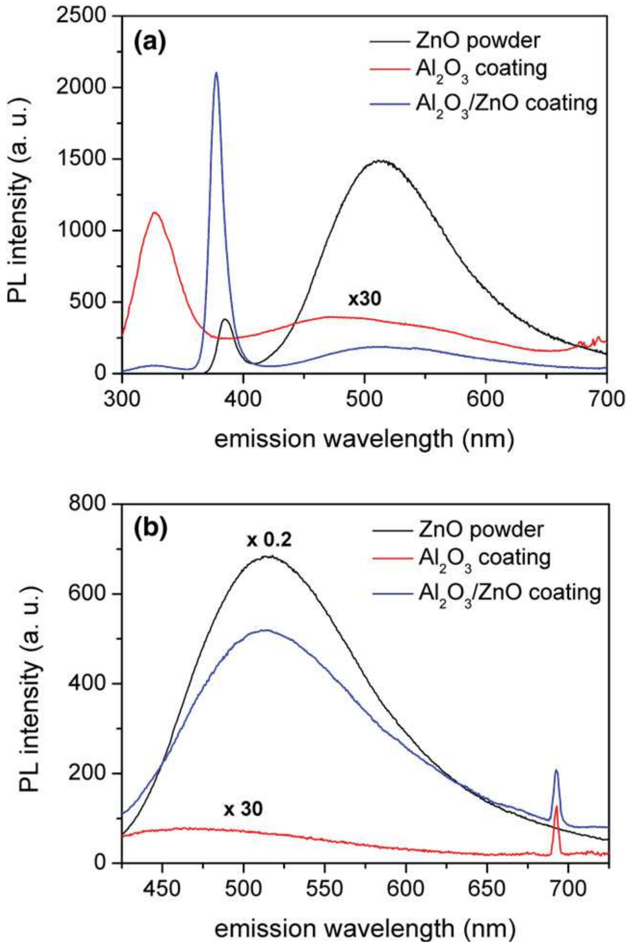

Fig. 9. PL emission spectra of ZnO powder, Al_2O_3, and Al_2O_3/ZnO coatings formed by PEO for 15 min: (a) emission PL spectra excited at 280 nm; (b) emission PL spectra excited at 380 nm.

of electrolytic solution. As the thickness of oxide coating increases with PEO time, electric field decreases and subsequently repulsive forces weaken allowing easier approach of ZnO particles to the outer layer, causing progressive increase of ZnO content on the top of the thicker oxide coatings.

We have already discussed that the phase composition of Al_2O_3/ZnO coatings changes with increased PEO time. At the same time, a change of alumina texture occurs due to gradual crystallization, going from amorphous alumina through the gamma phase up to the alpha phase, as presented on Fig. 5 (XRD data). Accordingly, specific surface area of alumina dramatically drops from several hundred m^2/g for its amorphous phase to a few m^2/g for alpha phase as a result of alumina sintering on the higher temperatures [28]. Process of sintering can capture ZnO making it inaccessible either to the light as immaterial reagent or to organic dye, causing the photoactivity of samples processed for PEO time over 10 min to be probably suppressed as a result of significant loss of surface area as alpha alumina appears. Simultaneously, there is an enrichment of ZnO on the surface of obtained oxide coatings (Table 1) and the contribution of these individual processes to the overall photoactivity becomes complex. It is also worth mentioning that similar photocatalytic behavior is observed for Al_2O_3/ZnO coatings obtained after 15 and 30 min of PEO processing. This suggests that some kind of photoactivity plateau is reached which rules out the influence of coating thickness on photocatalytic activity, i.e. it points out to the existence of mass transfer (for organic dye) and/or photon penetration limitations.

In order to investigate the influence of ZnO concentration on photocatalytic properties of obtained coatings another set of measurements was conducted in boric acid + borax solution with various ZnO concentrations (Fig. 11). Obviously, there is no difference in photoactivity for ZnO concentrations of 1 g/L, 2 g/L, and 4 g/L, but concentration of 0.5 g/L causes significant drop in photoactivity. Saturation of photoactivity is related to the comparable number of available photocatalytically active sites, i.e. only limited amount of ZnO can be present on the surface of obtained oxide layers. This data offers another possibility for fine tuning of ZnO surface content by varying its

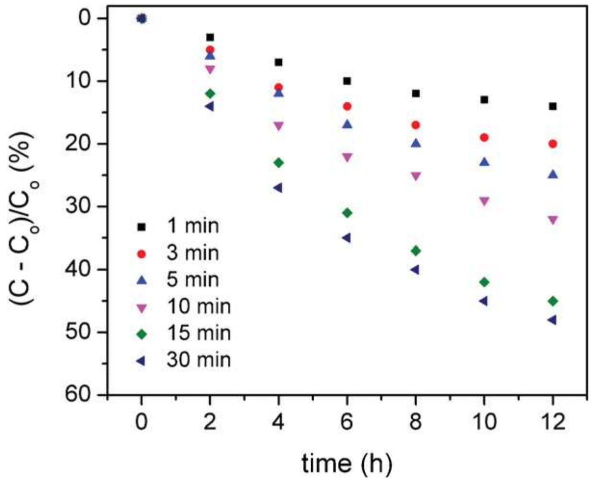

Fig. 10. Photocatalytic performance of Al_2O_3/ZnO coatings formed in various stages of PEO process.

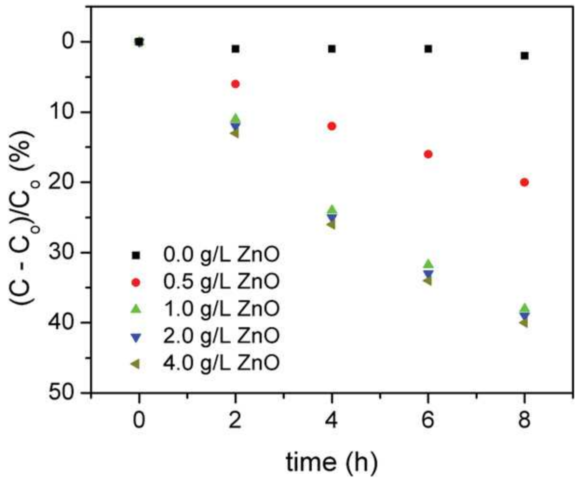

Fig. 11. Photocatalytic performance of Al_2O_3/ZnO coatings formed for 15 min in 0.1 M boric acid + 0.05 M borax + various concentrations of ZnO.

concentration in the electrolyte below 1 g/L. At the same time, photocatalytic activity of the sample prepared in the solution without ZnO nanoparticles excludes the effect of other electrolyte species on photocatalytic properties of obtained oxide coatings.

4. Conclusions

This paper reports on the formation of Al_2O_3/ZnO oxide coatings formed by plasma electrolytic oxidation of aluminum in water based boric acid + borax electrolyte with an addition of ZnO nanoparticles. Morphology, phase and chemical compositions of formed oxide coatings strongly depend on PEO time. Based on experimental results, a mechanism for ZnO incorporation into the oxide coating in the early and in the later stage of PEO is suggested.

PL spectra of formed oxide coatings feature well pronounced bands native to Al_2O_3 and ZnO oxides. PL spectrum of mixed Al_2O_3/ZnO oxide suggests that higher level of crystallinity results in higher PL intensity and identifies oxygen vacancies as centers of luminescence. Photocatalytic decomposition of MO under simulated sunlight shows that photoactivity is related to PEO process time. Most photocatalytically active samples were obtained after 30 min of PEO, but a negligible increase in photoactivity was noticed in comparison with samples processed for 15 min.

Acknowledgments

This work is supported by the Ministry of Education, Science, and Technological Development of the Republic of Serbia under project Nos. 171035, 172022, and 172026. Authors would also like to acknowledge M. Rados for his admirable work in collecting SEM/EDS data.

References

[1] J.L. Gomez, O. Tigli, Zinc oxide nanostructures: from growth to application, J. Mater. Sci. 48 (2013) 612–624.
[2] X. Ren, W. Zi, Q. Ma, F. Xiao, F. Gao, S. Hu, Y. Zhou, S. Liu, Topology and texture controlled ZnO thin film electrodeposition for superior solar cell efficiency, Sol. Energy Mater. Sol. Cells 134 (2015) 54–59.
[3] X. Mo, G. Fang, H. Long, S. Li, H. Huang, H. Wang, Y. Liu, X. Meng, Y. Zhang, C. Pan, Near-ultraviolet light-emitting diodes realized from n-ZnO nanorod/p-GaN direct-bonding heterostructures, J. Lumin. 137 (2013) 116–120.
[4] S.I. Inamdar, V.V. Ganbavle, K.Y. Rajpure, ZnO based visible–blind UV photodetector by spray pyrolysis, Superlattice. Microst. 76 (2014) 253–263.
[5] S. Joshi, M.M. Nayak, K. Rajanna, Effect of post-deposition annealing on transverse piezoelectric coefficient and vibration sensing performance of ZnO thin films, Appl. Surf. Sci. 296 (2014) 169–176.
[6] C. Tian, Qi Zhang, A. Wu, M. Jiang, Z. Liang, B. Jianga, H. Fu, Cost-effective large-scale synthesis of ZnO photocatalyst with excellent performance for dye photodegradation, Chem. Commun. 48 (2012) 2858–2860.
[7] S. Stojadinović, R. Vasilić, M. Perić, Investigation of plasma electrolytic oxidation on valve metals by means of molecular spectroscopy — a review, RSC Adv. 4 (2014) 25759–25789.
[8] S. Stojadinovic, R. Vasilic, I. Belca, M. Petkovic, B. Kasalica, Z. Nedic, Lj. Zekovic, Characterization of the plasma electrolytic oxidation of aluminium in sodium tungstate, Corros. Sci. 52 (2010) 3258–3265.
[9] A.L. Yerokhin, X. Nie, A. Leyland, A. Matthews, S.J. Dowey, Plasma electrolysis for surface engineering, Surf. Coat. Technol. 122 (1999) 73–93.
[10] J.W. Digle, T.C. Downie, C.W. Goulding, Anodic oxide films on aluminium, Chem. Rev. 69 (1969) 365–405.
[11] M. Albella, I. Montero, J.M. Martinez-Duart, A theory of avalanche breakdown during anodic oxidation, Electrochim. Acta 32 (1987) 255–258.
[12] G. Sundararajan, L. Rama Krishna, Mechanisms underlying the formation of thick alumina coatings through the MAO coating technology, Surf. Coat. Technol. 167 (2003) 269–277.
[13] L.O. Snizhko, A.L. Yerokhin, A. Pilkington, N.L. Gurevina, D.O. Misnyankin, A. Leyland, A. Matthews, A model for galvanostatic anodising of Al in alkaline solutions, Electrochim. Acta 49 (2004) 2085–2095.
[14] M.J. Shen, X.J. Wang, M.F. Zhang, High-compactness coating grown by plasma electrolytic oxidation on AZ31 magnesium alloy in the solution of silicate–borax, Appl. Surf. Sci. 259 (2012) 362–366.
[15] W.L. Xu, M.J. Zheng, S. Wu, W.Z. Shen, Effects of high-temperature annealing on structural and optical properties of highly ordered porous alumina membranes, Appl. Phys. Lett. 85 (2004) 4364–4366.
[16] A. Sahai, N. Goswami, Structural and vibrational properties of ZnO nanoparticles synthesized by the chemical precipitation method, Physica E 58 (2014) 130–137.
[17] A.K. Ojha, M. Srivastava, S. Kumar, R. Hassanein, J. Singh, M.K. Singh, A. Materny, Influence of crystal size on the electron–phonon coupling in ZnO nanocrystals investigated by Raman spectroscopy, Vib. Spectrosc. 72 (2014) 90–96.
[18] R. Krishnan, R. Kesavamoorthy, S. Dash, A.K. Tyagi, B. Raj, Raman spectroscopic and photoluminescence investigations on laser surface modified α-Al_2O_3 coatings, Scr. Mater. 48 (2003) 1099–1104.
[19] P.S. Xu, Y.M. Sun, C.S. Shi, F.Q. Xu, H.B. Pan, The electronic structure and spectral properties of ZnO and its defects, Nucl. Inst. Methods Phys. Res. B 199 (2003) 286–290.
[20] M. Anpo, Y. Kubokawa, Photoluminescence of zinc oxide powder as a probe of electron–hole surface processes, J. Phys. Chem. 88 (1984) 5556–5560.
[21] S. Stojadinovic, R. Vasilic, Z. Nedic, B. Kasalica, I. Belca, Lj. Zekovic, Photoluminescent properties of barrier anodic oxide films on aluminum, Thin Solid Films 519 (2011) 3516–3521.
[22] P.G. Li, M. Lei, W.H. Tang, Raman and photoluminescence properties of α-Al_2O_3 microcones with hierarchical and repetitive superstructure, Mater. Lett. 64 (2010) 161–163.
[23] T. Wang, H. Wu, C. Chen, C. Liu, Growth, optical, and electrical properties of nonpolar M-plane ZnO on p-Si substrates with Al_2O_3 buffer layers, Appl. Phys. Lett. 100 (2012) 3 (011901).
[24] D.M. Bagnall, Y.F. Chen, Z. Zhu, T. Yao, S. Koyama, M.Y. Shen, T. Goto, High temperature excitonic stimulated emission from ZnO epitaxial layers, Appl. Phys. Lett. 73 (1998) 1038–1040.
[25] A. Achour, K. Ait Aissa, M. Mbarek, K. El Hadj, N. Ouldhamadouche, N. Barreau, L. Le Brizoual, M.A. Djouadi, Enhancement of near-band edge photoluminescence of ZnO film buffered with TiN, Thin Solid Films 538 (2013) 71–77.
[26] W. Bai, X. Zhu, Z. Zhu, J. Chu, Synthesis of zinc oxide nanosheet thin films and their improved field emission and photoluminescence properties by annealing processing, Appl. Surf. Sci. 254 (2008) 6483–6488.
[27] R. Marsalek, Particle size and zeta potential of ZnO, APCBEE Procedia 9 (2014) 13–17.
[28] G. Busca, Structural, surface, and catalytic properties of aluminas, Adv. Catal. 57 (2014) 319–404.

Available online at www.sciencedirect.com

ScienceDirect

Ceramics International 41 (2015) 13189–13200

CERAMICS INTERNATIONAL

www.elsevier.com/locate/ceramint

Multiferroic (NiZn) Fe_2O_4–$BaTiO_3$ composites prepared from nanopowders by auto-combustion method

A.S. Dzunuzovic[a], M.M.Vijatovic Petrovic[a], B.S. Stojadinovic[b], N.I. Ilic[a], J.D. Bobic[a], C.R. Foschini[c], M.A. Zaghete[d], B.D. Stojanovic[a,*]

[a]*Institute for Multidisciplinary Research University of Belgrade, Belgrade, Serbia*
[b]*Institute of Physics, University of Belgrade, Serbia*
[c]*UNESP, Faculty for Engineering, Bauru, SP, Brazil*
[d]*UNESP, Institute for Chemistry, Araraquara, SP, Brazil*

Received 24 June 2015; received in revised form 10 July 2015; accepted 16 July 2015
Available online 4 August 2015

Abstract

Nickel zinc ferrite (NZF) and barium titanate (BT) were prepared by auto-combustion synthesis as an effective, simple and rapid method. Multiferroic composites with the general formula $yNi_{1-x}Zn_xFe_2O_4-(1-y)BT$ ($x=0.3$, 0.5, 0.7, $y=0.5$) were prepared by mixing NZF and BT powders in a liquid medium in the ball mill. The FEG micrographs indicated the primary particle size less than 100 nm for both, barium titanate and nickel zinc ferrite phases. X-ray analysis and Raman spectroscopy indicated the formation of well crystallized structure of NZF and BT phase in the composite powders and ceramics, with a small contribution of the secondary phase. The homogenous phase distribution in obtained composites was also confirmed. Impedance spectroscopy measurements were carried out in order to investigate the electrical resistivity of materials, showing that grain boundaries have greater impact on the total resistivity than grains. Saturation magnetization and remnant magnetization continuously decrease with barium titanate phase increase.

Keywords: A. Powders: chemical preparation; B. Composites; C. Impedance; D. $BaTiO_3$ and titanates; D. Ferrites

1. Introduction

Miniaturization of the solid-state electronics is achieved by downscaling and multifunctionality. Ferroics and multiferroics are among the most attractive multifunctional materials [1]. These nanostructured materials stimulated a sharply increasing interest to their significant technological promise in novel devices due to fact that the combination of dissimilar materials in ferroic-based oxide nanocomposites resulted in totally novel functionality.

The term multiferroic (MF) was first used by Schmid in 1994. His definition referred to multiferroics as a single phase materials which simultaneously possess two or more primary ferroic (ferroelectric, ferromagnetic and ferroelastic) properties. Today the term multiferroic has been expanded to include materials which exhibit any type of long range magnetic ordering, spontaneous electric polarization, and/or ferroelasticity. Working under this expanded definition the history of magnetoelectric multiferroics can be traced back to the 1960s [1–3]. In the most general sense the field of multiferroics was born from studies of magnetoelectric systems [4–6]. After an initial burst of interest, research remained static until early 2000. In 2003 the discovery of large ferroelectric polarization in epitaxially grown thin films of $BiFeO_3$ [7] and the discovery of strong magnetic and electric coupling in orthorhombic $TbMnO_3$ and $TbMn_2O_5$ have stimulated activity in the field of multiferroics. Besides scientific interest in their physical properties, multiferroics are interesting due to their potential applications as transducers, actuators, switches, magnetic field

---

[*] Corresponding author.
E-mail address: bstojanovic80@yahoo.com (B.S. Stojadinovic).

http://dx.doi.org/10.1016/j.ceramint.2015.07.096

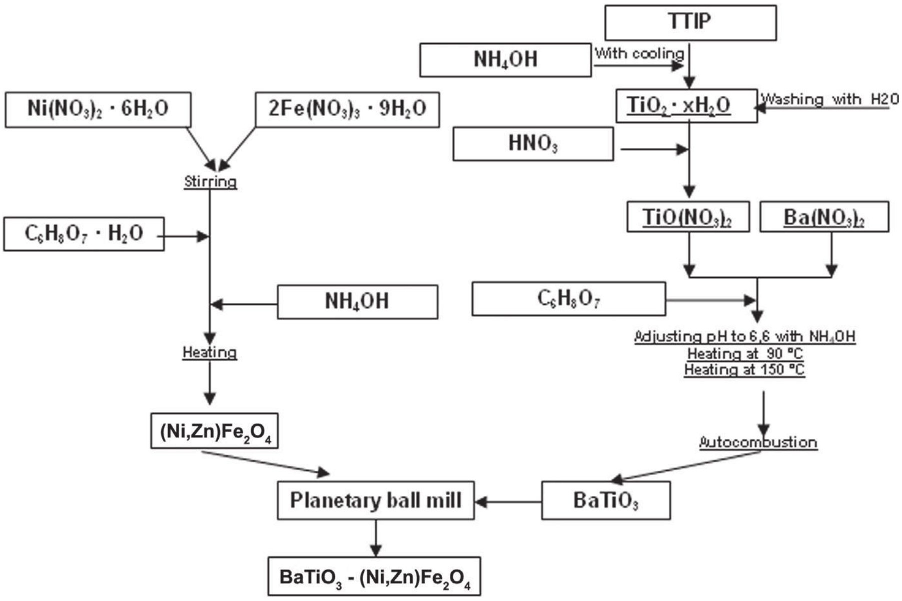

Fig. 1. Scheme of NZF, BT and composites preparation.

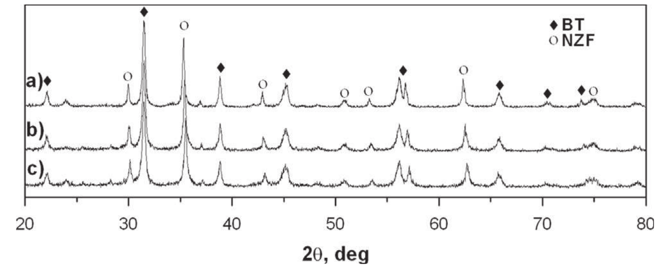

Fig. 2. The X-ray diffraction patterns of (a) NZF(30–70) – BT, (b) NZF(50–50) – BT and (c) NZF(70–30)–BT powders.

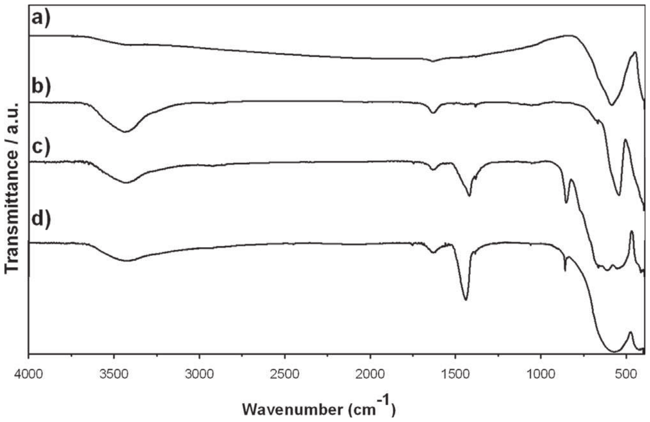

Fig. 3. FT-IR spectra of (a) NF, (b) ZF, (c) BT and (d) NZF(70–30) – BT powders.

sensors, new types of electronic memory devices, capacitive/inductive passive filters for telecommunications, etc. [8,9]. A large number of publications have been dedicated to multiferroics, dealing with theoretical, experimental, and application aspects [2,10]. In spite of hundreds of publications focused to single or composite multiferroic materials in the last years, they remain highly controversial concerning their preparation methods, phase stability, intrinsic polarization and switching, ferroelectric, ferromagnetic and magnetoelectric properties, etc. [10].

Multiferroic properties can appear in a large variety of materials [11]. The ferroelectric–ferromagnetic composites, as two-phase multiferroic materials, are desired not only for the fundamental research of magneto-electric effect, but also for the potential applications in many electronic devices [12]. The most widely studied systems correspond to Co or Ni ferrites, with PZT, PNT, BT or BST [13]. Among them, the Ni–Zn ferrites/$BaTiO_3$ systems need to be further investigated because of high electrical resistivity, chemical stability and excellent electromagnetic properties of the Ni–Zn ferrites, and high permittivity, low dielectric loss and high tunability of $BaTiO_3$ [4–6]. Those composites have attracted considerable attention as a new class of nanoferrites, expanding their use in other areas, such as drug delivery, heterogeneous catalysis, levitated railway system, magnetic-refrigeration, microwave devices, antennas, etc. [14].

To obtain the multiferroics, several routes for conventional material fabrication are being applied. Popular techniques within the multiferroic community are: solid state synthesis, hydrothermal synthesis, sol–gel processing, vacuum based deposition or other wet chemical synthesis methods. However, some types of multiferroics require specific processing conditions within more appropriate techniques. Consequently, multiferroic composites request methods for the synthesis both components: ferroelectric and ferromagnetic.

Ferrites crystallize in three crystal type: spinel, garnet type and magnetoplumbite type [15,16]. Meanwhile, the main attention is stressed to spinel type of ferrites that can be synthesized by a sol–gel method, conventional solid state reaction, mechanical attrition, hydrothermal synthesis, self-propagating combustion method, thermolysis, wet chemical co-precipitation technique, self-propagating, microemulsion,

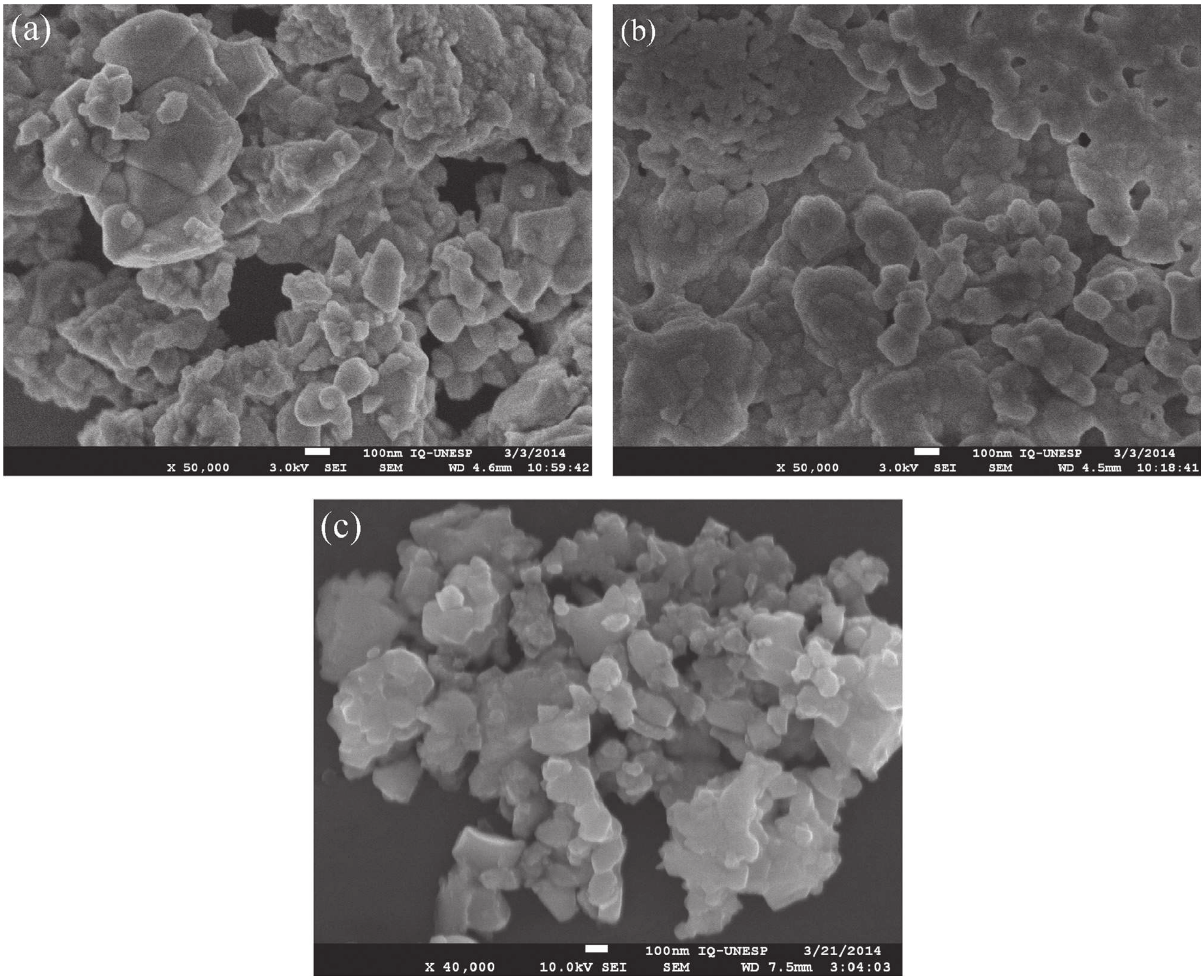

Fig. 4. SEM images of (a) NZF(70–30), (b) BT and (c) NZF(70–30)−BT powders.

microwave synthesis, etc. [17,18]. Recently, auto-combustion synthesis starts to be popular as rapid, cheap and rather simple technique. Ferroelectric component in multiferroic composites, such as barium titanate – $BaTiO_3$ (BT) can be produced using a huge number of various well-known methods. However, to obtain barium titanate through an advanced synthesis method like auto-combustion synthesis is under some difficulties due to lack of the literature data for the preparation of the BT by this method [5].

The aim of this study was to prepare multiferroic composites (Ni–Zn) ferrite–barium titanate from nanopowders obtained by an auto-combustion technique. It was shown that auto-combustion synthesis is very convenient for obtaining the ferrite powder as a pure phase with good properties. To obtain barium titanate by this method is not so simple due to the possible appearance of secondary phases which later may complicate the process of obtaining satisfactory properties of multifferoic composites. A number of different methods were used to characterize obtained powders and ceramic composites in order to fabricate functional multiferroic material with both, ferroelectric and magnetic properties.

2. Material and methods

The multiferroic composite materials, consisting of $Ni_{1-x}Zn_xFe_2O_4$ ($x=0.3$, 0.5, 0.7, denoted as NZF(70–30), NZF(50–50), NZF(30–70) and $BaTiO_3$ (BT), were obtained using the synthesis route shematically presented in Fig. 1.

The raw materials used for the synthesis of nickel zinc ferrite were $Fe(NO_3)_3 \cdot 9H_2O$ (Alfa Aesar, 98.0–101.0%), $Ni(NO_3)_2 \cdot 6H_2O$ (Alfa Aesar, 99.9985%), $Zn(NO_3)_2 \cdot 6H_2O$ (Alfa Aesar, 99%), $C_6H_8O_7 \cdot H_2O$ (Carlo Erba, 99.5–100.5%) and NH_4OH (Lach Ner, 25%). The molar ratio of Fe-ions, Ni+Zn-ions, citric acid was 2:1:1. Metal nitrates and citric acid solution were mixed by dissolving in a minimum amount of deionised water. The pH value of the solution was adjusted to 7 using the ammonia solution. After that the solution was heated and stirred at the temperature of about 90 °C until it converted into a xerogel, which was further heated in a heating calotte at 200 °C when self-propagation reaction was achieved. The formed powder was calcined at 1000 °C/1 h with heating rate 2 °C/min [19].

Starting reagents used for BT synthesis were $Ti(OCH(CH_3)_2)_4$ (TTIP) (Alfa Aesar, 98.0–101.0%), HNO_3, $C_6H_8O_7 \cdot H_2O$ (Carlo

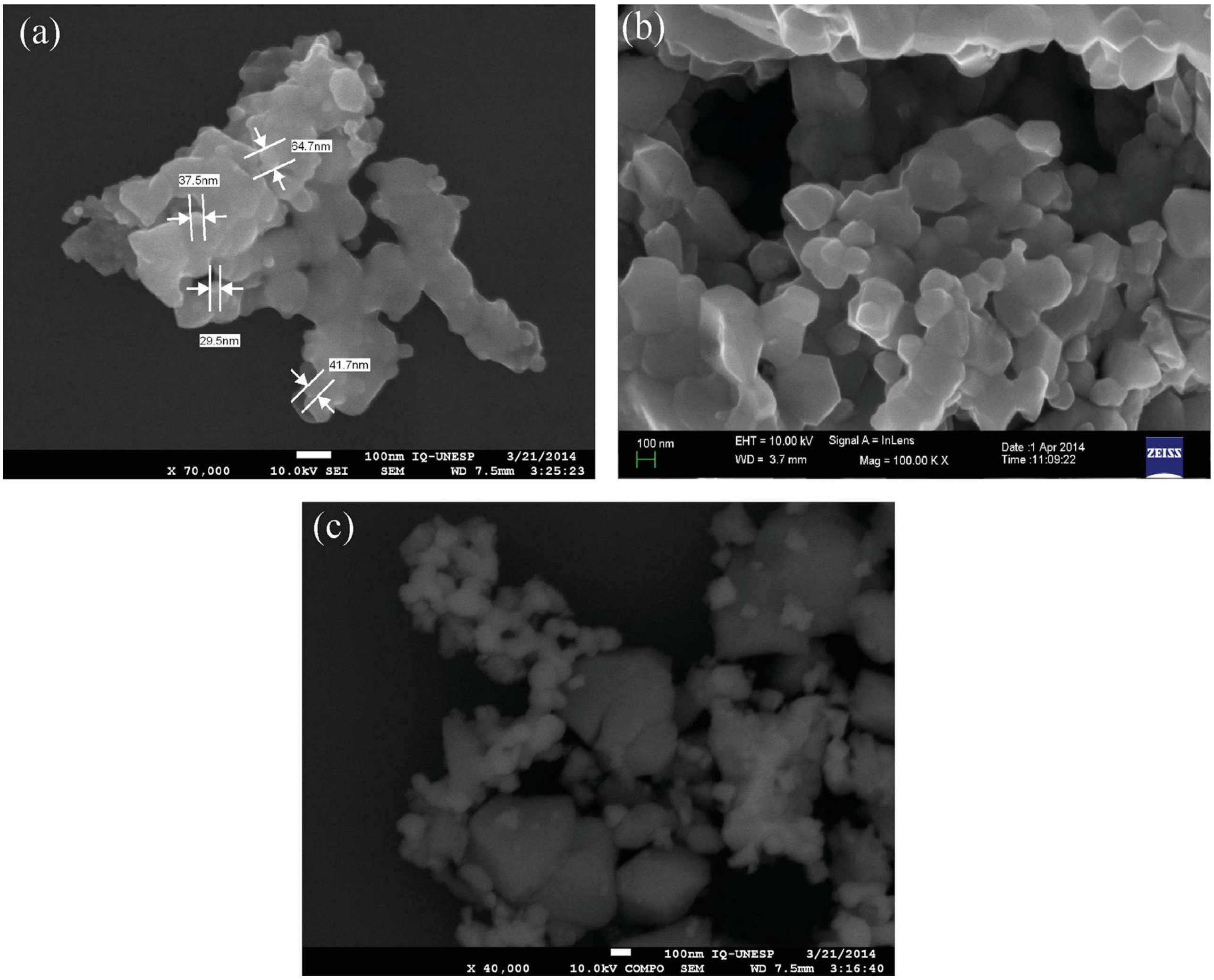

Fig. 5. FEG micrographs of (a) BT, (b) NZF(70–30) and (c) NZF(70–30)–BT powders.

Erba, 99.5–100.5%), $Ba(NO_3)_2$ and NH_4OH (Lach Ner, 25%). Firstly, ammonium hydroxide was added to TTIP solution, with constant cooling. During this process, the yellow precipitate was formed. It was washed with deionized water in a Buchner funnel on a vacuum pump. The obtained residue was dissolved in diluted HNO_3. Solutions of $TiO(NO_3)_2$ and $BaNO_3$ were mixed and citric acid was added as a fuel. pH value of solution was adjusted to 6.6 using NH_4OH. When solution was turned to xerogel, by heating at 90 °C, temperature was raised to 150 °C and self-ignition reaction occurs. It is very fast and exothermic reaction, and gray ash formed during combustion process represents the BT precursor powder. This powder was calcined at 900 °C for 2 h, with a heating rate of 5 °C/min (Electron-UK oven).

Multiferroic composites NZF–BT were prepared by mixing chemically obtained powders of the NZF and BT in the planetary ball mill for 24 h. The mass ratio of NZF and BT was always 1:1 for all obtained samples. Wolfram carbide balls and iso-propanol were used as a milling media. The composites powders were uniaxially pressed at 196 MPa into pellets and sintered at 1200 °C for 2 h.

The phase and crystal structure analysis was carried out by X-ray diffraction technique (Rotate anode Rigaku RINT2000, Experimental conditions: 40 kV, 60 mA. Linear detector D/teX Ultra – Rigaku, Divergence slit: 0, 25, Horizontal aperture slit: 5 mm). Micro-Raman spectra of the synthesized composites were collected at room temperature in the backscattering configuration using a JobinYvon T64000 spectrometer. The 514-nm laser line of a mixed Ar^+/Kr^+ laser was used as an excitation source with an incident laser power 60 mW in order to minimize heating effects. The ceramic composite samples were measured in the range 200–800 cm^{-1}. The FT-IR spectra were recorded with a Bruker Equinox-55 instrument. The morphology of the powders and microstructure of ceramics were examined using scanning electron microscope (SEM Model TESCAN SM-300) and field emission microscope (FE-SEM, JEOL, JSM-7500F). The grain size is determined using ImageJ program. The impedance measurements were performed using an LCR meter (model 9593-01, HIOKI HITESTER). Samples were prepared by coating their polished surfaces with Ag paste to improve the electrical contact. The real and imaginary parts of the complex impedance were measured in the frequency range of 42 Hz to 1 MHz and temperature range of 50–200 °C and referred as the Nyquist plot. Collected data were analyzed using the commercial software package Z-view. Magnetic measurements of materials were carried out using a superconducting quantum interferometric magnetometer SQUID (Quantum Design).

3. Results and discussion

XRD patterns of NZF(70–30)–BT, NZF(50–50)–BT and NZF(30–70)–BT powders, presented in Fig. 2, shows that nickel zinc ferrite, according to JCPDS files no. 10-0325, and barium titanate phases, according to JCPDS files no. 05-0626, were obtained.

FT-IR spectra of calcined nickel ferrite (NF), zinc ferrite (ZF), BT and NZF(70–30)–BT powders, recorded in the wave number range of 400–4000 cm^{-1} at room temperatures, are presented in Fig. 3. FT-IR spectra of NF and ZF display three bands at 560, 1640 and 3400 cm^{-1}. Strong peak at 560 cm^{-1} corresponds to metal ion-oxygen complexes in the tetrahedral sites. Small peak at 1640 cm^{-1} was assign to the adsorbed water or humidity. The peak at 3400 cm^{-1} corresponds to stretching and banding vibration of O–H bonds [20].

Absorption band near 3500 cm^{-1} can be observed in FTIR spectra of barium titanate. This peak was assigned to the stretching mode of internal OH$^-$ ions [21]. The broad bands at 590–680 cm^{-1} correspond to stretching of Ti–O bond [22].

Fig. 4 shows SEM images of the pure NZF(70–30), BT and composite NZF(70–30)–BT powders. It is possible to notice that the powders indicated the strong agglomeration with small primary particle size (< 100 nm). Small particles produced by chemical synthesis usually tend to form the agglomerates, as it was observed in the investigated case. That problem will be studied more carefully in the future period, having in mind the importance of composite materials properties. The use of attrition milling after calcination could be one of the possible solutions for the agglomeration reduction [23].

The FE-SEM micrographs of the obtained powders (Fig. 5) mostly indicated the rounded shapes of barium titanate particles with primary particle size less than 50 nm. The shape of ferrite particles is pyramidal like. In the composite ferroelectric–ferromagnetic powders obtained by homogenization of individual ferroelectric and ferromagnetic phase, two separate constituents could be clearly noticed, the one with rounded particles that belongs to BT and the other one with pyramidal particle shape that belongs to ferrite, demonstrating that multifferoic composites were obtained with a good dispersion of the nickel–zinc ferrite spinel phase in the BT ferroelectric matrix. The average particle size in the multiferroic composite powders is below 100 nm for BT and 150–300 nm for ferrites.

The XRD difractograms for sintered samples of obtained composites are presented in Fig. 6. The formation of both phases, NZF and BT was detected (JCPDS files no. 10-0325, JCPDS files no. 05-0626). Series of small peaks at 2θ angles of 32.2, 34.1, 37.1, 40.2, 54.9 and 63.1°, according to JCPDS files no. 84-0757, indicated barium ferrite ($BaFe_{12}O_{19}$) as a secondary phase present in the sintered composites.

The relative contribution of the secondary phase, around 8%, was calculated from XRD patterns of ceramics composites, according to the most intensive peak at the 32°. Therefore, it is evident that the amount of the secondary phase is the highest in the case of NZF(70–30)–BT. The appearance of $BaFe_{12}O_{19}$ was noticed in a few published articles, as well [24,25]. Therefore, from the available literature data was concluded that the presence of small amount of this secondary phase cannot significantly affect the magnetic properties of obtained composites. However, for further investigation, an effort will be done to obtain pure phase composites, in order to provide clearer information about influence of secondary phases on the properties of ferroelectric–ferromagnetic composites.

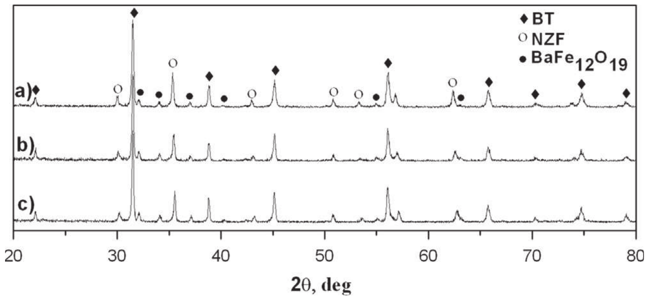

Fig. 6. The XRD patterns of (a) NZF(30–70)–BT, (b) NZF(50–50)–BT and (c) NZF(70–30)–BT ceramics.

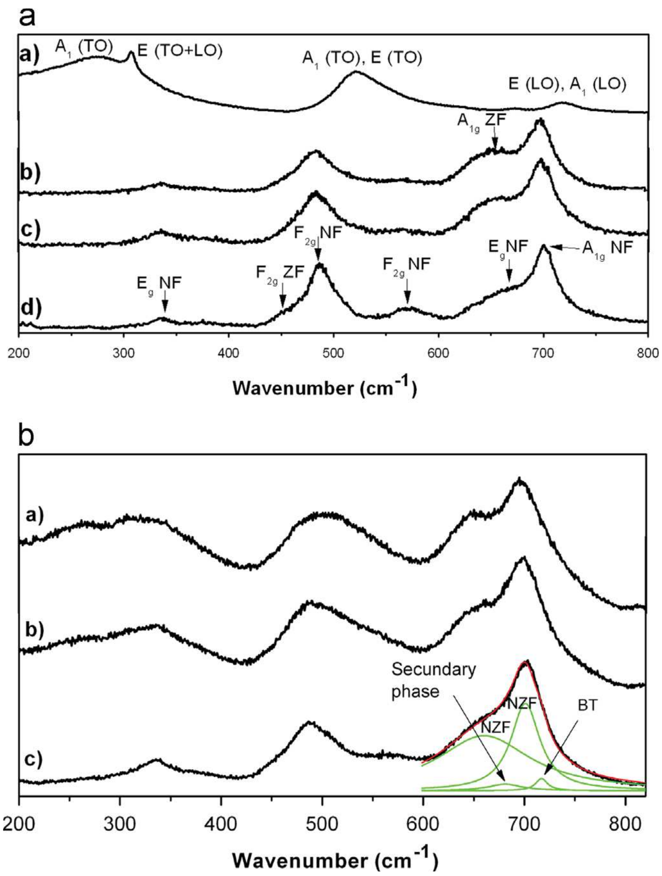

Fig. 7. (a) Raman spectra of (a) BT, (b) NZF(30–70), (c) NZF(50–50), and (d) NZF(70–30) and (b) Raman spectra of composites (a) NZF(30–70)–BT, (b) NZF(50–50)–BT and (c) NZF(70–30) at room temperature.

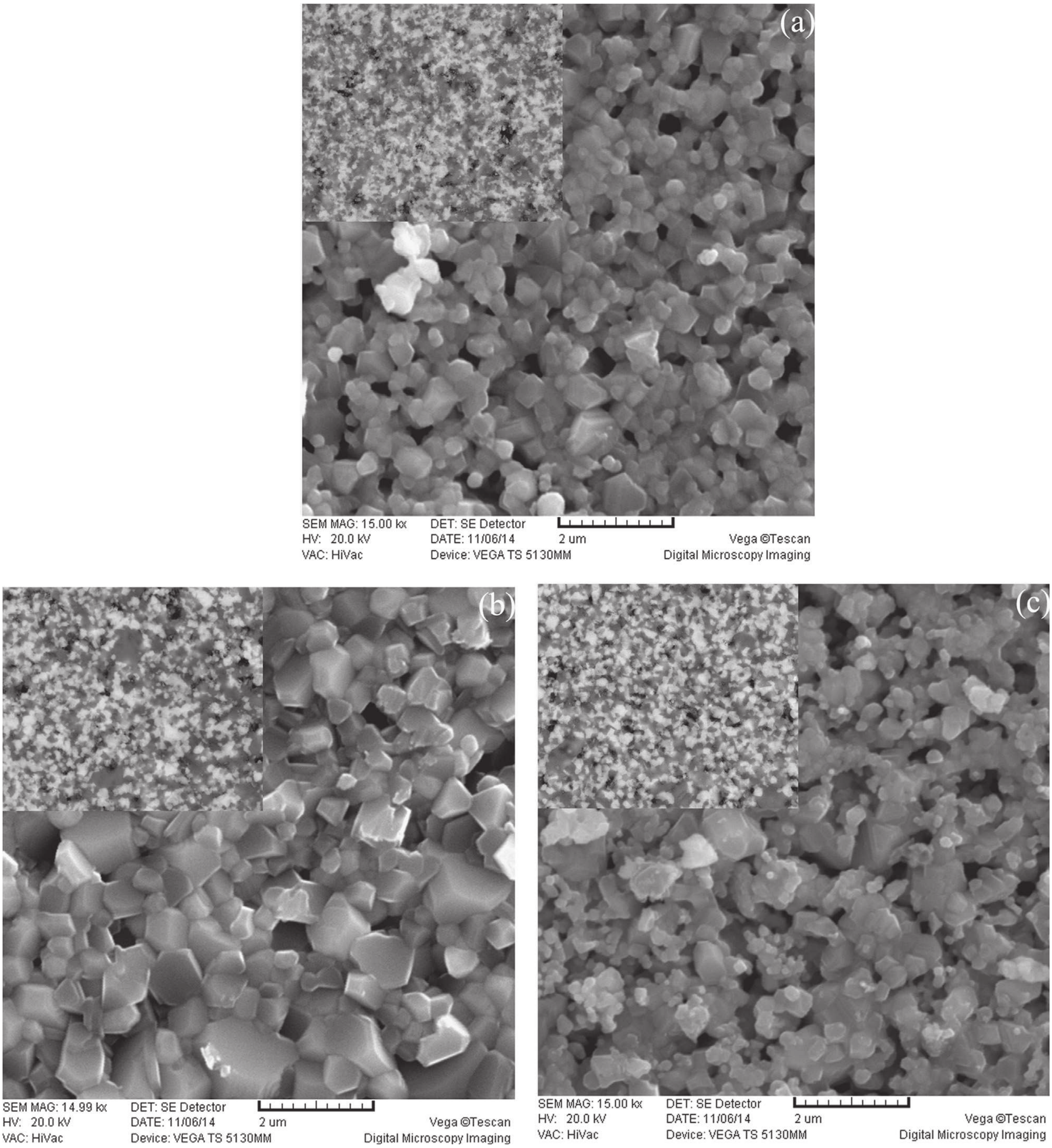

Fig. 8. SEM images of (a) NZF(30–70)–BT, (b) NZF(50–50)–BT, and (c) NZF(70–30)–BT ceramics.

The Raman spectra of $BaTiO_3$ and $Ni_{1-x}ZnFe_2O_4$ ceramics (x=0.3, 0.5 and 0.7) are given in Fig. 7a) for the comparison with obtained composite materials. In the spectra of NZF(70–30) ceramics the most intense Raman modes of nickel ferrite phase are two F_{2g} modes at 482 and 575 cm^{-1}, one E_g mode at 335 cm^{-1} and one A_{1g} mode at 702 cm^{-1} with a shoulder at 666 $cm^{-1}$of E_g symmetry [26,27]. The most prominent modes of the zinc ferrite phase are the F_{2g} mode at 451 cm^{-1} and broad A_{1g} mode at around 647 cm^{-1} of low intensity [28,29]. With increasing content of Zn in the $Ni_{1-x}Zn_xFe_2O_4$ samples, the F_{2g} mode of zinc ferrite becomes more intense and the E_g mode of nickel–ferrite at 660 cm^{-1} shifts to the lower frequency, approaching the frequency of zinc–ferrite A_{1g} mode. The other F_{2g} mode of nickel ferrite phase at 575 cm^{-1} almost disappears in the NZF(30–70) sample.

The Raman spectrum of the $BaTiO_3$ tetragonal phase presented the most prominent Raman modes are a broad band at about 270 cm^{-1} [A_1 (TO)], a sharp peak at ~303 cm^{-1} [E (TO+LO) mode], a mode at 516 cm^{-1}[A_1 (TO), E (TO)] and a mode at around 720 cm^{-1} [E (LO), A_1 (LO)] [30].

The Raman spectra of the sintered composites are presented in Fig. 7b). In the Raman spectra of NZF(70–30)–BT sample, several Raman modes of nickel ferrite suffered changes in the position, intensity and bandwidth. The Raman mode at 482 cm^{-1} is asymmetrically broadened towards higher frequencies, whereas the intensity of 575 cm^{-1} mode decreases. The width of the A_{1g} mode at 702 cm^{-1} increases reflecting the presence of more than two phases. In the fitting range from 600 to 800 cm^{-1} for NZF (70–30)–BT ceramics, it could be seen that this mode is well fitted with three phases, nickel ferrite, BT phase and a secondary phase, $BaFe_{12}O_{19}$ [31,32]. This result is in agreement with previously discussed XRD results.

The noticeable changes were seen in the Raman spectra of the NZF(50–50)–BT and NZF(30–70)–BT samples. In the NZF(50–50)–BT sample, the mode at 335 cm^{-1} of nickel ferrite phase was substantially broadened, whereas the mode of BT phase at around 265 cm^{-1} appeared. The deformation of the nickel ferrite mode at 482 cm^{-1} and its shift to higher frequencies, due to the presence of BT phase, is obvious. With further reduction of nickel ferrite phase in the NZF(30–70)–BT sample, the broad Raman mode at about 500 cm^{-1} is composed of F_{2g} and [A_1 (TO), E (TO)] modes of nickel zinc ferrite and $BaTiO_3$.

SEM images of sintered ceramic samples on the free surface are presented in Fig. 8. Insets of the images are displaying backscattered micrographs, demonstrating the homogenous phase distribution in obtained composites. Grains are nano-sized with different shapes, polygonal grains typical for nickel zinc ferrite, rounded grains characteristic for barium titanate and plate like grains that most likely correspond to the barium ferrite phase. All phases possess similar grain size, around 1 µm. The densities of composites were 5.09 g/cm^3 for NZF (70–30)–BT, 5.28 g/cm^3 for NZF(50–50)–BT, 5.15 g/cm^3 for NZF(30–70)–BT which corresponds to 89.6%, 93.0% and 90.8% of theoretical densities, respectively, showing the increasing trend with Zn content up to NZF(50–50)–BT and then with further increase of Zn the density starts to decrease. Theoretical values of density are 6.01 g/cm^3, 5.35 g/cm^3, 5.36 g/cm^3 and 5.33 g/cm^3 for the pure BT, NZF(70–30), NZF(50–50) and NZF(30–70) phases, respectively. Achieved ceramics densities are rather small due to high agglomeration and this can evidently affect the electrical (dielectric, ferroelectric) properties. This problem can be possibly solved by a treatment in the attrition mill, which may enable the preparation of ceramic composites with improved properties. The FE-SEM microstructure of composites is presented in Fig. 9. It is possible to notice two different phases: ferrites (platelike or pyramidal grains) and barium titanate with more rounded grains. It is important to notice that no reaction between parent components was observed.

The impedance spectroscopy (IS) is important method to study the electrical properties of one material, because it gives the information about resistive and reactive components in the material. IS was used to evaluate the contributions of various components such as grain and grain boundary to the overall electrical properties of NZF–BT ceramics composites. Fig. 10 shows the impedance plots for NZF(70–30)–BT, NZF(50–50)–BT,

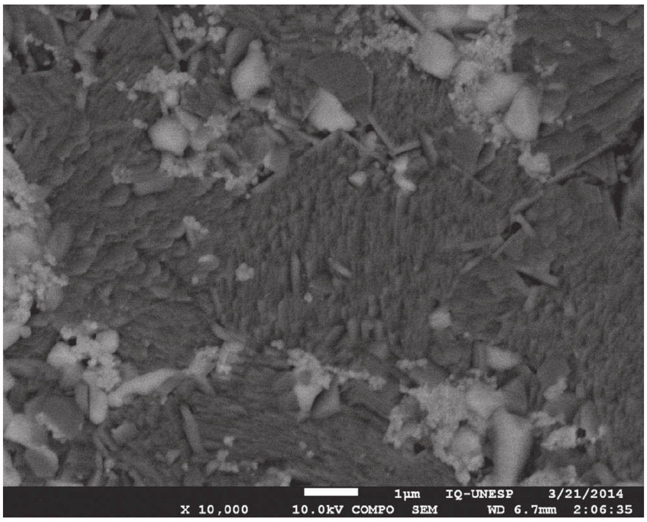

Fig. 9. FEG microstructure of NZF(70–30)–BT composite sintered at 1200 °C for 2 h.

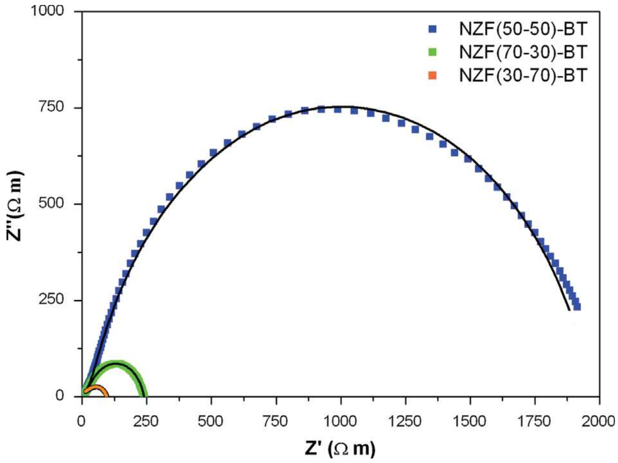

Fig. 10. Complex impedance spectra of all ceramics measured at 200 °C.

Table 1
Grain resistance, grain boundary resistance, total resistance and capacitance for all samples.

Sample	From Z'' to Z'				From Z'' to f	
	T (°C)	R_g (Ω m)	R_{gb} (Ω m)	R_{total} (Ω m)	R_{gb} (Ω m)	C_{gb} (nF/m)
NZF(30–70)–BT	50	155	7113	7268	4326	72.17
	100	117	1296	1413	822	74.45
	150	76	390	466	268	74.13
	200	22	74	96	52	72.12
NZF(50–50)–BT	50	250	54,039	54,289	30,882	109.71
	100	234	9231	9465	6844	135.27
	150	208	6562	6770	5380	160
	200	39	1929	1968	1504	146.24
NZF(70–30)–BT	50	585	36,480	37,065	24,590	99.63
	100	430	16,401	16,831	11,850	94.63
	150	57	492	549	398	85.87
	200	31	207	238	172	78.4

NZF(30–70)–BT ceramics at 200 °C. The impedance spectra were analyzed using commercially available Z-View software. For all samples, a one depressed semicircular arcs is present, indicating the possible overlapping of two arcs that correspond to grain and grain boundary contributions. The Z view software and equivalent circuit consisted of two parallel R-CPE elements connected in series, which were used to evaluate the grain boundary resistivity at low frequencies and grain contribution at high frequencies. The existence of two different phases (ferroelectric and ferromagnetic) in one composite material can make the interpretation of impedance results of these materials rather complicated. The appearance of two semicircular arcs could be also the indication of the presence of two different crystallographic phases. When compared to resistivity values of pure BT and NZF phases [19,33], quite a difference in the resistivity magnitude can be observed. BT, ferroelectric phase, is more resistive in comparison with NZF phase, indicating its dominant effect in the total resistivity of the composite materials. The values of the grain, grain boundary and total electrical resistivity of obtained ceramic composites are presented in Table 1.

With increasing temperature, the resistance of the grain and the grain boundary decreases for all composites (Table 1), as it was expected. Comparing the total resistance at the same temperature, it can be noticed that NZF(50–50)–BT possesses the highest values. With increase of Zn content up to 50% the resistance increases, probably because zinc leads to better structure ordering and results in the reduction of defects. Most likely, oxide ion vacancies $Vo^{\bullet\bullet}$ were formed due to loss of oxygen in the sintering process and present the main conductive species in the obtained ceramics [19].

The temperature dependence of the resistance can be presented by the equation [34]:

$$\sigma = \sigma_0 \exp\left(-\frac{E_a}{k_b T}\right) \tag{1}$$

where E_a, σ_0 and k_b are the activation energy of the carriers for conduction, the pre-exponential factor and the Boltzmann constant, respectively. Arrhenius plots of the grain, σ_g, and grain boundary conductivity, σ_{gb}, for NZF(30–70)–BT, NZF(50–50)–BT and NZF (70–30)–BT ceramics are presented in Fig. 11. The activation energy can be calculated from the slope of the given diagrams. The values of the grain and grain boundary activation energies were: $E_a(g) = 0.15$ eV, $E_a(gb) = 0.39$ eV for NZF(30–70)–BT, $E_a(g) = 0.17$ eV, $E_a(gb) = 0.27$ eV for NZF(50–50)–BT and $E_a(g) = 0.28$ eV, $E_a(gb) = 0.49$ eV for NZF(70–30)–BT. Generally, the activation energies for electron hopping are lower than for hole

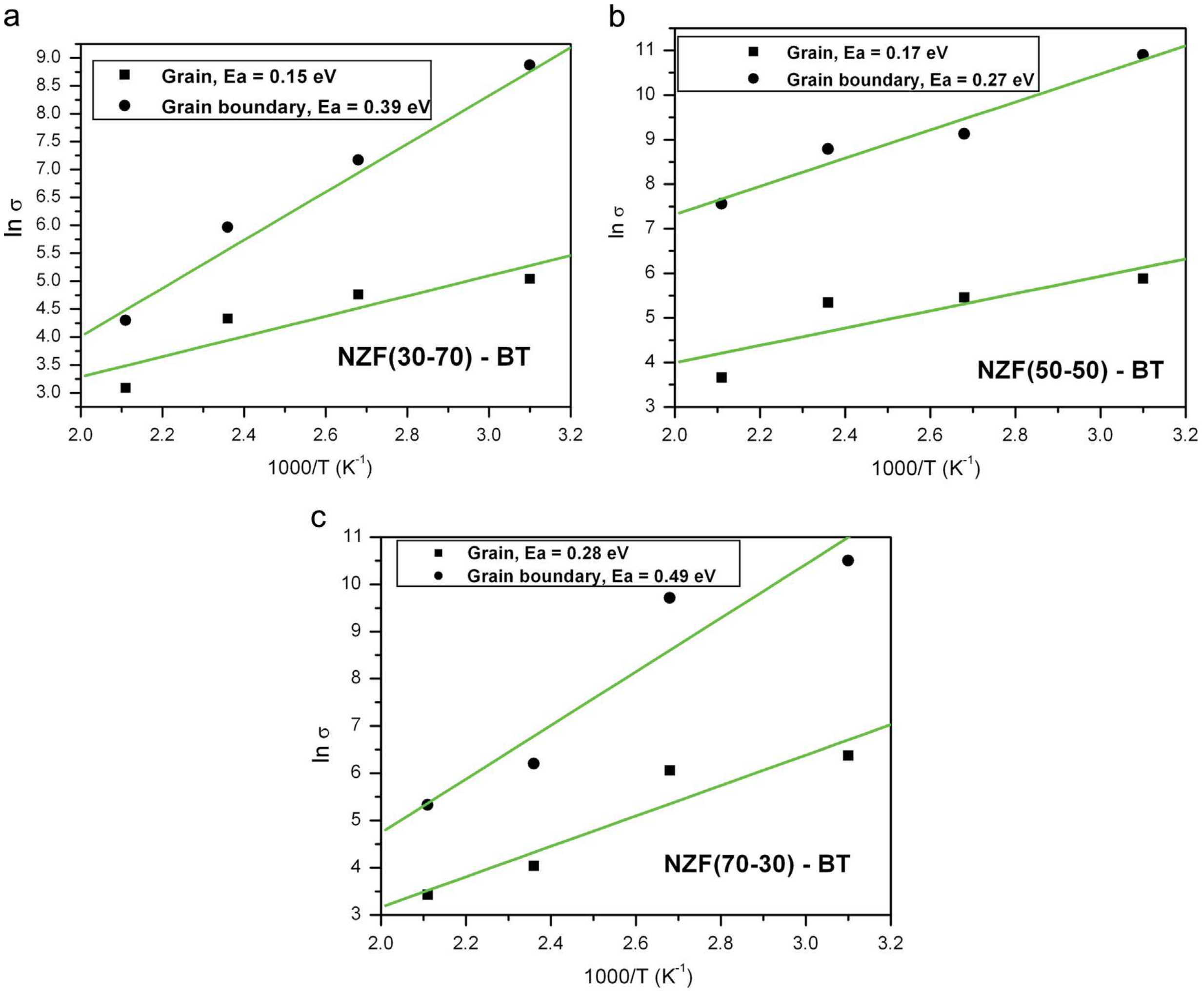

Fig. 11. Arrhenius plots of grain (σ_g) and grain boundary (σ_{gb}) conductivity for all ceramic samples.

hopping. In the polaron conduction, the activation energy of holes is usually used to be greater than 0.2 eV [35]. On this basis, the calculated activation energies indicate that the conduction in obtained materials is a consequence of polaron hopping. The conduction in ferrites, ferroelectrics and its composites can be explained by polaron hopping process among the localized sites. Hopping conduction is favored in ionic lattices in which the same kind of cation is found in two different states [36]. Thus, in the obtained composite materials the hopping of 3d electrons among Fe^{2+} and $Fe^{3}+$ as well as between Ni^{2+} and Ni^{3+} in the ferrite phase and also Ti^{4+} to Ti^{3+} in the ferroelectric phase, could play an important role in the conduction processes. These values for E_a are also in agreement with the results obtained for barium strontium titanate–nickel zinc ferrite composites in the study of other authors [25,37]. The activation energy for the conduction process through the grain boundaries in all measured samples was higher compared to the values of the activation energy for the conduction process through the grains. Therefore, the grain boundary effect can be ascribed as the dominant effect in total conduction of ceramic composites.

Complex modulus plots (M''–M') at the different temperatures for NZF(30–70)–BT, NZF(50–50)–BT, NZF(70–30)–BT are shown in Fig. 12. Values of M'' and M' were calculated from equations $M''=\omega C_o Z'$ and $M'=\omega C_o Z''$, respectively, where C_o is equal to $\varepsilon_o A/h$ and angular frequency ω is equal to $2\pi f$. The complex electric modulus analysis can be used to separate the electrode polarization effect from the grain boundary conduction process and also to determine the conductivity relaxation times [25]. In the presented diagrams two semicircular arcs can be noticed in NZF(70–30)–BT, NZF (50–50)–BT and NZF(30–70)–BT composites, even though, they were not fully resolved in the complex impedance plots. This is also the indication of the presence of different relaxation processes, due to contribution of grain, grain boundary and/or different crystallographic phases.

Complex impedance plots Z''–f for all ceramic composites are presented in Fig. 13. With increasing temperature the positions of peaks shift toward high frequency side, which leads to the conclusion that the dielectric relaxation is thermally activated process [38]. A relative lowering in the magnitude of Z'' with a shift of the peaks towards the higher frequency arises is possibly due to the presence of space charge polarization or accumulation at the grain boundaries [25]. Broadening of the peaks with rise in temperature can be

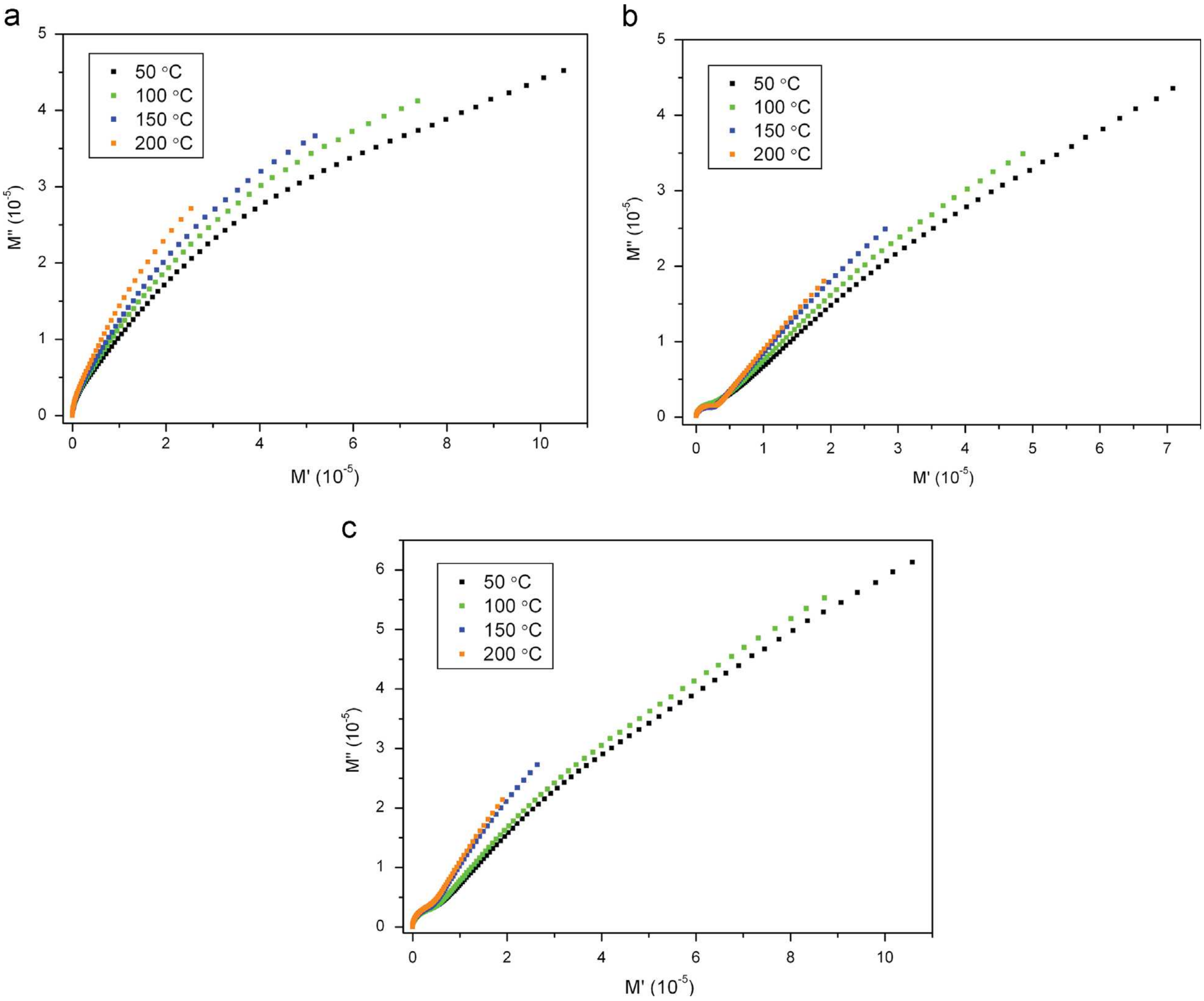

Fig. 12. Modulus complex plots of (a) NZF(30–70)–BT, (b) NZF(50–50)–BT, and (c) NZF(70–30)–BT at different temperatures.

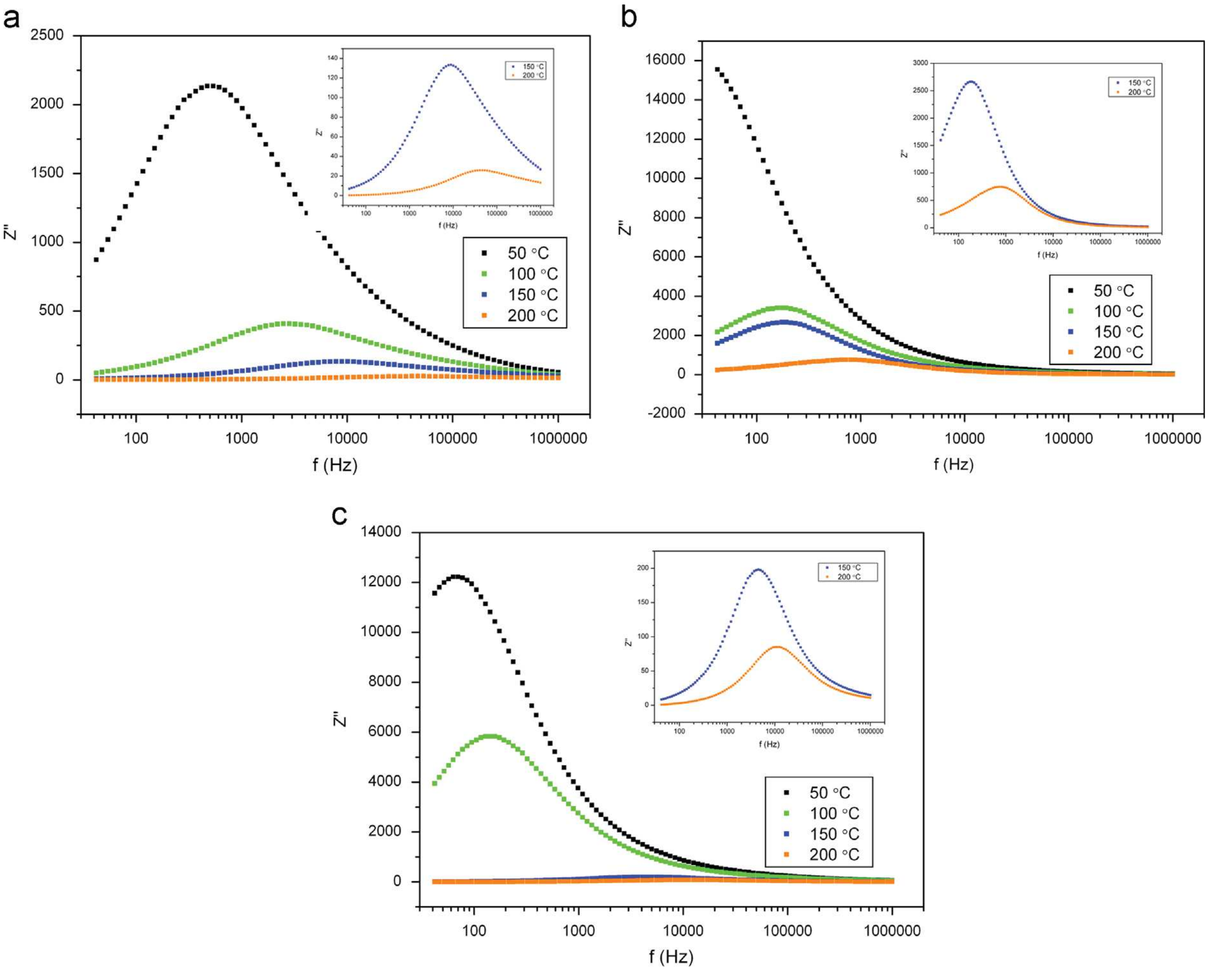

Fig. 13. Frequency dependence of imaginary parts of the impedance spectra (Z'') of (a) NZF(30–70)–BT, (b) NZF(50–50)–BT, and (c) NZF(70–30)–BT at different temperatures.

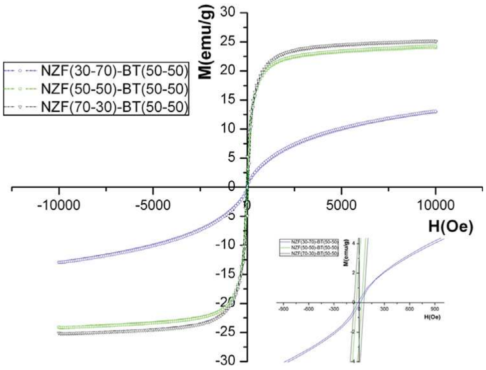

Fig. 14. Magnetic hysteresis loops at room temperature for all composites ceramics.

an indication of the presence of immobile species at low temperature and defects at higher temperatures [39]. The corresponding capacitances and resistivities were calculated from the maximum value of the Z'' peak and associated f_{max} value, using the relationships $C=1/2\pi f_{max}R$, where R is equal to $2Z''_{max}$ [40]. The obtained values for C and R are presented in Table 1. Obtained resistivity data were used for the calculation of activation energies of relaxation processes at the grain boundary and they are in accordance with E_a obtained from the complex impedance analysis.

Table 2
Saturation magnetization moment, saturation fields, residual magnetization and coercive field for $y\text{Ni}_{1-x}\text{Zn}_x\text{Fe}_2\text{O}_4-(1-y)\text{BT}$ ($x=0.3$, 0.5, 0.7, $y=0.5$) composite materials.

Sample	M_{sat} (emu/g)	H_{sat} (kOe)	M_r (emu/g)	H_c (Oe)
NZF (70–30)–BT	23.64	2.55	4.31	19.8
NZF (50–50)–BT	22.23	2.05	2.89	25.4
NZF (30–70)–BT	10.42	1.95	0.17	17.6

Magnetization results are presented in Fig. 14 and Table 2. In pure nickel zinc ferrite, with addition of Zn, magnetization increases because the balance between Fe^{3+} ions in tetrahedral and octahedral sites, which is conditioned by migration of the Fe^{3+} ions inter this sites. This leads to the weakening of A–B exchange interaction, causing the increase of magnetization. The change of the magnetic properties with reducing amount of magnetic phase was expected. In composites, a dilution effect exists, which means that BT does cause intimate change in the magnetic properties, leading to the reduction of the magnetic moment [41]. The saturation magnetization and remnant magnetization have shown a decrease with increasing Zn content, likely due to already mentioned dilution effect. M_s, at first slightly decreases with increase of Zn content up to 0.5 mol% and then significantly decreases with further increase of Zn. In comparison with pure NZF phases, M_s also decreases, due to the presence of non-magnetic barium titanate phase [19]. The fields at which saturation occurs were around 2 kOe for NZF(30–70)–BT and NZF(50–50)–BT and slightly higher for NZF(70–30)–BT. The coercive field, the field required to overcome the defects in the material, was higher for composites in the comparison with pure NZF phases, which can be explained by the fact that the composite possesses a higher anisotropy field than the NZF at the same applied field [35]. The coercive field was the highest for NZF(50–50)–BT ceramic composites.

4. Conclusion

A series of nickel zinc ferrite–barium titanate with general formula $y\mathrm{Ni}_{1-x}\mathrm{Zn}_x\mathrm{Fe}_2\mathrm{O}_4-(1-y)\mathrm{BT}$ ($x=0.3$, 0.5, 0.7, $y=0.5$) were successfully prepared by mixing of previously prepared powders of nickel zinc ferrite and barium titanate. The composites materials formation was confirmed by XRD and Raman spectroscopy for powders and ceramics, with small amount of secondary phase. SEM analysis indicated a high level of powder agglomeration and ceramic composites with different shapes grains of around 1 μm. Impedance analysis has shown that for all obtained ceramic samples grain boundary resistance has the highest contribution to the total resistance. The resistance was found to decrease with the increasing temperature for all measured samples, and it can be noticed that NZF(50–50)–BT possesses the highest values of total resistance. The calculated activation energy indicates that the conduction in the composite materials is a consequence of polaron hopping. Results of the magnetic measurements show that the magnetization in the composites ceramics is reduced in comparison with pure nickel zinc ferrite ceramics due to the presence of barium titanate phase. The fields at which saturation occurs were almost the same for all investigated compositions.

Acknowledgments

The authors gratefully acknowledge the financial support of the Ministry of Education, Science and Technological Development of the Republic of Serbia (Project III 45021), COST MP 0904 and IC 1208. Special thanks to Dr. Lavinia Curecheriu from Faculty of Physics, Al.I. Cuza University, Iasi, Romania for magnetic measurements and to Dr. Sonia Zanetti from Institute for Chemistry UNESP, Araraquara, Brazil for FEG microstructure measurements. Also we would like to thank Dr. Zorana Dohcevic-Mitrovic from Institute of Physics, University of Belgrade for useful suggestions about Raman spectroscopy measurements.

References

[1] H. Schmid, Multi-ferroic magnetoelectrics, Ferroelectrics 162 (1994) 317–338.

[2] T. Kimura, T. Goto, H. Shintani, K. Ishizaka, T. Arima, Y. Tokura, Magnetic control of ferroelectric polarization, Nature 426 (2003) 55–58.

[3] N. Hur, S. Park, P.A. Sharma, J.S. Ahn, S. Guha, S.W. Cheong, Electric polarization reversal and memory in a multiferroic material induced by magnetic fields, Nature 429 (2004) 392–395.

[4] L. Mitoseriu, Magnetoelectric phenomena in single-phase and composite systems, Bol. Soc. Esp. Ceram. 44 (3) (2005) 177–184.

[5] M.E. Botello-Zubiate, D. Bueno-Baques, J. de Frutos, L.E. Fuentes, J.A. Matutes-Aquino, Synthesis and magnetoelectric characterization of cobalt ferrite–barium titanate composites using a new pulsed magnetic field method, Integr. Ferroelectr. 83 (2006) 33–40.

[6] C.W. Nan, M.I. Bichurin, S. Dong, D. Viehland, G. Srinivasan, Multiferroic magnetoelectric composites: historical perspective status and future directions, J. Appl. Phys. 103 (2008) 031101.

[7] M.A. Khan, T.P. Comyn, A.J. Bell, Growth and characterization of tetragonal bismuth ferrite–lead titanate thin films, Acta Mater. 56 (2008) 2110–2118.

[8] N. Ikeda, H. Ohsumi, K. Ohwada, K. Ishii, T. Inami, K. Kakurai, Y. Murakami, K. Yoshii, S. Mori, Y. Horibe, H. Kito, Ferroelectricity from iron valance ordering in the charge-frustrated system $\mathrm{LuFe_2O_4}$, Nature 436 (2005) 1136–1138.

[9] S.W. Cheong, M. Mostovoy, Multiferroics: a magnetic twist for ferroelectricity, Nat. Mater. 6 (2007) 13–20.

[10] W. Eerenstein, N.D. Mathur, J.F. Scott, Multiferroic and magnetoelectric materials, Nature 442 (2006) 759.

[11] D.B. Litvin, Ferroic classifications extended to ferrotoroidic crystals, Acta Cryst. A 64 (2008) 316–320.

[12] T. Lottermoser, T. Lonkai, U Amann, D. Hohlwein, J. Ihringer, M. Fiebig, Magnetic phase control by an electric field, Nature 430 (2004) 541–544.

[13] B.B. van Aken, T.T. Palstra, A. Filippetti, N.A. Spaldin, The origin of ferroelectricity in magnetoelectric $\mathrm{YMnO_3}$, Nat. Mater. 3 (2004) 164–170.

[14] H. Kavas, N. Kasapoglu, A. Baykal, Y. Koseoglu, Characterization of $\mathrm{NiFe_2O_4}$ nanoparticles synthesized by various methods, Chem. Pap. 63 (4) (2009) 450–455.

[15] J.V. Boomgaard, R.A.J. Born, A sintered magnetoelectric composite material $\mathrm{BaTiO_3}$–Ni(Co, Mn)$\mathrm{Fe_2O_4}$, J. Mater. Sci. 13 (1978) 1538–1548.

[16] N.R. Reddy, E. Rajagopal, K.V. Sivakumar, K.K. Patankar, V.R.K. Murthy, Effect of temperature on the elastic and anelastic behaviour of magnetoferroelectric composites $\mathrm{Ba_{0.8}Pb_{0.2}TiO_3+Ni_{0.93}Co_{0.02}Mn_{0.05}Fe_{1.95}O_{4-\delta}}$ in the ferroelectric rich region, J. Electroceram. 11 (2003) 167–172.

[17] G.R. Amiri, M.H. Yousefi, M.R. Abolhassani, S. Manouchehri, M.H. Keshavarz, S. Fatahian, Magnetic properties and microwave absorption in Ni–Zn and Mn–Zn ferrite nanoparticles synthesized by low-temperature solid-state reaction, J. Magn. Magn. Mater. 323 (2011) 730–734.

[18] D. Chen, R. He, Synthesis of nickel ferrite nanoparticles by sol–gel method, Mater. Res. Bull. 36 (2001) 1369–1377.

[19] A.S. Džunuzović, N.I. Ilić, M.M. Vijatović Petrović, J.D. Bobić, B. Stojadinović, Z. Dohčević-Mitrović, B.D. Stojanović, Structure and properties of Ni–Zn ferrite obtained by auto-combustion method, J. Magn. Magn. Mater. 374 (2015) 245–251.

[20] S. Zahi, Synthesis, permeability and microstructure of the optimal nickel–zinc ferrites by sol–gel route, J. Elctromagn. Anal. Appl. 2 (2010) 56–62.

[21] M.H. Frey, D.A. Payne, Grain-size effect on structure and phase transformations for barium titanate, Phys. Rev. B 54 (1996) 3158–3168.

[22] P.R. Arya, P. Jha, G.N. Subbanna, A.K. Ganguli, Polymeric citrate precursor route to the synthesis of nano-sized barium lead titanates, Mater. Res. Bull. 38 (2003) 617–628.

[23] M.M. Vijatovic Petrovic, J.D. Bobic, A.M. Radojkovic, J. Banys, B.D. Stojanovic, Improvement of barium titanate properties induced by attrition milling, Ceram. Int. 38 (2012) 5347–5354.

[24] L. Mitoseriu, V. Buscaglia, M. Viviani, M.T. Buscaglia, I. Pallecchi, C. Harnagea, A. Testino, V. Trefiletti, P. Nanni, A.S. Siri, $\mathrm{BaTiO_3}$–$\mathrm{(Ni_{0.5}Zn_{0.5})Fe_2O_4}$ ceramic composites with ferroelectric and magnetic properties, J. Eur. Ceram. Soc. 27 (2007) 4379–4382.

[25] K. Verma, S. Sharma, Impedance spectroscopy and dielectric behavior in barium strontium titanate-nickel zinc ferrite composites, Phys. Status Solidi B 249 (2012) 209–216.

[26] G. Dixit, J.P. Singh, R.C. Sriavastava, H.M. Agrawal, Study of 200 MeV Ag^{15+} ion induced amorphisation in nickel ferrite thin films, Nucl. Instrum. Methods B 269 (2011) 133-139.

[27] A. Ahlawat, V.G. Sathe, V.R. Reddy, A. Gupta, Mossbauer, raman and X-ray diffraction studies of superparamagnetic $NiFe_2O_4$ nanoparticles prepared by sol–gel auto-combustion method, J. Magn. Magn. Mater. 323 (2011) 2049–2054.

[28] A. Ahlawat, V.G. Sathe, Raman study of $NiFe_2O_4$ nanoparticles, bulk and films: effect of laser power, J. Raman Spectrosc. 42 (2011) 1087–1094.

[29] J.P. Singh, G. Dixit, R.C. Srivastava, H.M. Agrawal, Ravi Kumar, Formation of latent tracks and their effect on the structural and magnetic properties of nanosized zinc ferrite, J. Alloy. Compd. 551 (2013) 370–375.

[30] Y. Shiratori, C. Pithan, J. Dornseiffer, R. Waser, Raman scattering studies on nanocrystalline $BaTiO_3$, J. Raman Spectrosc. 38 (2007) 1288–1299.

[31] X. Liu, J. Wang, J. Ding, M.S. Chen, Z.X. Shen, The effects of mechanical activation in synthesizing ultrafine barium ferrite powders from co-precipitated precursors, J. Mater. Chem. 10 (2000) 1745–1749.

[32] J. Kreisel, S. Pignard, H. Vincent, J.P. Senateur, G. Lucazeau, Raman study of $BaFe_{12}O_{19}$ thin films, Appl. Phys. Lett. 73 (1998) 1194.

[33] S. Sharma, K. Shamim, A. Ranjan, R. Rai, P. Kumari, S. Sinha, Impedance and modulus spectroscopy characterization of lead free barium titanate ferroelectric ceramics, Ceram. Int. 41 (2015) 7713–7722.

[34] M. Shah, M. Nadeem, M. Idrees, M. Atif, M.J. Akhtar, Change of conduction mechanism in the impedance of grain boundaries in $Pr_{0.4}Ca_{0.6}MnO_3$, J. Magn. Magn. Mater. 332 (2013) 61–66.

[35] M. Atif, M. Nadeem, Interplay between the ferromagnetic and ferroelectric phases on the magnetic and impendance analysis of $(x)Pb(Zr_{0.52}Ti_{0.48})O_3-(1-x)CoFe_2O_4$ composites, J. Alloy. Compd. 623 (2015) 447–453.

[36] C.E. Ciomaga, A.M. Neagu, M.V. Pop, M Airimioaei, S. Tascu, G. Schileo, C. Galassi, L. Mitoseriu, Feroelectric and dielectric properties of ferrite–ferroelectric ceramic composites, J. Appl. Phys. 113 (2013) 074103.

[37] M.I. Klinger, Two-phase polaron model of conduction in magnetite-like solids, J. Phys. C: Solid State Phys. 8 (1975) 3595.

[38] F Borsa, D.R. Torgeson, S.W Martin, H.K. Patel, Relaxation and fluctuations in glassy fast-ion conductors: wide-frequency-range NMR and conductivity measurements, Phys. Rev. B 46 (1992) 795.

[39] A.K. Behera, N.K. Mohanty, B. Behera, P. Nayak, Impendance properties of $0.7(BiFeO_3)$–$0.3(PbTiO_3)$ composite, Adv. Mater. Lett. 4 (2) (2013) 141–145.

[40] F.D. Morrison, D.C. Sinclair, A.R. West, Characterization of lanthanum doped barium titanate ceramics using impedance spectroscopy, J. Am. Ceram. Soc. 84 (3) (2001) 531–538.

[41] L.P. Curecheriu, M.T. Buscaglia, V. Buscaglia, L. Mitoseriu, P. Postolache, A. Ianculescu, P. Nanni, Functional properties of $BaTiO_3$–$Ni_{0.5}Zn_{0.5}Fe_2O_4$ magnetoelectric ceramics prepared from powders with core–shell structure, J. Appl. Phys. 107 (2010) 104–106.

Journal of Magnetism and Magnetic Materials 374 (2015) 245–251

Contents lists available at ScienceDirect

Journal of Magnetism and Magnetic Materials

journal homepage: www.elsevier.com/locate/jmmm

Structure and properties of Ni–Zn ferrite obtained by auto-combustion method

A.S. Džunuzović [a], N.I. Ilić [a], M.M. Vijatović Petrović [a,*], J.D. Bobić [a], B. Stojadinović [b], Z. Dohčević-Mitrović [b], B.D. Stojanović [a]

[a] Institute for Multidisciplinary Research, University of Belgrade, Kneza Višeslava 1, Belgrade, Serbia
[b] Institute of Physics, University of Belgrade, Pregrevica 118, Zemun, Serbia

ARTICLE INFO

Article history:
Received 20 May 2014
Received in revised form
11 August 2014
Available online 20 August 2014

Keywords:
Auto-combustion synthesis
Ferrites
Magnetic measurements
Raman spectroscopy
Impedance spectroscopy

ABSTRACT

Nanosized nickel zinc ferrite powders with general formula $Ni_{1-x}Zn_xFe_2O_4$ ($x=0.0$, 0.3, 0.5, 0.7, 1.0) were synthesized by an auto-combustion method starting from metal nitrates. X-ray analysis indicated the formation of well crystallized Ni–Zn ferrite phases, and Raman spectroscopy enabled a precise phases identification. The change of the grain size and density with increasing Zn content was confirmed by scanning electron microscopy. Magnetization of saturation and remnant magnetization, both, continuously increase up to $x=0.3$ of Zn, and then decrease for more Zn. The influence of the grain size of investigated systems on the saturation magnetization was studied. Impedance spectroscopy measurements were carried out in order to investigate the electrical resistivity of materials, showing that grain boundaries have greater impact on total resistivity that grains.

1. Introduction

There is a growing interest in magnetic ferrite nanomaterials such as $NiFe_2O_4$ and $(Ni,Zn)Fe_2O_4$, due to their applications as a part of the sensors, catalysis, magnetic drug delivery, permanent magnets, recording heads, antenna rods, loading coils, telecommunication devices, magnetic refrigeration, magnetic liquids, as a microwave absorber etc [1,2]. In addition, the applicability of these ferrite material increases because of their possible use as a component in the magnetoelectric (multifferoic) devices. In recent years there is an increasing interest for multiferroic materials in which at least two of ferroic properties (ferrolectric, ferromagnetic and ferroelastic) are combined [3–6]. Having in mind that ferrites possess ferromagnetic (antiferromagnetic) properties, especially nanostructured one, recently attracted attention in the field of multiferroic materials. However, to ensure the applicability of ferrites as a component in multiferroic devices, it is necessary to pay special attention to processing methods and properties of ferrites that are important for its functionality in multiferroic materials.

Nickel ferrite ($NiFe_2O_4$) with an inverse spinel structure shows ferrimagnetism, which originates from magnetic moments of anti-parallel spins between Fe^{3+} ions at tetrahedral sites and $Fe^{3+}$and Ni^{2+} ions at octahedral sites [7]. In the Ni–Zn spinel ferrite, Zn^{2+} ions occupy tetrahedral sites, causing migration of some Fe^{3+} ions from tetrahedral to octahedral sites, so the structure can be presented as $(Zn_x^{2+}Fe_{1-x}^{3+})[Ni_{1-x}^{2+}Fe_{1+x}^{3+}]$, where round brackets imply tetrahedral sites, and square brackets octahedral ones [8].

The Ni–Zn ferrites are produced by numerous methods such as solid state reaction [9], microwave-assisted solid state reaction [10,11], sonochemical process [12], citrate precursor techniques [13], coprecipitation [14], mechanical alloying [15], reactive milling [16], sol–gel technique [17] and pulsed wire discharge [18]. Some

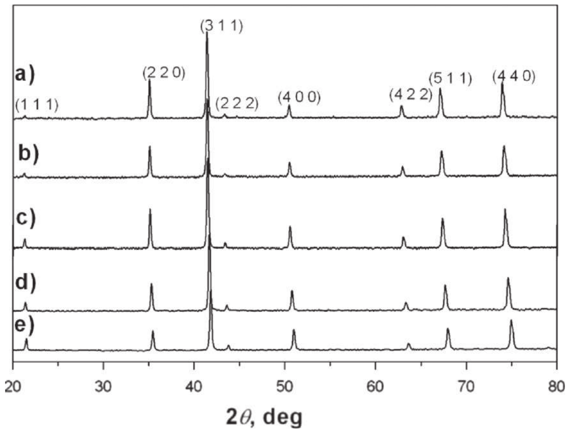

Fig. 1. XRD patterns of: a) ZF, b) NZF (30–70) c) NZF (50–50) d) NZF (70–30) and e) NF calcined powders.

---

[*] Corresponding author. Tel.: +381 11 2085 039; fax: +381 11 2085062.
E-mail address: miravijat@yahoo.com (M.M. Vijatović Petrović).

http://dx.doi.org/10.1016/j.jmmm.2014.08.047
0304-8853/© 2014 Elsevier B.V. All rights reserved.

disadvantages of these methods are complicated procedure, high reaction temperature, long reaction time, and use of reduction agents, which potentially upset the environment. Recently, a combustion synthesis method has emerged as a very popular method for synthesis and processing of advanced ceramic materials, composites and ferromagnetic nanomaterials. Higher purity of materials prepared by the combustion process is ascribed to expulsion of impurities as volatile species at high temperatures typically achieved during these reactions. The improvement in reactivity and mechanical properties is attributed to the high defect concentration as a result of high temperatures and the relatively rapid cooling rates following the formation of nanocrystalline powders [19].

In this paper, the formation of nickel and nickel zinc ferrite nanoparticles by the auto-combustion method was reported. Combustion synthesis is used as an attractive method because of short reaction time and low costs compared to the conventional methods. The purpose of present study is to investigate the effect of Zn content on the morphological, structural, magnetic and electrical properties

Table 1
Crystallite sizes of all powders (D_{XRD}), lattice parameters (a), grain size (D_{SEM}) and density of all ceramics.

Sample	D_{XRD} (nm)	a(Å)	D_{SEM} (μm)	Density (% of theor.)
NF	38.0	8.2801	0.825	73.1
NZF (70–30)	38.0	8.3160	0.957	75.4
NZF (50–50)	39.5	8.3278	1.068	78.9
NZF (30–70)	41.0	8.3955	1.216	85.1
ZF	45.0	8.4020	1.080	88.2

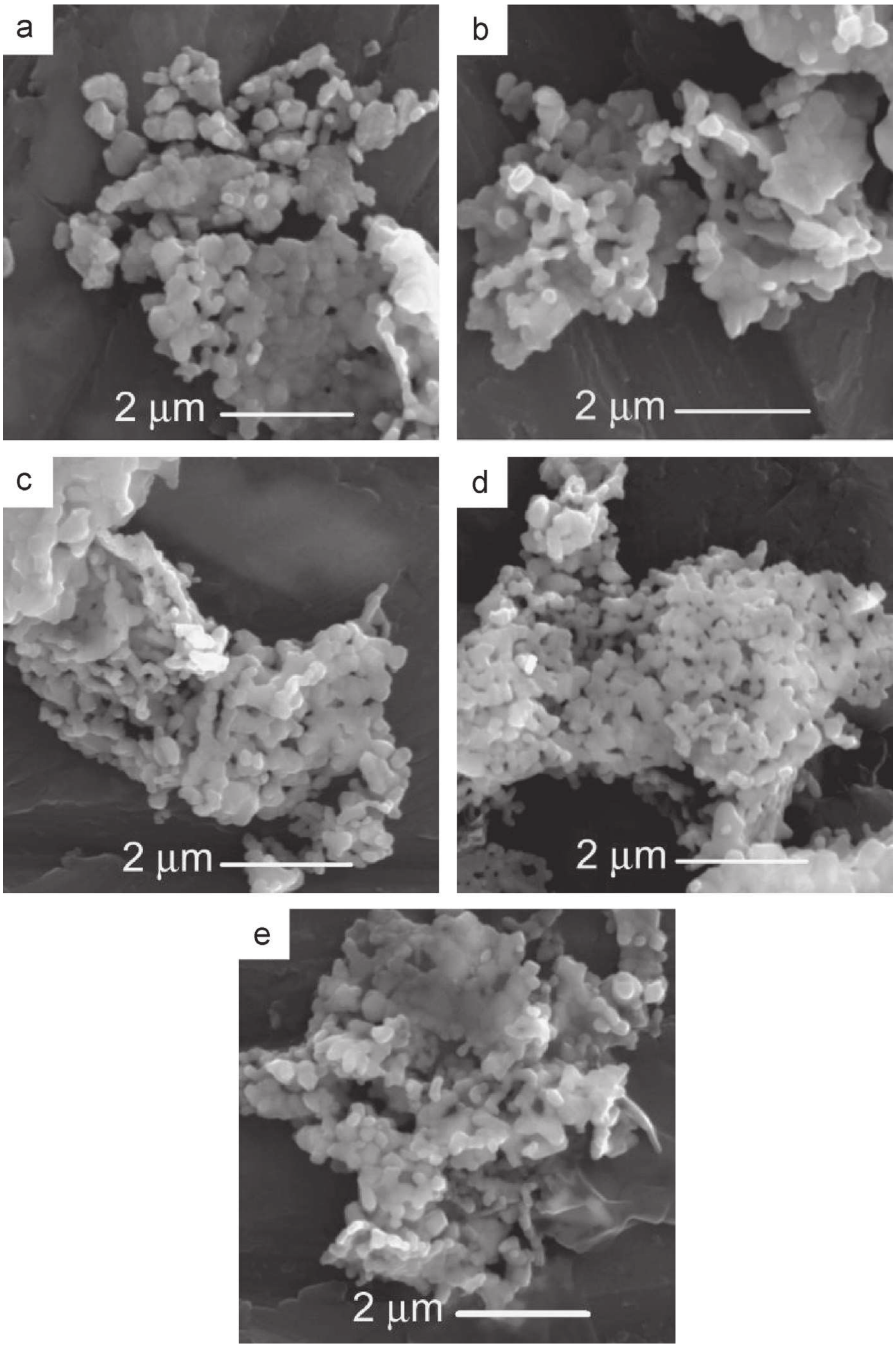

Fig. 2. SEM images of: a) NF, b) NZF (70–30) c) NZF (50–50) d) NZF (30–70) e) ZF powders.

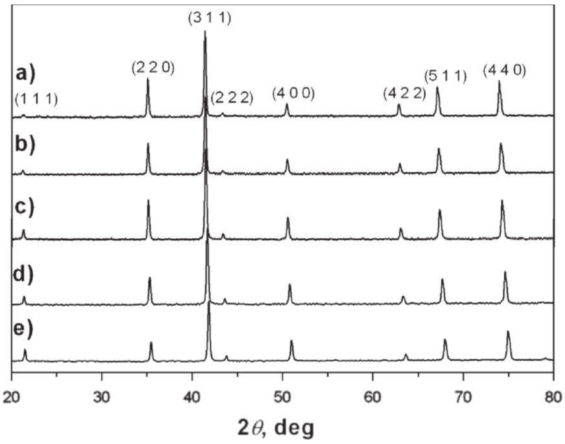

Fig. 3. XRD patterns of: a) ZF b) NZF (30–70) c) NZF (50–50) d) NZF (70–30) and e) NF sintered at 1250 °C for 4 h.

of nickel ferrite nanopowders and ceramics having in mind possible use of ferrites as a component in the multifferoic devices.

2. Materials and methods

The nanoparticles of $Ni_{1-x}Zn_xFe_2O_4$ (x=0.0, 0.3, 0.5, 0.7, 1.0, denoted as NF, NZF (70–30), NZF (50–50), NZF (30–70) and ZF) were synthesized by the auto-combustion method. The raw materials used for the synthesis were $Fe(NO_3)_3 \cdot 9H_2O$ (Alfa Aesar, 98.0–101.0%), $Ni(NO_3)_2 \cdot 6H_2O$ (Alfa Aesar, 99.9985%), $Zn(NO_3)_2 \cdot 6H_2O$ (Alfa Aesar, 99%) and $C_6H_8O_7 \cdot H_2O$ (Carlo Erba, 99.5–100.5%) and NH_4OH (Lach Ner, 25%). The molar ratio of iron ions, nickel ions, citric acid was 2:1:1. Metal nitrates and citric acid solutions were prepared by dissolving raw materials in a minimum amount of deionized water, and after that they were mixed together in a dish. pH value of the solution was adjusted to 7 using the ammonia solution. After that the solution was heated and stirred at the temperature of about 90 °C until it was transformed into a xerogel. The dish with xerogel was transferred into the heating calotte at 200 °C when self-propagation reaction was achieved.

The formed powder was calcined at 1000 °C with a heating rate of 2 °C/min (Electron-UK oven). The powder was pressed at 196 MPa into pellets of 8 mm in diameter. Sintering was performed at 1250 °C for 4 h in the tubular furnace (Lenton, UK) at a heating rate of 5 °C/min. Samples were cooled spontaneously in air atmosphere.

The phase and crystal structure analysis was carried out by an X-ray diffraction technique (Model Phillips PW1710 diffractometer, Co Kα radiation, 0.5°/min). The average crystallite size was calculated by Debye–Scherrer's equation using data obtained from X-ray diffractograms. Raman spectra were collected in the backscattering micro-Raman configuration using a Jobin Yvon T64000 spectrometer equipped with a nitrogen-cooled CCD detector. The argon ion (Ar^+) laser line at λ=514.5 nm was used as an excitation source. The measurements were performed at room temperature. The morphology and microstructure of obtained powders and ceramics were examined using a scanning electron microscope (SEM Model TESCAN SM-300). The grain size was determined using an ImageJ program. Magnetic measurements of materials were carried out using a superconducting quantum interferometric magnetometer SQUID (Quantum Design). The impedance measurements were performed for all sintered samples using an LCR meter (model 9593-01, Hioki Hitester). Samples were prepared by coating their polished surfaces with Ag paste. The real and imaginary parts of the complex impedance were measured in the frequency range of 42 Hz–1 MHz at the room temperature, which is referred as the Nyquist plot.

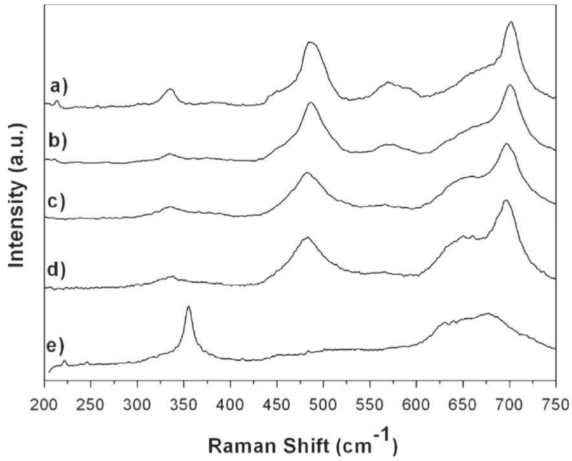

Fig. 4. Raman spectra of: a) NF, b) NZF (70–30) c) NZF (50–50) d) NZF (30–70) e) ZF samples.

3. Results and discussion

3.1. Structural and microstructural properties

XRD patterns of powders calcined at 1000 °C, presented in Fig. 1 showed that pure nickel ferrite and nickel zinc ferrite phases were obtained. This was confirmed by the existence of the reflections (111), (220), (311), (400), (422), (511) and (440), which indicated the presence of the cubic spinel structure (identified using the JCPDS files No. 10-0325) [2]. The average crystallite size, D_{XRD}, was calculated using the Debye–Scherrer's equation:

$$D_{XRD} = 0.9\ \lambda/B\ \cos\ \theta \tag{1}$$

where λ is the wavelength of Co cathode ray tube (0.17889 nm), θ is the angle of the Bragg diffraction, and B is the full width at half maximum of the most intensive peak, in degrees.

Calculated crystallite sizes are presented in Table 1. It can be seen that the size of the crystallites slightly increases when more Ni^{2+} ions were replaced by Zn^{2+} ions. This could be explained by a larger size of Zn^{2+} ions (0.83 Å) compared to Ni^{2+} ions (0.78 Å) [20]. The average crystallite sizes were between 38 and 45 nm for the investigated materials.

Fig. 2 shows SEM images of all synthesized powders. It can be noticed that the powder particles are very small ($<$200 nm) with a high tendency to form agglomerates. A high level of agglomeration appears mostly in the chemically prepared nanopowders and it is probably caused by a very small primary particles that tend to join together [21,22].

XRD patterns of the sintered samples are shown in Fig. 3 indicating that single ferrite phase is formed at 1250 °C for 4 h without presence of any impurities or unreacted phases. The lattice parameters were calculated using the numerical calculation of diffraction patterns data (Table 1). The lattice parameter a is slightly increased (from 8.2801 Å to 8.4020 Å) with zinc content increase. This dependence was almost linear, showing that the (Ni, Zn)Fe_2O_4 system obeys Vegard's law [23]. It is evident that larger Zn^{2+} ions displaces the smaller Fe^{3+} ions (0.67 Å) from the tetrahedral to octahedral sites causing the elongation of the NZF crystal lattice.

Raman spectroscopy confirmed that cubic spinel structure belonging to the space group Oh^7 (Fd3m) was obtained. Although the full unit cell contains 56 atoms (8 molecules per unit cell) only 14 atoms are in the asymmetric unit and therefore 42 vibrational modes are expected. Group theory predicts the following modes in spinel structure [24,25]:

$$A_{1g}(R)+E_g(R)+F_{1g}+3F_{2g}(R)+2A_{2u}+2E_u+4F_{1u}(IR)+2F_{2u} \quad (2)$$

The most intensive Raman modes of nickel ferrite were three F_{2g} (212, 483 and 577 cm^{-1}), one E_g (333 cm^{-1}) and one A_{1g} (702 cm^{-1}) [26,27] modes, whereas for zinc ferrite the most prominent modes were three F_{2g} (221, 355 and 451 cm^{-1}), one E_g (246 cm^{-1}) and one A_{1g} (647–674 cm^{-1}) mode [28]. F_{1g}, A_{2u}, E_u and F_{2u} modes are silent.

Fig. 4 shows the Raman spectra of all ceramic samples. The characteristic peaks in the NF sample appeared at 213, 334, 485, 577 and 702 cm^{-1} with a shoulder at 660 cm^{-1}. Raman modes of nickel ferrite sample showed a shoulder-like feature at the lower wavenumber side of all the Raman active bands. This doublet-like features originate from different local structures in the octahedral sites of nickel ferrite which are occupied either by Ni or Fe ions. One peak corresponds to the unit cell with all Fe ions and the other one to the unit cell with mixed Fe and Ni ions [29].

Raman spectrum of ZF displays five Raman modes at 221, 246, 355, 452, 647 cm^{-1}. In the Raman spectra of NZF samples, with lowering Zn content, a mode at 480 cm^{-1} was shifted to the value characteristic for pure NF phase, becoming at the same time more intense. Other NF mode at 334 cm^{-1} has become very intense in the sample with the highest Ni content. The mode centered around 650 cm^{-1} in NZF (30–70) sample was shifted to the lower energies regarding the corresponding NF Raman mode (shoulder at 660 cm^{-1}) probably because of the mixed Fe/Ni/Zn–O bonds formed in NZF samples [29]. The intense mode of ZF phase at 355 cm^{-1} was not observed in NZF samples.

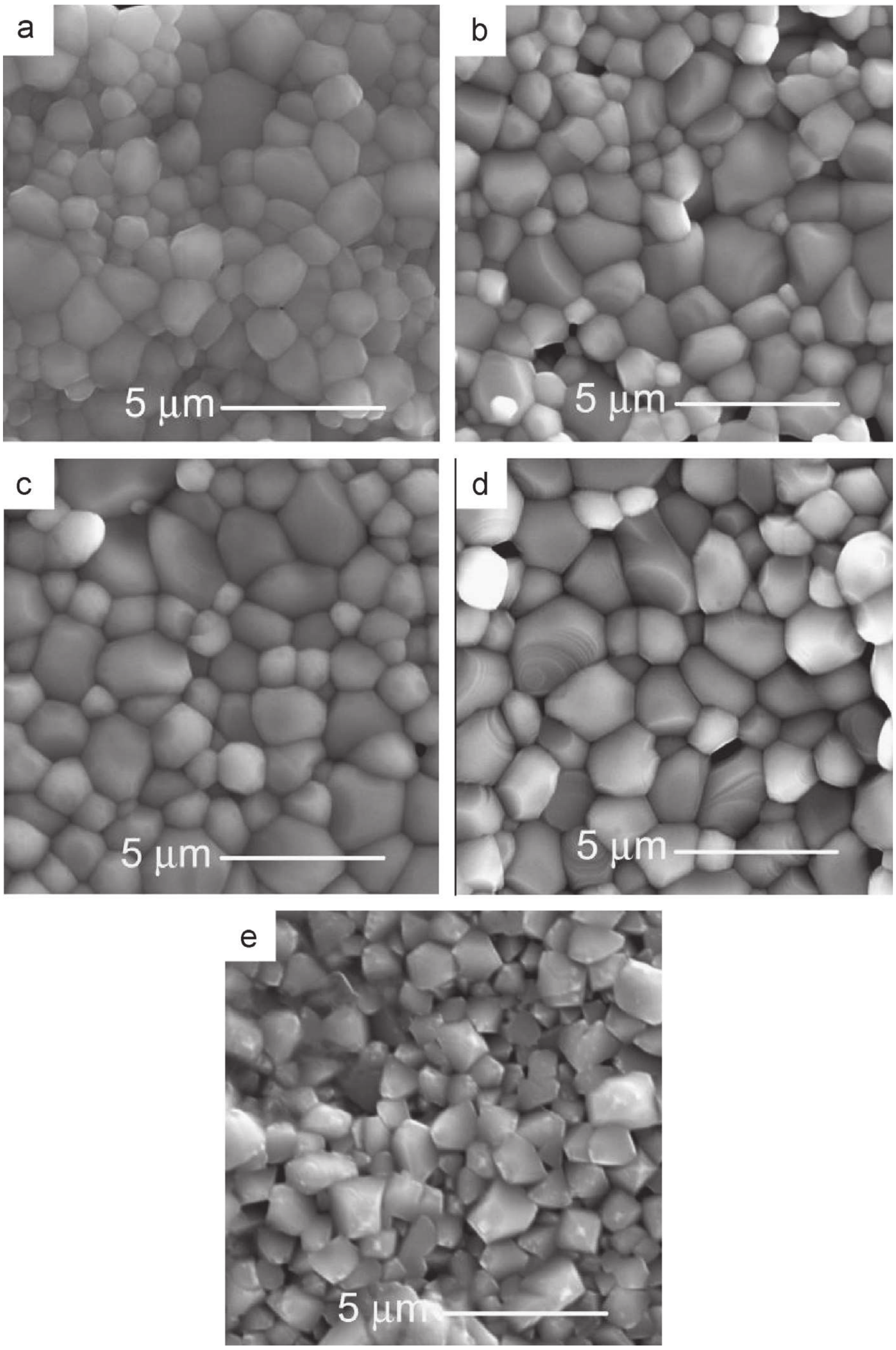

Fig. 5. SEM images of: a) NF, b) NZF (70–30), c) NZF (50–50) and d) NZF (30–70) e) ZF ceramics.

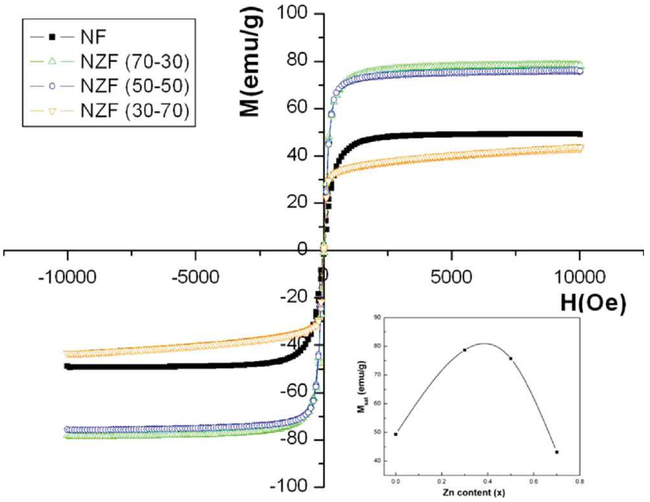

Fig. 6. Magnetization vs magnetic field for a) NF, b) NZF (70–30), c) NZF (50–50), d) NZF (30–70) samples.

Table 2
Saturation magnetization moment, saturation fields, residual magnetization and coercive field for all samples.

Sample	M_{sat} (emu/g)	H_{sat} (kOe)	M_r (emu/g)	H_c (Oe)
NF	49.39	1.84	2.27	15.7
NZF (70–30)	78.68	1.61	2.64	0.018
NZF (50–50)	75.72	1.53	1.41	0.72
NZF (30–70)	43.12	1.35	1.08	1.9

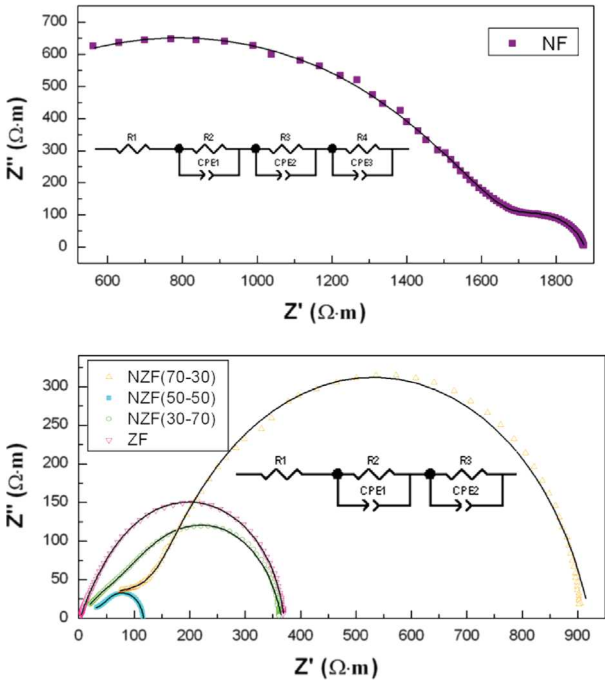

Fig. 7. Complex impedance plot of: a) NF b) NZF (70–30), NZF (50–50), NZF (30–70), ZF at room temperature.

SEM images of the sintered ceramic samples at the free surface are shown in Fig. 5. The average grain sizes of all samples are given in Table 1. The increase of zinc content led to the increase of the average grain size, except for ZF sample, where it was smaller than in NZF (30–70). It can be observed that the shape of the grains in the case of ZF is more pyramidal compared to polygonal grains of NZF. SEM images indicated that with increase of molar fraction of Zn, the density increases. This increase in density may be a consequence of Zn^{2+} concentration that slightly promotes the grain growth and improves densification, which was also observed in the work of Shirsath et al. [30].

Table 3
Grain resistance, grain boundary resistance and total resistance for all samples.

Sample	R_g (Ω m)	R_{gb} (Ω m)	R_e (Ω m)	R_{total} (Ω m)
NF	666	1364	149	2179
NZF (70–30)	242	725	/	967
NZF (50–50)	40	64	/	104
NZF (30–70)	144	220	/	364
ZF	52	314	/	366

3.2. Magnetization measurements

Magnetization results showed ferromagnetic behavior of the NF and NZF materials (Fig. 6). These curves are typical for soft magnetic materials [31]. Saturation magnetization moment of NF was lower than that for NZF (70–30) and NZF (50–50), but slightly higher than that for NZF (30–70) (Table 2). With the addition of Zn (which is nonmagnetic), the migration of Fe^{3+} ions from tetrahedral sites (A) to octahedral sites (B) take place, resulting in the weakening of A–B exchange interaction [32]. Thus, the balance between Fe^{3+} ions in those two positions is disrupted causing the increase of magnetization

On the other hand, the increase of Zn content above $x=0.3$ led to the increase of grains contribution to grain interface, which decreased the magnetization saturation. These values are in agreement with results reported by other authors [33,34]. The fields at which saturation occurs were almost the same for nickel based ferrite around 1.5 kOe (Table 2). The observed values for saturation magnetization, for NZF (70–30) and NZF (50–50) (79 and 76 emu/g), are slightly higher than for the NZF (65–35) and NZF (50–50) prepared by the citrate precursor method (73 and 69 emu/g) [33]. In comparison with mechano-synthesized NF, the saturation magnetization of obtained sample was also higher (49 vs. 24 emu/g) [35] indicating the significant influence of the powder processing route.

There are two effects that impact the coercivity of Zn substituted NF materials. First, the presence of Zn promotes sintering and leads to the increase of the grain size [36], which was confirmed by SEM measurements. Larger grains tend to consist of a greater number of domain walls. The magnetization caused by domain wall movement requires less energy than that required by domain rotation. As the number of domain walls increases with grain size, caused by the addition of Zn, the contribution of wall movement to magnetization is more expressed than that of domain rotation. Therefore, samples having larger grains are expected to have a low coercivity, H_C [37]. Second, Zn was reported to bring better arrangement in the ferrite crystal structure [38]. Since the domain walls pin to the defects in the structure, in order to pass them, some amount of energy is needed. This energy is provided by an applied magnetic field. The field required to overcome those defects is coercive field [31]. These two effects interact and reduce the coercive field of NZF samples. On the other hand, coercive fields of samples with Zn are very low. However, slight increase of coercive field with the increase of molar fraction of Zn was observed. Thus, the clear dependence of coercive field and Zn concentration above NZF (70–30) cannot be firmly claimed.

3.3. Impedance measurements

The impedance spectroscopy is an important method to study the electrical properties of ferrites because it gives the information about resistive and reactive components in the material. Fig. 7 shows the impedance plot for ceramic samples at room temperature. The impedance measurements were analyzed using commercially available Z-View software. The conduction mechanism in ferrites was explained with exchange of electrons between the ions of the same elements that have multiple valence states [8]. All samples showed two semicircular arcs, one due to the influence of the grain boundary conduction at the low frequencies, and other one due to influence of the grain conduction at the high frequencies. For NF samples the third semicircular arc was observed corresponding to the influence of electrode. The values of the grain, grain boundary and total electrical resistivity are given in Table 3.

The increase of zinc content leads to the decrease of total resistance up to NZF (50–50) and then with further increase of Zn the resistance starts to increase. The decreasing resistivity is attributed to the decrease of the number of grain boundaries caused by the grain size increase (induced by addition of Zn). With further increase of zinc, resistivity starts to increase. It can be assumed that more zinc leads to better structure ordering and results in the reduction of defects (vacancies) which are main conductive species in ceramics. Although the grain size increase in all compositions, this effect of Zn on the structure ordering dominates in NZF (30–70) and ZF and leads to an increase of total resistance of these compounds. Generally, the resistance of obtained ceramics was less than expected for ferrites (greater than 10^4 Ω m) [39] probably due to the low density.

4. Conclusion

A series of Ni–Zn ferrite with general formula $Ni_{1-x}Zn_xFe_2O_4$ where x=0.0, 0.3, 0.5, 0.7, 1.0 were prepared by the auto-combustion method. The pure phase formation was confirmed by XRD for powders and ceramics. Raman spectroscopy confirmed the formation of the cubic structure. SEM analysis indicated a high level of powder agglomeration. The size of the crystallites slightly increases when more Ni^{2+} ions were replaced by Zn^{2+} ions. Magnetic measurements showed that magnetization was rising with increasing of Zn content up to 30%, and followed by a further decrease. The fields at which saturation occurs were almost the same for all investigated compositions. In the comparison with NZF ceramics prepared by other synthesis methods, the value of the saturation magnetization of ferrites obtained in this study was enhanced. The resistance was found to decrease with the increase in zinc content up to NZF (50–50) and then increase. For all obtained ceramic samples grain boundary resistance has the highest contribution to the total resistance.

Although auto-combustion method has been shown as appropriate for obtaining pure nanosized nickel and nickel–zinc ferrites, it would be necessary to achieve higher density and higher resistance if we want to get ferrites as the final product. However, since our goal was focused on getting ferrites as ferromagnetic component for multiferroic composite, it might be noted that very encouraging results were achieved using the auto-combustion synthesis method.

Acknowledgments

The authors gratefully acknowledge the financial support of the Ministry of Education, Science and Technological Development of the Republic of Serbia (project III 45021), and COST MP0904 Action SIMUFER: “Single- and multiphase ferroics and multiferroics with restricted geometries”. Special thanks to Dr. Lavinia Curecheriu from Faculty of Physics, Al.I. Cuza University, Iasi for magnetic measurements.

References

[1] S. Maensiri, C. Masingboon, B. Boonchom, S. Seraphin, A simple route to synthesize nickel ferrite ($NiFe_2O_4$) nanoparticles using egg white, Scr. Mater. 56 (2007) 797–800.

[2] H. Kavas, N. Kasapoglu, A. Baykal, Y. Koseoglu, Characterization of $NiFe_2O_4$ nanoparticles synthesized by various methods, Chem. Pap. 63 (4) (2009) 450–455.

[3] R. Grigalaitis, M. Vijatovic Petrović, J. Bobić, A. Dzunuzovic, R. Sobiestianskas, A. Brilingas, B.D. Stojanovic, J. Banys, Dielectric and magneticproperties of $BaTiO_3$–$NiFe_2O_4$ multiferroic composites, Ceram. Int. 40 (2014) 6165–6170.

[4] L.P. Curecheriu, M.T. Buscaglia, V. Buscaglia, L. Mitoseriu, P. Postolache, A. Ianculescu, P. Nanni, Functional properties of $BaTiO_3$–$Ni_{0.5}Fe_2O_4$ magnetoelectric ceramics prepared from powders with core-shell structure, J. Appl. Phys. 107 (2010) 104–106.

[5] L. Mitoseriu, V. Buscaglia, M. Viviani, M.T. Buscaglia, I. Pallecchi, C. Harnagea, A. Testino, V. Trefiletti, P. Nanni, A.S. Siri, $BaTiO_3$–$(Ni_{0.5}Zn_{0.5})Fe_2O_4$ ceramic composites with ferroelectric and magnetic properties, J. Eur. Ceram. Soc. 27 (2007) 4379–4382.

[6] A. Sakanas, R. Grigalaitis, J. Banys, L. Mitoseriu, V. Buscaglia, P. Nani, Broadband dielectric spectroscopy of $BaTiO_3$–$Ni_{0.5}Zn_{0.5}Fe_2O_4$ composite ceramics, J. Alloys Compd. 602 (2014) 241–247.

[7] S.A. Seyyed Ebrahimi, S.M. Masoudpanah, H. Amiri, M. Yousefzadeh, Magnetic properties of MnZn ferrite nanoparticles obtained by SHS and sol–gel auto-combustion techniques, Ceram. Int. 40 (2014) 6713–6718.

[8] A.S. Fawzi, A.D. Sheikh, V.L. Mathe, Structural, dielectric properties and AC conductivity of $Ni_{(1-x)}Zn_xFe_2O_4$ spinel ferrites, J. Alloys Compd. 502 (2010) 231–237.

[9] G.R. Amiri, M.H. Yousefi, M.R. Abolhassani, S. Manouchehri, M.H. Keshavarz, S. Fatahian, Magnetic properties and microwave absorption in Ni–Zn and Mn–Zn ferrite nanoparticles synthesized by low-temperature solid-state reaction, J. Magn. Magn. Mater. 323 (2011) 730–734.

[10] Y. Liu, J. li, F. Min, J. Zhu, M. Zhang, Microwave-assisted synthesis and magnetic properties of $Ni_{1-x}Zn_xFe_2O_4$ ferrite powder, J. Magn. Magn. Mater. 354 (2014) 295–298.

[11] N. Gupta, A. Verma, S. Kashuap, D. Dube, Micro structural, dielectric and magnetic behavior of spindeposited nanocrystalline nickel-zinc ferrite thin films for microwave applications, J. Magn. Magn. Mater. 308 (2007) 137–142.

[12] K. Shafi, Y. Koltypin, A. Gedanken, R. Prozorov, J. Balogh, J. Lendvai, I. Felner, Sonochemical preparation of nano-sized amorphous $NiFe_2O_4$ particles, J. Phys. Chem. B 101 (1997) 6409–6414.

[13] S. Prasad, N. Gajbhiye, Magnetic studies of nanosized nickel ferrite particles synthesized by the citrate precursor technique, J. Alloys Compd. 265 (1998) 87–92.

[14] J. Yang, W. Tsuo, F. Yen, Preparation of ultrafine nickel ferrite powders using mixed Ni and Fe tartarates, J. Solid State Chem. 145 (1999) 50–57.

[15] Y. Shi, J. Ding, X. Liu, J. Wang, $NiFe_2O_4$ ultrafine particles prepared by co-precipitation/mechanical alloying, J. Magn. Magn. Mater. 205 (1999) 249–254.

[16] T.F. Marinca, I. Chicinas, O. Isnard, V. Pop, F. Popa, Synthesis, structural and magnetic characterization of nanocrystalline nickel ferrite- $NiFe_2O_4$ obtained by reactive milling, J. Alloys Compd. 509 (2011) 7931.

[17] D. Chen, R. He, Synthesis of nickel ferrite nanoparticles by sol–gel method, Mater. Res. Bull. 36 (2001) 1369–1377.

[18] Y. Kinemuchi, K. Ishizaka, H. Suematsu, W. Jiang, K. Yatsui, Magnetic properties of nanosize $NiFe_2O_4$ particles synthesized by pulsed wire discharge, Thin Solid Films 407 (2002) 109–113.

[19] R. Parthasarathi, L. Berchmans, R. Preetha, G. Senguttuvan, G. Umapathu, Combustion synthesis of nanocrystalline nickel ferrite using hexamine as a fuel, Int. J. Self-Propag. High-Temp. Synth. 20 (2011) 236–240.

[20] K. Rama Krishna, K. Vijaya Kumar, D. Ravinder, Structural and electrical conductivity studies in nickel-zinc ferrite, Adv. Mater. Phys. Chem. 2 (2012) 185–191.

[21] Adam F. Gross, Michael R. Diehl, Kristen C. Beverly, Erik K. Richman, Sarah H. Tolbert, Controlling magnetic coupling between cobalt nanoparticles through nanoscale confinement in hexagonal mesoporous silica, J. Phys. Chem. B 107 (2003) 5475–5482.

[22] M. Vijatovic Petrovic, J. Bobic, H. Ursic, J. Banys, B. Stojanovic, The electrical properties of chemically obtained barium titanate improved by attrition milling, J. Sol–Gel Sci. Technol. 67 (2013) 267–272.

[23] L. Vegard, The constitution of mixed crystals and the space occupied by atoms, Z. Phys. 5 (1921) 17.

[24] L. Fraas, J. Moore, Raman selection rule violation for a spinel crystal, Rev. Bras. Educ. Fís. 2 (1972) 299.

[25] P. Graves, C. Johnston, J. Campaniello, Raman scattering in spinel structure ferrites, Mater. Res. Bull. 23 (1988) 1651.

[26] G. Dixit, J.P. Singh, R.C. Sriavastava, H.M. Agrawal, Study of 200 MeV Ag^{15+} ion induced amorphisation in nickel ferrite thin films, Nucl. Instrum. Methods B 269 (2011) 133–139.

[27] A. Ahlawat, V.G. Sathe, V.R. Reddy, A. Gupta, Mossbauer, Raman and X-ray diffraction studies of superparamagnetic $NiFe_2O_4$ nanoparticles prepared by sol–gel auto-combustion method, J. Magn. Magn. Mater. 323 (2011) 2049–2054.

[28] J.P. Singh, G. Dixit, R.C. Srivastava, H.M. Agrawal, Ravi Kumar, Raman and Fourier-transform infrared spectroscopic study of nanosized zinc ferrite irradiated with 200 MeV Ag^{15+} beam, J. Alloys Compd. 551 (2013) 370–375.

[29] A. Ahlawat, V.G. Sathe, Raman study of $NiFe_2O_4$ nanoparticles, bulk and films: effect of laser power, J. Raman Spectrosc. 42 (2011) 1087–1094.

[30] S.E. Shirsath, S.M. Patange, R.H. Kadam, M.L. Mane, K.M. Jadhav, Structure refinement, cation site location, spectral and elastic properties of Zn^{2+} substituted $NiFe_2O_4$, J. Mol. Struct. 1024 (2012) 77–83.
[31] N.A. Spaldin, Magnetic Materials, Fundamentals and Applications, second ed., Cambridge University Press, Cambridge, 2011.
[32] S.S. Kumbhar, M.A. Mahadik, V.S. Mohite, K.Y. Rajpure, J.H. Kim, A.V. Moholkar, C.H. Bhosale, Structural, dielectric and magnetic properties of Ni substituted zinc ferrite, J. Magn. Magn. Mater. (2014) (http://dx.doi.org/10.1016/j).
[33] A. Verma, T.C. Goel, R.G. Mendiratta, P. Kishan, Magnetic properties of nickel zinc ferrites prepared by the citrate precursor method, J. Magn. Magn. Mater. 208 (2000) 13–19.
[34] H. Jamadar, M. Shelar, M. Bhandare, A. Shaikh, B. Chougule, Magnetic properties of nanocrystalline nickel zinc ferrites prepared by combustion synthesis, Int. J. Self- Propag. High-Temp. Synth. 20 (2011) 118–123.
[35] V. Sepalak, I. Bergmann, A. Feldhoff, P. Heitjans, F. Krumeich, D. Menzel, F. Litterst, S. Campbell, K. Becker, Nanocrystalline nickel ferrite, $NiFe_2O_4$: mechanosynthesis, nonequilibrium cation distribution, canted spin arrangement, and magnetic behavior, J. Phys. Chem. C 111 (2007) 5026–5033.
[36] A. Verma, T.C. Goel, R.G. Mendiratta, Frequency variation of initial permeability of NiZn ferrites prepared by the citrate precursor method, J. Magn. Magn. Mater. 210 (2000) 274–278.
[37] A.C. Costa, E. Tortella, M.R. Morelli, R.H. Kiminami, Synthesis, microstructure and magnetic properties of Ni–Zn ferrites, J. Magn. Magn. Mater. 256 (2003) 174–182.
[38] A. Verma, T.C. Goel, R.G. Mendiratta, M.I. Alam, Dielectric properties of NiZn ferrites prepared by the citrate precursor method, Mater. Sci. Eng. B 60 (1999) 156–162.
[39] A. Verma, T.C. Goel, R.G. Mendiratta, R.G. Gupta, High-resistivity nickel-zinc ferrites by the citrate precursor method, J. Magn. Magn. Mater. 192 (1999) 271–276.

Variation of electric properties across the grain boundaries in $BiFeO_3$ film

2016 J. Phys. D: Appl. Phys. 49 045309

(http://iopscience.iop.org/0022-3727/49/4/045309)

IOP Publishing Journal of Physics D: Applied Physics
J. Phys. D: Appl. Phys. **49** (2016) 045309 (9pp) doi:10.1088/0022-3727/49/4/045309

Variation of electric properties across the grain boundaries in $BiFeO_3$ film

Bojan Stojadinović[1], Borislav Vasić[1], Dimitrije Stepanenko[1], Nenad Tadić[2], Radoš Gajić[1] and Zorana Dohčević-Mitrović[1]

[1] Center for Solid State Physics and New Materials, Institute of Physics Belgrade, University of Belgrade, Pregrevica 118, 11080 Belgrade, Serbia
[2] Faculty of Physics, University of Belgrade, Studentski trg 12-16, 11000 Belgrade, Serbia

E-mail: bvasic@ipb.ac.rs and zordoh@ipb.ac.rs

Received 13 October 2015, revised 3 December 2015
Accepted for publication 8 December 2015
Published 29 December 2015

Abstract

Stark differences in charge transport properties between the interior and the boundary regions of grains in an undoped $BiFeO_3$ thin film have been found. The material is ferroelectric and each grain is a single domain. A spatial resolution that distinguishes between the grain interior and the boundary between the grains has been achieved by using piezoelectric force microscopy and conductive atomic force microscopy measurements. The local electric properties, as well as the local band gap show hysteresis only when probed in the grain interior, but do not show hysteresis when probed in the region around the boundary between two grains. The leakage current is more pronounced at the grain boundaries, and the region that carries significant current increases with the applied voltage.

Keywords: multiferroics, thin films, electrical properties, grain boundaries, scanning probe microscopy

S Online supplementary data available from stacks.iop.org/JPhysD/49/045309/mmedia

(Some figures may appear in colour only in the online journal)

1. Introduction

Multiferroic materials exhibit at least two ferroic properties among magnetic, electric, and elastic responses. Simultaneous presence of at least two hysteretic responses and interaction between the associated orders has spurred interest in the mechanisms that govern the phase transitions in multiferroics [1–3]. The explanation of the multiferroic order remains an interesting open problem of condensed matter physics. A pair of ferroic properties causes nonlinear and nonstandard responses, e.g. a material will produce electric polarization when exposed to an external magnetic field. Such responses make the multiferroics interesting from a practical point of view by allowing for novel forms of control. The most sought-after applications of multiferroics are electrically controlled magnetic memories [4], and emerging spintronic devices based on the simultaneous use of electric polarization, based on the orbital order, and magnetization, based on the spin order [2, 5].

The properties of multiferroic materials structured at the nanoscale can be drastically different from the corresponding properties of the bulk. Integration of materials into current semiconductor technology requires fabrication and structuring of thin films, leading to the interest in variation of the material properties with the nanoscale structure, as well as to the development of methods for their synthesis [6, 7]. In addition to reduced dimension, the thin films often show granular structure on the characteristic length scale of the order of 10 nm. Details of the grain structure contribute to the variation of the properties of both the material and the devices.

One of the most well-known multiferroic materials is the bismuth ferrite ($BiFeO_3$). It shows high critical temperatures, both for the ferroelectric ordering below 1104 K [8] and the antiferromagnetic ordering below 643 K [9]. The interest in $BiFeO_3$ stems from the possibility of having all the technologically desirable properties of multiferroics at and above the room temperature. A major obstacle for the applications of $BiFeO_3$ is the existence of relatively large leakage currents which severely limit the electric fields that a material can sustain. The leakage currents have been explained by the existence of charge defects, for example the oxygen and bismuth vacancies [10]. Attempts at minimizing the leakage currents in $BiFeO_3$ thin films drive the interest in their electronic transport properties and their modification either by doping [11–14] or by modifying the conditions of film growth [15, 16].

The properties of multiferroic $BiFeO_3$ granular thin film strongly depend on the grain size. The Neel temperature was shown to correlate with the volume of the grains which affects the polar displacements of cations and changes in polarization [17]. The mechanical properties also depend on the grain size [18]. Therefore, the regions in proximity to the grain boundaries may play an important role in determining the material properties.

We have studied a film of an undoped, single crystallographic phase, $BiFeO_3$. The film has been produced by sol–gel spin coating. The film has shown granular structure, and we have probed the variation of the electronic properties on the spatial scale commensurate with the grain size. Our film did not have any holes and all the measured grains lied on the top of the film, and not on the substrate. The variation at probed length scale are therefore properties of the grain morphology and independent of the thickness or large-scale roughness of the film.

In our measurements, the local electric properties of the film have varied on two characteristic length scales, corresponding to the sizes of grains and boundary regions. In scanning probe measurements, we have found mild variations between the interiors of different grains when probing their band structure. On the other hand, the differences between the grain interiors and the grain boundaries have been drastic. We have measured the local electric properties of the $BiFeO_3$ film across the grain boundary, and have found that the boundary regions differ from the grain interior in the density of states, charge transport mechanism, and the absence of hysteresis in the I–V curves. Remarkably, all the measured properties have shown a hysteresis when measured in the grain interior, but there were no sings of hysteresis when probed at the boundary.

2. Experimental procedure

$BiFeO_3$ thin film was prepared via the sol–gel spin coating method. The details of preparation are presented in the supplementary material (stacks.iop.org/JPhysD/49/045309/mmedia).

Structural characterization was carried out using x-ray diffraction (XRD) with Cu–Kα radiation on a Rigaku Ultima IV diffractometer ($2\theta = 20°–60°$). Raman spectroscopy was used to study the vibrational properties of $BiFeO_3$ thin film. Micro-Raman spectra were collected using a Jobin Yvon T64000 spectrometer with a liquid-nitrogen-cooled CCD camera.

The morphology and phenomena at short length scales were recorded by atomic force microscopy (AFM). AFM imaging was performed using tapping mode on NT-MDT system Ntegra Prima and silicon NSG01 probes with the tip curvature radius of 6 nm. The phase lag of the cantilever oscillation was recorded simultaneously with the topography image.

We have investigated the electromechanical response of our sample by piezoresponse force microscopy (PFM). During PFM measurements, an AC bias with the amplitude of 10 V and frequency of 150 kHz has been applied between the tip and the substrate on which the $BiFeO_3$ film is grown. PFM measurements were done using TiN coated NSG01 probes with a tip curvature radius of 35 nm, a typical force constant of 5.1 N $m^{-1}$and typical resonant frequency of 150 kHz. The conductive tip was scanning the surface of the sample in contact mode while AC bias was applied to the tip. The AC bias was inducing the contraction and expansion of the sample, and these changes of the shape were monitored by the tip deflection. This local piezoelectricity of $BiFeO_3$ thin film was recorded in out-of-plane and in-plane polarization.

The local electrical conductivity of a $BiFeO_3$ film was probed by conductive atomic force microscopy (C-AFM). During C-AFM measurements, a DC bias voltage (from +2 to +6 volts) was applied between the tip and the substrate. Surface topography and current maps were obtained simultaneously by using a conducting probe in contact with the sample. The measurements were performed with the DCP20 probe of a nominal curvature radius of 50–70 nm and typical force constant of 48 N m^{-1}. In the same mode, the electrical measurements of current-voltage (I–V) characteristics were recorded in the bias voltage range from −10 V to +10 V. The I–V curves were measured using C-AFM at the points within the grain interior and at the points on the grain boundary. We have determined the band gap value of BiFeO3 film according to the same procedure as in references [20–22]. Thus, we have measured the local density of states and the local band gap in $BiFeO_3$ film using C-AFM. At each point we have repeated the measurements a few times, and therefore proved the reproducibility. Differential conductance spectra were obtained by averaging and differentiating five current-voltage curves measured on an individual grain of $BiFeO_3$ film. All AFM measurements were performed at ambient conditions (room temperature and air atmosphere).

3. Results and discussion

The crystallographic phase and structure of our sample have been determined by XRD. The XRD pattern of the $BiFeO_3$ thin film is shown in figure 1(a). The XRD peaks of $BiFeO_3$ film with a rhombohedrally distorted $BiFeO_3$ perovskite structure, belonging to the R3c space group have been indexed. No peaks originating from the secondary phase were observed. The absence of the impurity phase signal from XRD measurement does not imply that the sample itself is ultra pure. However, it does imply that there are no regions of impurity phase of appreciable size. From the Williamson–Hall plot [19], we have estimated the grain size in our film to ∼38 nm and the microstrain to ∼0.3%, as shown in figure 1(b). The diffraction peaks corresponding to the perovskite structure have been clearly observed. Figure 1(c) shows the histogram of the grain size distribution from the AFM measurement of the $BiFeO_3$ film. Raman spectrum of $BiFeO_3$ film has confirmed the rhombohedrally distorted structure without the presence

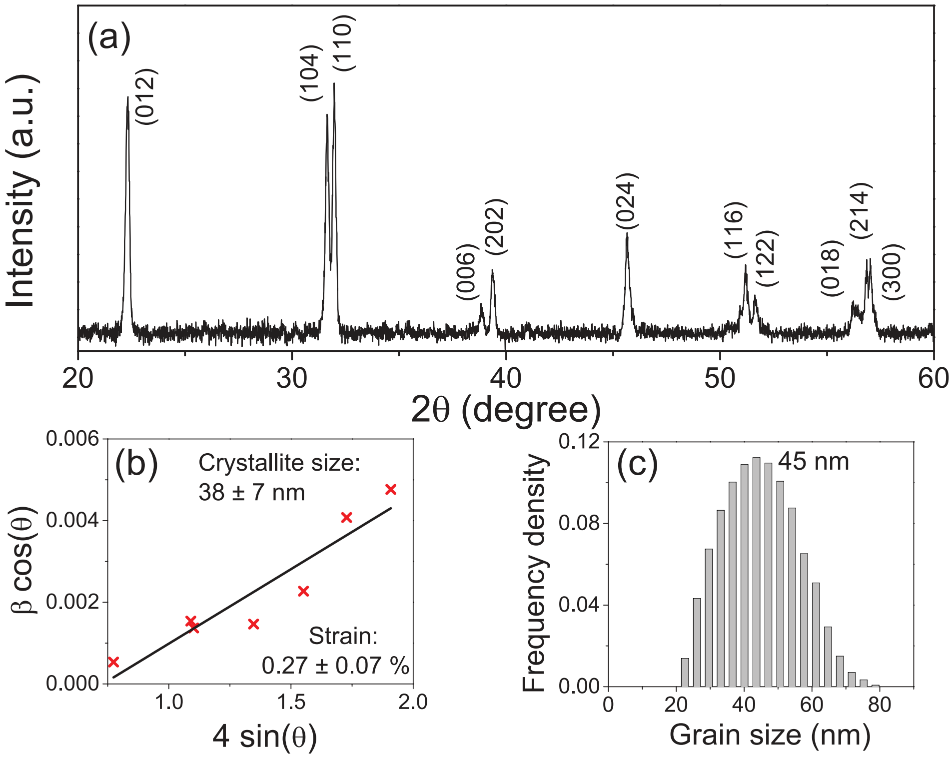

Figure 1. (a) X-ray diffraction pattern of the $BiFeO_3$ film fabricated by the sol–gel method, (b) Williamson–Hall plot for $BiFeO_3$ film with calculated crystallite size and strain, and (c) histogram of grain size distribution of $BiFeO_3$ film obtained from AFM image (see supplementary material (stacks.iop.org/JPhysD/49/045309/mmedia)).

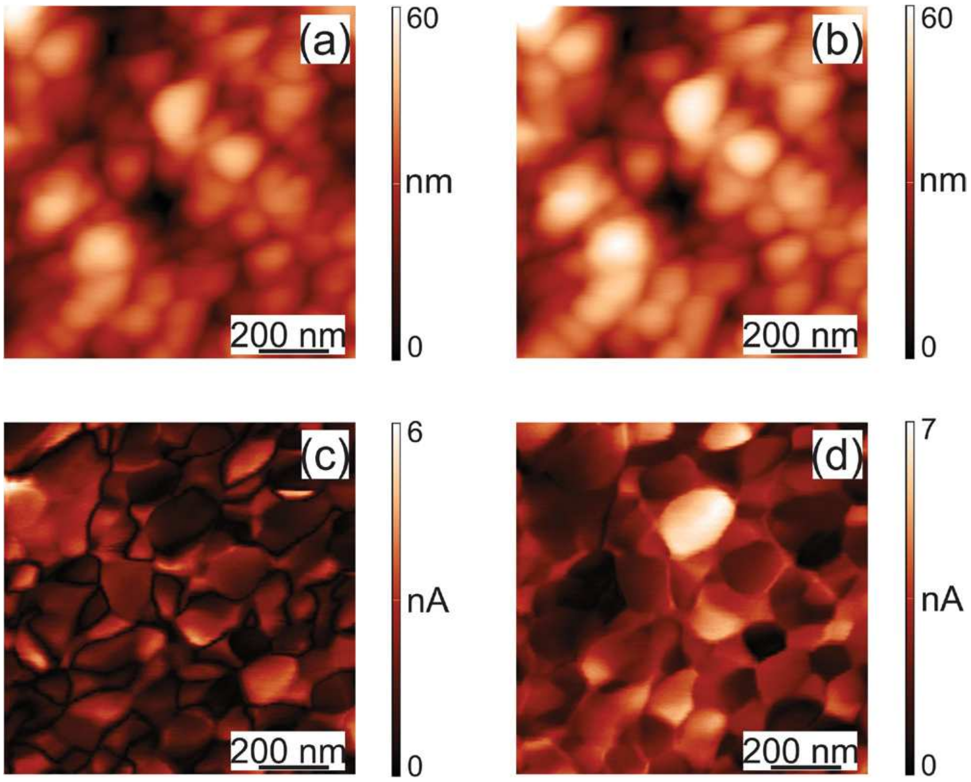

Figure 2. Topography (a) and out-of-plane PFM magnitude (c), topography (b) and in-plane PFM magnitude (d), showing the polarization components of $BiFeO_3$ film. The grains, visible on the topography images (a) and (b), correspond to the ferroelectric domain captured by the PFM magnitudes in (c) and (d).

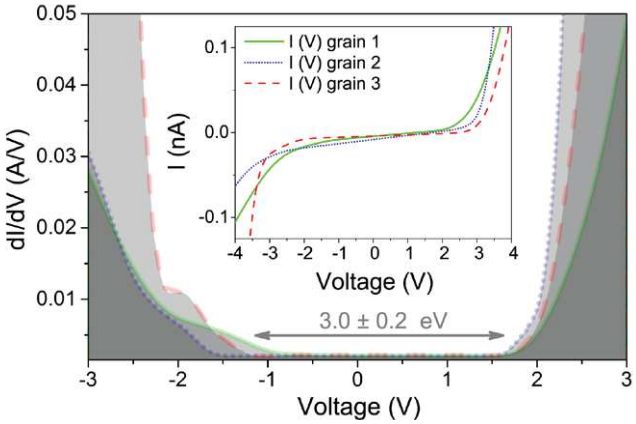

Figure 3. Representative differential conductance spectra measured on interior points of three different grains on $BiFeO_3$ film. Arrow shows the averaged band gap value. The corresponding I–V curves are shown in the inset in a wider voltage range, from −4 to 4 V.

of secondary phase. Raman scattering spectrum of the $BiFeO_3$ film is presented in supplementary material (stacks.iop.org/JPhysD/49/045309/mmedia).

Ferroelectric domains occur when the minimization of the electrostatic and elastic energy favors an inhomogeneous distribution in a material with unsaturated bulk electric polarization. The domain shapes and sizes are governed by various stresses that appear in the process of thin film growth [23, 24]. The granular structure of the $BiFeO_3$ film is dictated by lattice, morphology and thermal expansion coefficient mismatch between the $BiFeO_3$ film and the substrate [25, 26], the film thickness, and the temperature [27]. We have measured the polarization domains in the film, and found that they change on the characteristic length scale of ∼40 nm. We have measured both the out-of-plane and the in-plane polarization, based on normal and lateral deflection of the AFM cantilevers during PFM measurements (figures 2(c) and (d)). Therefore, we have identified both the in-plane and out-of-plane polarization components. Comparison with the sample topography, figures 2(a) and (b), has shown that the domain boundaries coincide with the grain boundaries. Therefore, each grain in the film has been a single-domain particle. This kind of the domain distribution is characteristic for the small grains, while larger grains generically show a multi-domain structure [24]. In our film, we could not identify any multi-domain grains.

Knowledge of the charge transport mechanism is essential in the design of memory devices based on $BiFeO_3$ film. The granular film contains rough surfaces that cause an inhomogeneous behavior of conductivity [28]. We have investigated the spatial distribution of the density of states and of the band gap. We have achieved high resolution by measuring the I–V characteristics locally using C-AFM, and by extracting the corresponding differential conductances.

Figure 3 shows the characteristic spectra of local differential conductance as a function of voltage. The measurements have been performed on interior points of different grains, far away from any boundaries with the neighboring grains. The density of states has varied slightly between the grains. The estimated band gap is $E_g = 3.0 \pm 0.2$ eV, in agreement with the optical measurements [29–31]. Conduction at negative bias voltages corresponds to the states in the valence band, while the conduction at the positive bias corresponds to the states in the conduction band. The flat plateau around zero voltage represents the band gap. These results show that the grain interiors are very similar, even though the grain's immediate surroundings vary. Therefore, we claim that the properties at the length scale of the grain size are not influenced by the distant regions of the film, and therefore should not depend on the film thickness, as long as it is larger than the grain dimension.

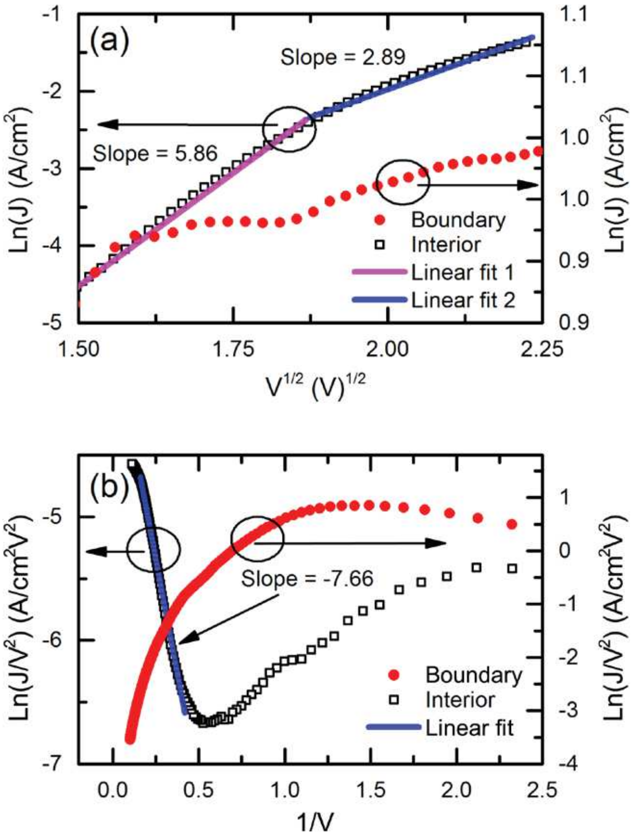

Figure 4. (a) Schottky thermionic emission plot, $\ln(J)$ versus $V^{1/2}$ and (b) Fowler–Nordheim plot, $\ln(J/V^2)$ versus $1/V$ at positive bias curves of the grain interior (left scale) and grain boundary (right scale) of the $BiFeO_3$ film.

We have observed a difference between the grain boundary and the grain interior in the local measurements of the current as a function of bias voltage. In the resulting I–V curves the conduction has been higher at the boundary. Conduction through semiconductor heterostructures is well researched, and various transport mechanisms have been proposed and observed [32, 33]. In our case, the distribution of electric polarization (see figure 2), and the typical gap sizes (see figure 3), suggest that the interior of the grain behaves as a semiconductor of fairly large band gap, ∼ 3 eV. In the grain interior, the transport has been consistent with the tunneling through a barrier, either via Schottky or Fowler–Nordheim mechanism [32–34]. We have fitted the I–V curves in the spatial region of the grain interior, and in the voltage region $V > 2$ V, to the predictions of the tunneling transport theory. Up to $V \approx 5$ V, the Schottky mechanism of thermal excitations across the barrier explains the observed behavior. At larger voltages,

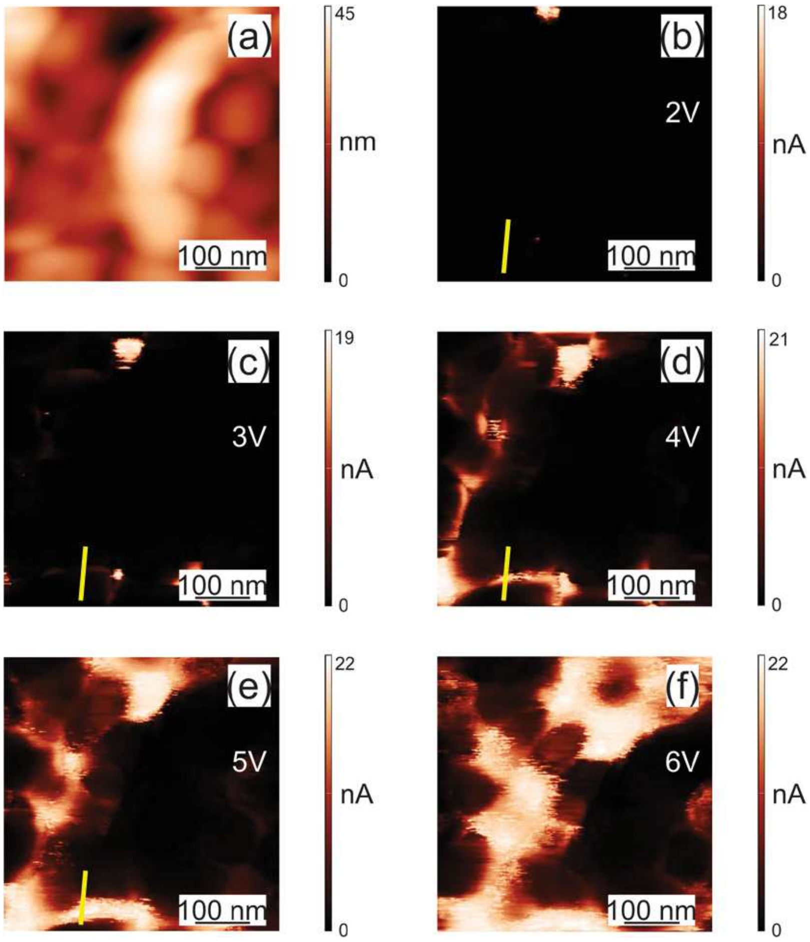

Figure 5. (a) Topography and ((b)–(f)) current maps (C-AFM images) according to bias voltages $V = 2, 3, 4, 5, 6$ V respectively. Bright regions means higher current. Notice the enhanced conductivity at grain boundaries and no conductivity regions in the grains interior. Bright line indicates the places between two grains where we have measured the current as a function of the position (shown in figure 6).

the results are consistent with the Fowler–Nordheim mechanism. Figure 4(a) shows the plot of $\ln(J)$ versus $V^{1/2}$ measured at various points in the BiFeO$_3$ film in the voltage range from 2 to 5 V. For the leakage current governed by the tunneling, $\ln(J/V^2)$ versus $1/V$ plot shows linearity for bias voltage well bellow the gap, i.e. $V < 2$ V (figure 4(b)), as we have observed in our film. At low fields, $V < 1.5$ V the grain interior has shown a plain Ohmic behavior (see supplementary material (stacks.iop.org/JPhysD/49/045309/mmedia)). As opposed to the grain interior, I–V curves of the grain boundary have not followed any standard transport model.

The local current distributions and the I–V characteristic of the BiFeO$_3$ film have been studied by the C-AFM. Current maps (C-AFM images) and topography images have been probed in the same spatial region of the sample. In C-AFM images, figure 5, the bright parts are conducting regions, while the dark regions are non-conducting. From the morphological and PFM measurements we have found that the BiFeO$_3$ film is inhomogeneous. A difference in electric transport properties between the grain interior and its boundary can appear for several reasons. Due to the different crystal orientation of the grains and the possible strain between the grains, the polarizations of neighboring grains are not equal and generically point in different directions. Furthermore, different polarizations of the neighboring grains cause strong electric fields in the region of the boundary between the grains. A similar phenomenon was observed in HoMnO$_3$ [35].

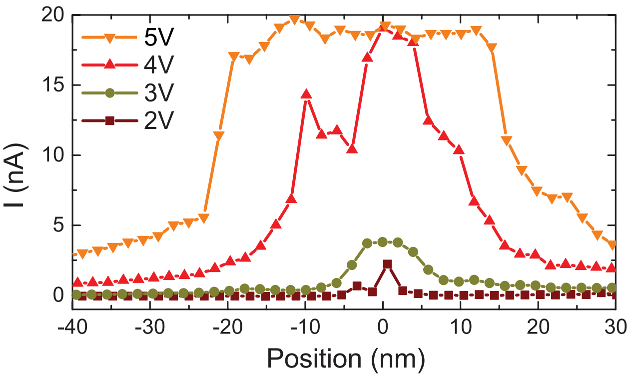

Figure 6. The current profiles of cross-sectional analysis along the bright solid line in figure 5.

Our measurements have demonstrated that the local conduction pathways of the BiFeO$_3$ film coincide with the grain boundaries, while the interior of the grains remain insulating [36], as indicated in figure 5, and consistent with the measurements on the interior points of various grains, presented in figure 3. The charge transport of BiFeO$_3$ film has been

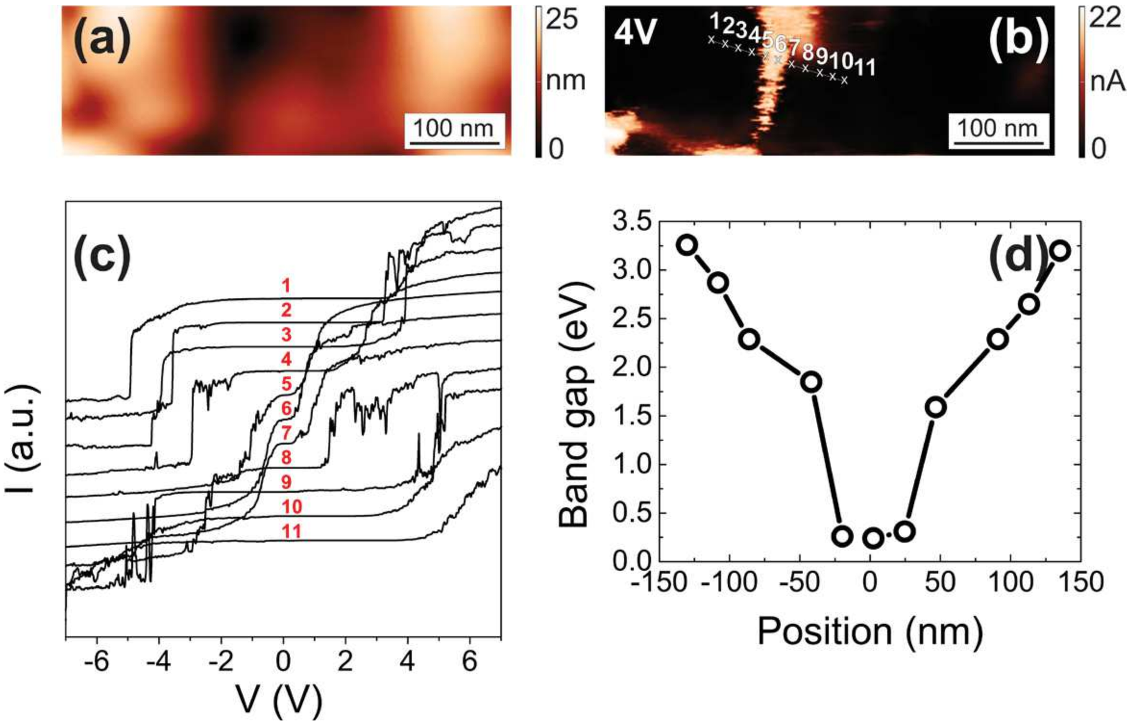

Figure 7. (a) Topography, (b) C-AFM image with line across the grain boundary, (c) I–V characteristics for 11-points across grain boundary and (d) behavior of the band gap as a function of the position of the grain boundary.

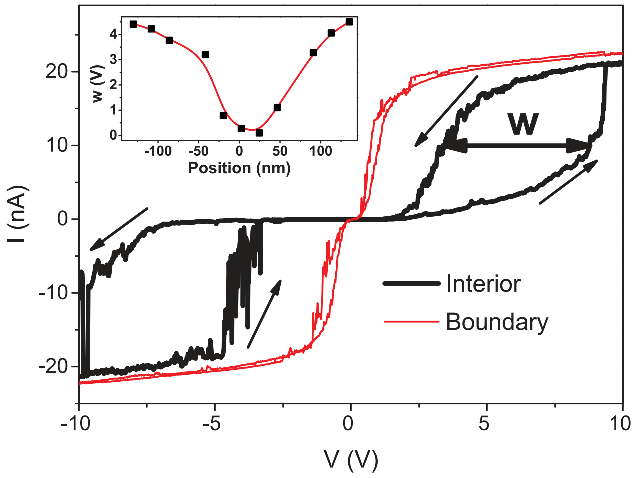

Figure 8. Dramatic I–V hysteresis in the grain interior (heavy line) and the absence of the hysteresis in the grain boundaries (thin line) of the $BiFeO_3$ film. In the inset, the width of the hysteresis curve (w) is shown as a function of the position across the grain boundary. Solid line in the inset is a guide to the eye.

investigated at different applied bias voltages, both slightly smaller and larger than the band gap. Topography image (figure 5(a)) and the corresponding C-AFM images at bias voltage ranged from 2 to 6 V (figures 5(b)–(f)) have confirmed high correlation between the granular structure of the film and the shape of the conduction pathways. Under low bias voltages, narrow charge transport pathways form (figures 5(b) and (c)) at the places that are low in the topographic image of the film, and are barely visible. As the bias voltage increases, both the width of the conduction pathways and the intensity of the current that flows through them increases.

The evolution of the conduction pathways with the increasing bias voltage is shown in figure 6. The current through the film has been measured at the points that lie both near the grain boundaries and deep within the grain, along line that crosses the grain boundary at the right angle. The measurements were repeated for various bias voltages. The geometry is indicated by the bright solid line in figures 5(b)–(e). With the increase of the bias voltage, the conduction path broadens. Initial broadening is slow, the currents are weak, and the path is narrow as long as the bias voltage is below the band gap. At the bias voltage of about 4 V, which is larger than the band gap, the path suddenly broadens dramatically, and the local currents increase. At such high biases, the interior of the grain also begins to conduct. Similar behavior was previously observed in doped $BiFeO_3$ film [28].

In order to better understand the microscopic charge transport process in the grain boundaries, we have measured the I–V characteristics across the grain boundary and observed the changes in the conduction. A pair of particularly large grains and the boundary between them have been chosen, so that we can reach a relatively high spatial resolution when compared to the dimensions of the grains. Figure 7 shows topography (a) and C-AFM image (b) under the 4 V bias with a line across the grain boundary and 11 points on it. The I–V characteristics taken at these points are shown in figure 7(c). As a general trend, the grain boundaries have almost Ohmic behavior, but at the point in the grain interior, the I–V characteristics are typical of semiconductors. Figure 7(d) shows the evolution of the band gap across the grain boundary. We have found the band gap of about 3.2 eV on the grain interior, consistent with the measurements on other grains, see figure 3. As the probe approaches the boundary, the band gap narrows down. At the

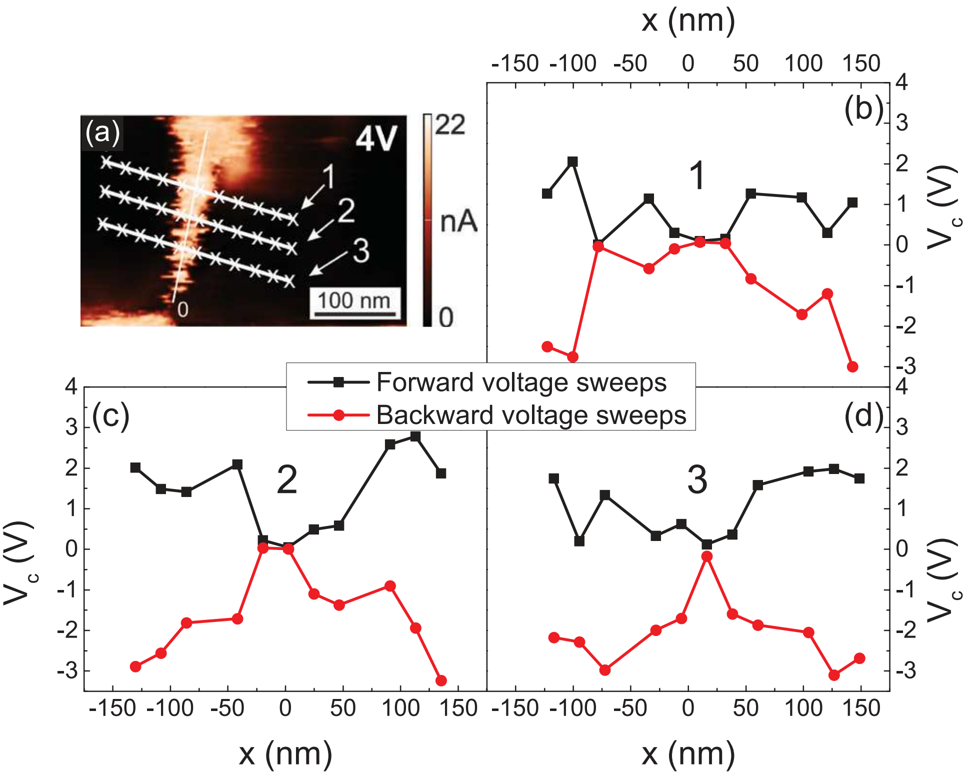

Figure 9. (a) C-AFM image with 3 lines across grain boundary and ((b)–(d)) center of band gap across lines 1, 2, and 3 in the C-AFM image. Solid lines are a guide to the eye.

three points located at the grain boundary (5, 6, and 7) the band gap is very narrow, and the material behaves similarly to a conductor. The fact that we do not find the band gap to be constant across the sample suggests that, at the level of single grains, the film is not homogeneous with well-defined and constant band structure throughout the sample.

The hysteretic dependence of polarization on the external electric field is well known in bulk ferroelectric $BiFeO_3$. The hysteretic phenomena are necessary for the applications of $BiFeO_3$ films in memory devices. Reorganization of charge associated with the variation of electric polarization causes strong internal fields in the sample, and we may expect similar hysteretic behavior in the quantities related to the charge transport. The I–V characteristics and the phenomenon of resistive switching in polycrystalline thin films shows some signatures of the hysteresis [37–39]. However, the hysteresis of electric polarization in the electric field exists only in insulators, whereas the conductors cannot support the electric fields in the interior. We have studied the local hysteresis in the I–V curves, and have probed both the region where the grain is insulating, i.e. the grain interior, and the region where the grain is conductive, i.e. the grain boundary. We have defined the hysteresis width, w, as the difference of voltage that produces a 10 nA current in forward- and backward voltage sweep, see figure 8. The hysteresis width vanishes at the grain boundary, and turns on in the interior with the characteristic length scale of 50 nm, see inset of figure 8. The measured points are presented in figure 7(b). Figure 8 shows the I–V curves in the forward and backward sweep at the grain interior (thick line) and at the grain boundary (thin line). Note that the typical grain diameter is 40 nm.

The bulk $BiFeO_3$ shows both the ferroelectric and the antiferromagnetic order. Both orders are characterized by hysteretic response to external fields. We have found the hysteresis in conductivity in the interior of the grain, but not at the grain boundary (see figure 8). Another property of the grain that can be studied locally is the density of states. We have measured the local density of states across the grain boundary and have found, again, the hysteretic behavior within the grain interior, but not on the boundary. We have chosen the center of the band gap as a representative quantity that describes the band structure. The definition of the center of band gap is illustrated graphically in the supplementary material (stacks.iop.org/JPhysD/49/045309/mmedia). In a series of C-AFM measurements, we have measured the density of states in a forward- and backward voltage sweeps at a set of points that extends across the grain boundary.

Figure 9(a) shows a C-AFM image of grain boundary. Within this region, we have recorded 11 I–V curves through three different lines (see picture). Three representative lines (1–3) across the leakage current pathways of different widths are selected for detailed study of the local density of states. The center of flat plateau in the I–V characteristics is defined as the center of the band gap. Figures 9(b)–(d) show the potential at the band gap centers, V_c, across marked lines 1–3 in figure 9(a).

The density of states is hysteretic, and the center of the band gap is hysteretic within the grain, but not within the boundary layer, see figure 9. The motion of the center of the band gap, V_c, as the probe position x moves in real space across the grain boundary is more pronounced in the backward voltage sweeps, and less in the forward ones. The local hysteresis is manifested by the difference in the positions of the band gap centers as measured in the forward- and backward voltage sweeps while the position of the probe within the sample is kept fixed. Comparison of the $V_c(x)$ curves from the figures 9(b)–(d) with the image of conductivity obtained by C-AFM shows that the narrower boundary region as defined by conductivity (figure 9(a)) also implies a narrower region with the absent hysteresis in $V_c(x)$ (figures 9(b)–(d)). Note, however that the boundary region as would naively be defined from $I(V)$ is much narrower than the absence of hysteresis would imply.

In thin $BiFeO_3$ films, a similar shift of the band gap was observed at the ferroelectric domain boundaries [40]. Discontinuity in polarization and the consequent charge accumulation on the surface causes potential discontinuity and moves the band gap. Such a potential difference should enhance the electrical conductivity by causing carriers in the material to accumulate at the domain wall to screen the polarization discontinuity [41, 42]. In our sample, the grains are single domains, see above, and a similar charge accumulation appears at the boundaries between the grains.

4. Conclusions

We have observed a difference in electrical properties between the grain interior and the grain boundary in $BiFeO_3$ thin film obtained by sol–gel spin coating process. Leakage current was more pronounced at the grain boundaries. The onset of large leakage current with the increasing bias voltage happens as the region of large conductivity expands from the grain boundaries towards the grain interiors. The leakage mechanism in grain interior have been identified with Schottky and Fowler–Nordheim processes, while the leakage current through the grain boundaries does not appear to be dominated by any standard mechanism of conduction. In the measurement with the local probes, we have also found that the band gap varies slightly among the different grains, but varies strongly between the grain boundary and the grain interior. In the grain interior, we have observed hysteresis in various properties of the material connected to the charge transport. The shape of the density of states is itself hysteretic. As a consequence, the conductivity as a function of slowly varying voltage is also hysteretic. As opposed to the grain interior, no hysteresis was observed with the local probe at the grain boundary.

Acknowledgments

This work was financially supported by the Ministry of Education, Science and Technological Development of the Republic of Serbia under the projects OI171032, OI171005, III45018 and SNF through SCOPES IZ73Z0152500.

References

[1] Sergienko I A and Dagotto E 2006 Role of the Dzyaloshinskii-Moriya interaction in multiferroic perovskites *Phys. Rev.* B **73** 094434

[2] Cheong S W and Mostovoy M 2007 Multiferroics: a magnetic twist for ferroelectricity *Nat. Mater.* **6** 13

[3] Picozzi S, Yamauchi K, Sergienko I A, Sen C, Sanyal B and Dagotto E 2008 Microscopic mechanisms for improper ferroelectricity in multiferroic perovskites: a theoretical review *J. Phys.: Condens. Matter* **20** 434208

[4] Catalan G and Scott J F 2009 Physics and applications of bismuth ferrite *Adv. Mater.* **21** 2463

[5] Ramesh R and Spaldin N A 2007 Multiferroics: progress and prospects in thin films *Nat. Mater.* **6** 21

[6] Ren X R, Tan G Q, Miao H Y and Li Z Y 2012 Controllability study on the preparation of pure phase $BiFeO_3$ thin films by liquid phase self-assembled method *Appl. Surf. Sci.* **258** 8040

[7] Schwartz R W 1997 Chemical solution deposition of perovskite thin films *Chem. Mater.* **9** 2325

[8] Roginskaya Y E, Tomashpol'Skiĭ Y Y, Venevtsev Y N, Petrov V M and Zhdanov G S 1966 Nature of dielectric and magnetic properties of $BiFeO_3$ *Sov. Phys.—JETP* **23** 47

[9] Kiselev S V, Ozerov R P and Zhdanov G S 1963 Detection of magnetic order in ferroelectric $BiFeO_3$ by neutron diffraction *Sov. Phys.—Dokl.* **7** 742

[10] Wang Y and Nan C W 2006 Enhanced ferroelectricity in Ti-doped multiferroic $BiFeO_3$ thin films *Appl. Phys. Lett.* **89** 052903

[11] Mao W *et al* 2014 Effect of Ln (Ln = La, Pr) and Co co-doped on the magnetic and ferroelectric properties of $BiFeO_3$ nanoparticles *J. Alloys Compd.* **584** 520

[12] Pradhan S K and Roul B K 2011 Effect of Gd doping on structural, electrical and magnetic properties of $BiFeO_3$ electroceramic *J. Phys. Chem. Solids* **72** 1180

[13] Liu J, Li M, Pei L, Wang J, Yu B, Wang X and Zhao X 2010 Structural and multiferroic properties of the Ce-doped $BiFeO_3$ thin films *J. Alloys Compd.* **493** 544

[14] Qi X, Dho J, Tomov R, Blamire M G and MacManus-Driscoll J L 2005 Greatly reduced leakage current and conduction mechanism in aliovalent-ion-doped $BiFeO_3$ *Appl. Phys. Lett.* **86** 062903

[15] Jang H W *et al* 2009 Domain engineering for enhanced ferroelectric properties of epitaxial (0 0 1) $BiFeO_3$ thin films *Adv. Mater.* **21** 817

[16] Lu H X, Zhao J L, Sun J R, Wang J and Shen B G 2011 Ferroelectric domain structure of the $BiFeO_3$ film grown on different substrates *Physics* B **406** 305

[17] Selbach S M, Tybell T, Einarsrud M A and Grande T 2007 Size-dependent properties of multiferroic $BiFeO_3$ nanoparticles *Chem. Mater.* **19** 6478

[18] Armstrong R W 1970 The influence of polycrystal grain size on several mechanical properties of materials *Metall. Mater. Trans.* B **1** 1169

[19] Williamson G K and Hall W H 1953 X-ray line broadening from filed aluminium and wolfram *Acta Metall. Mater.* **1** 22

[20] Alperson B, Cohen S, Rubinstein I and Hodes G 1995 Room-temperature conductance spectroscopy of CdSe quantum dots using a modified scanning force microscope *Phys. Rev.* B **52** R17017

[21] Alperson B, Rubinstein I and Hodes G 2001 Identification of surface states on individual CdSe quantum dots by room-temperature conductance spectroscopy *Phys. Rev.* B **63** 081303

[22] Kwon S, Lee S J, Kim S M, Lee Y, Song H and Park J Y 2015 Probing the nanoscale Schottky barrier of metal/semiconductor interfaces of Pt/CdSe/Pt nanodumbbells by conductive-probe atomic force microscopy *Nanoscale* **7** 12297

[23] Johann F, Morelli A, Biggemann D, Arredondo M and Vrejoiu I 2011 Epitaxial strain and electric boundary condition effects on the structural and ferroelectric properties of $BiFeO_3$ films *Phys. Rev.* B **84** 094105

[24] Castillo M E, Shvartsman V V, Gobeljic D, Gao Y, Landers J, Wende H and Lupascu D C 2013 Effect of particle size on ferroelectric and magnetic properties of $BiFeO_3$ nanopowders *Nanotechnology* **24** 355701

[25] Speck J S and Pompe W 1994 Domain configurations due to multiple misfit relaxation mechanisms in epitaxial ferroelectric thin films. I. Theory *J. Appl. Phys.* **76** 466

[26] Speck J S, Seifert A, Pompe W and Ramesh R 1994 Domain configurations due to multiple misfit relaxation mechanisms in epitaxial ferroelectric thin films. II. Experimental verification and implications *J. Appl. Phys.* **76** 477

[27] Kwak B S, Erbil A, Budai J D, Chisholm M F, Boatner L A and Wilkens B J 1994 Domain formation and strain relaxation in epitaxial ferroelectric heterostructures *Phys. Rev.* B **49** 14865

[28] Zhou M X, Chen B, Sun H B, Wan J G, Li Z W, Liu J M, Song F Q and Wang G H 2013 Local electrical conduction in polycrystalline La-doped $BiFeO_3$ thin films *Nanotechnology* **24** 225702

[29] Allibe J *et al* 2010 Optical properties of integrated multiferroic $BiFeO_3$ thin films for microwave applications *Appl. Phys. Lett.* **96** 182902

[30] Kumar A *et al* 2008 Linear and nonlinear optical properties of $BiFeO_3$ *Appl. Phys. Lett.* **92** 121915

[31] Chen X, Zhang H, Wang T, Wang F and Shi W 2012 Optical and photoluminescence properties of $BiFeO_3$ thin films grown on ITO-coated glass substrates by chemical solution deposition *Phys. Status Solidi* A **209** 1456

[32] Yan F, Lai M O, Lu L and Zhu T J 2011 Variation of leakage mechanism and potential barrier in La and Ru co-doped $BiFeO_3$ thin films *J. Phys. D: Appl. Phys.* **44** 435302

[33] Chen Z, He L, Zhang F, Jiang J, Meng J, Zhao B and Jiang A 2013 The conduction mechanism of large on/off ferroelectric diode currents in epitaxial (1 1 1) $BiFeO_3$ thin film *J. Appl. Phys.* **113** 184106

[34] Chiu F C 2014 A review on conduction mechanisms in dielectric films *Adv. Mater. Sci. Eng.* **2014** 578168

[35] Wu W, Horibe Y, Lee N, Cheong S W and Guest J R 2012 Conduction of topologically protected charged ferroelectric domain walls *Phys. Rev. Lett.* **108** 077203

[36] Cheng Z, Bin C, Xiao-Jian Z, Zheng-Hu Z, Yi-Wei L, Yuan-Fu C, Qing-Feng Z and Run-Wei L 2011 Local leakage current behaviours of $BiFeO_3$ films *Chin. Phys.* B **20** 117701

[37] Yang C H *et al* 2009 Electric modulation of conduction in multiferroic Ca-doped $BiFeO_3$ films *Nat. Mater.* **8** 485

[38] Yin K, Li M, Liu Y, He C, Zhuge F, Chen B, Lu W, Pan X and Li R W 2010 Resistance switching in polycrystalline $BiFeO_3$ thin films *Appl. Phys. Lett.* **97** 042101

[39] Wang C, Jin K J, Xu Z T, Wang L, Ge C, Lu H B, Guo H Z, He M and Yang G Z 2011 Switchable diode effect and ferroelectric resistive switching in epitaxial $BiFeO_3$ thin films *Appl. Phys. Lett.* **98** 192901

[40] Seidel J *et al* 2010 Domain wall conductivity in la-doped $BiFeO_3$ *Phys. Rev. Lett.* **105** 197603

[41] Seidel J *et al* 2009 Conduction at domain walls in oxide multiferroics *Nat. Mater.* **8** 229

[42] Maksymovych P, Seidel J, Chu Y H, Wu P, Baddorf A P, Chen L Q, Kalinin S V and Ramesh R 2011 Dynamic conductivity of ferroelectric domain walls in $BiFeO_3$ *Nano Lett.* **11** 1906

Journal of Alloys and Compounds 657 (2016) 866–872

Contents lists available at ScienceDirect

Journal of Alloys and Compounds

journal homepage: http://www.elsevier.com/locate/jalcom

Comparative study of structural and electrical properties of Pr and Ce doped $BiFeO_3$ ceramics synthesized by auto-combustion method

B. Stojadinović [a], Z. Dohčević-Mitrović [a, *], N. Paunović [a], N. Ilić [b], N. Tasić [b], I. Petronijević [c], D. Popović [c], B. Stojanović [a]

[a] Center for Solid State Physics and New Materials, Institute of Physics Belgrade, University of Belgrade, Pregrevica 118, 11080 Belgrade, Serbia
[b] Institute for Multidisciplinary Research, University of Belgrade, Kneza Višeslava 1, 11000 Belgrade, Serbia
[c] Faculty of Physics, University of Belgrade, Studentski trg 12-16, 11000 Belgrade, Serbia

ARTICLE INFO

Article history:
Received 11 June 2015
Received in revised form
21 September 2015
Accepted 27 September 2015
Available online 20 October 2015

Keywords:
$BiFeO_3$ ceramics
Pr(Ce) doping
Chemical synthesis
Structural characterization
Ferroelectricity
Dielectric properties

ABSTRACT

Polycrystalline $Bi_{1-x}Pr(Ce)_xFeO_3$ ceramics ($x = 0$, 0.03, 0.05 and 0.10) were prepared by auto-combustion method using urea as a fuel. The influence of Pr(Ce) doping on structural, vibrational, morphological, dielectric and ferroelectric properties of $BiFeO_3$ polycrystalline ceramics was investigated. From X-ray diffraction (XRD) and scanning electron microscopy measurements it was observed that Pr(Ce) doping generated a reduction of the crystallite (grain) size of $BiFeO_3$ and contraction of the rhombohedral cell due to the increased compressive strain. The changes seen in the XRD and Raman spectra of 10% Pr(Ce)-doped samples, pointed to a probable appearance of orthorhombic (pseudotetragonal) crystal structure. The pristine $BiFeO_3$ exhibited rounded shape, non-saturated ferroelectric hysteresis loop. The dielectric constant and dielectric loss have shown strong dispersion at lower frequencies, typical for conductive $BiFeO_3$. Dielectric and ferroelectric properties at room temperature were improved with Pr doping. Concerning the Ce-doped samples, only the 3% Ce-doped sample exhibited a better shaped hysteresis loop and improved dielectric properties compared to the pristine $BiFeO_3$. With further increase of Ce content the ferroelectric properties degraded.

1. Introduction

Materials which exhibit multiferroic behavior are very rare, and usually have low magnetic ordering temperature which constrains their application [1]. Among multiferroic materials, $BiFeO_3$ with a rhombohedrally distorted perovskite structure of space group R3c, belongs to a very few known magnetoelectric materials which exhibits both ferroelectricity and magnetic ordering at and above room temperature (ferroelectric Curie temperature $T_C \sim 1100$ K and Neel temperature $T_N \sim 640$ K) [2,3]. These features make $BiFeO_3$ particularly applicable in the fields of microelectronics, digital recording or magnetoelectric sensors [4,5]. $BiFeO_3$ can be potentially used in ferroelectric random access memory (FeRAM) applications [6] due to large spontaneous polarization [7–9], but of particular interest is to investigate the possible existence of magnetoelectric coupling in $BiFeO_3$ and its potential application in magnetic random access memories (MRAM) [10]. However, main disadvantages for the application of $BiFeO_3$ in devices is low resistivity (i.e. high leakage current) which causes large dielectric loss, poor ferroelectric loop at room temperature and small remnant polarization due to the presence of oxygen vacancies and secondary phases.

Doping of $BiFeO_3$ with rare earth ions at A-site [11–15], as well as doping with alkaline earth divalent ions such as Ca^{2+}, Ba^{2+} and Sr^{2+} [16] proved to be an effective way to improve its ferroelectric properties. In fact, A-site doping with ions of smaller radius influences the Fe–O–Fe bond angle, giving a more insulating character to $BiFeO_3$ [17]. The codoping with 4*f* elements at A-site and 3*d* elements at B-site is another effective way to reduce the leakage current in $BiFeO_3$ and to improve its multiferroic properties [18–21]. In the majority of previous reports referring the rare earth ions doping of $BiFeO_3$, only a few studies have been devoted to the investigation of ferroelectric properties of Pr(Ce)-doped $BiFeO_3$ ceramics [22–26] or thin films [27–29]. It can be expected that Bi substitution with $Pr^{3+/4+}$($Ce^{3+/4+}$) ions will prevent Bi volatilization and reduce the oxygen vacancy concentration, enhancing at the

---

* Corresponding author.
E-mail address: zordoh@ipb.ac.rs (Z. Dohčević-Mitrović).

http://dx.doi.org/10.1016/j.jallcom.2015.09.235

same time the insulating properties of $BiFeO_3$. Furthermore, Pr(Ce) doping can induce larger structural distortion and, even a structural transformation in $BiFeO_3$, which can have strong influence on ferroelectric properties of these materials [29,30].

In this paper, Pr(Ce)-doped $BiFeO_3$ ceramics were synthesized by auto-combustion method which represents a very facile, fast and low-cost method. A systematic study of the effect of Pr(Ce) doping on the structural, vibrational, ferroelectric, and dielectric properties of $BiFeO_3$ ceramics has been reported.

2. Experimental details

Pristine and Pr(Ce)-doped $BiFeO_3$ ($Bi_{1-x}Pr(Ce)_xFeO_3$, $x = 0.03$, 0.05 and 0.1) polycrystalline samples were synthesized by auto-combustion method using urea as a fuel. The fuel, besides providing the energy for the reaction, acts as a complexant and prevents the precipitation of metal ions in the form of hydroxides [31]. The $Bi_{1-x}Pr(Ce)_xFeO_3$ precursor solutions were prepared using $Bi(NO_3)_3 \cdot 6H_2O$ (Alfa Aesar, 98.0%), $Ce(NO_3)_3 \cdot 6H_2O$ (Acros Organics, 99.5%), $Pr(NO_3)_3 \cdot 6H_2O$ (Sigma–Aldrich, 99.9%), $Fe(NO_3)_3 \cdot 9H_2O$ (Alfa Aesar, 98.0–101.0%), HNO_3 (65%) and urea (Riedel-de Haen, 99.0–100.5%) as starting materials. The iron(III), cerium and praseodymium nitrates were dissolved in a minimal amount of distilled water, whereas bismuth nitrate was dissolved in a minimal amount of diluted nitric acid. The solutions were mixed and stirred for 15 min, after which the solution of urea was added. The molar ratio of urea to nitrates was 5:1. The obtained suspension was stirred and heated at 80–90 °C. During the heating a small amount of the precipitate, formed after urea addition, was dissolved and the clear solution was obtained. After a partial water evaporation, a yellow-white precipitate was formed and the solution was turned into gel. At the same time the self-ignition started. The reaction was fast and had finished in a few minutes. Large amount of gasses was released, without a flame. A black resin, remained after the auto-combustion reaction, was dried at 150–200 °C for one hour. The dried product was then grinded in a mortar and the obtained reddish powder was annealed at 600 °C for two hours with a heating rate of 10 °C/min. The powders were pressed into disks under the pressure of 300 MPa and sintered at 800 °C for 1 h in a closed dish, together with a small amount of Bi_2O_3 added in order to compensate the Bi loss during the heat treatment.

The structure and crystallinity of the $Bi_{1-x}Pr(Ce)_xFeO_3$ polycrystalline ceramics were investigated by X-ray diffraction (XRD) method, using Phillips PW1710 diffractometer with Cu Kα radiation. The surface morphology was studied by scanning electron microscopy (SEM, TESCAN SM-300). SEM micrographs were recorded on gold sputtered non-treated surfaces of ceramic samples.

Raman spectra were recorded in backscattering configuration using Tri Vista 557 Raman system equipped with a nitrogen-cooled CCD detector. The $\lambda = 514.5$ nm line of Ar^+/Kr^+ mixed laser was used as an excitation source with an incident laser power less than 60 mW in order to minimize the heating effects. The ferroelectric hysteresis loops were acquired at 1 kHz using a Radiant Precision Multiferroic Analyzer. The dielectric properties of the samples were examined in the frequency range from 80 Hz to 120 kHz using a Digital Programmable LCR Bridge HM8118 (Hameg). Each sample was placed in a closed capacitor cell housed in a Faraday cage with an AC signal of 1.5 V applied across the cell. The disk-shaped samples had a diameter close to the diameter of cell electrodes (8 mm). The same capacitor cell and Digital LCR Meter 4285A (HP/Agilent) were also used for the measurement of the dielectric properties at frequencies from 80 kHz to 8 MHz. All measurements were performed at room temperature.

3. Results and discussion

3.1. Structural and morphological properties

Fig. 1a shows XRD patterns of pristine $BiFeO_3$ and $Bi_{1-x}Pr_xFeO_3$ ceramics. All diffraction peaks of the pristine $BiFeO_3$ sample match with the rhombohedral structure (R3c) without the presence of a secondary phase. Polycrystalline $Bi_{1-x}Pr_xFeO_3$ samples crystallize in a slightly distorted R3c structure. The slight lattice distortion is manifested by a gradual shift of XRD peaks to higher 2θ values with Pr doping. The shift of XRD peaks to higher 2θ values can be ascribed to the unit cell contraction i.e. the decrease in lattice parameters due to the substitution of Bi^{3+} ions with smaller Pr dopant. The unit cell parameters of pristine $BiFeO_3$ and

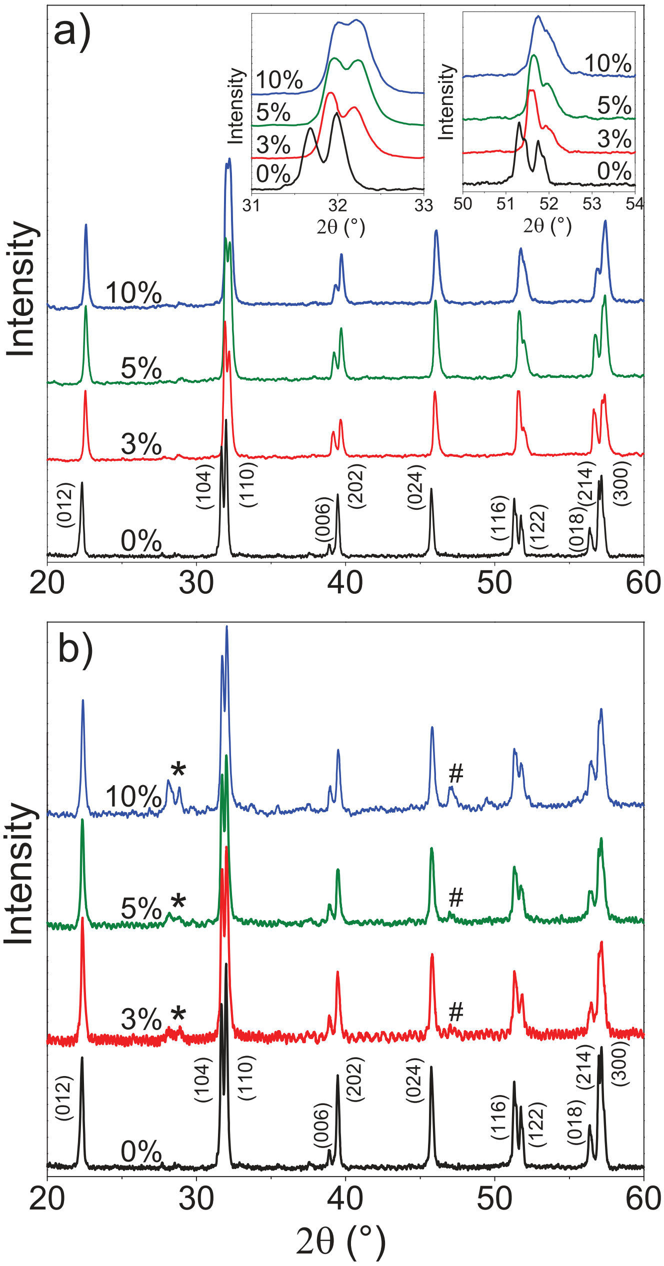

Fig. 1. X-ray diffraction patterns of the a) $Bi_{1-x}Pr_xFeO_3$ and b) $Bi_{1-x}Ce_xFeO_3$ samples ($0 \le x \le 0.1$). The (*) and (#) designate the appearance of additional phases discussed in the text.

$Bi_{1-x}Pr_xFeO_3$ samples are listed in Table 1. As can be seen from Table 1, with increasing Pr content, a reduction of both *a* and *c* lattice parameters, i.e. a contraction of the $BiFeO_3$ lattice, was observed.

The doublet peaks corresponding to the (104) and (110) planes around 2θ ~ 32°, and (116) and (122) planes around 2θ ~ 52°, with doping were shifted to higher 2θ values and almost merged into a single peak for the 10% Pr-doped sample. According to the literature data [32–34], these changes point to the beginning of partial phase transition from a rhombohedral (R3c) to an orthorhombic (Pbnm) structure. The enlarged 2θ regions where these peaks appear are presented in the insets of Fig. 1a. The partial structural transition can produce a distortion of the FeO_6 octahedron due to the changes in Fe–O bond length and O–Fe–O bond angles, affecting the electrical properties of $BiFeO_3$ [33,35]. Moreover, no additional peaks related to a secondary phase or other impurity phases have been observed in the sintered samples, implying a good solubility of Pr dopant in the $BiFeO_3$ lattice.

The XRD patterns of $Bi_{1-x}Ce_xFeO_3$ samples are presented in Fig. 1b and indexed to the rhombohedral $BiFeO_3$ structure. However, some weak diffraction peaks (marked with an asterisk) which correspond to a mullite ($Bi_2Fe_4O_9$) phase [36] appeared and became more pronounced with increased content of Ce dopant. As in the case of $Bi_{1-x}Pr_xFeO_3$ samples, lattice parameters (*a* and *c*) slightly decreased (see Table 1) implying that Ce substitution leads to the contraction of the unit cell and distortion of R3c structure. In addition, with increasing Ce content the peak at 2θ ~ 46° (marked with #) splits into two peaks. This is particularly noticeable for the 10% Ce-doped sample. According to Liu et al. [29], these peaks can be indexed as (200) and (002) peaks of pseudotetragonal structure. Such a behavior suggests that in 10% Ce-doped sample partial structural transformation from a rhombohedral to the pseudotetragonal phase started.

The crystallite size and strain in the $Bi_{1-x}Pr(Ce)_xFeO_3$ polycrystalline samples were calculated using the Williamson-Hall (W–H) plots [37] and are presented in Table 1. The example of W–H plots for pure and 3% Pr(Ce)-doped $BiFeO_3$ samples are given in Fig. S1. From Table 1, it can be seen that the average crystallite size was reduced with doping, whereas the strain values increased and reached the highest value for the 10% Pr(Ce)-doped samples. It can be concluded that Pr(Ce) doping induces increased compressive strain responsible for the $BiFeO_3$ lattice contraction. The similar contraction of the $BiFeO_3$ lattice due to the compressive strain (stress) has been seen in Sm-doped $BiFeO_3$ thin films [38]. Furthermore, the increased strain in $Bi_{1-x}Pr(Ce)_xFeO_3$ samples can produce a distortion of rhomohedral structure, which can induce gradual structural phase transformation as in a case of Y-doped $BiFeO_3$ nanopowders [39].

The surface morphology of $BiFeO_3$ and $Bi_{1-x}Pr(Ce)_xFeO_3$ ($x = 0.05, 0.1$) samples is shown in Fig. 2. The undoped (Fig. 2a) and Pr-doped $BiFeO_3$ samples (Fig. 2b and c) exhibit rather dense microstructure (82 and 78% of the theoretical density for undoped $BiFeO_3$ and 10% Pr-doped samples) with a clearly visible grains and grain boundary. The morphology of Ce-doped samples (Fig. 2d and e) is different from that of pure and Pr-doped samples. These samples exhibit less pronounced grain boundary microstructure with increased intergranular porosity and lower sample density (65% of the theoretical density for 10% Ce-doped sample). SEM images showed that in Pr(Ce)-doped samples the grain size decreased. The grain size decrease in Pr(Ce)-doped samples can be explained by inhibiting effect of increased Pr(Ce) dopant content on grain growth or can be attributed to the suppressed oxygen vacancy formation in these samples, as oxygen vacancies favorize the grain growth during the sintering process [33]. In addition, if there is a decrease of oxygen vacancy concentration, the reaction rate in the solid phase is slowed down, grains remain smaller and the

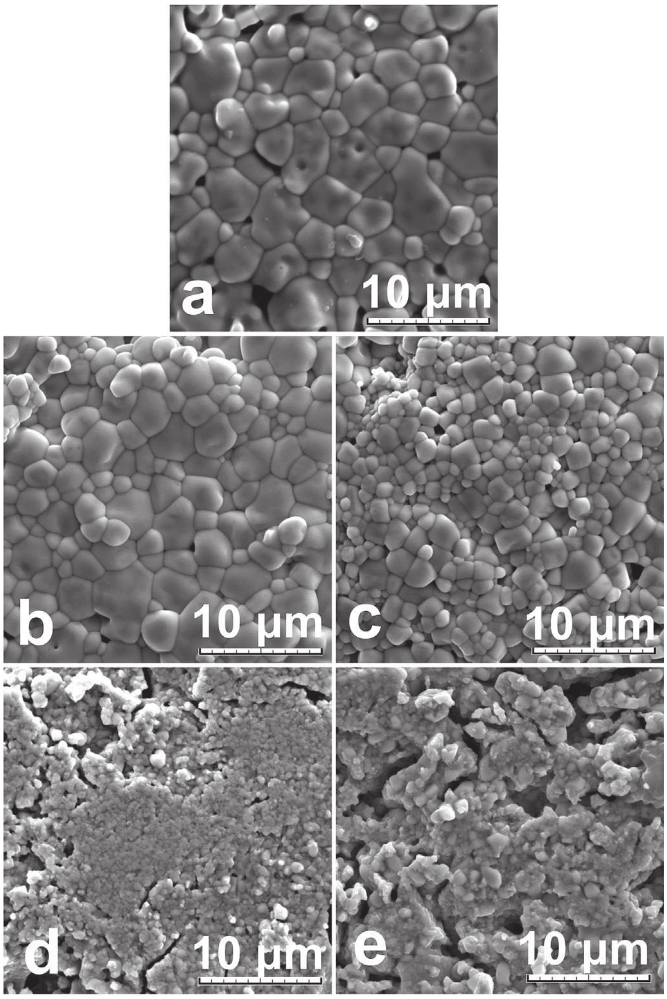

Fig. 2. SEM images of the surface morphology of a) $BiFeO_3$, b) $Bi_{0.95}Pr_{0.05}FeO_3$, c) $Bi_{0.90}Pr_{0.10}FeO_3$, d) $Bi_{0.95}Ce_{0.05}FeO_3$, and e) $Bi_{0.90}Ce_{0.10}FeO_3$ samples.

Table 1
The lattice parameters, average crystallite size and strain values for $Bi_{1-x}Pr(Ce)_xFeO_3$ samples.

Samples	Lattice parameter *a* (Å)	Lattice parameter *c* (Å)	Strain (%)	Crystalite size (nm)
$BiFeO_3$	5.617 ± 0.004	13.760 ± 0.010	0.10 ± 0.02	28.9 ± 2.2
$Bi_{0.97}Pr_{0.03}FeO_3$	5.587 ± 0.005	13.686 ± 0.012	0.16 ± 0.03	22.2 ± 1.6
$Bi_{0.95}Pr_{0.05}FeO_3$	5.582 ± 0.003	13.672 ± 0.007	0.18 ± 0.04	21.9 ± 1.9
$Bi_{0.90}Pr_{0.10}FeO_3$	5.576 ± 0.004	13.657 ± 0.009	0.36 ± 0.05	19.3 ± 1.9
$Bi_{0.97}Ce_{0.03}FeO_3$	5.597 ± 0.004	13.735 ± 0.013	0.20 ± 0.01	25.2 ± 0.9
$Bi_{0.95}Ce_{0.05}FeO_3$	5.598 ± 0.005	13.736 ± 0.010	0.24 ± 0.01	24.0 ± 1.6
$Bi_{0.90}Ce_{0.10}FeO_3$	5.595 ± 0.003	13.730 ± 0.011	0.32 ± 0.04	22.9 ± 2.6

densification is weaker.

3.2. Raman analysis

The structural evolution of $BiFeO_3$ structure with Pr(Ce) ion substitution can be reflected through the Raman spectra as well. For R3c rhombohedral structure, the group theory analysis predicts 13 Raman active modes (4 A_1 and 9 doubly degenerate E modes) [40–45], but the number of clearly seen Raman modes at room temperature is much less than predicted [43]. The room temperature Raman spectra of $BiFeO_3$ and $Bi_{1-x}Pr(Ce)_xFeO_3$ samples are presented in Fig. 3.

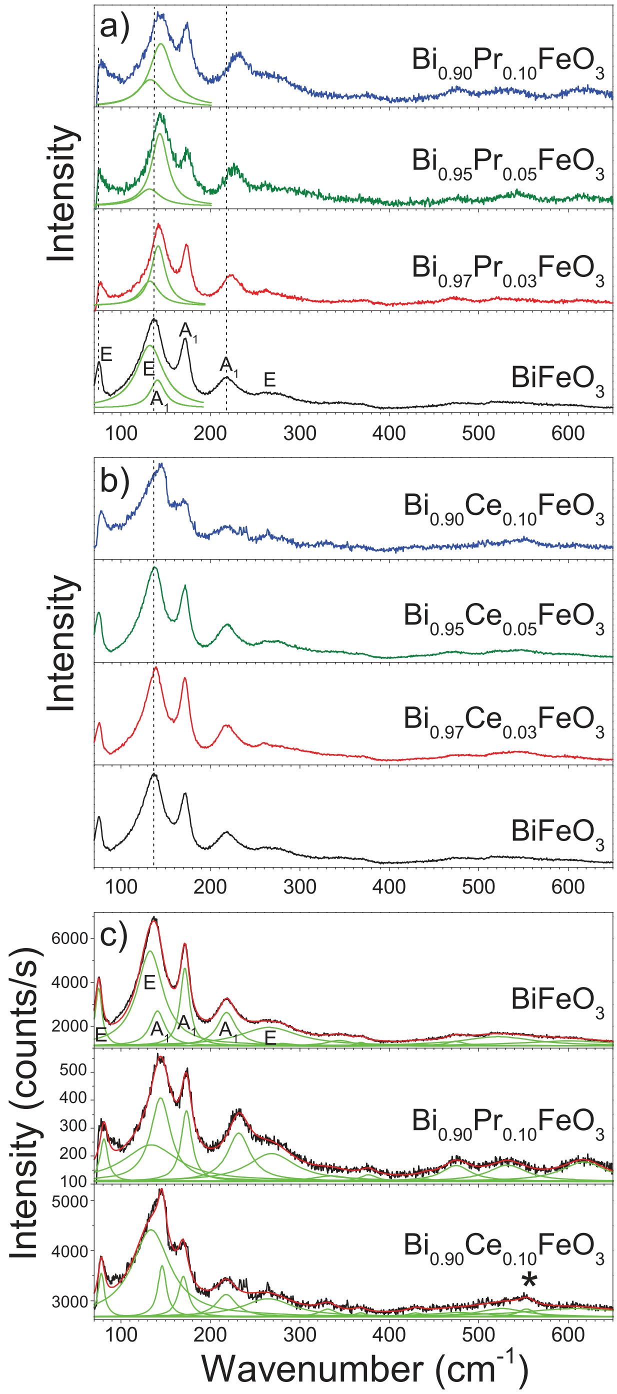

Fig. 3. Room-temperature Raman spectra of (a) $Bi_{1-x}Pr_xFeO_3$ and (b) $Bi_{1-x}Ce_xFeO_3$ samples ($0 \leq x \leq 0.1$), together with (c) deconvoluted Raman spectra of $BiFeO_3$, $Bi_{0.90}Pr_{0.10}FeO_3$ and $Bi_{0.90}Ce_{0.10}FeO_3$ samples.

In the Raman spectrum of $BiFeO_3$ sample (Fig. 3a), two A_1 modes at 171 and around 218 cm^{-1} [39] and two E modes at 75 and 265 cm^{-1} [43] can be clearly seen. The strong and wide Raman peak at 136 cm^{-1} is composed of two modes, E mode at 132 cm^{-1} and A_1 mode at around 140 cm^{-1}, which can be resolved by parallel polarization measurements at low temperatures [43]. The other E phonon modes at around 330, 368, 428, 475, 520 and 599 cm^{-1} are barely visible. In the Raman spectra of $Bi_{1-x}Pr_xFeO_3$ samples, the E mode at 75 cm^{-1} and A_1 mode at around 218 cm^{-1} exhibit shift to higher frequencies. The Raman peak at 136 cm^{-1} is also shifted to higher frequencies. After deconvolution of the 136 cm^{-1} peak using Lorentzian profiles, the position of the E mode remained unchanged, whereas the A_1 mode was shifted to higher frequencies (see dashed line in Fig. 3a). The other E modes (around 475, 520 and 599 cm^{-1}) become more prominent with increasing Pr content. In the Raman spectra of $Bi_{1-x}Ce_xFeO_3$ samples, more pronounced changes in the Raman modes position and intensity are observed in the case of 10% Ce-doped sample.

The exact positions of the Raman modes in the 10% Pr(Ce)-doped samples, for which the possible structural phase transformation was observed, were determined using the Lorentzian fit. In Fig. 3c are shown the deconvoluted Raman spectra of $BiFeO_3$, $Bi_{0.90}Pr_{0.10}FeO_3$ and $Bi_{0.90}Ce_{0.10}FeO_3$ samples. The obtained mode positions are summarized in Table 2.

As can be seen from Table 2, the E and A_1 modes (75, 140 cm^{-1}) which are related to Bi—O bonds, as well as the E modes (428, 520 and 599 cm^{-1}) which are characteristic for the Fe—O bonds [44,46], are shifted to higher frequencies for both $Bi_{0.90}Pr_{0.10}FeO_3$ and $Bi_{0.90}Ce_{0.10}FeO_3$ samples. The A_1 mode at around 218 cm^{-1}, which is characteristic for Bi—O bonds is shifted to higher frequencies in $Bi_{0.90}Pr_{0.10}FeO_3$ sample. The blueshift of the E and A_1 modes, for which the contribution of Bi—O bonds dominates, is expected when the substitution with smaller atomic mass Pr(Ce) ions at Bi-site happens, because the Raman mode frequency is dependent on the atomic mass (M) of the substituent according to the relation $\omega \sim (k/M)^{1/2}$ [22,26]. The appearance of the increased compressive strain in $BiFeO_3$ lattice with increased amount of Pr(Ce) dopant is also responsible for the blueshift of the frequency of the Raman A_1 and E modes, characteristic for both Bi—O and Fe—O bonds.

The E mode at 599 cm^{-1}, which is of low intensity in the pristine $BiFeO_3$ and almost invisible in $Bi_{0.90}Ce_{0.10}FeO_3$, becomes very prominent in $Bi_{0.90}Pr_{0.10}FeO_3$ sample. Compared to the pristine $BiFeO_3$, the relative intensity ratio of A_1 modes at about 140 and 171 cm^{-1} (I_{140}/I_{171}) is increased in 10% Pr(Ce)-doped samples ($I_{140}/I_{171} = 0.69$, 1.1, and 2.1 for $BiFeO_3$, 10% Ce and 10% Pr-doped samples, respectively). The change of the relative intensity of these two A_1

Table 2
Positions of the Raman modes for $BiFeO_3$, $Bi_{0.90}Pr_{0.10}FeO_3$, and $Bi_{0.90}Ce_{0.10}FeO_3$ samples.

Raman modes (in cm^{-1})	$BiFeO_3$	$Bi_{0.90}Pr_{0.10}FeO_3$	$Bi_{0.90}Ce_{0.10}FeO_3$
E	75.4	81.2	77.4
E	132.3	132.9	132.7
A_1	140.8	144.5	145.0
A_1	171.2	172.7	169.6
A_1	218.7	231.6	217.5
E	265.2	269.0	265.1
E	330.6	333.3	331.3
E	368.6	376.0	367.1
E	428.4	440.6	429.2
E	475.8	475.0	476.8
E	520.4	532.8	526.9
E	599.2	617.7	611.7

modes reflects the change in Bi–O bonds and the stereochemical activity of Bi lone electron pair with Pr(Ce) doping [23]. Furthermore, any changes in the position or intensity of the 140, 171 and 599 cm^{-1} modes are related to the changes in the ferroelectric properties of BiFeO$_3$ as well [22,45]. In the Raman spectrum of Bi$_{0.90}$Ce$_{0.10}$FeO$_3$ appears an additional mode (marked with an asterisk in Fig. 3c) at around 553 cm^{-1}. This mode can be ascribed to the mode of Bi$_2$Fe$_4$O$_9$ phase [47]. The appearance of this mode is in accordance with the XRD pattern of Bi$_{0.90}$Ce$_{0.10}$FeO$_3$ in which the presence of a mullite phase has been seen. The changes observed in the Raman spectra of doped samples gave a clear evidence about the lattice distortion induced by Pr(Ce) doping.

3.3. Dielectric properties

The frequency dependence of the dielectric constant (ε′) and loss tangent (tan δ) of Bi$_{1-x}$Pr(Ce)$_x$FeO$_3$ samples are shown in Fig. 4. It can be observed from Fig. 4a that the dielectric constant of the pristine BiFeO$_3$ at low frequencies has the highest value ($\varepsilon' = 159$) and shows a strong dispersion in the low-frequency region. Such a behavior is characteristic for the presence of oxygen or bismuth vacancies, which are responsible for the appearance of charge carriers at grain boundaries or interfaces (i.e. the local space charge), and an increased conductivity in BiFeO$_3$ [48]. The contribution of the local space charge to the dielectric constant usually manifests as a strong dispersion at low frequencies. The presence of oxygen vacancies also increases the probability of a hopping conduction mechanism between Fe^{2+} and Fe^{3+} ions, which can be reflected through an increased value of the dielectric constant [48].

The dielectric constant of Pr(Ce)-doped samples significantly decreases and exhibits much smaller dispersion at low frequencies (Fig. 4a). The overall decrease of the dielectric constant can be attributed to a reduced conductivity and a decreased space charge relaxation at the interface [49], but can also originate from the contraction of the unit cell volume when Bi ions are substituted with smaller Pr(Ce) ions. The unit cell contraction can result in a decreased polarization because of less free volume for the displacement of Fe^{3+} ions in FeO$_6$ octahedra. The dielectric constant of Bi$_{1-x}$Pr$_x$FeO$_3$ samples exhibits relatively small ($x = 0.03, 0.05$) or almost no dielectric dispersion ($x = 0.1$). Such a behavior can be explained by the fact that the incorporation of Pr$^{3+/4+}$ ions into the BiFeO$_3$ lattice reduces the oxygen vacancy concentration and conductivity of BiFeO$_3$ [49, 29]. Ce-doped samples ($x = 0.03, 0.05$) have lower value of dielectric constant than Pr-doped ones and show almost no frequency dispersion. The value of dielectric constant and its dispersion increases for the Bi$_{0.90}$Ce$_{0.10}$FeO$_3$ sample. The increase of dielectric constant can originate from the increased oxygen vacancy concentration and the appearance of local space charges at the grain boundaries or interfaces [48,49]. The change of the dielectric constant with frequency in BiFeO$_3$ and Bi$_{1-x}$Pr(Ce)$_x$FeO$_3$ samples can be well explained by the Maxwell–Wagner relaxation effect which refers to the interfacial polarization [48,49].

The loss tangent (tan δ) shows a similar variation with frequency as the dielectric constant. At low frequencies, the loss tangent of the undoped BiFeO$_3$ sample shows a higher value, due to the increased defect concentration and conductivity and shows a broad relaxation peak in the intermediate frequency range (10 kHz–1 MHz). The broad relaxation peaks are usually caused by inhomogenous grain conductivity [49]. The tan δ curves show dispersive characteristics in the low-frequency region for Pr-doped samples, with much less pronounced relaxation peaks. At frequencies higher than 10 kHz, the value of tan δ is reduced and is significantly lower than in the pristine BiFeO$_3$, due to reduced oxygen vacancy concentration and conductivity. The Ce-doped samples with lower content of Ce ($x = 0.03, 0.05$) have low value of tan δ over the whole frequency range. The tan δ becomes much higher in the case of Bi$_{0.90}$Ce$_{0.10}$FeO$_3$ sample, pointing to increased conductivity of Bi$_{0.90}$Ce$_{0.10}$FeO$_3$ sample.

3.4. Ferroelectric properties

The ferroelectric hysteresis (P–E) loops for Bi$_{1-x}$Pr(Ce)$_x$FeO$_3$ samples are presented in Fig. 5. In the inset of Fig. 5b is given P–E loop of the pristine BiFeO$_3$.

The BiFeO$_3$ exhibited a rounded shape i.e. a non-saturated (lossy) P–E loop, and was not able to withstand applied electric field stronger than 2 kV, which is typical for a conductive BiFeO$_3$ material. The ferroelectric performances of pristine BiFeO$_3$ are consistent with the dielectric measurements. The ferroelectric loops of the Pr(Ce)-doped samples (Fig. 5a and b), exhibited less pronounced leakage effect than for the pristine BiFeO$_3$, but were still non-saturated. This is an expected behavior, since the incorporation of Pr$^{3+/4+}$(Ce$^{3+/4+}$) ions in the BiFeO$_3$ lattice should suppress the formation of bismuth and oxygen vacancies. With increasing Pr content, the maximal polarization (P$_M$) and the remnant polarization (P$_R$) have increased and reached the values of 0.4 and 0.35 μC/cm^2 for Bi$_{0.90}$Pr$_{0.10}$FeO$_3$. The P$_M$ and P$_R$ values are comparable with the previously reported data on BiFeO$_3$ ceramics

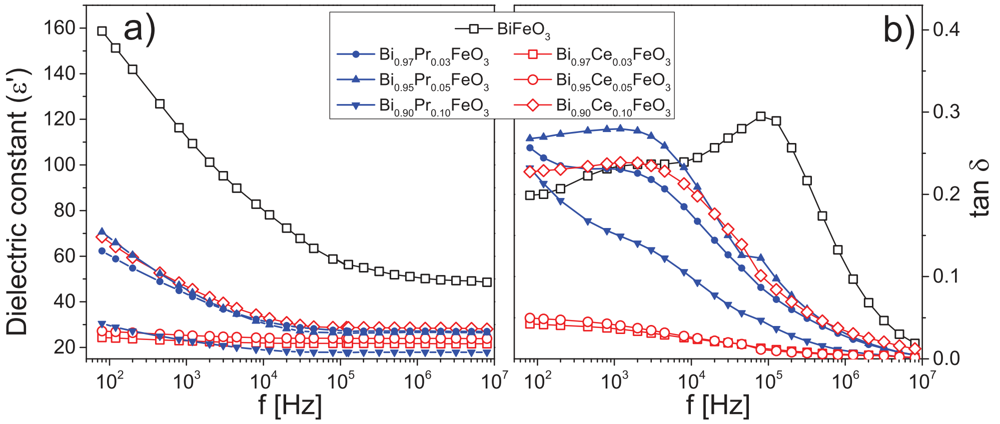

Fig. 4. Room temperature (a) dielectric constant (ε′) and (b) loss tangent (tan δ) of Bi$_{1-x}$Pr(Ce)$_x$FeO$_3$ samples ($0 \leq x \leq 0.1$) as a function of frequency.

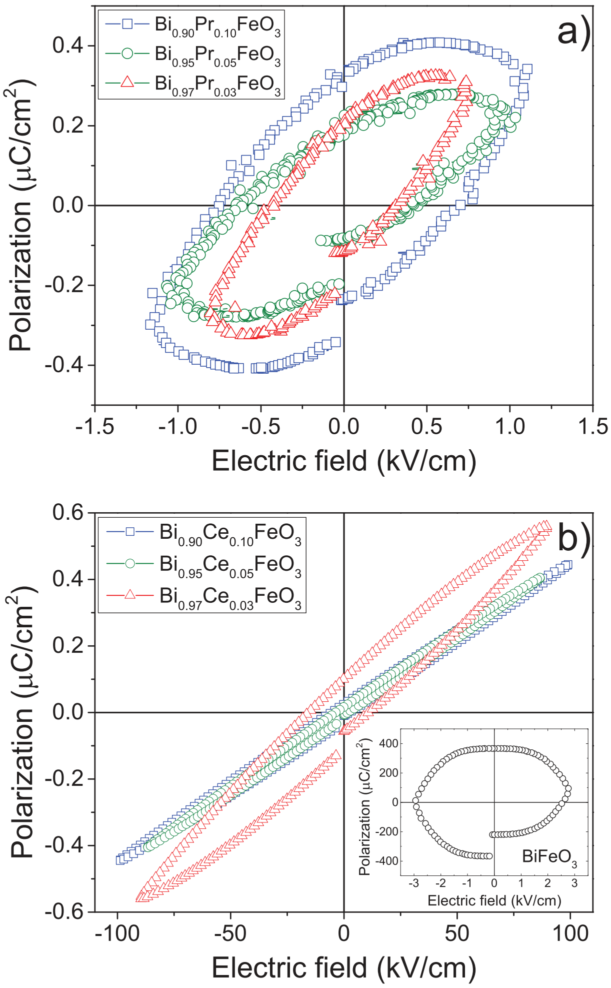

Fig. 5. Room-temperature P–E hysteresis loops for (a) $Bi_{1-x}Pr_xFeO_3$ and (b) $Bi_{1-x}Ce_xFeO_3$ samples ($0.03 \leq x \leq 0.1$). In the inset is presented P–E hysteresis loop for the pristine $BiFeO_3$.

doped with similar content of Pr [24,49]. However, the breakdown electric field for Pr-doped samples is still as low as in the case of the pristine $BiFeO_3$.

Initial Ce doping increases the ability of $BiFeO_3$ to withstand higher electric fields [50], in our case up to 100 kV/cm. This enhancement can be attributed to a decrease of oxygen vacancy concentration, as the substitution of Bi ions with higher valence Ce^{4+} ions would suppress the formation of oxygen vacancies and consequently reduce the leakage current. The polarization has the highest value of about 0.56 $\mu C/cm^2$ in the 3% Ce-doped sample, and the P_R value is about 0.1 $\mu C/cm^2$. With further increase of Ce content, the values of P_M, P_R and coercive field decreased and the samples exhibited a poor P–E loop. This result suggests that the ferroelectric properties were degraded with further increase of Ce content.

Several reasons can be responsible for the lower values of P_R in Pr(Ce)-doped samples. The contraction of $BiFeO_3$ unit cell with Pr(Ce) doping, i.e. the partial phase transition from rhombohedral to orthorhombic (pseudotetragonal) phase can reduce the remnant polarization, as the direction of the spontaneous polarization can be changed [51,29]. Another reason can be found in lowering of the crystal anisotropy and a decrease of Curie temperature with rare earth ion doping [52,53].

Therefore, we can conclude that Pr(Ce) doping causes a distortion of R3c structure and in 10% Pr(Ce) doped samples, there is an indication that partial structural phase transformation from rhombohedral to orthorhombic (pseudotetragonal) phase started. Pr doping suppresses the formation of oxygen vacancies, decreasing the conductivity of Pr-doped $BiFeO_3$ samples. In the case of Ce-doped samples, improved dielectric and ferroelectric properties exhibited the sample with 3% of Ce. Further increase of Ce content caused the deterioration of ferroelectric properties and in the 10% Ce-doped sample both the dielectric and ferroelectric properties of $BiFeO_3$ ceramics were degraded. The reduction of ferroelectric polarization for $Bi_{0.95}Ce_{0.05}FeO_3$ sample can originate from the presence of impurity $Bi_2Fe_4O_9$ phase which increases the conductivity of $BiFeO_3$. Further, deterioration of dielectric and ferroelectric properties for $Bi_{0.90}Ce_{0.10}FeO_3$ can originate from lower percentage of Ce^{4+} ions in this sample (see Fig. S2 Supplementary material) and increasing content of $Bi_2Fe_4O_9$ phase. On the other hand, the increased Ce content can decrease the stereochemical activity of Bi ions and can lead to the partial transition from ferroelectric to paraelectric phase, like in La-doped $BiFeO_3$ [54].

4. Conclusion

In summary, polycrystalline $Bi_{1-x}Pr(Ce)_xFeO_3$ ceramics ($x = 0$, 0.03, 0.05 and 0.10) were prepared by auto-combustion method. SEM and XRD analysis have shown that the crystallite and grain sizes slightly decreased in Pr(Ce)-doped samples, whereas the compressive strain increased. XRD and Raman spectra of 10% Pr(Ce)-doped samples pointed to probable appearance of orthorhombic (pseudotetragonal) phase. The presence of secondary phase was evident only in Ce-doped samples. The pristine $BiFeO_3$ showed lossy P–E loop, large dispersion of dielectric constant and tan δ at low frequencies, and a broad relaxation peak in tan δ in the intermediate frequency range. The dielectric properties were improved by the Pr substitution, i.e. the dielectric constant had lower values than in the pristine $BiFeO_3$ and exhibited smaller or almost no dispersion in the investigated frequency range, whereas with increasing Pr content the loss tangent decreased and had low values at higher frequencies. Pr-doped samples exhibited better shaped ferroelectric loops with much less pronounced leakage effect. The remnant and maximal polarization increased with increased Pr doping. Such an improvement in dielectric and ferroelectric properties can be attributed to decreased interfacial polarization and reduced conductivity of $BiFeO_3$ ceramic samples. Regarding the Ce-doped samples, the best dielectric and ferroelectric properties were observed in the 3% Ce-doped sample, whereas with further increase of Ce dopant up to 10% these properties were degraded. The reduced polarization and increased dielectric loss may be attributed to the appearance of conducting $Bi_2Fe_4O_9$ phase and decreased stereochemical activity of Bi-sites by Ce doping due to the possible appearance of the pseudotetragonal phase.

Acknowledgment

This work was financially supported by the Ministry of Education, Science and Technological Development of the Republic of Serbia under the projects ON171032 and III45018. Special thanks to Prof. Piter Hammer, Instituto de Quimica, Universidade Sao Paolo, Araraquara, Brazil for the XPS data.

Appendix A. Supplementary data

Supplementary data related to this article can be found at http://dx.doi.org/10.1016/j.jallcom.2015.09.235.

References

[1] N.A. Spaldin, Science 309 (2005) 391.
[2] I. Sosnowska, T. Peterlin-Neumaier, E. Steichele, J. Phys. C: Solid State Phys. 15 (1982) 4835–4846.
[3] G. Catalan, J.F. Scott, Adv. Mater. 21 (2009) 2463–2485.
[4] R. Ramesh, N.A. Spaldin, Nat. Mater. 6 (2007) 21–29.
[5] S.-W. Cheong, M. Mostovoy, Nat. Mater. 6 (2007) 13–20.
[6] A.N. Kalinkin, E.M. Kozhbakhteev, A.E. Polyakov, V.M. Skorikov, Inorg. Mater. 49 (2013) 1031–1043.
[7] C. Ederer, N.A. Spaldin, Phys. Rev. Lett. 95 (2005) 257601.
[8] J. Li, J. Wang, M. Wuttig, R. Ramesh, N. Wang, B. Ruette, A.P. Pyatakov, A.K. Zvezdin, D. Viehland, Appl. Phys. Lett. 84 (2004) 5261–5263.
[9] K.Y. Yun, D. Ricinschi, T. Kanashima, M. Noda, M. Okuyama, Jpn. J. Appl. Phys. 43 (2004) L647–L648.
[10] J.F. Scott, Nat. Mater. 6 (2007) 256–257.
[11] S.B. Emery, C.J. Cheng, D. Kan, F.J. Rueckert, S.P. Alpay, V. Nagarajan, I. Takeuchi, B.O. Wells, Appl. Phys. Lett. 97 (2010) 152902.
[12] K.S. Nalwa, A. Garg, A. Upadhyaya, Mater. Lett. 62 (2008) 878–881.
[13] G.L. Yuan, S.W. Or, J.M. Liu, Z.G. Liu, Appl. Phys. Lett. 89 (2006) 052905.
[14] J.H. Lee, H.J. Choi, D. Lee, M.G. Kim, C.W. Bark, S. Ryu, M.A. Oak, H.M. Jang, Phys. Rev. B 82 (2010) 045113.
[15] G.S. Lotey, N.K. Verma, J. Nanopart. Res. 14 (2012) 742.
[16] V.A. Khomchenko, D.A. Kiselev, J.M. Vieira, L. Jian, A.L. Kholkin, A.M.L. Lopes, Y.G. Pogorelov, J.P. Araujo, M. Maglione, J. Appl. Phys. 103 (2008) 024105.
[17] C.H. Yang, D. Kan, I. Takeuchi, V. Nagarajan, J. Seidel, Phys. Chem. Chem. Phys. 14 (2012) 15953–15962.
[18] W. Liu, G. Tan, X. Xue, G. Dong, H. Ren, A. Xia, Ceram. Int. 40 (2014) 12179–12185.
[19] W. Ye, G. Tan, G. Dong, H. Ren, A. Xia, Ceram. Int. 41 (2015) 4668–4674.
[20] Y.J. Kim, J.W. Kim, C.M. Raghavan, J.J. Oak, H.J. Kim, W.J. Kim, M.H. Kim, T.K. Song, S.S. Kim, Ceram. Int. 39 (2013) S195–S199.
[21] C.M. Raghavan, J.W. Kim, S.S. Kim, Ceram. Int. 39 (2013) 3563–3568.
[22] D. Varshney, P. Sharma, S. Satapathy, P.K. Gupta, J. Alloys Compd. 584 (2014) 232–239.
[23] P. Sharma, D. Varshney, S. Satapathy, P.K. Gupta, Mater. Chem. Phys. 143 (2014) 629–636.
[24] N. Kumar, N. Panwar, B. Gahtori, N. Singh, H. Kishan, V.P.S. Awana, J. Alloy. Compd. 501 (2010) L29–L32.
[25] S.K. Pradhan, B.K. Roul, Phys. B 407 (2012) 2527–2532.
[26] M. Arora, M. Kumar, Ceram. Int. 41 (2015) 5705–5712.
[27] B. Yu, M. Li, Z. Hu, L. Pei, D. Guo, X. Zhao, S. Dong, Appl. Phys. Lett. 93 (2008) 182909.
[28] X. Wang, H. Liu, B. Yan, J. Eur. Ceram. Soc. 29 (2009) 1183–1187.
[29] J. Liu, M. Li, L. Pei, J. Wang, B. Yu, X. Wang, X. Zhao, J. Alloy. Compd. 493 (2010) 544–548.
[30] J. Liu, M. Li, L. Pei, B. Yu, D. Guo, X. Zhao, J. Phys. D. Appl. Phys. 42 (2009) 115409.
[31] S. Lorentzou, K. Karadimitra, C. Agrafiotis, A.G. Konstandopoulos, in: Proceedings of the PARTEC 2004, International Conference for Particle Technology, Nuremberg, Germany, March 16–18, 2004.
[32] L. Chen, L. Zheng, Y. He, J. Zhang, Z. Mao, X. Chen, J. Alloys Compd. 633 (2015) 216–219.
[33] P.C. Sati, M. Arora, S. Chauhan, M. Kumar, S. Chhoker, Ceram. Int. 40 (2014) 7805–7816.
[34] V. Singh, S. Sharma, M. Kumar, R.K. Kotnala, R.K. Dwivedi, J. Magn. Magn. Mater. 349 (2014) 264–267.
[35] S.K. Pradhan, B.K. Roul, J. Phys. Chem. Solids 72 (2011) 1180–1187.
[36] N.I. Ilić, A.S. Džunuzović, J.D. Bobić, B.S. Stojadinović, P. Hammer, M.M. Vijatović Petrović, Z.D. Dohčević-Mitrović, B.D. Stojanović, Ceram. Int. 41 (2015) 69–77.
[37] G.K. Williamson, W. Hall, Acta Metall. 1 (1953) 22–31.
[38] X. Xu, T. Guoqiangn, R. Huijun, X. Ao, Ceram. Int. 39 (2013) 6223–6228.
[39] R.K. Mishra, D.K. Pradhan, R.N.P. Choudhary, A. Banerjee, J. Phys. Condens. Matter 20 (2008) 045218.
[40] M.N. Iliev, M.V. Abrashev, D. Mazumdar, V. Shelke, A. Gupta, Phys. Rev. B 82 (2010) 014107.
[41] M.K. Singh, H.M. Jang, S. Ryu, M.H. Jo, Appl. Phys. Lett. 88 (2006) 42907.
[42] P. Hermet, M. Goffinet, J. Kreisel, Ph. Ghosez, Phys. Rev. B 75 (2007) 220102(R).
[43] H. Fukumura, S. Matsui, H. Harima, T. Takahashi, T. Itoh, K. Kisoda, M. Tamada, Y. Noguchi, M. Miyayama, J. Phys. Condens. Matter 19 (2007) 365224.
[44] M.K. Singh, S. Ryu, H.M. Jang, Phys. Rev. B 72 (2005) 132101.
[45] G.L. Yuan, S.W. Or, H.L. Chan, Z.G. Liu, J. Appl. Phys. 101 (2007) 024106.
[46] Y. Yao, W. Liu, Yu Chan, C. Leung, C. Mak, B. Ploss, Int. J. Appl. Ceram. Technol. 8 (2011) 1246–1253.
[47] M.N. Iliev, A.P. Litvinchuk, V.G. Hadjiev, M.M. Gospodinov, V. Skumryev, E. Ressouche, Phys. Rev. B 81 (2010) 024302.
[48] A. Reetu, S. Agarwal, Ashima Sanghi, J. Appl. Phys. 110 (2011) 073909.
[49] V. Kumar, A. Gaur, N. Sharma, J. Shah, R.K. Kotnala, Ceram. Int. 39 (2013) 8113–8121.
[50] Z. Quan, W. Liu, H. Hu, S. Xu, B. Sebo, G. Fang, M. Li, X. Zhao, J. Appl. Phys. 104 (2008) 084106.
[51] X. Li, X. Wang, Y. Li, W. Mao, P. Li, T. Yang, J. Yang, Mater. Lett. 90 (2013) 152–155.
[52] H. Ushida, R. Ueno, H. Funakubo, S. Koda, J. Appl. Phys. 100 (2006) 014106.
[53] P. Pandit, S. Satapathy, P. Sharma, P.K. Gupta, S.M. Yusuf, V.G. Sathe, Bull. Mater. Sci. 34 (2011) 899–905.
[54] G.L. Yuan, S.W. Or, H.L. Chan, J. Phys. D. Appl. Phys. 40 (2007) 1196–1200.

Ceramics International 43 (2017) 16531–16538

Contents lists available at ScienceDirect

Ceramics International

journal homepage: www.elsevier.com/locate/ceramint

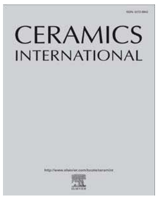

Dielectric and ferroelectric properties of Ho-doped $BiFeO_3$ nanopowders across the structural phase transition

Bojan Stojadinović[a], Zorana Dohčević-Mitrović[a,*], Dimitrije Stepanenko[a], Milena Rosić[b], Ivan Petronijević[c], Nikola Tasić[d], Nikola Ilić[d], Branko Matović[b], Biljana Stojanović[d]

[a] Center for Solid State Physics and New Materials, Institute of Physics Belgrade, University of Belgrade, Pregrevica 118, 11080 Belgrade, Serbia
[b] Institute for Nuclear sciences, Centre of Excellence-CextremeLab "Vinča", University of Belgrade, 11000 Belgrade, Serbia
[c] Faculty of Physics, University of Belgrade, Studentski trg 12-16, 11000 Belgrade, Serbia
[d] Institute for Multidisciplinary Research, University of Belgrade, Kneza Višeslava 1, 11000 Belgrade, Serbia

ARTICLE INFO

Keywords:
Sol-gel processes
X-ray methods
Dielectric properties
Ferroelectric properties
Perovskites

ABSTRACT

We have studied Ho-doped $BiFeO_3$ nanopowders ($Bi_{1-x}Ho_xFeO_3$, x = 0–0.15), prepared via sol-gel method, in order to analyse the effect of substitution-driven structural transition on dielectric and ferroelectric properties of bismuth ferrite. X-ray diffraction and Raman study demonstrated that an increased Ho concentration ($x \geq 0.1$) has induced gradual phase transition from rhombohedral to orthorhombic phase. The frequency dependent permittivity of $Bi_{1-x}Ho_xFeO_3$ nanopowders was analysed within a model which incorporates Debye-like dielectric response and dc and ac conductivity contributions based on universal dielectric response. It was shown that influence of leakage current and grain boundary/interface effects on dielectric and ferroelectric properties was substantially reduced in biphasic $Bi_{1-x}Ho_xFeO_3$ ($x > 0.1$) samples. The electrical performance of $Bi_{0.85}Ho_{0.15}FeO_3$ sample, for which orthorhombic phase prevailed, was significantly improved and $Bi_{0.85}Ho_{0.15}FeO_3$ has sustained strong applied electric fields (up to 100 kV/cm) without breakdown. Under strong external fields, the polarization exhibited strong frequency dependence. The low-frequency remnant polarization and coercive field of $Bi_{0.85}Ho_{0.15}FeO_3$ were significantly enhanced. It was proposed that defect dipolar polarization substantially contributed to the intrinsic polarization of $Bi_{0.85}Ho_{0.15}FeO_3$ under strong electric fields at low frequencies.

1. Introduction

Multiferroics, materials which simultaneously exhibit at least two ferroic properties among electric, magnetic, and elastic responses, are quite rare. They are of great interest for both fundamental physics and potential applications. Among multiferroic materials, bismuth ferrite ($BiFeO_3$) possesses unique property, i.e. exhibits multiferroic behavior at room temperature. Having high ferroelectric ($T_C \sim 1100$ K) and antiferromagnetic ($T_N \sim 640$ K) transition temperatures, $BiFeO_3$ is a promising material for the applications in spintronic devices, electrically controlled magnetic memories and functional sensors [1,2]. Nevertheless, problems of low resistivity and sinterability and appearance of secondary phases present a serious obstacle for the application of $BiFeO_3$ (BFO) in devices. BFO suffers from high leakage current which causes large dielectric loss and degradation of the ferroelectric properties. The main cause of leakage is disorder, usually in the form of charge defects, like oxygen or bismuth vacancies and secondary phases. Attempts at minimizing the leakage current density through doping with rare earth ions at Bi sites, have led to improvement of electric and magnetic properties of BFO [3–6]. These studies have demonstrated that substitution of Bi sites with rare-earth ions effectively controls the volatility of Bi^{3+} ions and the amount of defects, while suppressing the secondary phase appearance.

Despite a significant body of work dealing with rare-earth doped BFO [3,4,7–10], BFO doped with Ho is less investigated. There are several studies dealing with the influence of Ho doping on leakage current, and on magnetic or ferroelectric properties of BFO, for which BFO is either phase stabilized [11–16] or exhibits biphasic character with increased Ho doping [17–20]. Among these studies, only Song and coauthors [20] showed that dielectric constant was significantly increased with small amount of Ho substitution (x = 0.05, 0.10) for which BFO retained rhombohedral structure and then decreased when the orthorhombic phase appeared with higher doping (x = 0.15, 0.20). They also deduced that the dielectric loss of doped samples behaves in a complicated manner, probably influenced by the conductivity of material. Song and coauthors did not analyse the reasons of obtaining

---

[*] Corresponding author.
E-mail address: zordoh@ipb.ac.rs (Z. Dohčević-Mitrović).

http://dx.doi.org/10.1016/j.ceramint.2017.09.038
Received 3 July 2017; Received in revised form 22 August 2017; Accepted 5 September 2017

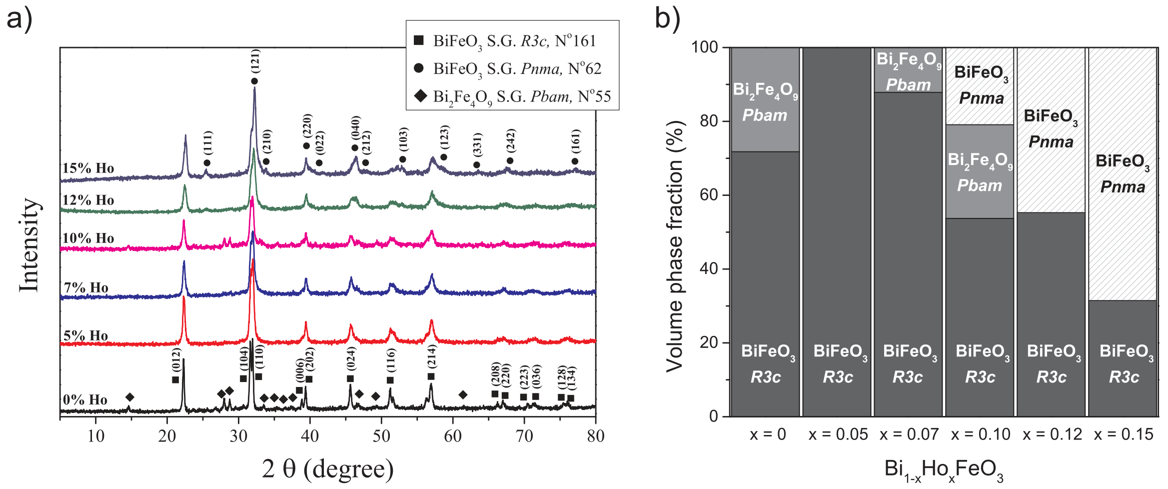

Fig. 1. a) X-ray diffraction patterns and b) volume phase fraction analysis of the $\mathrm{Bi}_{1-x}\mathrm{Ho}_x\mathrm{FeO}_3$ ($0 \le x \le 0.15$) samples.

colossal dielectric constant, nor assumed that quite often these phenomena can be explained by Maxwell-Wagner-type contributions of depletion layers at the interface between sample and contacts or at grain boundaries. Furthermore, it is quite reasonable to assume that various polarization mechanisms can appear in biphasic BFO and influence the dielectric and ferroelectric properties of BFO. To the best of our knowledge, influence of structural phase transformation caused by Ho doping on polarization mechanisms, which can exert a strong influence on the dielectric and ferroelectric properties of BFO, has not been studied.

Herein, we investigated how the structural phase transformation induced by Ho doping influenced the dielectric and ferroelectric properties of $\mathrm{Bi}_{1-x}\mathrm{Ho}_x\mathrm{FeO}_3$ nanopowders. Detailed analysis of the frequency dependent permittivity, using combined model which incorporated Debay-like dielectric relaxation, as well as dc and ac conductivity contributions, was performed. This analysis enabled us to estimate the influence of leakage current and grain boundary/interface effects on the dielectric and ferroelectric properties of single phase and biphasic $\mathrm{Bi}_{1-x}\mathrm{Ho}_x\mathrm{FeO}_3$ nanopowders. Origin of improved electric performances of biphasic $\mathrm{Bi}_{1-x}\mathrm{Ho}_x\mathrm{FeO}_3$ nanostructures, for which orthorhombic phase prevailed, was discussed in detail. These results may provide new insight into modified electrical properties of BiFeO_3 by Ho doping, which can be important for potential applications.

2. Experimental procedure

2.1. Materials synthesis

$\mathrm{Bi}_{1-x}\mathrm{Ho}_x\mathrm{FeO}_3$ ($x = 0$, 0.05, 0.07, 0.10, 0.12, and 0.15) powders were synthesized by a sol-gel method. The stoichiometric amounts of bismuth nitrate ($\mathrm{Bi(NO_3)_3{\cdot}6H_2O}$), iron nitrate ($\mathrm{Fe(NO_3)_3{\cdot}9H_2O}$), and holmium nitrate ($\mathrm{Ho(NO_3)_3{\cdot}5H_2O}$) were used. 2-Methoxyethanol and acetic acid ($\mathrm{CH_3COOH}$) were mixed and stirred for 30 min, before adding the nitrates. Obtained solutions were stirred and heated at 80 °C. After a partial liquid evaporation, the solutions have turned into brown gels. The gels were dried for 45 min at 150 °C. Dried samples were calcinated at 650 °C for 6 h. The pristine and doped samples were named according to the Ho content as BFO, BHFO5, BHFO7, BHFO10, BHFO12 and BHFO15.

2.2. Materials characterization

The phase composition and crystal structure of $\mathrm{Bi}_{1-x}\mathrm{Ho}_x\mathrm{FeO}_3$ samples were analysed using X-ray diffractometer Rigaku Ultima IV with nickel filtered Cu K_α radiation in the 2θ range of 10–80° with the step of 0.02° and the scanning rate of 0.5°/min. XRD pattern analysis was performed using Powder Cell programme (http://powdercell-for-windows.software.informer.com/2.4/) [21]. The TCH pseudo-Voigt profile function gave the best fit to the experimental data. The surface morphology was studied by scanning electron microscopy (SEM, TESCAN SM-300). The micro-Raman spectra were measured at room temperature using a Jobin Yvon T64000 spectrometer equipped with a nitrogen-cooled CCD detector. The $\lambda = 532$ nm line of solid state Nd:YAG laser was used as an excitation source with an incident laser power less than 40 mW in order to minimize the heating effects. The dielectric properties of the samples were examined in the frequency range of 80 Hz to 8 MHz. The Digital Programmable LCR Bridge HM8118 (Hameg) was used in the range 80 Hz–120 kHz, and the Digital LCR Meter 4285 A (HP/Agilent) was used in the range 80 kHz–8 MHz. Each sample was placed in a closed capacitor cell housed in a Faraday cage with an AC signal of 1.5 V applied across the cell. The disk-shaped samples had a diameter close to the diameter of the cell electrodes (8 mm). Standard bipolar measurements in the frequency range 1 Hz–1 kHz were performed on Precision Multiferroic Test System (Radiant Technologies, Inc.), using a triangular electric field waveform. All measurements were performed at room temperature.

3. Results and discussion

Fig. 1(a) shows XRD patterns of the $\mathrm{Bi}_{1-x}\mathrm{Ho}_x\mathrm{FeO}_3$ ($0 \le x \le 0.15$) samples. The XRD pattern of pristine BFO matches the rhombohedral *R3c* structure with a presence of weak diffraction peaks which correspond to the orthorhombic $\mathrm{Bi_2Fe_4O_9}$ secondary phase of *Pbam* space group (Nº 55, ICSD #20067). XRD spectra of the BHFO5 and BHFO7 samples maintain *R3c* structure. No secondary peaks were detected in BHFO5 sample, whereas the traces of secondary phase were observed in the BHFO7 sample. Addition of Ho dopant induced a gradual broadening of XRD peaks and their shifts towards higher angles. These changes suggest structural distortion of BFO lattice and can be attributed to the unit cell contraction due to the substitution of Bi^{3+} ions with smaller Ho^{3+} dopant. Significant changes with increased Ho concentration were observed in doublet (104) and (110) diffraction peaks at $2\theta \sim 32°$. These peaks were shifted towards larger 2θ values, and in the samples with higher Ho content ($x > 0.07$) they gradually merged into a single broad peak (BHFO15 sample). In addition, the (006), (116) and (202) diffraction peaks of *R3c* phase became weak and disappeared in the samples with higher Ho concentration ($x > 0.1$). In the spectra of BHFO12 and BHFO15 samples, a new single peak appeared at $2\theta \sim 38°$, whereas additional peak at $2\theta \sim 25°$ was found in BHFO15 sample.

Such changes have already been seen in the XRD spectra of doped

Table 1
The lattice parameters (Å), volume of the unit cell (Å^3) and volume phase fraction (vol%).

Phase	BFO	BHFO5	BHFO7	BHFO10	BHFO12	BHFO15
$BiFeO_3$ rhombohedral *R3c*	a = 5.5722 c = 13.8511 V = 372.45 71.75%	a = 5.5636 c = 13.8216 V = 370.51 100.00%	a = 5.5575 c = 13.8145 V = 369.51 87.86%	a = 5.5651 c = 13.8143 V = 370.51 53.72%	a = 5.5675 c = 13.8542 V = 371.91 55.27%	a = 5.5441 c = 13.8127 V = 367.68 31.45%
$Bi_2Fe_4O_9$ orthorhombic *Pbam*	a = 7.9477 b = 8.4582 c = 6.0050 V = 403.68 28.25%	/	a = 7.9769 b = 8.5299 c = 5.9448 V = 404.50 12.14%	a = 7.9501 b = 8.4580 c = 5.9976 V = 403.29 25.36%	/	/
$BiFeO_3$ orthorhombic *Pnma*	/	/	/	a = 5.5830 b = 7.8825 c = 5.4192 V = 238.49 20.92%	a = 5.5993 b = 7.8679 c = 5.4540 V = 240.27 44.73%	a = 5.5907 b = 7.8129 c = 5.4297 V = 237.17 68.55%
Rp	5.81	6.27	5.94	4.86	6.18	5.42
Rwp	7.44	7.92	7.60	6.14	7.92	6.91
Rexp	0.11	0.12	0.09	0.06	0.07	0.09

$BiFeO_3$ nanoparticles [17,22], ceramics [23–25] and films [26], and were ascribed to the presence of orthorhombic phase. All these notable changes in the XRD spectra indicate structural phase transformation from rhombohedral to orthorhombic phase in the samples doped with higher Ho content ($x = 0.10$, 0.12 and 0.15). $Bi_2Fe_4O_9$ phase is still present in the BHFO10 sample, but with further increase of Ho doping (BFHO12 and BFHO15 samples) the secondary $Bi_2Fe_4O_9$ phase is completely suppressed. Furthermore, the absence of diffraction peaks which correspond to Ho oxides, even at higher concentrations, implies that Ho ions have entered substitutionally into BFO lattice.

The measured XRD patterns were further refined using PowderCell programme in order to calculate the structural parameters and estimate the volume fraction of each phase. The best fits of the measured data were obtained using rhombohedral *R3c* structure for BHFO5 and BHFO7 samples. The orthorhombic phase appeared in BHFO10 samples and with further Ho doping this phase becomes dominant in BHFO15 sample. Unit cell parameters and the estimated volume fractions of different phases are presented in Table 1 for pristine and Ho-doped BFO samples. The decreasing trend in lattice constants and the unit cell contraction of *R3c* phase confirm that Bi^{3+} ions are substituted with smaller Ho^{3+} ions. A similar behavior has been reported in Tb-doped $BiFeO_3$ [10] as well as in rare-earth doped $BiFeO_3$ ceramics [27,28]. The slight increase of *R3c* phase lattice parameters in BHFO10 and BHFO12 samples can be ascribed to increased strain at phase boundary between rhombohedral and orthorhombic crystal structure. Levin et al. have also found abrupt expansion of the *R3c* unit cell volume at the rhombohedral-orthorombic phase transition in Nd-substituted $BiFeO_3$ [29]. The results of quantitative phase analysis of the $Bi_{1-x}Ho_xFeO_3$ samples are presented in Fig. 1(b).

The influence of structural changes on surface morphology of BFO is illustrated in Fig. 2, where the SEM images of pristine and BHFO15 samples are shown for comparison. Changes in the surface morphology are clearly visible. Certain amount of intergranular porosity and non-uniformity of particles can be observed in the BFO sample, including very small spherical particles and big clumps. With incorporation of Ho^{3+} ions in BFO, the particles became more uniform and compact, whereas the particle size was reduced, as seen in 10% Ho-doped BFO [30]. In the enlarged images (Fig. 2c and d) it can be seen that pure and Ho-doped BFO samples consist of small particles and large irregularly shaped agglomerates.

Changes of $Bi_{1-x}Ho_xFeO_3$ crystal structure are reflected in the changes of $BiFeO_3$ vibrational properties, i.e. through the changes in intensity, position, and width of the Raman modes. Fig. 3 shows the room-temperature Raman spectra of $Bi_{1-x}Ho_xFeO_3$ samples. Raman spectrum of undoped $BiFeO_3$ was deconvoluted using Lorentzian profiles and all 13 Raman active modes ($4A_1+9E$) of the rhombohedral $BiFeO_3$ [31] are observed. The most prominent Raman modes for *R3c* structure (marked as E-1, A_1-1, A_1-2, and A_1-3) are positioned at 75, 140, 171, and 218 cm^{-1}, respectively and are related to Bi–O bonds. The A_1-4 mode at 430 cm^{-1} and eight E modes at 124, 274, 344, 369, 468, 520, 550 and 598 cm^{-1} with quite weak scattering intensity are related to Fe–O bonds.

Raman spectroscopy is sensitive to atomic displacements. The A_1-1, A_1-2 and A_1-3 modes are blue-shifted due to the substitution of Bi^{3+} ions with smaller Ho^{3+} ions. Modes E-1, A_1-1, A_1-2 and A_1-3 became broader and of reduced intensity, whereas higher frequency E modes (E-4, E-5) have almost disappeared. The peak broadening and reduced intensities of Raman modes imply the distortion of rhombohedral structure with incorporation of Ho. With increasing Ho concentration ($x \geq 0.1$), further changes in the Raman spectra are the result of decreased stereochemical activity of Bi lone electron pair. The intensities of A_1 and E modes are drastically reduced in BHFO10 and BHFO12 samples. These modes are barely visible in the Raman spectra of BHFO15 sample. Moreover, in BHFO12 sample three new modes approximately at 300, 400, and 510 cm^{-1}, are observed. Reduced intensities of phonon modes, characteristic for rhombohedral phase, and the presence of additional modes suggest the appearance of new crystalline phase. In the Raman spectrum of BFHO15 sample which is significantly different from the spectrum of pristine BFO, the most prominent modes are at ~ 300, 400, and 510 cm^{-1}. These modes are characteristic for orthorhombic perovskite $LaMnO_3$ and $YMnO_3$ structures [32] and are also observed in doped BFO powders [17]. All notable changes in the Raman spectra of BHFO12 and BHFO15 samples are consistent with the results of XRD analysis, confirming a structural transformation from rhombohedral to orthorhombic paraelectric phase. Hence, Raman spectroscopy is powerful tool for detecting changes of Bi–O covalent bonds during the phase transition.

Fig. 4(a) and (b) illustrate the frequency dependence of real (ε') and imaginary (ε'') part of the complex permittivity ε of $Bi_{1-x}Ho_xFeO_3$ samples. In the lower frequency range, both ε' and ε'' decrease with increasing frequency and become nearly constant at higher frequencies. Among the samples with *R3c* structure, BHFO5 sample has shown pronounced dispersion at lower frequencies and higher values of ε' and ε'' than BFO. The BHFO7 sample displayed almost no dispersion over the whole frequency range. Among the samples with higher Ho content in which orthorombic phase appears, BHFO10 sample displayed more dispersive characteristic than BHFO12 and BHFO15 samples for which permittivity dispersions were negligible.

BFO nanostructures in the form of nanopowders or thin films usually suffer from large leakage current due to the presence of oxygen vacancies, Fe^{2+} ions or some other impurities. The inhomogeneity of BFO microstructure and composition originates from the regions with

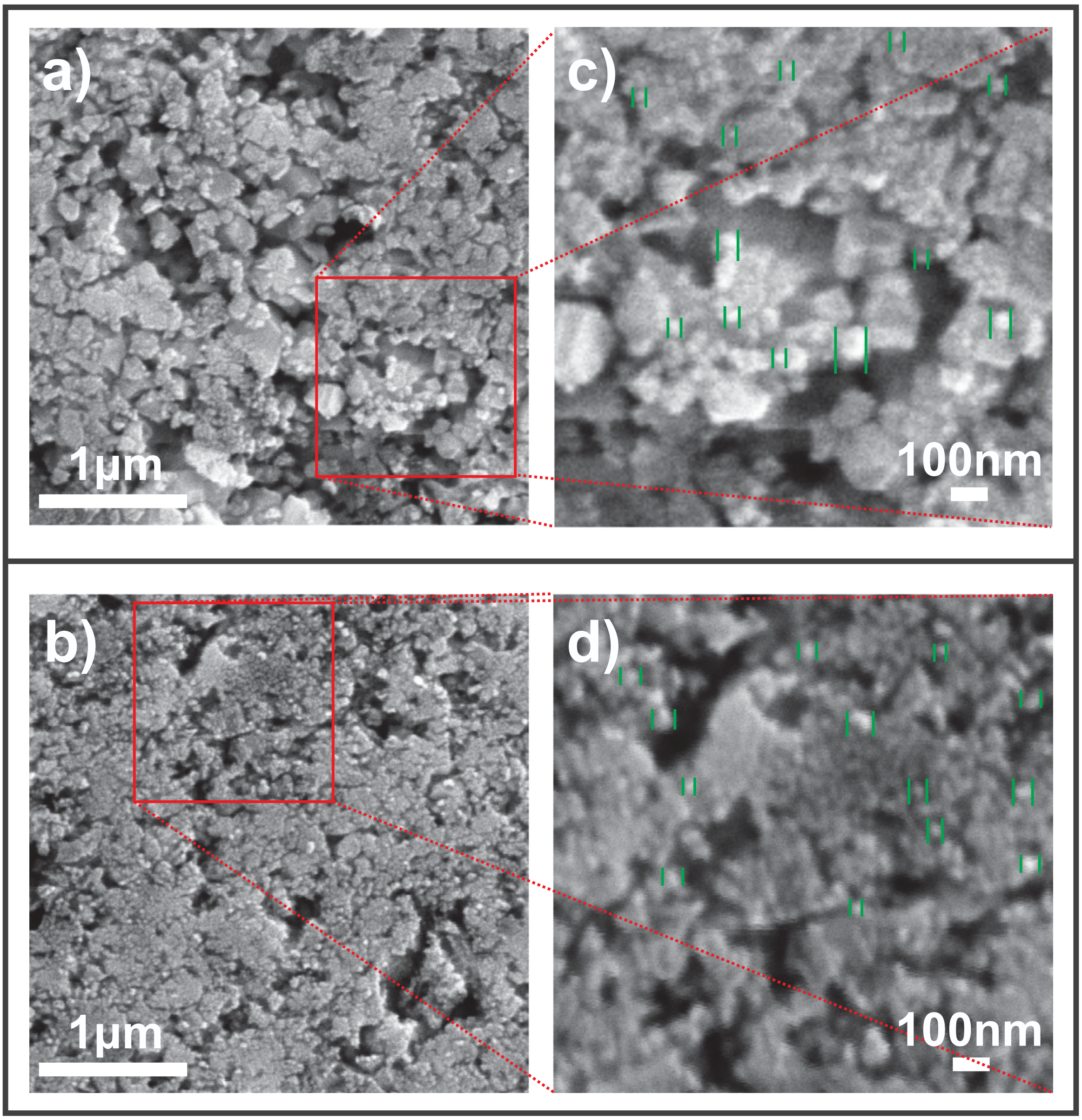

Fig. 2. SEM images of a) $BiFeO_3$ and b) $Bi_{0.85}Ho_{0.15}FeO_3$ samples. High-magnification SEM images of the c) $BiFeO_3$ and d) $Bi_{0.85}Ho_{0.15}FeO_3$ samples.

different conductivity, for example bulk and grain boundaries or from depletion layers formed at the interface of the electrode/sample surface. In addition to the dipolar or orientational polarization which occurs in the frequency range of 10^3–10^6 Hz, the grain boundary or interface effects give rise to the Maxwell-Wagner polarization which can substantially contribute to the permittivity and its dispersion at lower frequencies [3].

The dielectric relaxation processes in pure and Ho-doped BFO nanopowders were analysed within a model which includes Cole-Cole empirical expression, dc and ac conductivity terms. This model describes dielectric relaxation processes due to dipole relaxation, and the contributions from leakage current and grain boundary/interface effects. The advantages of this model for analyzing the dielectric properties of pristine $BiFeO_3$ films have been shown by Li and coworkers [33]. The total complex permittivity is of the form [33,34]:

$$\varepsilon = \varepsilon' + i\varepsilon'' = \frac{\varepsilon_s - \varepsilon_\infty}{1+(i\omega\tau)^{1-\alpha}} + \frac{\sigma_0}{\varepsilon_0} tan\left(\frac{\pi s}{2}\right)\omega^{s-1} + i\left(\frac{\sigma_{DC}}{\omega\varepsilon_0} + \frac{\sigma_0}{\varepsilon_0}\omega^{s-1}\right) \quad (1)$$

The first term in Eq. (1) corresponds to the Cole-Cole formula, where ε_s and ε_∞ are static and high frequency dielectric permittivity, τ is the relaxation time, andα, taking the value between 0 and 1, describes the distribution of relaxation times. For an ideal Debye relaxation $\alpha = 0$. For $\alpha < 0$ the loss peaks are broader and deviate in shape from the symmetric Debye peak [35]. The frequency-independent dc conductivity contributes only to the imaginary part of permittivity (ε'') through the term $\sigma_{DC}/\omega\varepsilon_0$, whilst the frequency-dependent ac conductivity represented by UDR ansatz [34,35], influences both ε' and ε'' through terms $(\sigma_0/\varepsilon_0)tan\left(\frac{\pi s}{2}\right)\omega^{s-1}$ and $(\sigma_0/\varepsilon_0)\,\omega^{s-1}$, where σ_0 is a pre-power term and s is a frequency exponent which takes values between 0 and 1.

The fits of $\varepsilon'(\omega)$ and $\varepsilon''(\omega)$, based on Eq. (1), are presented with solid lines on Figs. 4(a) and 4(b) and the values of fit parameters for $Bi_{1-x}Ho_xFeO_3$ samples are summarized in Table 2. The values of σ_{DC} and σ_0 for $Bi_{1-x}Ho_xFeO_3$ samples, based on the fitting results, are presented in Fig. 4(d). BFO sample has relatively high σ_{DC} value of $6.1\cdot10^{-9}\,\Omega^{-1}\,cm^{-1}$, whereas the value of σ_0 is an order of magnitude lower. These values are comparable with reported data [15,33,36]. It can be concluded that the permittivity of BFO sample is dominated by the leakage current contribution, whereas the ac dependent mechanisms are less prominent. Among the Ho-doped samples with *R3c*

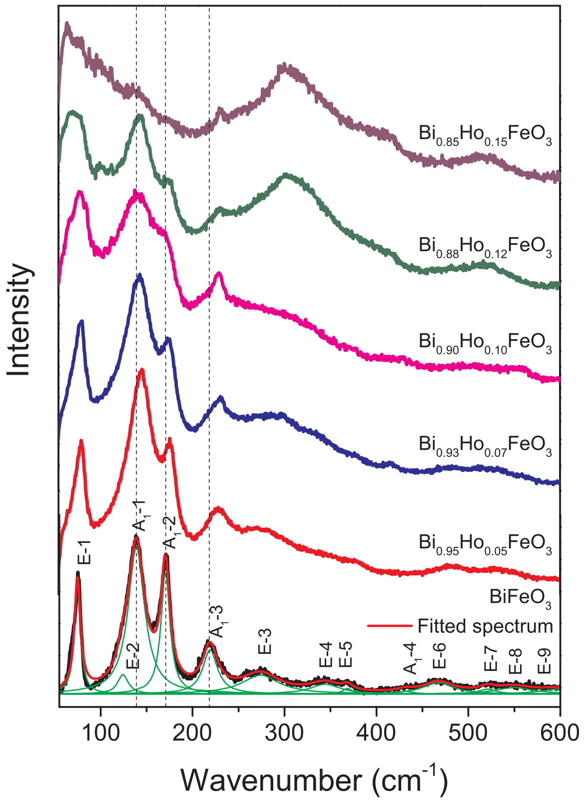

Fig. 3. Room-temperature Raman spectra of the $Bi_{1-x}Ho_xFeO_3$ ($0 \le x \le 0.15$) samples together with the deconvoluted Raman spectrum of pristine $BiFeO_3$.

structure, the highest dc and ac conductivity exhibits the BFHO5 sample, meaning that leakage current and grain boundary or interface effects can be a cause of permittivity dispersion and its higher value at lower frequencies. This finding offers an explanation for the collosal dielectric constant of Ho doped samples found by Song et al. [20]. The σ_{DC} and σ_0 values of BHFO7 sample are much lower than in BFO and BHFO5 samples. Despite the fact that the amount of secondary phase in BFHO7 is almost the same as in pristine BFO and having in mind that BFHO5 sample is phase pure, it seems that BHFO5 and BFO samples are more conductive than BHFO7 sample. This fact can explain the flat frequency dependence of $\varepsilon'(\omega)$ and $\varepsilon''(\omega)$ (Figs. 4(a) and (b)) of BHFO7 sample and imply that the presence of secondary phase has no great influence on the BFO conductivity, but defects in the form of oxygen vacancies and grain boundary or interface effects play a major role in the conductivity of BHFO5 and BFO samples. A significant increase of σ_{DC} value, which is almost twice as large as in pristine BFO and BHFO5 samples, was found in a case of BHFO10. Although it is expected that increased Ho doping reduces the leakage current due to the suppressed concentration of oxygen and bismuth vacancies, this sample seems to be more leaky than the pristine BFO. The σ_{DC} value, higher than in all the other samples, and pronounced dispersion of $\varepsilon''(\omega)$ implies that the leakage current affects the dielectric properties of BHFO10 to a great extent.

The changes in dielectric properties of BHFO10 sample can be related to the appearance of orthorhombic phase, because the dielectric properties are dependent on the sample structure and therefore can be modified near the phase transformation boundary [3]. The dc and ac conductivities were significantly reduced in BHFO12 sample, whereas BHFO15 sample, for which orthorhombic phase prevails, had an order of magnitude lower dc conductivity ($5.7 \cdot 10^{-10}\ \Omega^{-1}\ cm^{-1}$) than the BFO ($6.1 \cdot 10^{-9}\ \Omega^{-1}\ cm^{-1}$). Therefore, we argue that higher Ho content reduces the leakage current, and weakens the ac conductivity contribution to the dielectric response. The frequency dependence of dielectric loss ($tan\,\delta$) of $Bi_{1-x}Ho_xFeO_3$ samples is presented in Fig. 4(c). The dielectric loss follows a trend similar to the permittivity in the frequency range of 100 Hz to 8 MHz, i.e. it decreases with increasing frequency. The BFO, BHFO5 and BHFO10 samples have higher *tan δ* value than other Ho-doped samples with pronounced dispersion at lower frequencies. There is an indication of dielectric relaxation peak in conductive BFO and BHFO10 samples at frequency of 5 kHz, which can be ascribed to the carrier hopping process between Fe^{2+} and Fe^{3+} ions inside the particles [37] or to the hopping along the Fe^{2+}-$V_O^{\bullet}$ -Fe^{3+} chain [38]. This peak is slightly shifted to lower frequency in BHFO5 sample. This low frequency relaxation can be attributed to the grain boundary conduction [39]. Reduced *tan δ* values and the absence of relaxation peaks in BHFO7, BHFO12 and BHFO15 samples point at an increased resistivity of these samples.

Polarization-electric field (P-E) hysteresis loops of $Bi_{1-x}Ho_xFeO_3$ samples, measured at frequency of 100 Hz, are presented in Fig. 5(a). The BFO sample has an unsaturated P-E loop due to non negligible contribution of leakage current ($\sigma_{DC} = 6.1 \cdot 10^{-9}\ \Omega^{-1}\ cm^{-1}$). The maximal polarization, remnant polarization (P_r), and coercive field (E_c) reached the highest values in BFO sample and decreased with Ho-doping. The BHFO5 sample has a pinched P-E loop, characteristic for leaky materials. The permittivity analysis has shown that BHFO5 is less resistive than BFO and that grain boundary effects and leakage current dominate its dielectric properties. Therefore, the degraded ferroelectric properties can be attributed to the presence of oxygen vacancies and valence fluctuations of Fe ions (between Fe^{3+} and Fe^{2+}), because the appearance of oxygen vacancies and Fe^{2+} ions, especially at grain boundaries, is unfavorable for the polarization switching. The study of dielectric properties has shown that BHFO7 is more resistive than BFO and BHFO5. This fact explains slightly improved P-E loop compared to BHFO5 sample, but still lower P_r and E_c values than in BFO can originate from a decrease in stereochemical activity of Bi lone electron pair with increase of Ho content. P-E loops of the BHFO10, BHFO12 and BHFO15 samples are very similar to the P-E loops of BHFO5 sample. The degraded ferroelectricity of BHFO10 mainly originates from the contribution of dc conductivity (σ_{DC}) which is the highest among all analysed samples (see Fig. 4(d) and Table 2). Although BHFO12 and BHFO15 samples are more resistive than BFO and all the other Ho-doped samples, their ferroelectric properties are degraded because of the possible appearance of paraelectric phase regions in highly Ho doped BFO. This is supported by the changes noticed in the Raman spectra of these samples. Near the ferroelectric-paraelectric phase transition, the intensities of the Raman modes characteristic for Bi–O bonds [28] were reduced in BHFO12 sample and have almost disappeared in BHFO15 sample.

Furthermore, the presence of orthorhombic phase increases the breakdown field strength of $Bi_{1-x}Ho_xFeO_3$ samples (inset of Fig. 5(a)). The breakdown in BFO and $Bi_{1-x}Ho_xFeO_3$ samples with rhombohedral structure ($x < 0.1$) happens at the applied electric fields of around 20 kV/cm. The BHFO10 and BHFO12 samples, in which rhombohedral and orthorhombic phase coexist, withstand applied fields that are approximately twice as high. The BHFO15 sample in which orthorhombic phase prevails, withstands even higher electric fields (> 50 kV/cm) without breakdown (marked with arrow on the inset). The reason can be found in reduced dc conductivity of BHFO15 and in increasing number of Ho–O bonds with large bond energy, almost two times larger than the Bi–O bond [15]. Knowing that BHFO15 sample withstands high external fields without breakdown, the P-E loops of BHFO15 sample were measured at different testing frequencies from 2 Hz to 100 Hz under the applied field of 50 kV/cm, as shown in Fig. 5(b). It is obvious that P-E loops exhibit frequency-dependent behavior by showing rapid increase of P_r, E_c and maximal polarization at lower frequencies. Frequency dependence of the $2P_r$ for BHFO15 sample is presented in the top-left inset of Fig. 5(b), from which it is clear that $2P_r$ has the highest value of 0.21 μC/cm^2 at 2 Hz and rapidly decreases to 0.07 μC/cm^2 at 20 Hz. The P-E loops of BHFO15 measured in a high amplitude electric field of 100 kV/cm and at low frequencies of 1 Hz

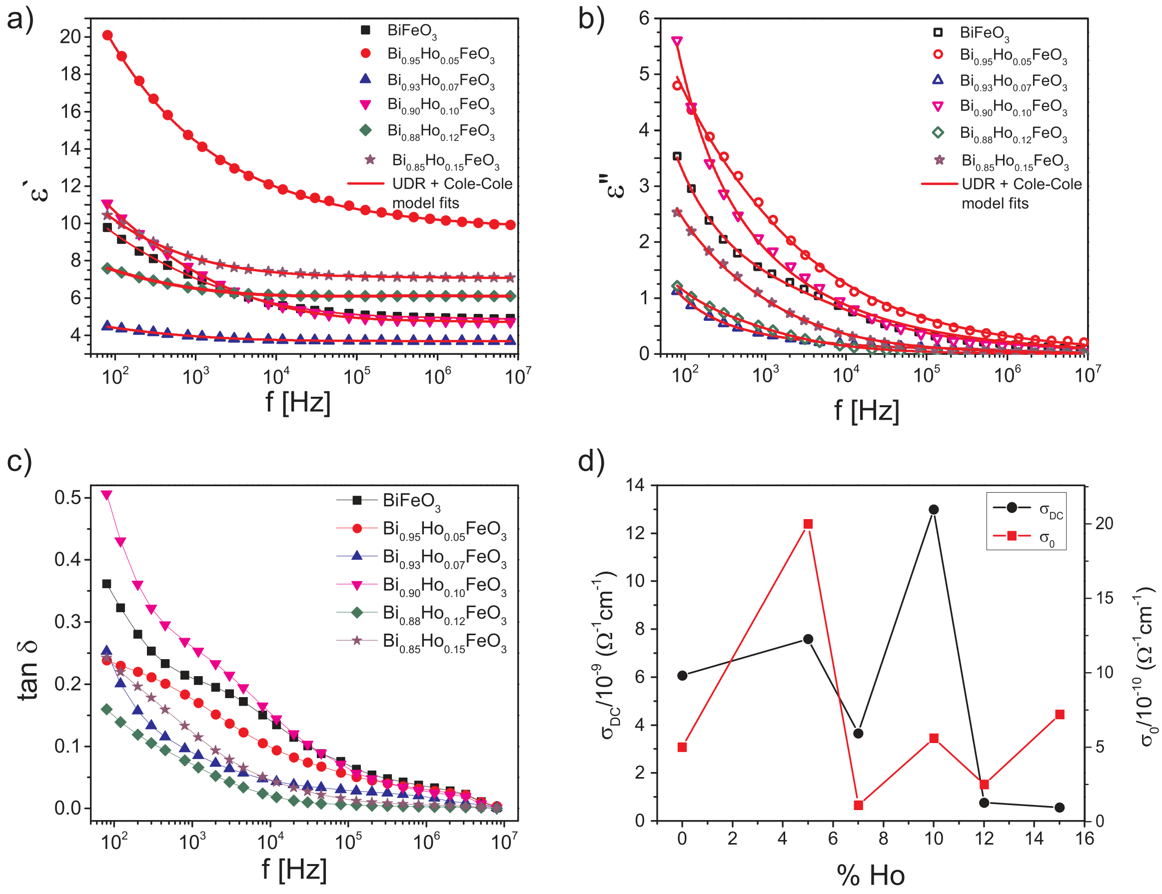

Fig. 4. Room-temperature (a) real (ε') and (b) imaginary (ε'') part of the complex permittivity. Full lines present the corresponding fits applying the combined model (Eq. 1), (c) loss tangent (*tan δ*) and (d) the dependence of σ_{DC} and σ_0 values on Ho content for $Bi_{1-x}Ho_xFeO_3$ samples.

and 2 Hz are presented in the right-bottom inset of Fig. 5(b). The $2P_r$ value is larger by a factor of two than the one obtained at the same frequency in the field of 50 kV/cm. Such a behavior can be explained by the effect of external field on the reorientation of defect dipoles and their role in domain wall switching in BFO. The presence of mobile, single defects (like V_{Bi}''', $V_O^{\bullet}$ or $V_O^{\bullet\bullet}$) or defect complexes (oxygen vacancy-cation associated dipoles) in BFO plays an important role in the domain wall pinning. It leads to the deterioration of polarization-switching properties by suppression of intrinsic polarization and increase of leakage current. The ferroelectric domain depinning can be achieved by applying high electric field or can be favoured at elevated temperatures and a secondary re-oxidation annealing [40–43]. On the other hand, in high electric fields the defect complexes can orient along the direction of spontaneous polarization and follow the domain switching, enhancing polarization properties of BFO [42–45]. Inherent defect dipoles are expected not to switch during fast field cycling, since their reorientation takes more time than the domain switching process. Therefore, the influence of defect dipole polarization on the overall polarization can be seen in high fields at low frequencies, as defect complexes can keep up with reversal of the field and contribute to the bulk ferroelectric polarization [40,44]. It is plausible to suppose that inherent defect complexes like $V_{Bi}''' - V_O^{\bullet\bullet}$, $Fe'_{Fe^{2+}} - V_O^{\bullet}$ or $Fe'_{Fe^{2+}} - V_O^{\bullet\bullet}$ form during the crystallization process in $Bi_{1-x}Ho_xFeO_3$ samples. Among all $Bi_{1-x}Ho_xFeO_3$ samples, only BHFO15 sample has supported high external field of 50 kV/cm which can induce defect dipole reorientation. By applying strong external field at low frequencies, defect dipoles can orient along the direction of spontaneous polarization following the domain switching. With increasing of the field strength to 100 kV/cm and by lowering the frequency to 1 Hz, the effect of defect dipolar polarization was more pronounced. Therefore, the reorientation of internal defect complexes under high external field gives rise to the enhancement of intrinsic polarization of BHFO15 sample.

4. Conclusions

In summary, the phase transformation from rhombohedral to orthorhombic phase induced by increased Ho substitution, affected to a great extent the dielectric and ferroelectric properties of $Bi_{1-x}Ho_xFeO_3$ nanopowders. The frequency dependent permittivity was analysed using combined model which incorporated Debye-like dielectric

Table 2
The fitting parameters for $Bi_{1-x}Ho_xFeO_3$ samples obtained from combined model.

Parameter	BFO	BHFO5	BHFO7	BHFO10	BHFO12	BHFO15
α	0.55	0.69	0.65	0.69	0.60	0.67
τ(s)	$5.3 \cdot 10^{-6}$	$2.2 \cdot 10^{-6}$	$5.2 \cdot 10^{-5}$	$1.2 \cdot 10^{-5}$	$5.6 \cdot 10^{-5}$	$3.2 \cdot 10^{-5}$
s	0.79	0.66	0.80	0.85	0.78	0.75
$\sigma_0(\Omega^{-1}\ cm^{-1})$	$5.0 \cdot 10^{-10}$	$1.8 \cdot 10^{-9}$	$1.1 \cdot 10^{-10}$	$5.6 \cdot 10^{-10}$	$2.5 \cdot 10^{-10}$	$7.2 \cdot 10^{-10}$
$\sigma_{DC}(\Omega^{-1}\ cm^{-1})$	$6.1 \cdot 10^{-9}$	$7.6 \cdot 10^{-9}$	$3.6 \cdot 10^{-9}$	$1.3 \cdot 10^{-8}$	$7.7 \cdot 10^{-10}$	$5.7 \cdot 10^{-10}$

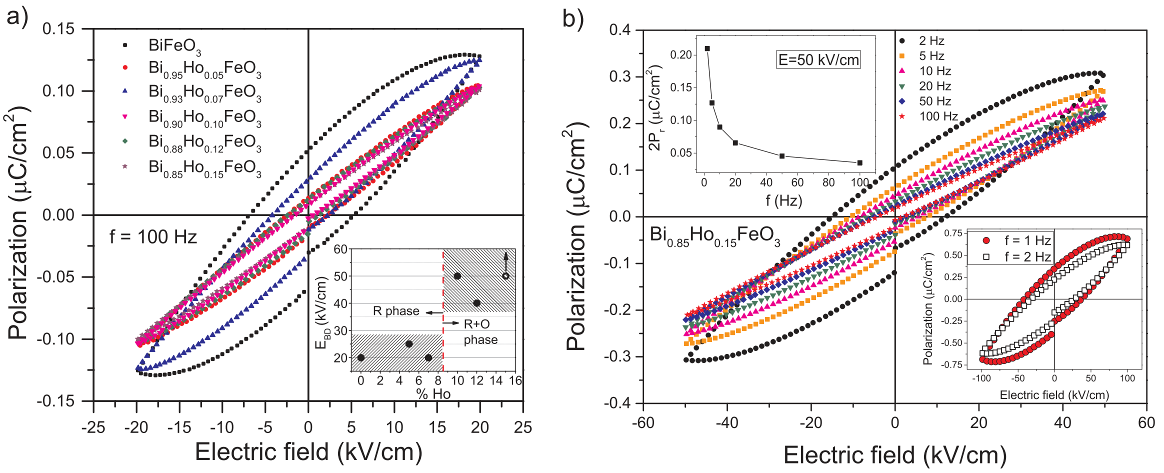

Fig. 5. a) Room-temperature P-E loops of $Bi_{1-x}Ho_xFeO_3$ samples. Inset presents breakdown fields for all samples except for BHFO15. b) P-E loops of BHFO15 sample taken at different frequencies. The frequency dependence of $2P_r$ is shown in the top-left corner inset, and the P-E loops in the field of large amplitude at low frequencies are shown in the bottom-right corner inset.

response and dc and ac conductivity contributions. It was shown that not only dc conductivity, but also grain boundary and interfacial effects were much reduced in biphasic $Bi_{1-x}Ho_xFeO_3$ (x > 0.1) samples. The dominant presence of orthorhombic phase in $Bi_{0.85}Ho_{0.15}FeO_3$ sample has stabilized the perovskite structure of BFO, significantly increased the breakdown field and improved BFO electrical performances. In high external electric fields (50 kV/cm and 100 kV/cm), P-E loops of $Bi_{0.85}Ho_{0.15}FeO_3$ sample manifested strong frequency dependence and abrupt increase of remnant polarization and coercive field at low frequencies. It was proposed that defect dipoles were oriented along the direction of spontaneous polarization, following the domain switching, and were therefore a primary cause of the enhanced polarization properties of $Bi_{0.85}Ho_{0.15}FeO_3$ sample. Although it is well established opinion that appearance of orthorhombic paraelectric phase degrades ferroelectricity of BFO, our study contributes to better understanding of polarization mechanisms in biphasic bismuth ferrite.

Acknowledgments

This work was financially supported by the Ministry of Education, Science and Technological Development of the Republic of Serbia under the projects ON171032 and III45018.

References

[1] G. Catalan, J.F. Scott, Physics and applications of bismuth ferrite, Adv. Mater. 21 (2009) 2463–2485.
[2] R. Ramesh, N.A. Spaldin, Multiferroics: progress and prospects in thin films, Nat. Mater. 6 (2007) 21–29.
[3] S.K. Pradhan, B.K. Roul, Effect of Gd doping on structural, electrical and magnetic properties of $BiFeO_3$ electroceramic, J. Phys. Chem. Solids 72 (2011) 1180–1187.
[4] G.L. Yuan, Siu Wing Or, J.M. Liu, Z.G. Liu, Structural transformation and ferroelectromagnetic behavior in single-phase $Bi_{1-x}Nd_xFeO_3$ multiferroic ceramics, Appl. Phys. Lett. 89 (2006) 052905.
[5] G.L. Yuan, S.W. Or, H.L.W. Chan, Reduced ferroelectric coercivity in multiferroic $Bi_{0.825}Nd_{0.175}FeO_3$ thin film, J. Appl. Phys. 101 (2007) 024106.
[6] J. Liu, M. Li, L. Pei, J. Wang, B. Yu, X. Wang, X. Zhao, Structural and multiferroic properties of the Ce-doped $BiFeO_3$ thin films, J. Alloy. Compd. 493 (2010) 544–548.
[7] K.S. Nalwa, A. Gart, A. Upadhyaya, Effect of samarium doping on the properties of solid-state synthesized multiferroic bismuth ferrite, Mater. Lett. 62 (2008) 878–881.
[8] W. Sun, J.F. Li, Q. Yu, L.Q. Cheng, Phase transition and piezoelectricity of sol-gel-processed Sm-doped $BiFeO_3$ thin films on Pt(111)/Ti/SiO_2/Si substrates, J. Mater. Chem. C 3 (2015) 2115–2122.
[9] D. Varshney, P. Sharma, S. Satapathy, P.K. Gupta, Structural, magnetic and dielectric properties of Pr-modified $BiFeO_3$ multiferroic, J. Alloy. Compd. 584 (2014) 232–239.
[10] Y. Wang, C.W. Nan, Effect of Tb doping on electric and magnetic behavior of $BiFeO_3$ thin films, J. Appl. Phys. 103 (2008) 024103.
[11] S. Chatuvedi, R. Bag, V. Sathe, S. Kulkarni, S. Singh, Holmium induced enhanced functionality at room temperature and structural phase transition at high temperature in bismuth ferrite nanoparticles, J. Mater. Chem. C 4 (2016) 780–792.
[12] P. Suresh, P.D. Babu, S. Srinath, Effect of Ho substitution on structure and magnetic properties of $BiFeO_3$, J. Appl. Phys. 115 (2014) 17D905.
[13] S.K. Pradhan, B.K. Roul, D.R. Sahu, Enhancement of ferromagnetism and multiferroicity in Ho doped Fe rich $BiFeO_3$, Solid State Commun. 152 (2012) 1176–1180.
[14] S.K. Pradhan, J. Das, P.P. Rout, V.R. Mohanta, S.K. Das, S. Samantray, D.R. Sahu, J.L. Huang, S. Verma, B.K. Roul, Effect of holmium substitution for the improvement of multiferroic properties of $BiFeO_3$, J. Phys. Chem. Solids 71 (2010) 1557–1564.
[15] N. Jeon, D. Rout, W. Kim, S.-J.L. Kang, Enhanced multiferroic properties of single-phase $BiFeO_3$ bulk ceramics by Ho doping, Appl. Phys. Lett. 98 (2011) 072901.
[16] H. Singh, K.L. Yadav, Enhanced magnetization with unusual low temperature magnetic ordering behaviour and spin reorientation in holmium-modified multiferroic $BiFeO_3$ perovskite ceramics, J. Phys. D: Appl. Phys. 48 (2015) 205001.
[17] Y. Wu, J. Zhang, X.-K. Chen, X.-J. Chen, Phase evolution and magnetic property of $Bi_{1-x}Ho_xFeO_3$ powders, Solid State Commun. 151 (2011) 1936–1940.
[18] Z.L. Hou, H.F. Zhou, L.B. Kong, H.B. Jin, X. Qi, M.S. Cao, Enhanced ferromagnetism and microwave absorption properties of $BiFeO_3$ nanocrystals with Ho substitution, Mater. Lett. 84 (2012) 110–113.
[19] Y.Q. Liu, Y.J. Wang, J. Zhang, M. Gao, Y.J. Zhang, M.B. Wei, J.H. Yang, Effect of Ho substitution on structure and magnetic property of $BiFeO_3$ prepared by solgel method, Mater. Sci. Semicond. Proc. 40 (2015) 787–795.
[20] G.L. Song, G.J. Ma, J. Su, T.X. Wang, H.Y. Yang, F.G. Chang, Effect of Ho^{3+} doping on the electric, dielectric, ferromagnetic properties and TC of $BiFeO_3$ ceramics, Ceram. Int. 40 (2014) 3579–3587.
[21] W. Kraus, G. Nolze, POWDER CELL – a program for the representation and manipulation of crystal structures and calculation of the resulting X-ray powder patterns, J. Appl. Cryst. 29 (1996) 301.
[22] L. Chen, L. Zheng, Y. He, J. Zhang, Z. Mao, X. Chen, The local distortion and electronic behavior in Mn doped $BiFeO_3$, J. Alloy. Compd. 633 (2015) 216–219.
[23] V. Singh, S. Sharma, M. Kumar, R.K. Kotnala, R.K. Dwivedi, Structural transition, magnetic and optical properties of Pr and Ti co-doped $BiFeO_3$ ceramics, J. Magn. Magn. Mater. 349 (2014) 264–267.
[24] P.C. Sati, M. Arora, S. Chauhan, M. Kumar, S. Chhoker, Structural, magnetic, vibrational and impedance properties of Pr and Ti codoped BiFeO3 multiferroic ceramics, Creram. Int. 40 (2014) 7805–7816.
[25] B. Stojadinović, Z. Dohčević-Mitrović, N. Paunović, N. Ilić, N. Tasić, I. Petronijević, D. Popović, B. Stojanović, Comparative study of structural and electrical properties of Pr and Ce doped $BiFeO_3$ ceramics synthesized by auto-combustion method, J. Alloy. Compd. 657 (2016) 866–872.
[26] V.A. Khomchenko, D.V. Karpinsky, A.L. Kholkin, N.A. Sobolev, G.N. Kakazei, J.P. Araujo, I.O. Troyanchuk, B.F.O. Costa, J.A. Paixão, Rhombohedral-to-orthorhombic transition and multiferroic properties of Dy-substituted $BiFeO_3$, J. Appl. Phys. 108 (2010) 074109.
[27] P.C. Sati, M. Kumar, S. Chhoker, M. Jewariya, Inuence of Eu substitution on structural, magnetic, optical and dielectric properties of $BiFeO_3$ multiferroic ceramics, Creram. Int. 41 (2015) 2389–2398.
[28] P. Pandit, S. Satapathy, P. Sharma, P.K. Gupta, S.M. Yusuf, V.G. Sathe, Structural, dielectric and multiferroic properties of Er and La substituted $BiFeO_3$ ceramics, B, Mater. Sci. 34 (2011) 899–905.
[29] I. Levin, M.G. Tucker, H. Wu, V. Provenzano, C.L. Dennis, S. Karimi, T. Comyn, T. Stevenson, R.I. Smith, I.M., Reaney displacive phase transitions and magnetic structures in Nd-substituted $BiFeO_3$, Chem. Mater. 23 (2011) 2166–2175.
[30] X. Xue, G. Tan, W. Liu, H. Ren, Comparative study on multiferroic ($Bi_{0.9}RE_{0.1}$)($Fe_{0.97}Co_{0.03}$)$O_{3-\delta}$ (RE = Ce and Ho) thin films: structural, electrical and optical properties, Creram. Int. 40 (2014) 6247–6254.
[31] P. Hermet, M. Goffinet, J. Kreisel, P. Ghosez, Raman and infrared spectra of multiferroic bismuth ferrite from frst principles, Phys. Rev. B 75 (2007) 220102.
[32] M. Iliev, M. Abrashev, H.G. Lee, V. Popov, Y. Sun, C. Thomsen, R. Meng, C. Chu,

Raman spectroscopy of orthorhombic perovskitelike $YMnO_3$ and $LaMnO_3$, Phys. Rev. B 57 (1998) 2872–2877.

[33] Y.W. Li, Z.G. Hu, F.Y. Yue, P.X. Yang, Y.N. Qian, W.J. Cheng, X.M. Ma, J.H. Chu, Oxygen-vacancy-related dielectric relaxation in $BiFeO_3$ films grown by pulsed laser deposition, J. Phys. D: Appl. Phys. 41 (2008) 215403.

[34] P. Lunkenheimer, V. Bobnar, A.V. Pronin, A.I. Ritus, A.A. Volkov, A. Loidl, Origin of apparent colossal dielectric constants, Phys. Rev. B 66 (2002) 052105.

[35] A.K. Jonscher, The universal dielectric response, Nature 267 (1977) 673–679.

[36] Q. Yun, Y. Bai, J. Chen, W. Gao, A. Bai, S. Zhao, Improved ferroelectric and fatigue properties in Ho doped $BiFeO_3$ thin films, Mater. Lett. 129 (2014) 166–169.

[37] E. Markiewicz, B. Hilczer, M. Blaszyk, A. Pietraszko, E. Talik, Dielectric properties of $BiFeO_3$ ceramics obtained from mechanochemically synthesized nanopowders, J. Electroceram. 27 (2011) 154–161.

[38] Q. Ke, X. Lou, Y. Wang, J. Wang, Oxygen-vacancy-related relaxation and scaling behaviors of $Bi_{0.9}La_{0.1}Fe_{0.98}Mg_{0.02}O_3$ ferroelectric thin films, Phys. Rev. B 82 (2010) 024102.

[39] S. Mukherjee, R. Gupta, A. Garg, V. Bansal, S. Bhargava, Inuence of Zr doping on the structure and ferroelectric properties of $BiFeO_3$ thin films, J. Appl. Phys. 107 (2010) 123535.

[40] B. Li, G. Li, Q. Yin, Z. Zhu, A. Ding, W. Cao, Pinning and depinning mechanism of defect dipoles in PMnNPZT ceramics, J. Phys. D: Appl. Phys. 38 (2005) 1107–1111.

[41] I. Bretos, R. Jiménez, C. Gutiérrez-Lázaro, I. Montero, L. Calzada, Defect-mediated ferroelectric domain depinning of polycrystalline $BiFeO_3$ multiferroic thin films, Appl. Phys. A 104 (2014) 092905.

[42] D. Guo, C. Wang, Q. Shen, L. Zhang, M. Li, J. Liu, Effect of measuring factors on ferroelectric properties of $Bi_{3.15}Nd_{0.85}Ti_3O_{12}$ thin films prepared by solgel method for non-volatile memory, Appl. Phys. A 97 (2009) 877–881.

[43] J. Lv, X. Lou, J. Wu, Defect dipole-induced poling characteristics and ferroelectricity of quenched bismuth ferrite-based ceramics, J. Mater. Chem. C 4 (2016) 6140–6151.

[44] L. Zhang, E. Erdem, X. Ren, R.-A. Eichel, Reorientation of (Mn_{Ti}''-$V_O^{\bullet\bullet}$)X defect dipoles in acceptormodified BaTiO3 single crystals: an electron paramagnetic resonance study, Appl. Phys. Lett. 93 (2008) 202901.

[45] Y. Chrishima, Y. Noguchi, Y. Kitanaka, M. Miyayama, Defect control for polarization switching in $BiFeO_3$ single crystals, IEEE Trans. Ultrason. Ferroelectr. Freq. Control 57 (2010) 2233–2236.

Processing and Application of Ceramics 11 [4] (2017) 304–310
https://doi.org/10.2298/PAC1704304M

Influence of Mg doping on structural, optical and photocatalytic performances of ceria nanopowders

Branko Matović[1,*], Jelena Luković[1], Bojan Stojadinović[2], Sonja Aškrabić[2], Aleksandra Zarubica[3], Biljana Babić[1], Zorana Dohčević-Mitrović[2]

[1]Institute for Nuclear Sciences, Centre of Excellence-CextremeLab Vinca, University of Belgrade, Belgrade, Serbia
[2]Institute of Physics Belgrade, Pregrevica 118, University of Belgrade, Belgrade, Serbia
[3]Faculty of Sciences and Mathematics, Department of Chemistry, University of Nis, Nis, Serbia

Received 21 July 2017; Received in revised form 14 November 2017; Accepted 6 December 2017

Abstract

Nanosized Mg-doped ceria powders were obtained by self-propagating room temperature reaction without using surfactants or templates. X-ray diffraction analysis and field emission scanning microscopy results showed that the doped samples are solid solutions with fluorite-type structure and spherical morphology. Raman spectra revealed an increase in the amount of oxygen vacancies with the increase of Mg concentration. This increasing results in a narrowing of the bandgap of CeO_2. The photocatalytic performances of the Mg-doped ceria solid solutions were evaluated by decomposing an organic dye, crystal violet under UV irradiation. The Mg-doped ceria solid solutions exhibit significantly better photocatalytic activity than the pure CeO_2 and commercial TiO_2. The higher first rate constant of the Mg-doped samples demonstrated that they are much more efficient than TiO_2 and CeO_2 under UV light. Mg^{2+} dopant ions and oxygen vacancies play a significant role in the enhancement of photocatalytic performances of the Mg-doped ceria.

Keywords: *ceria, solid solution, oxygen vacancies, UV light illumination, nanocatalysis*

I. Introduction

Nano ceria (CeO_2) has been extensively studied as an active or supporting catalytic material due to its superior oxygen storage-and-release properties [1]. Since ceria is a good electron acceptor, it can provide lattice oxygen in chemical reactions because of lower formation energy for oxygen vacancy [2–4]. Also, CeO_2 promotes the chemical activity of the material by facilitating electron transfer from suitable adspecies into an oxide surface [5,6]. A higher catalytic activity is related to the type, size, and distribution of oxygen vacancies. It is demonstrated that surface defects were more readily formed in CeO_2 nanostructures with special morphology, such as cubes, nanobelts, nanowires and nanotubes. Therefore, for the design of ceria based materials with high oxygen storage and transport capacity, it is important to know how to increase the number of structural defects (oxygen vacancies) and to maintain at the same time a fluorite-type crystal structure. This can be done either by the promotion of Ce^{4+} reduction into Ce^{3+} or by doping with transition or rare-earth elements [7]. CeO_2 is not generally considered as a photocatalytic material due to its wide band gap and specific 4f electron configuration. Despite the fact that little work was carried out in the field of photocatalytic applications of CeO_2 [8–10] recent studies demonstrated that improvement of ceria photocatalytic properties can be done by proper choice of dopant elements and their incorporated amounts [11] or by creating surface defects as the most reacting sites which can enhance the visible light activity of nanostructured ceria [12]. In addition, the preparation methods have also a significant influence on the ceria structure (homogeneity, morphology, grain size, crystal defects etc.) and its optical and photocatalytic properties. Therefore, tuning the band gap energy and tailoring the reactivity of ceria-based catalysts is still a challenging task.

---

[*] Corresponding authors: tel/fax: +381 11 3408 224
e-mail: *mato@vinca.rs*

In this work the Mg-doped ceria nonpowdered solid solutions ($Ce_{1-x}Mg_xO_{2-\delta}$, $0 \leq x \leq 0.4$) were prepared by facile and cost-effective self-propagating room temperature reaction (SPRT). The influence of Mg content on structural, optical and photocatalytic properties was examined. The evaluation of photocatalytic activity of synthesized catalysts has been carried out by degradation of crystal violet as a model pollutant. The mechanism for the band gap narrowing of Mg-doped ceria and the enhancement of the photocatalytic performances are also proposed.

II. Materials and methods

The solid solutions of magnesium-doped samples were prepared by a SPRT method using metal nitrates and sodium hydroxide as the starting materials. This technique gives the possibility of producing very fine powders with very precise stoichiometry in accordance with the tailored compositions [13–16]. Preparation of $Ce_{1-x}Mg_xO_{2-\delta}$ powders was performed by hand mixing chemicals according to:

$$\begin{aligned} &2\,[(1-x)\mathrm{Ce(NO_3)_3}\cdot 6\,\mathrm{H_2O} + x\mathrm{Mg(NO_3)_2}\cdot 6\,\mathrm{H_2O}] + 6\,\mathrm{NaOH} + \\ &+ (\tfrac{1}{2}-\delta)\mathrm{O_2} \longrightarrow 2\,\mathrm{Ce}_{1-x}\mathrm{Mg}_x\mathrm{O}_{2-\delta} + 6\,\mathrm{NaNO_3} + 15\,\mathrm{H_2O} \end{aligned} \tag{1}$$

The compositions of the reacting mixtures were calculated according to the nominal composition of the final reaction product. Compositions of $Ce_{1-x}Mg_xO_{2-\delta}$ were synthesized with x ranging from 0.0 to 0.4. The described reaction belongs to a group of double exchange reactions and develops spontaneously after being initiated, terminating extremely rapidly. After the mixture of reactants ($Ce(NO_3)_3 \cdot 6\,H_2O$, Aldrich, $Mg(NO_3)_2 \cdot 6\,H_2O$, Aldrich) was mechanically activated (by hand mixing instead by heating) the reaction took place at room temperature and terminated very quickly. The obtained mixtures of reaction products according to Eq. (1) were subjected to a centrifuge treatment to eliminate $NaNO_3$ and drying at 80 °C.

After drying, the composition of the solid solutions was identified by means of powder XRD on a Rigaku IV, XRD diffractometer with CuKα radiation at room temperature. The average crystallite size was measured from the 111 XRD peak using the Scherrer formula. The values of the unit cell parameters of all the analysed powders are calculated on the basis of the equation:

$$\frac{4\sin^2\theta}{\lambda^2} = \frac{1}{d_{hkl}^2} = \frac{h^2+k^2+l^2}{a^2} \tag{2}$$

where θ is the Bragov angle, hkl are Miller indices, λ is the wavelength (1.54184 Å), and a is parameter of the unit cell of the crystal [17].

SEM analysis using Zeiss DSM 982 Gemini scanning electron microscope proved that the obtained powders were in the nanometric size range. The room-temperature Raman spectra were obtained using a U-1000 (Jobin-Ivon) double monochromator in back scattering geometry. The Raman spectra were excited by the 514 nm line of an Ar^+/Kr^+ ion laser operating at low incident power (~20 mW) in order to avoid sample heating. The measurements of UV-Vis absorption spectra of the samples were carried out on a Specord M40 Carl Zeiss spectrophotometer in a spectral range 200–600 nm, at room temperature.

The specific surface area and the pore size distribution (PSD) of the doped CeO_2 samples were analysed using the Surfer (Thermo Fisher Scientific, USA). PSD was estimated by applying BJH method [18] to the desorption branch of isotherms and mesopore surface and micropore volume were estimated using the t-plot method [19].

Photocatalytic activity of the synthesized Mg-doped samples was evaluated by the degradation of crystal violet (CV) under UV light irradiation. The photochemical reactor consisted of UV lamp (Roth Co., 16 W, 2.5 mW/cm^2, $\lambda_{max} = 366$ nm) positioned annularly to the 50 ml quartz flask. The acidity of solutions was not additionally adjusted and pH values were in the range from 6.7 to 7.0. The rates of photocatalytic degradations of CV were followed at initial concentration of 0.01 mmol/dm^3. The amount of used catalyst was 30 ± 2 mg. CV photolysis test was performed prior to photocatalytic measurements and no significant dye degradation was observed. The prepared $Ce_{1-x}Mg_xO_{2-\delta}$ samples were immersed into CV solution and the solution was continuously stirred and kept in the dark for 1 h to establish adsorption-desorption equilibrium before being irradiated. Photocatalytic activity of the $Ce_{1-x}Mg_xO_{2-\delta}$ solid solutions were compared to commercial standard TiO_2 sample - Degussa P25 (having specific surface area, S_{BET}, of 56 m^2/g, pore volume of 0.25 cm^3/g, average pore size of 17.5 nm, crystallite size of 21 nm and the following phase composition: anatase, 81 vol.% and rutile, 19 vol.%) and the undoped CeO_2 sample.

The reaction rate constant (k) was determined assuming quasi first order kinetics using the following equation:

$$\ln\frac{C_0}{C_t} = k \cdot t \tag{3}$$

where C_0 is the initial dye concentration, C_t is the concentration at time t. The slope of the $\ln(C_0/C_t)$ versus time plot gives the value for the rate constant k.

III. Results

3.1. Characterization of Mg-doped ceria

XRD spectra of the $Ce_{1-x}Mg_xO_{2-\delta}$ samples, presented in Fig. 1, revealed that the obtained powders are a single phase with the fluorite crystal structure. Main diffraction peaks in each sample were significantly broadened indicating small crystallite size and/or strain. New peak is observed for the sample doped with 40 at.% of Mg, indicating that the limit of Mg solubility in ceria crystal lattice is in the range from 30 to 40 at.%. This high sol-

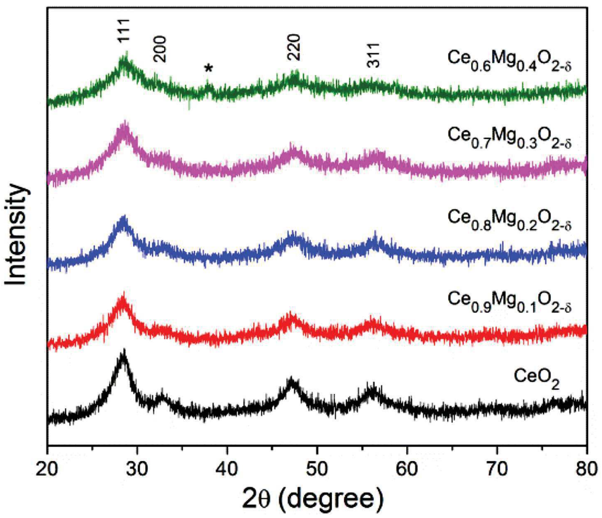

Figure 1. X-ray diffraction patterns of synthesized of $Ce_{1-x}Mg_xO_{2-\delta}$ nanopowders (* - brucite phase)

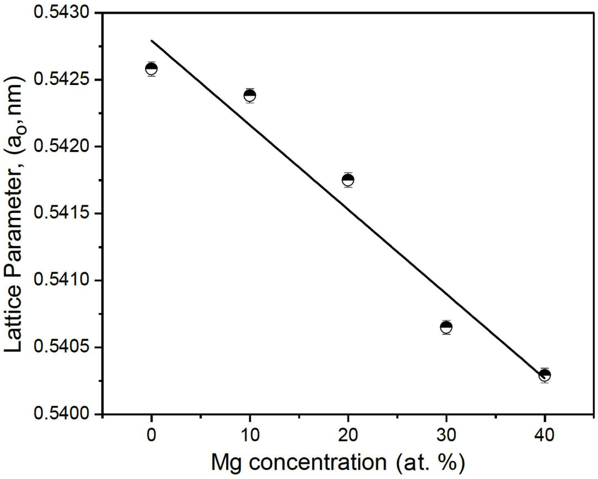

Figure 2. Lattice parameter (a_0) $Ce_{1-x}Mg_xO_{2-\delta}$ samples as a function of Mg content

ubility may be attributed to the nanometric nature of the obtained powders. Excess of Mg is very reactive and in contact with moisture make a brucite phase $Mg(OH)_2$, marked with asterisks in Fig. 1. XRD spectra exhibit very diffuse diffraction lines with increasing Mg content, which makes difficult to indicate precisely some atomic planes (*hkl*: 200, 220, 311, 420).

Calculation of cell parameters (Fig. 2) based on X-ray results, shows the linear dependence of unit cell parameter versus concentration of Mg^{2+} ions. With increasing of Mg^{2+} ion concentration the cubic ceria lattice shrinks. According to Shannon's compilation [19], the ionic radii of Ce^{4+} and Mg^{2+} for coordination number (CN) 8, are 0.97 and 0.89 Å, respectively. Thus, doping with a smaller sized Mg^{2+} ion and increasing of dopant concentration, will lead to the contraction of the ceria lattice. Also, lattice parameter (a_0) of doped ceria versus Mg^{2+} content, obeys Vegard's law, implying that Mg^{2+} substitutionally entered into ceria lattice. The crystallite size, calculated on the basis of XRD data, for all powders is less than 5 nm.

Room-temperature Raman spectra of the Mg-doped ceria are presented in Fig. 3, whereas in the inset is given the Raman spectrum of the undoped CeO_2. Room-temperature Raman spectrum of the undoped CeO_2 sample shows the strong peak at ~455 cm^{-1} corresponding to the triply degenerate F_{2g} mode characteristic for the fluorite cubic CeO_2 structure. The red shift of this mode compared to its bulk counterpart (464 cm^{-1}) and pronounced asymmetry on the low-energy side originates from the phonon confinement, strain and the presence of defects [20,21]. In the sample doped with 10 at.% of Mg, F_{2g} mode is shifted to ~457 cm^{-1}, due to the substitutional incorporation of Mg, as ion of smaller ionic radius, into ceria lattice. With further increasing of Mg content, F_{2g} mode shifts to higher energies and in the 40 at.% Mg doped sample, this mode is positioned at ~460 cm^{-1}.

Another mode of lower intensity, positioned at ~600 cm^{-1}, is characteristic for nanometric ceria and is attributed to the presence of intrinsic oxygen vacancies [20,22], due to the partial reduction of Ce^{4+} to Ce^{3+}. This mode is also presented in the Mg-doped samples. From the Lorentzian fit procedure (insets in Fig. 3), it

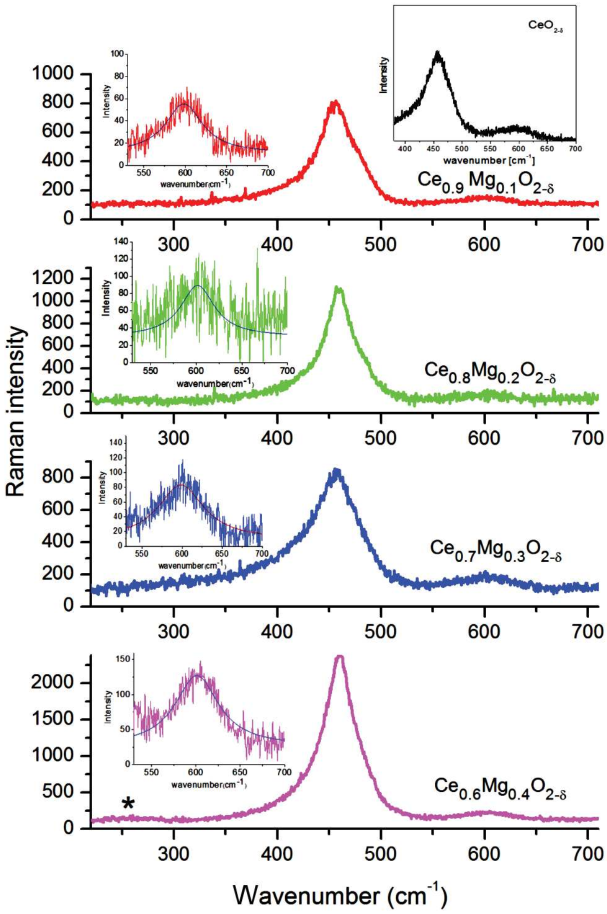

Figure 3. Room temperature Raman spectra of Mg-doped samples (insets present Raman spectrum of undoped CeO_2 and Lorentzian fits of intrinsic vacancy mode)

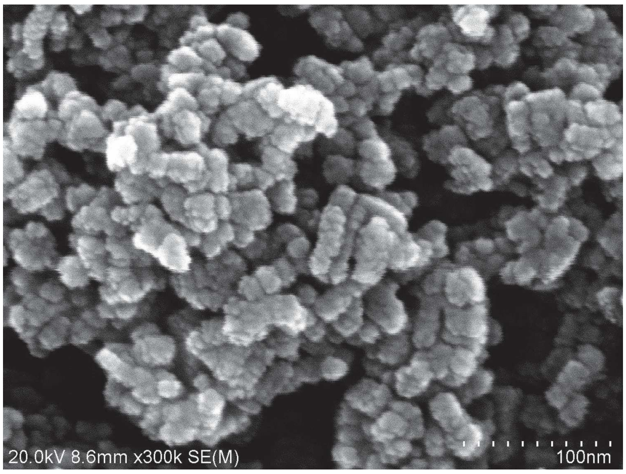

Figure 4. Typical FESEM images of 20 at.% Mg-doped ceria sample

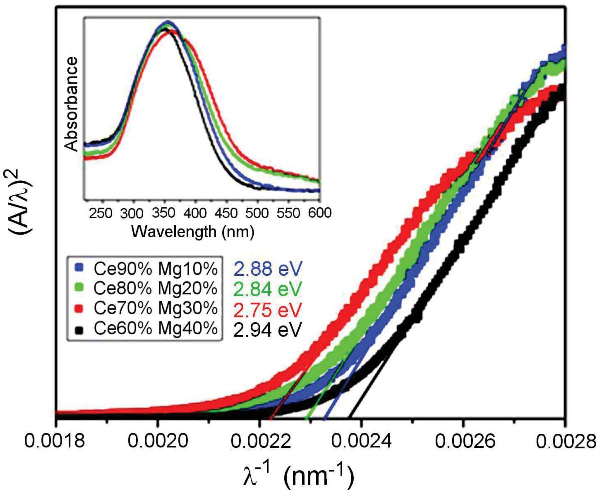

Figure 5. $(A/\lambda)^2$ plots for Mg-doped samples (inset presents absorption spectra of doped samples)

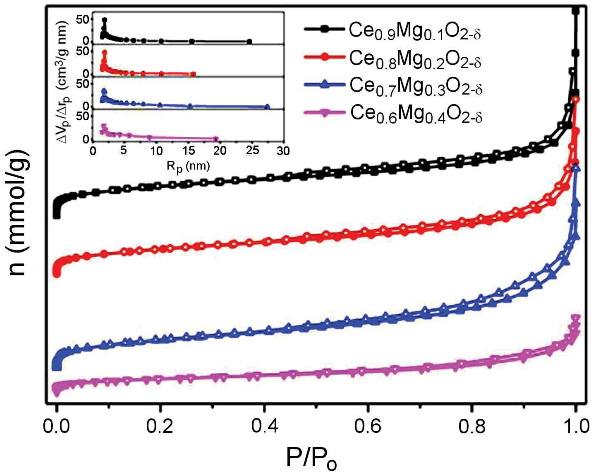

Figure 6. N_2 adsorption (solid symbols)/desorption (open symbols) isotherms and the pore size distribution (inset) of Mg-doped samples

was obtained that intensity of this mode increases with an increase of Mg content, pointing at increased intrinsic oxygen vacancy concentration [22]. In the spectra of the sample with 40 at.% Mg, new broad, low intensity mode around 270 cm^{-1} is observed. This mode (marked with asterisks in Fig. 3) can be ascribed to the E_g mode of $Mg(OH)_2$ (brucite) phase, which is in good agreement with XRD measurement [23]. It is evident from the Raman spectra of the sample with 40 at.% Mg that limits of Mg solubility in ceria crystal lattice is less than 40 at.%.

The as-prepared ceria powders consist of rounded particles with size less than 10 nm, roughly estimated (Fig. 4). The particles are linked in the form of blackberry, which together form cauliflower morphology. There is no difference of morphology and particle size between the Mg-doped ceria samples. It seems that various doping concentration has no influence on the microstructure of the powders.

The optical band gap of the undoped CeO_2, which corresponds to the O 2p $\longrightarrow$ Ce 4f^0 transition, was previously determined to be around 3.6 eV [24]. From the absorption spectra of the solid solutions $Ce_{1-x}Mg_xO_{2-\delta}$ (x = 0.1, 0.2, 0.3 and 0.4), presented in the inset of Fig. 5, the band gap energies of the Mg-doped samples were obtained using Tauc law for direct transition and applying absorption spectrum fitting method [25]. The plots of $(A/\lambda)^2$ vs. $1/\lambda$ are presented in Fig. 5, where A is the absorbance and λ is the wavelength. The linear extrapolation of $(A/\lambda)^2$ to zero gives a wavelength λ_g which corresponds to the optical band gap. The band gap values can be obtained using well known relation $E_g = 1240/\lambda_g$. The estimated direct band gap values (E_g) for $Ce_{1-x}Mg_xO_{2-\delta}$ samples are given in Fig. 5. It can be seen that with Mg doping up to 30 at.% band gap values decreased from 2.88 to 2.75 eV due to the formation of defect (localized) levels inside the gap with Mg doping [26]. In the sample with 40 at.% of Mg dopant the E_g is slightly increased to 2.94 eV. Such an increase can be a consequence of the presence of $Mg(OH)_2$ phase which has higher band gap value than CeO_2 [27] or to the Burstein-Moss effect caused by increased electron concentration and lifting of the Fermi-level because of increased Mg content and oxygen vacancies concentration [28].

Nitrogen adsorption/desorption isotherms for the Mg-doped samples, are shown in Fig. 6. According to the IUPAC classification [29] isotherms of samples are of type IV and with a hysteresis loop which is associated with mesoporous materials. In all samples, the shape of hysteresis loop is of type H3. Isotherms revealing type H3 hysteresis do not exhibit any limiting adsorption at high P/P_0, which is observed with nonrigid aggregates of plate-like particles giving rise to slit-shaped pores [30]. Specific surface areas calculated by BET equation, S_{BET}, are listed in Table 1. S_{BET} values for all Mg-doped samples are comparable (between 110–120 m^2/g), i.e. the amount of dopant does not have

Table 1. Porous properties of $Ce_{1-x}Mg_xO_{2-\delta}$ nanopowders

Sample	S_{BET} [m^2/g]	S_{meso} [m^2/g]	S_{mic} [m^2/g]	V_{mic} [cm^3/g]	r_m [nm]
CeO_2	70	45	25	0.013	-
$Ce_{0.9}Mg_{0.1}O_2$	114	104	10	0.003	3.7
$Ce_{0.8}Mg_{0.2}O_2$	110	110	0	0	4.3
$Ce_{0.7}Mg_{0.3}O_2$	120	120	0	0	5.2
$Ce_{0.6}Mg_{0.4}O_2$	113	113	0	0	4.4

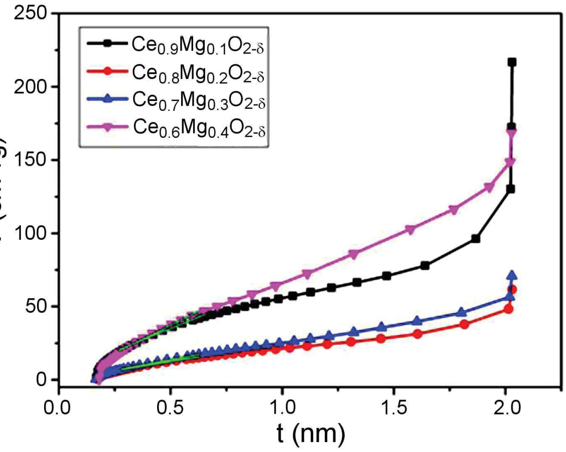

Figure 7. *t*-plots of Mg-doped samples

an essential influence on the overall specific surface area of the doped nanopowders. On the contrary, the undoped ceria sample has significantly smaller specific surface area than the doped ones. Therefore, the Mg doping increases the porosity of ceria. Pore size distribution (PSD) of samples possesses sharp PSD peak with most of the pore radius between 2–20 nm (inset of Fig. 6) implying that the samples are mesoporous. Values of mean pore radius, for all samples, are presented in Table 1.

The *t*-plot, obtained on the basis of the standard nitrogen adsorption isotherm, is shown in Fig. 7. The straight line in the medium *t*-plot region gives a mesoporous surface area including the contribution of the external surface, S_{meso}, determined by its slope, and the micropore volume, V_{mic}, which is given by the intercept. The calculated porosity parameters (S_{meso}, S_{mic}, V_{mic}) are given in Table 1. *t*-plot analysis confirmed that all samples are mesoporous, although a small amount of micropores (pore radius below 2 nm) was detected in the sample with 10 at.% of Mg and undoped ceria.

3.2. Photocatalytic performance of Mg-doped ceria

The influence of the dopant concentration on the photocatalytic activity of the Mg-doped ceria nanopowders has been studied through the photocatalytic removal of organic dye crystal violet (CV) under UV light irradiation. The kinetics of degradation of CV is represented in Fig. 8. As can be seen from Fig. 8, the pure ceria has shown modest photocatalytic activity. With increasing Mg content, the degradation of CV became significant. The samples with higher Mg content (>10 at.% Mg) have shown even better photocatalytic activity than the commercial TiO_2 Degussa P25, which is known as one of the most efficient photocatalysts for dye degradation.

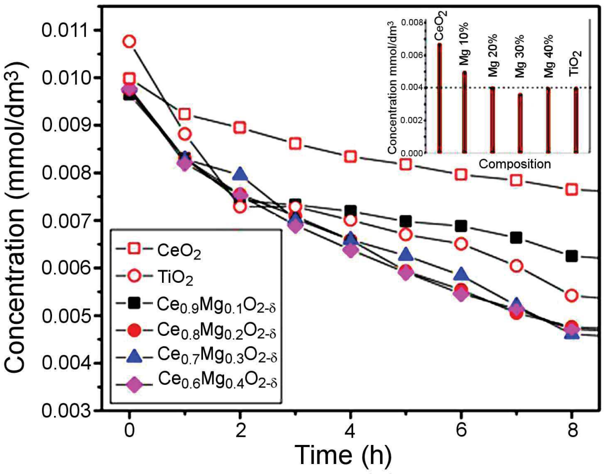

Figure 8. Photocatalytic degradation of CV in the presence of $Ce_{1-x}Mg_xO_{2-\delta}$ nanopowders and TiO_2 (insert represents photocatalytic efficiency after 24 h)

The reaction kinetics from Fig. 8, follows the first order and the degradation rate constants for 30 and 40 at.% Mg-doped samples, together with TiO_2 and CeO_2 as reference samples, are summarized in Table 2. It can be seen that the degradation rate constant for the $Ce_{0.7}Mg_{0.3}O_{2-\delta}$ and $Ce_{0.6}Mg_{0.4}O_{2-\delta}$ samples are higher than reference samples, implying that higher concentration of Mg in CeO_2 lattice improves the photocatalytic efficiency of ceria.

Table 2. The pseudo-first rate constants for CV after exposition time of 8 h

Sample	k [h^{-1}]	R^2
$Ce_{0.7}Mg_{0.3}O_{2-\delta}$	0.081	0.980
$Ce_{0.6}Mg_{0.4}O_{2-\delta}$	0.078	0.998
CeO_2	0.026	0.982
TiO_2	0.056	0.910

After 24 h the photocatalytic activity of the solid solutions with concentrations of 20 and 40 at.% of Mg respectively, are the same as a TiO_2 standard, whereas the $Ce_{0.7}Mg_{0.3}O_{2-\delta}$ sample exhibited higher activity (inset of Fig. 8). Such high photocatalytic activity of the $Ce_{0.7}Mg_{0.3}O_{2-\delta}$ sample can be attributed to its large specific surface area, the largest one among all the studied nanopowders, regular mesoporosity and favourable average pore size. A slightly lower photocatalytic activity of the ceria sample with 40 at.% Mg can be explained by the appearance of secondary brucite phase.

In Fig. 9 an illustration of the proposed mechanism of photocatalytic reactions is given. Upon UV light illumination photogenerated electrons and holes can be trapped by dopant ions, i.e. Mg^{2+} ions can be electron acceptors and/or hole donors. Reduction of the band gap of the Mg-doped samples implies that Mg^{2+} ions introduce states into the band gap of CeO_2. In such a

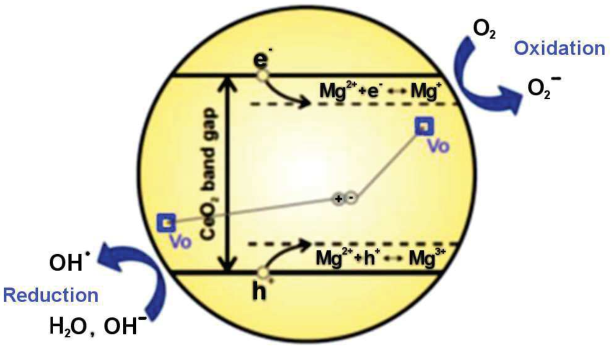

Figure 9. Illustration of the photocatalytic mechanism at Mg-doped CeO_2 interface under the UV light irradiation

way, Mg doping could be effective in delay of electron-hole recombination process, increasing the lifetime of the charge separation. The trapped electrons can be subsequently scavenged by molecular oxygen, which is adsorbed on the CeO_2 surface, to generate the superoxide radical ($O_2^{-\bullet}$). Superoxide radicals in contact with H_2O molecules form OH^- ions and finally $OH^\bullet$ radicals, which attack the dye in aqueous solution leading to its degradation. Due to high oxidative potential, the positive holes act as good oxidizing agents for dye degradation. The trapped holes can directly attack the dye or can interact with OH^- or water molecules present on the surface of the catalyst forming hydroxyl radicals ($OH^\bullet$).

Ceria nanoparticles are prone to the formation of oxygen vacancies (VO) which promote the formation of Ce^{3+} ions in the grain boundary region [30]. In order to attain charge neutrality with Mg doping, oxygen vacancies will be created in the ceria lattice. This fact is confirmed from Raman measurements. V_O as defects can also introduce localized state below the conduction band of CeO_2 [24] reducing the band gap. Furthermore, a high concentration of surface donor defects (V_O and Ce^{3+}) can serve as charge carrier traps and adsorption sites which transfer charge to adsorbed species like O_2 or H_2O on ceria surface. In such a way, oxygen vacancies can delay the electron-hole recombination process and support the charge carrier transfer to the ceria surface, improving the photocatalytic efficiency of ceria. Theoretical and experimental results on TiO_2 and ZnO have shown that excess electrons localized on the oxygen vacancy states affect surface adsorption and increase photocatalytic activity of TiO_2 and ZnO [31,32]. Therefore, it is reasonable to assume that besides Mg^{2+} ions as trapping centres, oxygen vacancies have a strong impact on the increased photocatalytic activity of Mg-doped ceria.

IV. Conclusions

Mg-doped ceria nanopowders ($Ce_{1-x}Mg_xO_{2-\delta}$, $0 \leq x \leq 0.4$) have been successfully fabricated via self-propagating room temperature reaction without any surfactant or template. The obtained samples are of fluorite cubic structure, composed of rounded particles with size less than 10 nm with the higher specific surface area than the pure CeO_2. Substitutional doping with lower valence Mg^{2+} ions promotes the formation of oxygen vacancies in ceria lattice, the amount of which increases with an increase of dopant concentration. The increased dopant concentration results in an effective red shift of the band gap value of the $Ce_{1-x}Mg_xO_{2-\delta}$ samples due to the formation of localized states inside the ceria gap. Only the sample with 40 at.% of Mg exhibited slight blueshift of the band gap due to the appearance of brucite phase. The photocatalytic activity of the Mg-doped CeO_2 for degradation of azodye crystal violet was examined under UV light irradiation. It was found that the samples with Mg content higher than 10 at.% have much better photocatalytic performances than the undoped CeO_2 and commercial Degussa P25. Localized electronic states of Mg^{2+} ions and oxygen vacancies can capture photogenerated charge carriers delaying recombination process, but can also serve as active sites on ceria surface to transfer charge to adsorbed species like O_2 or H_2O forming reactive radicals.

Acknowledgement: This work was financially supported by the Ministry of Education, Science and Technological Development of the Republic of Serbia under the projects III 45012 and ON171032. The authors would like to thank Nenad Tadić, Faculty of Physics, University of Belgrade for the UV-Vis measurements.

References

1. G.A. Deluga, J.R. Salge, L.D. Schmidt, X.E. Verykios, “Renewable hydrogen from ethanol by autothermal reforming”, *Science*, **303** (2004) 993–997.
2. M.V. Ganduglia-Pirovano, J.L.F.D. Silva, J. Sauer, “Density-functional calculations of the structure of near-surface oxygen vacancies and electron localization on CeO_2 (111)”, *Phys. Rev. Lett.*, **102** (2009) 026101.
3. A. Migani, G.N. Vayssilov, S.T. Bromley, F. Illas, K.M. Neyman, “Greatly facilitated oxygen vacancy formation in ceria nanocrystallites”, *Chem. Commun.*, **46** (2010) 5936–5938.
4. M. Nolan, S.C. Parker, G.W. Watson, “The electronic structure of oxygen vacancy defects at the low index surfaces of ceria”, *Surface Sci.*, **595** (2005) 223–232.
5. G.N. Vayssilov, Y. Lykhach, A. Migani, T. Staudt, G.P. Petrova, N. Tsud, T. Skala, A. Bruix, F. Illas, K.C. Prince, V. Matolin, K.M. Neyman, J. Libuda, “Support nanostructure boosts oxygen transfer to catalytically active platinum nanoparticles”, *Nature Mater.*, **10** (2011) 310–315.
6. M. Baron, H. Abbott, O. Bondarchuk, D. Stacchiola, A. Uhl, S. Shaikhutdinov, H.J. Freund, C. Popa, M.V.G. Pirovano, A.J. Sauer, “Resolving the atomic structure of vanadia monolayer catalysts: Monomers, trimers, and oligomers on ceria”, *Angewandte Chemie Int. Edition*, **48** (2009) 8006–8009.
7. M. Mogenson, N.M. Sammes, G.A. Tompsett, “Physical, chemical and electrochemical properties of pure and doped ceria ”, *Solid State Ionics*, **129** (2000) 63–94.
8. J.M. Coronado, A.J. Maira, A. Martínez-Arias, J.C. Conesa, J. Soria, “EPR study of the radicals formed upon

UV irradiation of ceria-based photocatalysts", *J. Photochem. Photobio. A: Chem.*, **150** (2002) 213–221.

9. G.R. Bamwenda, T. Uesigi, Y. Abe, K. Sayama, H. Arakawa, "The photocatalytic oxidation of water to O^{-2} over pure CeO_2, WO_3, and TiO_2 using Fe^{3+} and Ce^{4+} as electron acceptors", *Appl. Catal. A: Gen.*, **205** (2001) 117–128.
10. M.D. Hernández-Alonso, A.B. Hungría, A. Martínez-Arias, M. Fernández-García, J.M. Coronado, J.C. Conesa, J. Soria, "EPR study of the photoassisted formation of radicals on CeO_2 nanoparticles employed for toluene photooxidation", *Appl. Catal. B: Environ.*, **50** (2004) 167–175.
11. L. Yue, X.-M. Zhang, "Structural characterization and photocatalytic behaviors of doped CeO_2 nanoparticles", *J. Alloys Compd.*, **475** (2009) 702–705.
12. M.M. Khan, S.A. Ansari, D. Pradhan, D.H. Han, J. Lee, M.H. Cho, "Defect-induced band gap narrowed CeO_2 nanostructures for visible light activities", *Ind. Eng. Chem. Res.*, **53** (2014) 9754–9763.
13. B. Matovic, Z. Dohcevic-Mitrovic, M. Radovic, Z. Brankovic, G. Brankovic, S. Boskovic, Z.V. Popovic, "Synthesis and characterization of ceria based nanometric powders", *J. Power Sources*, **193** (2009) 146–149.
14. B. Matovic, J. Pantic, J. Lukovic, S. Ilic, N. Stankovic, M. Kokunesovski, M. Miljevic, "Synthesis and characterization of (Ba,Yb) doped ceria nanopowders", *Process. Appl. Ceram.*, **5** (2011) 69–72.
15. M. Prekajski, Z. Dohčević-Mitrović, M. Radović, B. Babić, J. Pantić, A. Kremenović, B. Matović, "Nanocrystaline solid solution CeO_2-Bi_2O_3", *J. Eur. Ceram. Soc.*, **32** (2012) 1983–1987.
16. M. Stojmenović, S. Bošković, S. Zec, B. Babić, B. Matović, D. Bučevac, Z. Dohčević-Mitrović, F. Aldinger, "Characterization of nanometric multidoped ceria powders", *J. Alloys Compd.*, **507** (2010) 279–285.
17. Lj. Karanović, D. Poleti, *X-ray Structural Analysis*, Institute for Textbooks and Teaching Resources, Belgrade, 2003.
18. E.P. Barret, L.G. Joyner, P.P. Halenda, "The determination of pore volume and area distributions in porous substances. I. Computations from nitrogen isotherms", *J. Am. Chem. Soc.*, **73** (1951) 373–380.
19. B.C. Lippens, B.G. Linsen, J.H. d. Boer, "Studies on pore systems in catalysts I. The adsorption of nitrogen; apparatus and calculation", *J. Catal.*, **3** (1964) 32–37.
20. R.D. Shannon, "Revised effective ionic radii and systematic studies of interatomie distances in halides and chaleogenides", *Acta Crystallogra. Section A*, **32** [5] (1976) 751–767.
21. Z.D. Dohčević-Mitrović, M.J. Šćepanović, M.U. Grujić-Brojčin, Z.V. Popović, S.B. Bošković, B.M. Matović, M.V. Zinkevich, F. .Aldinger, "The size and strain effects on the Raman spectra of $Ce_{1-x}Nd_xO_{2-\delta}$ ($0 \leq x \leq 0.25$) nanopowders", *Solid State Commun.*, **137** (2006) 387–390.
22. P.J. Colomban, G. Gouadec, "Raman spectroscopy of nanostructures and nanosized materials", *J. Raman Spectrosc.*, **38** (2007) 598–603.
23. Z.D. Dohčević-Mitrović, M.U. Grujić-Brojčin, M.J. Šćepanović, Z.V. Popović, S.B. Bošković, B.M. Matović, M.V. Zinkevich, F. Aldinger, "$Ce_{1-x}Y(Nd)_xO_{2-\delta}$ nanopowders: potential materials for intermediate temperature SOFCs", *J. Phys.: Condens. Mat.*, **18** (2006) S2061–S2068.
24. P. Dawson, C.D. Hatfield, G.R. Wilkinson, "The polarized infra-red and Raman spectra of $Mg(OH)_2$ and $Ca(OH)_2$", *J. Phys. Chem. Solids*, **34** (1973) 1217–1225.
25. M. Radović, B. Stojadinović, N. Tomić, A. Golubović, B. Matović, I. Veljković, Z. Dohčević-Mitrović, "Investigation of surface defect states in CeO_{2-y} nanocrystals by Scanning - tunneling microscopy /spectroscopy and ellipsometry", *J. Appl. Phys.*, **116** (2014) 234305.
26. N. Ghobadi, "Band gap determination using absorption spectrum fitting procedure", *Int. Nano Lett.*, **3** (2013) 1–4.
27. M. Radović, Z. Dohčević-Mitrović, A. Golubović, V. Fruth, S. Preda, M. Šćepanović, Z.V. Popović, "Influence of Fe^{3+}-doping on optical properties of CeO_{2-y} nanopowders", *Ceram. Int.*, **39** (2013) 4929–4936.
28. K. Mageshwari, R. Sathyamoorthy, "Studies on photocatalytic performance of MgO nanoparticles prepared by wet chemical method", *Trans. Indian Instit. Metals*, **65** (2012) 49–55.
29. V. Etacheri, R. Roshan, V. Kumar, "Mg-doped ZnO nanoparticles for efficient sunlight-driven photocatalysis", *ACS Appl. Mater. Inter.*, **4** (2012) 2717–2725.
30. B. Choudhury, A. Choudhury, "Ce^{3+} and oxygen vacancy mediated tuning of structural and optical properties of CeO_2 nanoparticles", *Mater. Chem. Phys.*, **131** (2012) 666–671.
31. F. Kayaci, S. Vempati, I. Donmez, N. Biyikliab, T. Uyar, "Role of zinc interstitials and oxygen vacancies of ZnO in photocatalysis: a bottom-up approach to control defect density", *Nanoscale*, **6** (2014) 10224–10234.
32. X. Pan, M.Q. Yang, X. Fu, N. Zhang, Y.J. Xu, "Defective TiO_2 with oxygen vacancies: synthesis, properties and photocatalytic applications", *Nanoscale*, **5** (2013) 3601–3614.

Ceramics International 43 (2017) 1256–1264

Contents lists available at ScienceDirect

Ceramics International

journal homepage: www.elsevier.com/locate/ceramint

$BiFeO_3$ perovskites: A multidisciplinary approach to multiferroics

Maria Čebela[a], Dejan Zagorac[a,*], Katarina Batalović[b], Jana Radaković[b], Bojan Stojadinović[c], Vojislav Spasojević[d], Radmila Hercigonja[e]

[a] *Materials Science Laboratory, Institute of Nuclear Sciences Vinča, Belgrade University, Belgrade, Serbia*
[b] *Laboratory for Nuclear and Plasma Physics, Institute of Nuclear Sciences Vinča, Belgrade University, Belgrade, Serbia*
[c] *Center for Solid State Physics and New Materials, Institute of Physics, University of Belgrade, Pregrevica 118, 11080 Belgrade, Serbia*
[d] *Laboratory of Theoretical and Condensed Matter Physics, Institute of Nuclear Sciences Vinča, Belgrade University, Belgrade, Serbia*
[e] *Faculty of Physical Chemistry, Belgrade University, Belgrade, Serbia*

ARTICLE INFO

Keywords:
A. Powders: chemical preparation
B. X-ray methods
C. Magnetic properties
D. Perovskites

ABSTRACT

Bismuth ferrite ($BiFeO_3$) is one of the most studied multiferroic system with a large number of published articles. This is mainly because $BiFeO_3$ material possesses both ferromagnetic and ferroelectric properties observed at room temperature, which opens great possibility for industrial and technological applications. Well-crystallized single-crystal $BiFeO_3$ nanopowder has been successfully synthesized with the hydrothermal method. The phase composition of the synthesized samples was determined by the x-ray diffraction (XRD) analysis, and the results showed that synthesized material crystallizes in the space group *R*3*c* as α-$BiFeO_3$ phase, which was confirmed by the previous experiments. In addition, a structure prediction has been performed and 11 additional $BiFeO_3$ modifications have been proposed. In the next phase, an *ab initio* optimization of predicted structures has been performed and the structure of the γ-form has been elucidated. Furthermore, electronic and magnetic properties of $BiFeO_3$ were investigated using combination of experimental and theoretical methods. Spectroscopic Ellipsometry has been used to study electronic properties of $BiFeO_3$, while magnetic behavior of synthesized material was investigated by SQUID. Finally, theoretical studies were performed using a full potential linearized augmented plane-waves plus local orbital (FP(L)APW+lo) method, based on density functional theory (DFT).

1. Introduction

In the recent years multiferroics have been an intriguing study field due to their well-known magnetoelectric phenomena that offer a wide range of potentially new applications including spintronics, new data-storage media and multiple-state memories [1–5]. In the past years, bismuth ferrite ($BiFeO_3$) was one of the most studied multiferroic system with a large number of published articles for this is unique nature of $BiFeO_3$ having both (anti) ferromagnetic and ferroelectric properties, observed at room temperature [1–5].

Single phase $BiFeO_3$ has received special attention due to its ferroelectric transition temperature of 1100 K and an antiferromagnetic Néel temperature up to 640 K [1–5]. The preparation of pure single-phased $BiFeO_3$ is the main issue caused by the narrow interval of its thermal stability and formation of secondary phases, such as $Bi_{25}FeO_{40}$ and $Bi_2Fe_4O_9$ [6,7]. According to the phase diagram of Bi_2O_3–Fe_2O_3, $BiFeO_3$ is an incongruently melting compound [8,9] and the kinetics of phase formation in the Bi_2O_3–Fe_2O_3 system can easily lead to the appearance of above-mentioned impurities during the solid state reaction route [6,7]. It has also been reported that successful syntheses of single phase of $BiFeO_3$ essentially may be dependent on the purity (99.9995%) of the starting materials [7,8]. To overcome these difficulties the other methods have been developed, such as ferrioxalate precursor method [9], sol–gel process [10], co-precipitation [11,12], spark plasma sintering [13] and hydrothermal method [14,15].

At standard conditions, the experimentally known modification of bismuth ferrite crystallizes in the perovskite structure type (α-$BiFeO_3$) with rhombohedral space group *R*3*c* (no. 161). [16–18]. A very important structural parameter of the perovskite is the rotation angle of the oxygen octahedron and this angle would be 0° for a cubic perovskite with perfectly matched ionic sizes [2]. Using a Goldschmidt tolerance (G_t) factor, [19] it is possible to calculate how well the ions fit into a perovskite unit cell. For $BiFeO_3$ compound G_t =0.88 using the ionic radii of Shannon [20], where Bi^{+3} is in sixfold coordination (with the 8-fold coordination G_t, decreases) and Fe^{+3} is in sixfold coordina-

---

[*] Corresponding author.
E-mail address: dzagorac@vin.bg.ac.rs (D. Zagorac).

http://dx.doi.org/10.1016/j.ceramint.2016.10.074
Received 12 July 2016; Received in revised form 10 October 2016; Accepted 11 October 2016

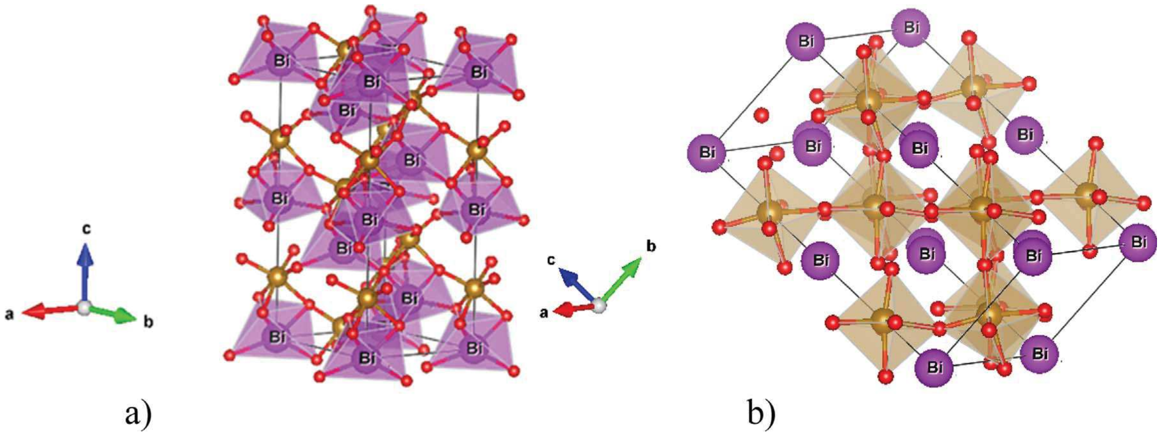

Fig. 1. Visualization of the synthesized and calculated α-$BiFeO_3$ structure: (a) sixfold coordination (CN=6) of the Bi atom by O atom; (b) sixfold coordination (CN=6) of the Fe atom by O atom.

tion with high spin. It is known from the literature that when $G_t < 1$, the oxygen octahedron must buckle in order to fit into a smaller cell [2].

Other important structural issues of $BiFeO_3$ are the anion-cation distances, angles and coordination polyhedra. There are two cations in bismuth ferrite, Bi^{3+} occupying A site, where the polarization is mostly caused by the lone pair ($6s^2$ orbital), while the magnetization comes from the B site (Fe^{3+}) [1,2]. Therefore, the α-$BiFeO_3$ modification is shown in Fig. 1, where Bi^{3+} has sixfold coordination with truncated prisms which are corner connected (Fig. 1a), while Fe^{3+} has same sixfold coordination**,** but with corner connected distorted octahedrons of oxygen (Fig. 1b). Finally, a very important structural issue is Fe–O–Fe angle, because it determines the magnetic ordering temperature and the conductivity, and in α-$BiFeO_3$ this angle is measured to be between 154 and 156° [17–21].

It has also been established that residual porosity location, microstructure, size, grain growth habit and grain boundary geometry of the sintered specimen are very important factors in determining the electrical as well as magnetic properties of $BiFeO_3$ [1–6,18–21]. However, among the large number of published papers on bismuth ferrite there are still some open questions *e.g.* synthesis of a pure single phase of $BiFeO_3$ at equlibrium or (meta)stability of non-equlibrium phases and their influence on materials properties [1–4].

2. Materials and methods

2.1. Synthesis and characterization of $BiFeO_3$ nanopowders

The preparation of pure single-phased $BiFeO_3$ is one of the main issues of this compound caused by the narrow interval of its thermal stability and formation of secondary phases [6,7]. However, in the past years many synthesis and characterizations of single crystals and nanopowders have been performed by the same authors [22–24]. The chemical compounds used in this work were bismuth nitrate ($Bi(NO_3)_3x5H_2O$), iron nitrate ($Fe(NO_3)_3x9H_2O$), and potassium hydroxide (KOH) and all the chemicals were of analytical grade. The applied synthesis route was proposed by Han [25]. The equi-molar mixtures of $Bi(NO_3)_3x5H_2O$ and $Fe(NO_3)_3x9H_2O$ were dissolved in 40 mL of KOH. The molar ratio of the alkali mineralizer was adjusted by dissolving certain amounts of KOH pellets into distilled water.

The mixture was stirred vigorously for 30 min and transferred into autoclave. The KOH concentration was set to 8 M. The hydrothermal treatments were conducted under autogenous pressure with temperature of 200 °C for 6 h. The produced powders were collected at the bottom of the autoclave after cooling to room temperature. The products were washed at least five times by repeated cycles of centrifugation in distilled water, and dispersed in ethanol by sonicating for 45 min. Subsequently, powders were obtained by evaporating ethanol in a mortar heated at 60 °C.

The structure of obtained powder was determined by X-ray powder diffraction on a Rigaku ULTIMA IV XRPD diffractometer with Cu $K\alpha_{1,2}$ radiations, at room temperature. Data for structural refinement were taken in the 2θ range 20–80°, with a step width of 0.02° 2θ and 5 s per step. The refinement was performed with the FullProf [26] computer program which adopts the Rietveld calculation method. In the present approach the grain size broadening was represented by a Lorentzian function, and strain broadening by a Gaussian function.

2.2. Computational details

Our general approach to the crystal structure prediction and optimization of structure candidates has been given in detail elsewhere [27–29]. Only the main steps of the method will be outlined and specific information will be provided. The Structure Prediction Diagnostic Software (SPuDS) [30] has been used to produce new structure candidates of $BiFeO_3$ perovskites. The SPuDS program has been developed to predict the crystal structures of perovskites, including those distorted by tilting of symmetric octahedra or caused by Jahn-Teller distortions [29–31]. The stability of the perovskite structures is determined by comparing the calculated bond valence sums and the ideal formal valences. This quantity is known as the global instability index (*GII*) and it is calculated according to the chemical composition in the 11 different Glazer tilt systems for a single B-site cation [32].

Theoretical determination and identification of the predicted structures was performed using the KPLOT program [33]. The symmetry of the predicted structures was analyzed with the algorithms SFND ("Symmetry FiNDer" [34]) and RGS („Raum Gruppen Sucher" or space group seeker [35]). Duplicate structures are removed using the CMPZ-algorithm [36] and the CCL algorithm has been used in investigation of nanosized structures [37].

The structural optimizations were performed using a full-potential linearized augmented plane waves plus local orbital (FP(L)APW+lo) method [38], and implemented in Wien2k [39], a program package based on density functional theory (DFT). General calculation parameters were kept the same in all calculations, in order to compare the stability of various crystal phases. The radii of the muffin-tin, non-overlapping spheres centered at the atomic nucleus, R_{mt}, were set to 2.07 Bohr for Bi, 1.75 bohr for Fe and 1.6 bohr for O. The parameter that determines the number of basis functions used, $R_{mt}K_{max}$, was set to 8.5, and the cutoff energy between the core and valence states was −7 Ry. Inside the muffin-tin spheres the wave functions were expanded into spherical harmonics up to l_{max}=10, and charge density was Fourier expanded up to G_{max}=20 Ry.

The Brillouin zone integration was achieved using tetrahedron method, and the number of k points was tested with respect to total energy in each case to ensure that convergence criteria were fulfilled. The volume of unit cell was optimized, and the investigated structures were relaxed until the forces acting on all atoms were less than 1 mRy/bohr. Magnetic structure of $BiFeO_3$ was addressed by the use of spin-unrestricted calculations. The exchange and correlation effects were included within the generalized gradient approximation (GGA), while “Hubbard-U” scheme with U_{eff}=3.8 eV was used for a better treatment of localized Fe d orbitals [40]. The core states were treated fully relativistic, while the valence states were treated within the scalar relativistic approximation. Self-consistency was achieved by demanding that the convergence of the integrated charge difference between the two successive iterations was less than 10^{-5} electrons. Taking into account all convergence criteria, differences in total energy between various phases were calculated with precision higher than 0.001 Ry.

The investigated structures were visualized using KPLOT [33] and VESTA [41] software. A detailed summary of computational details is presented in the Supporting information, Table S1.

2.3. Electrical and magnetic measurements

The ellipsometric measurements were performed at incidence angle θ_i=65°, in the UV–vis spectral range, using high resolution variable angle spectroscopic ellipsometer (SOPRA GES5E-IRSE) of the rotating polarizer type. Magnetic measurements were performed by using Quantum Design MPMS XL-5 SQUID magnetometer. DC magnetization measurements were carried out as a function of temperature (T=5–300 K) in the magnetic field of 100 Oe. Magnetization *vs.* magnetic field strength measurements were performed at temperatures 5 and 300 K in the fields up to 50 kOe. Summary of parameters used for experimental measurements (XRD, electrical and magnetic measurements) are presented in the Supporting information, Table S2.

3. Results and discussion

3.1. Structural properties of $BiFeO_3$ compound

3.1.1. X-Ray Powder Diffraction (XRPD) and Rietveld refinement of $BiFeO_3$

After synthesizing $BiFeO_3$ nanopowders data reported by Palewicz [21] were used as starting structural model for Rietveld refinement. The resulting x-ray powder pattern after refinement is shown in Fig. 2.

It was found out that all reflection can be indexed to a pure rhombohedral $BiFeO_3$ crystal phase which crystallize in *R3c* (no. 161) space group. However it may be seen that in representation of cell parameters and atom positions represented in Table 1, hexagonal setting have been used. Refined structure and microstructural parameters show that crystal size is in the nanometric range at about 30 nm. Reasonable values of R factors (Table 1) are an indication of good refinement and obtained results were in good agreement with previous research, where this equilibrium phase was named α- $BiFeO_3$ structure [1–4,16–18,21].

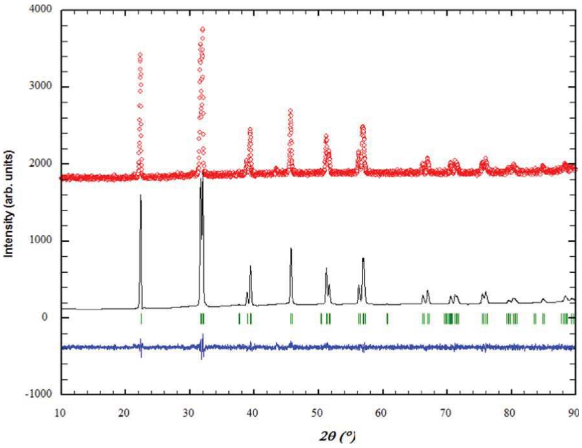

Fig. 2. XRD pattern after structural refinement procedure using Rietveld's method. Red circles denotes experimental pattern, and black line represent calculated pattern. A difference (observed-calculated) plot is shown beneath with the blue line. (For interpretation of the references to color in this figure legend, the reader is referred to the web version of this article.)

Table 1
Space group, cell parameters and atomic positions of α-$BiFeO_3$ refined structure and microstructural parameters after X-Ray Powder Diffraction (XRPD) and Rietveld refinement. In addition, Bi^{3+} and Fe^{3+} coordination number (CN), Bi–O and Fe–O distances has been presented.

Structure parameter	**Value**
Space group	*R3c* (no. 161)
Cell parameters	a=b=5.5870 (7) Å c=13.8898 (2) Å α=β=90°, γ=120°
Crystallite size (nm)	29.3
Strain (%)	0.25
Goodness of refinement	R_{wp}=7.08 R_p=5.5 R_{exp}=5.55 χ^2=1.6273

Element	**x**	**y**	**z**	**Occupancy**	**Temperature factor**
Bi	0.0000	0.0000	0.0000	1.000	1.024
Fe	0.0000	0.0000	0.221(4)	1.000	0.658
O	0.447(3)	0.018(3)	0.953(6)	1.000	1.042

Modification	Space group	Distance Bi–O	Bi^{3+} CN and mean distance	Distance Fe–O	Fe^{3+} CN and mean distance
α-BiFeO3	*R3c*	3×2.339 (1)	6	3×1.967(1)	6
		3×2.433 (2)	2.386 (2)	3×2.0937 (1)	2.0302(2)

3.1.2. Structure prediction of $BiFeO_3$ perovskites

Beside experimentally observed α-$BiFeO_3$ perovskite structure (see Fig. 2 and Table 1), SPuDS software was used to obtain 11 additional perovskite-related structure candidates marked from $BiFeO_3$-(1) to $BiFeO_3$-(11), in different space groups and sorted according to their global instability index (*GII*) values (see Table 2). Based on the *GII* criterion, the most stable $BiFeO_3$ perovskite structure closest to the experimentally observed one is $BiFeO_3$-(1) in the space group $R\bar{3}c$, with *GII*=0.00047 (see Table 2). As the number of the structure candidates increases, their stability decreases, and the most unstable structure is

Table 2
Calculated values of the global instability index (*GII*) and tilt system for 11 $BiFeO_3$ modifications using SPuDS software.

Name	**Space group**	**Tilt system**	**GII (a.u.)**
BiFeO3-(1)	*R-3c*	$a^-a^-a^-$	0.00047
BiFeO3-(2)	*Pnma*	a–b+a–	0.01123
BiFeO3-(3)	*Imma*	$a^ob^-b^-$	0.01592
BiFeO3-(4)	P_4/mbm	$a^oa^oc^-$	0.09595
BiFeO3-(5)	I_4/mcm	$a^oa^oc^-$	0.09595
BiFeO3-(6)	$P4_2/nmc$	$a^+a^+c^-$	0.09783
BiFeO3-(7)	C_2/c	$a^-b^-b^-$	0.15273
BiFeO3-(8)	*Cmcm*	$a^+b^oc^-$	0.17060
BiFeO3-(9)	*Im-3*	$a^+a^+a^+$	0.24293
BiFeO3-(10)	I_4/mmm	$a^ob^+b^+$	0.27773
BiFeO3-(11)	*Pm-3m*	$a^oa^oa^o$	0.74669

the cubic $Pm\bar{3}m$ perovskite $BiFeO_3$-(11) with GII=0.47669 (see Table 2). A summary of all predicted structure candidates is presented in the Supporting information (Table S3).

According to the literature data, at approximately 825 °C there is a first-order phase transition from α-$BiFeO_3$ modification to a high-temperature *β*-$BiFeO_3$ phase [2,4,42]. Although, there is disagreement about the exact symmetry of the β-$BiFeO_3$ modification [2,44–49], it was observed that at high temperatures this *α-β* phase transition changes the properties of $BiFeO_3$ from ferroelectric to paraelectric compound. In order to further investigate this effect the first part of our research was focused on structural properties of $BiFeO_3$.

Recent experimental [47–49] and theoretical results [50] show high temperature rhombohedral modification of $BiFeO_3$ in the space group $R\bar{3}c$ (no. 167). This recently discovered structure corresponds to our $BiFeO_3$-(1) predicted modification (see Table 2 and Supporting information). At similar temperatures and with influence of high pressure (up to 10 GPa) another candidate for a *β*-$BiFeO_3$ phase has been observed in the experiment [18,43,51] and *ab initio* calculations [52–55] showing orthorhombic space group *Pnma* (no. 62). This particular structure corresponds to our $BiFeO_3$-(2) modification. An alternative orthorhombic structure $BiFeO_3$-(3) is next in the line according to GII ranking (see Table 2) showing *Imma* space group (no. 74)**,** and has never been reported before.

Furthermore, alternative tetragonal phases of $BiFeO_3$ have been previously observed [45,56] and calculated [52,57] at high temperatures. Our structure prediction also favors tetragonal phase in $BiFeO_3$ compound, and four tetragonal modifications have been shown: $BiFeO_3$-(4) in space group *P4/mbm* (no. 127), $BiFeO_3$-(5) in space group *I4/mcm* (no. 140), $BiFeO_3$-(6) in space group $P4_2/nmc$ (no. 137), and $BiFeO_3$-(10) in space group *I4/mmm* (no. 139) (see Table 2 and Supporting information). The first three have the same *GII* index, while $BiFeO_3$-(10) has much higher values and therefore is more unstable.

In the same temperature range, additional monoclinic [18,45,46,58–60] and rhombohedral [47–50,58,61] structures in different space groups have been reported. Our study also show the formation of additional monoclinic $BiFeO_3$-(9) modification in the space group *C2/c* (no. 15) and orthorhombic $BiFeO_3$-(8) in the space group *Cmcm* (no. 63) (see Table 2 and Supporting information). However, their *GII* indexes show that these structures are quite unstable at equilibrium conditions indicating the low possibility of observing these structures at low temperatures and/or low pressures.

At high temperatures above 930 °C, a cubic γ-$BiFeO_3$ phase has been observed [51,62] and calculated in the previous research [40,52]. This γ-$BiFeO_3$ structure corresponds to our $BiFeO_3$-(11) modification showing space group $Pm\bar{3}m$ (no. 221). Alternative cubic structure could exist in the space groups $Im\bar{3}$ (no. 204) (see Table 2) or $Fm\bar{3}m$ (no. 225).[52]. However, $BiFeO_3$ is highly unstable at the high temperatures of the β-γ transition region and it rapidly decomposes into more stable phases $Bi_2Fe_4O_9$ or Fe_2O_3[1–6]. Therefore, there are still many open questions regarding *γ*-$BiFeO_3$ phase, as well as other $BiFeO_3$ modifications, observed in the transition regions at high temperatures and/or pressures. In order to address some of these questions *ab initio* calculations have been performed in this study.

3.1.3. Ab initio structure optimization

The set of structure candidates generated using the procedures described above, as well as equilibrium structure from experimental synthesis, were submitted to the *ab initio* local optimization. These local optimizations were performed using full potential linearized augmented plane-waves plus local orbital (FP(L)APW+lo) method based on density functional theory (DFT). The exchange and correlation effects were included within the generalized gradient approximation (GGA+*U*). A summary of our results is shown in Tables 3 and 4, where the structural parameters and total energies of all optimized structures on *ab initio* level are presented.

As a starting point for the study of the electronic structure, the structural parameters of the synthesized α-$BiFeO_3$ phase were optimized on *ab initio* level (see Figs. 1, 2 and Table 1). Obtained values amounted to $a=b=5.55$ Å and $c=13.84$ Å, which is in good agreement with our experimental results from the Rietveld refinement and previous experiments [1–4,16–18,21].

Although, the $BiFeO_3$-(1) in the space group *R*-3*c* is the closest structure to equilibrium α-$BiFeO_3$ according to *GII* index, the index value is close to 0, which indicates unstable structure that will be easily converted to equilibrium α-$BiFeO_3$ structure and may not be found to exist as a separate minimum. This is later confirmed in our *ab initio* calculations, which are in agreement with previous calculations [29]. The reason for this particular discrepancy is found in the SPuDS software which does not penalize Bi–O and O–O distances that are too short [63], resulting in a GII value unrealistically low. Therefore, the next in line was considered, which is $BiFeO_3$-(2) in the *Pnma* space group and with *GII*=0.01123. Our $BiFeO_3$-(2) structure was successfully compared to previous experimental [18,43,51] and theoretical findings [52–55] of β-$BiFeO_3$ structure using CMPZ algorithm [36] implemented in the KPLOT software [33] (see Fig. 3).

The $BiFeO_3$-(2) structure can be described by edge and corner connected dodecahedrons of oxygen around bismuth, with eightfold coordination (CN=8) of the Bi^{3+} cation by O^{2-} anion, and corner connected tilted octahedrons of oxygen around iron, with sixfold coordination (CN=6) of the Fe^{3+} cation by O^{2-} anion. It is known that at approximately 825 °C there is a first-order phase transition from *α*-$BiFeO_3$ modification to a high-temperature β-$BiFeO_3$ phase, and this rhombohedral to orthorombic phase transition is common in perovskites [2,4,43,63]. There are some literature results describing α→β phase transition and magnetic properties of $BiFeO_3$ compound with Fe octahedron tilting [1,2]. However, it is important to point Bi^{3+} coordination changing from six fold in α-$BiFeO_3$ to eight fold in β-$BiFeO_3$ modification, which can largely influence polarization of $BiFeO_3$ compound (see Supporting information, Table S4) [1,2].

With further increase of temperature above 930 °C, a cubic γ-$BiFeO_3$ phase has been observed in the experiment [51,62], which we have successfully compared to our $BiFeO_3$-(11) predicted structure, and optimized on *ab initio* level. Refined structure parameters of cubic γ-$BiFeO_3$ phase are published in Table 3 for the first time to our knowledge. The γ-$BiFeO_3$ structure can be described by face sharing cuboctahedrons of oxygen around bismuth, with 12-fold coordination (CN=12) of the Bi^{3+} cation by O^{2-} anion, and corner connected perfect octahedra of oxygen around iron, with six fold coordination (CN=6) of the Fe^{3+} cation by O^{2-} anion (see Fig. 4). It is also known from the literature that the distortions away from the ideal perovskite cubic structure occur according to various tilt systems, resulting in a change of symmetry (see Table 2) [29,63,64]. Therefore, according to these results as one of the probable high temperature and/or pressure transition route of $BiFeO_3$ from rhombohedral α-$BiFeO_3$ (CN=6) over intermediate orthorhombic β-$BiFeO_3$ (CN=8) to cubic γ-$BiFeO_3$ (CN=12) may be proposed Fig. 4.

In addition, our structure prediction favors tetragonal phase in $BiFeO_3$ compound and alternative tetragonal phases of $BiFeO_3$ have been previously observed [45,56] and calculated [52,57] at high temperatures. $BiFeO_3$-(4) in space group *P4/mbm* (no. 127) has been optimized on *ab initio* level and results are shown in Tables 3, 4 and Fig. 5. This is the first report of this kind of tetragonal phase of $BiFeO_3$ to be proposed to our knowledge. The $BiFeO_3$-(4) is a very good candidate energetically (see Table 4) located between β and γ phases, and structurally, with 8 fold coordination of bismuth by oxygen atom (see Table S4 in the Supporting information) similar to the β phase, and tetragonal symmetry, closer to the cubic γ phase. Thus, it might be considered that tetragonal $BiFeO_3$-(4) modification can be good candidate along β→γ phase transition in $BiFeO_3$. On the other hand, other tetragonal candidates are less realistic, *e.g.* $BiFeO_3$-(6) modification increases Fe coordination number to 10 (CN=10).

Table 3
Structural data of the most favorable $BiFeO_3$ perovskite modifications before and after *ab inito* optimization using GGA+*U* method.

Modification, space group and Wyckoff position	Cell parameters (Å), unit-cell volume (Å^3) and fractional coordinates[a]	Cell parameters (Å), unit-cell volume (Å^3) and fractional coordinates optimized with FP (L)APW +lo	Birch–Murnaghan EOS bulk moduli (GP)
α-$BiFeO_3$	a=5.5870, c=13.8898	a=5.550 c=13.840	B_0=112.61
*R*3*c*(161)	V=375.47	V_0=369.192, Vp=61.53	BP=6.56
Bi 6*a*	0 0 0	0 0 0	
Fe 6*a*	0 0 0.2208	0 0 0.7755	
O 18*b*	0.4474 0.0175 0.9528	0.08363 0.31631 0.37511	
β-$BiFeO_3$	a=5.6008, b=7.7667,	a=5.662, b=7.852,	B_0=140.88
Pnma(62)	c=5.395	c=5.455	BP=3.778
	V=234.720	V_0=242.519, Vp=60.63	
Bi 4*c*	0.5595 1/4 0.5205	0.5551 1/4 0.0119	
Fe 4*b*	1/2 0 0	1/2 0 1/2	
O1 4*c*	−0.0180 1/4 0.4016	0.9761 1/4 0.9099	
O2 8*d*	0.2957 0.0492 0.7008	0.2976 0.0452 0.2049	
$BiFeO_3$-(4)	a=5.3610, c=4.0309	a=5.4212, c=4.11635	B_0=148.86
*P*4/*mbm*(127)	V=115.851	V_0=120.577, Vp=60.29	BP=2.530
Bi 2*c*	0 1/2 1/2	0 1/2 1/2	
Fe 2*a*	0 0 0	0 0 0	
O1 2*b*	0 0 1/2	0 0 1/2	
O2 4*g*	0.1596 0.6596 0	0.18917 0.68917 0	
γ-$BiFeO_3$	a=4.0309	a=3.9538	B_0=162.96
$Pm\bar{3}m$(221)	V=65.496	V_0=61.808, Vp=61.81	BP=4.112
Bi 1*b*	1/2 1/2 1/2	1/2 1/2 1/2	
Fe 1*a*	0 0 0	0 0 0	
O 3*d*	0 0 1/2	0 0 1/2	

[a] In the first column are the results of the experimental synthesis, while others represent predicted structures using SpuDS software.

Table 4
Ground-state energy and stability compared to α-$BiFeO_3$ (AFM) phase calculated using GGA+*U* method. The total energies (E_0) per formula unit shown in second column are in Rydberg (Ry), while energy difference show in third column is converted to electronvolts (eV).

Modification	E_O/f.u. (Ry)	E_O-$E_{O\ (BiFeO3\text{-}eq)}$ (eV)
α-$BiFeO_3$ (AFM)	−46160.15377	0
β-$BiFeO_3$	−46160.12874	+0.34055
$BiFeO_3$-(4)	−46160.09749	+0.76573
γ-$BiFeO_3$	−46160.05814	+1.30111

Finally, *GII* ranking from BVC calculations has been compared with *ab initio* energy ranking using GGA calculations (see Supporting information, Table S5). We note that predicted structures optimized using GGA method had great overlap with *GII* ranking which is in agreement with previous theoretical studies [29]. The existence of predicted $BiFeO_3$ structures has been further confirmed by high precision GGA+*U* corrected method as shown in Table 3. It may be seen that α→β phase transition is accompanied by a sudden volume contraction (see Table 3), which has been observed in the literature [51,62]. The transition is also accompanied by a peak in the dielectric constant [2,62] which has been taken as an indication of a ferroelectric–paraelectric transition [2]. However, volume expansion was detected at β→γ phase transition (see Table 3), which has not been reported before. The decrease of cation-anion mean distance should be point out if second coordination polyhedron (see Supporting information, Table S4) was considered. Total energies and stability of predicted $BiFeO_3$ structures compared to equilibrium α-$BiFeO_3$ (AFM) phase has been shown in Table 4. Again, it is clear that *GII* stability ranking of

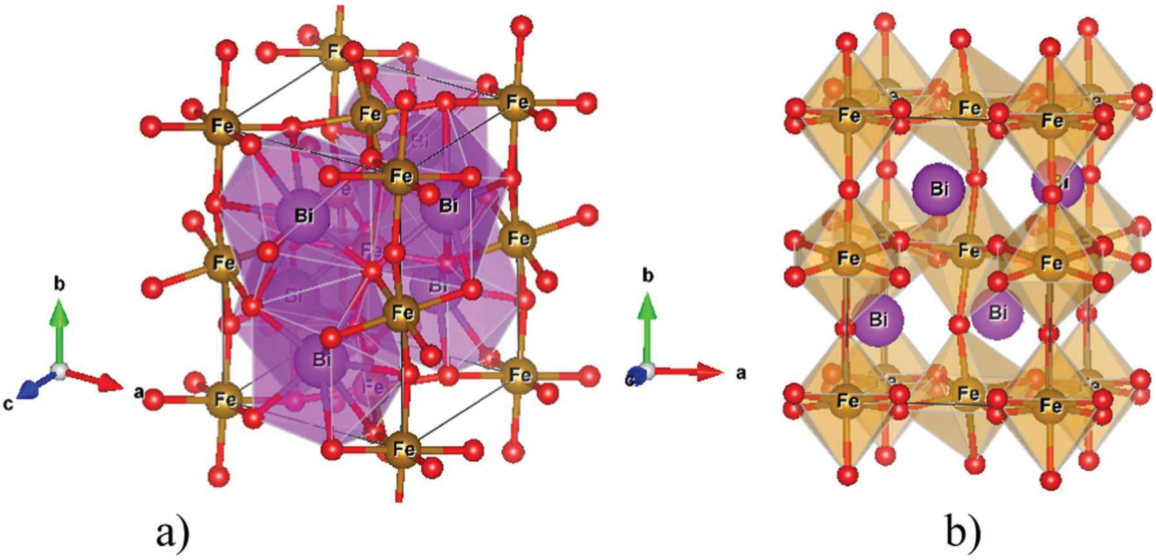

Fig. 3. Visualization of the calculated β-$BiFeO_3$ structure: (a) eight fold coordination (CN=8) of the Bi^{3+} cation by O^{2-} anion; (b) six fold coordination (CN=6) of the Fe^{3+} cation by O^{2-} anion.

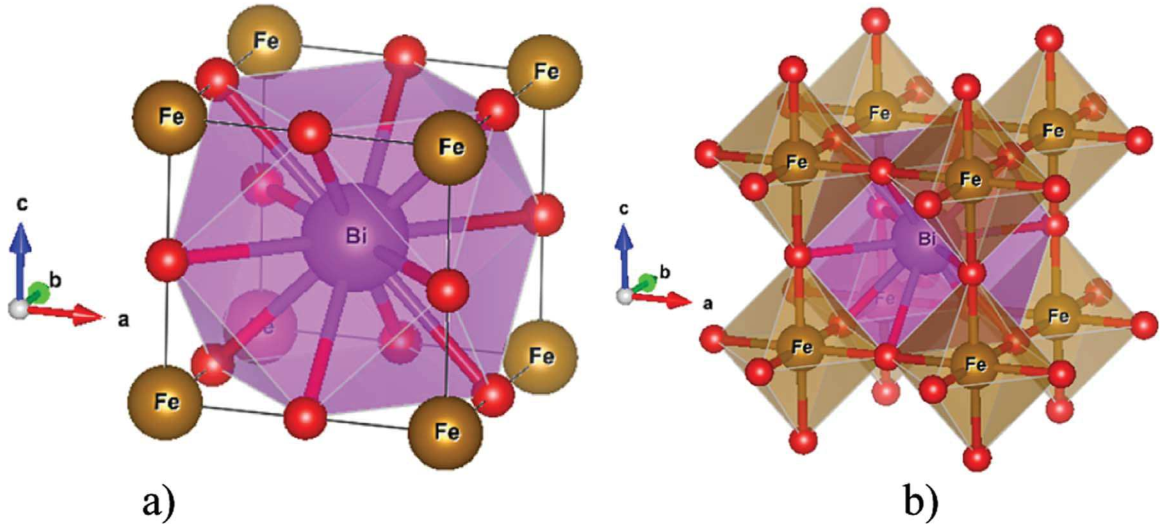

Fig. 4. Visualization of the calculated cubic γ- $BiFeO_3$ structure: (a) twelve fold coordination (CN=12) of the Bi atom by O atom; (b) six fold coordination (CN=6) of the Fe atom by O atom.

predicted $BiFeO_3$ structures overlap with *ab initio* total energy ranking at GGA and GGA+U level of calculation.

3.2. Electronic and magnetic properties of $BiFeO_3$

3.2.1. Spectroscopic ellipsometry

The pseudo-dielectric function ⟨ε⟩ represents an expectation value obtained directly from the measurements of ellipsometric angles Ψ and Δ. Assuming the two-phase model approximation (air/$BiFeO_3$ nanoparticles), the pseudo-dielectric function spectra was calculated directly from the complex reflectance ratio $\rho=\tan(\psi)\, e^{i\Delta}$ using the Eq. [1]:

$$\langle\varepsilon\rangle = \varepsilon_t = \sin^2\theta_i\left[1 + \tan^2\theta_i\left(\frac{1-\rho}{1+\rho}\right)^2\right] \tag{1}$$

Measurement of pseudo-dielectric function enables direct determination of the extinction coefficient k of the bismuth ferrite powder which is shown in the inset of Fig. 6. Literature data showed that the bismuth ferrite has the band gap value around 2.77 eV [63]. In order to obtain the band gap energy Tauc Law was used and the plot of $(\alpha E)^2$ *vs* E is presented in Fig. 6, where α is the absorption coefficient (α=4πk/λ) and E is the photon energy. The linear extrapolation of $(\alpha E)^2$ to zero gives a band gap value at 2.71 eV, as shown in Fig. 6., which is in good agreement with the data obtained from the literature [63].

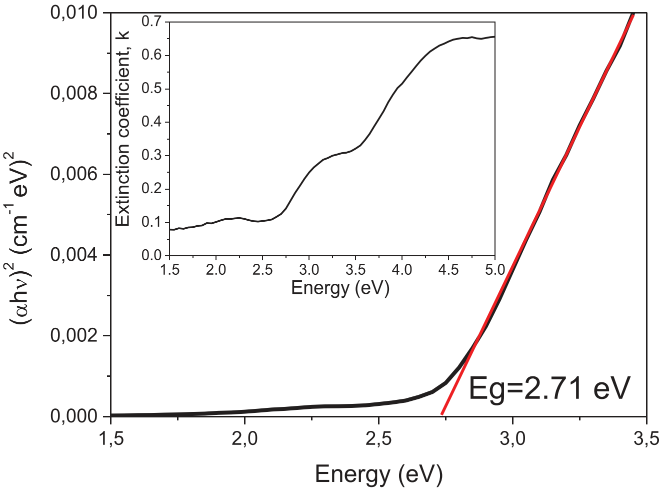

Fig. 6. Tauc plots *vs*. photon energy *E* for direct band gap (*Eg*) transition together with a linear extrapolation of $(\alpha E)^2$. Inset shows the complex extinction coefficient (n, k) of the bismuth ferrite powder obtained from spectroscopic ellipsometry.

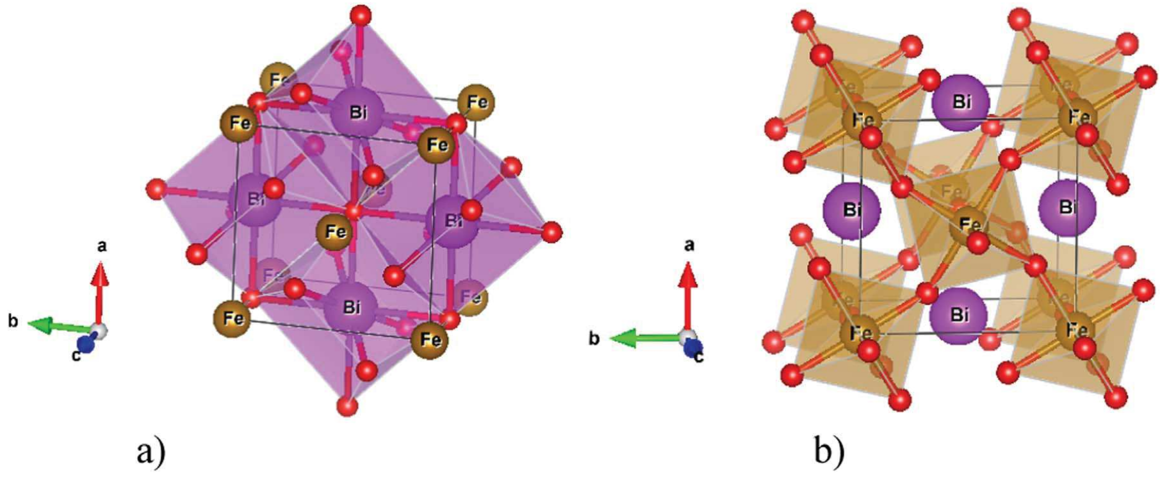

Fig. 5. Visualization of the calculated $BiFeO_3$-4 structure: (a) eightfold coordination (CN=8) of the Bi atom by O atom; (b) sixfold coordination (CN=6) of the Fe atom by O atom.

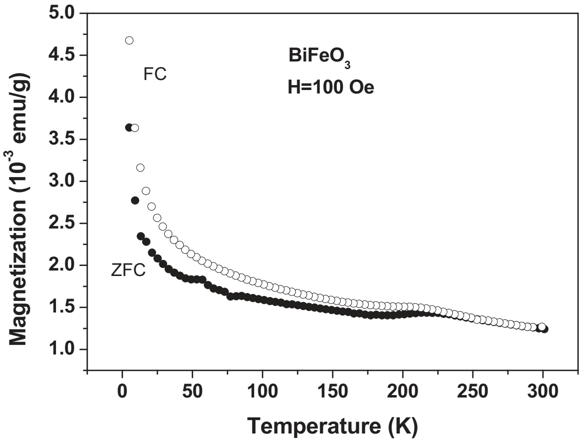

Fig. 7. Temperature dependence of BiFeO$_3$ magnetization.

3.2.2. Magnetic properties investigation using SQUID

Temperature dependence of DC magnetization for BiFeO$_3$ measured in the magnetic field of 100 Oe is depicted in Fig. 7. Two measurement procedures are applied: on heating after zero-field cooling (ZFC), as well as on cooling in the magnetic field (FC). It can be seen that system at about T_N=220 K shows pronounced maximum which can be assigned to the phase transition from antiferromagnetic to the paramagnetic state (Néel temperature). This temperature is due to nanometric dimensions of the particles significantly lower than those reported for bulk samples (T_N=651 K) [64]. Below Néel temperature ZFC and FC curves are splitting, and magnetization for both branches, increases with the temperature decrease. The same behavior was also observed for the samples obtained by different synthesis procedures [65,66], and can be explained due to a small presence of paramagnetic Fe^{3+} ions. These ions probably belong to the small amount of Bi$_{25}$FeO$_{39}$ phase which is formed during BiFeO$_3$ synthesis. At T=50 K, ZFC branch shows cusp which represents transition to super-spin glass state. Similar transition was also observed for doped and undoped BiFeO$_3$ nanopowders [67].

M(H) dependence recorded at 5 K and 300 K is shown in the Fig. 8. M(H) curve recorded at 5 K shows weak hysteresis behavior, without reaching saturation up to 5 T, is a sign of antiferromagnetic ordering. However, the small coercive field of about 300 Oe (see Fig. 8 inset) speaks in favor of weak ferromagnetic ordering. It is well known that this arrangement occurs when the particle diameter is less than the period of the long-range cycloidal spiral (62 nm) which is characteristic structure for this compound [65,68]. At the room temperature M(H) curve is linear and M(5 T)=0.36 emu/g (0.02 μ_B/f.u.) which is in accordance with the literature data for the BiFeO$_3$ nanoparticles of the similar diameter size [65].

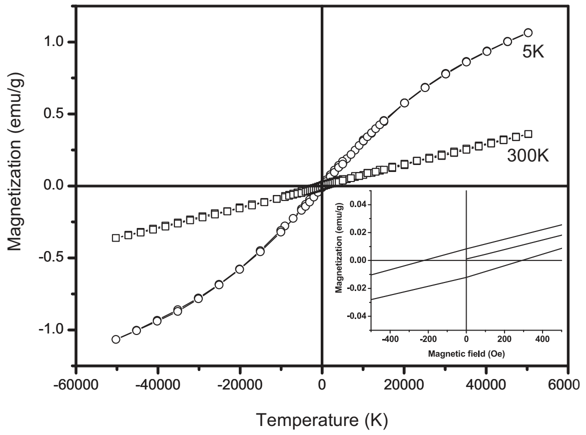

Fig. 8. Magnetization curve *vs.* applied magnetic field at 5 K and room temperature. Inset: Details of M(H) behavior at 5 K.

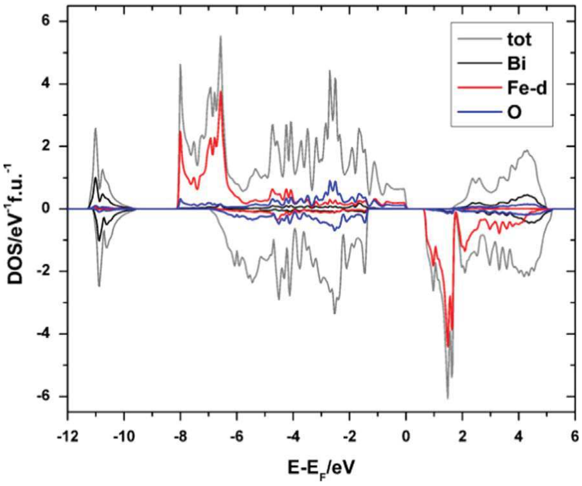

Fig. 9. Spin-polarized total and partial density of states for the ferromagnetic BiFeO$_3$; spin-up states shown as positive and spin-down states shown as negative.

3.2.3. Calculations on *ab initio* level

Previous studies reported that the calculated electronic ground state strongly depends on the nature of magnetic ordering, even when spin-polarization was introduced into the calculations [40,50]. Electronic structure of α-BiFeO$_3$ is studied by observing the behavior of its spin-up and spin-down density of states (DOS) around the Fermi level. Fig. 9 presents total DOS, as well as DOS decomposed according to individual Bi and O atoms, in addition to Fe *d* electron states for the ferromagnetic BiFeO$_3$. Density of states is presented for both spin-up and spin-down states, and by convention Fermi level is set to 0 eV. Total density of states shows the effect of spin-polarization in the region of occupied states, mainly from −8 to 0 eV, but also in the region of unoccupied states, from 0.5 to 5 eV. When total DOS is decomposed according to individual atoms of studied compound, it is evident that the spin-polarization is expressed primarily in Fe. This was expected, considering the magnetic nature of this atom. In order to address this, *d* electron states of Fe are extracted and presented in the same Figure. Two pronounced peaks of spin-up and spin-down *d* states are present in the region from −8 eV to −6 eV, and from 0.5 to 5 eV, respectively. It should also be indicated that Bi states are located in the band about 10 eV below the Fermi level, while O states are broader and found overlapping with the Fe *d* states.

In addition to studying the density of states, magnetic moment per Fe atom was also calculated. It amounts to 3.98 μB, which is in good agreement with experimental value for the cubic ferromagnetic phase, 3.75*(2)* μB [69].

In Fig. 10, total DOS, as well as DOS decomposed according to individual Bi, O and Fe atoms are presented for the BiFeO$_3$ obtained in spin-polarized calculations by imposing opposite orientations of magnetic moments on Fe atoms and therefore resulting zero magnetic moment of the unit cell, which is in agreement with magnetic measurements presented in previous chapter.

Bi states are located in the band about 10 eV below the Fermi level, similar to Fig. 9, while O states are broader and found overlapping with the Fe states. Calculated band gap is 2.1 eV using DFT-GGA, which is in good agreement with our electronic spectroscopy, concerning that calculated value is strongly dependent on the value of effective potential used in calculations and size of the measured particles, which is in agreement with other experimental and theoretical results. [1–6,40,50,70].

Furthermore, based on the Bader's theory of atoms in molecules [71], charge transfer in the studied compound is calculated. The values

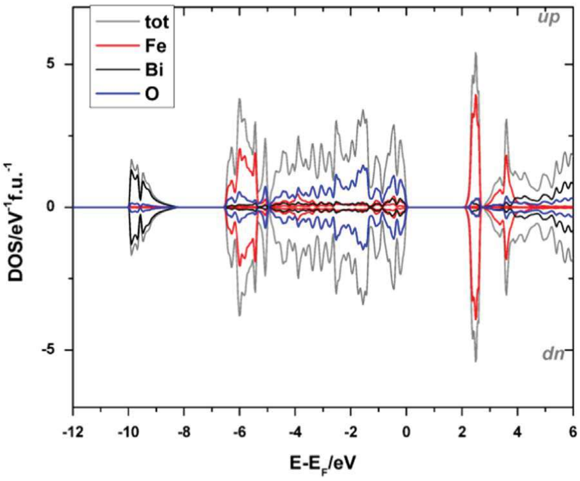

Fig. 10. Spin up (positive) and spin-down (negative) total and partial density of states for the antiferromagnetic $BiFeO_3$.

of Bader's charges are equal to the difference in the number of electrons of given atom and number of electrons in the atomic basin belonging to that atom in the studied compound. For the studied α-$BiFeO_3$ modification, obtained values of the Bader's charge were 1.86 for Fe and Bi, and −1.24 for O. This result indicates that the equal charge transfer occurred from both Fe and Bi metals to O atom, and is in agreement with general trend that Bader's charge follows electronegativity of the atoms [72].

4. Conclusions

Nanosized bismuth ferrite powder has a potential application in the production of lead free piezoelectric materials for actuators as well as magnetoelectric sensors. Here we show simple, low-costing and energy-saving hydrothermal method, which has advantages over the conventional methods. $BiFeO_3$ powders were synthesized using $Bi(NO_3)_3{\cdot}5H_2O$ and $Fe(NO_3)_3{\cdot}9H_2O$ as starting material and 8 M KOH as mineralizer. It was detected that all reflections can be indexed to a pure rhombohedral α-$BiFeO_3$ crystal phase which crystallizes in *R*3*c* (no. 161) space group. Refined structure and microstructural parameters show that the crystal size is in the nanometric range at about 30 nm. The structure prediction method has been used and 11 additional perovskite-related structure candidates in different space groups were obtained. After *ab initio* optimization equilibrium α-$BiFeO_3$ modification was confirmed by experimental results. Besides, β-$BiFeO_3$ and γ-$BiFeO_3$ modification at elevated temperatures and/or pressures were identified as well as their respective transition route. Calculations proved to be in good agreement with previous experimental and theoretical results.

In addition, a novel tetragonal $BiFeO_3$–4 phase which has never been reported before, was identified in this study. Finally, electromagnetic properties of $BiFeO_3$ were investigated using combination of experimental and theoretical methods. Temperature dependence of magnetization shows antiferromagnetic-paramagnetic phase transition at T_N=220 K, while below this temperature weak ferromagnetic ordering is detected. The results of this study offer an overall conclusion that the local magnetic properties of pure $BiFeO_3$ nanoparticles mainly depend on the particle size and their diverse morphology due to the different preparation methods and annealing temperatures. DFT calculations on electronic and magnetic properties of $BiFeO_3$ show good agreement with respective measurements studied here, previous experimental and theoretical work.

Acknowledgements

Authors would like to thank M. Jovanovic, M. Prekajski and J. Zagorac for valuable discussions. This work has been supported by the Grant nos. 45012 and 171001 from the Ministry of Education, Science and Technological Development of the Republic of Serbia.

Appendix A. Supporting information

Supplementary data associated with this article can be found in the online version at doi:10.1016/j.ceramint.2016.10.074.

References

[1] L.W. Martin, S.P. Crane, Y.-H. Chu, M.B. Holcomb, M. Gajek, M. Huijben, C.-H. Yang, N. Balke, R. Ramesh, Multiferroics and magnetoelectrics: thin films and nanostructures, J. Phys.: Condens. Matter 20 (2008) (2008) 434220–434233.
[2] G. Catalan, J.F. Scott, Physics and applications of bismuth ferrite, Adv. Mater. 21 (2009) 2463–2485.
[3] T. Rojac, A. Bencan, B. Malic, G. Tutuncu, J.L. Jones, J.E. Daniels, D. Damjanovic, $BiFeO_3$ ceramics: processing, electrical, and electromechanical properties, J. Am. Ceram. Soc. 97 (2014) 1993–2011.
[4] J. Wang, J.B. Neaton, H. Zheng, V. Nagarajan, S.B. Ogale, B. Liu, D. Viehland, V. Vaithyanathan, D.G. Schlom, U.V. Waghmare, N.A. Spaldin, K.M. Rabe, M. Wuttig, R. Ramesh, Epitaxial $BiFeO_3$ multiferroic thin films heterostructures, Science 299 (2003) 1719–1722.
[5] J.R. Teague, R. Gerson, W.J. James, Dielectric hysteresis in single crystal $BiFeO_3$, Solid State Commun. 8 (1970) 1073–1074.
[6] T. Lottermoser, T. Lonkai, U. Amann, D. Hohlwein, J. Ihringer, M. Fiebig, Magnetic phase control by an electric field, Nature 430 (2004) 541–544.
[7] W. Eerenstein, N.D. Mathur, J.F. Scott, Multiferroic and magnetoelectric materials, Nature 442 (2006) 759–765.
[8] R. Ramesh, N.A. Spaldin, Multiferroics: progress and prospects in thin films, Nat. Mater. 6 (2007) 21–29.
[9] S. Ghosh, S. Dasgupta, A. Sen, H.S. Maiti, Low temperature synthesis of bismuth ferrite nanoparticles by a ferrioxalate precursor method, Mater. Res. Bull. 40 (2005) 2073–2079.
[10] J.K. Kim, S.S. Kim, W.-J. Kim, Sol-gel synthesis and properties of multiferroic $BiFeO_3$, Mater. Lett. 59 (2005) 4006–4009.
[11] H. Ke, W. Wang, Y. Wang, J. Xu, D. Jia, Z. Lu, Y. Zhou, Factors controlling pure-phase multiferroic $BiFeO_3$ powders synthesized by chemical co-precipitation, J. Alloy. Compd. 509 (2011) 2192–2197.
[12] T.P. Comyn, D.F. Kanguwe, J. He, A.P. Brown, Synthesis of bismuth ferrite lead titanate nano-powders and ceramics using chemical co-precipitation, J. Eur. Ceram. Soc. 28 (2008) 2233–2238.
[13] R. Mazumder, D. Chakravarty, D. Bhattacharya, A. Sen, Spark plasma sintering of $BiFeO_3$, Mater. Res. Bull. 44 (2009) 555–559.
[14] X.-Z. Chen, Z.-C. Qiu, J.-P. Zhou, G. Zhu, X.-B. Bian, P. Liu, Large-scale growth and shape evolution of bismuth ferrite particles with a hydrothermal method, Mater. Chem. Phys. 126 (2011) 560–567.
[15] B. Liu, B. Hu, Z. Du, Hydrothermal synthesis and magnetic properties of single-crystalline $BiFeO_3$ nanowires, Chem. Commun. 47 (2011) 8166–8168.
[16] J.M. Moreau, C. Michel, R. Gerson, W.J. James, Ferroelectric $BiFeO_3$ X-ray and neutron diffraction study, J. Phys. Chem. Solids 32 (1971) 1315.
[17] F. Kubel, H. Schmid, Structure of a ferroelectric and ferroelastic mono domain crystal of the perovskite $BiFeO_3$, Acta Crystallogr. B 46 (1990) 698–702.
[18] H.J. Feng, Magnetism and electronic properties of $BiFeO_3$ under lower pressure, J. Magn. Magn. Mater. 322 (2010) 3755–3759.
[19] V.M. Goldschmidt, Naturwissenschaften 14 (1926) 477–485.
[20] R.D. Shannon, Revised effective ionic radii and systematic studies of interatomic distances in halides and chalcogenides, Acta Crystallogr. A 32 (1976) 751–767.
[21] A. Palewicz, R. Przeniosło, I. Sosnowska, A.W. Hewat, Atomic displacements in $BiFeO_3$ as a function of temperature: neutron diffraction study, Acta Crystallogr. 63 (2007) 537–544.
[22] B. Matovic, J. Pantic, J. Lukovic, M. Cebela, S. Dmitrovic, M. Mirkovic, M. Prekajski, A novel reduction-oxidation synthetic route for hafnia, Ceram. Int. 42 (2016) 615–620.
[23] B. Matovic, J. Pantic, M. Prekajski, N. Stankovic, T. Minovic, M. Cebela, Synthesis and characterization of Pr_6O_{11} nanopowders, Ceram. Int. 39 (2013) 3151–3155.
[24] M.M. Mirkovic, T.D. Lazarevic Pasti, A.M. Dosen, M.Z. Cebela, A.A. Rosic, B.Z. Matovic, B.M. Babic, Adsorption of malathion on mesoporous monetite obtained by mechanochemical treatment of brushite, RSC Adv. 6 (2016) 12219–12225.
[25] S.H. Han, K.S. Kim, H.G. Lee, H.W. Kang, J.S. Kim, C.I. Cheon, Synthesis and characterization of multiferroic $BiFeO_3$ powders fabricated by hydrothermal method, Ceram. Int. 36 (2010) 1365–1372.
[26] J. Rodriguez-Carvajal, Recent advances in magnetic structure determination by neutron powder diffraction, Physica B 192 (1993) 55–69.
[27] J.C. Schön, M. Jansen, First step towards planning of syntheses in solid-state chemistry: determination of promising structure candidates by global optimization, Angew. Chem. Int. Ed. 35 (1996) 1286–1304 (in English).

[28] D. Zagorac, J.C. Schön, J. Zagorac, M. Jansen, Prediction of structure candidates for zinc oxide as a function of pressure and investigation of their electronic properties, Phys. Rev. B 89 (2014) 075201.

[29] J. Zagorac, D. Zagorac, A. Zarubica, J.C. Schön, K. Djuris, B. Matovic, Prediction of possible $CaMnO_3$ modifications using an ab initio minimization data mining approach, Acta Crystallogr. B 70 (2014) 809.

[30] M.W. Lufaso, P.M. Woodward, Prediction of the crystal structures of perovskites using the software program SpuDS, Acta Crystallogr. B 57 (2001) 725–738.

[31] M.W. Lufaso, P.M. Woodward, Jahn–Teller distortions, cation ordering and octahedral tilting in perovskites, Acta Crystallogr. B 60 (2004) 10–20.

[32] A. Salinas-Sanchez, J.L. Garcia-Muñoz, J. Rodriguez-Carvajal, R. Saez-Puche, J.L. Martinez, Structural characterization of R_2BaCuO_5 (R=Y, Lu, Yb, Tm, Er, Ho, Dy, Gd, Eu and Sm) oxides by X-ray and neutron diffraction, J. Solid State Chem. 100 (1992) 201–211.

[33] R.Hundt, KPLOT-program, University of Bonn, Germany 1979, Version 9, 6.15, ⟨www.crystalimpact.com/download/kplot.htm⟩, 2012.

[34] R. Hundt, J.C. Schön, A. Hannemann, M. Jansen, Determination of symmetries and idealized cell parameters for simulated structures, J. Appl. Crystallogr. 32 (1999) 413–416.

[35] A. Hannemann, R. Hundt, J.C. Schön, M. Jansen, A new algorithm for space-group determination, J. Appl. Crystallogr. 31 (1998) 922–928.

[36] R. Hundt, J.C. Schön, M. Jansen, CMPZ–an algorithm for the efficient comparison of periodic structures, J. Appl. Crystallogr. 39 (2006) 6–16.

[37] R. Hundt, J.C. Schön, S. Neelamraju, J. Zagorac, M. Jansen, CCL: an algorithm for the efficient comparison of clusters, J. Appl. Crystallogr. 46 (2013) 587–593.

[38] J.P. Perdew, K. Burke, M. Ernzerhof, Generalized gradient approximation made simple, Phys. Rev. Lett. 77 (1996) 3865–3868.

[39] P. Blaha, K. Schwarz, G. K. H. Madsen, D. Kvasnicka, J. Luitz, WIEN2k, An augmented plane wave+local orbitals program for calculating crystal properties, Karlheinz Schwarz, Techn. Universitat Wien, Austria, 2001

[40] I.A. Kornev, S. Lisenkov, R. Haumont, B. Dkhil, L. Bellaiche, Finite-temperature properties of multiferroic, Phys. Rev. Lett. 99 (2007) 227602.

[41] K. Momma, F. Izumi, VESTA: a three-dimensional visualization system for electronic and structural analysis, J. Appl. Crystallogr. 41 (2008) 653–658.

[42] D.C. Arnold, K.S. Knight, F.D. Morrison, P. Lightfoot, Ferroelectric-paraelectric transition in $BiFeO_3$: crystal structure of the orthorhombic β phase, Phys. Rev. Lett. 102 (2009) 027602.

[43] R. Haumont, J. Kreisel, P. Bouvier, F. Hippert, Phonon anomalies and the ferroelectric phase transition in multiferroic $BiFeO_3$, Phys. Rev. B 73 (2006) 132 101.

[44] R. Haumont, I.A. Kornev, S. Lisenkov, L. Bellaiche, J. Kreisel, B. Dkhil, Phase stability and structural temperature dependence in powdered multiferroic $BiFeO_3$, Phys. Rev. B 78 (2008) 134108.

[45] S.M. Selbach, T. Tybell, M.-A. Einarsrud, T. Grande, The ferroic phase transitions of $BiFeO_3$, Adv. Mater. 20 (2008) 3692–3696.

[46] S.M. Selbach, T. Tybell, M.-A. Einarsrud, T. Grande, Size-dependent properties of multiferroic $BiFeO_3$ nanoparticles, Chem. Mater. 19 (2007) 6478–6484.

[47] A.G. Gavriliuk, V.V. Struzhkin, I.S. Lyubutin, S.G. Ovchinnikov, M.Y. Hu, P. Chow, Another mechanism for the insulator-metal transition observed in Mott insulators, Phys. Rev. B 77 (2008) 155112.

[48] O.E. Gonzalez-Vazquez, J. Iniguez, Pressure-induced structural, electronic, and magnetic effects in $BiFeO_3$, Phys. Rev. B 79 (2009) 064102.

[49] R. Palai, R.S. Katiyar, H. Schmid, P. Tissot, S.J. Clark, J. Robertson, S.A.T. Redfern, G. Catalan, J.F. Scott, The beta phase of multiferroic bismuth ferrite and its beta-gamma metal-insulator transition, Phys. Rev. B 77 (2008) 014110.

[50] P. Ravindran, R. Vidya, A. Kjekshus, H. Fjellvåg, O. Eriksson, Theoretical investigation of magnetoelectric behavior in $BiFeO_3$, Phys. Rev. B 74 (2006) 224412.

[51] V.I. Zinenko, M.S. Pavlovskii, Lattice dynamics of $BiFeO_3$: the untypical behavior of the ferroelectric instability under hydrostatic pressure, JETP Lett. 87 (2008) 288–291.

[52] O. Dieguez, O.E. Gonzalez-Vazquez, J.C. Wojdel, J. Iniguez, First-principles predictions of low-energy phases of multiferroic $BiFeO_3$, Phys. Rev. B 83 (2011) 094105.

[53] H.D. Megaw, C.N.W. Darlington, Geometrical and structural relations in the rhombohedral perovskites, Acta Crystallogr. A 31 (1975) 161–173.

[54] Y. Liu, K.-K. Wang, L.-H. Ni, Z.-H. Ren, G. Xu, C.-L. Song, G.-R. Han, Soft-mode driven tetragonal-to-monoclinic phase transition in multiferroic $BiFeO_3$, Phys. Lett. A 376 (2012) 3303–3307.

[55] J.H. Feng, F. Liu, First-principles prediction of coexistence of magnetism and ferroelectricity in rhombohedral Bi_2FeTiO_6, Phys. Lett. A 372 (2008) 1904–1909.

[56] R.C. Lennox, M.C. Price, W. Jamieson, M. Jura, A. Daoud-Aladine, C.A. Murray, C. Tang, D.C. Arnold, Strain driven structural phase transformations in dysprosium doped $BiFeO_3$ ceramics, J. Mater. Chem. C 2 (2014) 3345–3360.

[57] A.A. Belik, H. Yusa, N. Hirao, Y. Ohishi, E. Takayama- Muromachi, Structural properties of multiferroic $BiFeO_3$ under hydrostatic pressure, Chem. Mater. 21 (2009) 3400–3405.

[58] R.J. Zeches, M.D. Rossell, J.X. Zhang, A.J. Hatt, Q. He, C.-H. Yang, A. Kumar, C.H. Wang, A. Melville, C. Adamo, G. Sheng, Y.-H. Chu, J.F. Ihlefeld, R. Erni, C. Ederer, V. Gopalan, L.Q. Chen, D.G. Schlom, N.A. Spaldin, L.W. Martin, R. Ramesh, A strain-Driven morphotropic phase boundary in $BiFeO_3$, Science 326 (2009) 977–980.

[59] J.F. Scott, R. Palai, A. Kumar, M.K. Singh, N.M. Murari, N.K. Karan, R.S. Katiyar, New phase transitions in perovskite oxides: $BiFeO_3$, $SrSnO_3$, and Pb $(Fe_{2/3}W_{1/3})_{1/2}$ $Ti_{1/2}O_3$, J. Am. Ceram. Soc. 91 (2008) 1762–1768.

[60] I.D. Brown, The Chemical Bond in Inorganic Chemistry, Oxford University Press, 2002.

[61] J.-G. Park, M.D. Le, J. Jeong, S. Lee, Structure and spin dynamics of multiferroic $BiFeO_3$, J. Phys. Condens. Matter 26 (2014) 433202.

[62] M. Polomska, W. Kaczmarek, Z. Pajak, Electric and magnetic properties of $(Bi_{1-X}La_X)FeO_3$ solid solutions, Phys. Status Solidi A 23 (1974) 567–574.

[63] A. Kumar, R. Rai, N. Podraza, S. Denev, M. Ramirez, Y. Chu, L. Martin, J. Ihlefeld, T. Heeg, J. Schubert, D. Schlom, J. Orenstein, R. Ramesh, R. Collins, J. Musfeldt, V. Gopalan, Linear and nonlinear optical properties of $BiFeO_3$, Appl. Phys. Lett. 92121915, 2008.

[64] P. Suresh, S. Srinath, Observation of high coercivity in multiferroic lanthanum doped $BiFeO_3$, J. Alloy. Compd. 554 (2013) 271–276.

[65] T.J. Park, G.C. Papaefthymiou, G.C. Viescas, A.R. Moodenbaugh, S.S. Wong, Size-dependent magnetic properties of single-crystalline multiferroic $BiFeO_3$ Nanoparticles, Nano Lett. 7 (2007) 766–772.

[66] S.T. Zhang, M.H. Lu, D. Wu, Y.F. Chen, N.B. Ming, Larger polarization and weak ferromagnetism in quenched $BiFeO_3$ ceramics with a distorted rhombohedral crystal structure, Appl. Phys. Lett. 87 (2005) 262907.

[67] X.Z. Chen, R.L. Yang, J.P. Zhou, X.M. Chen, Q. Jiang, P. Liu, Dielectric and magnetic properties of multiferroic $BiFeO_3$ ceramics sintered with the powders prepared by hydrothermal method, Solid State Sci. 19 (2013) 117–121.

[68] R. Safi, H. Shokrollahi, Physics, chemistry and synthesis methods of nanostructured bismuth ferrite ($BiFeO_3$) as a ferroelectro-magnetic material, Prog. Solid State Chem. 40 (2012) 6–15.

[69] W. Sosnowska, W. Schäfer, K.H. Kockelmann, Andersen, I.O. Troyanchuk, Crystal structure and spiral magnetic ordering of $BiFeO_3$ doped with manganese, Appl. Phys. A 74 (2002) S1040.

[70] K.A. McDonnell, N. Wadnerkar, N.J. English, M. Rahman, D. Dowling, Photo-active and optical properties of bismuth ferrite ($BiFeO_3$): an experimental and theoretical study, Chem. Phys. Lett. 572 (2013) 78–84.

[71] R.W. Bader, A quantum theory of molecular structure and its applications, Chem. Rev. 91 (1991) 893–928.

[72] K. Batalović, V. Koteski, D. Stojić, Hydrogen storage in martensite Ti–Zr–Ni Alloy: a density functional theory study, J. Phys. Chem. C 117 (2013) 26914–26920.

Available online at www.sciencedirect.com

ScienceDirect

Ceramics International 40 (2014) 13409–13418

CERAMICS INTERNATIONAL

www.elsevier.com/locate/ceramint

Synthesis of pure and La-doped anatase nanopowders by sol–gel and hydrothermal methods and their efficiency in photocatalytic degradation of alprazolam

A. Golubović[a], N. Tomić[a], N. Finčur[b], B. Abramović[b], I. Veljković[c], J. Zdravković[d], M. Grujić-Brojčin[a,*], B. Babić[e], B. Stojadinović[a], M. Šćepanović[a]

[a]*Center for Solid State Physics and New Materials, Institute of Physics, University of Belgrade, Pregrevica 118, 11080 Belgrade-Zemun, Serbia*
[b]*Department of Chemistry, Biochemistry and Environmental Protection, Faculty of Sciences, University of Novi Sad, Trg D. Obradovića 3, 21000 Novi Sad, Serbia*
[c]*Institute for Multidisciplinary Research, University of Belgrade, Kneza Višeslava 1, 11000 Belgrade, Serbia*
[d]*Innovation Center, Faculty of Technology and Metallurgy, University of Belgrade, Karnegijeva 4, 11000 Belgrade, Serbia*
[e]*Institute of Nuclear Sciences "Vinča", University of Belgrade, 11001 Belgrade, Serbia*

Received 31 January 2014; received in revised form 17 April 2014; accepted 12 May 2014
Available online 20 May 2014

Abstract

Pure and La^{3+} doped titanium dioxide (TiO_2) nanopowders were obtained by sol–gel and hydrothermal methods. A precursor was titanium tetrachloride and concentrations of dopants were 0.5 and 1.0 mol%. Procedures of both methods were the same, up to the last part of synthesis (the transformation from the mother liquor to oxide nanopowders), in order to find the influence of applied methods on the properties of nanopowders. XRD results have shown that all synthesized nanopowders were in the anatase phase. It was seen from DSC measurements that anatase to rutile phase transition took place at a higher temperature with a higher concentration of dopant (La^{3+}). The samples obtained by the sol–gel method had a higher temperature of phase transition than related samples obtained by the hydrothermal method. Nanopowder properties have been related to the photocatalytic activity, tested in degradation of the pharmaceutical alprazolam.

Keywords: A. Powders: chemical preparation; B. Porosity; C. Optical properties; D. TiO_2

1. Introduction

Advanced Oxidation Processes (AOPs) have been developed to remove the contaminants of drinking water and industrial effluents [1,2]. Among them, heterogeneous photocatalysis using TiO_2 is regarded as a promising method for the purification and treatment of both contaminated air and water [3,4] due to its performance such as low cost, non-toxicity, chemical stability, availability and the strong oxidizing power of its photogenerated holes. The size of the titanium dioxide particles is an important factor affecting the photocatalytic activity of this catalyst [5,6]. Therefore, it is not surprising that much research has been focused upon the reduction of the particle size. Nano-semiconductor materials doped with rare-earth elements have the ability of strong adsorption, good thermal stabilization, electron-type conductivity and high photocatalytic activity [7–9].

TiO_2 can be produced by many different methods and among them we are particularly interested for "wet" methods where the most representative are sol–gel and hydrothermal methods. Because of that, in this work pure and La-doped TiO_2 nanoparticles were prepared by sol–gel and hydrothermal methods. The content of La^{3+} in our investigation was 0.5 and 1 mol%, as these concentrations have been established as the most appropriate in photocatalytic applications [9,10].

---

*Corresponding author. Tel.: +38 1113713023; fax: +38 1113160531.
E-mail address: myramyra@ipb.ac.rs (M. Grujić-Brojčin).

http://dx.doi.org/10.1016/j.ceramint.2014.05.060
0272-8842/

In recent years, pharmaceuticals have been present in the aquatic environment as a consequence of their use in very high quantities throughout the world. Pharmaceuticals are large group of organic compounds which can enter the water system by means of direct disposal and excretion. They may be present in surface water at low concentration levels, depending on the efficiency of wastewater treatments. Despite these low concentrations, the ubiquity of pharmaceuticals in the aquatic environment together, with their persistent biological activities explains the concern over this specific group of water contaminants [11–13]. Until now, a large diversity of pharmaceuticals has been found in the environment: analgesics, antibiotics, antiepileptics, β-blockers, blood–lipid regulators, antidepressants, anxiolytics, sedatives, contraceptives, etc. [14].

Alprazolam (8-chloro-1-methyl-6-phenyl-4H-[1,2,4]triazole[4,3,-α]-[1,4]-benzodiazepine, CAS no. 28981-97-7, $C_{17}H_{13}ClN_4$, M_r=308.765) is a short-acting anxiolytic, which belongs to the benzodiazepine class of psychoactive drugs. It has unique clinical and neurochemical spectrum of action among benzodiazepine full agonists [15,16]. Alprazolam acts on the brain and central nervous system to produce a calming effect [17] and it is mainly used to treat anxiety disorders or anxiety associated to symptoms of depression [18]. The extensive use of alprazolam is a consequence of its antidepressant effect, its synergic action as an anxiolytic in combination with antidepressants in patients with advanced cancer, in the treatment of pathologies that imply anxiety disorders of chronic intensity as the social phobia and other psychosocial pathologies [16].

Since pharmaceuticals are being introduced into the environment on a continuous basis and its continuous input and persistence to the water system may result in a potential risk for aquatic and terrestrial organisms, special attention has recently been paid to the degradation of pharmaceuticals as a means of water decontamination. The aim of this work is to estimate the efficiency of pure and La^{3+} doped anatase nanopowders, synthesized by two different routes, in photocatalytic degradation of alprazolam, as well as to investigate the variations in anatase structure with La^{3+} doping.

2. Experimental details

2.1. Synthesis

All chemicals are used without further purifications.

2.2. Sol–gel method (SG)

$TiCl_4$ (99.0%, pure, Merck) was used as a precursor. An appropriate amount of $TiCl_4$ was dissolved in distilled water under vigorous stirring on an ice-bath. To obtain the hydrogel the aqueous solution of NH_4OH (29% Carlo Erba), was added under careful control of the pH value of the solution to achieve the alkaline conditions (pH ~ 9). After aging in mother liquor for 5 h the hydrogel was filtered and washed out with distilled water until the complete removal of chloride ions (the common analytical procedure with $AgNO_3$). Afterwards the obtained hydrogel was converted to its ethanol–gel by anhydrous ethanol. Alcogel was placed in a vessel, dried at 280 °C and calcined at a temperature of 550 °C for 4 h.

2.3. Hydrothermal method (HT)

The whole procedure was the same as the sol–gel process until the hydrogel was obtained (including the aging in mother liquor for 5 h). Then hydrogel was placed in a steel pressure vessel (autoclave) under a controlled temperature. The reaction of hydrothermal synthesis was carried out at 200 °C for 24 h. After that, the vessel contains were filtered and washed with distilled water until complete removal of chloride ions. The last step to obtain TiO_2 nanoparticles was drying at 105.5 °C for 72 h.

2.4. Characterization methods

Samples of pure and La^{3+}-doped TiO_2 obtained by both methods were analyzed by XRD using a Stoe Stadi MP diffractometer (CuKα_1 radiation, primary beam Ge monochromator, linear PSD detector, Bragg–Brentano geometry). Data were collected at every 0.01° in the 10–90° 2θ angular range, using a counting time of 80 s/step. The Fullprof computer program was used. The Williamson–Hall Method [19] was applied for determination of the average microstrain and the mean crystallite sizes.

Composition/quality of TiO_2 has been analyzed on SEM (JEOL JSM-6460LV, with the operating voltage of 20 keV) equipped with an EDS (INCAx-sight) detector and "INAx-stream" pulse processor (Oxford Instruments).

Non-contact atomic force microscopy (NC-AFM) measurements were carried out using Omicron B002645 SPM probe VT AFM 25.

The TG/DSC analysis of samples consisted in pure and La-doped TiO_2 (anatase) synthesized by sol–gel method and hydrothermal method was carried out on an SDT Q600 instrument (TA Instruments) up to 1100 °C in N_2 atmosphere (flow rate: 100 $cm^3\ min^{-1}$; heating rate: 10 °C min^{-1}). The pure indium and sapphire were used for the calibration of temperature and DSC signal, respectively.

The porous structure of anatase samples has been evaluated from adsorption/desorption isotherms of N_2 measured on TiO_2 samples, at −196 °C, using the gravimetric McBain method. The main parameters of the porosity such as specific surface area and pore volume have been estimated by the Brunauer–Emmett–Teller (BET) method and α_s-plot [20]. The pore size distribution has been estimated from hysteresis sorption data by the Barret–Joyner–Halenda (BJH) method [21].

Raman scattering measurements of TiO_2 samples was performed in the backscattering geometry at room temperature in the air using a Jobin-Yvon T64000 triple spectrometer, equipped with a confocal microscope and a nitrogen-cooled charge coupled device detector. The spectra were excited by 514.5 nm line of Ar^+/Kr^+ ion laser with output power less than 5 mW to avoid local heating due to laser irradiation.

2.5. Measurements of photocatalytic activity

The photocatalytic activity of the nanopowders was evaluated in the process of the degradation of the solution of alprazolam (Sigma-Aldrich). The photocatalytic degradation was carried out in a cell described previously [22]. A 125 W high-pressure mercury lamp (Philips, HPL-N, emission bands in the UV region at 304, 314, 335 and 366 nm, with maximum emission at 366 nm), together with an appropriate concave mirror, was used as the radiation source. Experiments were carried out using 20 cm^3 of 0.03 mmol dm^{-3} of alprazolam solution and the photocatalyst loading was 1.0 mg cm^{-3}. The aqueous suspension was sonicated (50 Hz) in the dark for 15 min before illumination, to uniformly disperse the photocatalyst particles and attain adsorption equilibrium. The suspension thus obtained was thermostated at 25 ± 0.5 °C in a stream of O_2 (3.0 cm^3 min^{-1}), and then irradiated. During irradiation, the mixture was stirred at a constant rate under continuous O_2 flow. In order to determine the reproducibility of the results, at least duplicated runs were carried out for each condition for averaging the results, and the reproducibility of kinetic measurements was 3–10%.

For the UFLC–DAD kinetic studies of alprazolam photodegradation, aliquots of 0.50 cm^3 were taken from the reaction mixture at the beginning of the experiment and at regular time intervals. Aliquot sampling caused a maximum volume variation of ca. 10% in the reaction mixture. The suspensions containing photocatalyst were filtered through a Millipore (Milex-GV, 0.22 μm) membrane filter. After that, a 10-μl sample was injected and analyzed on UFLC-Shimadzu equipped with an Eclypse XDB-C18 column (150 mm × 4.6 mm i.d., particle size 5 μm, 25 °C). The UV/vis DAD detector was set at 222 nm (wavelength of alprazolam maximum absorption). The mobile phase (flow rate 1 cm^3 min^{-1}) was a mixture of acetonitrile (99.8%, J. T. Baker) and water (40:60, v/v), the water being acidified with 0.1% H_3PO_4 (85%, Sigma-Aldrich).

3. Results and discussion

3.1. Synthesis

In the sol–gel synthesis experimental parameters were the same as in our previous experiments [23] except the duration of calcination of 4 h. It was found that using the duration of 4 h to synthesize TiO_2 nanoparticles (anatase phase) have the best photocatalytic properties in photodegradation of metoprolol [22] within samples with various durations of calcination (from 1 to 7 h) and our samples have mentioned set-up of experimental parameters.

In the hydrothermal synthesis experimental parameters were temperature of 200 °C (as in [24,25], although Ti-butoxide was the precursor, and the duration was 24 h (as in [26]). The charge from the vessel in autoclave was the same as in the case of sol–gel synthesis before the processes of drying and calcination due to reveal a influence of type of synthesis on a properties of obtained TiO_2 nanoparticles.

3.2. X-ray diffraction

The XRD patterns of pure TiO_2 and doped with La^{3+} doped nanopowders, synthesized by sol–gel and hydrothermal

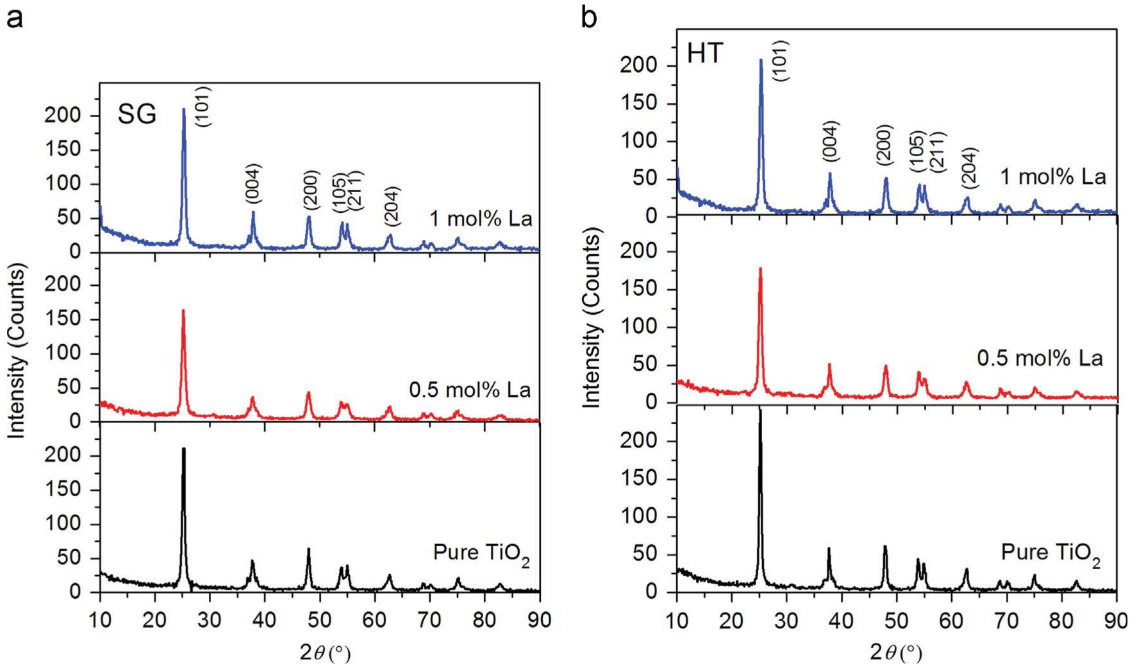

Fig. 1. XRD patterns of pure TiO_2 and La-doped TiO_2 nanopowders synthesized by sol–gel (a) and hydrothermal (b) methods. Characteristic diffractions of anatase phase given in parentheses.

Table 1
Crystallite size, lattice parameters, and average strain of pure and La^{3+} doped TiO_2 (anatase) obtained by sol–gel and hydrothermal methods.

	Crystallite size (nm)	Lattice parameters (nm)		Strain (%)
		a (=*b*)	*c*	
SG				
Pure TiO_2	16	0.3788 (6)	0.9526 (4)	0.12
0.5 mol% La	15	0.3795 (7)	0.9518 (9)	0.29
1 mol% La	15	0.3786 (5)	0.9462 (1)	0.86
HT				
Pure TiO_2	19	0.3796 (8)	0.9530 (0)	0.13
0.5 mol% La	17	0.3794 (4)	0.9536 (2)	0.24
1 mol% La	18	0.3791 (6)	0.9501 (6)	0.08

method are presented in Fig. 1. The diffraction peaks present in all samples coincide to the anatase TiO_2 structure (JCPDS card 21-1272, space group I41/amd), which is clearly indicated by the main anatase reflection at $2\theta \sim 25°$. Their positions are slightly shifted, indicating a change in lattice parameters in comparison to the bulk values for anatase ($a_0 = 0.37852$ nm, $c_0 = 0.95139$ nm), as shown in Table 1.

The average crystallite size of anatase nanoparticles, estimated by the Williamson–Hall method, is slightly greater in samples obtained by the hydrothermal method than those obtained by the sol–gel method, as listed in Table 1. The crystallite size in the range from 15 to 19 nm has been estimated from all diffraction patterns. Significant difference in microstrain has not been found in pure TiO_2 samples synthesized by both methods. Similarly, for both samples doped with 0.5% La^{3+}, corresponding values of microstrain were close, whereas much smaller microstrain (0.08%) has been detected in the sample doped with 1% La^{3+} obtained by the hydrothermal method in comparison to the sample synthesized by the sol–gel method (0.86%).

3.3. TG/DSC analysis

The TG analysis of pure, 0.5 mol% La^{3+} doped TiO_2 and 1 mol% La^{3+} doped TiO_2 nanopowders, obtained by SG and HT method has been performed. After heating the sample, from the room temperature up to 1100 °C, the total mass loss for both pure TiO_2 was 3.5%, while for the 0.5 mol% La doped TiO_2 and 1 mol% La doped TiO_2 synthesized either using SG or HT method total weight loss was around 5%. Unlike pure TiO_2, the doped samples have a slightly larger mass loss. It could be found that there are two main stages for all samples, where the first step occurs from room temperature up to 200 °C for pure TiO_2 and for doped samples up to 180 °C. For this step the rate of mass loss is around 2.5% and it could be ascribed to the release of some adsorbed water. The second step occurs up to 450 °C and it ranges from 1% for pure up to 1.3% for all doped samples and it could mainly resulted from the combustion decomposition of some organic matters.

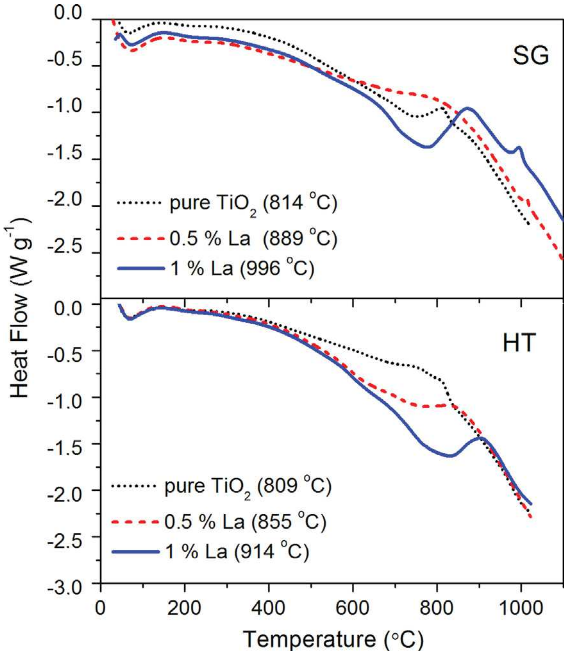

Fig. 2. DSC curves of pure and La-doped TiO_2 synthesized using sol–gel (a) and hydrothermal (b) methods.

In Fig. 2 DSC curves containing two broad exothermic peaks in general are presented. According to these curves, a wide peak at about 100 °C could be found, corresponding to the earlier mentioned desorption of water, as well as one highly overlapped releasing thermal peak with maxima around 350 °C, corresponding to the combustion decomposition of the organic matters. The interval from ~800 °C to 1000 °C has exhibited an obvious decalescence phenomena, possibly resulting from the phase transition from anatase to rutile [27]. Independently, in samples obtained both by SG or HT methods, the increasing of temperature of anatase to rutile the phase transition with increased La^{3+} concentration has been observed.

It can be concluded from the DSC curves of pure (undoped) TiO_2 nanopowders that the temperature of anatase to rutile phase transitions in these samples are almost the same, regardless of the process of synthesis. Also, the DSC peaks maxima are shifted towards higher temperatures with increasing concentration of La^{3+} in the samples synthesized by both methods. Samples obtained by the SG treatment (Fig. 3a) show higher increasing of temperature of anatase to rutile phase transition with increasing La^{3+} concentration, than samples obtained by the HT treatment (Fig. 3b). This phenomenon is directly related to the conditions of synthesis and the stoichiometric composition of the product, due to ability of La dopant to greatly inhibit anatase to rutile phase transition [28]. Generally, the temperature of the phase transition can be varied as a function of the preparation condition of the hydroxide gel (in our case, mother liquor). Namely, it has been found by studying XRD data of TiO_2 obtained by the sol–gel method that several weak peaks from the rutile phase appear in the sample calcined at 600 °C [29].

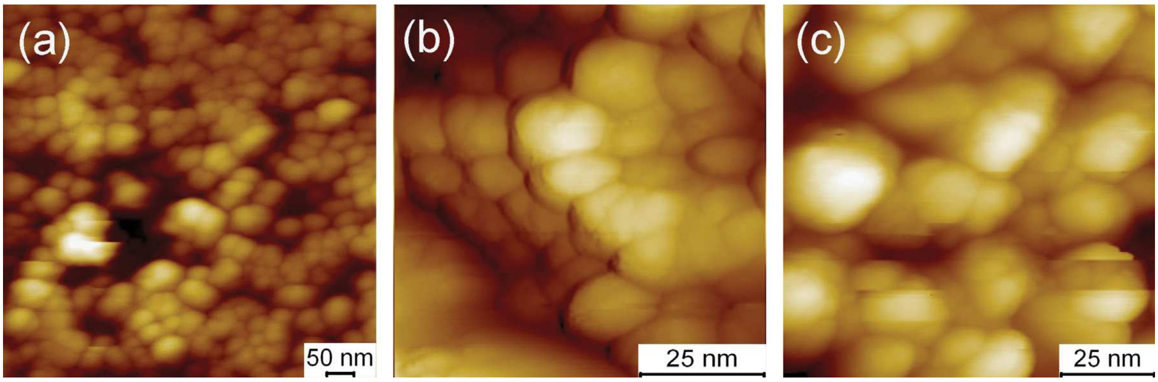

Fig. 3. The AFM images of (a) pure and (b) 0.5 wt% La doped TiO_2 synthesized by SG method, and (b) HT-synthesized TiO_2, nanopowder doped with 0.5 wt% La.

Table 2
EDS results for some TiO_2 nanopowders synthesized by SG and HT methods.

TiO_2 sample	O (wt%)	Ti (wt%)	La (wt%)	Total (wt%)
Sol–gel method				
Pure	43.28	56.72	0.00	100.00
0.5% La	47.99	52.01	0.00	100.00
1% La	43.56	55.97	0.47	100.00
Hydrothermal method				
Pure	43.16	56.84	0.00	100.00
0.5% La	43.02	56.98	0.00	100.00
1% La	43.03	56.17	0.80	100.00

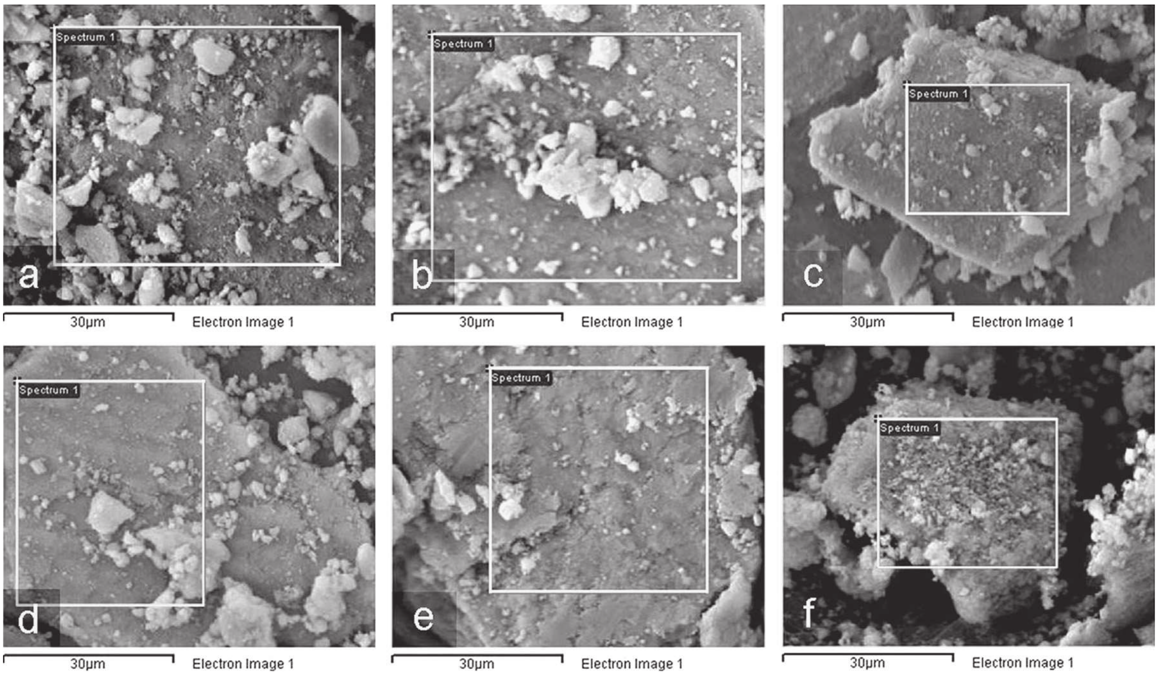

Fig. 4. The SEM images corresponding to EDS results of (a) pure, (b) 0.5 wt La doped and (c) 1 wt% La doped SG synthesized TiO_2 nanopowders; (d) pure, (e) 0.5 wt La doped and (f) 1 wt% La doped HT synthesized TiO_2 nanopowders.

3.4. Atomic force microscopy

The NC-AFM images of pure and 0.5 mol% La-doped TiO_2 samples synthesized by SG method are shown in Figs. 3(a) and (b), respectively. In Fig. 3(c) the image of 0.5 mol% La-doped TiO_2 nanopowder synthesized by the HT method is presented. It can be observed from these images that samples consist of small, spherical nanoparticles (~15–20 nm), as well as greater agglomerated particles, with slightly smaller particles in the SG synthesized doped sample. These results are in good agreement with size estimation obtained by XRD analysis (Table 1).

3.5. SEM-EDS

The chemical composition of pure and La-doped nanopowders synthesized by SG and HT methods has been estimated by the EDS method (Table 2). The micrographs of all synthesized samples are shown in Fig. 4, whereas the EDS spectra, collected from corresponding framed areas, are presented in Fig. 5. The oxygen weight percent is similar in SG and HT synthesized nanopowders (∼43 wt%), and above the value in stoichiometric TiO_2 (40 wt%). The La content has been detected in the samples doped with 1 wt% of La: 0.47 wt% in the SG synthesized sample, and 0.80 wt% in the HT synthesized sample. In the samples doped with 0.5 wt% of La, synthesized by both methods, the content of La could not be detected.

3.6. BET

In order to study the effects of synthesis method and La-doping on the pore structure and adsorption abilities of TiO_2 nanopowders, BET nitrogen sorption measurements have been carried out. The parameters of porosity, determined from the α_s-plots [20] obtained from the standard nitrogen adsorption isotherms have shown that the samples are fully mesoporous. In Fig. 6 the pore size distributions for pure and La-doped TiO_2 nanopowders synthesized by sol–gel and hydrothermal methods, obtained by the BJH model

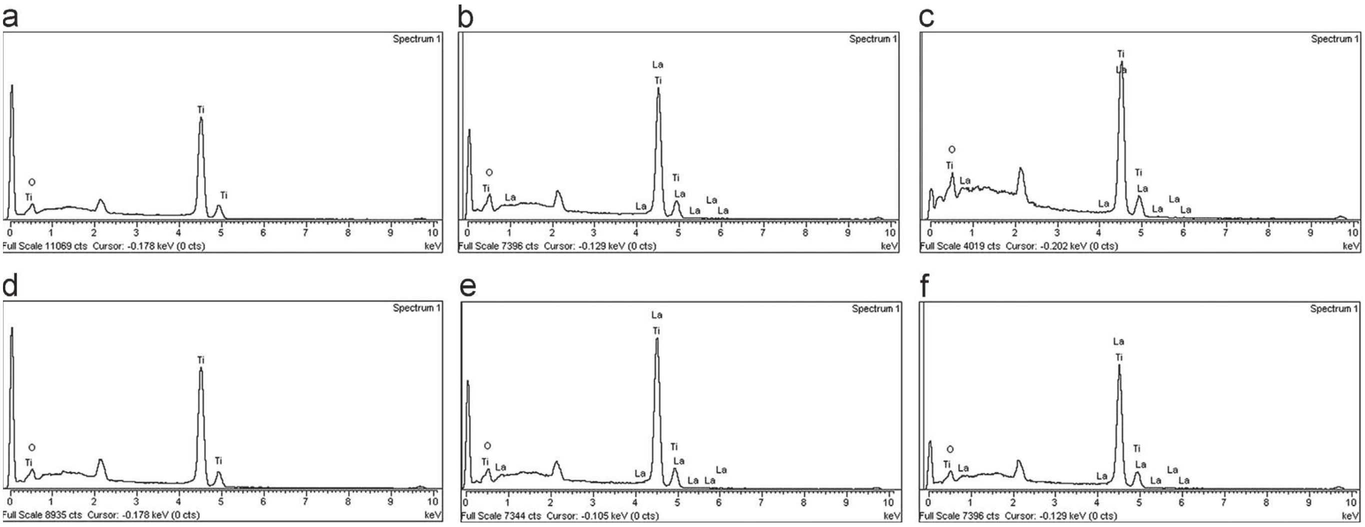

Fig. 5. The EDS spectra of (a) pure, (b) 0.5 wt% La doped and (c) 1 wt% La doped SG synthesized TiO_2 nanopowders; (d) pure, (e) 0.5 wt% La doped and (f) 1 wt% La doped HT synthesized TiO_2 nanopowders.

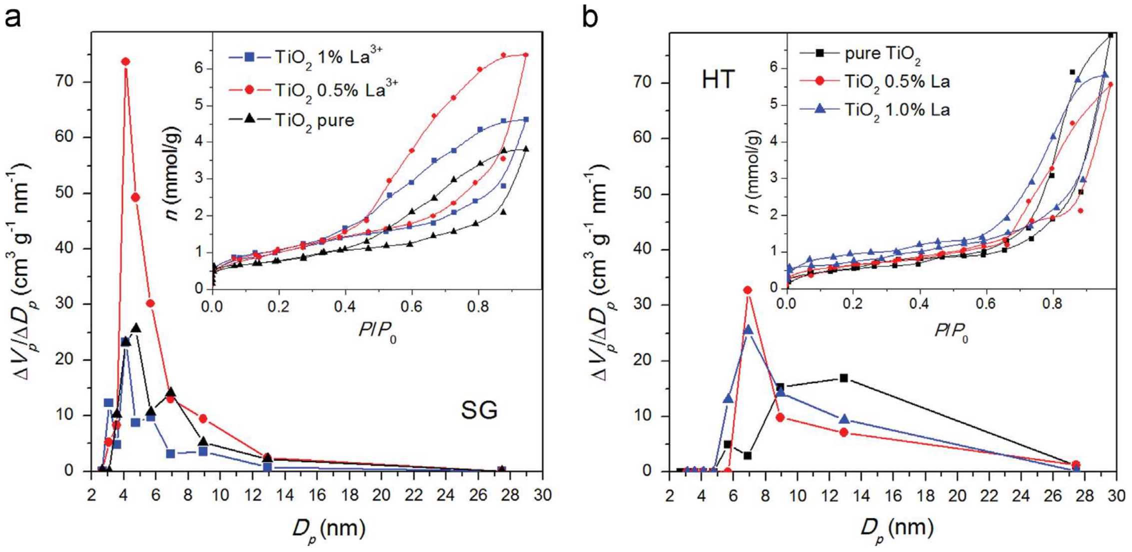

Fig. 6. The pore size distribution for pure and La-doped TiO_2 nanopowders synthesized by sol–gel (a) and hydrothermal (b) methods, obtained by BJH. Corresponding adsorption/desorption isotherm curves given in the insets.

[21], are shown, together with corresponding adsorption/desorption curves, given in the insets.

The pore parameters of the samples have been influenced by the synthesis method and the level of La-doping: in Table 3 the values of specific surface area (S_{BET}) and pore volume (V_p) for sol–gel and hydrothermally synthesized nanopowders, obtained by the BET method, are listed for comparison. Namely, in the sol–gel synthesized samples, the specific surface area is increasing with the increase of La content, from 60 $m^2\,g^{-1}$ in pure TiO_2 to $\sim$80 $m^2\,g^{-1}$ in La-doped samples (see Table 3). In hydrothermally synthesized samples S_{BET} values are lower than in the sol–gel synthesized samples. In those samples, S_{BET} is also increasing, from 49 $m^2\,g^{-1}$ in pure TiO_2 nanopowder to 51 and 58 $m^2\,g^{-1}$ in samples doped with 0.5 and 1 mol%, respectively (Table 3). Similar values of specific surface area have been obtained by the BJH method [21].

The mean diameters of mesopores, calculated from both BET and BJH (D_{BET}, D_{BJH}, respectively) for the samples obtained by both synthesis routes are also listed in Table 3. It may be noticed from these data that larger pore diameters have been registered in the hydrothermally synthesized sample.

3.7. Raman scattering measurements

The structure of synthesized pure and La-doped TiO_2 nanopowder samples have been analyzed by Raman

Table 3
The porous properties of pure and La-doped TiO_2 nanopowders synthesized by sol–gel and hydrothermal methods: specific surface area (S_{BET}, S_{BJH}), pore volume (V_p), and mean pore diameters (D_{BET}, D_{BJH}) obtained from BET and BJH methods.

	Sol–gel method			Hydrothermal method		
	Pure TiO_2	0.5% La	1% La	Pure TiO_2	0.5% La	1% La
S_{BET} ($m^2\,g^{-1}$)$=S_{meso}$	60	80	81	49	51	58
V_p ($cm^3\,g^{-1}$)	0.133	0.222	0.161	0.241	0.194	0.203
D_{BET} (nm)	5.7	7.2	5.1	12.6	9.8	9.0
S_{BJH} ($m^2\,g^{-1}$)	62	82	81	51	50	59
D_{BJH} (nm)	5.4	7.1	5.2	12.5	9.9	8.5

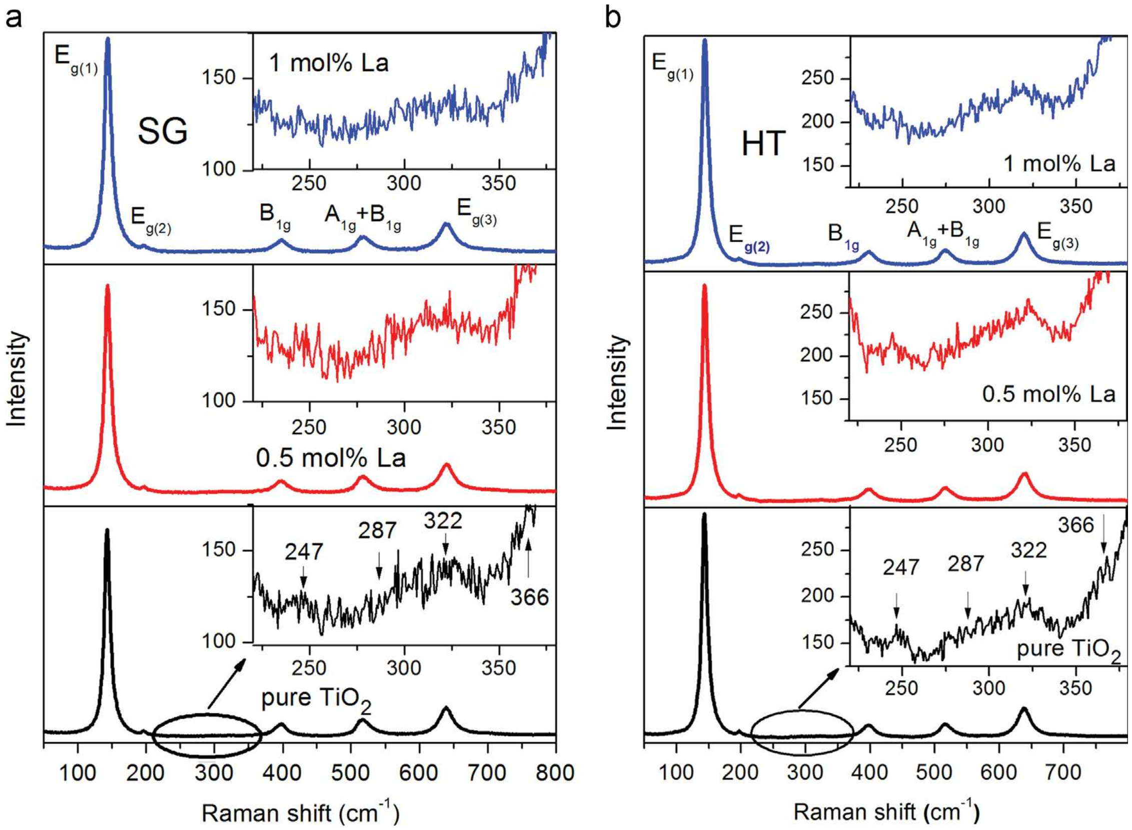

Fig. 7. The Raman spectrum of pure and La-doped TiO_2 nanopowders, synthesized by sol–gel (a) and hydrothermal (b) methods, with anatase modes denoted. Insets: the spectral region of 220–380 cm^{-1} with characteristic brookite modes.

spectroscopy, to reveal the influence of synthesis method and La-doping on measured Raman spectra. The most intensive Raman features in all spectra (Fig. 7) have been assigned to anatase [30]: $E_{g(1)}$ ($\sim$143 cm^{-1}), $E_{g(2)}$ ($\sim$199 cm^{-1}), B_{1g} ($\sim$399 cm^{-1}), $A_{1g}+B_{1g}$ ($\sim$518 cm^{-1}), and $E_{g(3)}$ ($\sim$639 cm^{-1}). Greater intensity of anatase modes, measured in the HT samples, points to better crystallinity in these samples in comparison to the SG synthesized samples. Besides anatase modes, some additional features of very low intensity have been detected in the range from 220 to 380 cm^{-1} in the Raman spectra of the samples synthesized by both sol–gel and hydrothermal method, as shown in the insets of Fig. 7(a) and (b). These features can be ascribed to the brookite phase [22]: A_{1g} ($\sim$247 cm^{-1}), B_{3g} ($\sim$287 cm^{-1}), B_{1g} ($\sim$322 cm^{-1}), and B_{2g} ($\sim$366 cm^{-1}). Low intensities and large linewidths of these modes should indicate a disorder and/or partial amorphization of the brookite phase [22,23], which is more pronounced in the sol–gel synthesized samples.

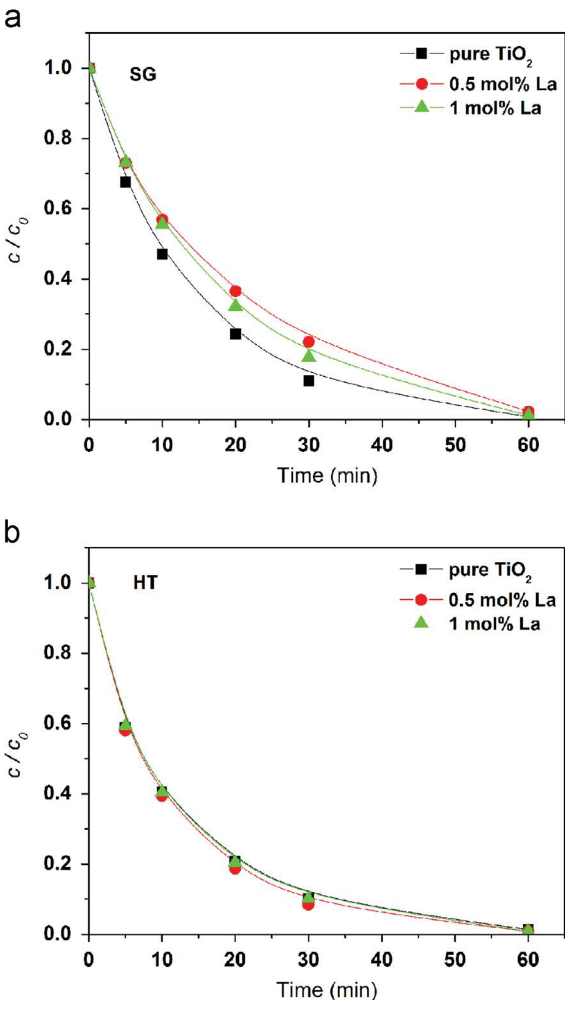

Fig. 8. The kinetics of photocatalytic degradation of alprazolam (c_0=0.03 mmol dm^{-3}) in the presence of different types of catalyst (1 mg cm^{-3}) under UV irradiation: (a) sol–gel and (b) hydrothermally synthesizes samples of pure and La doped TiO_2 nanopowders.

Table 4
Effect of type catalyst on reaction rate constant and reaction rate of photocatalytic degradation of alprazolam (c_0=0.03 mmol dm^{-3}).

	$k^a \times 10^2$ (min^{-1})	$R^b \times 10^6$ (mol dm^{-3} min^{-1})	r^c
SG			
Pure TiO_2	7.04	2.28	0.9991
0.5 mol% La	4.97	1.61	0.9966
1 mol% La	5.63	1.82	0.9995
HT			
Pure TiO_2	7.68	2.49	0.9938
0.5 mol% La	8.22	2.66	0.9960
1 mol% La	7.80	2.53	0.9948

[a] Reaction rate constant determined for the first 20 min of irradiation.
[b] Reaction rate determined for the first 20 min of irradiation.
[c] Linear regression coefficient.

3.8. Photocatalysis

Influence of two different routes of synthesis and concentrations of La^{3+} on the photocatalytic activity of nanopowders was studied in photocatalytic degradation of alprazolam under UV light irradiation. The results are presented in Fig. 8. On the basis of these kinetic curves, a linear dependence of ln(c/c_0) on the illumination time was obtained in the first period of heterogeneous photocatalysis for all synthesized samples, suggesting that the degradation reaction of the alprazolam is pseudo-first order kinetics (the linear correlation coefficients varied in the range 0.994–0.999), as shown in Table 4.

As can be seen, the presence of La^{3+} has a negative effect on the photocatalytic efficiency of nanopowders synthesized by the sol–gel method (Fig. 8(a), Table 4), while in the case of hydrothermal synthesis method La^{3+} content practically has no impact (within experimental error) on the efficiency of nanopowders in photocatalytic degradation of alprazolam (Fig. 8(b), Table 4).

When comparing photocatalytic activity of nanopowders obtained by both methods of synthesis (Fig. 8, Table 4) it can be concluded that the alprazolam degradation rate was somewhat higher in the case of used catalysts synthesized by the hydrothermal method, although the crystallite size of nanoparticles in this case were a slightly greater than nanoparticles obtained by the sol–gel method (Table 1), while the specific surface areas were slightly lower (Table 2). However, the catalysts synthesized by the hydrothermal method have greater mean pore diameter (calculated by two different methods, Table 2) than the catalyst synthesized by the sol–gel method. These relationships confirm the crucial role of pore size distribution in efficient photocatalytic degradation of relatively large pollutant molecules such as alprazolam and probably this is the reason for a slightly higher efficiency of the catalyst synthesized by the hydrothermal method. Similar results were obtained in the study of photocatalytic degradation of metoprolol by using mesoporous anatase nanopowders [22].

4. Conclusion

Mesoporous TiO_2 nanopowders doped with La^{3+} were prepared by the sol–gel synthesis performed at 550 °C and hydrothermal method performed at 200 °C in order to compare structural, morphological and photocatalytic properties of synthesized samples. According to XRD and Raman measurements nanoparticles with a dominant anatase phase have been obtained by both synthesis methods. These measurements have shown that slightly larger crystallites, with better crystalline structure, have been produced by HT than by the SG method. It has been observed from DSC measurements that La-doping shifted anatase-to-rutile phase transformation to higher temperatures, giving better thermal stability to these nanomaterials for applications in advanced technologies. Photocatalytic activity of synthesized nanopowders has been tested in degradation of alprazolam in water solution under UV light irradiation. A higher degradation rate has been detected for the catalysts synthesized by the hydrothermal method, in spite of their slightly greater crystallite size and lower specific surface area, in comparison to the nanoparticles obtained by the sol–gel method. Such improvement of photocatalytic performance of hydrothermally synthesized nanopowders may rather be related to their better crystallinity of both TiO_2 phases (anatase and brookite), as well as greater mean pore size. Also, La-doping have slightly degraded photocatalytic efficiency of nanopowders obtained by the applied sol–gel route in degradation of alprazolam, whereas there was no impact of La-content on photocatalytic performance of hydrothermally synthesized samples.

Acknowledgments

This work was supported by the Ministry of Education, Science and Technological Development, Republic of Serbia Projects no. III 45018, ON 171032, and ON 172042 as well as SASA Project F – 134.

References

[1] A. Fujishima, T.N. Rao, D.A. Tryk, Titanium dioxide photocatalysis, J. Photochem. Photobiol. C 1 (2000) 1–21.

[2] N. Daneshvar, A.R. Khataee, Removal of azo dye C.I. acid red 14 from contaminated water using Fenton, UV/H_2O_2, $UV/H_2O_2/Fe(II)$, $UV/H_2O_2/Fe(III)$ and $UV/H_2O_2/Fe(III)$/oxalate processes: a comparative study, J. Environ. Sci. Health A 41 (2006) 315–328.

[3] K. Pirkanniemi, M. Sillanpāā, Heterogeneous water phase catalysis as an environmental application: a review, Chemosphere 48 (2002) 1047–1060.

[4] N. Daneshvar, D. Salari, A.R. Khataee, Photocatalytic degradation of azo dye acid red14 in water: investigation of the effect of operational parameters, J. Photochem. Photobiol. A 157 (2003) 111–116.

[5] H. Jensen, A. Soloviev, Z. Li, E.G. Søgaard, XPS and FTIR investigation of the surface properties of different prepared titania nano-powders, Appl. Surf. Sci. 246 (2005) 239–249.

[6] K.L. Yeung, A.J. Maira, J. Stolz, E. Hung, N.K.-C. Ho, A.C. Wei, J. Soria, K.-J. Chao, P.L. Yue, Ensemble effects in nanostructured TiO_2 used in the gas-phase photooxidation of trichloroethylene, J. Phys. Chem. B106 (2002) 4608–4616.

[7] D. Xu, L. Feng, A. Lei, Characterization of lanthanum trivalent ions/TiO_2 nanopowders catalysis prepared by plasma spray, J. Colloid Interface Sci. 329 (2009) 395–403.

[8] K. Xu, G. Zhu, Preparation and characterization of nano-La (S, C)-TiO_2 oriented films by template hydrothermal synthesis, Appl. Surf. Sci. 255 (2009) 6691–6695.

[9] L. Jing, X. Sun, B. Xin, B. Wang, W. Cai, H. Fu, The preparation and characterization of La doped TiO_2 nanoparticles and their photocatalytic activity, J. Solid State Chem. 177 (2004) 3375–3382.

[10] S. Ahmed, M.G. Rasul, W.N. Martens, R. Brown, M.A. Hashib, Heterogeneous photocatalytic degradation of phenols in wastewater: a review on current status and developments, Desalination 261 (2010) 3–18.

[11] M. Huerta-Fontela, M.T. Galceran, F. Ventura, Fast liquid chromatography–quadrupole-linear ion trap mass spectrometry for the analysis of pharmaceuticals and hormones in water resources, J. Chromatogr. A 1217 (2010) 4212–4222.

[12] V. Calisto, V.I. Esteves, Psychiatric pharmaceuticals in the environment, Chemosphere 77 (2009) 1257–1274.

[13] A. Jurado, N. Mastroianni, E. Vàzquez-Suñé, J. Carrera, I. Tubau, E. Pujades, C. Postigo, M. López de Alda, D. Barceló, Drug of abuse in urban groundwater. A case study: Barcelona, Sci. Total Environ. 424 (2012) 280–288.

[14] O.A.H. Jones, N. Voulvoulis, J.N. Lester, Partitioning behavior of five pharmaceuticals compounds to activated sludge and river sediment, Arch. Environ. Contam. Toxicol. 50 (2006) 297–305.

[15] M. Reza Ganjali, H. Haji-Hashemi, F. Faridbod, P. Norouzi, M. Qomi, Potentiometric determination of alprazolam based on carbon paste and PVC membrane Electrodes, Int. J. Electrochem. Sci. 7 (2012) 1470–1481.

[16] B. Castañeda, W. Ortiz-Cala, C. Gallardo-Cabrera, N. Sbarbati Nudelman, Stability studies of alprazolam tablets: effect of chemical interactions with some excipients in pharmaceutical solid preparations, J. Phys. Org. Chem. 22 (2009) 807–814.

[17] G. Tulja Rani, D. Gowri Shankar, P. Kadgapathi, B. Satyanarayana, A validated RP HPLC method for simultaneous determination of propranolol hydrochloride and alprazolam in bulk and in pharmaceutical formulations, J. Pharm. Res. 4 (2011) 358–360.

[18] P. Pérez-Lozano, E. García-Montoya, A. Orriols, M. Miñarro, J.R. Ticó, J.M. Suñé-Negre, Development and validation of a new HPLC analytical method for the determination of alprazolam tablets, J. Pharm. Biomed. 34 (2004) 979–987.

[19] G.K. Williamson, W.H. Hall, X-ray line broadening from filed aluminium and wolfram, Acta Metall. 1 (1953) 22–31.

[20] K. Kaneko, C. Ishii, H. Kanoh, Y. Hanzawa, N. Setoyama, T. Suzuki, Characterization of porous carbons with high resolution α_S-analysis and low temperatures magnetic susceptibility, Adv. Colloid Interface 76–77 (1998) 295–320.

[21] E.P. Barret, L.G. Joyner, P.P. Halenda, The determination of pore volume and area distribution in porous substances. I. computation from nitrogen isotherms, J. Am. Chem. Soc. 73 (1951) 373–380.

[22] A. Golubović, B. Abramović, M. Šćepanović, M. Grujić-Brojčin, S. Armaković, I. Veljković, B. Babić, Z. Dohčević-Mitrović, Z.V. Popović, Improved efficiency of sol–gel synthesized mesoporous nanopowders in photocatalytic degradation of metoprolol, Mater. Res. Bull. 48 (2013) 1363–1371.

[23] A. Golubović, M. Šćepanović, A. Kremenović, S. Aškrabić, V. Berec, Z. Dohčević-Mitrović, Z.V. Popović, Raman study of the variation in anatase structure of TiO_2 nanopowders due to the changes of sol–gel synthesis conditions, J. Sol–Gel Sci. Technol. 49 (2009) 311–319.

[24] M. Akarsu, A. Asiltürk, F. Sayilkan, N. Kiraz, E. Arpaç, H. Sayilkan, A Novel, Approach to the hydrothermal synthesis of anatase titania nanoparticles and the photocatalytic degradation of rhodamine B, Turk. J. Chem. 30 (2006) 333–343.

[25] R.R. Djenadic, Lj.M. Nikolic, K.P. Giannakopoulos, B. Stojanovic, V.V. Srdic, One-dimensional titanate nanostructures: synthesis and characterization, J. Eur. Ceram. Soc. 27 (2007) 4339–4343.

[26] K. Yanagisawa, J. Overstone, Crystallization of anatase from amorphous titania using the hydrothermal technique: effects of starting material and temperature, J. Phys. Chem. B 103 (1999) 7781–7787.

[27] J. Liqiang, S. Xiaojun, C. Weimin, X. Zili, D. Yaoguo, F. Honggang, The preparation and characterization of nanoparticle TiO_2/Ti films and their photocatalytic activity, J. Phys. Chem. Solids 64 (2003) 615–623.

[28] J. Liqiang, S. Xiaojun, X. Baifu, W. Baiqi, C. Weimin, F. Honggang, The preparation and characterization of La doped TiO_2 nanoparticles and their photocatalytic activity, J. Solid State Chem. 177 (2004) 3375–3382.

[29] T. Sugimoto, X. Zhou, A. Muramatsu, Synthesis of uniform anatase TiO_2 nanoparticles by sol-gel method. 3. Formation process and size control, J. Colloid Interface Sci. 259 (2003) 43–52.

[30] T. Ohsaka, F. Izumi, Y. Fujiki, Raman spectra of anatase, TiO_2, J. Raman Spectrosc. 7 (1978) 321–324.

Available online at www.sciencedirect.com

ScienceDirect

www.elsevier.com/locate/matchar

Surface modification of sol–gel synthesized TiO_2 nanoparticles induced by La-doping

M. Grujić-Brojčin[a,*], S. Armaković[b], N. Tomić[a], B. Abramović[b], A. Golubović[a], B. Stojadinović[a], A. Kremenović[c], B. Babić[d], Z. Dohčević-Mitrović[a], M. Šćepanović[a]

[a]Institute of Physics, University of Belgrade, Pregrevica 118, 11080 Belgrade, Serbia
[b]Department of Chemistry, Biochemistry and Environmental Protection, Faculty of Sciences, University of Novi Sad, Trg D. Obradovića 3, 21000 Novi Sad, Serbia
[c]Faculty of Mining and Geology, Laboratory for Crystallography, University of Belgrade, Đušina 7, 11000 Belgrade, Serbia
[d]Institute of Nuclear Sciences "Vinča", University of Belgrade, 11001 Belgrade, Serbia

ARTICLE DATA

Article history:
Received 3 June 2013
Received in revised form
17 November 2013
Accepted 3 December 2013

Keywords:
TiO_2 nanopowder
La-doping
STM/STS
Optical spectroscopy
Photocatalysis

ABSTRACT

The influence of La-doping in the range of 0.5–6.0 mol% on structural and morphological properties of TiO_2 nanopowders synthesized by sol–gel routine has been investigated by XRPD, AFM, EDS and BET measurements, as well as Raman spectroscopy. The XRPD and Raman measurements have revealed the anatase phase as dominant in all nanopowders, with crystallite size decreasing from ~15 nm in pure TiO_2 to ~12 nm in La-doped samples. The BET data suggest that all samples are fully mesoporous, with mean pore diameters in the range of ~6–8 nm. The specific surface area and the complexity of pore structure are greater in doped samples than in pure TiO_2 sample. The spectroscopic ellipsometry has apparently shown that the band gap has been gradually increased with the increase of La content. The STM and STS techniques have been used successfully to evaluate the surface morphology and electronic properties of La-doped nanopowders. All investigated properties have been related to photocatalytic activity, tested in degradation of a metoprolol tartrate salt (0.05 mM), and induced by UV-radiation. All doped samples showed increased photocatalytic activity compared to pure TiO_2, among which the 0.65 mol% La-doped sample appeared to be the most efficient.

1. Introduction

Among the semiconductors investigated for the purpose of the degradation of pollutants in the water, titanium dioxide (TiO_2) is the most preferable material for the photocatalytic processes, due to its high photosensitivity, non-toxic nature, large band gap and stability ([1] and the references therein). In recent research, doping TiO_2 with lanthanum (La^{3+}) ions has been found to improve the activity of TiO_2 photocatalysts [2–4]. The reasons for such improvement in photocatalytic activity have been generally related to increasing surface area and pore volume, capacity for adsorption of organic compounds, as well as suppressing electron–hole recombination rates in La-doped TiO_2 photocatalyst during the photocatalytic reaction [2–4]. However, the variety of experimental conditions, sample preparation and determination of photoreactivity, as well as a lack of information on electronic structure, still make it difficult to explain the formation mechanism of lanthanum oxides and the changing of band gap energy with La-doping [5,6]. Namely, most of the literature is in agreement with the fact that La-doping is able to red shift the adsorption edges of TiO_2 to longer wavelengths, usually attributed to the La^{3+} replacing Ti^{4+}

---

[*] *Corresponding author at:* Institute of Physics, University of Belgrade, Pregrevica 118, 11080 Belgrade, Serbia. Tel.: +381 113713023; fax: +381 113162190.
E-mail address: myramyra@ipb.ac.rs (M. Grujić-Brojčin).

1044-5803/$ – see front matter © 2013 Elsevier Inc. All rights reserved.
http://dx.doi.org/10.1016/j.matchar.2013.12.002

ions in the TiO_2 lattice [6,7], but some recent studies have reported either a blue shift [8] or an absence of any shift [6]. This may be due to different synthesis conditions, and more insight is needed to determine which conditions are responsible for the specific behavior of the adsorption edge.

The sol–gel process appears to be the most popular doping technique since it is a low-cost, simple, and versatile method that can be easily manipulated. However, this process, followed by calcination at high temperature, can allow for lanthanum ions either to form oxides dispersed on the surface of the TiO_2 nanoparticles, or to incorporate in the titania lattice, as a less frequent outcome [7]. Therefore one of the goals of this research was to estimate which form of La^{3+} ions is dominant in TiO_2 nanopowders synthesized under the specified sol–gel synthesis conditions.

The TiO_2 mesoporous nanopowders, pure and doped with La^{3+} in the range of 0.5 to 6.0 mol% have been prepared by sol–gel routine using titanium tetrachloride ($TiCl_4$) as a precursor [9–11]. The effects of La-doping on the crystallite size, structure and phase composition of the synthesized samples have been investigated by X-ray powder diffraction (XRPD), energy-dispersive X-ray spectroscopy (EDS), and Raman scattering measurements.

The morphological properties have been studied by atomic force microscopy (AFM) and the Brunauer–Emmett–Teller (BET) measurements. The BET data have been analyzed by BJH (Barrett–Joyner–Halenda) and CPSM (corrugated pore structure model) methods to estimate the specific surface area and pore size distribution. Also, the pore structure tortuosity factor, as a feature of primary importance in catalysis, has been calculated by CPSM to obtain the information on the connectivity among the pores, which is essential to describe transport dynamics in porous media, and consequently determine the time of the catalytic reaction [12,13].

The electronic properties of nanopowders have been studied by scanning tunneling spectroscopy (STS) and spectroscopic ellipsometry (SE), to reveal the influence of doping on band gap energy and the energies of electronic transitions.

Experimentally observed structural, morphological and surface modifications of TiO_2 nanoparticles induced by La-doping have been related to the photocatalytic activity under ultraviolet (UV) irradiation. The efficiency of La-doped TiO_2 nanopowders have been tested in photocatalytic degradation of metoprolol tartrate salt, and compared to the performance of pure nanopowder under the same conditions [10,11,14]. Metoprolol tartrate salt (1-[4-(2-methoxyethyl) phenoxy]-3-(propan-2-ylamino)propan-2-ol tartrate (2:1), CAS no. 56392-17-7, $(C_{15}H_{25}NO_3)_2\ C_4H_6O_6$, $M_r = 684.81$, MET) is commonly used as selective β_1-blocker in treatment of cardiovascular diseases. Its continuous input and persistence in the aqueous system, even in trace concentrations, may result in an emerging environmental pollution [15].

2. Experimental Details

2.1. Synthesis

Anatase nanoparticles have been prepared by using a sol–gel procedure with $TiCl_4$ (99.0% pure, Merck) as a titanium precursor. The 5 ml of $TiCl_4$ was dissolved in 150 ml of distilled water under vigorous stirring on the ice-bath. In order to obtain the hydrogel, the aqueous solution of ammonium hydroxide (29%, Carlo Erba) has been added under careful control of the pH value of the solution (9.3). After aging in the mother liquor for 5 h, as-prepared hydrogel has been filtered and washed out with distilled water until complete removal of chloride ions. Obtained hydrogel has been converted to alcogel by repeated exchange with anhydrous ethanol for several times. To convert into nanoparticles, the alcogel was placed in a vessel, dried at 280 °C and calcined at a temperature of 550 °C for 7 h [9]. Also, an appropriate amount of $LaCl_3 \cdot 7H_2O$ (Merck) had been dissolved in water prior to the hydrolysis of $TiCl_4$, to obtain La-doped TiO_2 nanoparticles. The pure TiO_2 nanopowder and those doped with 0.5, 0.65, 1, 2, 3, 4, 5, and 6 mol% of La are labeled as TL(0), TL(0.5), TL(0.65) and from TL(1) to TL(6), respectively.

2.2. Characterization Methods

Powder X-ray diffraction has been used for the identification of crystalline phases, quantitative phase analysis and estimation of crystallite size and strain. The XRPD patterns for pure titanium dioxide nanopowder and those doped with 0.65 and 1 mol% of lanthanum ions have been collected on a Philips diffractometer (PW1710) employing Cu $K_{\alpha1,2}$, in the scanning range of 2θ between 20 and 80° with the step size of 0.06° and the counting time of 41 s/step. The patterns of the samples doped with higher La concentration have been collected in the same range by using a Stoe Stadi MP diffractometer (Cu $K_{\alpha1}$ radiation, primary beam Ge monochromator, linear PSD detector, Bragg–Brentano geometry), at every 0.01°, with a counting time of 80 s/step. The Fullprof computer program was used for the structure refinements, quantitative phase analysis and estimation of average crystallite sizes and strains [16]. For size-strain analysis the instrumental resolution function was obtained by parameterizing the profiles of the diffraction pattern of a LaB_6 (NIST SRM660a) standard specimen.

Composition/quality of TiO_2 has been analyzed on a SEM (JEOL JSM-6460LV, with the operating voltage of 20 keV) equipped with an EDS (INCAx-sight) detector and “INAx-stream” pulse processor (Oxford Instruments).

Non-contact atomic force microscopy (NC-AFM) measurements were carried out using an Omicron B002645 SPM probe VT AFM 25.

The porous structure of catalysts has been evaluated from adsorption/desorption isotherms of N_2 measured on TiO_2 samples, at −196 °C, using the gravimetric McBain method. The main parameters of the porosity such as specific surface area and pore volume have been estimated by BET method and α_s-plot ([17] and references therein). The pore size distributions have been estimated from experimental nitrogen sorption data by BJH and CPSM methods [11,18].

The Raman scattering measurements of TiO_2 samples were performed in the backscattering geometry at room temperature in the air using a Jobin-Yvon T64000 triple spectrometer, equipped with a confocal microscope and a nitrogen-cooled charge coupled device detector. The spectra have been excited by a 514.5 nm line of Ar^+/Kr^+ ion laser with an output power of less than 5 mW to avoid local heating due to laser irradiation.

The ellipsometric spectra of the TiO_2 nanopowders were measured using a SOPRA GES-5 variable angle ellipsometer in rotating polarizer configuration. The data were collected at room temperature, in the range from 1.5 to 6.5 eV with a resolution of 0.02 eV, for the incidence angle of 65°. Bulk calculations have been used to analyze the ellipsometric spectra and determine the dielectric functions of synthesized anatase nanopowders from measured SE data. The critical point (CP) method [19–21] has been applied to identify and evaluate the energy of the electronic transitions in nanopowders.

Scanning tunneling microscopy and spectroscopy (STM/STS) were employed to study the formation of La_2O_3 on an anatase nanoparticle surface. The measurements were performed at room temperature using the Omicron VT UHV system. Topography images were taken at several bias voltages in the range of 2.0–2.3 V and set-point currents with typical value of 200 pA, or less. Spectroscopic data were acquired at various locations of the tungsten tip above chosen nanoparticles in the range of ±4 V. The data represent an average of 100 measurements performed consecutively.

2.3. *Measurements of Photocatalytic Activity*

The photocatalytic activity of the TiO_2 powders doped with different amounts of La was evaluated by the degradation of the solution of metoprolol tartrate salt (≥99%, Sigma-Aldrich). The photocatalytic degradation was carried out as described in our previous research [10,11]. The initial MET concentration was 0.05 mM and the TiO_2 loading was 1.0 mg ml^{-1}. All experiments were performed at the natural pH. Kinetics of the MET photodegradation was monitored with liquid chromatography with diode array detection (LC–DAD) at 225 nm (wavelength of MET maximum absorption) [10]. The use of the gradient mode to follow the degradation kinetics of MET was necessary in order to separate the peaks originating from MET and intermediates, and shorten the time of the LC–DAD analysis. In order to determine the reproducibility of the results, at least duplicated runs were carried out for each condition for averaging the results, and reproducibility of kinetic measurements were 3–10%.

3. Experimental Results

3.1. *X-ray Powder Diffraction*

The XRPD patterns of pure and some La-doped TiO_2 nanopowders, are shown in Fig. 1. The most intensive diffraction peaks can be ascribed to the anatase crystal structure (JCPDS card 78-2486). Structure refinements have been performed by Rietveld method, and the lattice parameters, unit cell volume, average crystallite size and average strain in anatase are summarized in Table 1. The value of the anatase parameter a varies around its reference value (a_0 = 0.378479(3) nm), whereas the value of the c parameter is slightly smaller than the reference one (c_0 = 0.951237(1) nm). The unit cell volume of all samples is also smaller in comparison to the reference value, except in the pure TiO_2. The structural refinement has revealed that the anatase crystallite size of doped samples is decreased from ~15 nm in pure TL(0) to ~12 nm in La-doped samples, whereas the strain is slightly increased with doping (Table 1).

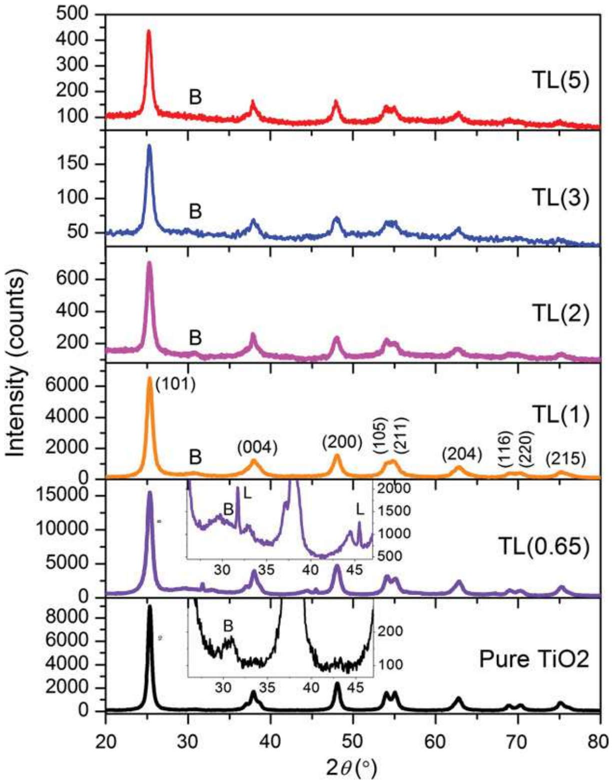

Fig. 1 – XRPD patterns of pure and selected La-doped TiO_2 nanopowders, with characteristic reflections of anatase phase given in the parentheses. The enlarged parts of diffractograms of the samples TL(0.65) and pure TiO_2 are shown in the insets. Characteristic reflections of brookite and La_2O_3 are denoted by "B" and "L", respectively.

The presence of a low intensity diffraction peak at $2\theta \approx 30.8°$ (denoted by "B" in Fig. 1), observed in all XRPD patterns, points to the brookite phase (JCPDS card 29-1360). The average crystallite size, the average strain, and the content of brookite phase have been also summarized in Table 1. The small crystallite size (down to 2 nm in TL(0.65)), as well as large values of the average strain in brookite phase indicate that this phase is highly disordered in all the samples. Therefore any attempt to obtain reliable unit cell parameters of brookite during the Rietveld refinement has failed. It also can be seen from Table 1 that brookite content, estimated from quantitative phase analysis, is greater in doped samples. A relatively large error in estimation of brookite content (defined as triple value of standard deviation, Table 1) is a consequence of the very low crystallinity of this phase followed by wide brookite diffraction peaks. Also, the lower intensity of brookite diffraction peaks in comparison to those of anatase, as well as a number of anatase and brookite reflections at very close values of diffraction angle, convoluting to one diffraction maximum, make the estimation of brookite presence even more complicated.

Moreover, very broad peaks at around 13.0, 29.5, 33.0 and 44.0° (as could be noticed from the pattern of the sample TL(0.65) shown in the upper inset of Fig. 1), which probably point to the presence of amorphous TiO_2 phase, as well as low signal intensity and great noise (samples TL(2), TL(3) and TL(5)), are

Table 1 – The results of the Rietveld analyses (the unit cell parameters and unit cell volume of anatase, average crystallite size and average strain in anatase and brookite phase and content of brookite phase) for pure and La-doped TiO_2 (the values in parentheses represent estimated standard deviations).

Sample	Anatase					Brookite		
	a (nm)	c (nm)	V (10^{-3} nm^3)	Crystallite size (nm)	Strain ($\times 10^{-3}$)	Content (%)	Crystallite size (nm)	Strain (10^{-3})
TL(0)	0.37884(1)	0.94980(5)	136.31(1)	15	3	10(2)	58	17
TL(0.65)	0.37895(2)	0.9485(1)	136.21(2)	12	4	42(5)	2	29
TL(1)	0.37880(2)	0.94780(1)	136.01(2)	10	5	24(3)	26	22
TL(2)	0.37853(2)	0.94908(9)	135.99(2)	12	8	21(1)	12	8
TL(3)	0.37823(6)	0.9471(3)	135.49(5)	12	8	21(4)	12	8
TL(5)	0.37874(3)	0.9485(1)	136.06(2)	12	8	22(2)	12	8

Reference values: a_0 = 0.378479(3) nm, c_0 = 0.951237(1) nm, and V_0 = 136.26(1) (10^{-3} nm^3).

confirming that the crystallinity of synthesized materials is of extremely low degree. It seems that La-doping induces additional disorder in both anatase and brookite phases.

The diffraction peaks at ~31.7 and 45.5°, characteristic for crystalline La_2O_3, have been found only in the pattern of the sample doped with 0.65 mol% La (the upper inset in Fig. 1). However, it does not exclude the presence of La-oxide in the amorphous phase in the samples doped with higher La concentration.

3.2. *Atomic Force Microscopy*

The NC-AFM images of pure, 1 mol% and 6 mol% La-doped TiO_2 samples are shown in Fig. 2. Note that images (a) and (c) are

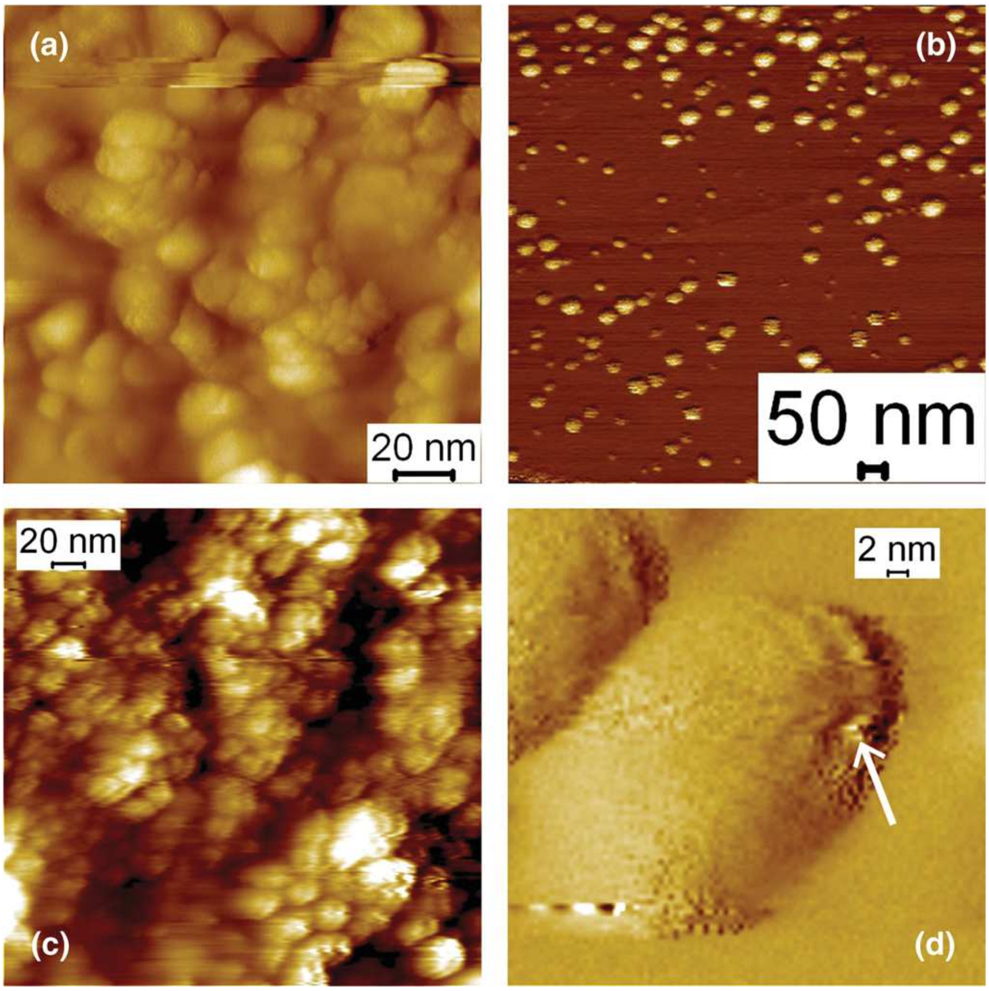

Fig. 2 – NC-AFM images of pure (a) and La-doped TiO_2 samples: 1 mol% La (b), 6 mol% La (c) and close-up image of the sample with 6 mol% La (d).

Table 2 – EDS results for pure and some La-doped TiO_2 nanopowders.

Sample	La (mol%)	EDS data			
		O (wt.%)	Ti (wt.%)	La (wt.%)	Total (wt.%)
TL(0)	0	39.46	60.54	0	100
TL(0.65)	0.65	42.91	57.09	0	100
TL(1)	1	49.71	49.44	0.85	100
TL(2)	2	44.59	53.45	1.96	100
TL(6)	6	41.71	52.39	5.91	100

taken from the pure and 6 mol% La doped nanopowders, respectively, pressed into the pellets, whereas the image (b) is recorded on nanopowder TL(1), previously dispersed in ethanol, deposited on freshly cleaved HOPG (highly oriented prolific graphite). From these images we can observe that samples consist of very small nanocrystals (up to 20 nm) and greater agglomerated particles. However, in the close-up image of the sample with 6 mol% La, as the most interesting, one could observe a granular structure (up to 2 nm) covering the surface of some nanoparticles.

3.3. EDS

The chemical composition of pure and some La-doped nanopowders has been estimated by EDS method (Table 2). The micrographs of chosen samples (pure TL(0) and doped TL(0.65), TL(1) and TL(6)) are shown in Fig. 3(a), whereas the EDS spectra of pure and maximally doped sample are presented in Fig. 3(b). The oxygen weight percent in pure TiO_2 nanopowder sample is close to stoichiometric TiO_2 (40 wt.%), whereas the percent of oxygen is higher in the La-doped samples. The final molar La/Ti ratio calculated from EDS data is lower than at the beginning of the synthesis process. It is estimated at around 63% of the starting value, except in the case of the sample doped with

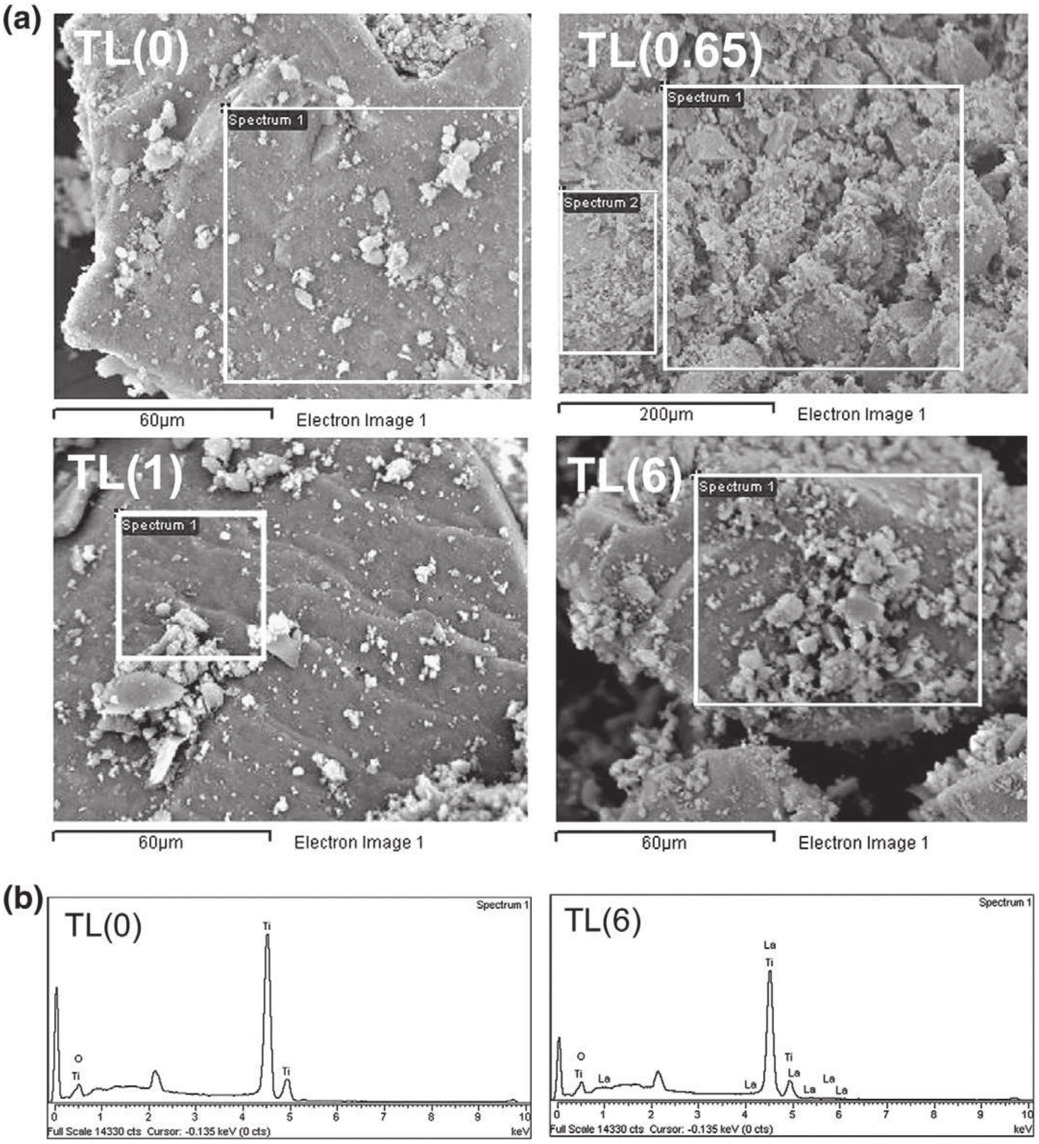

Fig. 3 – (a) The SEM images of pure TL(0) and some La-doped nanopowders TL(0.65), TL(1) and TL(6); (b) EDS spectra of pure TiO_2, TL(0), and nanopowder doped with the highest percent of La, TL(6).

0.65 wt.% of La, where such low content of La could not be detected by EDS method.

3.4. BET

To investigate the effects of lanthanum doping on the pore structure and adsorption abilities of TiO_2 nanopowders, the nitrogen sorption isotherm measurements have been carried out. The parameters of porosity, determined from the α_S-plots [17] obtained from the standard nitrogen adsorption isotherms suggest that the samples are fully mesoporous. The specific surface area (S_{BET}) and pore volume (V_p) obtained by BET method, and mesopore diameter calculated from both BET and BJH ($\overline{D}_{BET}$, $\overline{D}_{BJH}$, respectively) for chosen samples are listed in Table 3. The values of S_{BET} in La-doped samples (~80 $m^2\ g^{-1}$) are higher than those in pure nanopowder (58 $m^2\ g^{-1}$). Mean pore diameters, obtained from BET results as $\overline{D}_{BET} = 4V_p/S_{BET}$ are in good agreement with the diameters obtained by BJH method.

The pore size distribution (PSD) is estimated from the desorption branch of the hysteresis isotherm loops by usually used BJH method [18]. The mean pore diameters obtained by BJH method, listed in Table 3, are comparable to the corresponding diameters obtained by BET method. The CPSM method [12,22] for PSD evaluation has been also applied. In this method the pore structure is considered as a statistically large number of independent, nonintersected corrugated pores, made of a series of N_S cylindrical segments of equal length, with randomly distributed diameters of mesopores [11,12,22]. The pore volume distributions obtained by CPSM are shown in Fig. 4 (thick lines). Note that the distributions calculated by this method are somewhat wider than those obtained by BJH, although corresponding mean pore diameters are in good agreement (Table 3). The CPSM fitting parameter N_S, mentioned above, is also listed in Table 3: higher values of N_S have been obtained for doped samples, which can be associated with a more complex pore structure in doped samples [12]. As a result of CPSM, the pore tortuosity factor τ is also estimated (Table 3), as a measure of diffusion through porous media based on nitrogen sorption hysteresis data [11,12]. The dependence of tortuosity factor on the La-content in doped samples shows the same tendency as N_S: higher values of τ are obtained for doped samples, with the maximum in the sample TL(0.65) (τ = 5.3), pointing to the most complex pore structure consisting of interconnected pore segments with different diameters in this sample.

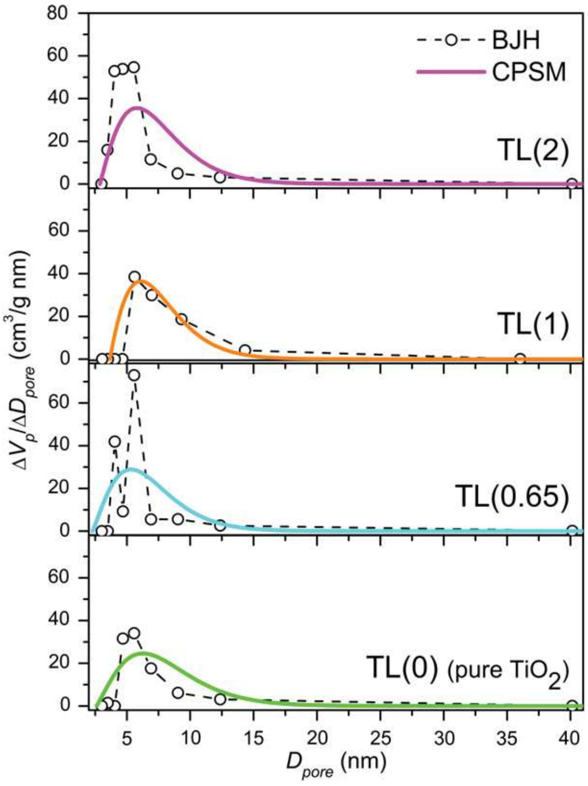

Fig. 4 – The pore size distribution for pure TiO_2 and some La-doped nanopowders obtained by BJH (symbols with thin dashed lines) and CPSM (thick lines) methods.

Table 3 – The porous properties of TiO_2 samples (TL(0), TL(0.65), TL(1), and TL(2)): specific surface area (S_{BET}), pore volume (V_p), mean pore diameters obtained from different methods ($\overline{D}_{BET}$,$\overline{D}_{BJH}$,$\overline{D}_{CPSM}$), CPSM fitting parameter N_S and predicted tortuosity factor τ.

	Sample			
	TL(0)	TL(0.65)	TL(1)	TL(2)
S_{BET} ($m^2\ g^{-1}$)	58	79	84	78
V_p ($cm^3\ g^{-1}$)	0.160	0.185	0.258	0.215
S_{BJH} ($m^2\ g^{-1}$)	58.2	79.4	83.8	78.1
$\overline{D}_{BET}$ (nm)	7.1	6.0	7.9	7.1
$\overline{D}_{BJH}$ (nm)	7.1	6.3	7.7	7.5
$\overline{D}_{CPSM}$ (nm)	8.1	6.9	7.7	7.5
N_S	8	13	12	11
τ	4.1	5.3	4.4	4.6

3.5. Raman Scattering

The Raman spectra of all synthesized nanopowders are dominated by anatase Raman modes [11,23]: $E_{g(1)}$ (~143 cm^{-1}), $E_{g(2)}$ (~199 cm^{-1}), B_{1g} (~399 cm^{-1}), $A_{1g}+B_{1g}$ (~518 cm^{-1}), and $E_{g(3)}$ (~639 cm^{-1}), as can be seen from the spectrum of TiO_2 nanopowder doped with 0.65 mol% La shown in Fig. 5. The $E_{g(1)}$ Raman mode is shifted and broadened in all synthesized nanopowders in comparison with corresponding bulk value [10,11]. By applying the phonon confinement model [24] on those experimental results, the anatase crystallite size has been estimated as ~12 nm in samples with 1–4 mol% of La, and ~15 nm in the other doped samples, as well as pure TiO_2 nanopowder, which is in good accordance with XRPD results. The broadening of the experimental Raman modes, which exceed the values ascribed to the phonon confinement effect only, also suggests the presence of defects and nonstoichiometry [11,24,25].

Additional Raman features, detected in the spectra of all samples, in the range from 210 to 380 cm^{-1} (shown enlarged in Fig. 7), can be ascribed to the brookite phase: A_{1g} (~247 cm^{-1}), B_{3g} (~288 cm^{-1}), B_{1g} (~322 cm^{-1}), and B_{2g} (~366 cm^{-1}) [10,11,25]. Low intensities and large linewidths of these modes indicate great disorder and partial amorphization of brookite in all the samples [10,11,25].

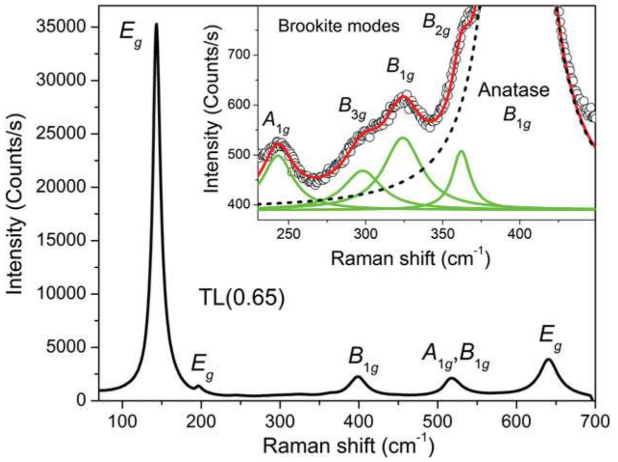

Fig. 5 – The Raman spectrum of doped TiO_2 nanopowdered sample TL(0.65) with anatase modes denoted. Inset: the region of 230–450 cm^{-1} with characteristic brookite modes.

The Raman spectra of pure and representative La-doped TiO_2 nanopowders (TL(0.65), TL(1) and TL(2)) in the C–H and O–H spectral region (2300–4000 cm^{-1}) are shown in Fig. 6. Few broad features have been noticed in this region. According to many other vibrational studies, carried out to determine the characteristics of water molecules and hydroxyl groups adsorbed on anatase surfaces ([26] and references therein), broad Raman structure in the frequency range of 2800–3800 cm^{-1} can be assigned to O–H stretching vibration of water molecules adsorbed on the surface of the particles and condensed in the pores of TiO_2 nanopowders [10,27], whereas the peak at ~2940 cm^{-1} can be assigned to the stretching mode characteristic for CH– species [10,28]. Moreover, a low intensity peak located at ~3700 cm^{-1} is noticed in the samples doped with low La content (TL(0.65) and TL(1)). This peak is assigned to the O–H stretching mode of isolated (free) hydroxyls [10,26], and can be related to the ability of the anatase samples to form the surface O–H groups with the important influence on their catalytic activity [10,29].

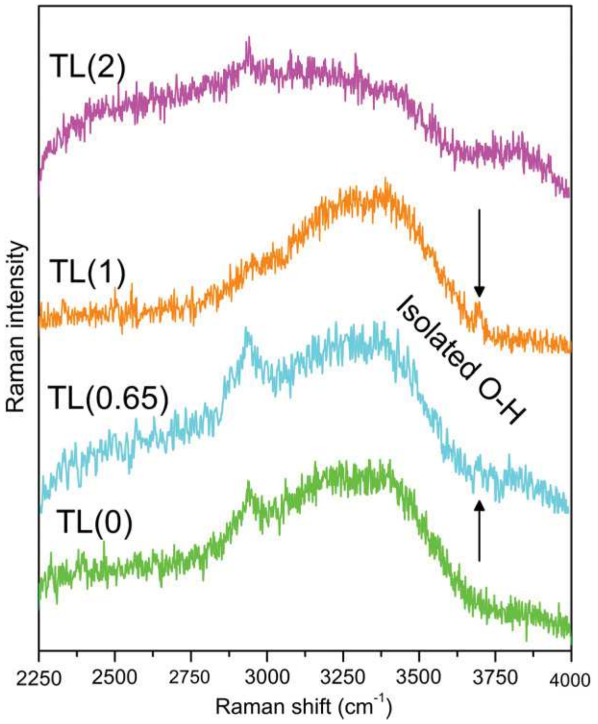

Fig. 6 – The Raman spectra of pure TiO_2 and selected La-doped TiO_2 nanopowders in the C–H and O–H spectral region (2300–4000 cm^{-1}). The mode ascribed to isolated OH groups in samples TL(0.65) and TL(1) is marked by the arrows. The spectra of doped samples are upshifted for clarity.

3.6. *Spectroscopic Ellipsometry*

The optical band gap energy has been estimated by means of the extinction coefficient k, obtained from SE data of pure and doped TiO_2 nanopowders, by using a so-called two phase model. In a case of large band gap semiconductors, in a small energy range in the vicinity of the optical band gap energy E_g, the absorption coefficient α is assumed to follow the well-known dependence $\alpha h\nu \approx A(h\nu - E_g)^{\gamma}$, where A is a sample-dependent constant parameter, γ is a constant equal to 1/2 and 2 for direct and indirect allowed transitions, respectively, and $h\nu$ is the photon energy. Then, E_g can be graphically estimated by a linear fit of the high energy tail of $(\alpha h\nu)1/\gamma$ [30]. The absorption coefficient has been evaluated from the extinction coefficient k of pure and doped anatase nanopowders, as $\alpha = 4\pi k / \lambda$, where λ is the wavelength of incident light. In the literature, both direct and indirect band to band transitions of nanocrystalline anatase titania are reported (1[30] and references therein). To establish the type of electronic transition of the synthesized samples, the absorption coefficient data were fitted to the equation for both indirect and direct band gap transitions. Fig. 7(a) shows the $(\alpha h\nu)^{1/2}$ plots versus the photon energy $h\nu$ for an indirect transition, whereas the $(\alpha h\nu)^2$ plots for a direct transition are given in Fig. 7(b). The dispersions of $(\alpha h\nu)^{1/2}$ of the samples under examination do not show an asymptotic linear behavior in the near-UV region (Fig. 7(a)). This finding confirms that, contrary to bulk anatase, synthesized TiO_2 nanoparticles do not exhibit an indirect type of band to band transition. In Fig. 7(b) the dispersions of $(\alpha h\nu)^2$ clearly show an asymptotic linear behavior in the near-UV region, and the intercepts of the linear-fit extrapolations with the horizontal axes led us to estimate the energy of the optical band gap corresponding to the direct electronic transition. The dependence of the optical band gap energy on mol% of La is presented in the inset of Fig. 7(b). The band gap values, found in the range from 3.62 to 3.82 eV, are higher than that of bulk anatase TiO_2 (3.2 eV) [30], and gradually increase with the increase of molar percent of La in titania nanopowders.

Spectroscopic ellipsometry has been also used to determine the room temperature pseudodielectric function spectra of pure and doped anatase nanopowders. The features observed in the range from 2 to 6 eV of the $\varepsilon(\omega)$ spectra are ascribed to interband critical points (CPs) [19,20,31], which are related to regions of the band structure with large or singular point electronic density of states [19]. Those structures are analyzed by standard analytic line shapes [20]: $\varepsilon(\omega) = C - A\exp(i\varphi)(\omega - E + i\gamma)^m$, where a CP is described by the amplitude A, threshold energy E, broadening γ and phase angle φ. The exponent m takes the values of −1/2 and 1/2 for one- (1D) and three-dimensional (3D) CPs, respectively. Two dimensional (2D) CPs are described with $m = 0$

and corresponding analytical line shape is given by $\varepsilon(\omega) = C - A\exp(i\varphi)\ln(\omega - E + i\gamma)$. Discrete excitons with a Lorentzian line shape (0D) are represented by $m = -1$. The values of the CP energy thresholds have been determined by theoretical fitting of both the second derivative and the module of the first derivative.

The 2nd derivative spectra of the complex dielectric function, $d^2\varepsilon(\omega) / d\omega^2$, have been calculated by a standard technique of smoothing polynomials to obtain the CP parameters [19]. It is given in analytic form as follows [21]:

$$\frac{d^2\varepsilon}{d\omega^2} = A'\Omega^{(m-2)/2}\left(\begin{array}{c} \cos\left((m-2)\arccos\left(\frac{\omega-E}{\Omega^{1/2}}\right)+\varphi\right) \\ +i\sin\left((m-2)\arccos\left(\frac{\omega-E}{\Omega^{1/2}}\right)+\varphi\right)\end{array}\right), \quad (1)$$

with $\Omega = (\omega - E)^2 + \gamma^2$. Note that for $\omega \neq 0$, $A' = -m(m - 1)A$, but for $m = 0$, A' must be equal to A. The parameters A, E, γ and φ have been calculated for all investigated nanopowders by fitting the numerically obtained second derivative spectra of the experimental $\varepsilon(\omega)$ to Eq. (1), considering the CPs of 2D and 3D types [31]. The 2nd derivatives of the real and imaginary parts ($\varepsilon_1(\omega)$ and $\varepsilon_2(\omega)$ respectively) of the complex dielectric function $\varepsilon(\omega)$ of pure (TL(0)) and one doped TiO_2 nanopowder (TL(1)), obtained from SE experimental data, are shown in Fig. 8(a). Corresponding fitting curves, taking into account the electronic transitions in the range from 2 to 6 eV, according to Eq. (1) are also shown. According to this procedure, the electronic transitions with energies at about 2.72, 3.35, 3.80, 4.20 and 4.93 eV have been registered in all samples, whereas the transition at about 5.5 eV has been noticed in doped nanopowders only. Thereby, the energies of the first three transitions listed above are gradually increasing with the molar percent of lanthanum.

The module of the first derivative of dielectric function $\varepsilon(\omega)$ for pure and several La-doped nanopowders, defined as $|d\varepsilon/d\omega|^2 = (d\varepsilon_1/d\omega)^2 + (d\varepsilon_2/d\omega)^2$, is shown in Fig. 8(b). Generally, the module of the first derivative of dielectric function shows peaks that correspond to CPs of energy transitions of the

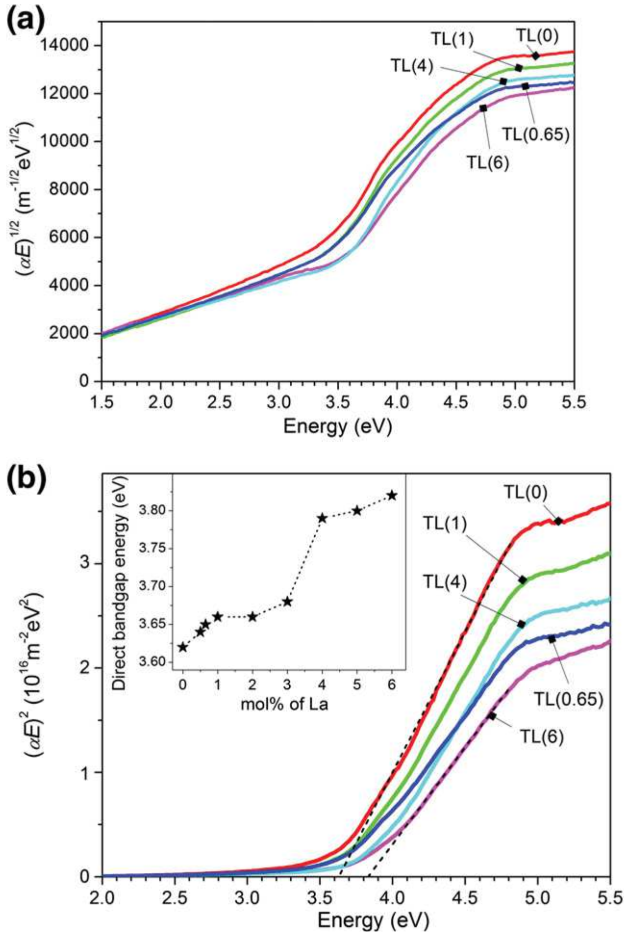

Fig. 7 – (a) The plot of $(\alpha E)^{1/2}$ versus E for indirect band gap transition in pure and selected La-doped TiO_2 nanopowders; (b) the plot of $(\alpha E)^2$ versus E for direct band gap transition in the same samples with characteristic tangent lines. Inset: the dependence of estimated direct band gap energy on mol% of La.

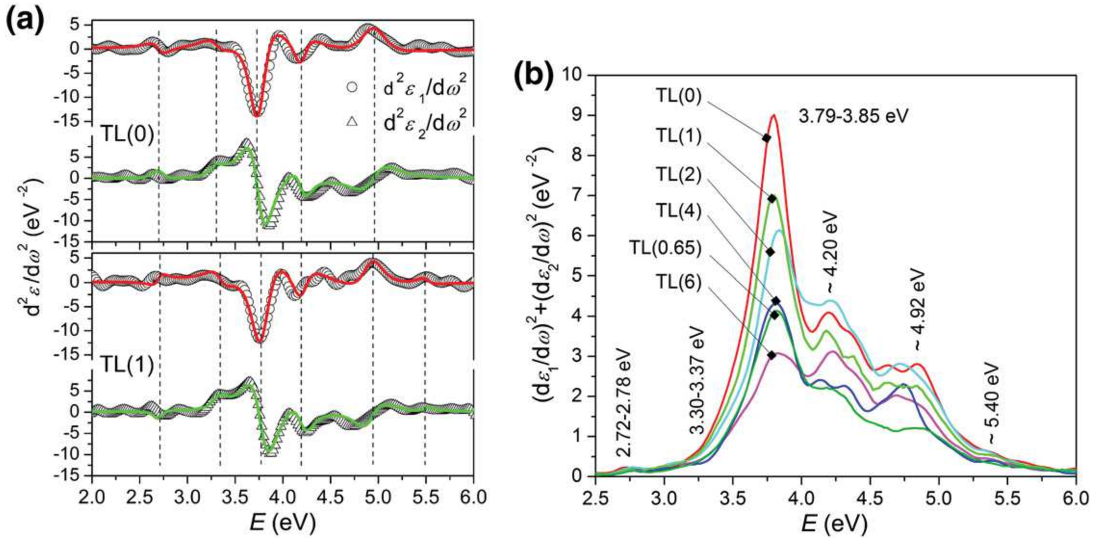

Fig. 8 – (a) The second derivatives of the real ($\varepsilon_1(\omega)$, denoted by circles) and imaginary ($\varepsilon_2(\omega)$, triangles) parts of the dielectric functions of TiO_2 nanopowders TL(0) and TL(1), obtained by SE measurements, together with the fitting curves (lines); (b) the module of the first derivative of dielectric function $\varepsilon(\omega)$ of pure and several La-doped anatase nanopowders.

electronic band structure [19]. The shift of the most intensive peak from 3.79 to 3.85 eV with the increase of mol% of La, is obvious from Fig. 8(b). Similar behavior is registered for the peak at 2.72–2.78 eV, whereas the peak at ~5.4 eV has approximately the same position in all doped samples. The position and behavior of other peaks denoted in Fig. 8(b) are hard to correlate with La content systematically, mostly because of the difficulties in precise evaluation of their energies in the spectra.

3.7. *STM/STS*

The AFM results, shown in Fig. 2, point to the existence of a great number of nanoparticles with rough granular surface (Fig. 2(d)) in the sample with 6 mol% of La. Since TiO_2 nanoparticles with both smooth and rough surfaces in that sample have also been distinguished by the STM, STS measurements have been used to obtain information on the surface band gap in the nanoparticles with different surface morphologies.

The tunneling spectroscopy was performed by positioning the tip over different isolated TiO_2 nanoparticles and measuring their *I–V* characteristics. The measurements of *I–V* characteristics have been always repeated several times and the signal has been finally averaged for 100 runs. The d*I*/d*V* versus *V* characteristics, corresponding to the characteristic density of states, have been obtained by numerical differentiation of measured *I–V* curves. Fig. 9(a) shows a typical d*I*/d*V* versus *V* characteristic of isolated TiO_2 particles with smooth surface. The STM image of such particle from the sample TL(6) is given in the inset of Fig. 9(a). From the presented STS data, the surface band gap of those particles has been estimated as ~3.2 eV, a value close to the band gap of the anatase phase [30]. However, in the same sample, for isolated TiO_2 particles covered with rough granular structure (Fig. 9(b)), the higher value of surface band gap (~4 eV) has been found.

3.8. *Photocatalysis*

The influence of different amounts of La^{3+} in the La-doped TiO_2 nanopowders on photocatalytic activity was studied through the photocatalytic degradation of MET under UV light irradiation. Kinetic curves for all investigated samples are presented in Fig. 10, together with the results obtained using pure TiO_2 and direct photolysis. On the basis of these kinetic curves, a linear dependence of $\ln(c/c_0)$ on illumination time was obtained in the first period (30 min) of heterogeneous photocatalysis for all synthesized samples suggesting that the degradation reaction of the MET is of pseudo-first kinetic order (the linear correlation coefficients varied in the range 0.994–0.999).

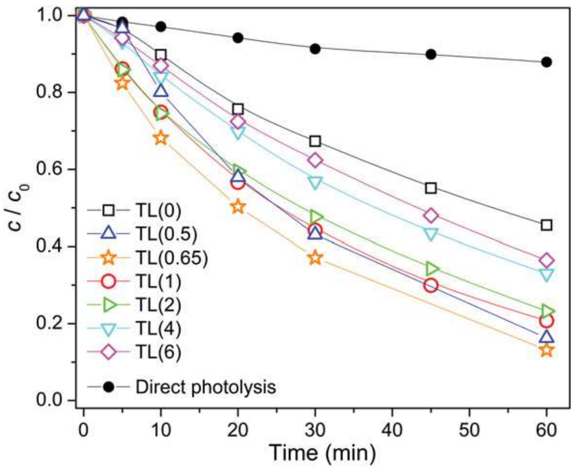

Fig. 10 – Kinetics of MET (0.05 mM) photodegradation under UV irradiation in the presence of La-doped TiO_2 nanopowders with various amounts of La, pure TiO_2, and direct photolysis. When present, the catalyst loading was 1 mg ml^{-3}.

As can be seen in Fig. 10, the photocatalytic activity of all doped samples with La^{3+} exhibited a significant increase in the MET photodegradation efficiency compared to pure TiO_2. It can be concluded (Fig. 11) that among all tested La-doped TiO_2 nanopowder samples the highest photocatalytic efficiency was exhibited by the sample TL(0.65), as it led to an 87% elimination of MET within 60 min. However, pure TiO_2 has eliminated only 55% of MET for the same time. These results

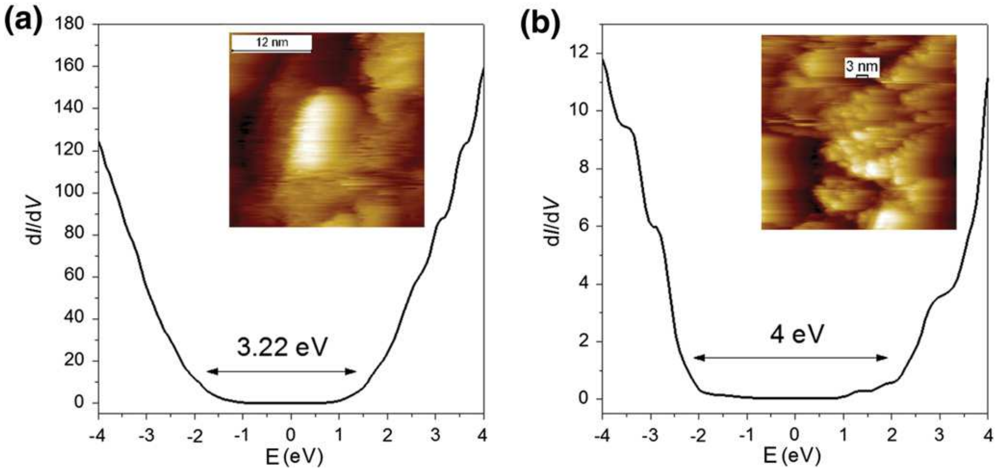

Fig. 9 – The dI/dV versus V characteristics of isolated TiO_2 nanoparticles of TL(6) sample, with smooth (a) and rough (b) surfaces obtained by STS, followed by corresponding STM images in the insets.

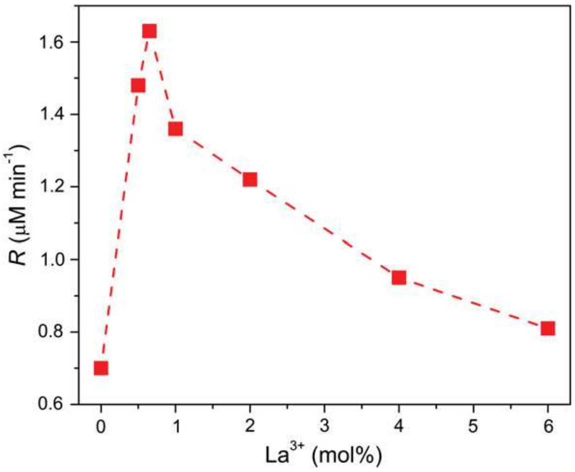

Fig. 11 – The influence of La doping content in TiO_2 nanopowders on MET (0.05 mM) photocatalytic degradation rate determined for the first 30 min of irradiation.

are in agreement with literature data [32]. Besides, as can be seen in Fig. 10, the addition of the photocatalysts, both undoped and doped with La^{3+} has markedly improved the degradation rate of MET in comparison to direct photolysis, i.e., in the absence of TiO_2.

4. Discussion

The experimental results obtained from XRPD and Raman measurements, presented in previous paragraphs, have shown that synthesized TiO_2 nanopowders retain their anatase structure as the dominant phase, with the brookite content slightly varying with La-doping. Thereby, the anatase crystallites in doped samples are smaller than those in pure sample TL(0), with the strain slightly increasing with doping. The XRPD data confirmed the formation of crystalline La_2O_3 oxide only in the sample TL(0.65). The absence of the peaks characteristic for lanthanum oxide in XRPD data of other doped samples may indicate that this oxide is highly dispersed and/or mainly amorphized [33]. Also, retaining the position of the main diffraction peak of anatase with La-doping (within experimental error) stands in favor of the assumption that lanthanum has rather formed an oxide, than substituted titanium in the anatase lattice, due to the much greater ionic radius of La^{3+} ions (1.22 Å) than that of Ti^{4+} (0.69 Å) [3,8].

Although Raman spectroscopy has rarely been applied to study the surface complex formation of anatase nanoparticles [27], because the Raman features are hard to resolve due to intensive sample luminescence in C–H and O–H spectral region, we have demonstrated the applicability of Raman spectroscopy to identify specified surface groups. In addition to broad Raman feature between 2800 and 3800 cm^{-1}, assigned to OH stretching vibrations, and the peak at ~2940 cm^{-1} assigned to the stretching mode of CH-species, both present in the spectra of all samples, we have found a low intensity peak at ~3700 cm^{-1} in the spectra of the samples doped by low La content (TL(0.65) and TL(1)). The peak at ~3700 cm^{-1} is assigned to the O–H stretching mode of isolated (free) hydroxyls, which are, according to several authors, the most photocatalytically active among all hydroxyl groups at the surface of TiO_2 nanoparticles [34].

The analysis of chemical composition by EDS method has shown that the ratio of Ti/O content is higher in doped samples in comparison to pure TiO_2. However, this method could not distinguish whether the excess oxygen participates in La_2O_3 or in interstitial oxygen, molecular oxygen at the surface and/or OH groups [10].

The morphological investigation of synthesized nanopowders, performed by nitrogen sorption isotherm measurements, has shown that doped samples are also fully mesoporous, and that La-doping increases the specific surface area to about 30%. Also, the total pore volume and pore structure complexity are increased in doped samples, which could be explained by the presence of La_2O_3 accumulated on the surface of TiO_2 nanoparticles, which inhibit the agglomeration of TiO_2 particles and produce more complex pores [35].

The analysis of SE data has shown that, contrary to bulk anatase, synthesized TiO_2 nanoparticles do not exhibit an indirect type of band to band transition, which confirms the findings of many authors, that TiO_2 nanoparticles with small crystalline domain exhibit a direct type of band to band transition [30]. These results have also shown that the energy of direct band gap transitions gradually increases with La-doping. The literature data have shown that the optical gap increases significantly with the increasing of La_2O_3 concentration in TiO_2 [8], whereas incorporation of La^{3+} in TiO_2 lattice usually leads to the slight shift of absorption edges of La-doped TiO_2 towards a longer wavelength (red shift) in comparison to pure TiO_2 [36]. So, the gradual increase of band gap registered in our doped samples can be related to increasing concentration of La_2O_3. Namely, when anatase TiO_2 is mixed with a larger band gap La_2O_3 (~5.5 eV [37]), the band gap of the composite semiconductor TiO_2/La_2O_3 should be shifted to a higher energy in comparison with pure TiO_2. Such conclusion is also supported by the results of the CP method. Namely, the electronic transition registered at ~5.4 eV has approximately the same energy for all doped samples, which implies that this transition may be related to the band gap of La_2O_3.

The STS data, recorded simultaneously with the STM topography, have provided direct experimental evidence for the modification of surface electronic properties by La-doping. The more prominent presence of granular structure at the surface of TiO_2 nanoparticles in the samples doped with a higher amount of La (6 mol%), as well as a higher value of surface band gap (~4 eV) in those particles, than in particles with smooth surface (~3.2 eV), most probably implies that the granular structure consisted of La_2O_3.

All these findings point out that, under specified sol–gel synthesis conditions, the La^{3+} ions rather form La_2O_3 oxide, mainly present in the surface layer of the doped TiO_2 nanopowders, than incorporate in the anatase lattice.

The investigations presented in this work have shown that La-doping does improve the photocatalytic activity of TiO_2 nanopowders, with higher efficiency obtained for lower La content. The kinetic analysis discussed here showed that an optimal La amount, with respect to the efficiency in photocatalytic degradation of MET, is 0.65 mol%, which is similar to the literature data obtained for the degradation of some other organic compounds ([38] and references therein). The improvement in photocatalytic properties of La-doped samples can be ascribed to the formation of La_2O_3 at the grain boundaries of anatase nanoparticles. This effect inhibits the growth of crystal grains, decreases anatase crystallite size and produces a more complex pore structure [35], which is confirmed by the results of XRPD, Raman and BET measurements presented in this work. However, the presence of isolated hydroxyl groups on the surface of TiO_2 nanoparticles, which can represent a decisive factor in high photocatalytic activity of TiO_2 [39], has been registered only in the nanopowders with a low level of La-doping—0.65 and 1 mol%. This implies that reduction of photocatalytic activity of TiO_2 nanopowders with further increase of La-doping amount may be related to the blocking of the active centers due to the accumulation of excess La_2O_3 on the surface of anatase grains, registered by both AFM and STM measurements.

5. Conclusion

Mesoporous La-doped TiO_2 photocatalysts, prepared by sol–gel method, have been extensively characterized by various sophisticated techniques. The photocatalytic activity of La-doped TiO_2 nanopowders has been evaluated for the degradation of MET in an aqueous solution under UV light irradiation. Doped samples have shown a higher rate of degradation than pure TiO_2, synthesized under the same condition, with a maximum rate for 0.65 mol% La loading. The enhanced photocatalytic activity of La-doped TiO_2 is mainly due to the smaller particle size, larger specific surface area and total pore volume, as well as higher pore structure complexity. Moreover, the presence of isolated (free) hydroxyls, as the most photocatalytically active hydroxyl groups, has been registered in the TiO_2 photocatalysts with low La content, which exhibit the highest photocatalytic efficiency.

This study has also shown that the spectroscopic ellipsometry is able to determine the type of electronic transition in TiO_2 materials, as well as to resolve the dilemma of whether or not large La^{3+} ions replace smaller Ti^{4+} ions in the TiO_2 lattice. Presented analysis of SE results has shown gradual increase of direct band gap energy with La-doping, which can be attributed to the surface modification of TiO_2 nanoparticles, confirmed by the STM/STS measurements.

Acknowledgments

This work was financially supported by the Serbian Ministry of Education and Science under the Project Nos. III45018, ON171032, and ON172042, as well as the SASA Project F-134. The authors also express their gratitude to MSc. Marko Radović for his help in AFM and ellipsometric measurements.

REFERENCES

[1] Chen W, Hua D, Jun-Ying T, Ji-Mei A. Photocatalytic activity enhancing for TiO_2 photocatalyst by doping with La. Trans Nonferrous Met Soc China 2006;16:s728–31.

[2] Kim HR, Lee TG, Shul YG. Photoluminescence of La/Ti mixed oxide prepared using sol–gel process and their pCBA photodecomposition. J Photochem Photobiol A 2007;185:156–60.

[3] Liqiang J, Xiaojun S, Baifu X, Baiqi W, Weimin C, Honggang F. The preparation and characterization of La doped TiO_2 nanoparticles and their photocatalytic activity. J Solid State Chem 2004;177:3375–82.

[4] Jin M, Nagaoka Y, Nishi K, Ogawa K, Nagahata S, Horikawa T, et al. Adsorption properties and photocatalytic activity of TiO_2 and La-doped TiO_2. Adsorption 2008;14:257–63.

[5] Zhao Z, Liu Q. Effects of lanthanide doping on electronic structures and optical properties of anatase TiO_2 from density functional theory calculations. J Phys D Appl Phys 2008;41:085417 [1–9].

[6] Sun L, Zhao X, Cheng X, Sun H, Li Y, Li P, et al. Synergistic effects in La/N codoped TiO_2 anatase (101) surface correlated with enhanced visible-light photocatalytic activity. Langmuir 2012;28:5882–91.

[7] Bingham S, Daoud WA. Recent advances in making nano-sized TiO_2 visible-light active through rare-earth metal doping. J Mater Chem 2011;21:2041–50.

[8] Zhang L, Sun Z-H, Yu F-M, Chen H-B. Bioinorganic chemistry and applications. Hindawi Publishing Corporation; 2001. http://dx.doi.org/10.1155/2011/853048.

[9] Golubović A, Šćepanović M, Kremenović A, Askrabić S, Berec V, Dohčević-Mitrović Z, et al. Raman study of the variation in anatase structure of TiO_2 nanopowders due to the changes of sol–gel synthesis conditions. J Sol Gel Sci Technol 2009;49:311–9.

[10] Šćepanović M, Abramović B, Golubović A, Kler S, Grujić-Brojčin M, Dohčević-Mitrović ZD, et al. Photocatalytic degradation of metoprolol in water suspension of TiO_2 nanopowders prepared using sol–gel route. J Sol–Gel Sci Technol 2012;61:390–402.

[11] Golubović A, Abramović B, Šćepanović M, Grujić-Brojčin M, Armaković S, Veljković I, et al. Improved efficiency of sol–gel synthesized mesoporous anatase nanopowders in photocatalytic degradation of metoprolol. Mater Res Bull 2012;48:1363–71.

[12] Salmas CE, Androutsopoulos GP. A novel pore structure tortuosity concept based on nitrogen sorption hysteresis data. Ind Eng Chem Res 2001;40:721–30.

[13] Zalc JM, Reyes SC, Iglesia E. The effects of diffusion mechanism and void structure on transport rates and tortuosity factors in complex porous structures. Chem Eng Sci 2004;59:2947–60.

[14] Šojić D, Despotović V, Orčić D, Szabó E, Arany E, Armaković S, et al. Degradation of thiamethoxam and metoprolol by UV, O_3 and UV/O_3 hybrid processes: kinetics, degradation intermediates and toxicity. J Hydrol 2012;472–473:314–27.

[15] Ikehata K, Naghashkar NJ, El-Din MG. Degradation of aqueous pharmaceuticals by ozonation and advanced oxidation processes: a review. Ozone Sci Eng 2006;28:353–414.

[16] Rodriguez-Carvajal J. FullProf computer program. http://www.ill.eu/sites/fullprof/index.html; 2008.

[17] Kaneko K, Ishii C, Kanoh H, Hanzawa Y, Setoyama N, Suzuki T. Characterization of porous carbons with high resolution α_s-analysis and low temperature magnetic susceptibility. Adv Coloid Interface Sci 1998;76–77:295–320.

[18] Barrett EP, Joyner LG, Halenda PP. The determination of pore volume and area distributions in porous substances. I. Computations from nitrogen isotherms. J Am Chem Soc 1951;73:373–80.

[19] Leòn M, Levcenko S, Nateprov A, Nicorici A, Merino JM, Serna R, et al. Dielectric functions and fundamental band gaps of $Cu_2In_4Se_7$, $CuGa_3Se_5$ and $CuGa_5Se_8$ crystals. J Phys D Appl Phys 2007;40:740–8.

[20] Lautenschlager P, Garriga M, Logothetidis S, Cardona M. Interband critical points of GaAs and their temperature dependence. Phys Rev B 1987;35:9174–89.

[21] Albornoz JG, Serna R, Leon M. Optical properties and electronic structure of polycrystalline $Ag_{1-x}Cu_xInSe_2$ alloys. J Appl Phys 2005;97:103515 [1–7].

[22] Androutsopoulos GP, Salmas CE. A new model for capillary condensation–evaporation hysteresis based on a random corrugated pore structure concept: prediction of intrinsic pore size distributions: part 1: model development. Ind Eng Chem Res 2000;39:3747–63.

[23] Ohsaka T, Izumi F, Fujiki Y. Raman spectrum of anatase, TiO_2. J Raman Spectrosc 1978;7:321–4.

[24] Šćepanović MJ, Grujić-Brojčin MU, Dohčević-Mitrović ZD, Popović ZV. Effects of confinement, strain and nonstoichiometry on Raman spectra of anatase TiO_2 nanopowders. Mater Sci Forum 2006;518:101–6.

[25] Šćepanović M, Aškrabić S, Berec V, Golubović A, Dohčević-Mitrović Z, Kremenović A, et al. Characterization of La-doped TiO_2 nanopowders by Raman spectroscopy. Acta Phys Pol A 2009;115:771–4.

[26] Soria J, Sanz J, Sobrados I, Coronado JM, Maira AJ, Hernandez-Alonso MD, et al. FTIR and NMR study of the adsorbed water on nanocrystalline anatase. J Phys Chem C 2007;111:10590–6.

[27] Watson S, Beydoun D, Scott J, Amal R. Preparation of nanosized crystalline TiO_2 particles at low temperature for photocatalysis. J Nanopart Res 2004;6:193–207.

[28] Brownson JRS, Tejedor-Tejedor MI, Anderson MA. Photoreactive anatase consolidation characterized by FTIR spectroscopy. Chem Mater 2005;17:6304–10.

[29] Yang D, Liu H, Zheng Z, Yuan Y, Zhao J, Waclawik ER, et al. An efficient photocatalyst structure: TiO_2(B) nanofibers with a shell of anatase nanocrystals. J Am Chem Soc 2009;131:17885–93.

[30] Ferrara MC, Pilloni L, Mazzarelli S, Tapfer L. Hydrophilic and optical properties of nanostructured titania prepared by sol–gel dip coating. J Phys D Appl Phys 2010;43:095301.

[31] Šćepanović M, Grujič-Brojčin M, Mirić M, Dohčević-Mitrović Z, Popović ZV. Optical characterization of laser-synthesized anatase TiO_2 nanopowders by spectroscopic ellipsometry and photoluminescence measurements. Acta Phys Pol A 2009;116:603–6.

[32] Wu H-H, Deng L-X, Wang S-R, Zhu B-L, Huang W-P, Wu S-H, et al. The preparation and characterization of La doped TiO_2 nanotubes and their photocatalytic activity. J Dispersion Sci Technol 2010;31:1311–6.

[33] Shi Z-L, Lai H, Yao S-H, Wang S-F. Preparation, characterization and photocatalytic activity of lanthanum doped mesoporous titanium dioxide. Chin J Chem Phys 2012;25:96–102.

[34] Bégin-Colin S, Gadalla A, Le Caer G, Humbert O, Thomas F, Barres O, et al. On the origin of the decay of the photocatalytic activity of TiO_2 powders ground at high energy. J Phys Chem C 2009;113:16589–602.

[35] Cao G, Li Y, Zhang Q, Wang H. Synthesis and characterization of $La_2O_3/TiO_{2-x}F_x$ and the visible light photocatalytic oxidation of 4-chlorophenol. J Hazard Mater 2010;178:440–9.

[36] Parida KM, Sahu N. Visible light induced photocatalytic activity of rare earth titania nanocomposites. J Mol Catal A Chem 2008;287:151–8.

[37] Yang C, Fan H, Qiu S, Xi Y, Fu Y. Microstructure and dielectric properties of La_2O_3 films prepared by ion beam assistant electron-beam evaporation. J Non-Cryst Solids 2009;355:33–7.

[38] Zhang S, Zheng Z, Wang J, Chen J. Heterogeneous photocatalytic decomposition of benzene on lanthanum-doped TiO_2 film at ambient temperature. Chemosphere 2006;65:2282–8.

[39] Liu G, Sun C, Cheng L, Jin Y, Lu H, Wang L, et al. Efficient promotion of anatase TiO_2 photocatalysis via bifunctional surface-terminating Ti–O–B–N structures. J Phys Chem C 2009;113:12317–24.